Investigation on Different Inverter Configurations and their Control Aspects for Distribution Systems

Thesis Submitted
in Partial Fulfillment of the Requirements for the
Degree of

DOCTOR OF PHILOSOPHY

in
Electrical Engineering

by:

SUDHANSHU MITTAL
(2K21/PhDEE/04)

Under the Supervision of
Prof. Alka Singh (Professor)
Dr. Prakash Chittora (Assistant Professor)
Department of Electrical Engineering
Delhi Technological University

DEPARTMENT OF ELECTRICAL ENGINEERING
DELHI TECHNOLOGICAL UNIVERSITY
(Formerly Delhi College of Engineering)
Shahbad Daulatpur, Main Bawana Road, Delhi-110042, India
May, 2025

DECLARATION

I hereby certify that the work which is being presented in the thesis entitled **"INVESTIGATION ON DIFFERENT INVERTER CONFIGURATIONS AND THEIR CONTROL ASPECTS FOR DISTRIBUTION SYSTEMS"** in partial fulfillment of the requirements for the award of the Degree of Doctor of Philosophy and submitted in the Department of Electrical Engineering of the Delhi Technological University is an authentic record of my own work carried out during the period from July, 2021 to December, 2024 under the supervision of Dr. Alka Singh, Professor, Department of Electrical Engineering and Dr. Prakash Chittora, Assistant Professor, Department of Electrical Engineering, Delhi Technological University The matter presented in this thesis has not been submitted by me for the award of any other degree of this or any other Institute.

Place: Delhi **(Sudhanshu Mittal)**
Date:

CERTIFICATE

On the basis of the declaration submitted by Mr. Sudhanshu Mittal, student of Ph.D., I hereby certify that the thesis titled "**INVESTIGATION ON DIFFERENT INVERTER CONFIGURATIONS AND THEIR CONTROL ASPECTS FOR DISTRIBUTION SYSTEMS**" which is submitted to the Department of Electrical Engineering, Delhi Technological University, Delhi in partial fulfilment of the requirement for the award of the degree of Doctor of Philosophy is an original contribution with existing knowledge and faithful record of research carried out by him under my guidance and supervision.

The contents of this research work have not been submitted in part or fully to any other Institute or University for the award of any degree.

Date:

(Prof. Alka Singh)	**Dr. Prakash Chittora**
Supervisor Department of Electrical Engineering	Co-Supervisor Department of Electrical Engineering
Delhi Technological University	Delhi Technological University
Delhi, India	Delhi, India

ACKNOWLEDGEMENT

I would like to express my deep and sincere gratitude to my supervisor **Prof. Alka Singh** for her valuable guidance and continuous monitoring of my research work. It was great honor for me to pursue my research work under her supervision. Prof. Alka Singh has been the main motivating and inspiring factor behind my research work. It's her vigor and hunger to perform in adverse situation, which has inspired me to thrive for excellence and nothing less.

I would also like to convey my sincere gratitude to Co-Supervisor **Dr. Prakash Chittora**, Assistant professor, DTU, whose continuous monitoring, valuable guidance and input has always been a driving force to complete my research work. I would like to thank the SRC members mainly Prof. Uma Nangia, who have given me valuable guidance and advice to improve quality of my research work. I am extremely thankful to staff members like Dr. Ajandra Singh, Mr. Hari Kishan Singh, Mr. Monu and Mrs. Komal of Power System Lab, DTU, Delhi for providing me immense facility and assistance to carry out my research work. I would like to thank other office staff, Central library and Computer Centre staff, for their valuable co-operation and support.

I would like my sincere thanks to **Dr. Manoj Badoni, Dr. Praveen Bansal, Dr. Amarendra Pandey** who has guided me to develop hardware at initial level of research work. Also, i would like to share my gratitude towards **Mr. Gaurav Kaushik, Dr. Inder Choudhary, Dr. Amitesh Kumar and Prof. Mukhtiar Singh**. His research publications have guided me during all time of my research work. I am extremely grateful to my research group and friends **Mr. Gaurav Yadav**, Mr. Brijendra Sangar, Mr. Divyansh, Mr. Atul Awasthi, Mr. Dipak Prasad, Dr. Kanchan Bala Rai, Vineet Kumar and Pankaj Verma for their valuable assistance, co-operation and great source of learning.

If I get any success today for my research work, the entire credit should go to my grand father Late. **Garun Bhagat,** Late. **Prof. Ram Naresh Prasad Verma,** Late. **Ramashray Bhagat, Kishori Bhagat, Atmesh Verma,** my grandmother Late. **Asarfi Devi**, my mother, **Smt. Asha Devi**, father **Shri Ravindra Prasad**, my elder brother **Mr. Himanshu Mittal**, younger sister **Dr. Ankita Mittal,** younger brothers **Mr. Vishal Krishna and Rajeev Ranjan.** I sincerely convey my gratitude to my fiancée, **Dr. Suryakanti,** who has encouraged me to carry out my research work. I want to thank other family members like **Raju Patel**, **Vaibhav** and **Ravi Shankar** who directly or indirectly support my research work.

Lastly, I thank Mother Nature and Almighty God for allowing me to pursue doctoral studies.

Place: Delhi **(Sudhanshu mittal)**

Date:

ABSTRACT

Modern distribution systems have considerable hurdles in preserving power quality as sensitive electronic equipment and nonlinear loads become more common. Power quality concerns, such as voltage deviations, harmonic distortions, and frequency changes, can cause equipment failures and inefficiencies in power transmission and distribution.

Several innovative technologies and tactics have been developed to overcome these issues. One viable strategy is to combine Distribution Static Synchronous Compensator (DSTATCOM) and Hybrid Power Filters (HPFs). This combination provides rapid reactive power adjustment and voltage support while efficiently suppressing harmonics and filtering out disturbances, improving system stability and power quality in distribution networks.

Electric vehicles (EVs) are gradually becoming recognised as a sustainable mode of transportation, thanks to technological developments, economic factors, and environmental concerns. Several factors contribute to the growing popularity of EVs, including the availability of low-cost models, lower battery costs, rising gasoline prices, and more awareness of the effects of climate change. EVs are viewed as a critical option for reducing greenhouse gas emissions in the transportation sector, encouraging supporting public policies worldwide

The entire thesis work has been split in to eight chapters. The first two chapters deal with the Introduction and Literature Review related to problems and mitigation techniques of DSTATCOM and EV Charging Systems. The third chapter deals with the design and analysis of grid connected systems. The configuration of DSTATCOM in one-phase and three-phase grid connected and EV charging systems are discussed. The fourth chapter discusses the DSTATCOM in single-phase and three phase grid connected systems. The control algorithms considered for compensation are Notch Filter (NF), Adaptive Leaky Least Mean Fourth (ALLMF) and Adaptive Radial Basis Function Neural Network (ARBFNN). The fifth chapter

using Multilevel Inverter (MLI) based DSTATCOM with same algorithms NF, ALLMF and ARBFNN are discuss in details. These algorithms are studied under varying load conditions i.e., non-linear conditions using Matlab/Simulink models. The algorithms have also been tested in the Simulink environment as well as hardware developed in the laboratory.

The six chapter deals with the single phase grid connected EV charging systems. In this chapter the control algorithms Second Order Generalized Integrator (SOGI), Least Mean Square (LMS) and Rodrigues Jacobi Polynomial (RJP) are used to control bidirectional AC -DC converter. The waveforms of charging and discharging condition are tested in both hardware and Simulink and it is found satisfactory.

The seventh chapter also deals with the three-phase grid connected PV and EV charging systems. The same algorithms SOGI, LMS and RJP are tested in Matlab/Simulink. The Simulink waveforms are well presented with and without PV in charging and discharging conditions.

The eighth chapter studies the Reduced Switch Multilevel Inverter (RSFLI) based grid connected EV charging systems. This system considers a battery integrated PV systems under single phase grid connected system. Control algorithm like Third Order Sinusoidal Integrator (TOSSI) is used and tested in Matlab/Simulink and OPAL-RT setup in the laboratory. The Simulink and OPAL-RT waveforms are well presented in this chapter.

The chapter nine presents the conclusion and future scope by analysing above chapters.

TABLE OF CONTENTS

Chapter 2 Literature Review 14

Chapter 8 Single Phase Grid Connected RSFLI with Solar PV

List of Figures

List of Tables

List of Symbols

PQ	Power Quality
PCC	Point Of Common Coupling
VSC	Voltage Source Converters
SAPF	Shunt Active Power Filter
DSTATCOMs	Distribution Static Compensators
DVRs	Dynamic Voltage Restorers
CHB-MLI	Cascaded Multilevel Inverter
MLI	Multilevel Inverter
RSFLI	Reduced Switch Five Level Inverter
PWM	Pulse Width Modulation
PS-PWM	Phase Shift Pulse Width Modulation
THD	Total Harmonic Distortion
LMS	Least Mean Sqaure
SRFT	Synchronous Reference Frame Theory
PLL	Phase Lock Loops
SOGI	Second –Order Generalized Integrator
TOSSI	Third-Order Sinusoidal Signal Integrator

ALLMF	Adaptive Leaky Least Mean Fourth
ARBFNN	Adaptive Radial Basis Function Neural Network
NF	Notch Filter
RJP	Rodrigous Jacobi Polynomial

List of Abbreviations

v_s	source voltage
v_{sa}, v_{sb}, v_{sc}	Three phase supply voltage
i_g/i_s	Grid/source current
i_{sa}, i_{sb}, i_{sc}	Three phase supply current
i_L	Load current
i_{La}, i_{Lb}, i_{Lc}	Three phase load current
i_c	Compensating current
i_{ca}, i_{cb}, i_{cc}	Three phase compensating current
V_{dc-ref}	Reference DC link voltage
V_{dc1}	DC link voltage across capacitor-1
V_{dc2}	DC link voltage across capacitor-2
V_{dc}	DC link voltage
f_{sw}	Switching Frequency
ΔI_{cr-pp}	Peak to Peak ripple current
i_f	Fundamental current
i_{fa}, i_{fb}, i_{fc}	Three phase fundamental current
i_{ref}	Reference current

$i_{sa}*, i_{sb}*, i_{sc}*$	Three phase reference current
f_{cr}	Carrier frequency
f_m	Modulating Frequency
v_α	In-phase component voltage
v_β	Quadrature component voltage
i_{avg}	average current
k_d	Proportional gain
k_i	Integral gain
i_T	Total effective average current
u_p	Unit vector template
u_{pa}, u_{pb}, u_{pc}	Unit template in three phase

Chapter 1

Introduction

1.1 Overview of power quality

Power quality, also known as PQ, is an essential component of electrical power systems. It refers to the consistency and dependability of the power supply that is provided to end users. It is distinguished by criteria such as the amplitude of the voltage, the frequency, and the continuity of the waveform, all of which are crucial for the effective operation of electrical systems in both household and industrial settings [1]. The term "power quality disturbances" (PQDs) refers to a wide range of phenomena, including voltage sags, swells, interruptions, harmonics, flicker, inter harmonics, spikes, notches, and transient effects. These phenomena can occur singly or in combination, and they have the potential to cause damage to system components as well as operational inefficiencies [2]. Power quality is especially important in industrial settings because sensitive equipment and manufacturing processes require reliable power. Voltage sags, harmonic distortions, and transient disturbances are all common difficulties that can cause production downtime and higher operational expenses [3]. To address these difficulties, a mix of proactive and reactive tactics are used. To prevent harmonic distortions, use proactive efforts such as selecting appropriate equipment, balancing loads, and using power factor correction devices. To handle voltage sags and transient events, reactive techniques such as installing surge suppressors and voltage regulators are used [4]. The incorporation of renewable energy sources and the development of smart grids have exacerbated power quality management, necessitating sophisticated detection, classification, and mitigation strategies. These include the employment of Dynamic Voltage Restorers (DVRs) and other Flexible AC Transmission Systems (FACTS) devices, which effectively repair voltage disturbances and improve overall power quality [5]. Research underlines the requirement of real-time monitoring and data analytics for spotting and fixing PQDs as well as the need of experimental investigations to better grasp these disruptions and create suitable mitigating solutions [6]. Minimizing equipment damage, lowering running costs, and guaranteeing the dependability and efficiency of power systems depend on maintaining excellent power quality generally [7].

1.2 Overview of Electric Vehicle

Electric vehicles (EVs) are gradually becoming recognised as a sustainable mode of transportation, thanks to technological developments, economic factors, and environmental concerns. Several factors contribute to the growing popularity of EVs, including the availability of low-cost models, lower battery costs, rising gasoline prices, and more awareness of the effects of climate change [8]. EVs are viewed as a critical option for reducing greenhouse gas emissions in the transportation sector, encouraging supporting public policies worldwide [9]. In terms of technology, EVs are classified into two types: battery electric cars (BEVs) and hybrid electric vehicles (HEVs), each with its own set of principles and functions . BEVs, in particular, are praised for their ability to alleviate energy crises and environmental concerns by lowering dependency on fossil fuels and improving air quality [10]. EVs' essential components include electric motors, energy storage devices, power electronics, and battery management systems, all of which are critical for effective energy management and peak performance [11]. The integration of EVs into the power grid poses issues, including higher energy demand and potential effects on power quality. Accurate load modelling is critical for addressing these difficulties, with methods ranging from deterministic to machine learning approaches, each with unique data requirements and advantages [12]. Furthermore, advances in battery charging infrastructure are crucial to increasing the range and appeal of EVs, making them more accessible to a larger user base [13]. Despite these advances, difficulties remain, including the need for increased supply chain efficiency and more reliable electrical sources to allow mass EV adoption [14]. As EV technology advances, it has the potential to revolutionise the automotive industry, expanding beyond personal vehicles to include electric buses and delivery vehicles, and thereby contributing to a more sustainable future .

1.3 Modern Distribution System and Power Quality

Modern distribution systems have considerable hurdles in preserving power quality as sensitive electronic equipment and nonlinear loads become more common. Power quality concerns, such as voltage deviations, harmonic distortions, and frequency changes, can cause equipment failures and inefficiencies in power transmission and distribution. Several innovative technologies and tactics have been developed to overcome these issues. One viable strategy is to combine Distribution Static Synchronous Compensator (DSTATCOM) and Hybrid Power Filters (HPFs). This combination provides rapid reactive power adjustment and voltage support while efficiently suppressing harmonics and filtering out disturbances, improving system stability and power quality in distribution networks [15]. Similarly, the Distributed Power Flow Controller (DPFC), a

Flexible AC Transmission System (FACTS) device, employs a number of small-sized converters to improve power quality by addressing system resonance and voltage fluctuations induced by nonlinear loads [16]. The usage of custom and advanced power devices such as DSTATCOM and DVR is also emphasised as a method of improving power quality. These devices are very successful at reducing voltage sags and maintaining voltage stability, as evidenced by MATLAB simulations . Furthermore, combining renewable energy sources, such as solar systems, with Unified Power Quality Conditioners (UPQC), can address power quality problems at the point of common coupling (PCC) by adjusting for sags and ensuring a steady power factor [17]. Furthermore, the use of Adaptive Neuro-Fuzzy Inference Systems (ANFIS) is a viable approach for real-time adaptation and reaction to dynamic power quality problems. ANFIS-based controllers enable precise control and decision-making, improving the robustness and flexibility of modern distribution systems, particularly as renewable energy is increasingly integrated [18]. To summarise, modern distribution systems can dramatically improve power quality by strategically integrating advanced technologies like DSTATCOM with HPFs, DPFC, UPQC, and ANFIS controllers. These solutions address a variety of power quality challenges, assuring the consistent and efficient operation of electrical networks in the face of changing technological demands.

1.4 STATE OF ART

Modern power distribution systems are confronted with two challenges: the integration of renewable sources like PV and the increase in power electronic-based demands. The primary focus of research in the modern power system is to mitigate the negative impacts of Power Quality (PQ) events and to supply clean, sustainable power to residential complexes and industrial facilities. The burden of power quality issues, such as harmonics prevalent in the system, is significantly increased by the significant increase in nonlinear loads for electronics devices, uninterruptible power supplies, and rectifiers[19]. The current harmonics are typically produced as a result of the harmonics in the voltage supply and are also influenced by the type of load. A Distribution Static Compensator (DSTATCOM) is a power electronic device that is designed to address power quality issues resulting from unbalances, reactive power burden, and harmonic distortions in electrical systems. This thesis examines a variety of topologies, including multilevel inverters, single phase and three phase inverters, in order to enhance Power Quality (PQ) for DSTATCOM. Different control algorithms like conventional, adaptive, neural network and polynomial based techniques can be used to address PQ issues like reactive power, harmonic unbalance, power fluctuations, etc[20]. These algorithms include Synchronous Reference Frame Theory (SRFT), P-Q theory, Second-Order Generalized Integrator (SOGI), LCL-filter-based DSTATCOM, ANOVA Kernel Kalman Filter (AKKF), Hermite function based ANN, optimized Multi-Layer Perceptron (MLP) neural network, Bernoulli polynomial-based control technique, Leaky Least Mean Fourth (LLMF), Rodrigous Jacobi Polynomial (RJP) technique, Proportionate Affine Projection Algorithm (PAPA), Laguerre Polynomial (LP) based algorithm , Adaptive RBFNN based control techniques, Instantaneous Symmetrical Components Theory (ISCT), Notch filter based control techniques, Normalized Least Mean Absolute Third (NLMAT) algorithm, Immune Feedback Control Algorithm etc.

The design part of Voltage Source Converter (VSC) to be operated as DSTATCOM is carried for single phase system and three phase system with non linear load and it includes simulation study verified further experimentally[21]. The single phase and three phase inverters based DSTATCOM are used to mitigate harmonics present in the grid connected nonlinear load systems. In addition, five level Cascaded H-Bridge (CHB) inverter based DSTATCOM has been further implemented to reduce harmonics present in the source current.

Moreover, DSTATCOM can also be used in Electric Vehicles (EVs) related technology which will help us to reduce the consumption of fossil fuel such as diesel and gasoline, whose prices are increasing every day. The disadvantage of using fossil fuel as the primary source for vehicle is also that the fuel may no longer exist in future. Due to these reasons the demand of Electric Vehicles (EV) is increasing day by day. EVs have the capability to reduce our dependency on fossil fuels. The bidirectional DC-DC converter with battery connected at the DC link of Voltage Source Converter (VSC), will operate as On board Electric Vehicle charger.

Bidirectional power electronic converters serve as the essential components of EV chargers, supporting the main functions of Vehicle to Grid (V2G) and Grid to Vehicle (G2V) operations[22]. Furthermore, these converters can be used to provide additional grid functions such as reactive power support, voltage regulation and harmonics suppression etc. DSTATCOMs can offer these functionalities using different control algorithms and have been studied in this thesis work. The control algorithms discussed extensively are Least Mean Square (LMS), Rodrigues Jacobi Polynomial (RJP), Second-Order Generalized Integrator (SOGI), Leaky Least Mean Fourth (LLMF) algorithm. A DSTATCOM with EV charger, for example, is designed to deliver the reactive power required by non-linear loads while also charging or discharging the battery of an electric vehicle. The combination can also be used as an active power filter to reduce harmonics present in grid current of a domestic network.

A single phase grid connected EV system comprises nonlinear loads, bidirectional AC-DC converter and bidirectional DC-DC converter which can be modelled to operate in both G2V and V2G modes of operation. The effect of harmonic distortion due to nonlinear load has also been analyzed. Pulse Width Modulation (PWM) as well as Hysteresis Current Control technique have been used for generating switching pulses of various power Electronics based devices such as DSTATOM, DC-DC converter etc [23]. The steady state and dynamic state performance have been analyzed using different control algorithms.

Similarly, in three phase system, the system comprises nonlinear loads, bidirectional AC-DC converter and bidirectional DC-DC converter. Further, considering an On-Board EV Charger and a PV source connected at DC link of the VSC, the PV feeds real power to EV and the grid. Both the G2V and V2G operations are implemented using bidirectional Buck-Boost converter which is an emergent area of research. The grid supplies power to charge the battery of EV in G2V mode of operation. In V2G mode of operation, the stored energy in the EV battery bank is reutilized to supply back to the utility grid, which helps in peak shaving, load balancing, voltage management and improving the system reliability. The bidirectional DC-DC converter, along with the battery bank are connected at the DC link of three phase VSC and controlled to implement charging and discharging modes.

PV (Photo Voltaic) is the abundant source of renewable energy with less maintenance, less area and no moving parts. The double stage topology consisting of MPPT and boost converter is used to integrate to the EV, grid and nonlinear load [24]. The PV based grid connected EV charger ensures the bidirectional flow of active power to the grid, battery as well as nonlinear load. The PV and EV based VSC performs shunt compensation to mitigate power quality problems. The DC link capacitance of the VSC in three phase grid connected system is integrated with both EV and PV system. The performance of PV with VSC and PV, EV with VSC is analyzed on MATLAB/Simulink platform. The PWM control technology is utilised to control charging and discharging mode of batteries. The dynamics of the system are analyzed and results are used to interpret the effectiveness of different control techniques. The performance analysis is also verified by the developed prototype model in the laboratory. The prototype model is examined under dynamic load circumstances like an increase in load during G2V and V2G operation. Using a

Hysteresis Control Techniques (HCC), gating pulses are produced to control the active filter part and mitigate harmonics present in the source current as per IEEE 519 standard (i.e less than 5%) during charging and discharging operation [25].

Furthermore, to study is conducted on Reduced Switch Multi Level Inverter (RSMLI) based DSTATCOM, which may be connected to single phase/three phase supply system and nonlinear loads at Point of Common Coupling (PCC) and can also solve PQ issues. The DC link of RSMLI is integrated with PV and EV to smooth operation of charging and discharging condition. The above inverter configuration is more effective and uses lesser number of switches and her other benefits like simple structure, improved performance available at a lower cost as compared with five level (CHB) inverter. The system design aspects integrate grid, nonlinear load, compensator, solar panel and EV charger. The complete closed loop controller is designed to charge as well as discharge the EV battery to support grid [26].

1.5 Custom Power Devices

Custom power devices are specialised power electronics systems intended to improve power quality (PQ) in electrical distribution networks. These devices solve a variety of power quality issues, including voltage fluctuations, harmonics, and transients, ultimately enhancing power system dependability and efficiency. The Distribution Static Compensator (DSTATCOM) is a popular bespoke power device that is very good in reducing current-related PQ difficulties in distribution systems. DSTATCOM works with a voltage source converter (VSC) and can be set up in three-phase systems. The 3P3W arrangement is notable for its simplicity and low active power requirements, whereas the 3P4W configuration provides neutral current compensation without the need for extra control mechanisms [27]. Another important bespoke power device is the UPQC, which addresses voltage and current PQ issues. The UPQC, as well as its photovoltaic counterpart (PV-UPQC), are extremely successful at controlling voltage fluctuations, transients, and harmonic distortions. These devices have been widely researched for their structural configurations and control tactics, which are critical for maximising their performance in distribution systems [28]. Composite filters (CFs), which combine passive filters (PFs) with series active power filters (SAPFs), are also used to improve PQ, especially in systems using electric arc furnaces (EAFs) that generate voltage harmonics. The CFs use advanced control algorithms based on vectorial theory to detect and mitigate harmonic distortions, hence improving PQ at the point of common coupling (PCC). Furthermore, machine learning approaches have been combined with specialised electronic devices such as DVR and DSTATCOM to improve their performance. These strategies aid in lowering harmonics and boosting the devices' tolerance to diverse power disturbances [29]. Overall, custom power devices play an important role in modern power systems, eliminating PQ difficulties and easing the incorporation of renewable energy sources, resulting in a more stable and efficient electrical grid.

1.6 Motivation and Research Objectives

The motivation and research objectives surrounding modern distribution systems and power quality are driven by the increasing complexity and demands of contemporary electrical networks. The integration of renewable energy sources, the proliferation of nonlinear loads, and the need for reliable and efficient power delivery are central themes in current research. One primary motivation is the challenge posed by the integration of distributed generation (DG) and renewable energy sources (RES) into conventional power distribution systems. This integration, while beneficial for reducing carbon emissions and dependency on fossil fuels, introduces significant power quality issues such as harmonics, voltage sags, and system stability concerns. These issues arise from the unplanned and arbitrary placement of DGs, which can disrupt system operation and control [30]. Therefore, research is focused on developing methods to assess and improve power quality in these complex systems. The research objectives in this field are multifaceted. One key objective is to develop advanced assessment methods for power quality that account for the uncertainties introduced by distributed power outputs. Traditional methods are often subjective and fail to provide accurate evaluations under these conditions. To address this, new frameworks, such as those based on cloud modeling and cloud entropy optimization, have been proposed to enhance the accuracy and reliability of power quality assessments [31]. Another significant objective is the development and implementation of intelligent control systems, such as Adaptive Neuro-Fuzzy Inference Systems (ANFIS), to enhance power quality. These systems offer precise control and decision-making capabilities, enabling real-time adaptation to dynamic power quality disturbances. ANFIS-based solutions are particularly effective in mitigating common issues like voltage sags, harmonics, and flicker, making them suitable for modern distribution systems with complex load profiles and high renewable energy integration [32]. Furthermore, the use of custom power devices, such as UPQC and Distributed Static Compensators (D-STATCOM), is a critical research focus. These devices are designed to address power quality issues by compensating for voltage fluctuations and reducing harmonic distortions. The integration of photovoltaic (PV) systems with UPQC, for instance, aims to minimize Total Harmonic Distortion (THD) in residential low-voltage feeders, thereby improving overall power quality [33] Additionally, the application of machine learning techniques and advanced control strategies, such as PID-Fuzzy approaches, is being explored to enhance the adaptability and effectiveness of power quality improvement measures. These techniques are crucial for managing the complex interactions within modern distribution networks and ensuring the stability and safety of electrical systems [34]. In summary, the motivation behind research in modern distribution systems and power quality is to address the challenges posed by the integration of RES and nonlinear loads. The objectives are to develop accurate assessment methods, implement intelligent control systems, and utilize advanced power devices to ensure reliable and efficient power delivery. These efforts are essential for maintaining system stability, protecting electrical equipment, and enhancing the overall safety of power distribution networks [35].

1.7 Scope of Work

The scope of work includes investigation on single phase and three phase grid connected DSTATCOM, Grid Integrated Multilevel Inverters, single phase grid connected EV system, three phase grid connected EV and solar PV system and RSFLI based grid connected solar PV and EV charging system.

1.7.1 Investigations on Single Phase and Three Phase Grid connected DSTATCOM

The single-phase and three-phase grid connected power distribution systems are connected to non-linear loads. These systems face power quality problems due to non-linear loads which inject harmonics in to the source side. The single phase and three phase VSC based DSTATCOM is connected at PCC with grid and non-linear load to mitigate supply current harmonics. The system is developed in MATLAB Simulink software. The designed parameters related calculations are also discussed in the proposed system. The proposed model of a single-phase grid-connected and three phase grid connected system consists of a grid, VSC with interfacing inductor, nonlinear loads (Rectifier with resistive and inductive load). The experimental setup of proposed system is developed in the laboratory. The simulation and experimental results are verified and found satisfactory. The digital signal processor (DSP) based dSPACE 1104 is used to control developed single phase grid connected system. Similarly, the three phase proposed prototype model is controlled by the use of Microlab box 1202. A single-phase and three-phase DSTATCOM is used and controlled in a single-phase and three-phase electrical system to reduce harmonic distortions, voltage control and enhance power factor. Various control algorithms are developed to reduce power quality problems in single-phase and three-phase grid connected systems. Such algorithms include Notch filter, Leaky Least Mean Fourth (LLMF) and Adaptive Radial Basis Function Neural Network (ARBFNN). These algorithms have been implemented in both single-phase and three-phase grid connected systems.

Both single-phase and three-phase systems perform well under normal steady state and dynamic state conditions. The Total Harmonic Distortion (THD) analysis for both single-phase and three-phase grid connected systems are discussed in the thesis work. The developed control algorithm and conventional techniques are compared for fundamental active load component and suitable comparisons are reported.

1.7.2 Investigations on Grid integrated Multilevel Inverters

A single-phase AC source supplies power to a rectifier load having R-L branch connected at DC side. Source resistance and source inductance parameters are denoted as RS and LS. Two converter configurations (two level (2L) and five level Cascaded H-Bridge (5L-CHB)) are connected one by one in shunt configuration to eliminate harmonic currents and also to compensate the PQ problems. The control of the proposed system requires input variables such as source voltage vs, source current is, load current iL, total DC link voltage (Vdc1+Vdc2). These are sensed with LEM based current and voltage sensors. These sensed voltage and current signals are fed through ADC channel of DSP (dSPACE 1104). The DSP generates the required gating pulses for DSTATCOM. An interfacing inductor (LC) is connected with converter to suppress the AC output ripples. The designed simulation and results of two level (2L) and five level (5L) converter configurations are analyzed.

In the laboratory, the hardware setup of both two level (2L) and five level (5L) Cascaded H-Bridge (CHB) converter configurations have been implemented as DSTATCOM in single phase grid connected system. The steady state and dynamic state results are observed for both hardware setup viz two level and five level CHB converter configurations and it is found that the performance of five level CHB converter is better w.r.t two level converter. Also, the THD is observed to be less in five level inverter configurations as comparised to two level converter and it follow the 5% less THD as per IEEE-519 standard.

Additionally, a proposed control technique Leaky Least Mean Fourth (LLMF) algorithm is compared with Adaptive Radial Basis Function Neural Network (A-RBFNN) and Notch filter. The proposed control techniques generate better fundamental current and the result analysis is also presented in the thesis.

1.7.3 Investigations on single phase grid connected EV System

A single phase grid, nonlinear loads, bidirectional AC-DC converter and bidirectional DC-DC converter is modelled to develop single phase grid interfaced Electric Vehicle (EV) charging system. The charging and discharging operations during G2V and V2G mode of operation are discussed in the thesis. The MATLAB/Simulink model is designed and verified to study the performance of proposed system. To verify and confirm the simulation results, a prototype model gets developed in the lab. The prototype model is examined under dynamic load circumstances like an increase in load during G2V and V2G operation.

A nonlinear load is connected at the PCC which can receive power from a single-phase AC supply. The source resistance and inductance are as RS and LS, respectively. The nonlinear load is configured as a series combination of load resistance (R) and inductance (L) on the rectifier's DC-side. A shunt configuration of AC-DC converter is applied as an active filter to reduce supply-side current harmonics. The bidirectional AC-DC converter is fed at the PCC which allows compensatory currents to suppress the output ripples from the converter to be provided via interfacing inductors (Lc). The bidirectional buck-boost converter is fed at DC link of AC-DC converter. The proposed system's control is based on input variables such as source voltage (vs), source current (is), load current (iL), DC link voltage (Vdc), battery voltage (Vbat) and battery current (Ibat). These variables are measured using LEM-based current and voltage sensors. These measured voltage and current signals are subsequently analysed by the Real Time System (RTS's) controllers of ADC channel to ensures four gating pulses with the application of hysteresis current controller (HCC) to control bidirectional AC-DC converter. A Pulse Width Modulation (PWM) technique is also used for generating switching pulses of bidirectional DC- DC converter. A Digital Signal Oscilloscope (DSO) is used to record different signals captured from the hardware and a power analyser analyses experimental parameters like power, current, and harmonics.

Furthermore, an innovative Rodrigues Jacobi polynomial (RJP) based control algorithm is designed to control single phase VSC to improve power quality during charging/discharging operation of EV. The RJP control algorithm is compared with Least Mean Square (LMS) and Second Order Generalised Integrator (SOGI) control algorithm for considered system.

1.7.4 Investigations on three phase grid connected Solar PV and EV Charger System

The three phase grid connected Solar PV and EV charging systems is designed by the combination of three phase AC source, nonlinear load, three phase VSC, bidirectional DC-DC converter, battery bank and PV with boost converter.

In the proposed three phase grid interfaced solar PV and EV charging systems, RJP control algorithm is developed to control three phase VSC. This algorithm is use to generate fundamental component of the load current. Further, the system considers an On-Board EV Charger and a PV source connected at DC link of the VSC. The PV feeds real power to EV and the grid. Both the G2V and V2G operations are implemented using bidirectional Buck-Boost converter which is an emergent area of research. The grid supplies power to charge the battery of EV in G2V mode of operation. In V2G mode of operation, the stored energy in the EV battery bank is reutilized to supply back to the utility grid, which helps in peak load shaving, load balancing, voltage management and improving the system reliability. The bidirectional DC-DC converter, along with the battery bank are connected at the DC link of three phase VSC and controlled to implement charging and discharging modes. The performance of PV with VSC and PV, EV with VSC is analysed on MATLAB/Simulink platform. The PWM control technology is used to regulate the voltage and current used for charging and discharging batteries. The dynamics of the proposed system are analyzed and results are shown in the thesis with the new proposed algorithm.

The RJP control algorithm is compared with Least Mean Square (LMS) and Second Order Generalised Integrator (SOGI) control algorithm and results are analysed.

1.7.5 Investigations on RSFLI based grid connected Solar PV and EV Charger System

Maintaining grid power quality under the large penetration of Renewable Energy Sources (RES) and EV is a challenging task. This needs development of fast and efficient control technique for the compensator. A novel topology of Reduced Switch Five Level Inverter (RSFLI) for the integration of photovoltaic based renewable energy source and EV charger is discussed in this chapter. The new RSFLI has simple structure with low cost due to reduced switch count and it also meets the requirement of high power, medium voltage in power plants and industries. The system design integrates grid, nonlinear load, compensator, solar panel and EV charger. The Third Order Sinusoidal Integrator (TOSSI) algorithm is used to control RSFLI in the presence of grid, PV and EV. The solar PV array is integrated at the DC link of this inverter and Maximum Power Point Tracking (MPPT) is required to inject power at PCC. Further, G2V and V2G modes of operation are smoothly facilitated using a bidirectional DC-DC converter in conjunction with the RSFLI. The RSFLI has two separate DC links. The suggested control technique regulates both DC link voltages of the RSFLI to almost equal values. The RSFLI is utilized as a compensator and coupled to a single phase power distribution system. The complete closed loop system is designed to charge as well as discharge the EV battery to support grid.

The single phase grid connected RSFLI with PV and EV charging system is designed and tested in OPAL-RT real-time simulator. The dynamic results are found satisfactory during charging and discharging operation and during load changes.

1.8 Organization of the Thesis

The content of the thesis work has been divided into the following chapters:

Chapter 1: This chapter discuss the introduction of power quality (PQ), PQ standards and mitigation of harmonics, introduction of single phase inverter, three phase inverter and multilevel inverters.

Chapter 2: This chapter presents a literature survey on the grid connected DSTATCOM such as different converter configurations (single phase VSC, three phase VSC, Multilevel inverter), single phase grid connected EV charging system, three phase grid connected solar PV and EV charging systems. This chapter also discusses literature survey regarding different control algorithms under various grid (single phase and three phase). The review on single phase grid connected multilevel inverter based EV charger is also discussed in the thesis.

Chapter 3: This chapter includes the design aspects of different converter configurations. The design of DC link voltage, DC link capacitance, interfacing inductor, design of voltage and current sensors, design of gating circuit, design of PV array, design of DC-DC bidirectional converter etc. are presented in the thesis.

Chapter 4: This chapter discuss and analyzes the single phase and three-phase grid-connected DSTATCOM. The designed system is first modeled in MATLAB/Simulink. The steady as well as dynamic waveforms at different control algorithms are presented and results are analysed.

The prototype experimental setup of both single phase and three phase are developed in the laboratory. The experimental setup uses power analyser, DSO, dSPACE 1104, Microlab box 1202, loads etc. The suggested control algorithms' performance is contrasted with that of the existing control algorithms.

Chapter 5: This chapter includes the analysis of multilevel inverter based DSTATCOM. The configuration and switching operation of five level multilevel inverter is discussed. The mathematical modeling of different control algorithms with control diagram of Notch filter, LLMF and ARBFNN and its comparison of fundamental current are presented in the thesis.

Chapter 6: This chapter presents the analysis of single phase grid connected EV charging system to operate under G2V and V2G condition. The harmonic analysis of this system is also presented during charging and discharging mode. The various control algorithms RJP , LMS and SOGI for considered system and its mathematical calculation with comparative analysis are discussed in the chapter. The simulation and experimental results are also presented and analysed.

Chapter 7: This chapter discusses the performance analysis of three phase grid interfaced Solar PV and EV charging systems. Simulation results of three phase grid interfaced EV with PV and without PV are presented and compared.

Chapter 8: In this chapter implementation of single phase grid connected reduced switch multilevel inverter with PV and EV charging system is presented. The integration of PV and EV to the grid in single-phase system is also summarized in this chapter. The results are validated using OPAL-RT.

Chapter 9: This chapter concludes the works of the future scope.

Chapter 2

Literature Review

This chapter presents a literature survey on the grid connected DSTATCOM with different converter configurations such as single phase VSC, three phase VSC, Multilevel inverter, single phase grid connected EV charging system, three phase grid connected solar PV and EV charging systems. This chapter also discusses literature survey regarding different control algorithms under various grid (single phase and three phase). The review on single phase grid connected reduced switch multilevel inverter based EV charger is also discussed in this chapter.

2.1 General

Power quality (PQ) is an important part of electrical systems and particularly critical in industrial applications where power fluctuation can lead to damaged machinery, production lines or even entire automation processes failing. It contains several quantities that determines the attributes of that power supply like- Voltage Magnitude, Frequency, Continuity of Waveform [36]. With the rapid development of science and technology, more penetration of various kinds of loads into modern electrical systems, power quality problems have become one of the most difficult problems in electricity application. These can be observed as sinusoidal voltage waveforms distortions translated into disturbances and power supply loss, which in turn lead to equipment damages [37]. Due to the widespread use of power electronic systems and integration of renewable energy sources, it is becoming more critical to address Power Quality (PQ) issues. Such problems can create a lack of robustness and failures in power distribution systems and sensitive devices, which require efficient mitigation methods [38]. Voltage sags, harmonic distortions, voltage fluctuations and transient disturbances can be some of the various manifestations of poor power quality problems that may lead to no/unit production output or equipment tripping at a higher load than its rating which in turn leads to product/output wastage making the complete process cycle inefficient and costly [39, 40]. Non-linear loads, such as power electronic converters for EV charging stations, are found to be a major source of many power quality problems. The non-linear behaviour of such loads, and the switching ripple due to power electronic devices can be amongst the greatest distortions on the distribution grid [41]. This can be further complicated by an increase in electricity demand, especially the EVs which could double the current electricity demand in few regions where they are predominant [42]. In brief Power Quality problems stem from the presence for Non-linear loads, such as EV charging stations and magnetic devices which result in fluctuation and disturbances into the electrical grid.

2.2 Literature Survey

The literature survey on presented topics are discuss in detail in below section.

2.2.1 Power quality problems and mitigation techniques

The performance of industrial machinery is significantly influenced by power quality issues, which are predominantly due to the sensitivity of modern equipment to electrical disturbances. Industrial systems are particularly susceptible to power quality issues, including voltage fluctuations, harmonic distortions, transient disturbances, voltage sags, swells, flicker and reactive power related issues. These are related to the utilization of non-linear loads on residential, commercial and industrial environments [43]. The irregularities disrupt the power-system normalcy. These are usually due to abrupt changes in load, network interruptions or other operational faults. Another harmonic distortion type, which is widely distributed in systems due to non-linear loads and can cause overheating and thereby reduce efficiency of an electrical system [44]. The PQ problems result in the inefficiency of power distribution systems and lead to malfunctions in sensitive devices and hence mitigate approaches are required [45]. Increasing complexity and sophistication of industrial systems, which necessitate high power efficiency and stability, exacerbate these issues [46].

Controlling these problems, the advanced power electronic-based solutions in the form of Custom Power Devices (CPDs) have been made commercially available. These devices are DVR, DSTATCOM and UPQC which provide an enhancement of power quality level by compensation of voltage sag, swell and fluctuation, current harmonics, etc., [47]. The UPQC in particular emerges as a reliable and efficient tool that uses both series and shunt compensators to mitigate various types of PQ problems. The series part such as a DVR takes care of voltage sags and swells and the shunt part which is often a DSTATCOM deals with current-related errors like harmonics [48]. The Fuzzy logic and optimization algorithms such as Hybrid Ant Colony Optimization (HACO) are also integrated to increase the performance of these devices by optimizing their control parameters that will ensure better system efficiency and reliability [48-50]. In general, the literature stresses that it is crucial to have a structured model for power quality management (which complements each other- traditional and new one) as PQ problems are multi-faceted. The use of case studies and simulations, provides practical insights into the application and effectiveness of the mitigation strategies [51]. In order to preserve and enhance power quality standards, it is imperative to conduct continuous research and development in this field as power systems continue to develop. The integration of renewable energy sources, particularly wind power, into the grid can exacerbate these issues due to their variable nature, necessitating the use of custom power devices such as SVC, STATCOM, and UPQC to mitigate these effects [52-53]. The high-frequency or supraharmonics disturbances, are arising as a new power quality challenge in the 2-150 kHz range. Modern power electronics is the primary cause of these disturbances, which can result in electromagnetic interference that impacts both domestic and utility equipment. The absence of standardisation in this frequency range complicates mitigation efforts, emphasising the necessity of additional research and the development of detailed analytical models to more effectively comprehend and resolve these issues [54]. In order to address these power quality issues; a variety of mitigation techniques and devices are implemented. D-STATCOM, hybrid active power filters, and DVR are among the solutions employed to better the source power factor, control harmonic distortions, and enhance voltage quality [55]. Furthermore, the optimisation of power distribution and the enhancement of overall system stability can be achieved through the implementation of Flexible AC Transmission Systems (FACTS) and Distributed Energy Resources (DERs) [56]. In order to achieve effective mitigation, it is necessary to implement a combination of advanced technologies and the strategic integration of renewable energy sources, which is further supported by ongoing research to resolve gaps in understanding and standardisation [57-59].

Although renewable energy sources (RES) can contribute to the mitigation of power quality issues, they also present certain obstacles as a result of their intermittent nature and the integration of nonlinear demands. Numerous studies have investigated strategies for improving the quality of power in renewable energy systems. A DVR is one method that is employed in hybrid renewable energy-based smart infrastructures. The objective of this approach is to enhance the overall quality of power by reducing harmonic distortion, reducing voltage surges, and improving voltage stability. In simulations, the implementation of a modified synchronous reference frame-based controller and a cascaded H-bridge DVR topology has demonstrated promising results, effectively addressing issues such as voltage regulation and total harmonic distortion [60-61]. An alternative approach involves the utilisation of an optimised Fractional Order Proportional Integral Derivative (FOPID) controller in conjunction with a UPQC. This method is intended to address power quality issues, including voltage sags/swells and harmonics, in grid-connected renewable energy systems. Through the implementation of sophisticated optimisation algorithms, the FOPID controller has demonstrated substantial enhancements in its ability to address power quality concerns, surpassing conventional PI controllers [62-63]. Furthermore, the utilisation of an open-end winding transformer can improve the quality of power by integrating hybrid renewable systems, such as the combination of solar photovoltaic and wind power. This configuration, in conjunction with active power filter-based control schemes, effectively mitigates voltage and current distortions, guaranteeing that harmonic distortions remain within acceptable limits [64]. Additionally, exhaustive reviews underscore the significance of advanced control strategies in enhancing the quality of power in renewable energy systems. These strategies, which are facilitated by power electronic converters, have the potential to substantially improve the quality of energy that is generated and distributed, thereby addressing issues such as network congestion and load imbalances [65].

2.2.2 Literature Review based on Power quality standards

The Power quality standards are indispensable for guaranteeing the compatibility of the electric supply system with end-use equipment, establishing a framework for performance evaluation, defining equipment requirements, and delineating responsibilities among stakeholders [66-67]. These standards are developed by a variety of organisations, including the IEEE and IEC, and they address a variety of issues, including harmonics, interharmonics, flicker, voltage imbalance, and voltage sag indices [68-69]. In an effort to address contemporary challenges, including grid modernisation, data analytics, and the integration of inverter-based resources (IBR) and distributed energy resources (DER), the IEEE has been actively engaged in the development of power quality standards [70-71]. These standards are essential for addressing the complexities that have been introduced by advanced grid technologies and renewable energy sources. The IEEE also offers guidelines for specific phenomena, such as harmonics and flicker, which are essential for the preservation of power quality in systems with a substantial amount of renewable energy penetration [72-73]. Power quality standards are changing globally to accommodate the growing integration of renewable energy sources, including solar and wind power facilities. These standards are essential for the stability and reliability of large-scale renewable installations, as they include interconnection requirements and guidelines for low voltage ride through (LVRT) [74]. In order to assure that these systems satisfy international benchmarks, the IEC establishes measurement criteria for power quality phenomena and characterises wind turbine equipment [75]. The development of power quality standards is a continuous process, with roadmaps in place to resolve emerging technologies and challenges. The evolution of standards is guided by these roadmaps to ensure that they remain effective and relevant in administering the dynamic nature of modern power systems [76-77]. These standards will be instrumental in enabling the transition to more sustainable and resilient energy systems as the energy landscape continues to evolve.

2.2.3 Configuration and Design of the DSTATCOM System

The two-leg topology is employed in single-phase DSTATCOM, whereas the three-phase, three-wire topology is employed in three-phase distribution systems. The accepted topology is the three-phase, three-wire topology, as it is compact, less cumbersome, and minimises switching losses. It does not employ a bulkier transformer [78-79]. The Direct and indirect control techniques are employed to generate reference current methods [80-81]. It has been determined that the direct control technique is superior to the indirect control technique. The Hysteresis Current Controller and Dead-Beat Current Controller can be used for DSTATCOM. The HCC outperforms Dead Beat Controller [82]. A few methods that have been considered and implemented in the literature to reduce harmonics include hybrid filters, passive filters, and active power line conditioners are [83,87]. The Switching technology has been recently developed, and there are less expensive methods to implement it, such as DSP/field-programmable-gate-array (FPGA)-based systems. Therefore, active power line conditioners are a suitable technique for harmonic compensation. Active power filters (APFs) of the shunt type are frequently employed to eliminate harmonics in the current. Several critical components and control strategies are required to optimise power quality and ensure efficient grid integration when a Distribution Static Compensator (DSTATCOM) system is configured and designed. Typically, a DSTATCOM system extracts power from a photovoltaic array by employing control strategies like sliding mode control to optimise power extraction. The system's performance is frequently evaluated using DSP, which generates control signals for the voltage-source inverter through a PQ control scheme, as illustrated in the work of Soujanya and Upendar [88]. This configuration is essential for enhancing power quality by minimising the present Total Harmonic Distortion (THD). An alternative method entails the implementation of a 3-phase DSTATCOM, which regulates reactive and active power by utilising a Weighted Chimp (WdCH) optimisation algorithm to improve power quality. In order to reduce THD and optimise load current reference values, this system employs a 3-phase Voltage

Source Converter (VSC) that is regulated by Sinusoidal Pulse Width Modulation (SPWM) [89]. Further developments in DSTATCOM design involve the integration of solar and photovoltaic (SPV) systems with a hybrid controller that integrates Maximum Power Point Tracking (MPPT) with perturb and observe (P&O). The SPV is connected to the DSTATCOM's DC-link using a DC-DC boost converter, which is regulated by a Greedy Control-based Monarch Butterfly Optimisation (GCMBO) strategy. This strategy significantly reduces THD [90]. In general, the design of a DSTATCOM system entails the integration of a series of sophisticated control algorithms and optimisation techniques to guarantee the efficient management of power quality and grid integration. Each approach provides distinct advantages and enhances the system's performance.

2.2.4 Control Algorithms of DSTATCOM

The control algorithms for DSTATCOM are essential for the improvement of power quality in electrical distribution systems. The efficacy of DSTATCOMs has been optimised through the development of a variety of control strategies, each with its own set of advantages and disadvantages. The Adaline model predictive control (MPC) strategy is a prominent approach that integrates MPC with a least mean square (LMS)-based Adaline current estimator. This method generates reference currents by estimating the fundamental frequency components of load currents. The DC-capacitor voltage is maintained by a proportional-integral (PI) controller, and the power quality is substantially improved by ensuring that the source currents track the reference currents through MPC [91]. The Parallel Tangent (PARTAN) LMS adaptive control is another innovative control algorithm that is specifically designed for cascaded multilevel inverters (CHB-MLI) that are utilised as DSTATCOM units. This method improves the power factor and exports reactive power to address power quality issues under distorted grid conditions. The system's efficacy in maintaining power quality within IEEE-519 limits is demonstrated through simulations and experiments, which validate its performance [92]. Furthermore, the utilisation of Instantaneous Reactive Power Theory (IRPT), MPC and Synchronous Reference Frame (SRF)is underscored in an overview of a variety of control techniques for DSTATCOMs. In both grid-connected and islanded modes of operation, these techniques are assessed for their capacity to enhance power quality and reduce transients [93]. In addition, the Weighted Chimp (WdCH) optimisation algorithm is introduced to optimise DSTATCOM control. This method is designed to reduce Total

Harmonic Distortion (THD) and improve power quality by adjusting the fundamental weight values of load currents to determine reference grid currents [94].

In general, the control algorithms for DSTATCOMs include a variety of techniques, including classical methods, advanced adaptive, and optimisation techniques, all of which contribute to the enhancement of power quality by resolving specific challenges, such as grid distortions and load variations. These strategies are indispensable for the preservation of power distribution systems that are both efficient and dependable [95].

2.2.4.1 Conventional Control Algorithms of DSTATCOM

The management of power quality issues in electrical distribution systems is contingent upon the implementation of conventional control algorithms for DSTATCOM. The primary objectives of these algorithms are to regulate reactive power flow, minimise Total Harmonic Distortion (THD), and ensure voltage stability. The use of the Second Order Generalised Integrator (SOGI) filter, which is frequently paired with a Proportional-Integral (PI) controller, is one of the traditional approaches. This method is effective in identifying and compensating for reactive power and harmonics in the system, as evidenced by simulations that demonstrate enhanced power quality under a variety of load conditions [96-97]. In environments with distorted and asymmetrical power supplies, the SOGI-based control is particularly beneficial, as it is capable of accurately detecting and compensating for the harmonic and reactive components of the load current [98]. The Synchronous Reference Frame (SRF) theory is another conventional approach that simplifies the control of active and reactive power by converting the three-phase system into a two-axis system. The robustness and effectiveness of this method in dynamic conditions are the reasons it is extensively employed [99]. Furthermore, Hysteresis Current Control is implemented due to its rapid dynamic response and straight forwardness, despite the potential for switching frequency fluctuations [100]. Model Predictive Control (MPC) is also acquiring popularity as a conventional control strategy because of its capacity to anticipate future system behaviour and address multivariable control issues. It guarantees minimal THD and enhanced power quality by providing precise control over the DSTATCOM's operations [101] These conventional algorithms frequently encounter obstacles, including steady-state errors and sluggish convergence rates, despite their effectiveness. Some algorithms, such as Notch Filter (NF), Sliding Discrete Fourier Transform (SDFT) and Third Order Sinusoidal Integrator (TOSSI) control algorithm, have been devised to address these issues [102-104]. The SDFT and SOGI control algorithms block also includes to manage distorted grid conditions, thereby guaranteeing that the Total Harmonic Distortion (THD) is within the IEEE-519 limits. The system's superiority under conventional algorithms has been demonstrated through simulations and laboratory experiments, which have validated its performance under dynamic load variations and distorted grid conditions [105]. These methods provide the management of power quality and assuring the reliability and efficiency of power distribution systems [106].

2.2.4.2 Adaptive Control Algorithms of DSTATCOM

Adaptive control algorithms for DSTATCOM are essential for the improvement of power quality by managing reactive power and reducing harmonics in distribution networks [107]. The adaptive control strategies have been devised, each with its own methodologies and advantages. One such approach is the Least Mean Square (LMS) adaptive control algorithm, which is intended for use as a DSTATCOM in a single phase or three phase grid connected systems [108]. Advanced algorithms, such as the Weighted Zero Attracting Variable Step Size LMS (WZAVSSLMS), Parallel Tangent (PARTAN) Least Mean Square (LMS), Normalised Huber (NH) Control Algorithm, Robust Shrine Affine Projection Sign (RSAPS) adaptive control algorithm, q-LMF (Quantum Calculus-based Least Mean Fourth) based control and Normalized Sign Regression Least Mean Mixed Norm (NSRLMMN) algorithm, have been devised to address these issues [109-110]. These methods provide substantial enhancements over conventional methods by reducing errors and increasing convergence rates [111]. This algorithm maintains a unity power factor on the supply side and effectively exports reactive power required by nonlinear loads. Other approaches are also intended for use as a DSTATCOM in a cascaded multilevel inverter (CHB-MLI), which is the Parallel Tangent (PARTAN) Least Mean Square (LMS) adaptive control algorithm, Improved Immune Control Algorithm etc. This method effectively reduces THD and improves power quality under both balanced and unbalanced loads by supplying gating pulses for a 1-phase VSC through Sinusoidal Pulse Width Modulation (SPWM) [112]. Another adaptive strategy is provided by the immune feedback control algorithm, which employs a three-phase VSC as a shunt compensator. This method maintains a unity power factor and minimizes supply current harmonics by estimating fundamental reference grid currents from nonlinear load currents. It has been demonstrated to effectively balance loads and compensate for nonlinear loads [113]. Simulations and experimental validations serve to illustrate the efficacy of each algorithm, which offers distinctive benefits.

2.2.4.3 Neural Network (NN) based Control Algorithms of DSTATCOM

Artificial neural networks are composed of three layers, input layer, hidden layer, and output layer. The hidden layer is composed of a preset number of neurons with a fixed activation function. All of these layers are trained and transmit signals to other neurons. These neurons in the hidden layers are updated with adjustable weights. The selection of neurons and hidden layers presents a challenge for the neural network [114]. A fuzzy logic controller is an adaptive neuro fuzzy inference system illustrated in [115-116] for shunt compensation. Using training data, these NN are trained offline, which may be a challenging and time-consuming process. As a result, a variety of gradient methods are introduced to facilitate the real-time training of neural networks (NN) in order to enhance PQ [117-119]. Finally, the neural network-based adaptive control algorithm utilises an Adaline (Adaptive linear element) neural network for VSC-based DSTATCOM. This method improves the system's performance by generating the fundamental current components of the load currents, which are essential for the elimination of harmonics and the compensation of reactive power at the point of common coupling (PCC) [120].

The adaptive euro Fuzzy inference system (ANFIS), the radial functional neural network (RFNN), the feed-forward ANN, Hermite function-based artificial neural network (HeANN) and the adaptive linear neural network (ADALINE) are among the numerous ANN topologies that have been published [121-123]. The feed forward ANN [124] is one of the most well-known and frequently used of these networks. It was used to investigate control methods based on ANFIS-LMS as a method of reducing PQ issues.

2.2.4.4 Polynomial based Control Algorithms of DSTATCOM

Polynomial-based control algorithms for DSTATCOMs are intended to improve power quality by effectively managing reactive power and mitigating harmonics in distribution networks. Several advanced control strategies have been devised, each of which optimises performance under a variety of conditions by utilising polynomial-based approaches [125]. A Bateman Polynomial algorithm is one such approach which generate the fundamental weight values of load currents to determine the magnitude and phase values of the reference grid currents [126]. This approach employs Sinusoidal Pulse Width Modulation (SPWM) to generate gating pulses for a 1-phase or 3-phase Voltage Source Converter, with the objective of reducing Total Harmonic Distortion (THD) and enhancing power quality in the presence of both balanced and unbalanced loads [127]. A Mittag Leffler Polynomial based Neural Network control algorithm is implemented in an additional innovative control strategy. This technique is particularly effective in distorted grid conditions, as it employs a 1-phase system to compensate reactive power and enhance the power factor to unity. The system's performance is also improved by the integration of some polynomials like Bernoulli Polynomial-based artificial neural network (BePANN), Gagenbuer Polynomial and Laguerre polynomial which guarantees that THD levels remain within the IEEE-519 constraints [128-129].

These control algorithms, which are based on polynomials, exhibit substantial progress in DSTATCOM technology, providing durable solutions for the enhancement of power quality. Modern power distribution systems can benefit from each method's distinctive advantages, including improved adaptability to grid disturbances, reduced THD, and enhanced convergence rates. The potential for further optimisation and innovation in power quality management is underscored by the integration of these algorithms into DSTATCOM systems.

2.3 Literature Survey on Single Phase Grid Connected DSTATCOM

Several major aspects and advancements in the field are highlighted in the literature on single-phase grid-connected DSTATCOM. In electrical grids with a distorted load current due to nonlinear load, single-phase DSTATCOM are essential for preserving stability, performance and mitigate harmonics present in the systems. Harmonics are introduced into the supply system by the non-linear demands. Single-phase grid-connected DSTATCOM are advantageous in terms of control strategies due to the implementation of advanced techniques which significantly reduce Total Harmonic Distortion (THD) and enhance the quality of power injected into the grid. These techniques are Adaptive Least Mean Square (LMF) control scheme is developed in [130], Second Order Generalised Integrator (SOGI) in [131], Notch Filter (NF) [132], Wrapped Filter (WF) [133], Lyapunov Function in [134-135], Normalized Sign Regression Least Mean Mixed Norm (NSRLMMN) algorithm in [136], Single phase inverter system with non-linear load consideration, ANOVA Kernel Kalman Filter in [137], adaptive Least Mean Square (LMS) in [138], EPLL based control algorithm in [139] for Power Quality Improvement in [140]. DSTATCOMs are instrumental in improving the transient stability of grid-connected systems. In general, the integration of DSTATCOMs in single-phase grid-connected systems is essential for the enhancement of power quality, stability, and efficiency. The research emphasises the necessity of ongoing development in single-phase systems to keep pace with the advancements observed in three-phase systems and the significance of advanced control strategies [141,142].

2.4 Literature Survey on Three Phase Grid Connected DSTATCOM

The literature on three-phase grid-connected DSTATCOMs emphasizes their critical role in improving the quality and stability of power in distribution networks. DSTATCOMs are shunt-connected devices that regulate reactive power and address power quality issues, including voltage sags, harmonic distortion, and load imbalances [143]. Power quality issues, including disturbances in supply current injected as a result of load, inadequate power factor, and load unbalancing, are common in three-phase grid-connected systems. In the literature, a variety of control techniques have been devised, including the PNKLMF-based technique presented by Nishant et al. [144], the Kalman filter in [145-146], and the Extended Kalman Filter in [147]. P. Shah [148] addressed FOGI-FLL. Badoni et al [149] examined a control technique that was based on Euclid. Chittora et al [150] examined the Chebyshev technique. B. Singh et al. addressed the following topics: Laplacian Regression Technique [151], MGI control in [152], ILST control algorithm in [153], Recursive Digital Filter in [154], and QNBP NN-based I cos ϕ in [155]. Jain et al. addressed HTF-Based Higher-Order Adaptive Control [156] and predictive model control in [157]. In [158], Rahamani et.al. addressed Lyapunov control, Naive Back Propagation-based I-cosĄ in [159], Learning-based Anti-Hebbian in [160], Variable Forgetting Factor Recursive Least Square Control Algorithm in [161], Conductance-based fryze in [162], Fast Zero Attracting Normalised Least Mean Fourth-Based Adaptive Control in [163], JAYA Optimization-based control algorithm in [164], and Leaky Least Logarithmic Absolute Difference-Based Control in [165]. In 3-phase grid-connected systems, the algorithms mentioned above are implemented. Prakash and Alka [166] underscore the importance of employing an Enhanced Phase Locked Loop (EPLL) algorithm to improve the performance of a three-phase DSTATCOM. This method enhances power quality by stabilising DC link voltage during load disturbances and minimising Total Harmonic Distortion (THD) through the DSTATCOM of reactive and active power control. They suggest the utilisation of a Voltage VSC and a T-linked transformer to address these concerns, emphasising the DSTATCOM's contribution to reactive power regulation and efficient load balancing. Manoj et al. [167] investigate the utilisation of Adaptive Generalized Maximum Versoria Criterion (AGMVC) to control DSTATCOM. This system has been utilised to supply active power to linear and nonlinear loads, incorporating power quality adjustment elements such as harmonics, excessive reactive power, and imbalance.

Peerzadah et al.[168] conduct a comparative analysis of a 3Φ-3W system that employs a DSTATCOM, with an emphasis on the reduction of THD and the correction of power factor. They employ the Synchronous Reference Frame (SRF) technique to generate reference currents, which are validated through real-time simulation. This underscores the DSTATCOM's efficacy in enhancing power quality in a variety of load conditions. Lastly, [169] addresses the integration of DSTATCOMs into grid-connected solar PV systems. The study emphasises the DSTATCOM's function in ensuring the stable operation of the solar-PV system by maintaining power factor correction and zero voltage regulation, despite insolation variations. In general, these studies collectively emphasise the versatility and efficacy of DSTATCOMs in improving power quality and stability in a variety of grid-connected scenarios. They employ a variety of control strategies and configurations to address specific challenges in distribution networks [170,172].

2.5 Literature Survey on Grid integrated multilevel inverter based DSTATCOM

According to the literature review, the SAPF is frequently used in single-phase distribution systems as a basic two-level inverter [173]. The high switching frequency and higher dv/dt stress on the switches in high power applications are the problems with this conventional inverter, which can lead to switch malfunctions. A supplementary line frequency transformer must be attached, hence augmenting the overall cost of the system for distribution at medium and high voltage levels. Consequently, its usefulness is constrained for high power applications. Nonetheless, MLI is developing as the favored configuration of DSTATCOM, particularly for high-power level applications [174-175]. It may operate at a low switching frequency, and the harmonic content decreases as the number of levels increases. The required flexibility is offered by the modular approach. Three typical topologies for MLI are available in literature, which are Neutral Point Clamped (NPC) [176], Flying Capacitor MLI (FCMLI) [177] and Cascaded H-bridge MLI (CHB-MLI) [178].

The first one, which is referred to as the 3-level Diode Clamped Multilevel Inverter (DCMLI), was introduced by Nabae and Takahashi [179]. The concept of midpoint Neutral Point Clamped (NPC) inverter was introduced in this paper. In the 1990s, Meynard and Foch [180] and Lavievilleet al. [181] introduced the Flying Capacitor MLI (FCMLI), which is the second most well-known configuration. It is based on the basic idea of using capacitors rather than clamping diodes and is also known as a capacitor constrained inverter. Baker and Bannister [182] put forth a succession of H-bridge connections in the mid-1970s, which are commonly referred to as cascaded H-bridge

MLI (CHB-MLI). The CHB-MLI configuration performs better than its counterparts due to its modular structure, inherent voltage balancing quality due to the absence of diodes and capacitors. The CHB-MLI is also known as Series Connected H-bridge MLI (SCHB-MLI) and it is also the most suitable topology for interconnecting renewable energy sources such as PV arrays or fuel cells [183].

In order to obtain the required voltage, it is customary to connect multiple inverters in series. The circuit design and control scheme of each inverter module are identical. Consequently, the CHB inverter exhibits a high level of modularity [184-186]. Furthermore, this advanced control strategy facilitates the prevention of defective units without impeding the power supply to the load terminals, thereby guaranteeing continuous availability [187-188]. Numerous cascaded multilevel inverter topologies have been designed as a DSTATCOM and implemented for a prominent role in the design of power electronics-based compensators. These devices are quick in operation and their control can also be modified easily. The examples include the UPQC, SAPF, DVR. Paper [189] shows that DSTATCOM is used to correct phase-shift of current and achieve unity power factor in a three-phase three-wire system feeding nonlinear loads. It can also be used to improve Power Quality (PQ) related problems. A few methods for mitigating PQ problems are described in the research paper [190] in which DSTATCOM accompanied with CHB-MLI is used.

The DSTATCOM can be configured to solve PQ problems such as harmonics filtering, reactive power compensation, voltage support in low voltage distribution networks, load balancing, lowering SPV power fluctuations etc. using several control algorithms. These algorithms include Synchronous Reference Frame Theory (SRFT) [191], P-Q theory[192], Salp Swarm Optimization Algorithm (SSOA) [193-194], cascaded enhanced second-order general integrator with a prefilter (CESOGI-WPF) control technique [124,195], LCL-filter-based DSTATCOM [196], ANOVA Kernel Kalman Filter (AKKF) [124,136], Hermite function based ANN [121],optimized Multi-Layer Perceptron (MLP) neural network [197], Bernoulli polynomial-based control technique [124,198], proportionate affine projection algorithm (PAPA) [199], Laguerre Polynomial (LP) based algorithm [124], Instantaneous Symmetrical Components Theory (ISCT) [200], Normalized Least Mean Absolute Third (NLMAT) algorithm [124,201-202], Immune Feedback Control Algorithm [203-204] etc. The DC link of the DSTATCOM can also be used to interface solar photovoltaic (SPV) arrays to extract DC power to three-phase system [205]. The modifications of system configuration have also been discussed in literature viz. three-phase, five-wire

DSTATCOM which helps to achieve Unity Power Factor (UPF) and Zero Voltage Regulation (ZVR) modes of operation [124].The five level cascaded H-bridge inverter based DSTATCOM may also be connected to asynchronous generator supply system and loads at point of common coupling (PCC) and can also solve PQ issues [124].

2.6 Literature Survey on Single Phase Grid Connected EV Charging Systems

The literature on single-phase grid-connected electric vehicle (EV) charging systems emphasises several critical components, such as power quality, converter design, and integration of DC-DC converter with battery bank [206-208]. The necessity for efficient and rapid charging systems is a substantial obstacle to the adoption of electric vehicles (EVs). This can be resolved by integrating solar and utility power sources. The presence of EVs in significant number unleashes an additional source of electric power when needed. Battery Electric Vehicles have nowadays gained popularity as an alternative mode of transportation due to their improved performance, zero emissions as well as the convenience of a longer driving range. This naturally leads to a more sustained and environmentally friendly way of transportation [209]. This also implies realization of V2G operations on a much larger scale in the near future and the economic merits of EVs which have been debated in recent decades [210]. The automotive industry and numerous government organisations are focusing more on electric vehicle sector, owing to government incentive schemes and development programmes. Several countries, notably the United States (US), the European Union, Canada, China, and India, have already implemented Zero Emission Vehicle legislation [211-212]. These programmes aim to encourage the use of EVs by providing financial incentives and supporting the development of EV charging infrastructure. Furthermore, there were over 26 million EVs on the road in 2023 across the globe. This number is expected to climb to over 1 billion EVs by 2050 [213].

However, it may also be noted the growing popularity of EVs has the ability to adversely affect the quality of grid power since it is a DC load. Therefore, battery chargers become crucial components of performance evaluation and fulfilling grid-side power quality requirements as specified in IEEE 519 standards becomes relevant. [214-216]

The chargers for Plug-in Electric Vehicles (PEV) can be broadly categorized as either on-board or off-board chargers. They may have the capability to facilitate bidirectional power flow, either from the grid to the vehicle or from the vehicle to the grid [217-218]. The on-board chargers (OBC) system must have characteristics such as high power density, efficient energy utilisation, a compact form factor, lightweight construction, high reliability, and cost-effectiveness. Moreover, they should also be environmentally sustainable and grid-compatible [219-220].

Bidirectional power electronic converters serve as the essential components of EV chargers, supporting the main functions of G2V and V2G operations [221]. Furthermore, these converters can be used to provide additional grid functions such as reactive power support, voltage regulation and harmonics suppression. The Static synchronous compensators (STATCOMs) have traditionally offered these functionalities using different control algorithms. These control algorithms are Enhanced Phase Locked Loop (EPLL) [222], Hopfield Neural Network [223], Bernoulli polynomial-based control technique, Hermite function-based artificial neural network, Fractional delay Newton structure for Lagrangian interpolation [224], Sliding Window Recursive Discrete Fourier Transform (SWRDFT) [225], Sign Regressor Least Mean Mixed Norm (SRLMMN) control technique [226], Laguerre polynomial function-based inverter control [227], Nonlinear adaptive normalized least mean absolute third algorithm [202], Leaky Least Mean Fourth (LLMF) control algorithm etc. An EV charger, for example, is designed to deliver the reactive power required by non-linear loads while also charging or discharging the battery of an electric vehicle. An EV charger can also be used as an active power filter to reduce harmonics in the current on the grid side of a domestic network. A single-phase EV charger can additionally adjust the voltage at the point of common coupling (PCC) by injecting leading or lagging volt-ampere reactive (VAR) into the grid [228]. The on-board charger comprises a single-phase grid-integrated VSC and a dual active bridge (DAB)-based dc-dc converter that provides galvanic isolation between the battery and the grid [229]. This EV charger has bidirectional power flow, allowing it to be used in vehicle-to-home (V2H) or vehicle-to-grid (V2G) applications. In addition to the traditional G2V battery charging function, it can give reactive power (VAR) support to the grid [230-232].

In order to surmount the protracted charging process, which is a significant impediment to the adoption of electric vehicles (EVs), it is imperative to implement fast charging systems. As a result of the increased demand on the grid, these systems are confronted with challenges such as power loss, voltage instability, harmonic distortion, and transformer saturation [233]. In grid-connected EV charging systems, power quality is a critical concern. The congestion and stability issues that can result from the variability in EV charging can also affect other users on the same network. In order to more effectively comprehend and mitigate these challenges, recent research has concentrated on the supra-harmonic frequency range (2 kHz to 150 kHz). A model study of a single-phase bidirectional AC/DC converter that is connected to the grid has been conducted to investigate power quality issues. The results indicate that high switching frequencies can result in substantial emissions within this range [234-236]. Improvements in converter design are essential for enhancing the reliability and efficacy of electric vehicle charging systems. A single-phase grid-connected fault-tolerant bi-directional power flow converter has been proposed, which is capable of preserving power quality in the presence of defective conditions [237]. In order to reduce total harmonic distortion (THD) and maintain a unity power factor, this system implements adaptive resonant control and an H-bridge configuration [238]. In a similar vein, a high DC-gain flyback converter has been created, which maintains efficiency with fewer switches than conventional converters, while simultaneously reducing THD and improving power factor [239]. In general, the efficacy of single-phase grid-connected EV charging systems is significantly improved by the integration of advanced converter technologies and the emphasis on power quality. The support of the increasing demand for electric vehicles (EVs) and the maintenance of stable and efficient grid operations are contingent upon these developments.

Single-phase grid-connected electric vehicle (EV) charging systems are intricate assemblies that incorporate numerous critical components to guarantee safe and efficient charging [206,218]. AC/DC converters, DC/DC converters, phase-locked loop (PLL) algorithms, and power factor correction (PFC) mechanisms comprise the primary components. The AC/DC conversion is typically administered by a pulse width modulated (PWM) rectifier, which is essential for converting alternating current (AC) from the grid to direct current (DC) that is suitable for charging EV batteries. Isolated converters are frequently implemented during the DC/DC conversion stage to regulate the voltage disparity between the energy storage system and the DC connector, thereby guaranteeing safety through galvanic isolation. This stage has the capacity to employ LLC-type resonant converters, which provide high input voltage operation and enhanced performance through resonant switching, thereby minimising reactive power and improving power flow regulation [240]. Additionally, a VSC at the front end is employed to achieve power factor correction, which reduces the phase difference between current and voltage and maintains a unity power factor, thereby minimising reactive power in the system [241]. This is essential for the stability of the grid and the efficient transmission of energy. The single-phase grid-connected EV charging systems are distinguished by their utilisation of VSCs for power factor correction, PWM rectifiers for AC/DC conversion, isolated DC/DC converters for voltage regulation, and PLL algorithms for grid synchronisation. These components collaborate to guarantee the efficient, safe, and reliable charging of electric vehicles (EVs) while simultaneously promoting grid stability and energy management [242].

2.7 Literature Survey on Three Phase Grid Connected Solar PV and EV Charging Systems

The integration of electric vehicle (EV) charging infrastructure with three-phase grid-connected solar photovoltaic (PV) systems is a promising approach to improve the efficiency and sustainability of EV charging [243-244]. Research paper [245] discusses a PV system with battery storage using a bidirectional DC-DC converter. This system has been designed for serving DC loads and EV battery charging is proposed in this paper. The PV array power is used to charge the EV's battery and DC loads during peak hours. During the hours when the sunlight is not available, the power of battery is used to supply DC loads.

A multi-port reconfigurable converter for grid-integrated hybrid PV/EV/battery system is proposed in [135]. The model is developed with PLECS software for time-domain simulation, and the converter is intended to charge electric vehicles at a rate of 10 kW. In order to achieve high power density and increased component utilization, the converter shares components across various power flow routes. A single transformer is used to exchange power between EV and the rest of the sources complying with EV isolation standards as well as attaining reduced magnetics. The research emphasises numerous critical components of this integration.

Initially, a study [246] conducted in Jeddah, Saudi Arabia, demonstrates the viability of utilising grid-connected PV systems for EV charging. The study found that a rooftop solar PV system was capable of satisfying the energy requirements of a petrol station, which included EV charging, while simultaneously reducing energy costs and CO2 emissions. This suggests that solar photovoltaic (PV) systems have the potential to economically and environmentally support electric vehicle (EV) charging infrastructure. The integration of both photovoltaic and grid power sources can be advantageous for fast charging systems, which are essential for the widespread adoption of EVs. This dual-source approach is designed to address the challenges associated with high demand in rapid charging stations, including power loss, voltage instability, and transformer overloading [247]. The integration of solar and grid power not only facilitates rapid charging but also alleviates grid variability concerns. In addition, the incorporation of renewable energy sources, including solar, into EV charging systems provides benefits such as cost reductions and reduced grid demand

[248]. Although hybrid and on-board charging systems present challenges in terms of cost and integration complexity, they enhance these benefits by providing faster charging and enhanced communication protocols [249]. The stability and efficiency of EV charging infrastructure are further improved by a three-phase, four-wire distribution network that incorporates PV and tiny hydro energy conversion systems. This configuration enables the seamless operation of both grid-tied and stand-alone modes, thereby reducing energy curtailment and enhancing power quality [250]. Additionally, the utilisation of bidirectional charge systems, which facilitate energy transfer between EVs and the grid, facilitates microgrid energy management. This method, which has been demonstrated through simulation, guarantees a consistent power supply and minimal harmonic distortion, underscoring the potential for EVs to function as energy storage systems within a grid-connected solar PV framework [251]. The integration of three-phase grid-connected solar PV systems with EV charging infrastructure provides substantial advantages in terms of sustainable development, grid stability, and efficiency. Nevertheless, in order to completely realise these advantages, it is necessary to address obstacles such as the complexity of integration, the cost, and the necessity of advanced control mechanisms.

2.8 Literature Survey on Grid Connected RSMLI with Solar PV and EV Charging Systems

The integration of solar photovoltaic (PV) systems and electric vehicle (EV) charging stations with grid-connected Reduced Switch Multilevel Inverters (RSMLI) is a promising approach to improve the efficacy and sustainability of EV charging infrastructure [252]. Research is going on [253] to improve the battery efficiency, range etc which are the main hurdles in today’s scenario. Keeping in mind future growth of EV, V2G and G2V modes are being explored by industries. Developments in the areas of battery technology, charging infrastructure and vehicle-to-grid integration have advanced as a result of the EV market's explosive growth. These developments have kept elevating the efficiency, range, and comfort of electric vehicles over the last decade.

Recent literature review [254] highlights the topology and the control aspects of EV chargers. Paper [255] discusses a charger which employs a Self Tuning Filter (STF) based control technique in Grid-Connected Operation (GCO) to estimate the fundamental load current and to provide synchronized sinusoidal reference current. A Sliding Mode Control (SMC) based DC-link voltage controller is presented in [256] to reduce DC-link voltage overshoot with finite-time convergence during external disturbances. A wide range high voltage gains bidirectional DC-DC converter utilizing a dead-beat controller is discussed in [257] which ensures smooth and accurate current control for both G2V and V2G operation. A single-phase bidirectional active neutral-point-clamped (ANPC) five-level converter (5LC) is proposed by the authors for use in V2G, vehicle-to-home (V2H) and G2V applications for active filtering [258]. An innovative, high-quality charging scheme for electric vehicles is demonstrated by the author using a Type-2 fuzzy logic driven shunt converter coupled system. Both the G2V and V2G modes of operation are made possible by the bidirectional converters. The decoupled current control approach combined with the DC-link voltage is utilized in ac-dc converters [258]. A reconfigurable Power Electronics Interface (PEI) known as the integrated multipurpose power electronics interface (IMPEI) combining the drive inverter and on-board charger into a single interface that can be used for multiple modes of operation, including G2V and vehicle-to-grid V2G operations with grid flexibility is discussed in [259]. The distributed model predictive control (DMPC) technique enables EV chargers to make use of reactive power V2G capabilities and engage in real-time voltage regulation of both balanced and unbalanced distribution networks without interfering with active power interchange. The implementation of a solar photovoltaic (PV) array powered grid-connected domestic EV charger that caters to the needs of an EV, household loads and the grid is discussed in [260]. In order to support local loads in an isolated situation, the charger is additionally equipped with vehicle-to-home power transfer and active/reactive grid power assistance. Maximum EV Hosting Capacity (HCmax) for low voltage distribution networks is presented in [261] to measure and evaluate the potential improvements to distribution networks that could result from the suggested phase-shifting technique. Paper [262] suggests a novel way to use the ripple injection load control signals for the regulation of EV charging load. Singh et al. and Jain et al. have shown an EV charging station [263]. In paper [264], the EV is charged solely from PV and the grid. However, if the PV array and grid are unavailable, the EV battery is not charged. This disadvantage is addressed in [266]. The paper [266] describes an efficient control technique for a multifunctional grid-connected solar photovoltaic (PV), EV charger that uses adaptive notch filters (ANFs) to power the EV batteries while also enhancing grid power quality.

Additionally, the use of (RES) Renewable Energy Sources like PV into EV charging infrastructures is gathering momentum as a result of advantages such as reduced fuel costs, reduce global warming effects and greater independence from the grid [95]. They demonstrate the DSTATCOM's ability to effectively address oscillation and stability issues by employing advanced control techniques such as Level Shifted Pulse Width Modulation (LSPWM) and Artificial Neural Networks (ANN) to enhance power stability and mitigate fault currents [267]. The literature also underscores the significance of advanced charging management systems and control algorithms in order to improve the efficacy and user experience of EV charging stations. These systems have the potential to enhance communication protocols, preserve battery life, and optimise recharge processes [268]. The integration of RSMLI with solar PV and grid-connected EV charging systems offers a viable solution to the obstacles associated with the adoption of electric vehicles. Although the prospective advantages are substantial, additional research is required to resolve technical obstacles and enhance system performance. This encompasses the examination of the feasibility of V2G technology and the development of sophisticated control algorithms in order to completely realise the potential of this integration [269-271].

2.9 Identified Research Gaps

The following research gaps are noted according to the findings of the comprehensive literature review:

- New and Improved control algorithms for Inverter control.
- Need of Impact analysis of PV system on grid.
- Modern control algorithms required for EV operation.
- Need to analyze different Inverter configurations.

2.10 Objectives of Current Research

The following are research objectives based upon the research gap identified

- Analysis and design different Inverter circuits for PQ improvement in distribution system.
- Impact of PV system on conventional grid along with PQ improvement.
- Integration of EV system for G2V and V2G modes of operation.
- Simulation and analysis of new Inverter topology for cost effective solution.

2.11 Conclusions

This chapter discusses the literature related to DSTATCOM, EV, PV, Single and Three phase grid and their control structure. On the basis of detailed review, research gaps are identified and finally objectives of the thesis are proposed.

Chapter 3

Design Aspects of Different Converter Configuration

This chapter includes the design aspects of different converter configurations. The design of DC link voltage, DC link capacitance, interfacing inductor, design of voltage and current sensors, design of gating circuit, design of PV array, design of DC-DC bidirectional converter etc. are presented in this chapter.

3.1 Design and Analysis of Single Phase Grid connected DSTATCOM

The proposed single phase grid connected system is shown in Fig 3.1. It comprises a single-phase, 50 Hz grid supply through a single-phase auto transformer. The supply, compensator, and load are connected at the PCC. The single phase VSC is connected in shunt with a DC link capacitor to simulate the DSTATCOM. Voltages and currents in the system are measured using LEM-made sensors. dSPACE1104 is a digital signal processor (DSP) that is employed to process input signals and generate appropriate gating pulses for the DSTATCOM's operation. In order to operate the VSC, four gating pulses are necessary. The designed interfacing inductors and the parameters is

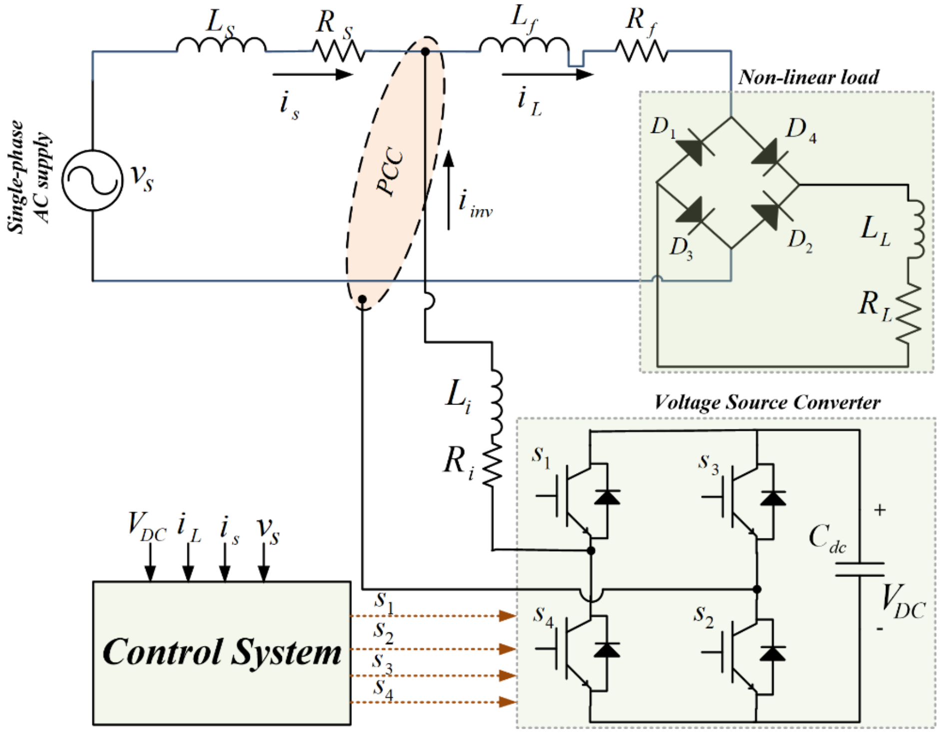

Fig 3.1 System diagram of single phase grid connected DSTATCOM

selected to connect the VSC to the PCC. Only nonlinear loads are types of loads that are examined in this analysis. The DSO is used to record the performance/system variables.

3.1.1 Calculation of DC link Voltage

The switching losses of IGBT switches ought to be injected with an adequate value of voltage from the DC link. For pulse width modulation (PWM) control to work properly in a single-phase system, the DC link voltage of the system must be higher than the peak supply voltage [272]. The single-phase system's peak value is estimated as

$$A_m = \sqrt{2}v_s \tag{3.1}$$

where, A_m is the peak amplitude of AC phase voltage, v_s is the source voltage of single phase system. The rating of single phase system is considered as 110V, 50Hz for simulation and experimental performance. The calculation of DC-link voltage can be given as:

$$V_{dc_{ref}} > A_m = \sqrt{2}v_s \tag{3.2}$$

The dc link voltage is calculated as 155V and it selected as 200V for the DSTATCOM operation.

3.1.2 Calculation of DC link Capacitance

The DC-link voltage of the VSC is extremely sensitive to the voltage of the input grid as well as the current of the load. It is important that the value of the DC-link capacitance be sufficiently high in order to maintain the DC-link voltage throughout the dynamics [272]. Calculating the DC-link capacitance can be done with the help of Eq. 3.3.

$$C_{dc} = \frac{v_g a i_s \tau g}{\frac{1}{2}\left(V_{dcref}^2 - V_{dcm}^2\right)} \tag{3.3}$$

The overloading factor is denoted by 'a' which is considered as 1.2. The source current is denoted by i_s whose maximum values is 8A, the time constant is denoted by τ (0.02s), the gain constant is denoted by g(0.5), the reference DC-link voltage is denoted by V_{dcref} (200V), and the minimum DC-link voltage is denoted by V_{dcm}(155.56V). By applying these values to Eq. 3.3. The computed values of C_{dc} is 1340μF.

$$C_{dc} \approx 1340\mu F \tag{3.4}$$

A value of DC-link capacitor higher than the calculated value has been chosen for simulation as well as experimental studies. The selected value of C_{dc} = 1500μF for further studies.

3.1.3 Calculation of Interfacing Inductor

An interfacing inductor is employed to eliminate current ripples. A larger inductance value enhances filtering efficacy; nevertheless, it concurrently increases power loss.

Therefore, the appropriate design of the interface or filter inductor (L_i) is essential and is shown in Eq.3.5.

$$L_i = \frac{m*V_{dc}}{4*a*f_s*\Delta i} \qquad (3.5)$$

In this case, m is the modulation index (m=1), V_{dcref} is the DC-link reference voltage, a is the overflow factor, f_s is the switching frequency, and Δi is the current ripple, which is set to 15% of the maximum current. For the purposes of modelling, the computed values of L_i is.

$$L_i \approx 2.77mH \qquad (3.6)$$

For simulation and experimental purpose, its value is selected as

$$L_i \approx 3mH \qquad (3.7)$$

3.1.4 Rating of IGBT Switches of DSTATCOM

The DSTATCOM is equipped with an IGBT switches. The IGBTs exhibit a low on-state voltage drop and a high voltage capability. Smoother turn-on/off waveforms are achieved through the use of IGBT. Additionally, the simplicity of driver circuit and the nearly zero gate drive current are additional benifit. The current limit and switching speed are the primary factors that determine the rating of switches. Given that the switching speed is 10 kHz and the I_{VSC} is 25 A, the SKM150GB12V IGBT module was chosen. The IGBT switch leg and schematic internal connection diagram of the IGBT switches employed is illustrated in Fig 3.3 (a-b). Three of these modules are employed in a three-phase SAPF. The IGBT specifications include a V_{CE} of 1200V, an I_C of 150A, a fs of 20kHz, a V_{GE} of 15V, and a top temperature range of -40°C to 150°C.

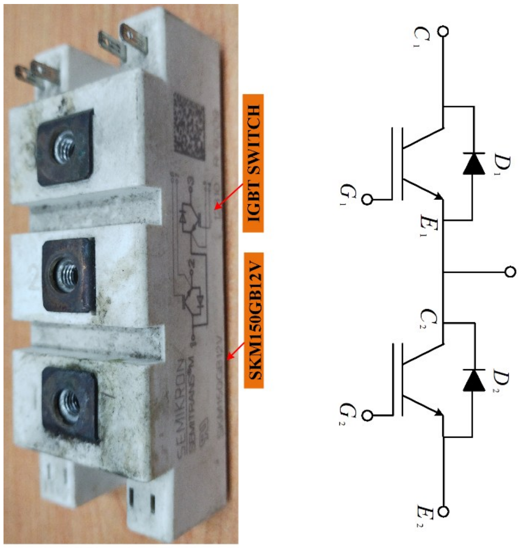

(a)

(b)

Fig 3.2 (a) Diagram of IGBT leg and (b) Schematic diagram of IGBT

3.1.5 Design of Voltage and Current Sensor Circuits

The design of voltage and current sensors are discussed in detail. In single phase systems two voltage and two current sensors are required.

(a) Design of Voltage Sensors

The LV-25P voltage sensors are used to measure the voltage across DC link capacitors and the voltage at the PCC. This sensor gives off a theoretical value of 25V and has a conversion ratio of 2500:1000. For this sensor to work, it needs a ±15V source. The signal for the input voltage is sent to the +HT and -HT terminals. The output voltage is measured across terminal M across resistance (Ro/p), and the amplification circuit is given another signal. Fig 3.3 shows connection diagram of the voltage sensor circuit and its developed circuit.

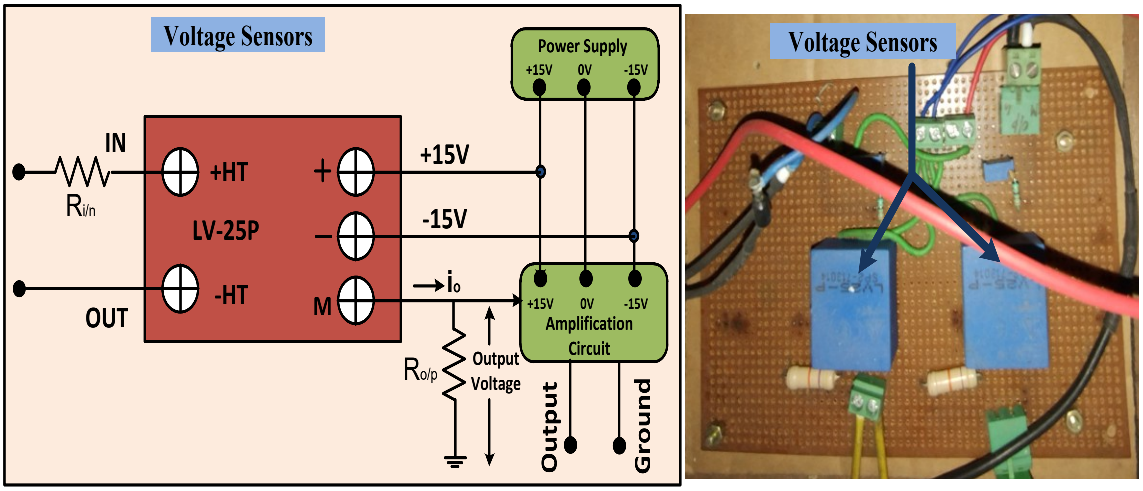

Fig 3.3 Circuit diagram of Voltage Sensor and developed sensor

(b). Design of Current Sensors

The LA-25P current monitor from LEM is used to measure both the grid current and the load

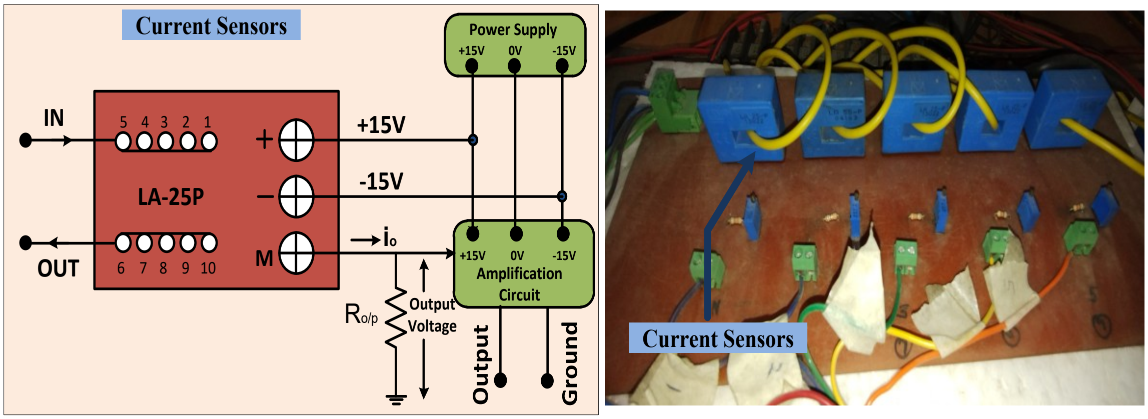

Fig 3.4 Circuit diagram of Current Sensor and developed sensor

current. It has a conversion ratio of 1000:1. This sensor needs a power source of ±15V to work. The output voltage is measured across resistance (Ro/p), and the signal is sent to the amplifier circuit. The connection diagram of current sensor and its developed sensor is shown in Fig 3.4.

3.1.6 Design of Amplifier Gating Circuit for IGBT Driver

The dSPACE-1104/MicroLab box 1202 generates PWM signal of nearly +5V and the voltage to needed to trigger the IGBTs is +15V. Therefore, an amplification circuit of gate driver as has to be connected between the dSPACE-1104/MicroLab box 1202 as shown in Fig 3.5 (a) and the experimental model is shown in Fig 3.5 (b). It consists of AND Gate IC-SN7406N and transistor 2N2222A. IC requires +5V DC supply and NPN transistor needes +15V DC supply to operate. The driver circuit contains SKYPER-32 pro with evaluation board as shown in Fig 3.5 (c) .

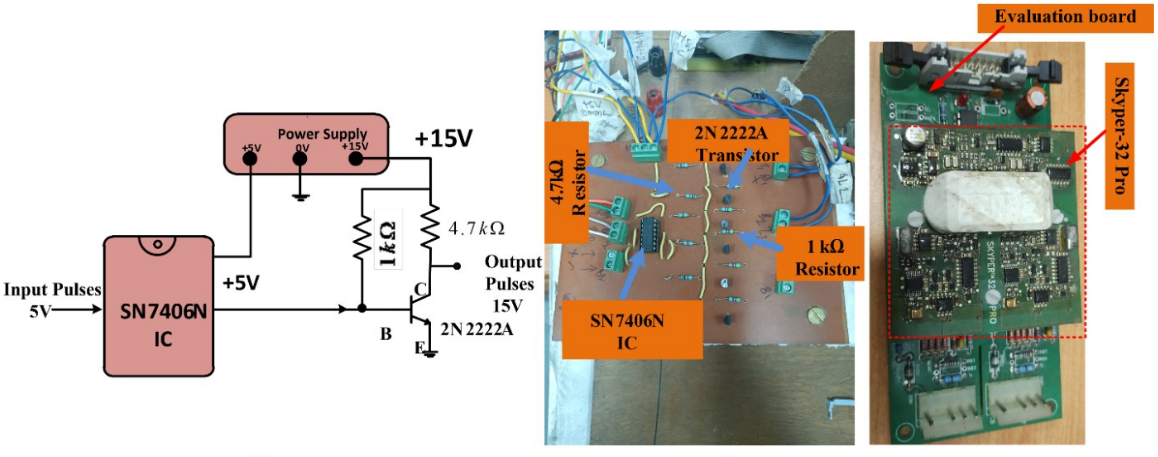

(a) (b) (c)

Fig 3.5 (a) Connection diagram of gate driving circuit (b) Practical Implementation of amplifier driver circuit and (c) Evaluation board with Skyper-32 Pro.

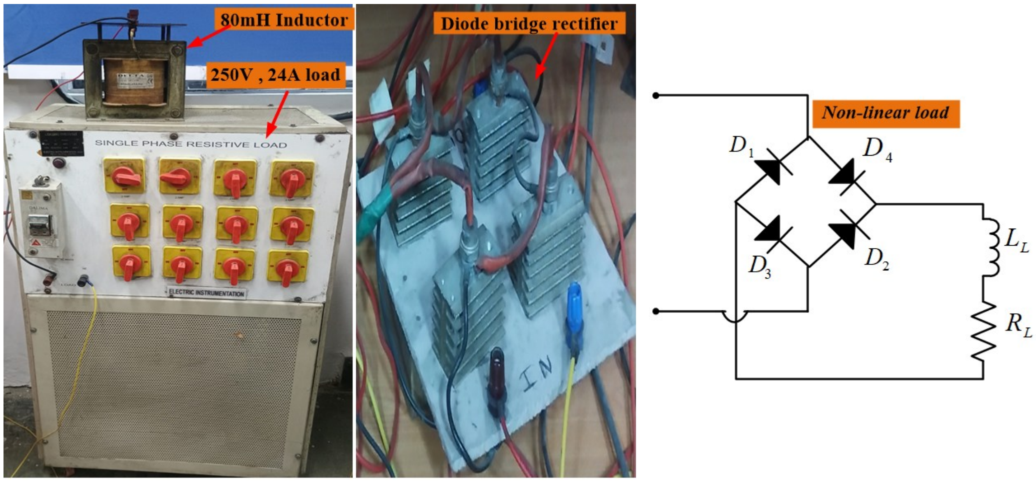

(a) (b) (c)

Fig 3.6 (a) Image of linear load (b) image of diode bridge rectifier (c) circuit of non-linear load

3.1.7 Rating of Non-linear loads

The linear loads of a rating of 250 V and 24 A are connected in single-phase systems. Non-linear loads are connected through a diode bridge rectifier as shown in Fig 3.6. The DC side of the diode bridge rectifier contains a variable resistor (20-120Ω) and a fixed inductor of 80 mH.

3.1.8 Experimental Set-up in the laboratory

In the laboratory, single phase grid connected DSTATCOM is developed to verify the feasibility of proposed technique. The system rating is 110V rms and 50 Hz frequency. This hardware setup requires two voltage sensors (LV-25P) for sensing (v_s, V_{dc}) and two current sensors (LA-25P) for sensing (i_s, i_L). These sensed voltage and current signals are processed by DSP (dSPACE 1104) to generate four gating pulses for VSC. The VSC is controlled as a DSTATCOM to inject compensating current at point of common coupling. Hardware results for steady state and dynamic states are captured using Power Analyzer and DSO respectively. The experimental setup is shown in Fig 3.7.

Fig 3.7 Experimental setup of single phase DSTATCOM

3.2 Design and Analysis of Three Phase Grid connected DSTATCOM

Fig 3.8 depicts system diagram of three phase grid connected DSTATCOM. It uses a three-phase auto transformer to receive power from the grid at 50 Hz in three phases. There is a connection for the supply, compensator, and load at the PCC. LEM based sensors are used to measure the system voltages and currents. In order to run DSTATCOM, a DSP called Microlab box 1202 processes input signals and generates the correct gating pulses. A three phase VSC shunted with a DC link capacitor is used to imitate the DSTATCOM. The operation of VSC requires six gating pulses. To link the VSC to the PCC, the interfacing inductors are created and selected with the proper value. In this study, the nonlinear loads are taken into account. A DSO is used to record the performance/system variables.

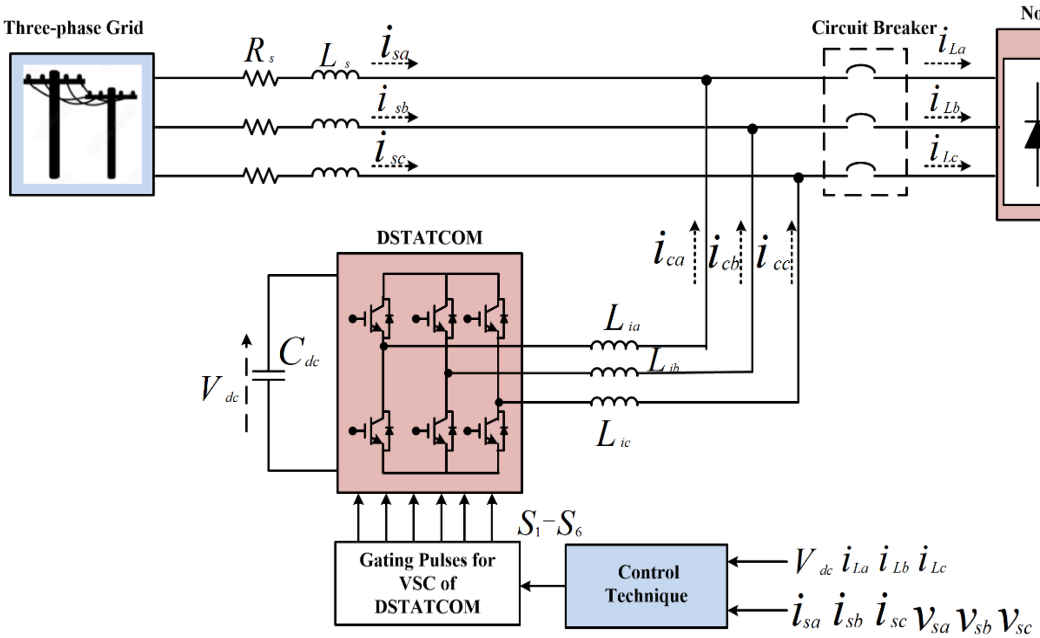

Fig 3.8 System diagram of three phase grid connected DSTATCOM

3.2.1 Calculation of DC link Voltage

The DC-link voltage will be used to contribute reactive power to the grid. Consequently, the grid voltage employed must be slightly higher than the DC-link voltage of the three-phase VSC [273]. It is possible to determine the grid voltage's magnitude by employing the factor Eq. 3.8.

$$A_m = \frac{2\sqrt{2}v_{LL}}{\sqrt{3}} \tag{3.8}$$

where A_m is the maximal amplitude of the AC phase voltage and v_{LL} is the line source voltage of the three-phase system. The 110V, 50Hz is the rating of the experimental performance. The DC-link voltage can be determined by the following formula:

$$V_{dc_{ref}} > A_m = \frac{2\sqrt{2}v_{LL}}{\sqrt{3}} \tag{3.9}$$

In the experiment, the DC link reference value is 155V and is set at 200V for the DSTATCOM operation in three phase grid connected systems.

3.2.2 Calculation of DC link Capacitance

A VSC's DC-link voltage is extremely sensitive to the input grid voltage and load current. A high enough DC-link capacitance value is required to keep the DC link voltage constant throughout dynamics [273]. Eq 3.10 can be used to get the capacitance of the DC link.

$$C_{dc} = \frac{6v_{ph}i_s a\tau g}{\left[V_{dc_{ref}}^2 - V_{dc_m}^2\right]} = 3172\mu\text{F} \tag{3.10}$$

where, v_{ph} denotes the phase voltage of a three-phase system, i_s represents the source current (i_s=8A), 'a' signifies the overloading factor, which is set at 1.2 for this application, 'τ' indicates the time constant, established at 0.02 seconds, 'g' refers to the gain constant (g=0.4), V_{dc_m} is the minimum DC link voltage ($V_{dc_m} = 155$), and $V_{dc_{ref}}$ is the DC link reference voltage ($V_{dc_{ref}} = 200V$). The DC link capacitance is selected as 3300µF.

3.2.3 Calculation of Interfacing Inductor

Current ripples are filtered out using an interface inductor. Better filtering is provided by inductors with greater values, but the loss is also higher [273]. As a result, it is crucial to properly design the interface or filter inductor (L_i), which is done by calculating by Eq.3.11.

$$L_i = \frac{\sqrt{3}mV_{dc_{ref}}}{12af_s\Delta i} = 4.8mH \tag{3.11}$$

where, m is the modulation index of 1, a is overloading factor of 1.2, f_s is the switching frequency of 10kHz and Δi is the ripple current and it is considered 10% of the maximum current. In experimental 5mH is selected.

3.2.4 Rating of IGBT Switches of DSTATCOM

The DSTATCOM is equipped with an IGBT switches. The IGBTs exhibit a low on-state voltage drop and a high voltage capability. Smoother turn-on/off waveforms are achieved through the use of IGBT. Additionally, the simplicity of driver circuit and the nearly zero gate drive current are additional benifit. The current limit and switching speed are the primary factors that determine the rating of switches. Given that the switching speed is 10 kHz and the IVSC is 25 A, the SKM150GB12V IGBT module was chosen. The IGBT switch leg and schematic internal connection diagram of the IGBT switches employed is illustrated in Fig 3.3 (a-b). Three of these modules are employed in a three-phase SAPF. The IGBT specifications include a VCE of 1200V, an IC of 150A, a fs of 20kHz, a VGE of 15V, and a top temperature range of -40°C to 150°C. Here, three legs of IGBT switches are required for three phase VSC.

3.2.5 Rating of Non-linear loads

The linear loads of a rating of 250 V and 24 A are connected in single-phase systems. Non-linear loads are connected through a diode bridge rectifier as shown in Fig 3.6.

The DC side of the diode bridge rectifier contains a variable resistor (20-120Ω) and a fixed inductor of 80 mH.

3.2.6 Experimental Set-up in the laboratory

Fig 3.9 depicts a experimental setup of three phase grid connected DSTATCOM that includes sensors, the Microlab box 1202 controller, VSC, interfacing inductors, Nonlinear load, programable DC supply, power analyzer, DSO, Point of Common Coupling (PCC) and a three-phase AC supply. three phase grid connected DSTATCOM systems are powered by a three-phase variable voltage transformer. The output of the three-phase variac and three phase DSTATCOM is connected to the PCC and load terminals. The DSTATCOM is connected to the three-phase power supply by interface inductors. The ADC ports of the Microlab box 1202 are used to sense and apply the following AC and DC voltages and currents: v_{sa}, v_{sb}, v_{sc}; i_{La}, i_{Lb}, i_{Lc}; and V_{dc}, the DC link voltage of the DSTATCOM. It is via the Digital to Analog Channel (DAC) of the Microlab box 1202 that the output gating pulses are produced, following signal processing with the proper control algorithms. A voltage level amplifier circuit then feeds these signals into the IGBT switches of the DSTATCOM. It is necessary to have two independent DC sources in order to

Fig 3.9 Experimental setup of three phase DSTATCOM

power the sensors circuit (-15 to +15 V) and the voltage amplifier circuit and IGBT switches (0-30 V).

3.3 Design and Description of Five Level CHB-MLI based DSTATCOM

A five-level cascaded H-bridge design is depicted in the circuit diagram as shown in Fig 3.10. A rectifier load with an R-L branch linked to the DC side receives power from a single-phase AC source. A source's inductance and resistance are represented by the symbols L_S and R_S, respectively. PQ issues can also be solved by connecting the Five Level Cascaded H-Bridge (5L CHB) converter in a shunt configuration utilizing two H-bridges. Variables such as source voltage v_s, source current i_s, load current i_L, and total dc link voltage $(V_{dc1}+V_{dc2})$ are required for the control of the given system. These are detected using current and voltage sensors that are based on LEMs. The ADC channels of the DSP (dSPACE 1104) receives the voltage and current signals that are sensed. For DSTATCOM, the necessary eight gating pulses are generated by the DSP. The converter is equipped with an interface inductor (L_i) to dampen the AC output ripples.

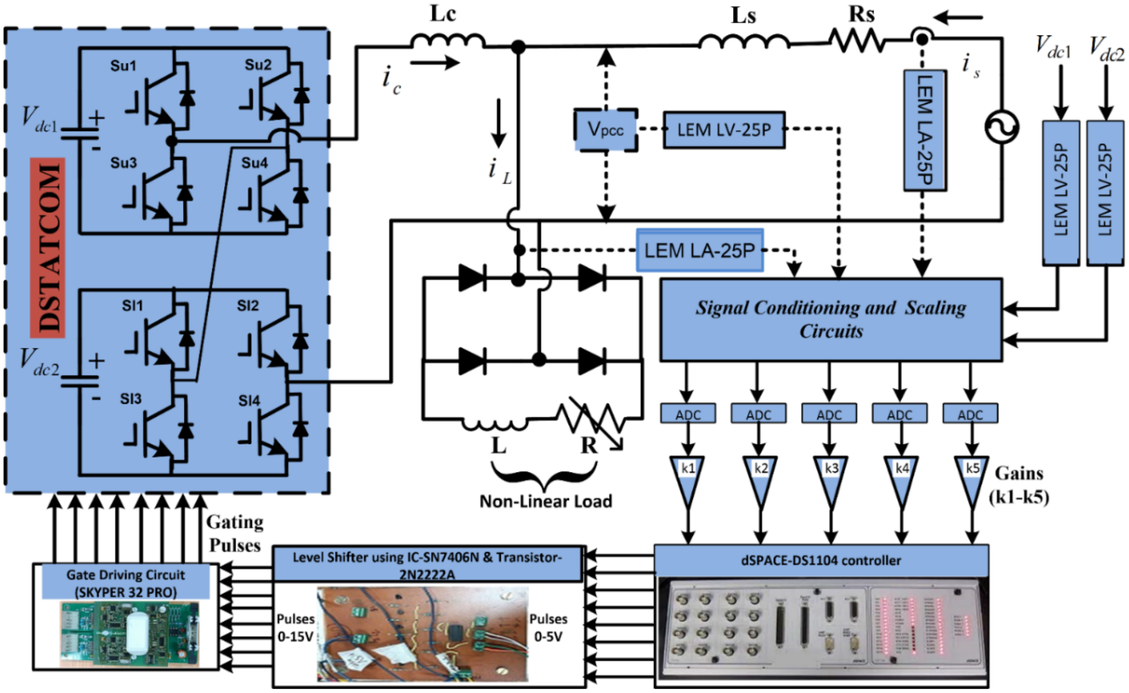

Fig 3.10 System Diagram of 5-level Distribution System

3.3.1 Inverter and Driver Circuit

A single-phase AC supply, dSPACE 1104 board, programmable DC supply, voltage and current sensors, two H-bridge VSC, DSO, interface inductor, nonlinear load are the main components needed for the setup. All components of a single-phase grid-connected system's design is thoroughly examined. The design quantities listed below have been taken into consideration.

3.3.1.1 DC link voltage
3.3.1.2 Interfacing inductors
3.3.1.3 DC link capacitance
3.3.1.4 Current and Voltage sensors
3.3.1.5 Design of pulse generation

3.3.1.1 Design of DC link Voltage

Usually, the DC link voltage must be higher than the peak of supply voltage for effective compensation. The DC capacitor voltage can be calculated as [274]

$$V_{dc-ref} = \frac{\sqrt{2}v_s}{\sqrt{3}m_f} \tag{3.12}$$

Here, v_s = 110V is the grid voltage, m_f=0.9 is the modulation index. The DC link voltage across capacitor in each H-bridge is calculated to be 99.97V. So, the total DC link voltage is 200V for 5L CHB converter.

3.3.1.2 Design of Interfacing Inductor

The value of L_i is calculated as [274]

$$L_i = \frac{V_{dc,ref}}{12\,(m-1)\,f_{sw}\,\Delta I_{cr-pp}} \tag{3.13}$$

Considering the total DC link voltage V_{dc-ref} = 200V, switching frequency f_{sw} = 5kHz, m= 5 representing voltage levels and peak to peak ripple current is ΔI_{cr-pp}= 0.2, the value of interfacing inductor is found to be 4.14mH. Hence, in the proposed system 5mH is selected in simulation studies as well as experiments.

3.3.1.3 Design of DC link Capacitance

The 5L CHB inverter contains two DC link capacitors and each capacitance is calculated using the following relation [274]

$$C_{dc} = \frac{K_L v_s i_c T}{2(V_{dc-ref}^2 - V_{dc}^2)} \tag{3.14}$$

where V_S is taken as 110V AC, i_c = 3.4A, T=0.02sec, V_{dc-ref} = 200V, V_{dc}=190V, considering a voltage drop of 10V, C_{dc}=2205.64 µF is calculated and for this system it is taken as 2400µF for simulation studies and 2500µF for experimental validation.

3.3.1.4 Design of voltage and current sensor

The design of voltage and current sensors are discussed in detail. In single phase systems two voltage and two current sensors are required.

(a) Design of Voltage Sensors

The LV-25P voltage sensors are used to measure the voltage across DC link capacitors and the voltage at the PCC. This sensor gives off a theoretical value of 25V and has a conversion ratio of 2500:1000. For this sensor to work, it needs a ±15V source. The signal for the input voltage is sent to the +HT and -HT terminals. The output voltage is measured across terminal M across resistance (Ro/p), and the amplification circuit is given another signal. Fig 3.3 shows connection diagram of the voltage sensor circuit and its developed circuit.

(b). Design of Current Sensors

The LA-25P current monitor from LEM is used to measure both the grid current and the load current. It has a conversion ratio of 1000:1. This sensor needs a power source of ±15V to work. The output voltage is measured across resistance (Ro/p), and the signal is sent to the amplifier circuit. The connection diagram of current sensor and its developed sensor is shown in Fig 3.4.

3.3.1.5 Design of pulse generation

Phase shift modulation control technique [275] is employed to generate the switching pulses of CHB-MLI. A signal generated by the sensed source current (i_s) and reference supply current (i_{ref}) is compared to a triangular carrier wave. The carrier signals in this modulation scheme are phase-shifted by angle and are represented by the following:

$$\phi_{cr} = \frac{360^0}{m-1} \tag{3.15}$$

where where m is the number of levels of output voltage. As a reference signal, the modulating signal is chosen in the proposed CHB-MLI SAPF. In order to determine the switching pulses of IGBT switches, it is compared with a triangular carrier signal (f=5kHz) at each instant. As shown in Fig 3.11, the PS-PWM technique is characterised by the modulation frequency (m_f) index, which is shown in Eq. 3.16.

$$m_f = \frac{f_{cr}}{f_m} \tag{3.16}$$

where f_{cr} and f_m are the frequencies of the carrier and modulating signals, respectively.

The inverter's switching frequency can be determined using the following equation.

$$f_{inv} = (m-1) f_m \times m_f \tag{3.17}$$

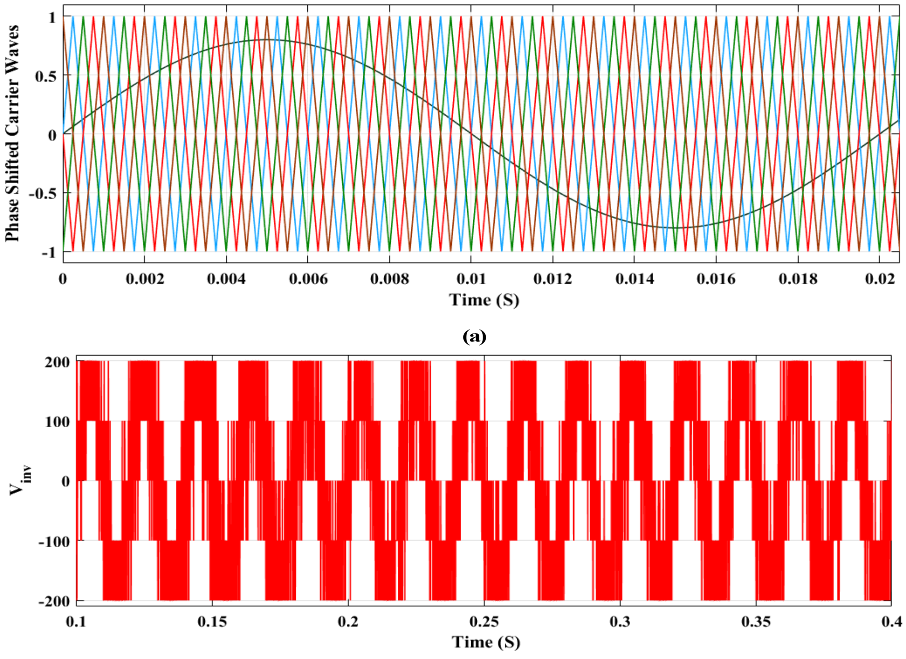

(a)

(b)

Fig 3.11 Waveform showing (a) Phase Shifted -PWM techniques of 5L-CHB converter (b) five level converter voltage output of CHB.

3.3.2 Power Supply Circuit

The design of power supply and its implemented hardware is shown in Fig 3.12. It is the combination of transformer, Integrated circuits (IC), Diode bridge rectifier (DBR) and Capacitors.

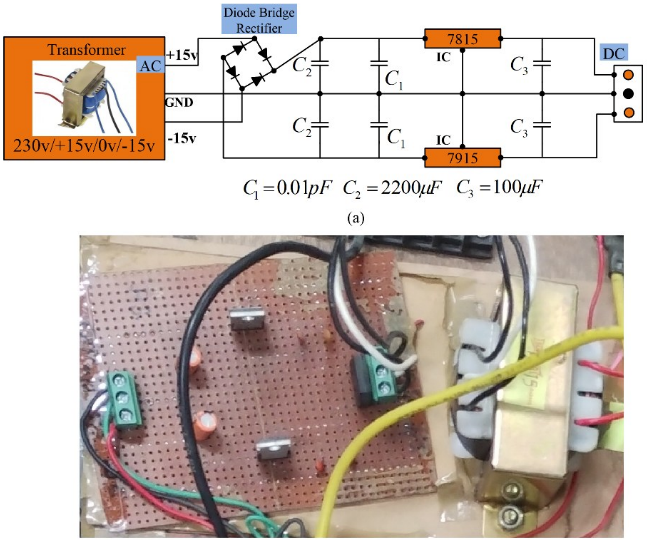

(a)

(b)

Fig 3.12 (a) Power supply circuit (b) Implemented hardware setup of power supply

The power supply is designed for 230V AC and ±15V DC. It is used to supply DC power to sensors and gate driver circuit.

3.4 Design and Description of Single Phase Grid Interfaced EV Charging Systems

The complete circuit diagram of the developed system incorporating grid, bidirectional AC-DC converter and bidirectional DC-DC converter for EV charger is shown in Fig 3.13. A nonlinear load is connected at the PCC which can receive power from a single-phase AC supply. The source resistance and inductance are shown in Fig 3.13 as R_S and L_S, respectively. It is observed that the connected load is nonlinear which distorts the load current. A shunt configuration of AC-DC converter is applied as an active filter to reduce supply-side current harmonics. The proposed system's control is based on input variables such as source voltage (v_s), source current (i_s), load current (i_L), DC link voltage (V_{dc}), battery voltage (V_{bat}) and battery current (I_{bat}). These variables are measured using LEM-based current and voltage sensors. These measured voltage and current signals are subsequently analysed by the Real Time System (RTS's) controllers of ADC channel. The designed control technique is applied to create the pulses of gate terminal via digital I/O channels. The gating terminal pulses have a magnitude of +5V, which is amplified to +15V by the level shifter circuit. An interface inductor (Lc) is interfaced with the bidirectional AC-DC converter to suppress the output ripples from the inverter.

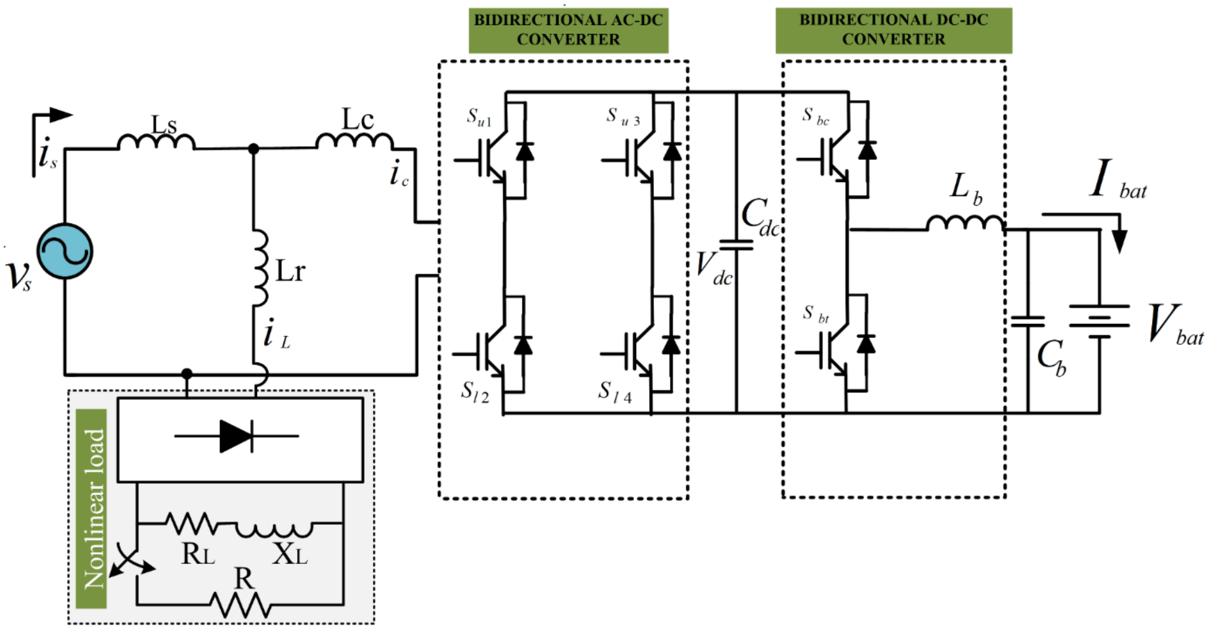

Fig 3.13 System diagram of single phase grid connected EV charging systems

3.4.1 AC-DC Converter and Gate Driver Circuit

The circuit design and its developed bidirectional AC-DC converter is depicted in Fig 3.14. Two IGBT legs make up the AC-DC converter (Semikron model number: SKM75GB12T4). Each leg has two IGBT switches and is rated at 1200 V/75 amps. Each IGBT leg's schematic is displayed in Fig 3.14. The DC link capacitor which is connected at the DC side, has an 800V and 1650 µF rating. To activate the switches, 15V pulses are needed, and the gate pulses are applied to driver.

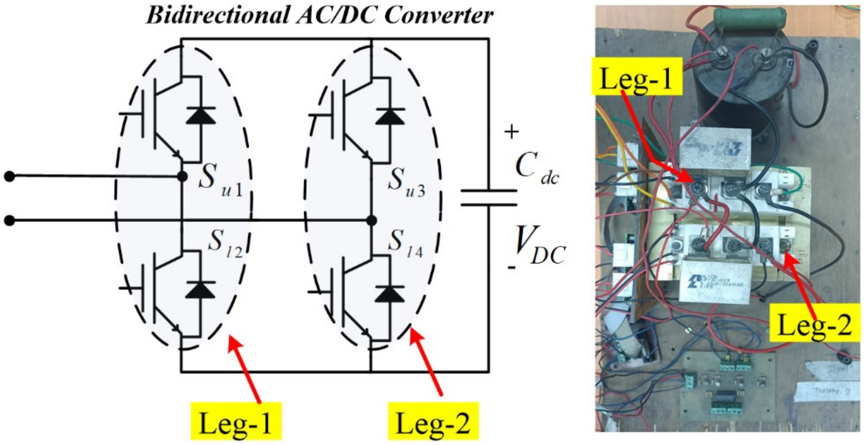

Fig 3.14 Design of bidirectional AC/DC Converter and developed converter

3.4.1.1 Design of DC link Voltage [276]

In single-phase EV charging systems, the DC link voltage must be greater than the peak of supply voltage. It is calculated as

$$V_{dc} = \sqrt{2}V_s = \sqrt{2} * 40 = 56.56\,V \tag{3.18}$$

where, V_{dc} is the peak amplitude of AC phase voltage, v_s is the source voltage of single phase system. The rating of single phase system is 40V, 50Hz for the experimental system. The dc reference value is higher than dc link voltage. The calculated V_{dc} is 56.56V and reference dc voltage (V_{dc_ref}) is set at 80V.

3.4.1.2 DESIGN OF INTERFACING INDUCTOR [276]

The calculation of interfacing inductor is already discussed in Section 3.1.3. The formula of interfacing inductor (L_i) is

$$L_i = \frac{m * V_{dc}}{4 * a * f_s * \Delta i} = 2.77mH \tag{3.19}$$

Here, m is the modulation index (m=1), V_{dcref} is DC-link reference voltage, a(1.2) is the overloading factor, f_s (10kHz) is the switching frequency and Δi is the ripple content in the current and it is considered as 5% of maximum current. The interfacing inductors of 3mH are selected for both simulation and experimental setup.

3.4.1.3 Design of DC link Capacitance

It is already discussed in section 3.1.2. The formula of DC-link capacitance is shown in Eq. 3.20.

$$C_{dc} = \frac{v_g a i_s \tau g}{\frac{1}{2}\left(V_{dcref}^2 - V_{dcm}^2\right)} \tag{3.20}$$

Here, the source current denoted by (i_s) (5A), the reference DC-link voltage is denoted by V_{dcref} (80V), and the minimum DC-link voltage is selected by V_{dcm} (56.56V). The result of applying these values to Eq. 3.21 is

$$C_{dc} \approx 1499\mu F \tag{3.21}$$

So, the selected value of C_{dc} is taken as1500µF.

3.4.2 DESIGN OF BIDIRECTIONAL DC-DC CONVERTER

As shown in Fig 3.15, the BDDC converter comprises a battery bank, filter capacitance (C_b), filter inductance (L_b), and two IGBT switches (S_{bc}, S_{bt}). The battery capacity is 48V, 42 Ah, with an initial state of charge (SOC) of 80% and a battery response time of 0.1s. The inductor filter design in buck mode is carried out as [277]. The value of D is selected as 0.6.

$$D = \frac{V_{bat}}{V_{dc}} = 0.6 \tag{3.22}$$

$$L_b = \frac{(Vdc - V_{bat})D}{\Delta I_{bat} * f_s} = 4.8\,mH \tag{3.23}$$

Here it is assumed that switching frequency is 5kHz and current ripple is 10% of battery current. For the inductor filter design in boost mode the duty cycle and inductor value are 5mH selected.

$$C_b = \frac{(1-D)V_{bat}}{8 * L_b * \Delta V_{bat} * f^2} \approx 40\mu\text{f} \tag{3.24}$$

The battery voltage is represented by V_{bat}, the DC link voltage by V_{dc} and the charging current ΔI_{bat} is 10% of I_{bat}, the switching frequency is considered as 5 kHz.

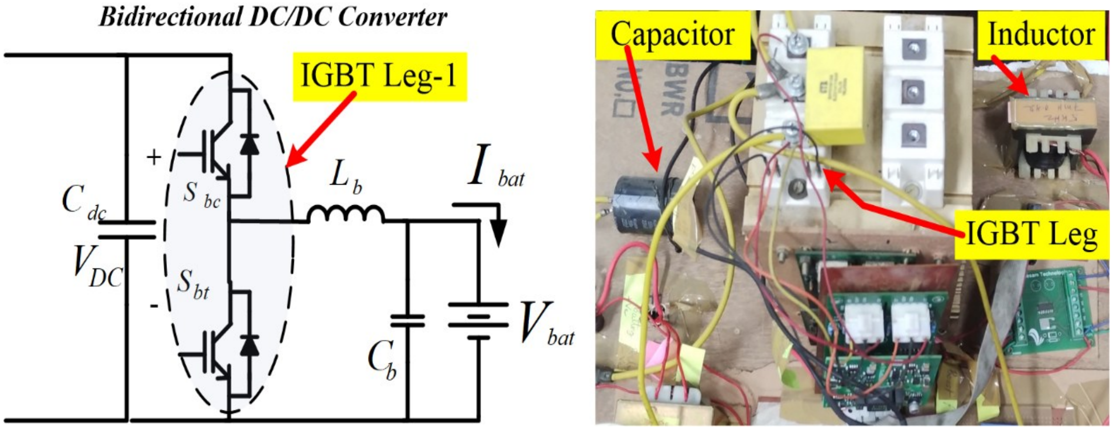

Fig 3.15 Design of bidirectional DC/DC Converter and developed converter

3.4.3 Design of Amplifier Gating Circuit for IGBT Driver

The dSPACE-1104/MicroLab box 1202 generates PWM signal of nearly +5V and the voltage to needed to trigger the IGBTs is +15V. Therefore, an amplification circuit of gate driver as has to be connected between the dSPACE-1104/MicroLab box 1202 as shown in Fig 3.5 (a) and the experimental model is shown in Fig 3.5 (b). It consists of AND Gate IC-SN7406N and transistor 2N2222A. IC requires +5V DC supply and NPN transistor needes +15V DC supply to operate. The driver circuit contains SKYPER-32 pro with evaluation board as shown in Fig 3.5 (c).

3.4.4 Design of Solar PV array

A standard Kyocera Solar KC175GT PV module from the Simulink library was utilized for modeling a 700W PV array. Fig. 3.16 shows the I-V and P-V characteristic of solar PV system. The design of inductor and capacitor of boost converter are shown in Eq. 3.25-3.26.

$$L_p = \frac{D * V_{mp}}{\Delta I_{PV} * f_{sw}} = 1.20\, mH \tag{3.25}$$

Lp is determined to be 1.20mH and is taken to be 3mH. The variables are D (duty cycle), Vmp (voltage at maximum power), ΔI_{PV} (inductor current ripple), and f_{SW} (IGBT switching frequency) is 10kHz.

$$C_p = \frac{D * I_{out}}{\Delta V_{out} * f_{sw}} = 86\mu F \tag{3.26}$$

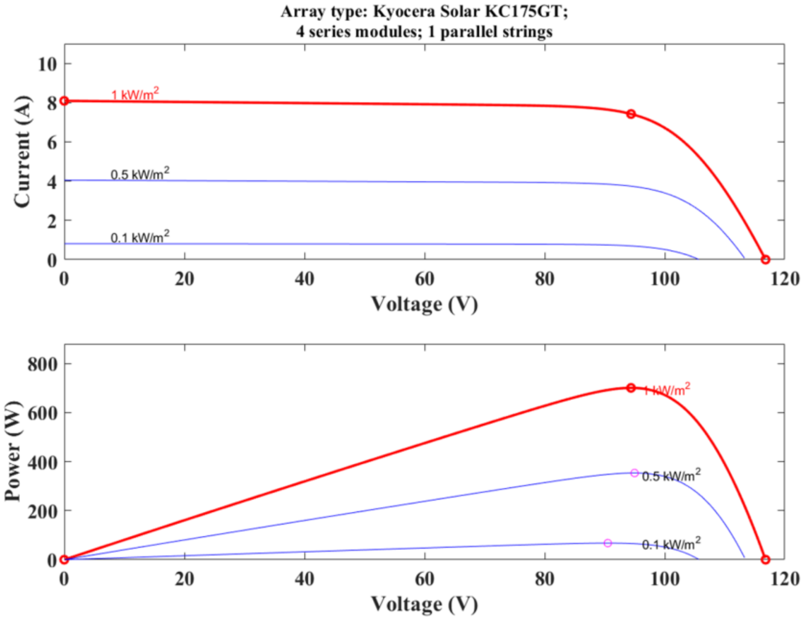

Fig 3.16 Characteristic of I-V and P-V curve at 1000W/m^2 irradiance.

where P_{PV} is the maximum power 700W selected as , I_{out} is the output current, ΔV_{out} is the ripple in boost output voltage which is 10% of the output voltage V_{out} and V_{out} is 58 V, Cp is selected to be 100μF.

Table 3.1: Parameters of single phase grid connected DSTATCOM

S.No.	Control parameters	Simulation values	Experimental values
1.	AC voltage Source (v_s)	110V (rms)	110V (rms)
2.	DC link voltage (V_{dc})	200V	200V
3.	DC link capacitance (C_{dc})	1340μF	1500μF
4.	Interfacing inductor (L_i)	2.77mH	3mH
5.	Non-linear load	R=30Ω and L=100mH	R=120Ω and L=80mH
6.	Switching frequency	10kHz	10kHz
7.	PI controller gains	K_p=0.1, K_i=5	K_p=0.15, K_i=5

Table 3.2: Parameters of three phase grid connected DSTATCOM

S.No.	Control parameters	Simulation values	Experimental values
1.	AC voltage Source (v_s)	110V (rms)	110V (rms)
2.	DC link voltage (V_{dc})	200V	200V
3.	DC link capacitance (C_{dc})	3300μF	4700μF
4.	Interfacing inductor (L_i)	4.8mH	5mH
5.	Non-linear load	R=30Ω and L=100mH	R=120Ω and L=80mH
6.	Switching frequency	10kHz	10kHz
7.	PI controller gains	K_p=0.5, K_i=2	K_p=0.08, K_i=0.1

Table 3.3: Parameters of five level CHB-MLI based DSTATCOM

S.No.	Control parameters	Simulation values	Experimental values
1.	AC voltage Source (v_s)	110V (rms)	110V (rms)
2.	DC link voltage (V_{dc})	200V	200V

3.	DC link capacitance (C_{dc})	2400µF	2500µF
4.	Interfacing inductor (L_i)	5mH	5mH
5.	Non-linear load	R=30Ω and L=100mH	R=120Ω and L=80mH
6.	Switching frequency	20kHz	5kHz
7.	PI controller gains	K_p=0.1, K_i=5	K_p=0.05, K_i=2

Table 3.4: Parameters of single phase grid interfaced EV charging system

S.No.	Control parameters		Simulation values	Experimental values
1.	AC voltage Source (v_s)		110V (rms)	40V (rms)
2.	DC link voltage (V_{dc})		200V	80V
3.	DC link capacitance (C_{dc})		1500µF	1500µF
4.	Interfacing inductor (L_i)		2.77mH	3mH
5.	Non-linear load		R=30Ω and L=100mH	R=120Ω and L=80mH
6.	Battery capacity		96V, 42Ah	48V, 42Ah
7.	Switching frequency	AC-DC Converter	10kHz	10kHz
		DC-DC Converter	5kHz	5kHz
8.	Duty Cycle		0.48	0.6
9.	PI controller gains	AC-DC Converter	K_p=0.5, K_i=10	K_p=0.08, K_i=0.15
		DC-DC Converter	K_p=0.5, K_i=5	K_p=0.1, K_i=5
10.	Battery Inductance (L_b)		3.12mH	≈5mH
11.	Battery Capacitance (C_b)		≈80µF	40µF

3.5 Conclusion

The design of single-phase and three phase grid-connected DSTATCOM, five level inverter based DSTATCOM and single phase grid connected EV charging system is performed in this chapter. The detailed parameters of different systems are also tabulated in Table 3.1 to Table 3.4. Based upon the detailed analysis and design equations experimental prototype setup is developed. Along with the design aspects of CHB-MLI 5-level inverters, its switching logic aspects has also been discussed in this chapter. At the end of the chapter a three-phase grid-connected EV with PV system is considered which is capable of accommodating a PV array and EV. This configuration will be very useful when the impact of EV system will increase in near future. The performance aspects of these configuration is studied in detail in subsequent chapters.

Chapter 4

Performance Analysis of Single Phase and Three Phase Grid Connected DSTATCOM

This chapter discusses and analyzes the single phase and three-phase grid-connected DSTATCOM system. The designed system is then modeled in MATLAB/Simulink. The steady state and dynamic waveforms for different control algorithms are presented and results are analysed. The prototype experimental setup of both single phase and three phase system are developed in the laboratory. The experimental setup uses power analyser, DSO, dSPACE 1104, Microlab box 1202, loads etc. The performance of the proposed control algorithms system is compared with the conventional control algorithms.

4.1 Introduction

In this chapter, the mathematical analysis of Adaptive Leaky Least Mean Fourth (ALLMF), Adaptive Radial Basis Functional Neural Network (A-RBFNN) and Notch filter are presented. These control algorithms are applied to control single phase VSC as well as three phase VSC. The VSC is connected in single phase and three power distribution system and modelled as a compensator. The voltage across DC links of the VSC is regulated to reference value by the proposed control algorithms. The closed loop system is designed and developed to mitigate Total Harmonic Distortion (THD) in the source current and improve power quality of the proposed system. The system is analyzed for steady state and dynamic state condition and the results are verified on the hardware prototype developed in the laboratory. The complete system comprising the grid, load and compensator is modeled in MATLAB/SIMULINK. The simulation and experimental results with each algorithm are discuss in detail. The comparative analysis of % Total Harmonic Distortion (THD) are also shown at the end. The proposed Adaptive Leaky Least Mean Fourth control algorithm is also compared with conventional Notch filter and Adaptive Radial Basis Functional Neural Network (ARBFNN) control algorithm on several parameters.

4.2 Brief theory and Mathematical Analysis of Different Control Algorithms

The description and mathematical analysis of Notch Filter (NF), Adaptive Leaky Least Mean Fourth (ALLMF) control algorithm, and Adaptive Radial Basis Functional Neural Network

(ARBFNN) control algorithm are presented below.

4.2.1 Mathematical Analysis of Conventional Notch Filter (NF) Control Algorithm

The NF is generally developed to reject all undesired frequencies (f) of the signal. NF are essentially bandpass or band reject filters, and as such, they are utilized as selector or rejector circuits in a variety of applications. [278].

This filter design involves two parameters, damping constant (ζ) and constant frequency (ω). In NF, the mechanism is to control the ζ and in this system the frequency is assumed to be constant. Moreover, due to constant frequency, the computational burden in the notch filter is reduced. Basically, notch filter uses two integrators to extract the fundamental component from the input signal. Bandwidth and settling time are varied by changing the damping constant (ζ). The NF circuit diagram is depicted in Fig 4.1. The transfer function of NF is shown in Eq. 4.1.

$$G(s) = \frac{s^2 + \omega^2}{s^2 + \xi\omega + \omega^2} \tag{4.1}$$

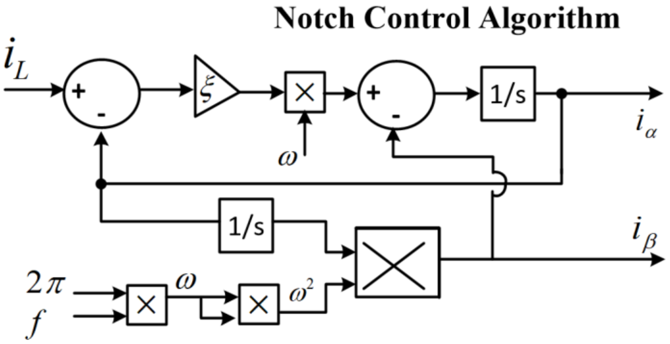

Fig 4.1 Circuit diagram of notch filter

4.2.2 Mathematical Analysis of Adaptive Radial Basis Function Neural Network Algorithm

The Conventional Radial Basis Function (CRBF) Neural Network has the capability to approximate any continuous function with accuracy, if there are enough hidden neurons. The CRBF Neural Network also has the benefit of being a universal approximator, which means it can approximate any function regardless of its complexity or dimension. The CRBFNN structure is shown in Fig 4.2(a). The structure contains three layers and it is a feed-forward network. The first layer is the input layer that receives the input data, which is typically a vector of values that represent the characteristics of the data under analysis and the input signals (x) travel from this layer to the second layer. The second layer is a hidden layer made up of RBF neural units. A Gaussian function's centre is represented by each neuron in the hidden layer. Each neuron's level of activation indicates how near the input vector is to the centre point that neuron represents. The third layer is known as the output layer and it is a linear combination of activation function from the hidden layer. The weights are updated in the output layer with LMS control technique.

Neural networks are proven to have good convergence, simple structure and faster learning capability. In Fig 4.2(b), the circuit diagram of CRBFNN controller is shown. Here, the weight is updated with the help of LMS algorithm. The load current (i_L) is passed through activation function (f_k) to estimate the actual output (L_{OUT}) which is compared with desired output d(n) to estimate error e(n). The updated weight is calculated by LMS control technique.

Fig 4.2 (a) also shows, the input layer of the p_{th} node $X_p=[x_1,x_2,....x_n]$, the centre vector of the k_{th} node $g_k=[g_1,g_2,.....g_m]$, Euclidean distance between the input layer and RBF layer is ||dist||, bias width of k^{th} node is b_k.

The activation function of k^{th} node in the RBF layer is

$$f_k = \exp(-S_k^2 / 2b_k^2) \tag{4.2}$$

where,

$$S_k = \| X_p - g_k \|$$

$$f_k = \exp(-\| X_p - g_k \|^2 / 2b_k^2) \qquad k=1,2......m,\ p=1,2......n \tag{4.3}$$

Now, L_{OUT} is the actual output of CRBFNN which is generated after the hidden layer and weight updation,

$$L_{out} = w_{p1}f_1 + w_{p2}f_2 + ... + w_{pm}f_m \tag{4.4}$$

$$L_{out} = \sum_{r=1}^{m} w_{pr} f_k \tag{4.5}$$

where, $w_{p1},w_{p2},........,w_{pm}$ are the updated weights.

In CRBFNN, the weight is updated with the help of Least Mean Square (LMS) controller and the error as shown in Eq. (4.6-4.7).

$$w(t+1) = w(t) - \gamma \frac{\partial C(t)}{\partial w(t)} \tag{4.6}$$

$$e(n) = [d(n) - L_{OUT}] \tag{4.7}$$

where, C(t)= [1/2 e^2(t)] denotes the minimum cost function and γ denotes the convergence factor having value less than 1.

The CRBFNN has fast self-learning ability, good generalization ability and the property of universal approximation which has been used for system control and development of nonlinear system model. Fig 4.2 (c) shows the circuit diagram of ARBFNN and it is used to extract fundamental weight of load current.

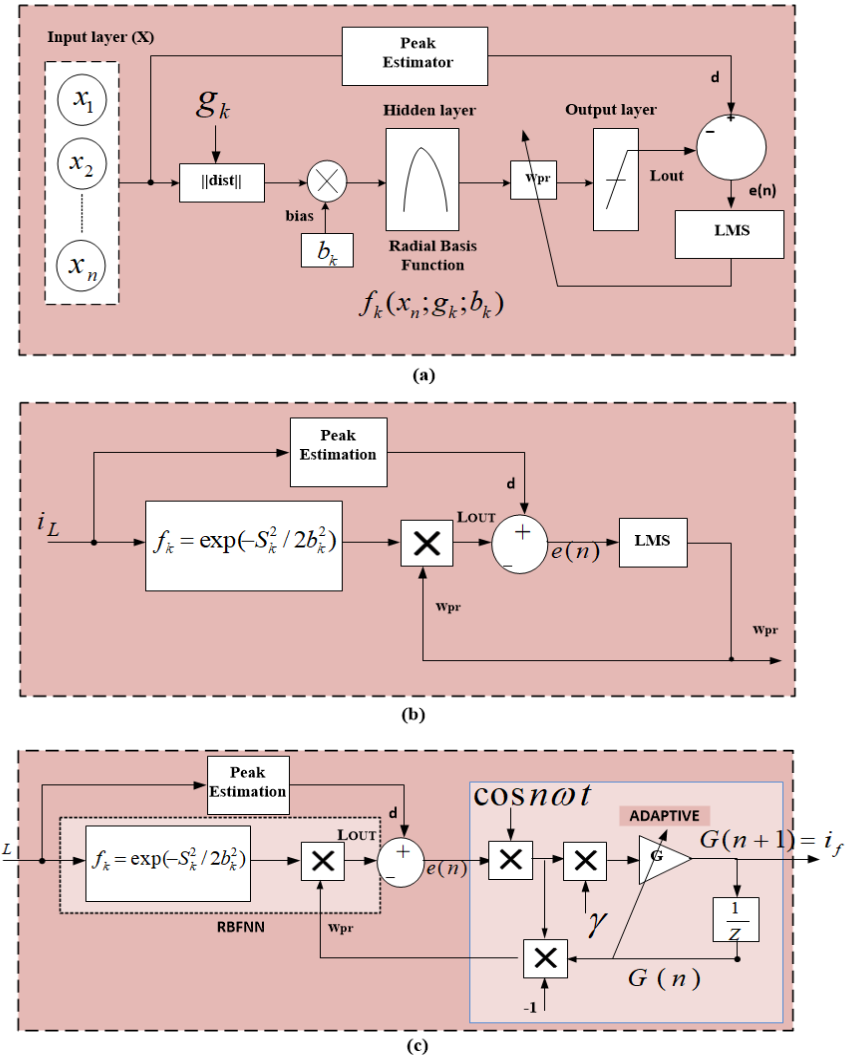

Fig 4.2 (a) Structure of CRBFNN (b) Circuit diagram of CRBFNN (c) Circuit diagram of A-RBFNN

The CRBFNN has self-learning ability, good generalization ability and the property of universal approximation which has been used for system control and development of nonlinear system model [279]. Now, the CRBFNN is modified and adaptive varying gain (G) is added to develop ARBFNN which is very fast self learning ability to control various DSTATCOM. Fig 4.2 (c) shows the circuit diagram of A-RBFNN and it is used to extract fundamental weight of load current.

In ARBFNN technique, the dynamics of the weight is control with the help of Adaptive varying gain G as shown in Eq. (4.8).

$$G(n+1) = G(n) - \gamma \frac{\partial w_{pr}}{\partial G} \tag{4.8}$$

The circuit diagram of ARBFNN as shown in Fig 4.2 (c) in which only one neuron (n=1) is considered, the output ‘w_{pr}’ is calculated as

$$w_{pr} = \int G(n) e \sin\omega t \, d\omega t \tag{4.9}$$

$$\therefore w_{pr} = -G(n) e \cos\omega t \tag{4.10}$$

The partial derivative of the cost function with respect to the weight vector is

$$\frac{\partial w_{pr}}{\partial G(n)} = -e\cos\omega t \tag{4.11}$$

Using Eq. (4.8), Eq. (4.10) and Eq. (4.11)

$$G(n+1) = G(n) + \gamma e \cos\omega t \tag{4.12}$$

Thus, the gain varies adaptively in A-RBFNN technique until convergence is obtained.

4.2.3 Mathematical Analysis of Adaptive Leaky Least Mean Fourth (ALLMF) Control Algorithm

The ALLMF algorithm belongs to a new class of stochastic gradient descent-based algorithms that aims to minimize the mean fourth error, which is a convex function of the adaptive weight vector [280]. The strength of ALLMF algorithm lies in its faster initial convergence and lower steady-state error compared to the conventional Least Mean Fourth (LMF) algorithm.

Fig 4.3 shows the weight updating structure of LLMF adaptive algorithm. As shown in Fig 4.3, *N* represents the total number of matrix vector. Assigning the interpolation intervals and determining the interval index i that corresponds to the input signal t(n), are the initial steps in interpolation. The look-up table (LUT) control points are represented by $A_N \in \Re^{A\times 1} = [A_1\ A_2\ A_3\ \ldots\ldots\ldots\ldots A_N]^T$, where A_i stands for the i^th^ control point and $A_N \in \Re^{4\times 1} = [A_{i-1}\ A_i\ A_{i+1}\ A_{i+2}]$ for the i^th^ span. Additionally, to produce an error e(n), the output of ALLMF interpolation is deducted from the real load current $i_L(n)$. After load dynamics, this adaptive process is continued until steady state is reached.

Assume that the signal B(n) is fed into the system with an unknown weight coefficient vector $w_p(n)=[w_p(0)\ w_p(1) w_p(2)\ldots. w_p(N-1)]^T$ and that the observed signal is $i_L(n)$.

where, $B(n)=[b(n)\ b(n-1)\ldots. b(n-N+1)]^T$ represents the vector of input signal.

The goal is to identify the unknown channel coefficient vector $w_p(n)$ adaptively using the input signal B(n) and observed signal $i_L(n)$.

The block diagram of ALLMF control algorithms is shown in Fig 4.4 and the weight updation using ALLMF control algorithm is shown in Fig 4.5. This controller is used to estimate the fundamental weight of load current and changes the weight of load current in real time. It has been observed that using ALLMF control technique reduces the error to zero quickly as compared to

Least Mean Fourth (LMF) method. The detailed description of extraction of fundamental active weight of nonlinear load current (i_L) by ALLMF technique is described below.

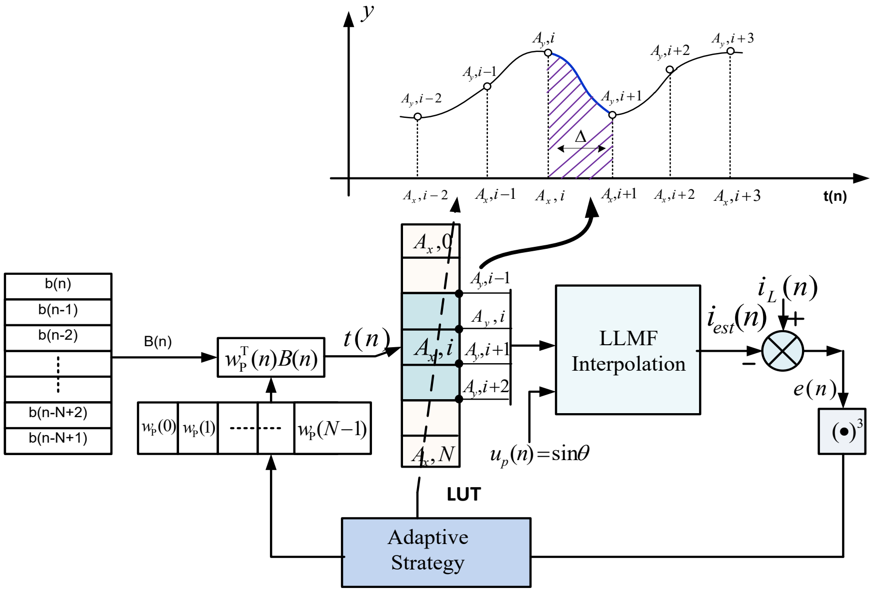

Fig 4.3 Weight updating structure of ALLMF adaptive algorithm

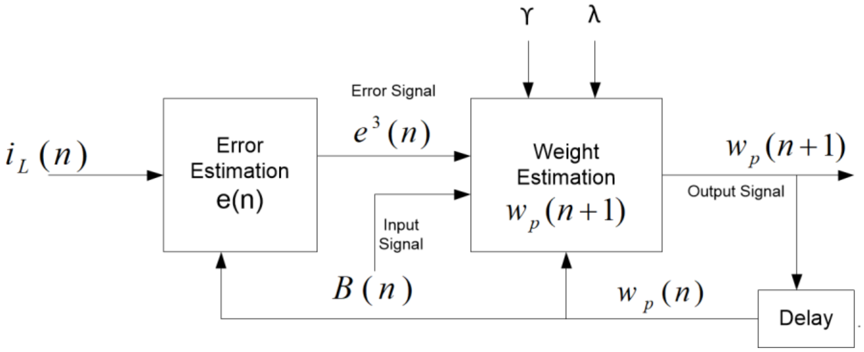

Fig 4.4 Block diagram of ALLMF control algorithm

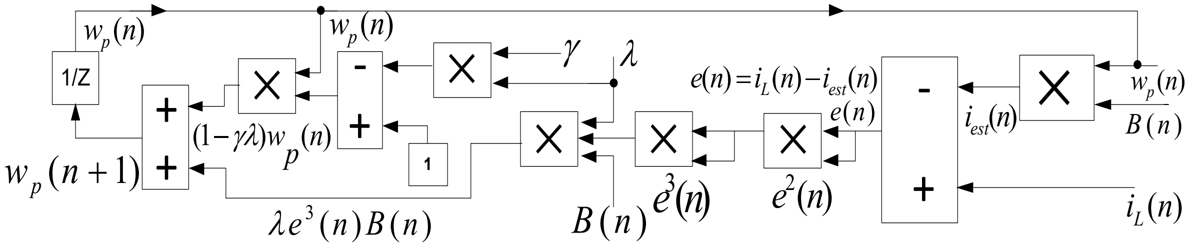

Fig 4.5 Weight updation using ALLMF control algorithm.

The load current (i_L) contains the sum of both fundamental as well as harmonic components, which are represented as;

$$i_L(t) = i_{L1}\sin(\omega t+\theta)+i_{L2}\sin(2\omega t+\theta)+.........\infty \tag{4.13}$$

$$i_L(t) = i_{L1}\sin(\omega t+\theta)+\sum_{r=2}^{\infty} i_{Lr}\sin(r\omega t+\theta_r) \tag{4.14}$$

where, r is the order of harmonics; $\boldsymbol{\theta_r}$ is the harmonic phase angle**;** ω is an angular frequency of the fundamental harmonics; $i_{L1}$is fundamental and i_{Lr} denotes the rth harmonic components of the current. Now, this equation can be expressed as;

$$i_L(t) = i_{L1}[\sin\omega t\cos\theta+\sin\theta\cos\omega t]+\sum_{r=2}^{\infty} i_{Lr}[\sin r\omega t\cos\theta_r+\cos r\omega t\sin\theta_r] \tag{4.15}$$

Replacing $i_{L1}\cos\boldsymbol{\theta}$**;** $i_{L1}\sin\boldsymbol{\theta}$**;** $i_{Lr}\cos\boldsymbol{\theta_r}$; $i_{Lr}\sin\boldsymbol{\theta_r}$ by $w_p(0)$; $w_p(1)$; $w_p(2)$;$w_p(3)$ and negelecting even harmonics.

$$i_L(t) = [w_p(0)\sin\omega t+w_p(1)\cos\omega t]+\sum_{r=3,5....}^{\infty}[w_p(2)\sin r\omega t+w_p(3)\cos r\omega t] \tag{4.16}$$

In matrix form,

$$= [w_p(0)\, w_p(1)\, w_p(2)\, w_p(3)......]\begin{bmatrix}\sin\omega t\\ \cos\omega t\\ \sin 3\omega t\\ \cos 3\omega t\\ .\\ .\\ \infty\end{bmatrix} \tag{4.17}$$

where,

$$B(n) = [\sin\omega t\cos\omega t\sin 3\omega t\cos 3\omega t......\infty]^T \tag{4.18}$$

$$w_p(n) = [w_p(0)\, w_p(1)\, w_p(2)\, w_p(3)......] \tag{4.19}$$

Now the controller is designed to extract only the fundamental current component, hence only unit template (sin(ωt)) is used further along with only one weight update component. Further; Eq. (4.18-4.19) can be used to estimate load current shown as,

$$i_{est}(n) = w_p(n)B(n) \tag{4.20}$$

Let $i_L(n)$ be the actual nonlinear load current and $i_{est}(n)$ be an estimated current to evaluate the error signal e(n).

$$e(n) = i_L(n) - w_p(n)B(n) \tag{4.21}$$

In case of LMF algorithm, the cost function 'C_{LMF}' to be minimized is given by

$$C_{LMF}(n) = \frac{1}{4}[e^4(n)] \tag{4.22}$$

$$= \frac{1}{4}[\{i_L(n) - w_p(n)B(n)\}]^4 \tag{4.23}$$

The modified LMF cost function is introduced to the ALLMF algorithm with the leakage parameter (γ) as shown in Eq.4.24.

Therefore; the minimum cost function of ALLMF is

$$C_{LLMF}(n) = \frac{1}{4}[e^4(n)] + 2\gamma\,|\,w_p(n)\,|^2 \tag{4.24}$$

As a result, the gradient estimation is defined as the partial derivative of the cost function with respect to the weight vector.

$$\frac{\partial C(n)}{\partial w_p(n)} = [\{\gamma\, w_p(n) - e^3(n)B(n)\}] \tag{4.25}$$

The minimum of C(n) can be sought recursively using the gradient method as shown below

$$w_p(n+1) = w_p(n) - \lambda \frac{\partial C(n)}{\partial w_p(n)} \tag{4.26}$$

$$= w_p(n) - \lambda[\{\gamma\, w_p(n) - e^3(n)B(n)\}] \tag{4.27}$$

$$w_p(n+1) = w_p(n) - \lambda[\{\gamma\, w_p(n) - e^3(n)B(n)\}] \tag{4.28}$$

where, λ is the adaptation constant and γ is learning rate and its value ranges between 0 and 1. The Eq. 4.28 shows the weight updating equation of ALLMF control technique, which is being used in the proposed controller to extract the fundamental active weight of the load current. The ALLMF technique is developed for the control of a Distribution Static Compensator (DSTATCOM), which provides the necessary compensating currents at PCC so that the supply current is almost sinusoidal.

4.3 Performance Analysis of Single Phase Grid connected DSTATCOM

The single phase grid connected DSTATCOM is designed in the laboratory to improve the PQ of the system. The diode bridge rectifier with series R-L load is non linear load. Fig 4.6 shows the system diagram with source impedance Z_S (source resistance R_S and inductance L_S), interfacing inductor L_i, ripple filter R_i, diode bridge rectifier, VSC with DC link capacitance all collectively connected at PCC. The conventional H-bridge configuration is selected for the VSC with four IGBT and antiparallel diodes. The DSTATCOM with the help of suitable control algorithm injects the compensating current at PCC to mitigate harmonics in grid currents caused by non-linear load. It also improves power factor to nearly unity, makes grid current sinusoidal and provides reactive power compensation. The DC link voltage is regulated using a tuned PI controller. The interfacing inductor are used to minimize ripples in the compensating current. The simulation and experimental parameters are listed in Appendix A.

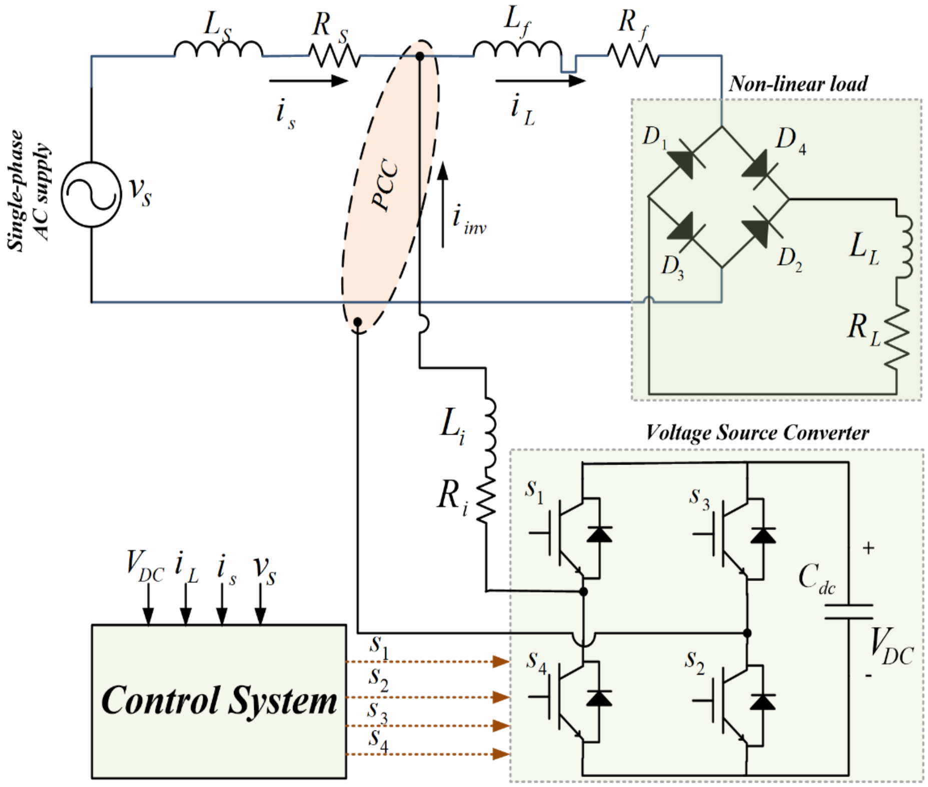

Fig 4.6 System diagram of single phase grid connected DSTATCOM

4.3.1 Control Algorithm using conventional Notch Filter

The control diagram of single phase VSC incorporating conventional Notch Filter is shown in Fig 4.7. The proposed algorithm is used to update the estimated weight signals output which is the fundamental component of the load current (i_f). The weight loss component (i_{loss}) is calculated by processing the DC-link voltage through the PI controller. The unit template is multiplied with the sum of the fundamental weights (i_f) and the PI controller's output to produce the reference current, i_{ref}. The reference current is perfectly sinusoidal (i_{ref}) and then compared with actual supply current i_s in HCC current controller to generate gating pulses for IGBT switching operation to control DSTATCOM. This ensures the grid current is perfectly sinusoidal and the entire reactive power demand of the load is met by the compensator.

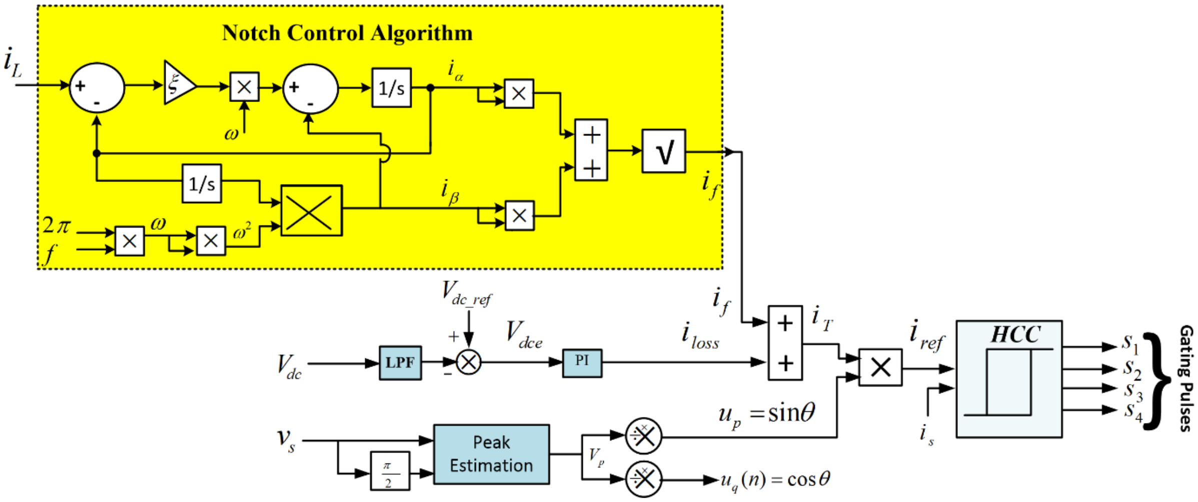

Fig 4.7 Control diagram using Notch Filter based control algorithm

4.3.2 Extraction of fundamental current using Conventional Notch Filter (NF)

The load current fundamental active magnitude (i_f) is extracted using Notch filter controller by using the Eq. 4.29.

$$i_f = \sqrt{(i_\alpha)^2 + (i_\beta)^2} \tag{4.29}$$

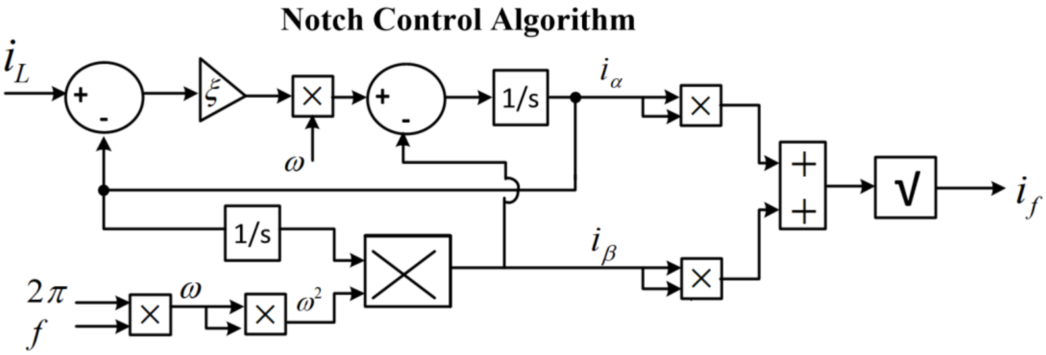

Fig 4.8 Circuit diagram of Notch Filter

where 'f 'is the frequency and i_f is the fundamental current magnitude of notch filter.

4.3.3 Calculation of current loss component

The DC link voltage (V_{dc}) and its reference voltage (V_{dc_ref}) is compared to find error (V_{dce}) as shown in Eq.4.30. The current loss component is now obtained by feeding the error V_{dce} to the Proportional Integral (PI) controller.

$$V_{dce} = V_{dc\_ref} - V_{dc} \tag{4.30}$$

$$i_{loss}(n) = [i_{loss}(n+1) + k_P\{V_{dce}(n+1) - V_{dce}(n)\} + k_i\{V_{dce}(n+1)\}] \tag{4.31}$$

4.3.4 Calculation of unit templates .

In order to determine unit templates, the grid voltage (v_s) and its quadrature phase shifted component

(v_p) as shown in Fig 4.9, are passed through the peak estimation block. In order to calculate peak voltage (v_m), the Eq. 4.32-4.33 are used.

The calculation of v_m as per Eq. 4.34.

$$v_s = v_m sin\omega t \tag{4.32}$$

$$v_p = v_m(sin\omega t + \frac{\pi}{2}) \tag{4.33}$$

Now, the peak voltage is,

$$\therefore v_m = \sqrt{v_p^2 + v_s^2} \tag{4.34}$$

The unit template is computed as

$$u_p = \frac{v_s}{v_m} = \sin \omega t \tag{4.35}$$

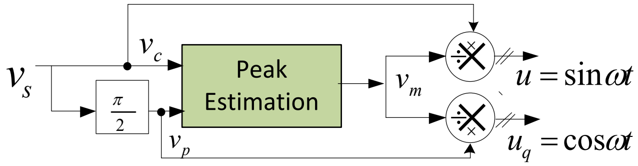

Fig 4.9 Generation of Unit Templates

4.3.5 Simulation results for NF Control Algorithm

The simulation results using Notch filter are shown in Figs 4.10-4.11. These simulations provide several waveforms for closed-loop control systems. The parameters of the Simulink model are detailed in the Appendix A, and the results are elaborated below.

The system's behaviour under dynamic circumstances is shown in Fig 4.10, which is obtained from the suggested Notch Filter (NF) controller architecture. The waveforms of the source voltage (v_s), source current (i_s), nonlinear load current (i_L), compensatory current via the active filter (i_c), DC link voltage (V_{dc}) is shown. At time t=0.8s, the load current is increased from 4A to 5A and at time t=1s, the load is decreased back to initial level of 4A. An increase in source current (i_s) occurs without any change in source voltage (v_s). Due to load variations, the DC-link voltage (V_{dc}) slight decrease, but the PI controller promptly reinstates it to the 200V reference level. Furthermore, the source current stays sinusoidal and in phase with the source voltage, illustrating the efficacy of the control mechanism based on the Notch Filter algorithm under dynamic load conditions. Fig 4.11 illustrates the waveforms of load current (i_L), fundamental current (i_f), reference current (i_{ref}) and unit template (u_p) during load disturbance. The reference current and fundamental current is also changed at t=0.8s due to load change but unit templates lie under sine limit of ±1.

The analysis of the THD profiles in the source voltage (v_s) exhibits harmonic performance with a negligible THD of 0.03%. The source current (i_s) shows a THD of 2.90% which reflecting good

harmonic quality. In contrast, the load current displays significant distortion with a THD of 30.61% as shown in Fig 4.12.

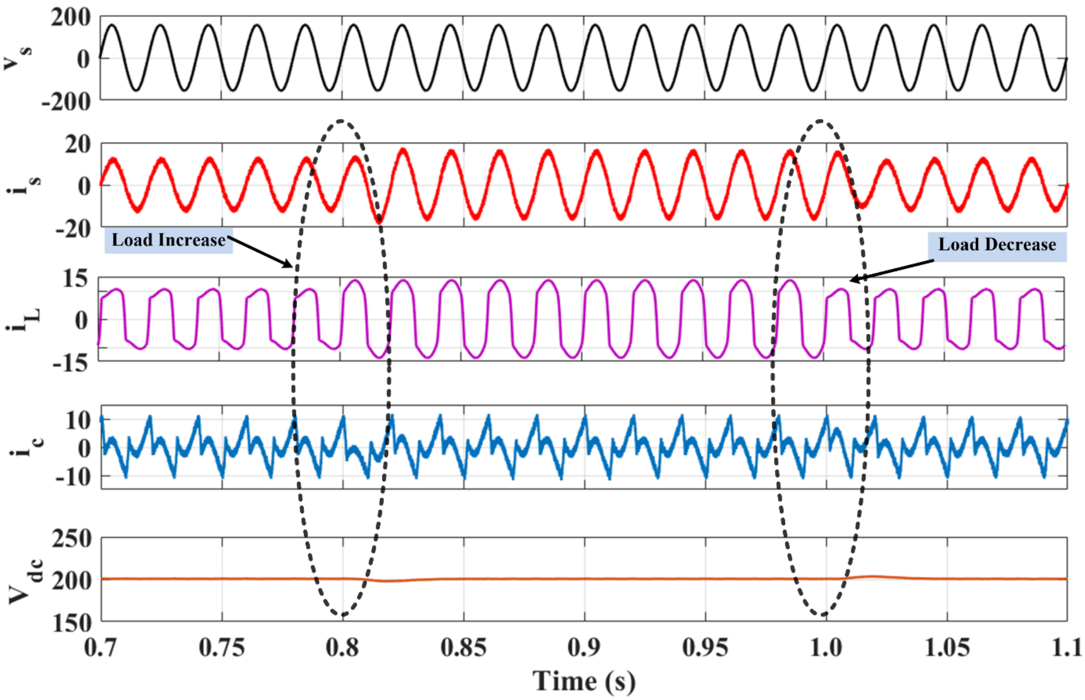

Fig 4.10 Simulation waveforms of source voltage (v_s), source current (i_s), load current (i_L), compensating current (i_C), DC link voltage (V_{dc}) during dynamic condition using NF.

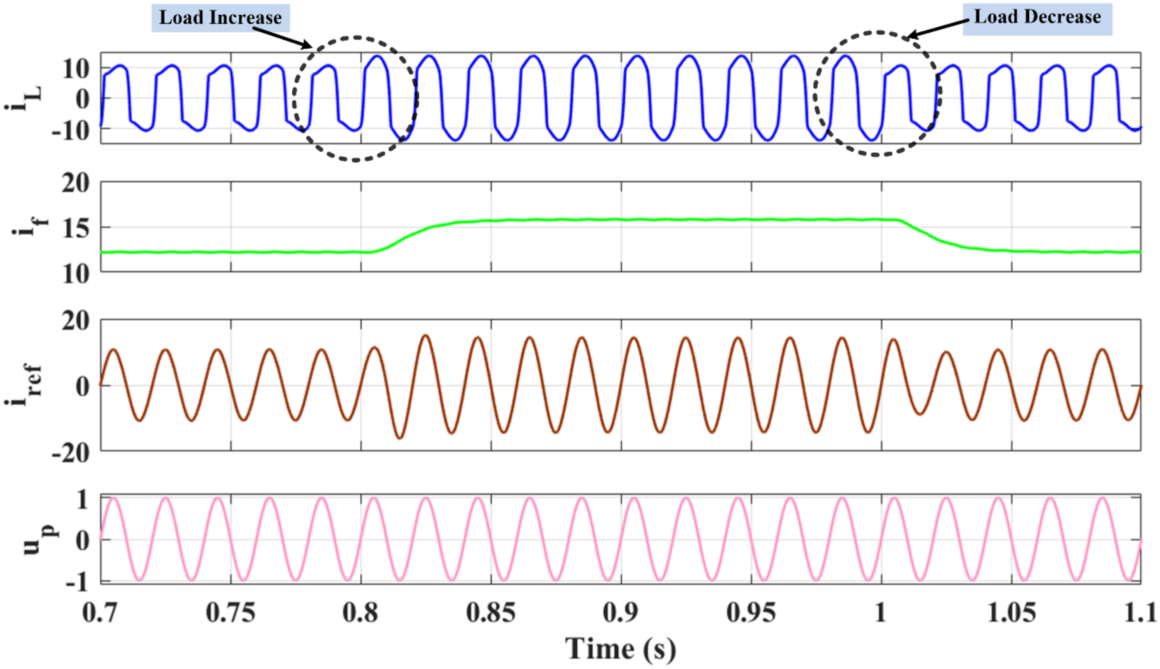

Fig 4.11 Simulation waveforms of load current (i_L), fundamental current (i_f), reference current (i_{ref}), unit template (u_p) during dynamic condition using NF

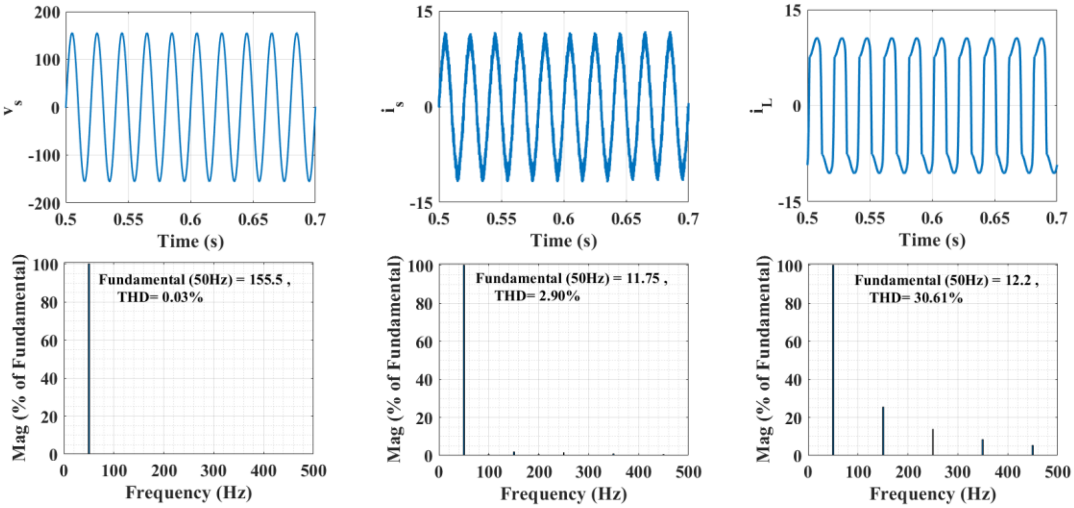

Fig 4.12 Simulation results: Harmonic analysis of a). v_s , THD = 0.03% b). i_s , THD = 2.90% c). i_L , THD = 30.61% during steady state conditions using NF

4.3.6 Experimental Results of Notch Filter

A prototype laboratory model as shown in Fig 4.13 is developed to validate the simulation findings. The developed model is evaluated at 110V (rms) and 50Hz alternating current supply, which powers a nonlinear load. The nonlinear load is arranged as a series combination of load resistance (R) and inductance (L) on the DC side of the rectifier. The VSC is supplied at the point of common coupling (PCC), enabling compensating currents to be sent via interface inductors to improve power quality in grid current. Multiple LEM sensors, namely the voltage sensor (LV-25P), are used for measuring vs and V_{dc} while current sensors (LA-25P) are used to detect i_s and i_L. The dSPACE-1104 controller is linked for communicating with these sensors. The developed controller ensures proper regulation of the VSC, with four gating pulses from the dSPACE driving the converter. A DSO records various signals obtained from the hardware, while a power analyser (HIOKI PQ3100) evaluates experimental characteristics such as power, current, and harmonics. The comprehensive details of the experimental setup are included in the Appendix A. This section thoroughly analyses the experimental performance under steady-state and dynamic conditions, as seen in Figs 4.14-4.17.

a). *Steady State Conditions*

Figs 4.14-4.16 show the various waveforms, harmonics analysis, and power analysis during steady state conditions.

Fig 4.13 Experimental setup of single phase DSTATCOM

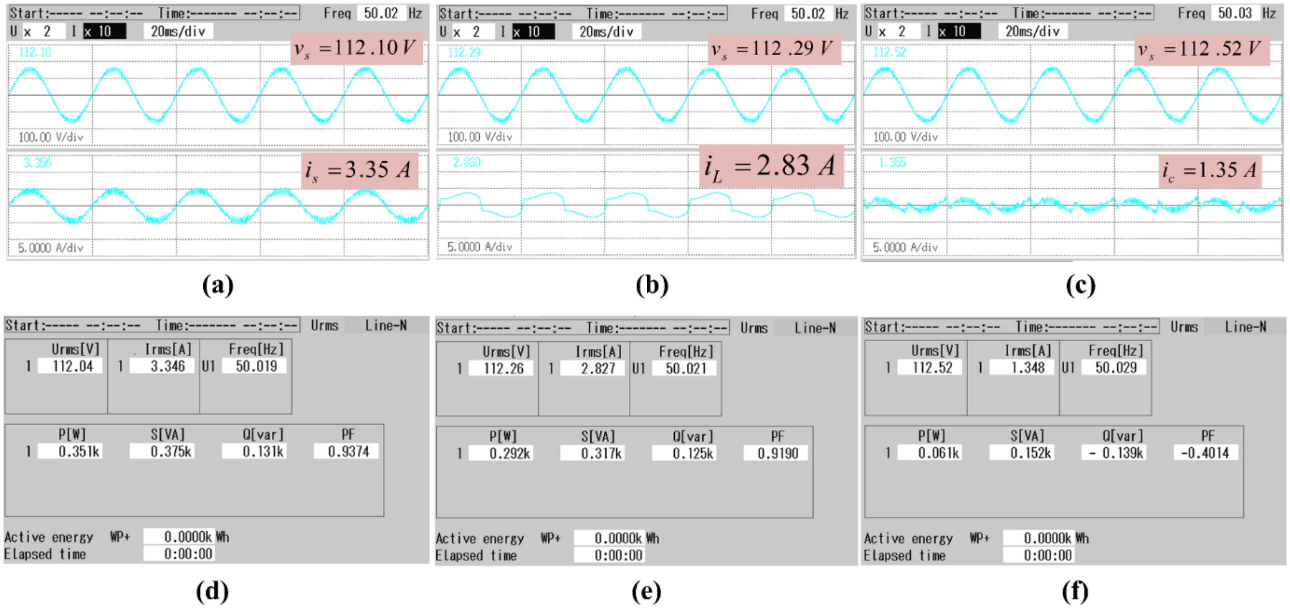

(a) (b) (c)

```
Start:----- --:--:--  Time:------- --:--:--  Urms   Line-N
   Urms[V]      Irms[A]     Freq[Hz]
1  112.04    1  3.346   U1  50.019

   P[W]       S[VA]       Q[var]      PF
1  0.351k     0.375k      0.131k      0.9374

Active energy  WP+   0.0000k Wh
Elapsed time         0:00:00
```

```
Start:----- --:--:--  Time:------- --:--:--  Urms   Line-N
   Urms[V]      Irms[A]     Freq[Hz]
1  112.26    1  2.827   U1  50.021

   P[W]       S[VA]       Q[var]      PF
1  0.292k     0.317k      0.125k      0.9190

Active energy  WP+   0.0000k Wh
Elapsed time         0:00:00
```

```
Start:----- --:--:--  Time:------- --:--:--  Urms   Line-N
   Urms[V]      Irms[A]     Freq[Hz]
1  112.52    1  1.348   U1  50.029

   P[W]       S[VA]       Q[var]      PF
1  0.061k     0.152k      - 0.139k    -0.4014

Active energy  WP+   0.0000k Wh
Elapsed time         0:00:00
```

(d) (e) (f)

Fig 4.14 Experimental results of a). v_s,i_s b). v_s,i_L c). v_s,i_C d). Supply power P_S e). Load power P_L f). Compensator power P_C during steady state condition using NF.

Fig 4.14 illustrates the results of the system's steady-state experiments, representing the waveforms of the v_s, i_s, i_L, and i_c. The distortion of the load current due to the connection of a non-linear load is most clearly seen in Fig 4.14 (b). The sinusoidal characteristics of source current, as seen in Fig 4.14 (a), with the supply voltage (v_s). Fig 4.14 (c) demonstrates that the compensating current (i_c) of 1.34A is injecting at point of common coupling to improve the quality of waveforms of source current.

Fig 4.14 (d-f) shows the steady-state active and reactive power flow. The reactive power required by the load is 0.125kVAR, while the active power need is 0.292 kW. The active filter raises the load's power factor (P.F.) from 0.919 to 0.937 by reducing its reactive power demand by 0.125kVAR, as seen in Fig 4.14 (d-e). The load's actual power demand plus switching losses is covered by the 0.351kW supplied by the grid.

Figure 4.15 depicts the single phase system's steady-state performance using the NF controller. Figures 4.15(a–c) demonstrate the harmonic content of the v_s, i_s, and i_L. The THD in i_L is 26.86%, as illustrated in Fig 4.15(b). The THD in v_s is 1.59% and THD in i_s is 4.12%, as shown in Fig 4.15(a), in accordance with the IEEE 519 standard. The compensator current, which is utilized to mitigate harmonics in a non-linear load, exhibits a THD of 76.48%, as illustrated in Fig 4.15 (c). The Notch Filter based single phase VSC performs harmonic reduction for supply currents in single system.

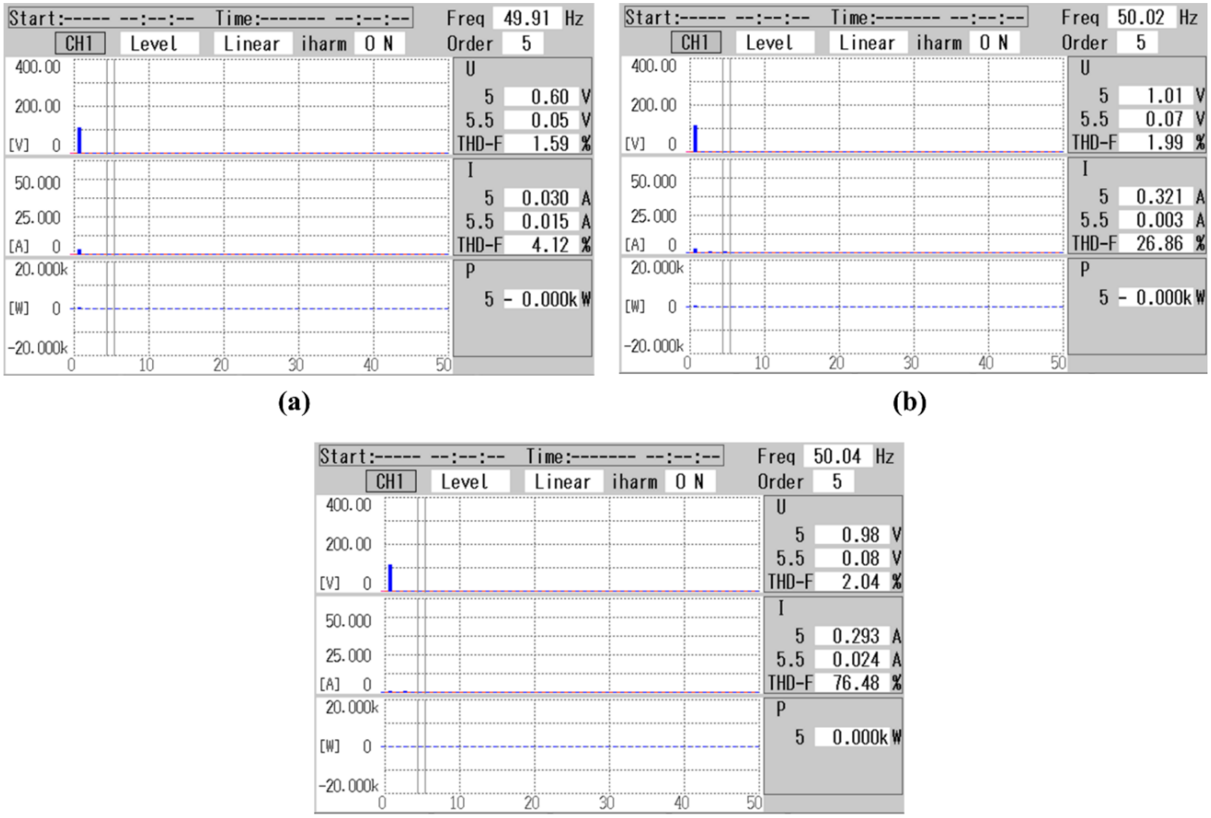

(a) (b)

(c)

Fig 4.15 Experimental results : Harmonic analysis of a). v_s,i_s with THD = 4.12% b). v_s,i_L with THD = 26.86% c). v_s,i_C with THD = 76.48% during steady state condition using NF.

b). *Dynamic State Conditions*

Fig 4.16 (a–d) shows the dynamic results of the proposed system under different load conditions. The waveforms show things that can change, such as source voltage (v_s), source current (i_s), load current (i_L), DC link voltage (V_{dc}), compensating current (i_c), fundamental weight (I_f), unit template (u_p) and reference current (i_{ref}).

Fig 4.16 (a–b) shows the waveforms of v_s, i_s, i_L, V_{dc}, and i_c as the load changes. The source current changes when the load changes, but the DC link voltage stays at 200V. The voltage on the DC link is well-regulated, and changes in the load have little effect on how well it regulates.

Fig 4.16 (c-d) illustrates the waveforms of load current (i_L), source current (i_s), fundamental current (i_f), reference current (i_{ref}) and unit template (u_p). The waveform indicates a change in the fundamental current caused by fluctuations in the load current. The Notch Filter based control algorithm accurately predicts the fundamental load current magnitude. The unit template (u_p) maintains unity and unchanged during load change.

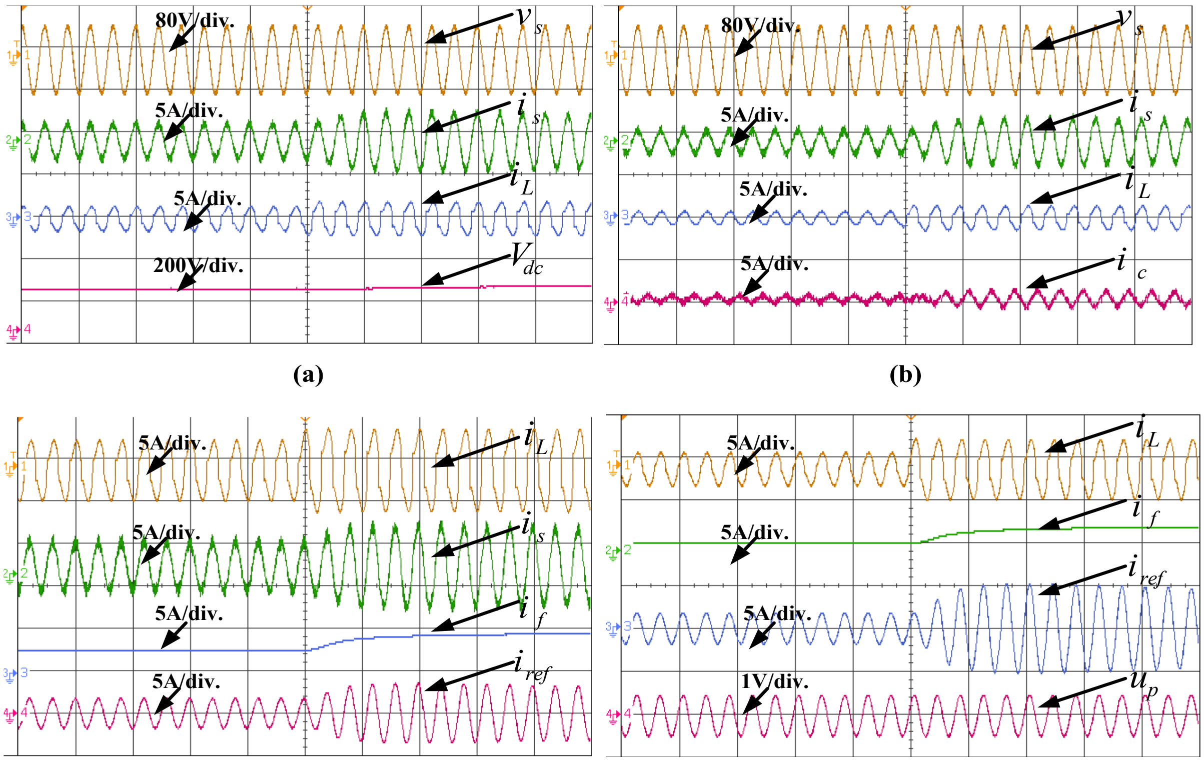

(a) (b)

(c) (d)

Fig 4.16 Experimental waveforms of a). v_s,i_s,i_L,V_{dc} b). v_s,i_s,i_L,i_C c). $i_L,i_s,,i_f,i_{ref}$ and d). i_L, i_f,i_{ref} ,u_p during dynamic condition using NF

The intermediate waveforms of load current (i_L), in phase component of load current (i_α), quadrature phase component of load current (i_β) and fundamental current are shown in Fig 4.17. It is observed that during, a sudden increase in load, the intermediate parameters i_α and i_β also change and fundamental current attains a new steady state position.

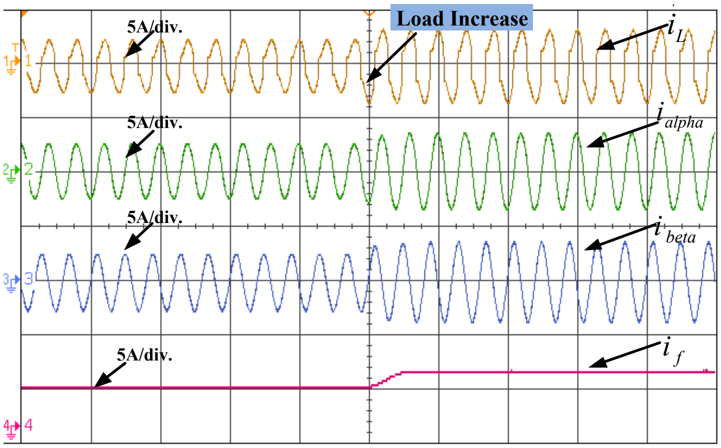

Fig 4.17 Experimental waveforms of i_L,i_α, i_β,i_f during dynamic load condition using NF

4.3.7 Control Algorithm using Adaptive LLMF Control Algorithm

Fig 4.18 illustrates the control diagram of the Adaptive Leaky Least Mean Fourth (ALLMF) algorithm. The fundamental weight of the load current is estimated by updating the estimated weight signal in real time. In order to estimate the weight loss component (i_L), a PI controller is implemented to regulate the DC-link voltage to a 200V reference. The effective weight i_T is the sum of the fundamental (i_f) and loss component (i_{loss}). This weight is multiplied by the unit

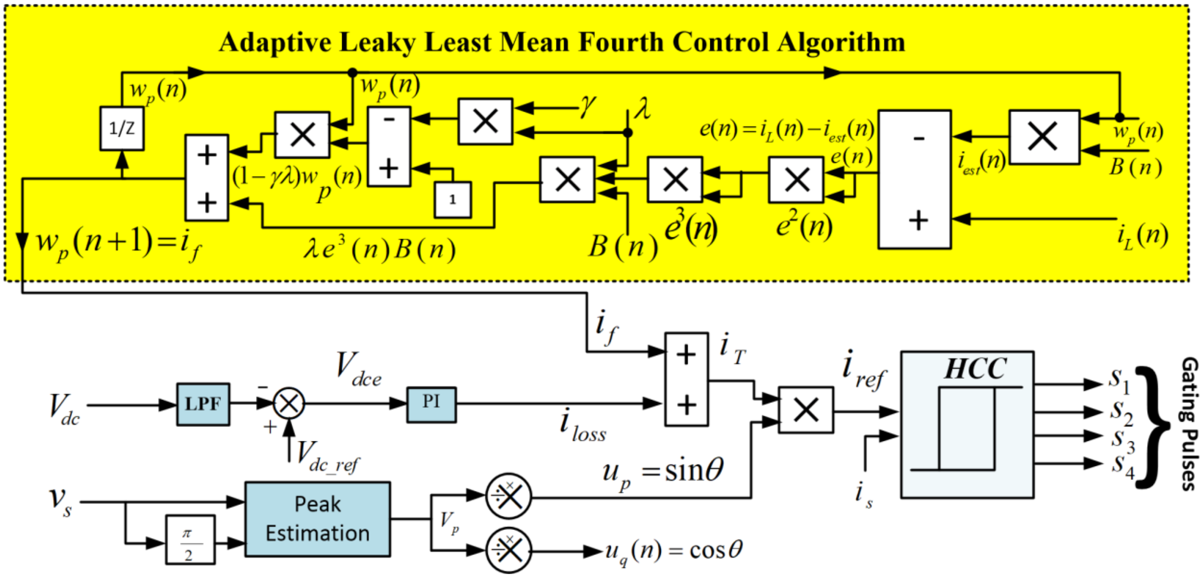

Fig 4.18 Control diagram of ALLMF algorithm

template to produce the reference current (i_{ref}). The actual reference current is passed through a PWM current controller to generate gating pulses for IGBT switching operation, which is used to control DSTATCOM. The reference current is flawlessly sinusoidal (i_{ref}). This guarantees that the grid current is precisely sinusoidal and that the compensator meets the entire reactive power demand of the load. The controller description includes the estimation of the fundamental weight current using ALLMF, the calculation of the unit template, the estimation of the active weight loss component, and the reference supply current.

4.3.8 Extraction of Fundamental Current using ALLMF

The main aim of the fundamental current extraction is to control DSTATCOM and this fundamental current is extracted by the application of ALLMF control algorithm as shown in Eq.4.36. The circuit diagram of ALLMF is shown in Fig 4.19.

$$w_p(n+1) = w_p(n) - \lambda[\{\gamma w_p(n) - e^3(n)B(n)\}] = i_f \qquad (4.36)$$

where $w_p(n+1) = i_f$ corresponds to the fundamental component of load current and λ is the learning rate, e(n) is the error signal.

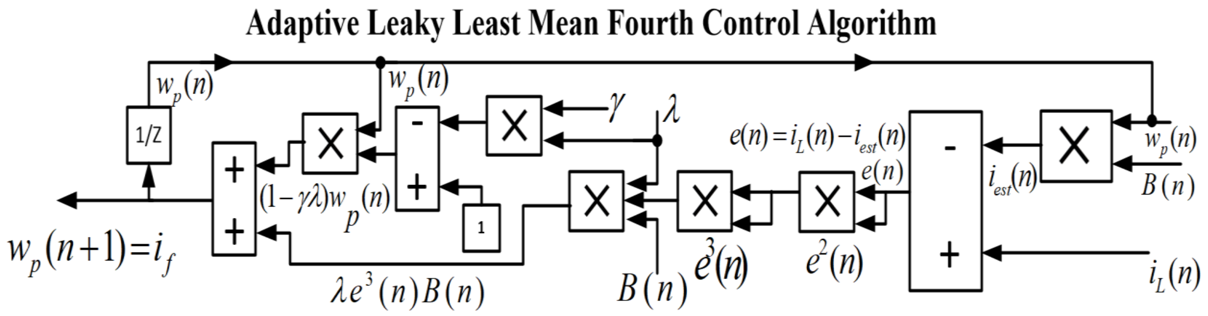

Fig 4.19 Circuit diagram of ALLMF algorithm using Matlab.

4.3.9 Calculation of loss component

The calculation of loss current is already discussed in section 4.3.3. The equation of loss current is shown in shown in Eq. 4.38.

$$V_{dce} = V_{dc\_ref} - V_{dc} \qquad (4.37)$$

$$i_{loss}(n) = [i_{loss}(n+1) + k_P\{V_{dce}(n+1) - V_{dce}(n)\} + k_i\{V_{dce}(n+1)\}] \qquad (4.38)$$

4.3.10 Calculation of unit templates

Similarly, the calculation of unit templates is given in detail in section 4.3.4. The unit template is shown in Eq. 4.39.

$$u(n) = \frac{v_s}{V_m} = sin\omega t \qquad (4.39)$$

4.3.11 Simulation results for ALLMF Control Algorithm

The MATLAB/Simulink environment is used to develop and analyse a model of the proposed system. Fig 4.20 - 4.22 shows the simulation waveforms under dynamic conditions and also %THD under steady state condition. The closed loop control system is developed for 110V, 50Hz. Fig

4.20 shows the dynamic behavior of proposed system for ALLMF control algorithm. In this figure,

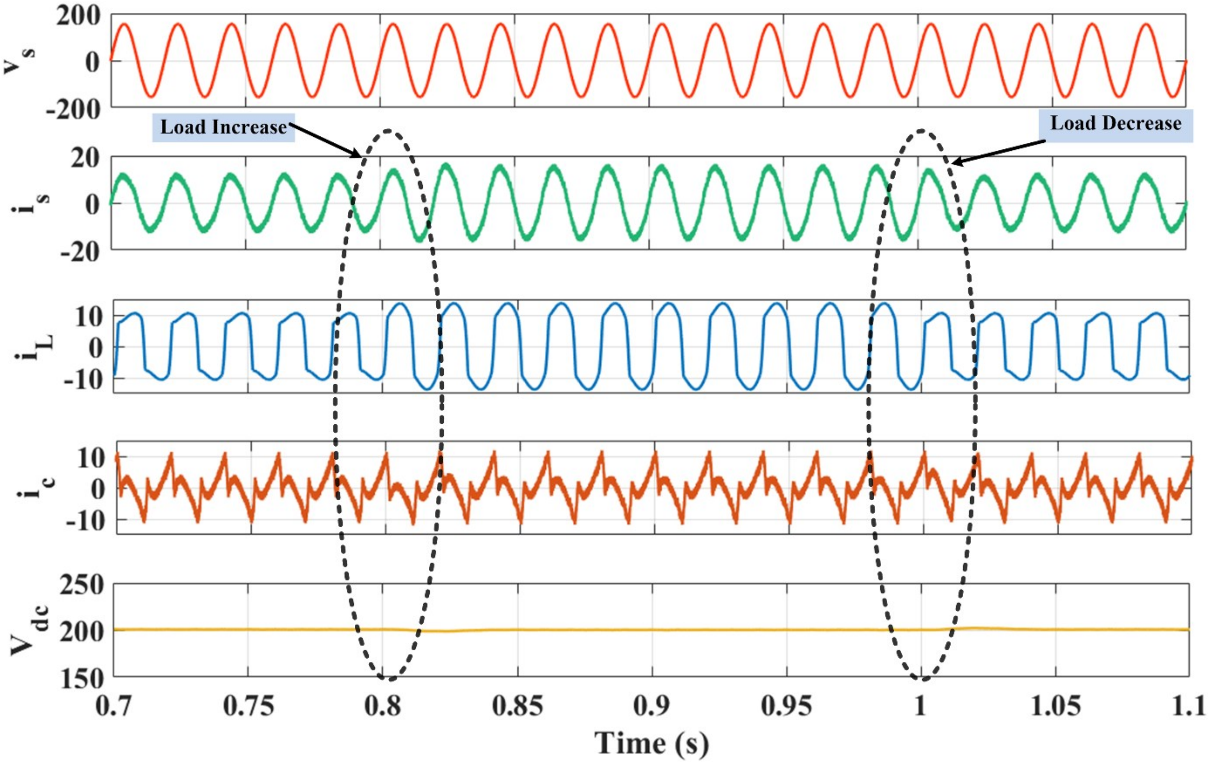

Fig 4.20 Simulation waveforms of source voltage (v_s), source current (i_s), load current (i_L), compensating current

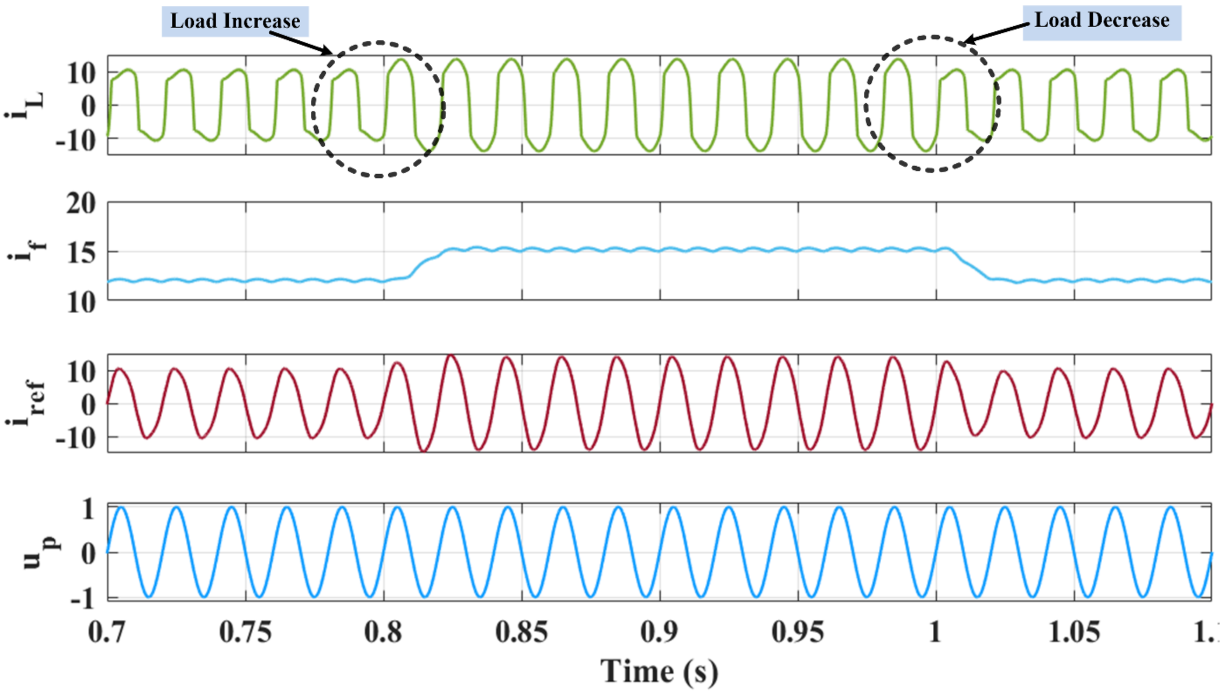

Fig 4.21 Simulation waveforms of load current (i_L), fundamental current (i_f), reference current (i_{ref}), unit template (u_p) during dynamic condition using ALLMF.

the waveform of grid voltage (v_s), grid current (i_s), nonlinear load current (i_L), compensating current through DSTATCOM (i_c), and total DC link voltage (V_{dc}) are shown. Effect of load perturbation on controller performance is studied. At time t=0.8s, the load is increased from 4A to 5A and at time t=1s, the load is decreased back to initial level of 4A. At the instant of load change, V_{dc} shows sudden disturbance during load increase/decrease but V_{dc} voltage again settles to 200 V due to action of PI controller. After compensation, it is found that the source current stays sinusoidal and in phase with the PCC voltage. This proves the effectiveness of the ALLMF control technique under dynamic load conditions.

Fig 4.21 shows the load current i_L (A), fundamental weight current if, reference current i_{ref} and unit template (u_p). During load change the fundamental current is observed to increase at time t=0.8s and then it decreases at t=1s as per the changes in the actual loading conditions. This result shows that the extraction of fundamental current using ALLMF technique is in accordance with the change in load current and reference current. It also observed that, there is no change in waveforms of unit template during load change and it maintained to unity.

The analysis of the THD profiles in the source voltage (v_s) exhibits harmonic performance with a negligible THD of 0.03%. The source current (i_s) shows a THD of 2.72% which reflecting good harmonic quality. In contrast, the load current displays significant distortion with a THD of 30.98%. as shown in Fig 4.22.

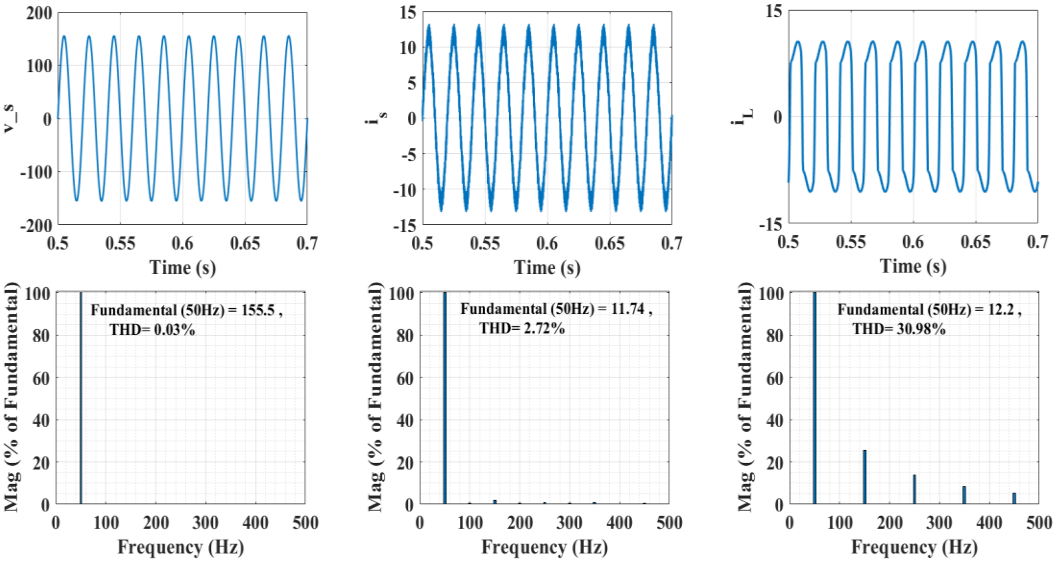

Fig 4.22 Simulation results : Harmonic analysis of a). v_s , THD = 0.03% b). i_s , THD = 2.72% c). i_L , THD = 30.98% during steady state condition using ALLMF.

4.3.12 Experimental results for ALLMF Control Algorithm

The proposed system model is being developed in the lab. The simulation results are validated with an experimental setup. The suggested system is powered by an alternating current source of 110 V and 50 Hz. The prototype hardware also exhibits a nonlinear load modelled as an R-L load on the rectifier's DC side. A DSTATCOM is linked to the PCC to provide compensating current via interface inductors. Several LEM current sensors (LA-25P) for sensing (i_s, i_L) and voltage sensors (LV-25P) for detecting (v_s, V_{dc}) are linked and interfaced with the DSP dSAPCE1104 board. Gating pulses from the DSP are supplied into DSTATCOM for proper system control. A DSO is used to record different hardware dynamic results. The power analyser (HIOKI PQ3100) captures the experimental data of power, current, and their harmonics. Appendix A includes information on the experimental parameters.

(a). Steady State Condition

The Figs 4.23(a-c) depicts the steady-state experimental results for the proposed system. It shows the waveforms of source voltage (v_s), source current (i_s), load current (i_L), and compensating current (i_c). As shown in Fig 4.23(a-b), the source voltage (v_s), source current (i_s), and load current (i_L) are all in the same phase. However, the load current is distorted. In Fig 4.23(c), the compensating current (i_c) is used to reduce harmonics in the source current.

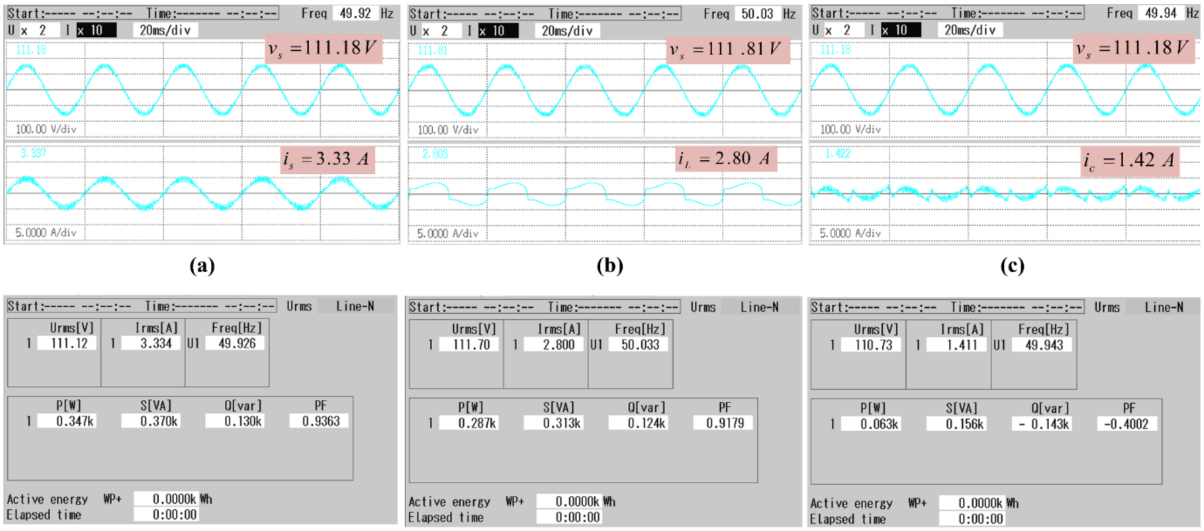

(a) (b) (c)

Start:----- --:--:-- Time:------- --:--:-- Urms Line-N
Urms[V] 1 111.12 Irms[A] 1 3.334 Freq[Hz] U1 49.926
P[W] 1 0.347k S[VA] 0.370k Q[var] 0.130k PF 0.9363
Active energy WP+ 0.0000k Wh
Elapsed time 0:00:00

Start:----- --:--:-- Time:------- --:--:-- Urms Line-N
Urms[V] 1 111.70 Irms[A] 1 2.800 Freq[Hz] U1 50.033
P[W] 1 0.287k S[VA] 0.313k Q[var] 0.124k PF 0.9179
Active energy WP+ 0.0000k Wh
Elapsed time 0:00:00

Start:----- --:--:-- Time:------- --:--:-- Urms Line-N
Urms[V] 1 110.73 Irms[A] 1 1.411 Freq[Hz] U1 49.943
P[W] 1 0.063k S[VA] 0.156k Q[var] - 0.143k PF -0.4002
Active energy WP+ 0.0000k Wh
Elapsed time 0:00:00

(d) (e) (f)

Fig 4.23 Experimental results of a). v_s, i_s b). v_s, i_L c). v_s, i_C d). Supply power P_S e). Load power P_L f). Compensator power P_C during steady state condition using ALLMF

Fig 4.23(d-f) depicts the steady-state active and reactive power flow using the present technique. The load's active and reactive power requirements are 0.287kW and 0. 124kVAR, respectively.

The switching loss equals 0.063kW. The DSTATCOM fulfils the load's reactive power demand of 0.124kVAR, resulting in a power factor (P.F) improvement from 0.917 to 0.936, as shown in Fig 4.20(d-e). The DSTATCOM meets the load's reactive power need by delivering 0.143kVAR, as shown in Fig 4.23(f). The grid provides 0.347kW to match the load's actual power while also accommodating switching losses.

Fig 4.24 shows the percentage THD of v_s, i_s, i_L and i_c. In Fig 4.24(a), the source current's THD is decreased to 3.67% which is nearly sinusoidal and the voltage distortion is 1.55%. Fig 4.24 (b) shows a significant harmonic distortion content of 26.76%. The DSTATCOM compensating current having THD 87.80% is observed and further it injects compensating current to cancels out the harmonics produced by the nonlinear load. The source current is sinusoidal in shape and synchronised with the source voltage. The observed waveforms demonstrate that the ALLMF method functions properly, and the obtained %THD of source current (i_s) is within the IEEE-519 standard limit of 5%.

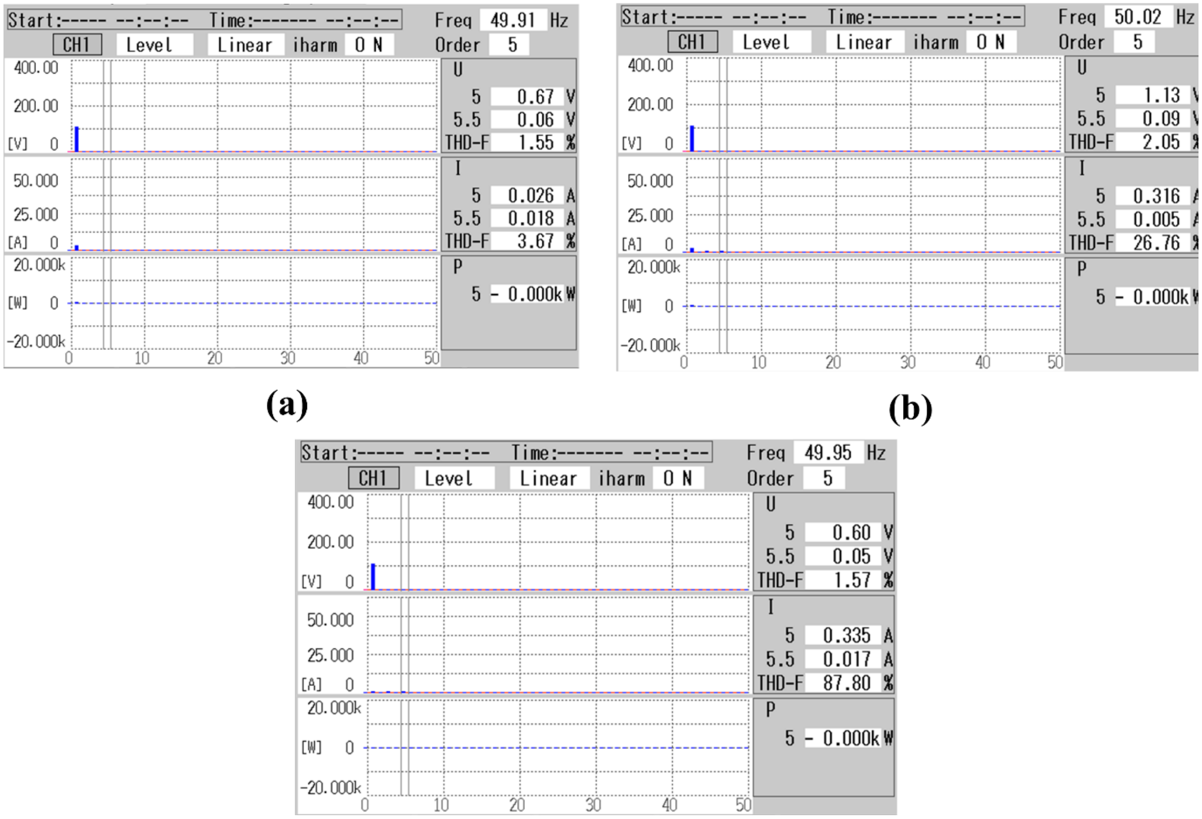

Freq 49.91 Hz
Order 5
U: 5 0.67 V; 5.5 0.06 V; THD-F 1.55 %
I: 5 0.026 A; 5.5 0.018 A; THD-F 3.67 %
P: 5 - 0.000k W

(a)

Freq 50.02 Hz
Order 5
U: 5 1.13; 5.5 0.09; THD-F 2.05
I: 5 0.316; 5.5 0.005; THD-F 26.76
P: 5 - 0.000k

(b)

Freq 49.95 Hz
Order 5
U: 5 0.60 V; 5.5 0.05 V; THD-F 1.57 %
I: 5 0.335 A; 5.5 0.017 A; THD-F 87.80 %
P: 5 - 0.000k W

(c)

Fig 4.24 Experimental results : Harmonic analysis of a). v_s, i_s with THD = 3.67% b). v_s, i_L with THD = 26.76% c). v_s, i_c with THD = 87.80% during steady state condition using ALLMF (b). Dynamic State Condition

The system's dynamic response under different load conditions is shown in Figs 4.25(a–d). During load variations, the following parameters are displayed: source voltage (v_s), source current (i_s), load current (i_L), DC link voltage (V_{dc}), compensating current (i_c), fundamental weight current (i_f), reference current (i_{ref}), and unit template (u_p). Fig 4.25(a-b) depicts the waveforms of v_s, i_s, i_L,i_c and V_{dc} as load changes. The waveforms of source current, load current and compensating current are increased due to change in load. It is also observed that the source voltage remains unchanged. The DC link voltage is able to maintain its stability and be well-regulated at around 200V. The compensating current (i_c) is injected at PCC through DSTATCOM to mitigate harmonics present in grid current.

The waveforms of i_L, i_s, i_f, i_{ref} and u_p as the load changes are shown in Fig 4.25(c-d). Due to change in load current, the fundamental current and reference current are increased but unit template maintains constant to sine limit. The satisfactory waveforms are obtained by the application of ALLMF in single phase grid connected DSTATCOM.

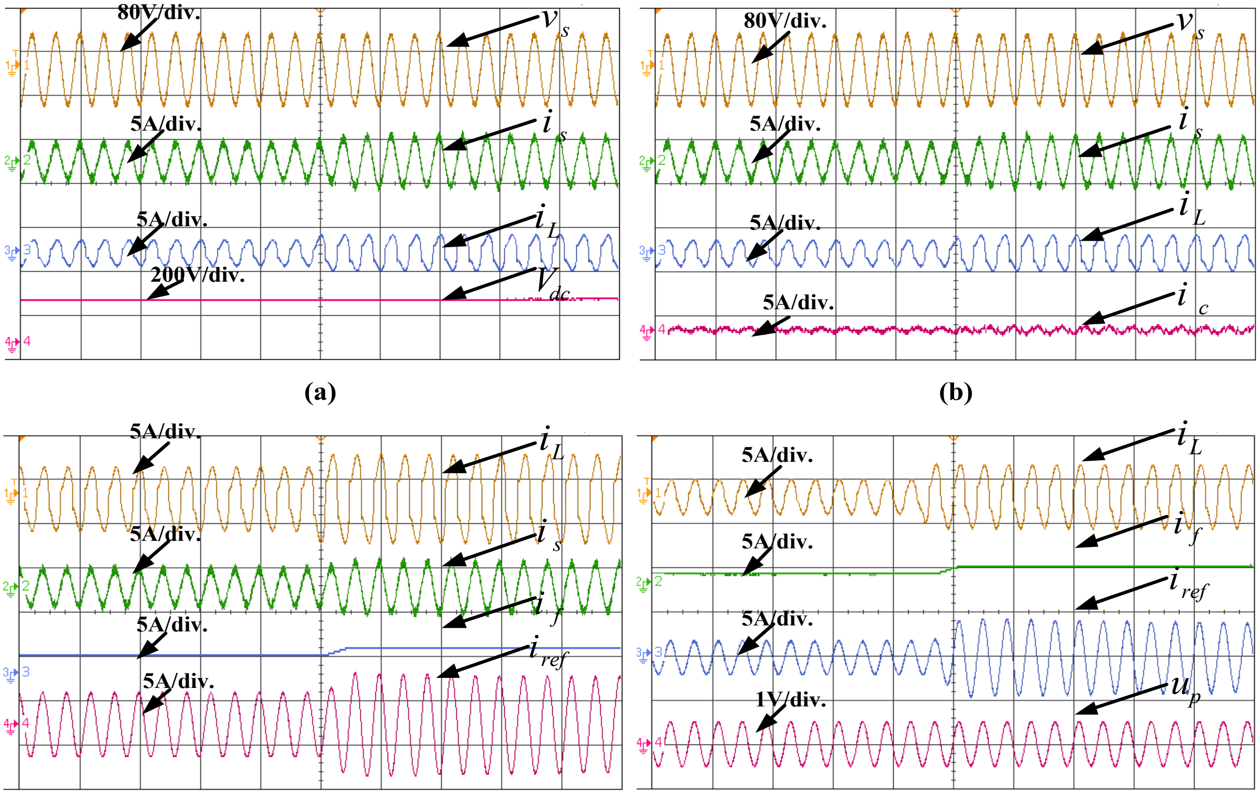

(a) (b)

(c) (d)

Fig 4.25 Experimental waveforms of a). v_s,i_s,i_L,V_{dc} b). v_s,i_s,i_L,i_c c). i_L,i_s,i_f,i_{ref} and d). i_L,i_f,i_{ref},u_p during dynamic condition using ALLMF.

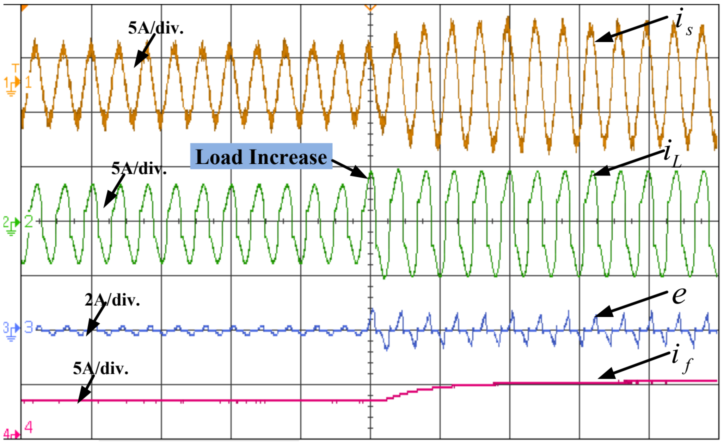

Fig 4.26 Experimental waveforms of i_s, i_L, e, i_f during dynamic load condition using ALLMF.

The intermediate signal waveforms of i_s, i_L, e, and i_f are displayed in Fig 4.26. It is observed that the load current increases during load change, the intermediate parameters (e, i_f) likewise also change. Additionally, it is noted that under dynamic load conditions, the error (e) is almost zero.

4.3.13 Control Algorithm using ARBFNN Algorithm

The complete control algorithm including both the control of DC links and details of ARBFNN are shown in Fig 4.27. The controller description comprises the calculation of unit template, the estimation of the fundamental weight signal, the estimation of active weight loss component and the reference supply current. The estimated weight signal is updated in real time to estimate the

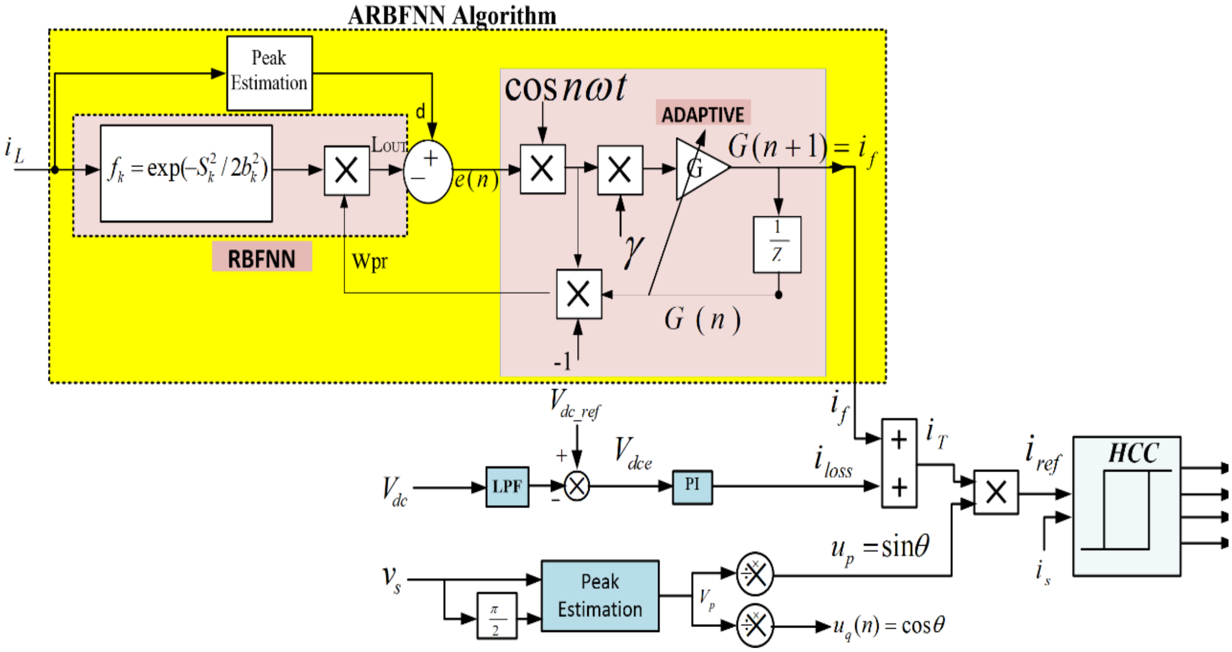

Fig 4.27 Control diagram using A-RBFNN algorithm

fundamental weight of load current. A PI controller is realized over the DC-link voltage to regulate it to 200V reference so as to estimate the weight loss component. The summation of both weights viz. fundamental (i_f) and loss component (i_{loss}) is effective weight (i_T) which is multiplied with unit template to generate reference current i_{ref}. The reference current is perfectly sinusoidal (i_{ref}) and the actual supply current is (i_s) passed through PWM current controller to generate gating pulses for IGBT switching operation to control DSTATCOM. This ensures the grid current is perfectly sinusoidal and the entire reactive power demand of the load is met by the compensator.

4.3.14 Extraction of Fundamental Current using ARBFNN

Eq. 4.40 presents the active magnitude of current fundamental retrieved with A-RBFNN controller as shown in Fig 4.28. The gain in A-RBFNN changes dynamically until convergence is reached.

$$G(n+1) = G(n) + \gamma e \cos \omega t = i_f \tag{4.40}$$

where G(n+1) = $i_f$corresponds to the fundamental component of load current and ϒ is the learning rate, ‘e’ is the error signal.

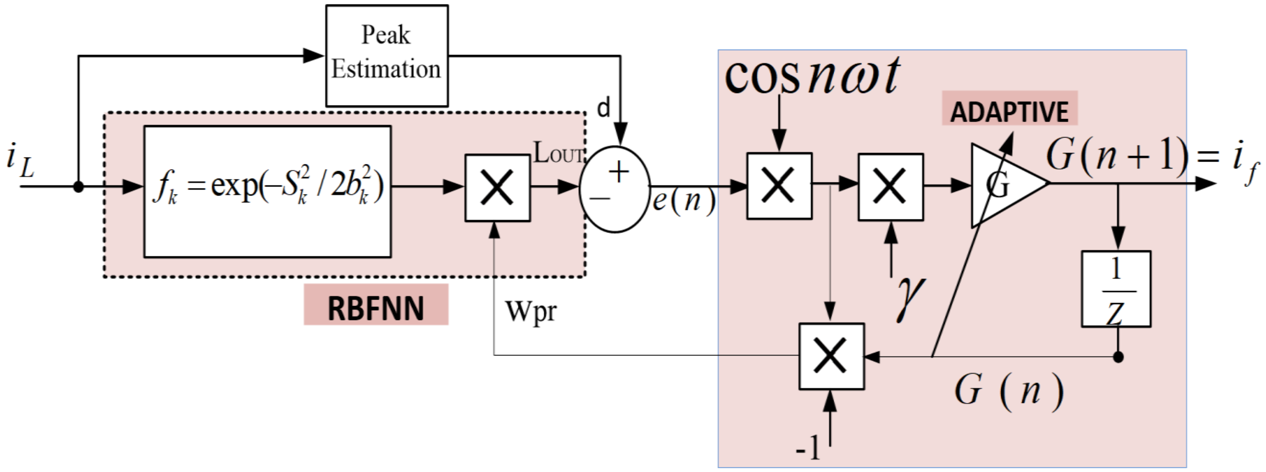

Fig 4.28 Circuit diagram of A-RBFNN algorithm

4.3.15 Calculation of loss component

It is similar discussed in section 4.3.3, the compared DC link voltage error (V_{dce}) as shown in Eq. 4.41, The current loss component is shown in Eq. 4.42.

$$V_{dce} = V_{dc\_ref} - V_{dc} \tag{4.41}$$

$$i_{loss}(n) = [i_{loss}(n+1) + k_P\{V_{dce}(n+1) - V_{dce}(n)\} + k_i\{V_{dce}(n+1)\}] \tag{4.42}$$

4.3.16 Calculation of unit templates

Similarly, as discussed in section 4.3.4, the unit template is shown in Eq. 4.43.

$$u(n) = \frac{v_s}{V_m} = sin\omega t \tag{4.43}$$

4.3.17 Simulation results for ARBFNN Control Algorithm

In the MATLAB/Simulink software, a model of the suggested system with ARBFNN algorithm is designed and evaluated. The simulation results under different conditions are displayed in Figs 4.29–4.31. The system is designed for 110V, 50Hz applied in closed loop control system.

Fig 4.29 shows the dynamic waveforms of source voltage v_s, source current i_s, load current i_L, compensator current i_c, and DC link voltage V_{dc}. The load is increased from 4A to 5A at time t=0.8s and decreased to its initial level of 4A at time t=1s. Due to load change, the load current, source current and compensating current are also changes but source voltage, and DC link voltage remains unchanged. It is observed that the source current stays sinusoidal and in phase with the source voltage after compensation. The DC link voltage is well regulated and maintained to its reference value of 200V under load dynamics.

The waveform of i_L, i_f, i_{ref} and u_p are shown in Fig 4.30. The fundamental current is observed to increase at time t=0.8s and then decrease at t=1s in accordance with the variations in the actual loading conditions during a load change. The fundamental current is extracted by utilizing

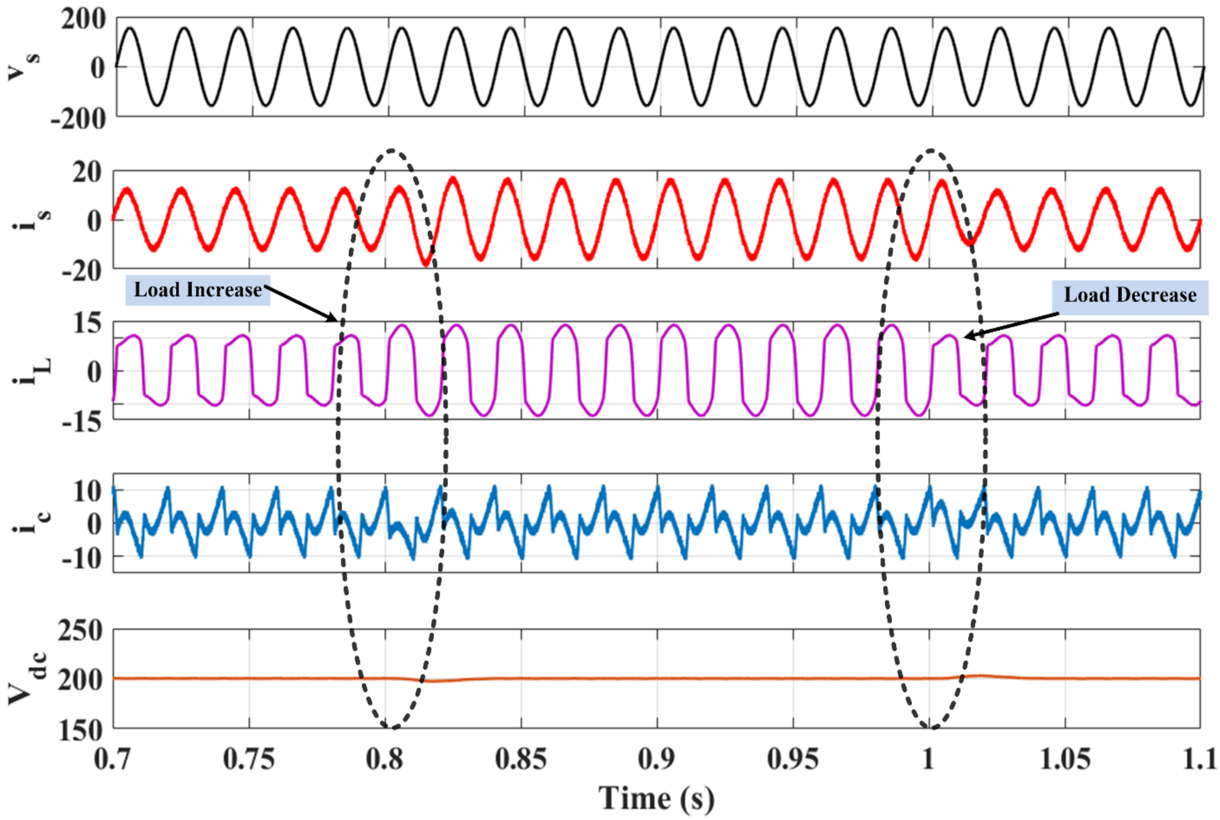

Fig 4.29 Simulation waveforms of source voltage (v_s), source current (i_s), load current (i_L), compensating current (i_c), DC link voltage (V_{dc}) during dynamic condition using ARBFNN

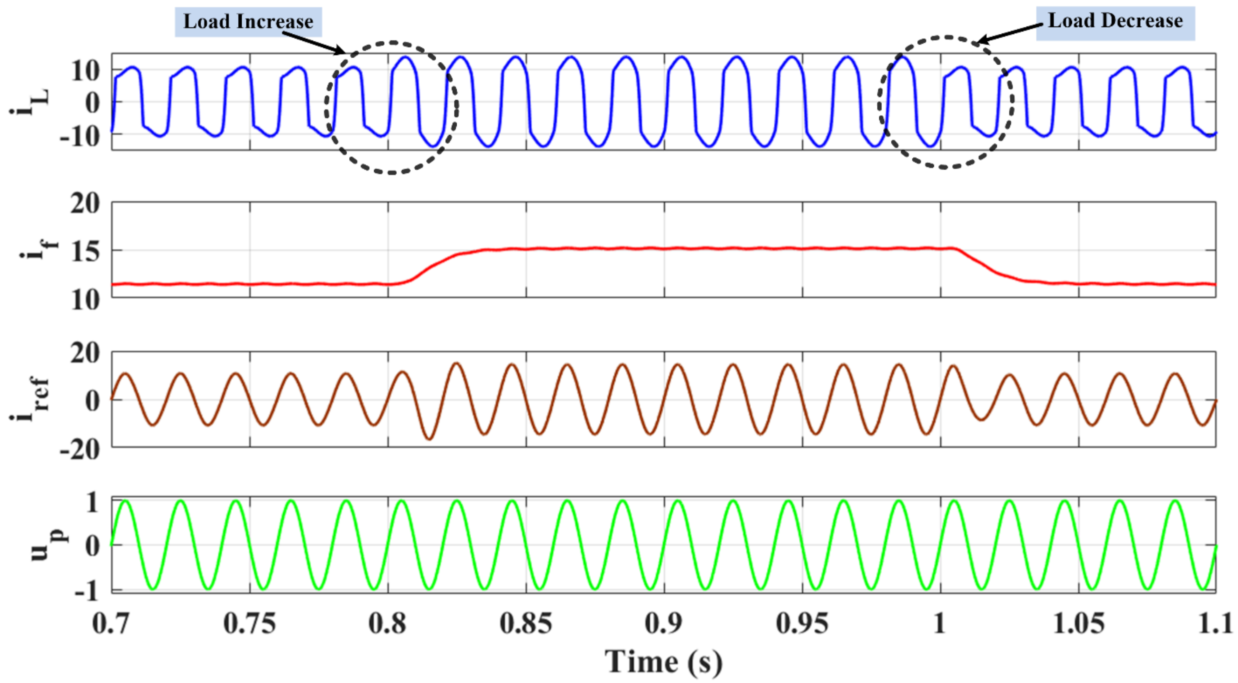

Fig 4.30 Simulation waveforms of load current (i_L), fundamental current (i_f), reference current (i_{ref}), unit template (u_p) during dynamic condition using ARBFNN.

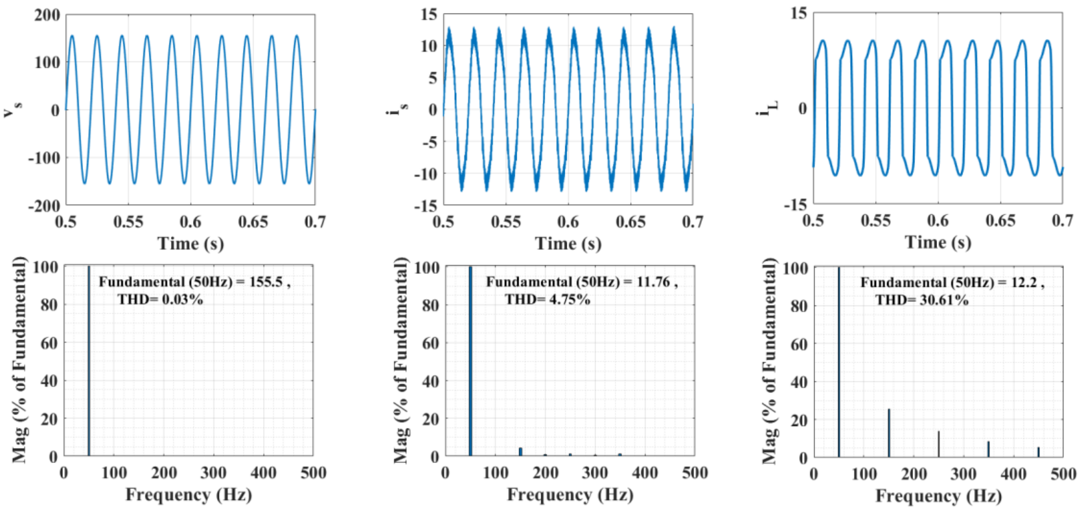

Fig 4.31 Simulation results: Harmonic analysis of a). v_s, THD = 0.03% b). i_s, THD = 4.75% c). i_L, THD = 30.61% during steady state condition using ARBFNN.

ARBFNN algorithm. The reference current also changes with change in load current but the unit template's waveforms remained constant at unity. Also, the fundamental current increases and reaches a new steady state value within less than one cycle, due to the A-RBFNN algorithm's effective control action.

The analysis of the THD profiles in the source voltage (v_s) exhibits harmonic performance with a negligible THD of 0.03% as shown in Fig 4.31. The source current (i_s) shows a THD of 4.75% which reflecting good harmonic quality. In contrast, the load current displays significant distortion with a THD of 30.61%.

4.3.18 Experimental results of ARBFNN

In the laboratory, single phase grid connected DSTATCOM is developed to verify the feasibility of proposed technique. The system rating is 110V rms and 50 Hz frequency. This hardware setup requires two voltage sensors (LV-25P) for sensing (v_s, V_{dc}) and two current sensors (LA-25P) for sensing (i_s, i_L). These sensed voltage and current signals are processed by DSP (dSPACE 1104) to generate eight gating pulses for VSC. The VSC are controlled to inject compensating current at point of common coupling. Hardware results for steady state and dynamic states are captured using Power Analyzer and DSO respectively.

(a). Steady State Condition

The results of single phase grid connected DSTATCOM configuration are now discussed. Fig 4.32(a-c) shows the supply voltage (v_s) along with source current (i_s), load current (i_L) and compensating current (i_c). After compensation, the supply current (i_s) is observed to be in phase with supply voltage and sinusoidal as shown in Fig 4.32(a) while the load current i_L is distorted as shown in Fig 4.32(b).

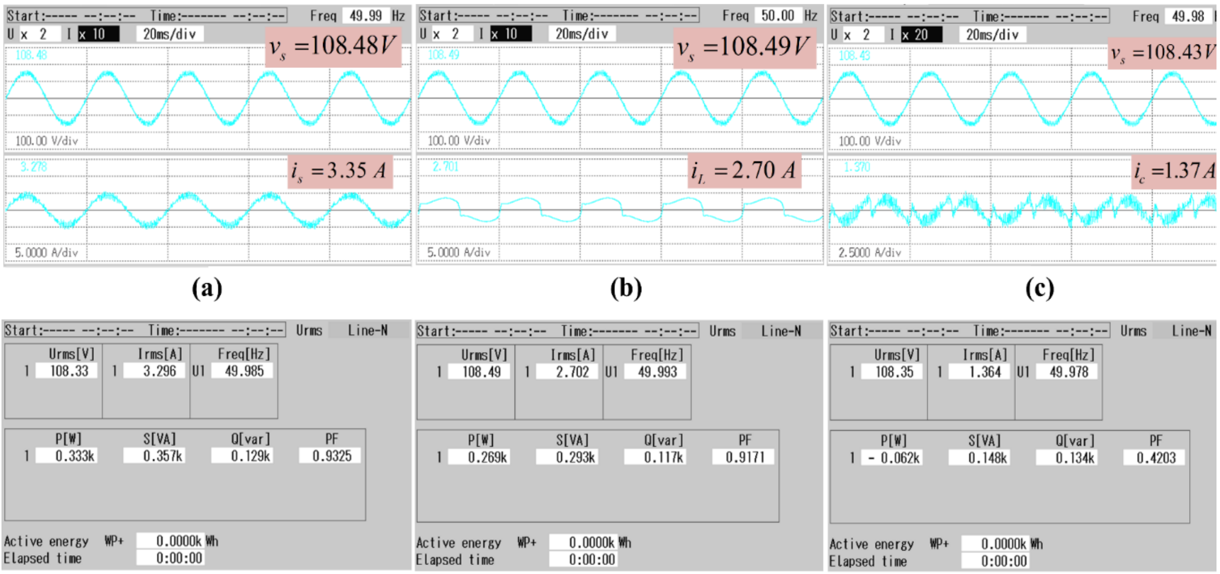

(a) (b) (c)

(d) (e) (f)

Fig 4.32 Experimental results of a). v_s, i_s b). v_s, i_L c). v_s, i_C d). Supply power P_S e). Load power P_L f). Compensator power P_C during steady state condition using ARBFNN.

The steady state active and reactive powers are shown in Fig 4.32(d-f). The active and reactive power demand of load is 0.269kW and 0.117kVAR. The grid supplies 0.333kW active and 0.139kVAR reactive power respectively. The compensator powers are 0.062kW and 0.134kVAR respectively. It is observed that the system active power demand is met by grid whereas most of the reactive power is provided by compensator. Thus, power factor at the supply end is improved from 0.9171 to 0.9325.

Fig 4.33(a-b) shows the THD analysis of source current and load current. The THD of 'i_s' is 4.97% as shown in Fig 4.33(a) and THD of i_L is 26.72% as shown in Fig 4.33(b). The load current is nonlinear (rectifier with R-L load) having high THD. The source current THD has been reduced due to DSTATCOM action and brought within prescribed IEEE standard 519.

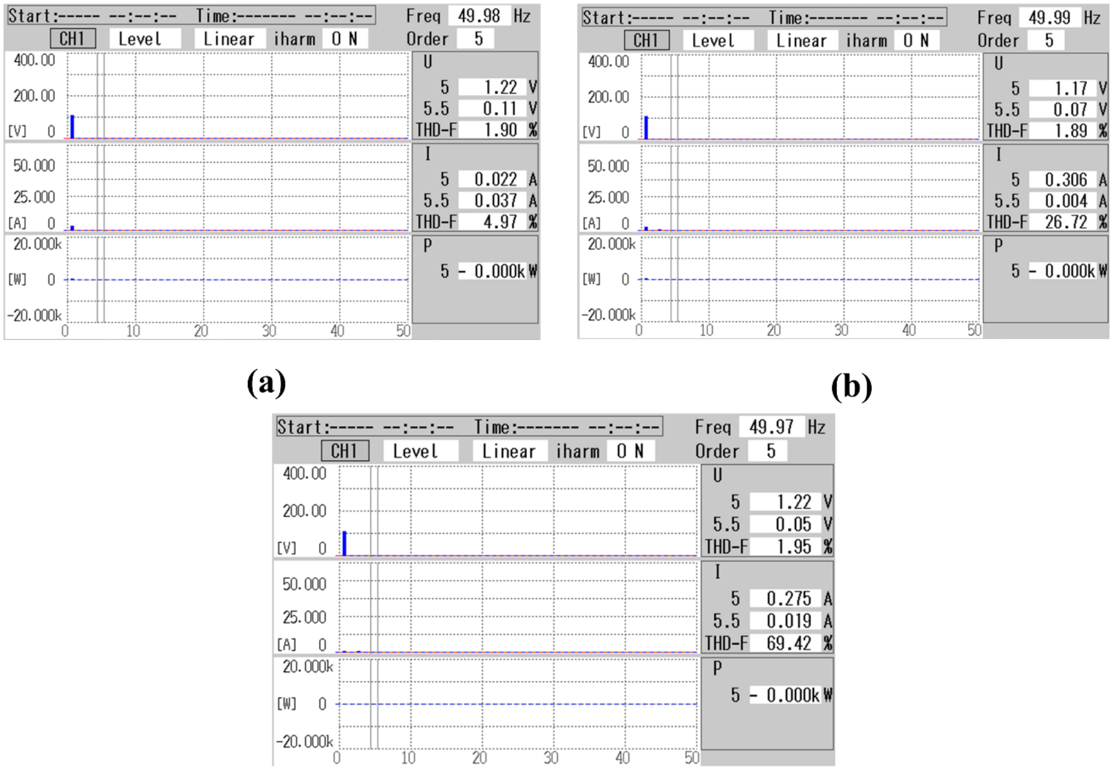

Start:----- --:--:-- Time:------- --:--:--
Freq 49.98 Hz
CH1 Level Linear iharm ON
Order 5
U
5 1.22 V
5.5 0.11 V
THD-F 1.90 %
I
5 0.022 A
5.5 0.037 A
THD-F 4.97 %
P
5 - 0.000k W

(a)

Start:----- --:--:-- Time:------- --:--:--
Freq 49.99 Hz
CH1 Level Linear iharm ON
Order 5
U
5 1.17 V
5.5 0.07 V
THD-F 1.89 %
I
5 0.306 A
5.5 0.004 A
THD-F 26.72 %
P
5 - 0.000k W

(b)

Start:----- --:--:-- Time:------- --:--:--
Freq 49.97 Hz
CH1 Level Linear iharm ON
Order 5
U
5 1.22 V
5.5 0.05 V
THD-F 1.95 %
I
5 0.275 A
5.5 0.019 A
THD-F 69.42 %
P
5 - 0.000k W

(c)

Fig 4.33 Experimental results : Harmonic analysis of a). v_s,i_s with THD = 4.97% b). v_s,i_L with THD = 26.72% c). v_s,i_c with THD = 69.42% during steady state condition using ARBFNN.

(b). Dynamic State Condition

Fig 4.34(a-b) shows the waveforms of source voltage v_s, source current i_s, load current i_L, DC link voltage V_{dc} and compensating current i_c under load increase condition. The DC link voltage is well regulated to its reference value of 200V under load dynamics as shown in Fig 4.34(a). Fig 4.34(b) shows, the supply voltage and current are in same phase before and after load increase. The compensating current (i_c) is also changed due to load change and it also inject compensating current to improve the waveform of source current.

The waveform of i_L,i_s, i_f ,i_{ref} and u_p are shown in Fig 4.34(c-d). It is to be observed that, the load and fundamental current both increase as expected. In less than two cycle, the fundamental active current also increases and reaches a new steady state value due to effective control action of ARBFNN algorithm. The reference current also changes with change in load current and sine template maintains ±1.

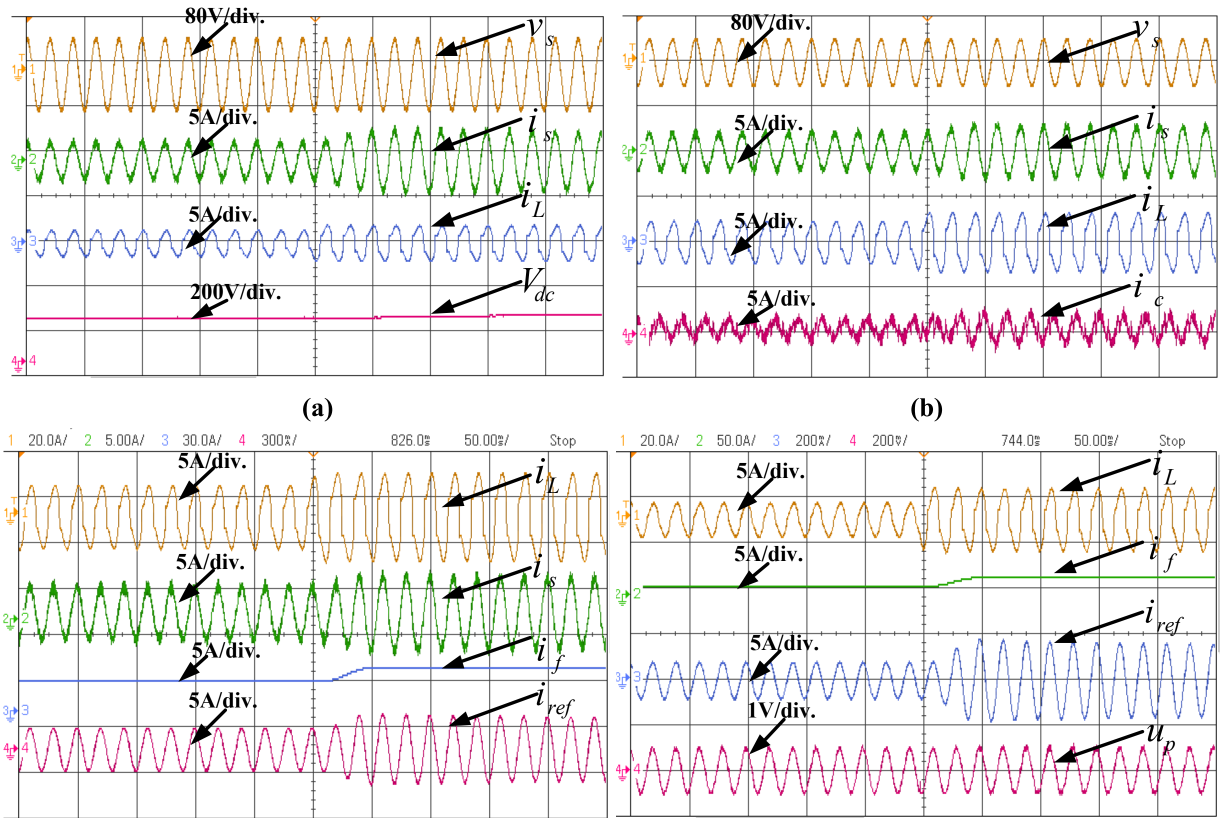

(a) (b)

(c) (d)

Fig 4.34 Experimental waveforms of a). v_s,i_s,i_L,V_{dc} b). v_s,i_s,i_L,i_C c). i_L,i_s,,i_f,i_{ref} and d). i_L, i_f,i_{ref} ,u_p during dynamic condition using ARBFNN.

Fig 4.35 shows the intermediate signal waveforms of is, i_L , e, i_f . It is seen that the intermediate parameters (e, i_f) also change whenever there is a sudden increase in load current. It is also observed that the error (e) is nearly zero under dynamic load condition.

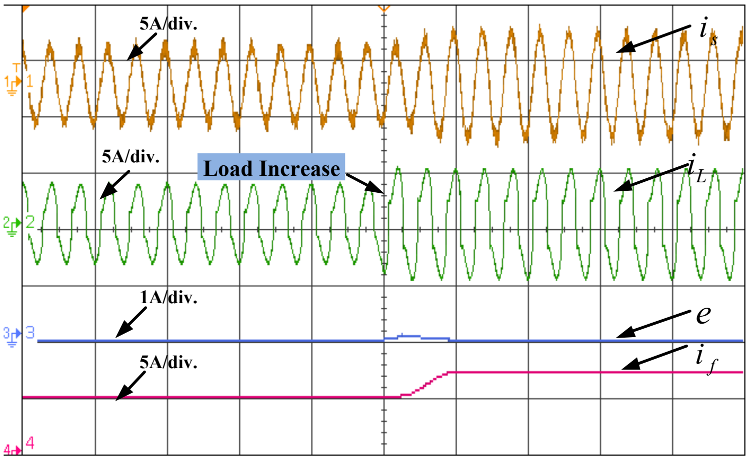

Fig 4.35 Experimental waveforms of i_s ,i_L,e, i_f during dynamic load condition using ARBFNN.

4.4 Comparative analysis of Notch Filter, ARBFNN and adaptive LLMF algorithm

The proposed control algorithms tested on single phase grid connected DSTATCOM. The comparison of all the three algorithms here is discussed based on the extraction of the fundamental current with load current as displayed in Fig 4.36. The comparative analysis of different control algorithms (Notch filter, ALLMF and ARBFNN) is also shown in Table 4.1. The proposed system and performance results for single phase grid connected DSTATCOM are thoroughly analysed. It is observed that the weight convergence is fastest for ALLMF controller and also the extracted fundamental current does not contain any oscillations. Whereas in other two algorithms, oscillations

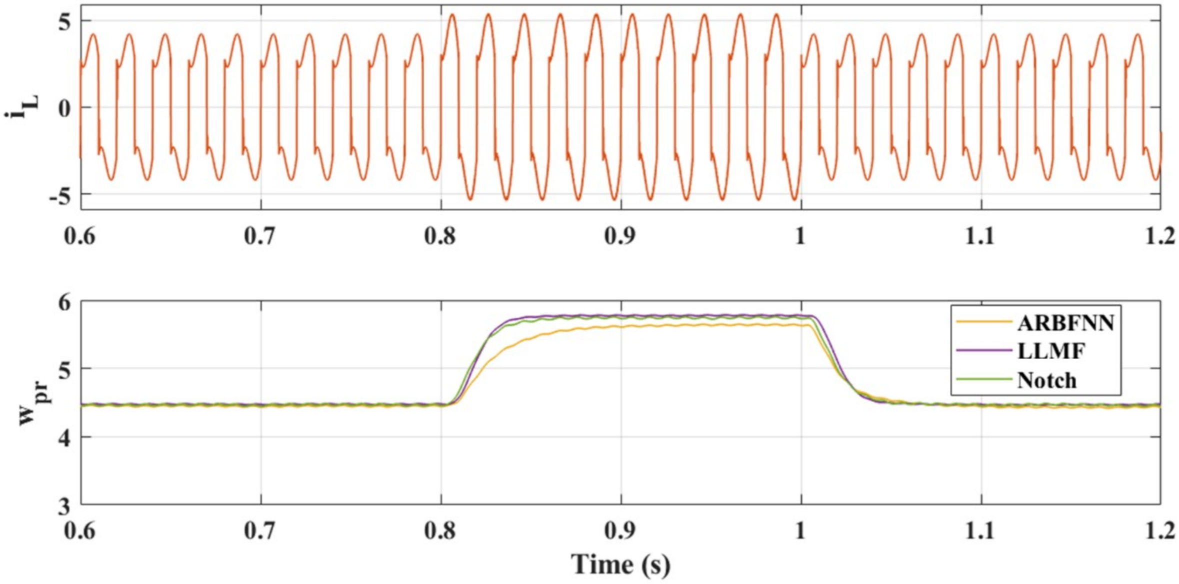

Fig 4.36 Comparative waveforms of load current (i_L) with fundamental current (i_f) at different algorithms

are observed. The ALLMF controller is adaptive algorithm while the Notch filter is a conventional, non-adaptive filter technique. Whereas, the ARBFNN is the neural network-based algorithm. The experimental harmonic content of the source current is obtained to be 4.97% and 4.12% for ARBFNN and Notch algorithms respectively, whereas the ALLMF technique achieves 3.67% THD when the load current has THD of 26.76%. The Convergence is also fast within two cycles with 3V DC link voltage variations under load change. Faster weight convergence guarantees that the proposed approach performs better and maintains closed-loop stability under varied load situations. It is concluded that the DSTATCOM with ALLMF algorithm shows better response in terms of THD of source current as shown in Table 4.2, lower switching losses and fast transient response.

Table 4.1: Comparative analysis of NF, ARBFNN and proposed ALLMF algorithm

S.no	Parameters	Notch	ARBFNN	ALLMF (Proposed)
1	Filter type	Non-Adaptive	Adaptive	Adaptive
2	THD of i_s	4.12%	4.97%	3.67%
3	Estimation of fundamental currents	Consist sustained oscillations	Consist small oscillations	Oscillations are absent
4	Oscillations Magnitude	±4%	±5%	Zero
5	Complexity	Medium	Medium	Medium
6	Sampling Time (T_s)	$50\mu s$	$50\mu s$	$50\mu s$
7	Degree of optimization	NA	Second order	Fourth order
8	DC link Voltage variations	4V	4-5V	3V
9	Convergence	Faster than ARBFNN (3~4 cycles)	Slow (4~6 cycles)	Fastest (2 cycles)

Table 4.2: %THD analysis of NF, ARBFNN and proposed ALLMF algorithm

Algorithms		**%T.H.D (v_s)**	**%T.H.D (i_s)**	**%T.H.D (i_L)**
Notch	Simulation	0.03	2.90	30.61
	Experimental	1.59	4.12	26.86
ALLMF	Simulation	0.03	**2.72**	30.98
	Experimental	1.55	**3.67**	26.76
ARBFNN	Simulation	0.03	4.75	30.61
	Experimental	1.90	4.97	26.72

4.5 Performance Analysis of Three Phase Grid Connected DSTATCOM

The three phase grid connected DSTATCOM is designed in the laboratory to improve the power quality of the systems which is shown in Fig 4.37. It consists of three-phase grid, VSC converter connected in shunt to the system and loads. The three-phase, three-leg configuration comprising six IGBT switches with antiparallel diodes is selected for VSC. The VSC is coupled to DC Link capacitor is referred to as DSTATCOM. The interfacing inductor is used to minimize the ripples in the compensating current. The DSTATCOM is used in mitigating power quality problems with the help of suitable control algorithms and this is discussed in successive sections. The DC link voltage is controlled with the help of PI controller. The simulation and experimental parameters are listed in Appendix A.

For the experimental verification, the three-phase three wire grid connected system is developed in the laboratory. The grid supply is varied through autotransformer. The load, compensator are connected at the point of common coupling (PCC). The compensator is realized as the three-phase, three leg configuration is selected for three-phase system. The DSTATCOM comprises a VSC with DC link capacitance connected in parallel. The interfacing inductors are suitably designed to minimize switching ripples in the DSTATCOM connected at PCC. The voltages and current are sensed and measured with the help of Hall effect sensors viz. LEM LA25 and LV25 current and voltage sensors respectively. The sensed voltage and current signals are processed and necessary computations are carried out inside the Microlab Box which produces the six gating signals for the

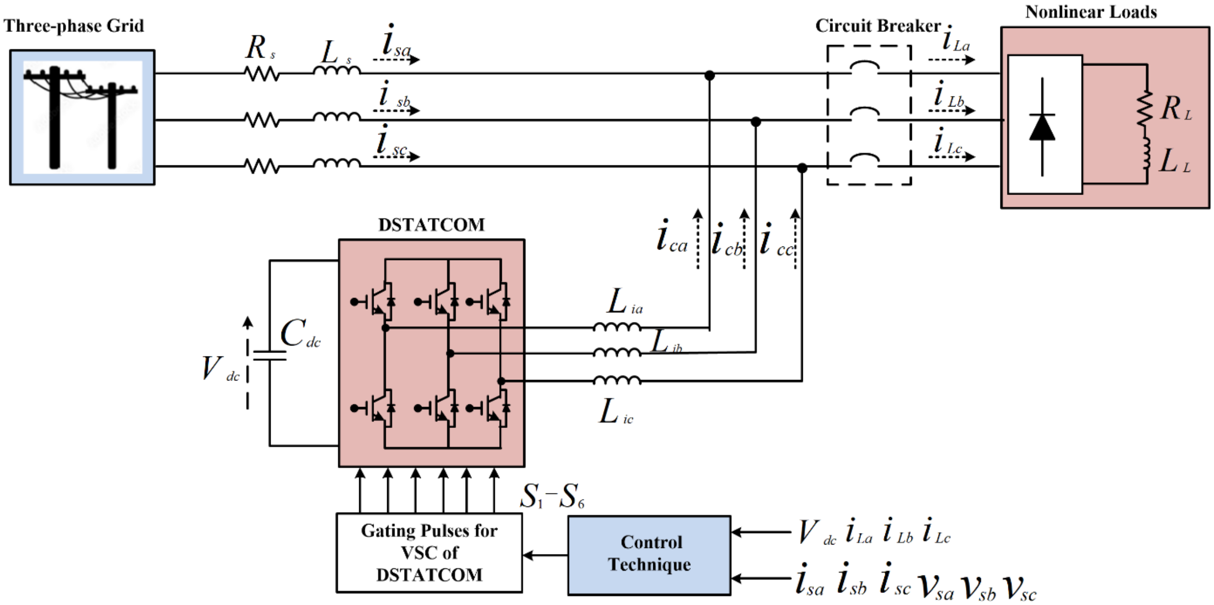

Fig 4.37: System diagram of three phase grid connected DSTATCOM

DSTATCOM. The performance of steady state and dynamic waveforms are recorded using Power Analyzer (HIOKI) and DSO respectively.

4.6.1 Control techniques developed using Conventional Notch Filter

The fundamental current component, active loss component, Unit templates and reference currents are all utilised to regulate the VSC, as illustrated in Fig 4.38. The phase load current is injected into the Notch Filter (NF) controller to derive the fundamental currents (i_{fa}, i_{fb}, i_{fc}). The average current (i_{avg}) is defined as one-third of the sum of fundamental currents. In order to estimate the current loss component, a PI controller is implemented to regulate the total DC-link voltage to a 200V reference. In order to produce reference currents (i_{sa}*, i_{sb}*, i_{sc}*), the effective total current iT is multiplied by unit templates (u_a, u_b, u_c) and the sum of both the average fundamental current (i_{avg}) and loss component (i_{loss}). The reference currents (i_{sa}*, i_{sb}*, i_{sc}*) are perfectly sinusoidal, while the actual supply currents (i_{sa}, i_{sb}, i_{sc}) and reference currents (i_{sa}*, i_{sb}*, i_{sc}*) are fed through a HCC to produce six gating pulses for the IGBT switching operation, which controls a three-phase VSC. This guarantees that the grid currents are precisely sinusoidal and that the compensator meets the entire reactive power demand of the load.

4.6.2 Extraction of Fundamental Current using NF

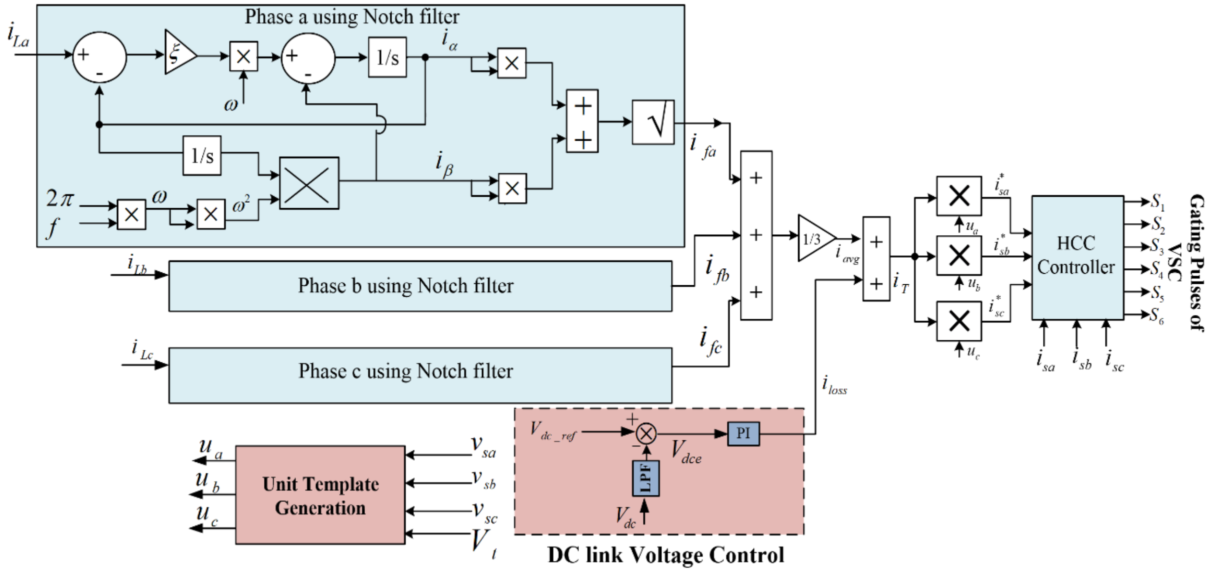

Fig 4.38: Control diagram using Notch filter

The fundamental current components for each phase i_{fa}, i_{fb} and i_{fc} is extracted by Notch Filter controller given by Eq. (4.44 – 4.46).

$$i_{fa} = \sqrt{(i_{\alpha a})^2 + (i_{\beta a})^2} \tag{4.44}$$

$$i_{fb} = \sqrt{(i_{\alpha b})^2 + (i_{\beta b})^2} \tag{4.45}$$

$$i_{fc} = \sqrt{(i_{\alpha c})^2 + (i_{\beta c})^2} \tag{4.46}$$

Now, the average fundamental current is calculated as

$$i_{avg} = \frac{1}{3}(i_{fa} + i_{fb} + i_{fc}) \tag{4.47}$$

4.6.3 Calculation of loss component

The error (V_{dce}) is determined by comparing the DC link voltage (V_{dc}) and its reference voltage (V_{dc_ref}) as shown in Eq.4.48. The current loss component is subsequently determined by supplying the error V_{dce} to the Proportional Integral (PI) controller.

$$V_{dce} = V_{dc\_ref} - V_{dc} \tag{4.48}$$

$$i_{loss}(n) = [i_{loss}(n+1) + k_P\{V_{dce}(n+1) - V_{dce}(n)\} + k_i\{V_{dce}(n+1)\}] \tag{4.49}$$

4.6.4 Calculation of Unit Templates

The unit templates (u_a, u_b, u_c) for each phase is calculated by using PCC terminal voltage as (V_t). The diagram of unit template generation is shown in Fig 4.36.

$$u_a = \frac{v_{sa}}{V_t}; u_b = \frac{v_{sb}}{V_t}; u_c = \frac{v_{sc}}{V_t} \tag{4.50}$$

where, the PCC voltage is

$$V_t = \sqrt{\frac{2}{3}(v_{sa}^2 + v_{sb}^2 + v_{sc}^2)} \tag{4.51}$$

4.6.5 Simulation results incorporating Notch Filter

The waveforms of three phase supply voltage (v_{sabc}), supply currents (i_{sabc}), load currents (i_{Labc}), compensator currents (i_{cabc}), and DC link voltage (V_{dc}) are depicted in Fig 4.39. The supply current maintains sinusoidal behaviour throughout both load change, even in the presence of distorted load currents due to non-linear load. The waveforms of load currents (I_L), fundamental current across a-phase (i_{fa}), reference current (i_{refa}) and unit template (u_{pa}) are depicted in Fig 4.40. The load current is increased at t=0.8s and decrease at t=1s. The source current, reference current and fundamental current of a-phase also follow the load change but unit template (u_{pa}) remains unity. The Notch Filter (NF) is responsible to extract fundamental current and further it provides the improved waveforms in three phase grids connected DSTATCOM.

The analysis of the THD profiles in the source voltage (v_s) exhibits harmonic performance with a negligible THD of 0.00%. The source current (i_s) shows a THD of 3.21% which reflecting good

harmonic quality. In contrast, the load current displays significant distortion with a THD of 17.68% as shown in Fig 4.41.

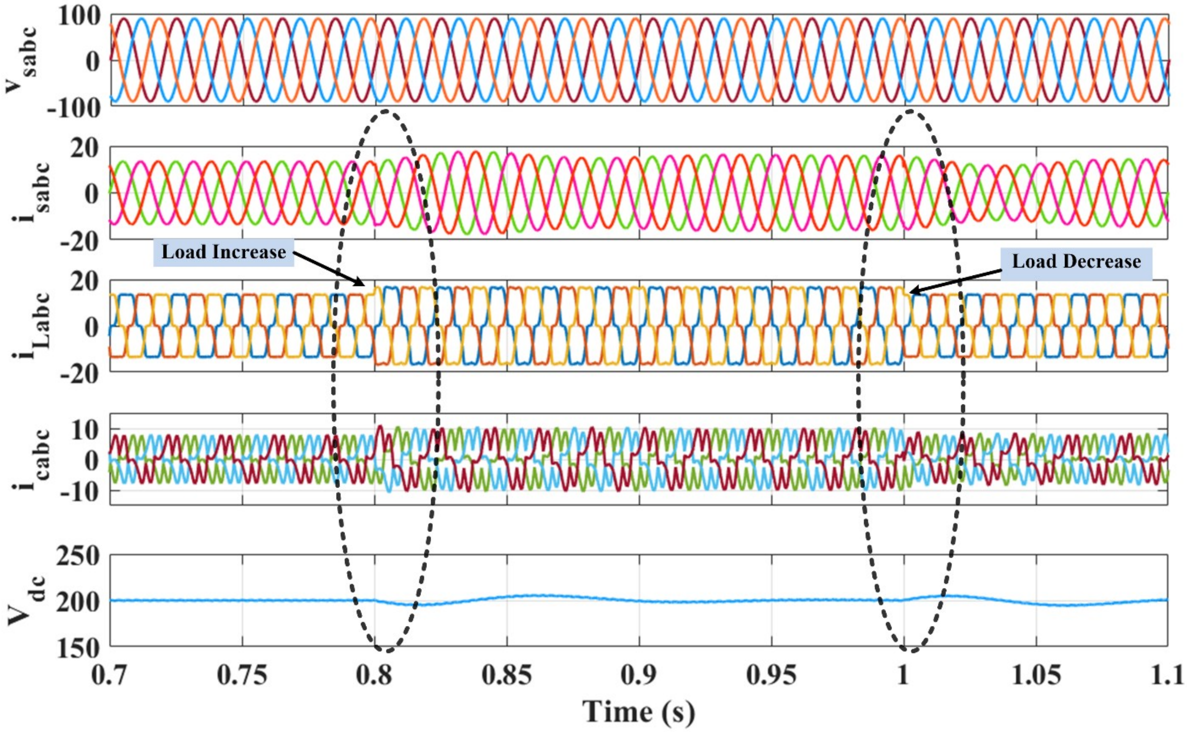

Fig 4.39 Simulation waveforms of source voltage (v_{sabc}), source current (i_{sabc}), load current (i_{Labc}), compensating current (i_{Cabc}), DC link voltage (V_{dc}) during dynamic condition using NF.

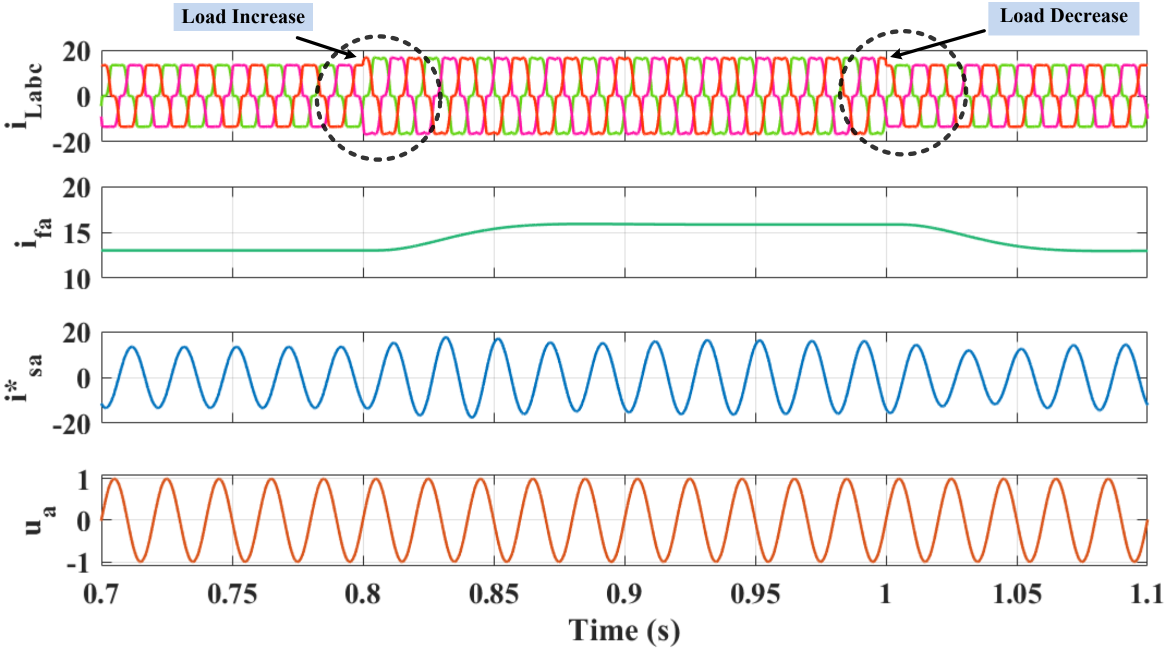

Fig 4.40 Simulation waveforms of load current (i_{Labc}), fundamental current (i_{fa}), reference current (i^*_{sa}), unit template (u_a) during dynamic condition using NF.

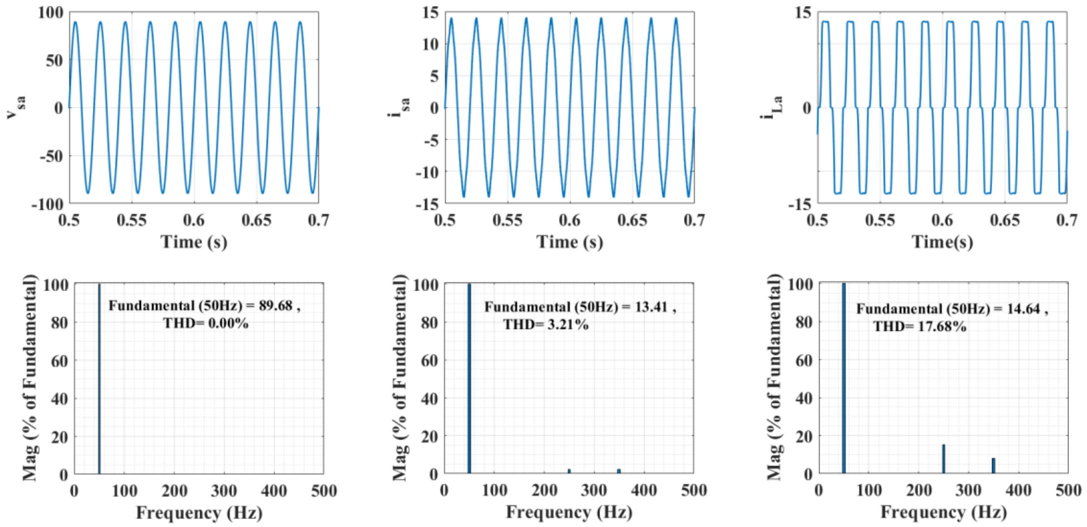

Fig 4.41 Simulation results : Harmonic analysis of a). v_s , THD = 0.00% b). i_s , THD = 3.21% c). i_L , THD = 17.68% during steady state condition using NF.

4.6.6 Experimental results using Notch Filter

The experimental setup of three phase grid connected DSTATCOM is shown in Fig 4.42. This setup includes sensors, the Microlab box 1202 controller, VSC, interfacing inductors, Nonlinear load, programable DC supply, power analyzer, DSO, PCC and a three-phase AC supply. The output of the three-phase variac and three phase DSTATCOM is connected to the PCC and load terminals. The purpose of developed hardware is to mitigate harmonics present in three phase source current.

Fig 4.42 Experimental setup of three phase DSTATCOM

The waveforms presented in Fig 4.43 and Fig 4.44 illustrates the performance of the three-phase grid connected DSTATCOM under steady state condition. In Fig 4.45 and Fig 4.46, the dynamic performance across a-phase in three-phase grid connected DSTATCOM are shown.

(a). Steady State Condition

For the system, the waveforms of three phase source voltage (v_{sabc}) with the three phase source current (i_{sabc}), load current (i_{Labc}) and compensator current (icabc) are shown in Fig 4.43(a-c).

The net power analysis across source (P_s), load (P_L) and compensator are also shown in Fig.4.43(d-f). The three phase grid power supplies 0.669kW and 0.124kVAR to the non-linear load as shown in Fig 4.43(d). The net power across load demands 0.603kW and 0.194kVAR as shown in Fig 4.43(e). The reactive power demand is fulfilled by compensator which inject 0.205kVAR and the switching loss power is 0.034kW as shown in Fig 4.43(f).

The analysis of total harmonic distortion (THD) is shown in Fig 4.44. The total harmonic distortion (THD) in the source voltage is 1.86%, and the THD in the source current is 4.27%, as shown in Fig 4.44(a), which adheres to the IEEE 519 standard. The total harmonic distortion (THD) of load current due to non-linear load is 23.67%. The THD in compensator current is 122.12%.

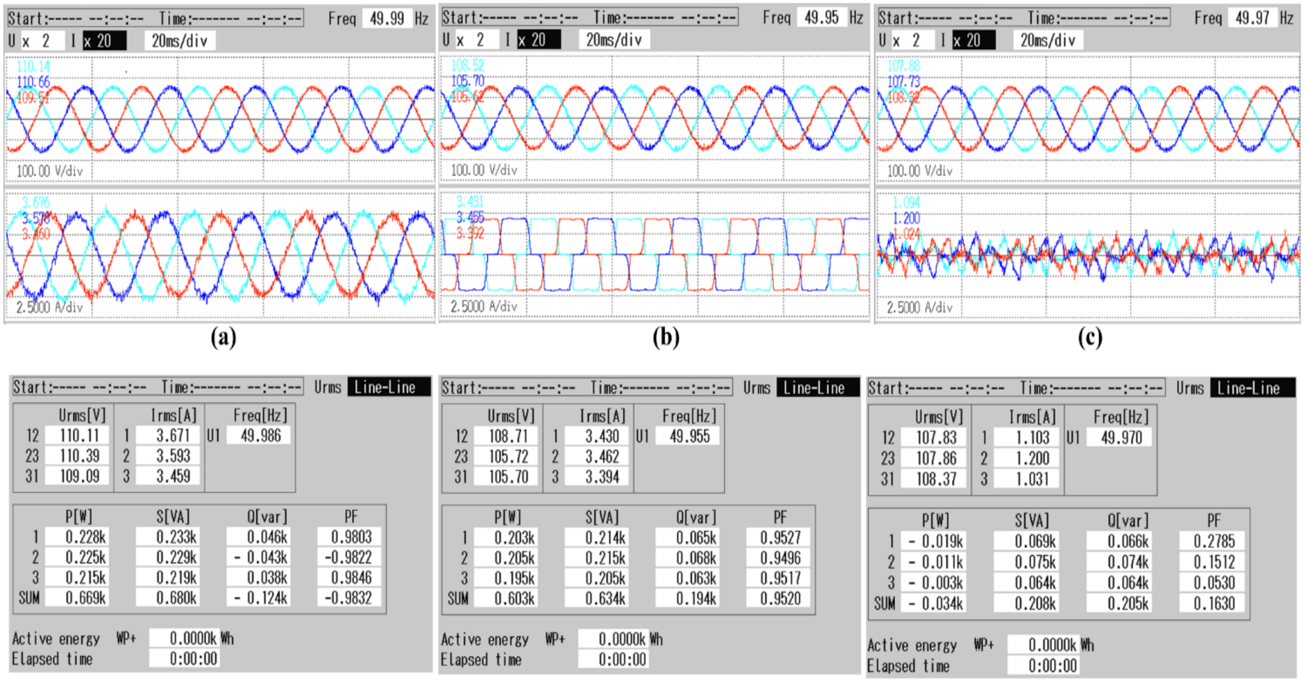

(d)

	Urms[V]		Irms[A]		Freq[Hz]
12	110.11	1	3.671	U1	49.986
23	110.39	2	3.593		
31	109.09	3	3.459		

	P[W]	S[VA]	Q[var]	PF
1	0.228k	0.233k	0.046k	0.9803
2	0.225k	0.229k	- 0.043k	-0.9822
3	0.215k	0.219k	0.038k	0.9846
SUM	0.669k	0.680k	- 0.124k	-0.9832

Active energy WP+ 0.0000k Wh
Elapsed time 0:00:00

(e)

	Urms[V]		Irms[A]		Freq[Hz]
12	108.71	1	3.430	U1	49.955
23	105.72	2	3.462		
31	105.70	3	3.394		

	P[W]	S[VA]	Q[var]	PF
1	0.203k	0.214k	0.065k	0.9527
2	0.205k	0.215k	0.068k	0.9496
3	0.195k	0.205k	0.063k	0.9517
SUM	0.603k	0.634k	0.194k	0.9520

Active energy WP+ 0.0000k Wh
Elapsed time 0:00:00

(f)

	Urms[V]		Irms[A]		Freq[Hz]
12	107.83	1	1.103	U1	49.970
23	107.86	2	1.200		
31	108.37	3	1.031		

	P[W]	S[VA]	Q[var]	PF
1	- 0.019k	0.069k	0.066k	0.2785
2	- 0.011k	0.075k	0.074k	0.1512
3	- 0.003k	0.064k	0.064k	0.0530
SUM	- 0.034k	0.208k	0.205k	0.1630

Active energy WP+ 0.0000k Wh
Elapsed time 0:00:00

Fig 4.43 Experimental results of a). v_s,i_s b). v_s,i_L c). v_s,i_C d). Supply power P_S e). Load power P_L f). Compensator power P_C during steady state condition using NF.

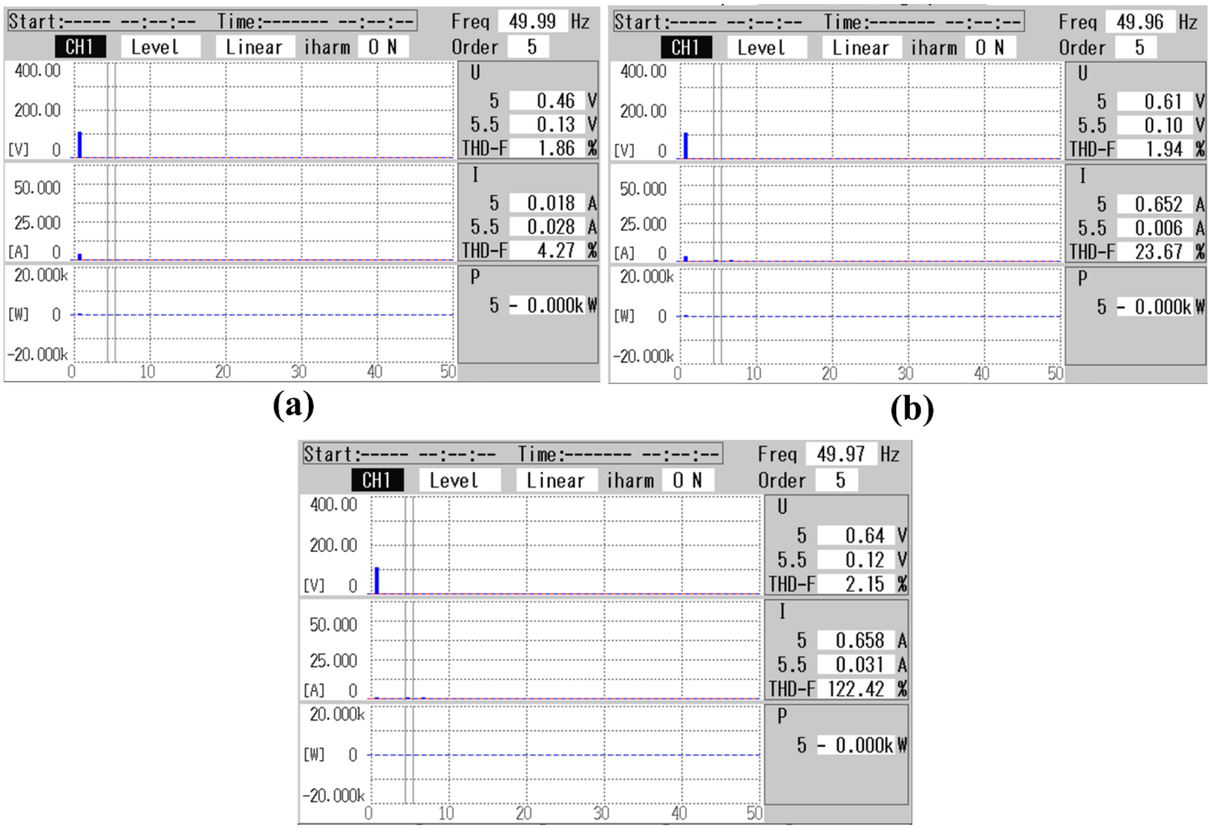

(a) **(b)**

(c)

Fig 4.44 Experimental results: Harmonic analysis of a). v_s,i_s with THD = 4.27% b). v_s,i_L with THD = 23.67% c). v_s,i_C with THD = 122.42% during steady state condition using NF.

(b). Dynamic State Condition

The a-phase waveforms of source voltage (v_{sa}), source current (i_{sa}), load current(i_{La}), DC link voltage (V_{dc}), compensating current(i_{ca}), fundamental current (i_{fa}), reference current (i_{refa}) and unit template (u_{pa}) are shown in Fig 4.45(a-d) under dynamic load condition. The current of load (i_{La}), source (i_{sa}), compensator (i_{ca}), fundamental (i_{fa}) and reference (i_{refa}) is changed due to load change. The V_{dc} remains constant and the i_s follows a sinusoidal pattern even when the load changes. Additionally, in accordance with the IEEE 519 standard, the harmonic content of the grid current is less than 5% observed.

The reference current changes in response to load variations, and the output weight exhibits rapid convergence. This suggests that the NF-based control technique functions satisfactorily under a dynamic load condition. Within one to two cycles of operation, the system attains a stable state.

The intermediate waveforms of Notch Filter (NF) controller are captured and display in Fig 4.46. The waveforms of in phase current (i_α) and quadrature current (i_β) is increased due to change in

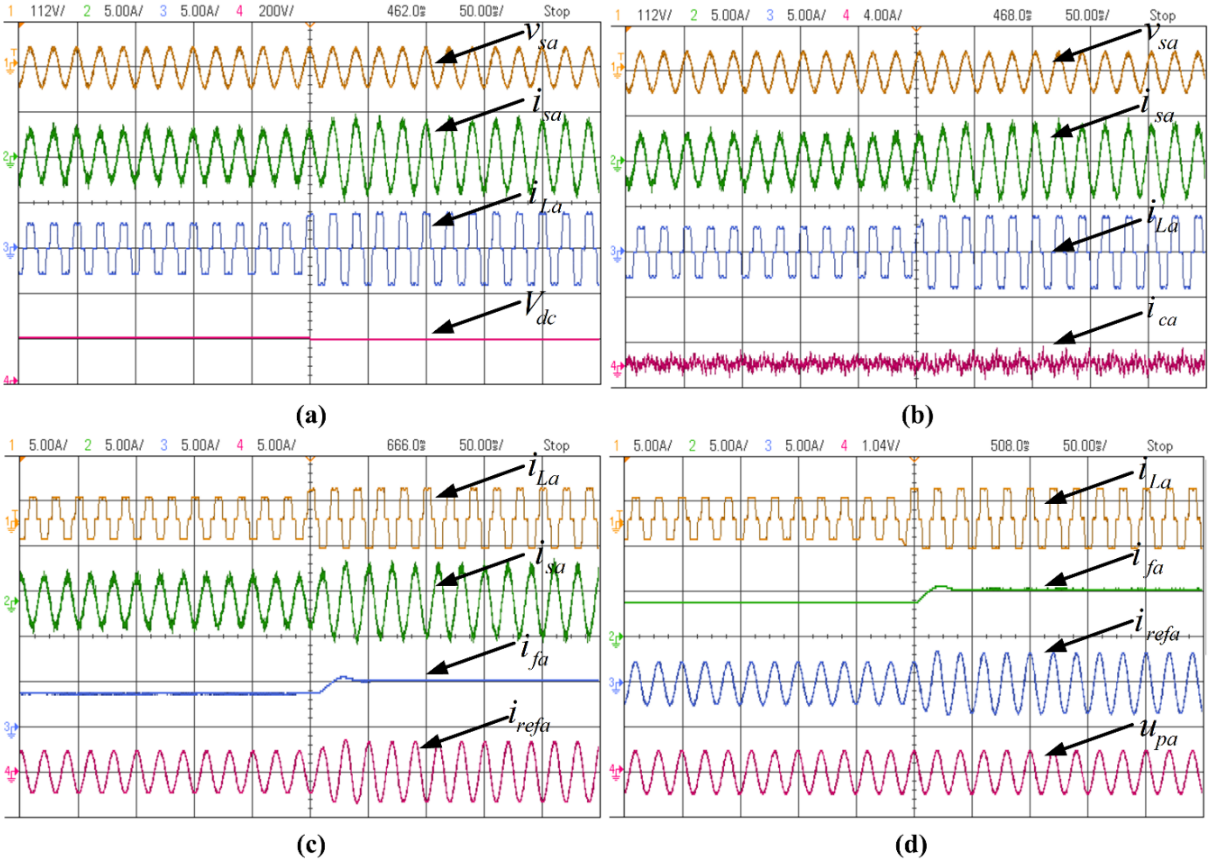

Fig 4.45 Experimental waveforms of a). v_s,i_s,i_L,V_{dc} b). v_s,i_s,i_L,i_C c). i_L,i_s,,i_f,i_{ref} and d). i_L, i_f,i_{ref} ,u_p during dynamic condition using NF.

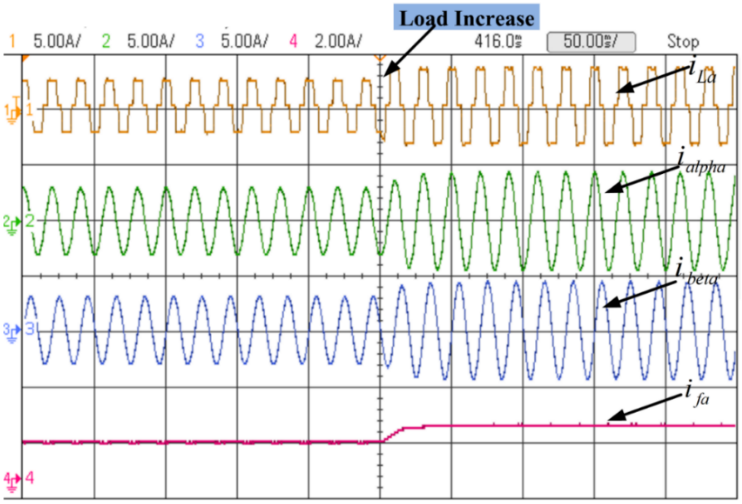

Fig 4.46 Experimental waveforms of i_{La},i_{α}, i_{β},i_{fa} during dynamic load condition using NF.

load current (i_{La}). The a-phase fundamental current (i_{fa}) is extracted to the application of NF which further used to control of three phase DSTATCOM.

4.6.7 Control Algorithm using Adaptive LLMF Algorithm

Fig 4.47 shows the system control diagram of ALLMF algorithm to control three phase VSC. The load currents of each phase are fed with separate ALLMF algorithm to generate fundamental currents (i_{fa}, i_{fb}, i_{fc}) of each phase. The mean of these fundamental currents is average current (i_{avg}). A PI controller is fed with the total DC-link voltage to regulate it to 200V reference so as to estimate the current loss component. The summation of both average fundamental current (i_{avg}) and loss component (i_{loss}) is effective total current i_T which is multiplied with unit templates (u_a, u_b, u_c) to generate reference currents (i_{sa}^*, i_{sb}^*, i_{sc}^*). It is observed that the reference currents (i_{sa}^*, i_{sb}^*, i_{sc}^*) are perfectly sinusoidal and the actual supply currents (i_{sa}, i_{sb}, i_{sc}) is fed through HCC to generate six gating pulses for IGBT switching operation to control three phase VSC. These VSC injecting compensating current to fulfill reactive power demand of the load and ensures the grid currents is perfectly sinusoidal.

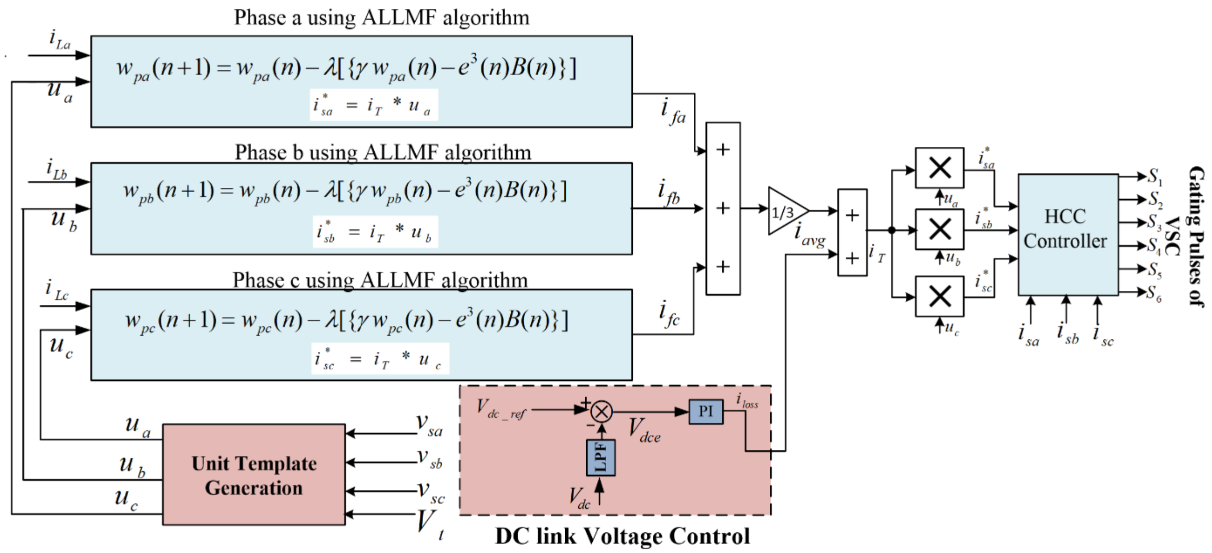

Fig 4.47: Control diagram using ALLMF algorithm

4.6.8 Extraction of Fundamental Current using ALLMF

The fundamental weight components for each phase i_{fa} ,i_{fb} and i_{fc} is extracted by ALLMF controller given by Eq. (4.52 – 4.54).

$$w_{pa}(n+1) = w_{pa}(n) - \lambda[\{\gamma w_{pa}(n) - e^3(n)B(n)\}] = i_{fa} \tag{4.52}$$

$$w_{pb}(n+1) = w_{pb}(n) - \lambda[\{\gamma w_{pb}(n) - e^3(n)B(n)\}] = i_{fb} \quad \ldots (4.53)$$

$$w_{pc}(n+1) = w_{pc}(n) - \lambda[\{\gamma w_{pc}(n) - e^3(n)B(n)\}] = i_{fc} \quad \ldots (4.54)$$

Now, the average weight is calculated as

$$i_{avg} = \frac{1}{3}(i_{fa} + i_{fb} + i_{fc}) \tag{4.55}$$

4.6.9 Calculation of loss current component

As discussed in Section 4.6.3, the calculation of loss current component. The current loss is shown in Eq. 4.57.

$$V_{dce} = V_{dc\_ref} - V_{dc} \tag{4.56}$$

$$i_{loss}(n) = [i_{loss}(n+1) + k_P\{V_{dce}(n+1) - V_{dce}(n)\} + k_i\{V_{dce}(n+1)\}] \tag{4.57}$$

4.6.10 Calculation of unit templates

As discussed in Section 4.6.4, the unit templates (u_a, u_b, u_c) is shown in Eq. 4.58 and the PCC voltage is shown in Eq. 4.59.

$$u_a = \frac{v_{sa}}{V_t}; u_b = \frac{v_{sb}}{V_t}; u_c = \frac{v_{sc}}{V_t} \tag{4.58}$$

$$v_t = \sqrt{\frac{2}{3}(v_{sa}^2 + v_{sb}^2 + v_{sc}^2)} \tag{4.59}$$

4.6.11 Simulation Results for ALLMF Control Algorithm

The MATLAB/SIMULINK software is utilized to observe the control strategies of three phase grid connected DSTATCOM that is controlled by utilised by ALLMF algorithms. The simulation research on the DSTATCOM system is being conducted to compensate with the intention of implementing innovative ALLMF control strategies is effective in relation to the enhancement of power quality (PQ). The simulation results of three-phase source voltage (v_{sabc}), supply currents (i_{sabc}), load currents (i_{Labc}), compensator currents (i_{cabc}), DC link voltage (V_{dc}), fundamental current (i_{fa}), reference current (i_{refa}), and unit template (u_{pa}) under dynamic conditions are displayed in Fig 4.48 and Fig 4.49, respectively. The dynamic performance waveforms of three phase grid connected DSTATCOM is satisfactory by the use of ALLMF control approach. These waveforms are obtained by the change in loads from t=0.8s to t=1s. The i_{sa}, i_{La}, i_{ca}, i_{fa}, and i_{refa} currents is vary as a result of the load change. In the event that the load is changed, the vsabc does not change, and the Vdc also settles at 200V after one cycle. Additionally, it has been found that the magnitude of the sine templates lies in the range of +1 to -1. In order to achieve a higher PQ, the DSTATCOM injects compensatory current.

The analysis of the THD profiles in the source voltage (v_s) exhibits harmonic performance with a negligible THD of 0.00%. The source current (i_s) shows a THD of 1.07% which reflecting good harmonic quality. In contrast, the load current displays significant distortion with a THD of 17.68% as shown in Fig 4.50.

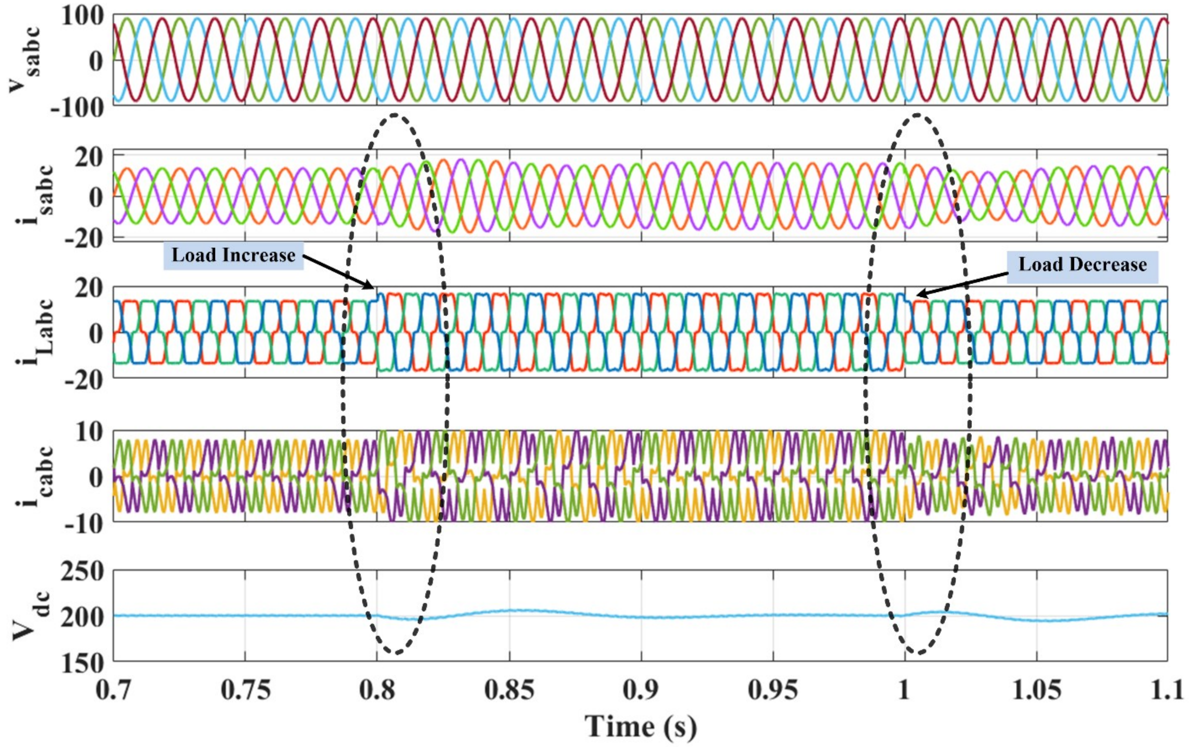

Fig 4.48 Simulation waveforms of source voltage (v_{sabc}), source current (i_{sabc}), load current (i_{Labc}), compensating current (i_{Cabc}), DC link voltage (V_{dc}) during dynamic condition using ALLMF.

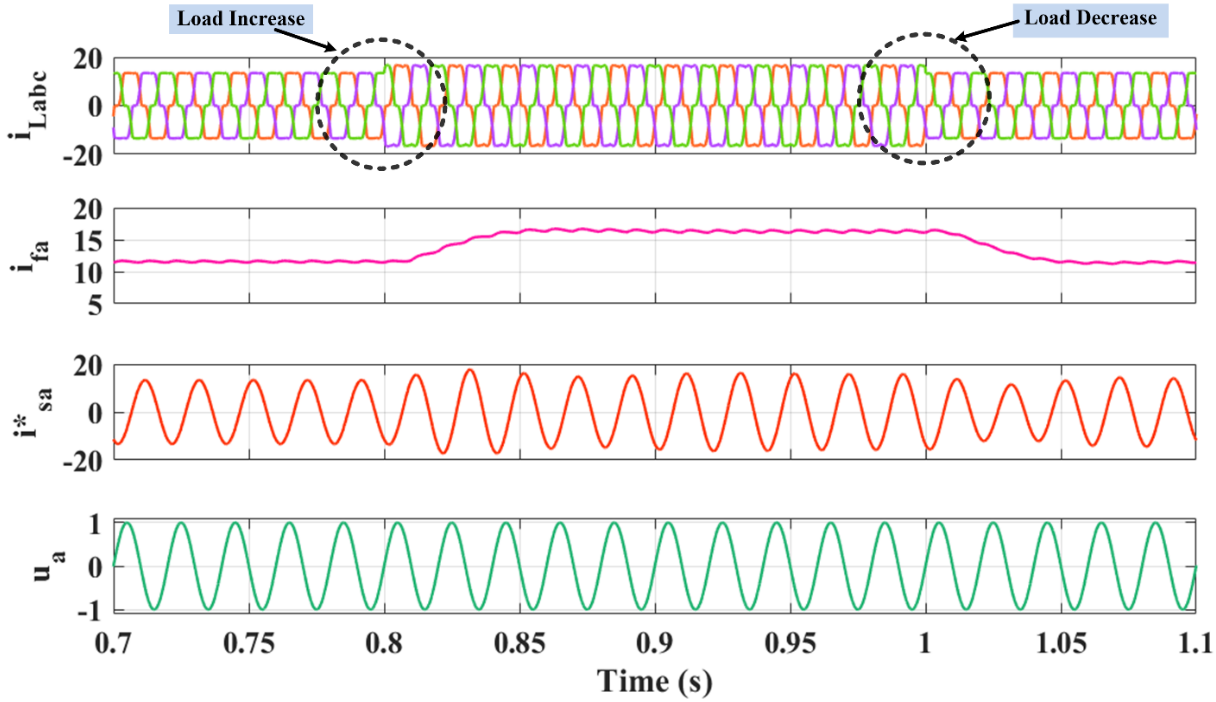

Fig 4.49 Simulation waveforms of load current (i_{Labc}), fundamental current (i_{fa}), reference current (i^*_{sa}), unit template (u_a) during dynamic condition using ALLMF.

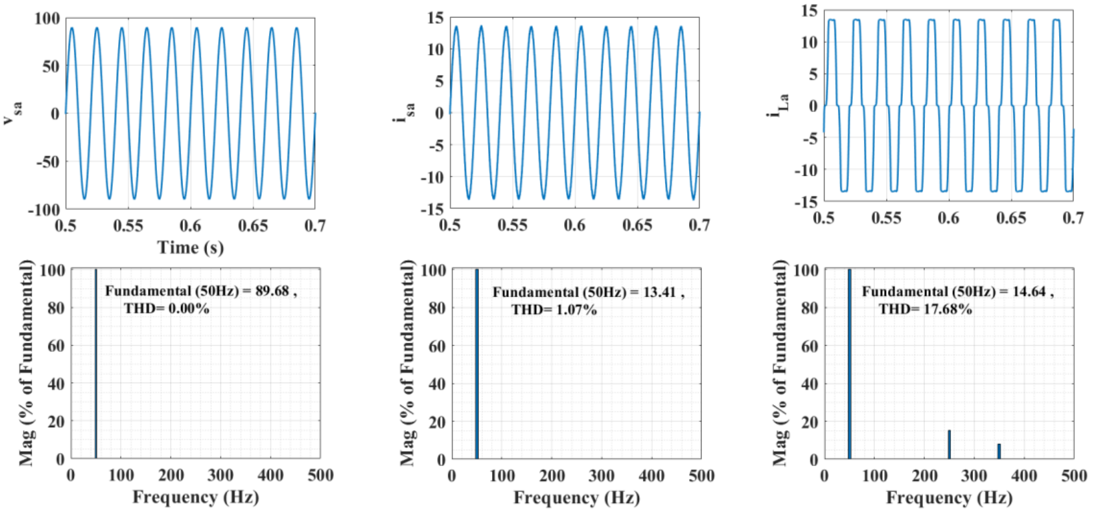

Fig 4.50 Experimental results : Harmonic analysis of a). v_s , THD = 0.00% b). i_s , THD = 1.07% c). i_L , THD = 17.68% during steady state condition using ALLMF.

4.6.12 Experimental Results for ALLMF Control Algorithm

The experimental results of the proposed system are shown in Fig 4.51 to Fig 4.54. The steady state and dynamic waveforms are well presented in this section.

(a). Steady State Condition

The steady state waveforms of phase voltages (v_{sa},v_{sb},v_{sc}) with three phase source current (i_{sa},i_{sb},i_{sc}), load current (i_{La},i_{Lb},i_{Lc}) and three phase compensator current (i_{ca},i_{cb},i_{cc}) are shown in Fig

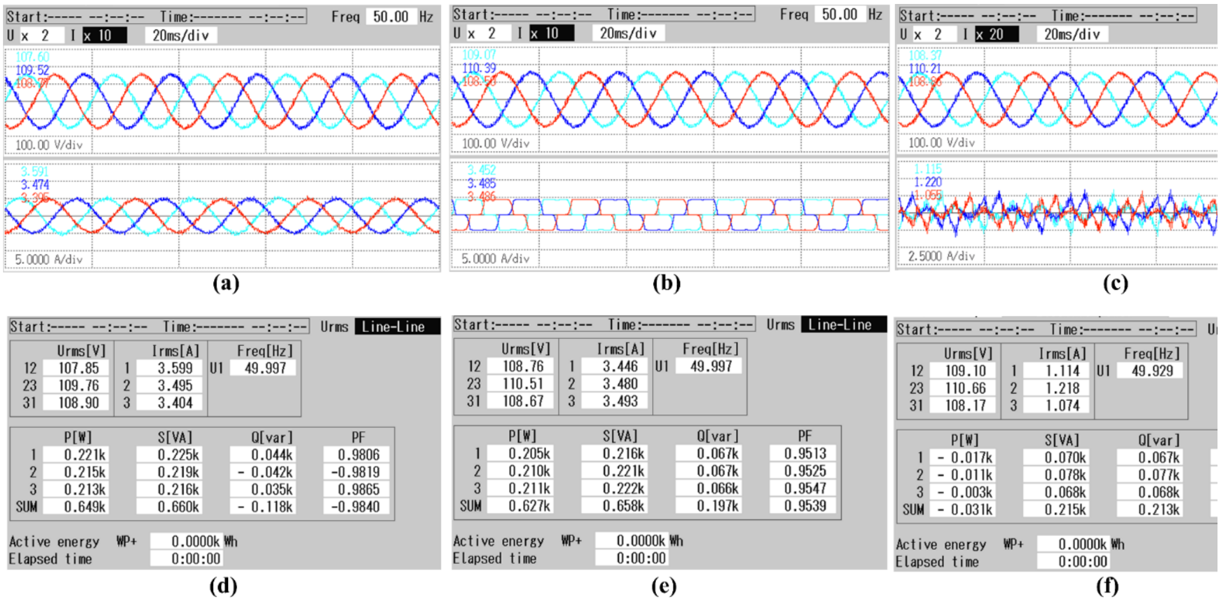

(a) (b) (c)

Start:----- --:--:-- Time:------- --:--:-- Urms Line-Line

	Urms[V]		Irms[A]		Freq[Hz]
12	107.85	1	3.599	U1	49.997
23	109.76	2	3.495		
31	108.90	3	3.404		

	P[W]	S[VA]	Q[var]	PF
1	0.221k	0.225k	0.044k	0.9806
2	0.215k	0.219k	- 0.042k	-0.9819
3	0.213k	0.216k	0.035k	0.9865
SUM	0.649k	0.660k	- 0.118k	-0.9840

Active energy WP+ 0.0000k Wh
Elapsed time 0:00:00

(d)

Start:----- --:--:-- Time:------- --:--:-- Urms Line-Line

	Urms[V]		Irms[A]		Freq[Hz]
12	108.76	1	3.446	U1	49.997
23	110.51	2	3.480		
31	108.67	3	3.493		

	P[W]	S[VA]	Q[var]	PF
1	0.205k	0.216k	0.067k	0.9513
2	0.210k	0.221k	0.067k	0.9525
3	0.211k	0.222k	0.066k	0.9547
SUM	0.627k	0.658k	0.197k	0.9539

Active energy WP+ 0.0000k Wh
Elapsed time 0:00:00

(e)

Start:----- --:--:-- Time:------- --:--:-- U

	Urms[V]		Irms[A]		Freq[Hz]
12	109.10	1	1.114	U1	49.929
23	110.66	2	1.218		
31	108.17	3	1.074		

	P[W]	S[VA]	Q[var]
1	- 0.017k	0.070k	0.067k
2	- 0.011k	0.078k	0.077k
3	- 0.003k	0.068k	0.068k
SUM	- 0.031k	0.215k	0.213k

Active energy WP+ 0.0000k Wh
Elapsed time 0:00:00

(f)

Fig 4.51 Experimental results of a). v_s,i_s b). v_s,i_L c). v_s,i_C d). Supply power P_S e). Load power P_L f). Compensator power P_C during steady state condition using ALLMF.

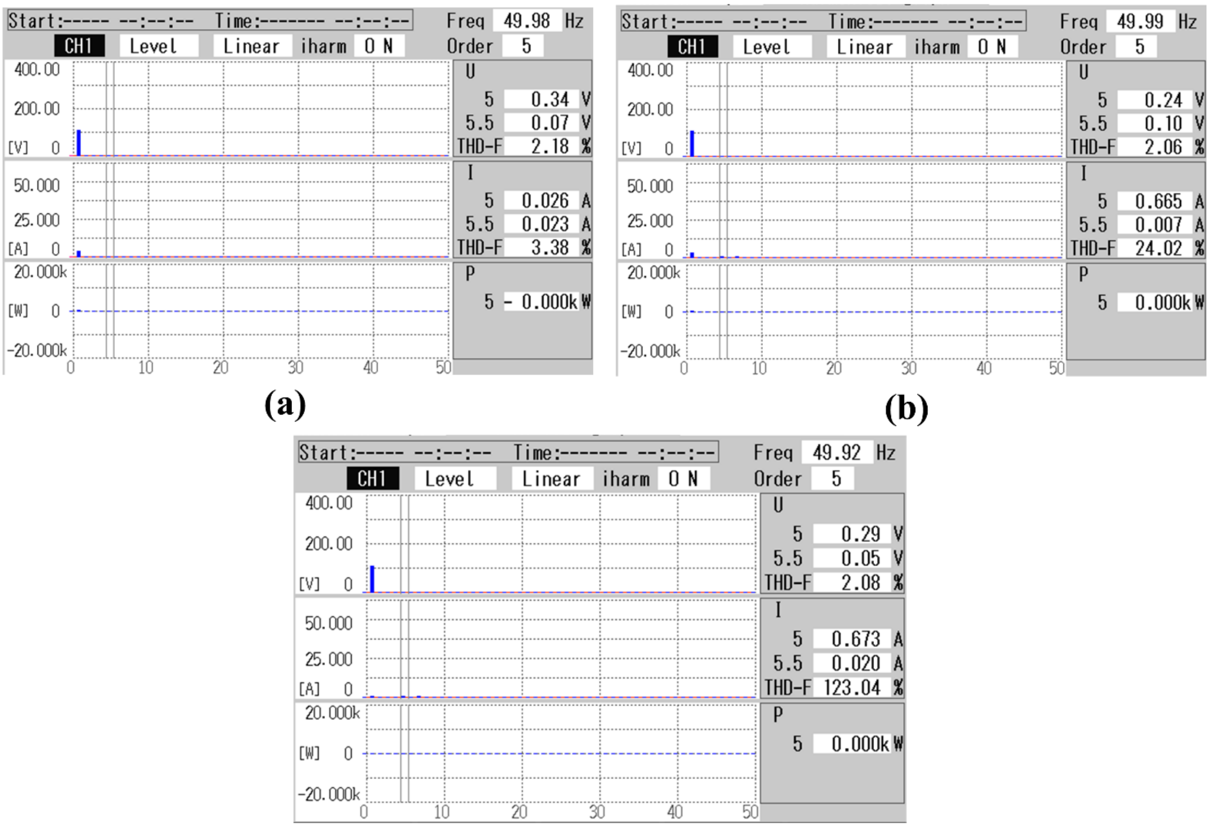

(a)

Freq 49.98 Hz
Order 5
U
5 0.34 V
5.5 0.07 V
THD-F 2.18 %
I
5 0.026 A
5.5 0.023 A
THD-F 3.38 %
P
5 - 0.000k W

(b)

Freq 49.99 Hz
Order 5
U
5 0.24 V
5.5 0.10 V
THD-F 2.06 %
I
5 0.665 A
5.5 0.007 A
THD-F 24.02 %
P
5 0.000k W

(c)

Freq 49.92 Hz
Order 5
U
5 0.29 V
5.5 0.05 V
THD-F 2.08 %
I
5 0.673 A
5.5 0.020 A
THD-F 123.04 %
P
5 0.000k W

Fig 4.52 Experimental results : Harmonic analysis of a). v_s,i_s with THD = 3.38% b). v_s,i_L with THD = 24.02% c). v_s,i_C with THD = 123.04% during steady state condition using ALLMF.

4.51(a-c). The nonlinear load current is fed with ALLMF controller in proposed system to improve the quality of source current and maintain sinusoidal.

The data of power is captured with HIOKI power analyser as shown in Fig 4.51 (d-f). The load power demand is 0.627kW and 0.197kVAR. The grid supply power of 0.649kW to the load and compensator injects reactive power of 0.213kVAR. The losses in the switches are 31W. The power factor is improved from 0.953 to 0.984.

After compensation, the total harmonic distortion of source voltage is 2.18% with source current is 3.38% as shown in Fig 4.52(a). Before compensation, the THD of load current is 24.02% as shown in Fig 4.52(b). The compensator injects THD of 123.04% as shown in Fig 4.52(c). The THD of source current is less than 5% as per IEEE standard.

(b). Dynamic State Condition

Fig 4.53 and Fig 4.54 shows the dynamic performance waveforms of three phase grid connected DSTATCOM. The proposed ALLMF control algorithm is presented to control DSTATCOM.

Further, the DSTATCOM is responsible to improve the quality of power. Fig 4.53 shows the improved waveforms of a-phase source voltage (v_{sa}), supply currents (i_{sa}), load currents (i_{La}), compensator currents (i_{ca}), DC link voltage (V_{dc}), fundamental current (i_{fa}), reference current (i_{refa}), and unit template (u_{pa}). The change in waveforms of currents due to varying load is well display. The source voltage (v_{sa}) is constant and in phase with source current (i_{sa}). During load change, the DC link voltage (V_{dc}) and unit templates (u_{pa}) remains stable at 200V and ±1 respectively. The response of proposed ALLMF controller provides satisfactory results with sinusoidal waveforms of i_{sa}.

In Fig 4.54, we can see the dynamic consequences of the a-phase variables i_{La}, i_{sa}, error (e), and i_{fa}. Rise in load causes a rise in i_{La}, i_{sa}, and i_{fa}. As an added bonus, using the ARBFNN algorithm yields the minimal error (e) and adequate system performance.

The dynamic waveforms of i_{La} and i_{sa} current with intermediate results of error (e) and i_{fa} are shown in Fig 4.54. The source current (i_s) sinusoidal and complies with the IEEE 519 standard for three-

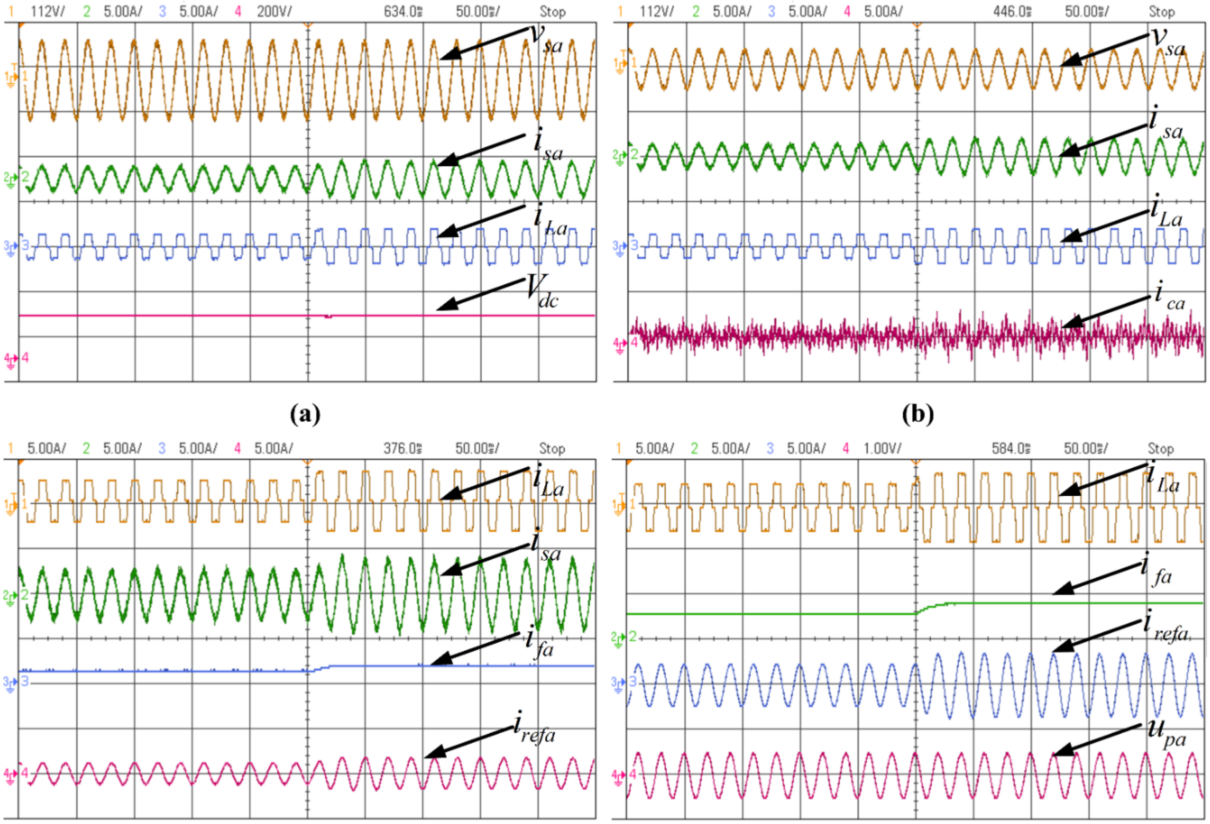

(a) **(b)**

(c) **(d)**

Fig 4.53 Experimental waveforms of a). v_s,i_s,i_L,V_{dc} b). v_s,i_s,i_L,i_C c). i_L,i_s,,i_f,i_{ref} and d). i_L, i_f,i_{ref} ,u_p during dynamic condition using ALLMF.

phase systems, despite the highly non-linear load current. The Adaptive Leaky Least Mean Fourth (ALLMF) controller is employed to calculate the fundamental current to control DSTATCOM. It is also observed that the system is stable.

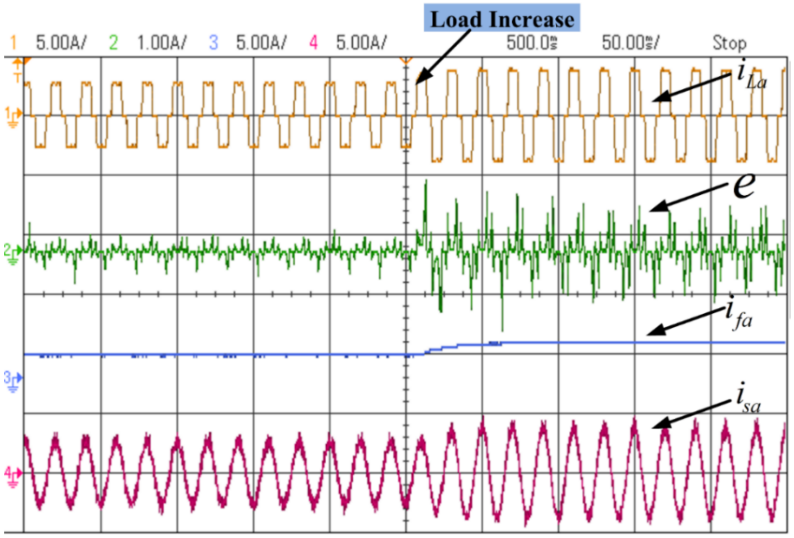

Fig 4.54 Experimental waveforms of i_{La},e, i_{fa} , i_{sa} during dynamic load condition using ALLMF.

4.6.13 Control Algorithms using ARBFNN Algorithm

The proposed ARBFNN algorithm is utilized to control three phase VSC. The six gating pulses (S_1, S_2, S_3, S_4, S_5 and S_6) are generated by the combination of Unit templates, the fundamental

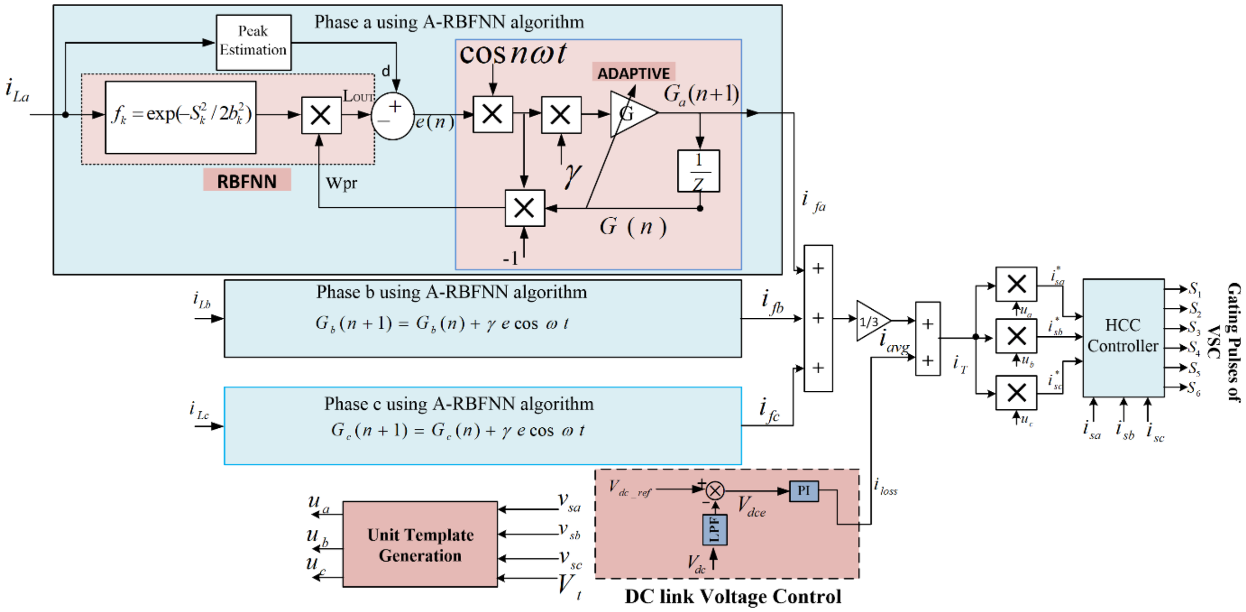

Fig 4.55 Control diagram using A-RBFNN algorithm

current component, active loss component, reference currents and hysteresis controller which are shown in Fig 4.55. The fundamental currents (i_{fa}, i_{fb}, i_{fc}) is extracted by processing phase load current with ARBFNN controller. The one third of the sum of all fundamental currents is average current (i_{avg}). A DC-link voltage and its reference voltage is compared and fed with PI controller to estimate the current loss component (i_{loss}). The effective total current i_T is the addition of both average fundamental current (i_{avg}) and loss component (i_{loss}). Further, it is multiplied with unit templates (u_a, u_b, u_c) to generate reference currents (i_{sa}^*, i_{sb}^*, i_{sc}^*). The actual supply currents (i_{sa}, i_{sb}, i_{sc}) and reference currents (i_{sa}^*, i_{sb}^*, i_{sc}^*) are now passed in HCC to provide gating pulses of three phase VSC. The VSC with interfacing inductor injects compensating current to improve the grid currents waveform.

4.6.14 Extraction of Fundamental Current using ARBFNN

The fundamental weight components (i_{fa} , i_{fb} and i_{fc}) for each phase is extracted by ARBFNN controller as shown in Eq. (4.60 – 4.63)

$$G_a(n+1) = G_a(n) + \gamma e \cos\omega t = i_{fa} \tag{4.60}$$

$$G_b(n+1) = G_b(n) + \gamma e \cos\omega t = i_{fb} \tag{4.61}$$

$$G_c(n+1) = G_c(n) + \gamma e \cos\omega t = i_{fc} \tag{4.62}$$

Now, the average weight is calculated as

$$i_{avg} = \frac{1}{3}(i_{fa} + i_{fb} + i_{fc}) \tag{4.63}$$

4.6.15 Calculation of loss current

As discussed in Section 4.6.3, the switching losses of the IGBT switches of the DSTATCOM can be calculated as shown in Eq. 4.65.

$$V_{dce} = V_{dc\_ref} - V_{dc} \tag{4.64}$$

$$i_{loss}(n) = [i_{loss}(n+1) + k_P\{V_{dce}(n+1) - V_{dce}(n)\} + k_i\{V_{dce}(n+1)\}] \tag{4.65}$$

4.6.16 Calculation of unit templates

As discussed in section 4.6.4, the unit templates (u_a, u_b, u_c) is shown in Eq. 4.66.

$$u_a = \frac{v_{sa}}{V_t}; u_b = \frac{v_{sb}}{V_t}; u_c = \frac{v_{sc}}{V_t} \tag{4.66}$$

where, the PCC voltage (vt) is shown in Eq.4.67.

$$V_t = \sqrt{\frac{2}{3}(v_{sa}^2 + v_{sb}^2 + v_{sc}^2)} \tag{4.67}$$

4.6.17 Simulation Results using ARBFNN algorithm

The control technique using ARBFNN algorithm is simulated in the MATLAB/SIMULINK. The purpose of the simulation study on the DSTATCOM system is to evaluate the efficacy of novel control technique for the improvement of PQ and load compensation in three phase grids connected DSTATCOM. Fig 4.56 and Fig 4.57 shows the simulation results of three phase source voltage (v_{sabc}), supply currents (i_{sabc}), load currents (i_{Labc}), compensator currents (i_{cabc}), DC link voltage (V_{dc}), fundamental current (i_{fa}), reference current (i_{refa}) and unit template (u_{pa}) under dynamic condition. The dynamic performance waveforms of DSTATCOM employing ARBFNN control technique is captured by an increase and decrease of loads at t=0.8s to t=1s. Due to load change, the current of source, load, compensator, fundamental and reference current are also changed. The v_{sabc} remains same and V_{dc} also settles at 200V in one cycle during load variation. It is also observed that the sine templates magnitude lies in between +1 to -1. The DSTATCOM inject compensating current to improve PQ.

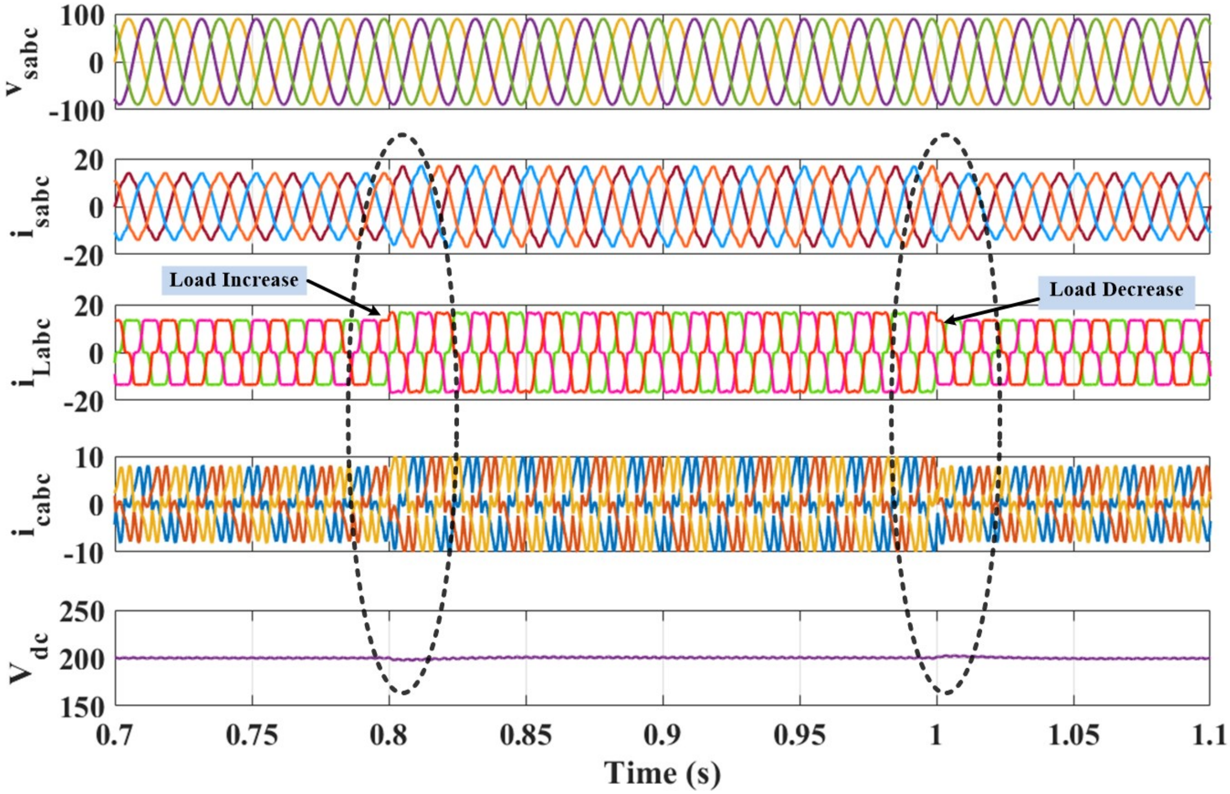

Fig 4.56 Simulation waveforms of source voltage (v_{sabc}), source current (i_{sabc}), load current (i_{Labc}), compensating current (i_{Cabc}), DC link voltage (V_{dc}) during dynamic condition

The analysis of the THD profiles in the source voltage (v_s) exhibits harmonic performance with a negligible THD of 0.02%. The source current (i_s) shows a THD of 4.02% which reflecting good

harmonic quality. In contrast, the load current displays significant distortion with a THD of 17.68% as shown in Fig 4.58.

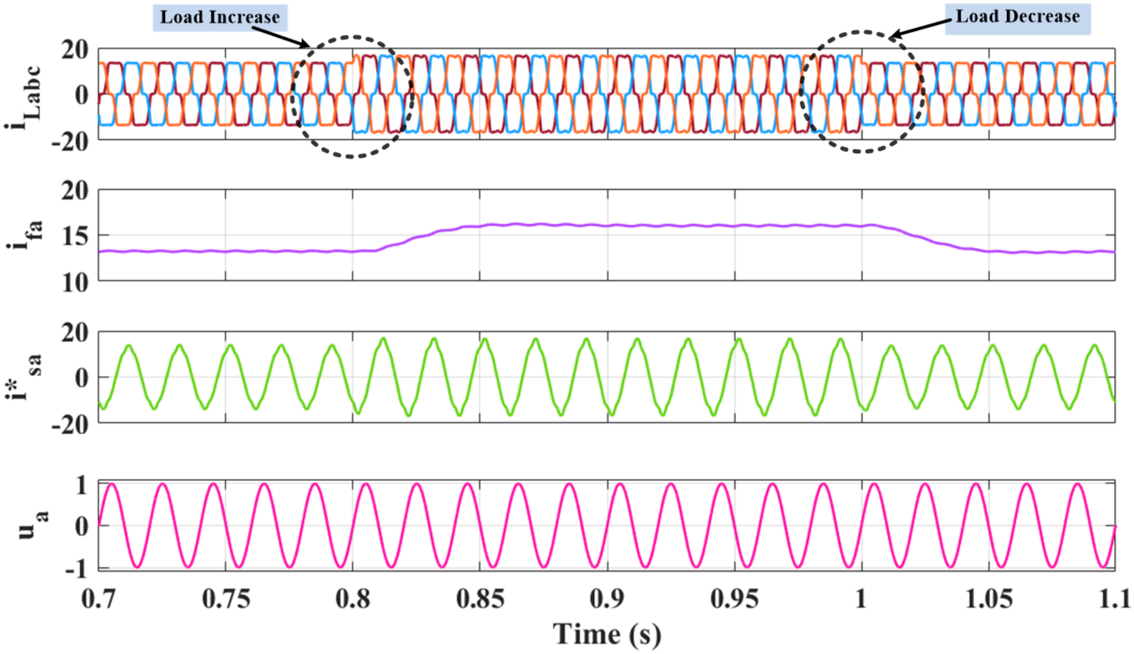

Fig 4.57 Simulation waveforms of load current (i_{Labc}), fundamental current (i_{fa}), reference current (i^*_{sa}), unit template (u_a) during dynamic condition using A-RBFNN.

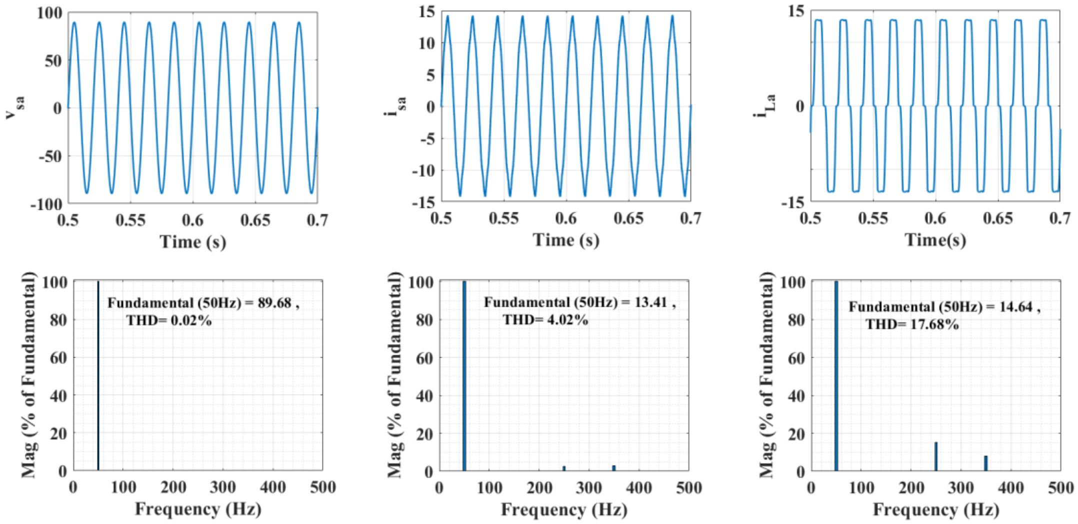

Fig 4.58 Experimental results : Harmonic analysis of a). v_s , THD = 0.02% b). i_s , THD = 4.02% c). i_L , THD = 17.68% during steady state condition using ARBFNN.

4.6.18 Experimental Results for ARBFNN algorithm

The hardware Prototype model of three phase grid connected DSTATCOM is designed and controlled by a Microcontroller box 1202. The Digital Signal Oscilloscope and HIOKI power analyser were used to test the hardware and record the signals in real-time. This section discusses the experimental outcomes.

(a). Steady State Condition

The three phase AC voltage supply (v_{sabc}) with ac currents of source, load and compensator are shown in Fig 4.59(a-c) under steady state condition. The distorted nonlinear load is processed by

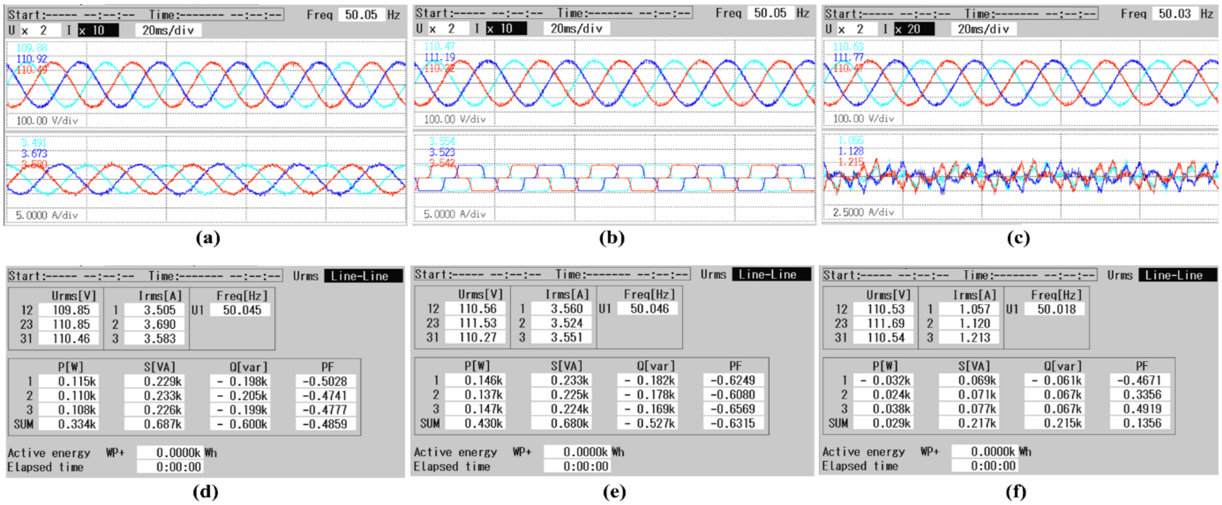

Start:----- --:--:-- Time:------- --:--:-- Urms Line-Line

	Urms[V]		Irms[A]		Freq[Hz]
12	109.85	1	3.505	U1	50.045
23	110.85	2	3.690		
31	110.46	3	3.583		

	P[W]	S[VA]	Q[var]	PF
1	0.115k	0.229k	- 0.198k	-0.5028
2	0.110k	0.233k	- 0.205k	-0.4741
3	0.108k	0.226k	- 0.199k	-0.4777
SUM	0.334k	0.687k	- 0.600k	-0.4859

Active energy WP+ 0.0000k Wh
Elapsed time 0:00:00

(d)

Start:----- --:--:-- Time:------- --:--:-- Urms Line-Line

	Urms[V]		Irms[A]		Freq[Hz]
12	110.56	1	3.560	U1	50.046
23	111.53	2	3.524		
31	110.27	3	3.551		

	P[W]	S[VA]	Q[var]	PF
1	0.146k	0.233k	- 0.182k	-0.6249
2	0.137k	0.225k	- 0.178k	-0.6080
3	0.147k	0.224k	- 0.169k	-0.6569
SUM	0.430k	0.680k	- 0.527k	-0.6315

Active energy WP+ 0.0000k Wh
Elapsed time 0:00:00

(e)

Start:----- --:--:-- Time:------- --:--:-- Urms Line-Line

	Urms[V]		Irms[A]		Freq[Hz]
12	110.53	1	1.057	U1	50.018
23	111.69	2	1.120		
31	110.54	3	1.213		

	P[W]	S[VA]	Q[var]	PF
1	- 0.032k	0.069k	- 0.061k	-0.4671
2	0.024k	0.071k	0.067k	0.3356
3	0.038k	0.077k	0.067k	0.4919
SUM	0.029k	0.217k	0.215k	0.1356

Active energy WP+ 0.0000k Wh
Elapsed time 0:00:00

(f)

Fig 4.59 Experimental results of a). v_S,i_S b). v_S,i_L c). v_S,i_C d). Supply power P_S e). Load power P_L f). Compensator power P_C during steady state condition

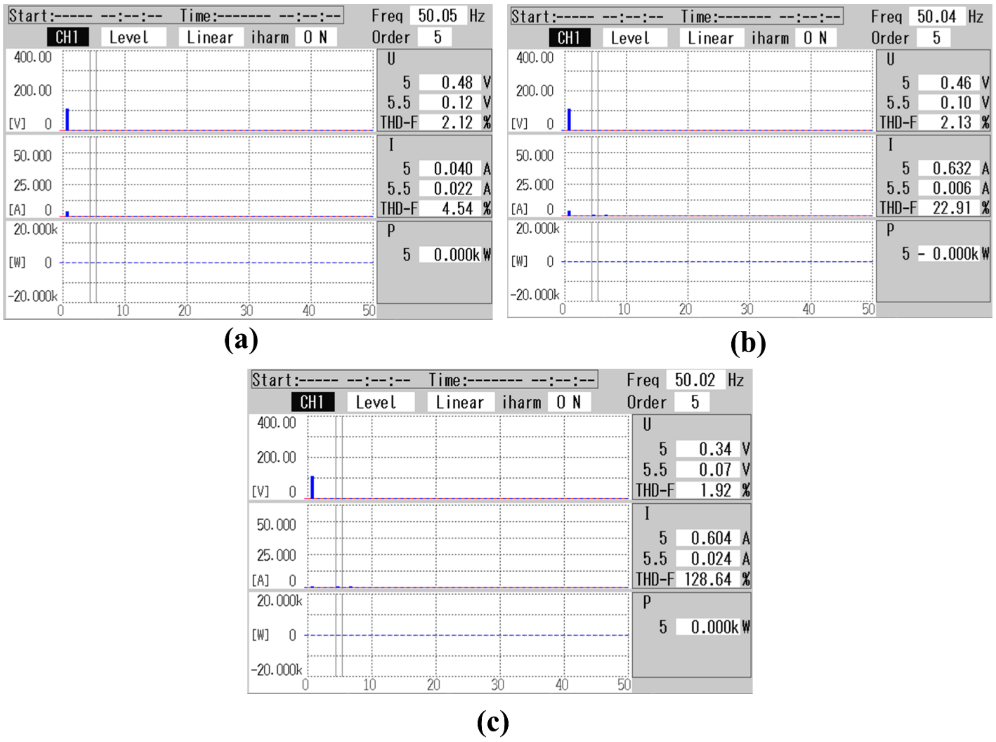

(a)
Freq 50.05 Hz
Order 5
U
5 0.48 V
5.5 0.12 V
THD-F 2.12 %
I
5 0.040 A
5.5 0.022 A
THD-F 4.54 %
P
5 0.000k W

(b)
Freq 50.04 Hz
Order 5
U
5 0.46 V
5.5 0.10 V
THD-F 2.13 %
I
5 0.632 A
5.5 0.006 A
THD-F 22.91 %
P
5 - 0.000k W

(c)
Freq 50.02 Hz
Order 5
U
5 0.34 V
5.5 0.07 V
THD-F 1.92 %
I
5 0.604 A
5.5 0.024 A
THD-F 128.64 %
P
5 0.000k W

Fig 4.60 Experimental results: Harmonic analysis of a). v_S,i_S with THD = 4.54% b). v_S,i_L with THD = 22.91% c). v_S,i_c with THD = 128.64% during steady state condition proposed techniques of ARBFNN algorithm to improve the waveform of source current and it is observed that the source waveform is sinusoidal.

The power flow in three phase grids connected DSTATCOM is shown in Fig 4.59 (d-f) under steady-state which is controlled by an ARBFNN-based algorithm. The HIOKI power quality analyser is used to measure the active and reactive power. The load requires 0.430kW of active power and 0.527kVARs of reactive power, whereas the supply offers 0.600kVARs of reactive power and 0.334kW of active power. The 29W compensator switching losses are fed by the supply. The 215 VARs are fed into the system by the DSTATCOM.

The total harmonic distortion of a-phase source voltage (v_{sa}) with source current (i_{sa}), load current (i_{La}) and compensator current is 2.12%, 4.54%,22.91% and 128.64% respectively are shown in Fig 4.60.

(b). Dynamic State Condition

The dynamic performance of the three phase grid connected DSTATCOM and ARBFNN control technique for non-linear load is illustrated in Fig 4.61 and Fig 4.62. The dynamic waveforms of

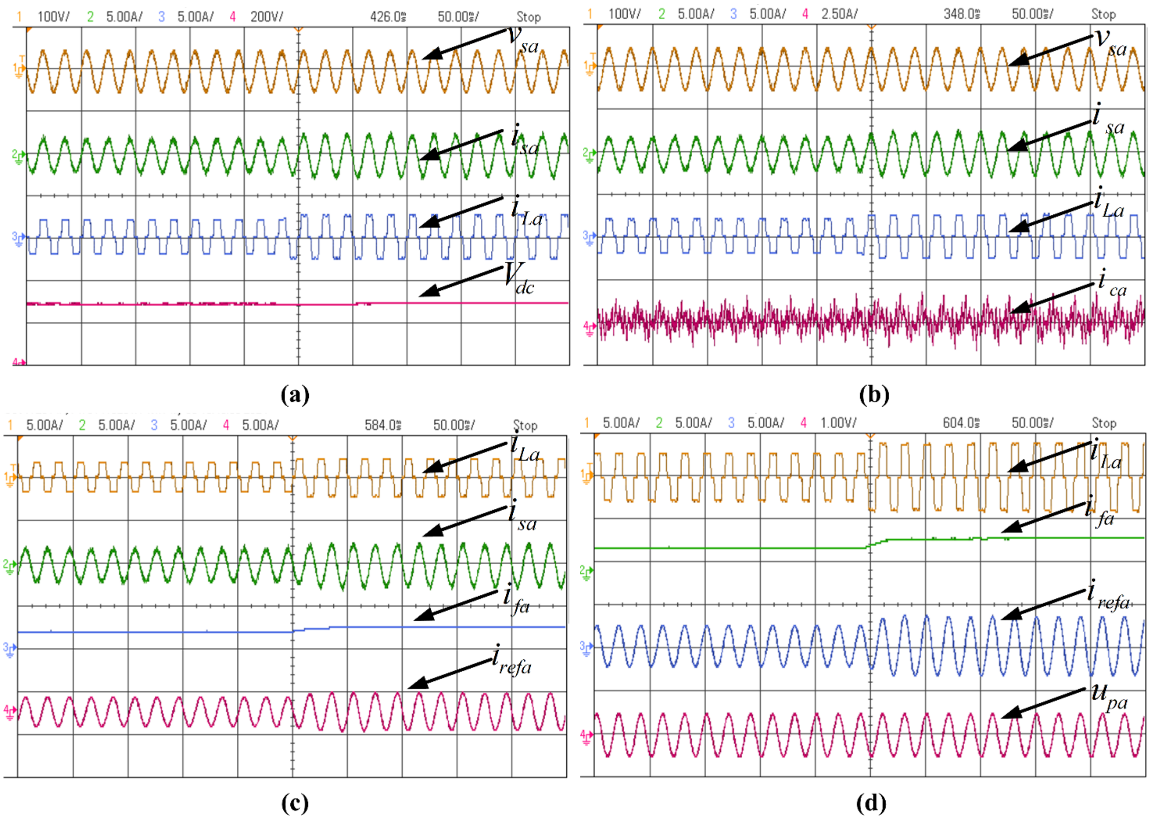

(a) (b)

(c) (d)

Fig 4.61 Experimental waveforms of a). v_{sa},i_{sa},i_{La},V_{dc} b). v_{sa},i_{sa},i_{La},i_{ca} c). i_{La},i_{sa},,i_{fa},i_{refa} and d). i_{La}, i_{fa},i_{refa} ,u_{pa} during dynamic condition phase-a is shown in between source voltage (v_{sa}), supply currents (i_{sa}), load currents (i_{La}), compensator currents (i_{ca}), DC link voltage (V_{dc}), fundamental current (i_{fa}), reference current (i_{refa}) and unit template (u_{pa}) in Fig 4.61. All the currents of phase-a increases due to load change but vsa remains stable with sinusoidal wave of i_{sa}. The DC link voltage also attains its initial position to 200V in few cycles during load change. It is also observed that the unit template is sinusoidal in limit and unchanged during load variations.

The intermediate results of a-phase i_{La}, i_{sa}, error (e) and ifa under dynamic condition are shown in Fig 4.62. The i_{La}, i_{sa} and i_{fa} are increased due to load increase. It is also absorbed that the minimum error (e) is obtained and the performance of the system is satisfactory by the application of ARBFNN algorithm.

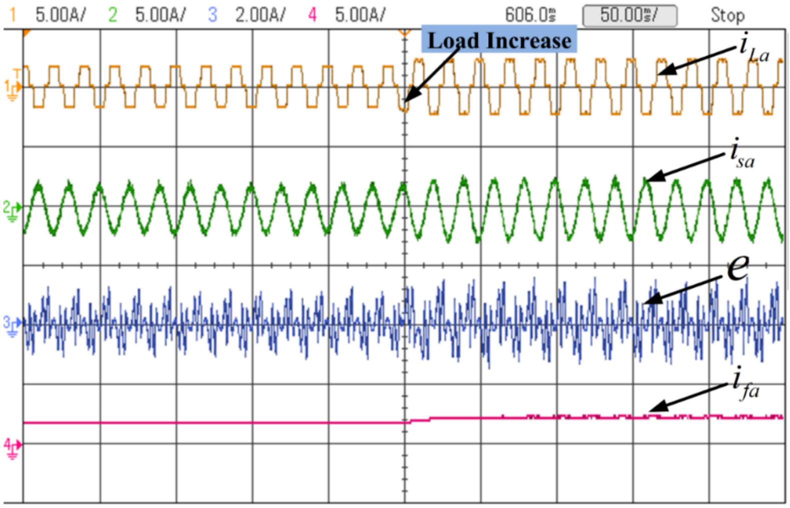

Fig 4.62 Experimental waveforms of i_{La}, i_{sa} ,e, i_{fa} during dynamic load condition

4.7 Comparative analysis of NF, ARBFNN and ALLMF algorithm in three phase system

The comparative analysis of fundamental currents of respective algorithms with load current are shown in Fig 4.63. During load current is increase at time t=0.8s and decrease at time t=1s, the fundamental currents of respective algorithm is also change. The response of the fundamental current extracted through ALLMF is oscillation free and fast response during load change. But in other algorithms, the response of NF and ARBFNN observes oscillation and also the response is slow for ARBFNN algorithm. The %THD analysis of ALLMF of source current (i_s) is less and performs better in comparison to other algorithms as shown in Table 4.3.

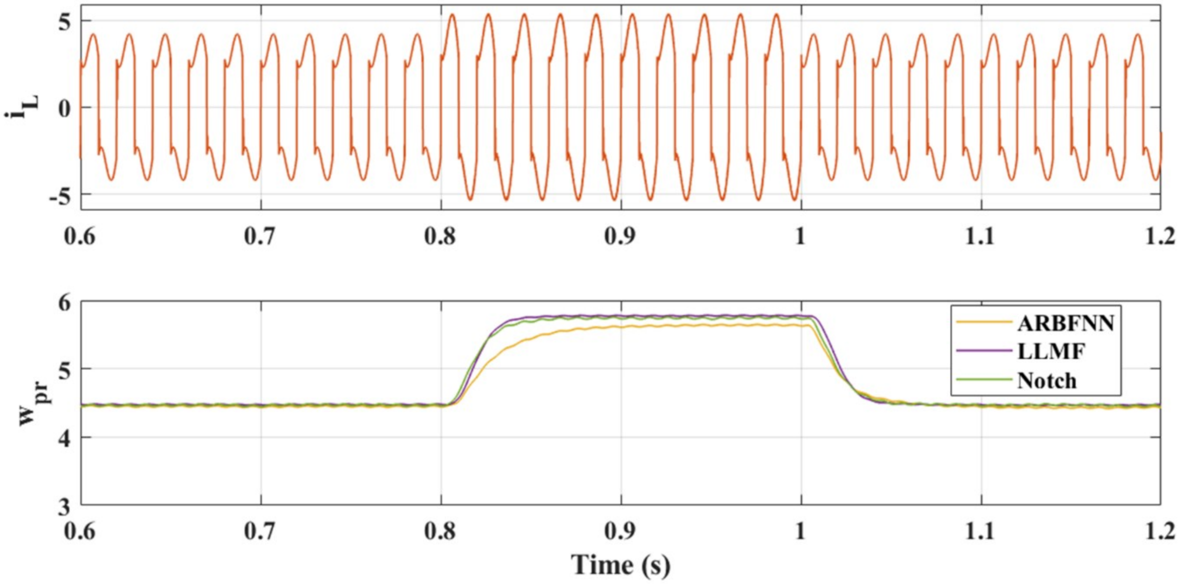

Fig 4.63 Comparative waveforms of load current (i_L), with fundamental current (i_{fa}) at different algorithms

Table 4.3: %THD analysis of NF, ARBFNN and proposed ALLMF algorithm

Algorithms		**%T.H.D (v_s)**	**%T.H.D (i_s)**	**%T.H.D (i_L)**
Notch	Simulation	0.00	3.21	17.68
	Experimental	1.86	4.27	23.67
ALLMF	Simulation	0.00	**1.07**	17.68
	Experimental	2.18	**3.38**	24.02
A-RBFNN	Simulation	0.02	4.02	17.68
	Experimental	2.12	4.54	22.91

4.8 Conclusion

In this chapter performance analysis of NF, ALLMF and ARBFNN based control technique is performed on single phase and three phase DSTATCOM system. Detailed simulation analysis is shown and to verify the simulation results the control techniques are further applied to single phase as well as three phase hardware prototype system. The detailed parameters are already tabulated in Table 3.1 of chapter 3. In this chapter THD analysis of supply voltage and current is also performed and it is observed that for both simulation as well as hardware setup, the THD obtained using all the three control technique is found to be below 5% which is required as per IEEE 519 standard. On detailed comparative analysis, it is found that the ALLMF control technique outperform the other two technique on the basis of source current THD and its dynamic performance.

Chapter 5

Performance Analysis of Grid integrated Multilevel Inverter to Improve Power Quality

---

This chapter discuss the performance analysis of the single phase grid-connected multilevel inverter based DSTATCOM. This chapter also presents the classification and configuration of multilevel inverter. The designed system is first modeled in MATLAB/Simulink. Subsequently, real-time simulation and experimental validation have been demonstrated. The cascaded H-bridge inverter is used as a DSTATCOM in single phase grid connected system to mitigate harmonics present in grid current. The steady state and dynamic waveforms for different control algorithms are presented and results are analysed.

5.1 Introduction

Fig 5.1 shows the circuit diagram of the proposed system with five level cascaded H-bridge configuration. A single-phase AC source supplies power to a rectifier load having R-L branch

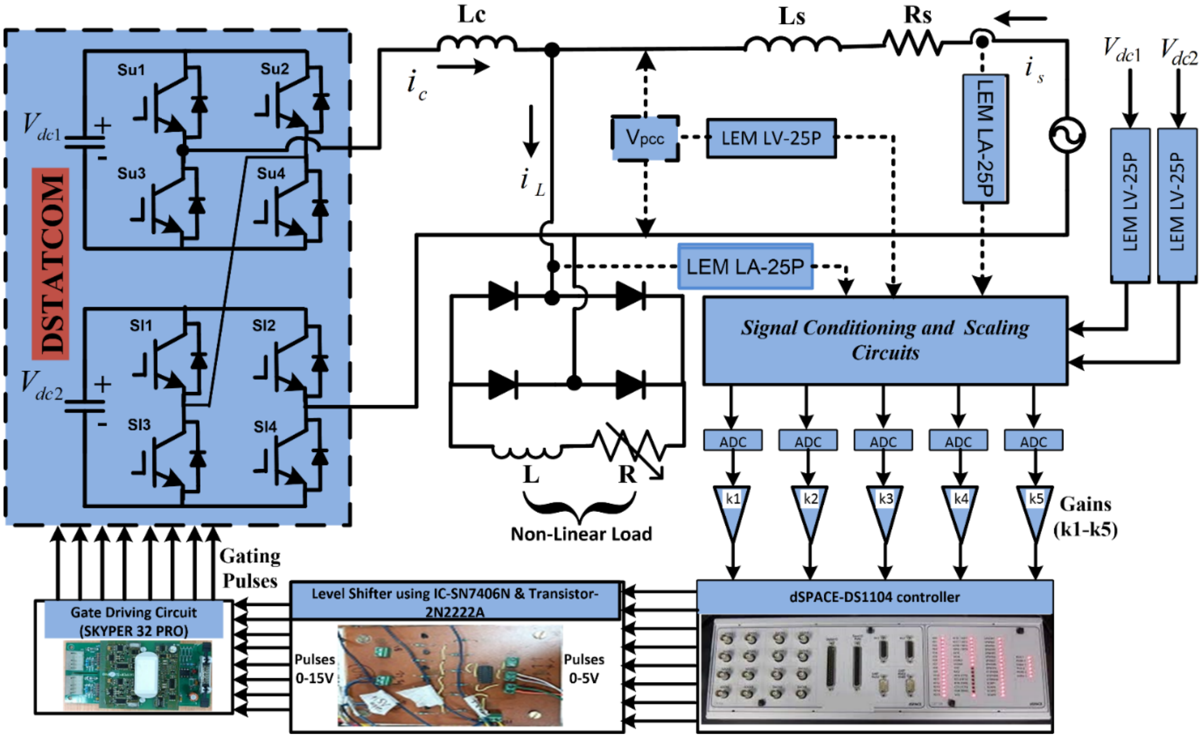

Fig 5.1 System Diagram of 5-level Distribution System

connected at DC side. Source resistance and source inductance parameters are denoted as R_S and L_S. The Five Level Cascaded H-Bridge (5L CHB) converter configurations is connected in shunt configuration to compensate the PQ problems. The control of the proposed system requires input variables such as source voltage v_s, source current i_s, load current i_L, total dc link voltage ($V_{dc1}+V_{dc2}$). These are sensed with LEM based current and voltage sensors. These sensed voltage and current signals are fed through ADC channel of DSP (dSPACE 1104). The DSP generates the required gating pulses for DSTATCOM. An interfacing inductor (L_i) is connected with converter to suppress the AC output ripples.

5.2 Description and Configuration of Selected Five Level CHB-MLI based

The conversion of DC supply into AC with desired frequency and voltage using conventional inverter results in some demerits like more switching stresses, higher distortion, and reduced efficiency [281]. The Cascaded H- Bridge (CHB) inverter produces output having reduced number of harmonics compared to conventional two-level H bridge inverter. The Five Level Series Connected H-bridge Multilevel Inverter (5L SCHB-MLI) used as DSTATCOM to improve PQ of the connected system.

A single H-bridge (SHB) inverter generates a two-level output $+V_{dc}$ and $-V_{dc}$ with a single DC link and four IGBT switches. The Multilevel Inverter (MLI) with higher number of levels results in an output voltage waveform having reduced harmonics. Two available topologies for MLI for increasing the number of levels is mentioned in literature viz. clamping diode multilevel configuration which requires larger number of diodes and the flying capacitor multilevel inverter which requires larger number of capacitors. Both these configurations of Multilevel Inverter (MLI) are costly and require more switches. The 5-level CHB inverter consists of double H-bridge configuration each having its own DC link and IGBT switches. The number of bridges can be increased to increase the number of levels. However, when the number of levels is increased, the number of power electronics switches also increases properly. Hence the scope of this paper is limited to 5L CHB configuration. In comparison to two level inverters as shown in Fig 5.2(a), switching stresses are less in 5-level inverters. In Fig 5.2(b), two H-bridge are connected in series with separate DC link voltage fed with PCC to generate higher voltage levels and reduced Total Harmonic Distortion (THD). The 5L CHB is appropriately switched on so as to obtain five voltage levels $+2V_{dc}$, $+V_{dc}$, 0, $-V_{dc}$, $-2V_{dc}$.

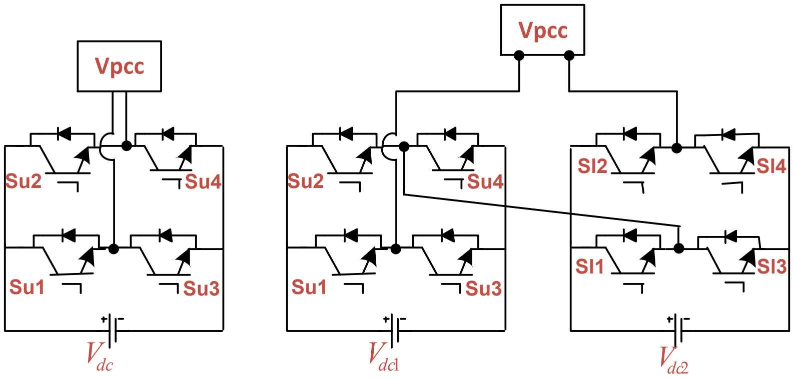

(a) (b)

Fig 5.2 Generalized configuration of (a) 2-level converter (b). 5-level CHB MLI

The power electronic switches are operated in only two states viz, turn-on and turn-off. The CHB configuration shows eight IGBT switches as shown in Fig 5.2b which requires eight gating pulses for the operation of CHB. The technique used in this paper is Pulse Width Modulation (PWM) in which reference signal is compared with high frequency triangular waveform for generating various voltage steps ($+2V_{dc}$, $+V_{dc}$, $0V_{dc}$, $-V_{dc}$, $-2V_{dc}$) and switching pattern of various IGBTs (S_{u1}, S_{u2}, S_{u3}, S_{u4}, S_{l1}, S_{l2}, S_{l3}, S_{l4}) as shown in Table 5.1. The combination of four switches in ON mode and remaining four switches in OFF mode to generate different voltages ($+2V_{dc}$, $+V_{dc}$, $0V_{dc}$, $-V_{dc}$, $-2V_{dc}$). The conducting switches are represented by 1 indicate the switch is ON while 0 indicates the particular switch is OFF. Here, S_{u1}, S_{u2}, S_{u3}, S_{u4} belong to first H-bridge and S_{l1}, S_{l2}, S_{l3}, S_{l4} belong to the second H-bridge which is also shown in Fig 5.2b. All the remaining possible cases listed in Table 5.1 are forbidden since the two switches in the same leg must not be switched on simultaneously.

Table 5.1:Switching table for 5L CHB-MLI

Modes	Conducting Switches 1 = ON ; 0 = OFF								Output Voltage $V_{dc1}= V_{dc2}= V_{dc}$
	S_{u1}	S_{u2}	S_{u3}	S_{u4}	S_{l1}	S_{l2}	S_{l3}	S_{l4}	
1	1	0	0	1	1	0	0	1	$+2V_{dc}$(mode1)
2	1	0	0	1	0	0	1	1	$+1V_{dc}$(mode2)
3	1	0	0	1	0	1	1	0	$0V_{dc}$(mode3)
4	0	1	1	0	0	0	1	1	$-1V_{dc}$(mode4)
5	0	1	1	0	0	1	1	0	$-2V_{dc}$(mode5)

5.3 Switching operation of Five Level CHB-MLI based DSTATCOM

The five modes of switching operation are discuss below and Fig 5.3 shows the five modes of

CHB to produce different voltage steps.

Mode 1: In this mode, switches S_{u1}, S_{u4}, S_{l1}, S_{l4} are ON and the remaining switches are OFF to obtain +2 V_{dc}.This is shown in Fig 5.3.

Mode 2: In this mode, switches S_{u1}, S_{u4}, S_{l3}, S_{l4} are ON, and the remaining switches are OFF to obtain +1 V_{dc}. This is shown in Fig 5.3.

Mode 3: In this mode, switches S_{u1}, S_{u4}, S_{l2}, S_{l3} are ON, and the remaining switches are OFF to obtain 0 V_{dc}. This is shown in Fig 5.3.

Mode 4: In this mode, switches S_{u2}, S_{u3}, S_{l3}, S_{l4} are ON, and the remaining switches are OFF to obtain -1 V_{dc}. This is shown in Fig 5.3.

Mode 5: In this mode, switches S_{u2}, S_{u3}, S_{l2}, S_{l3} are ON and the remaining switches are OFF to obtain -2 V_{dc}. This is shown in Fig 5.3.

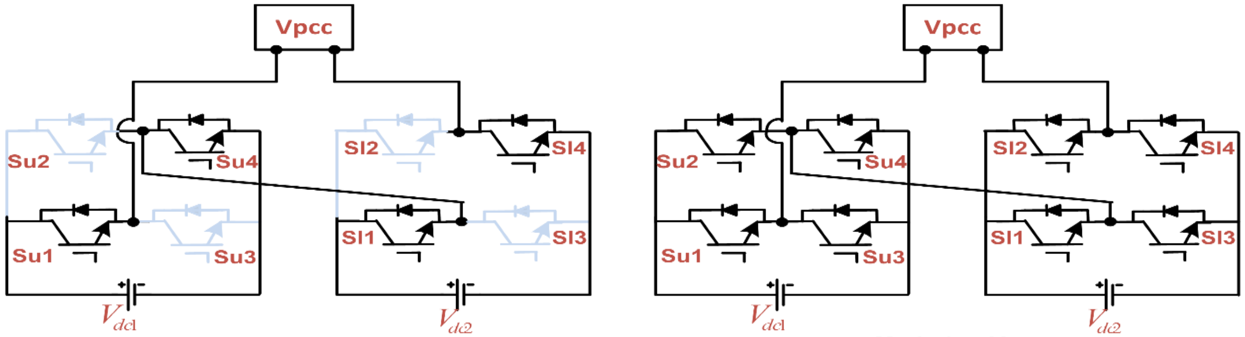

Mode 1: +2 Vdc **Mode 2: + Vdc**

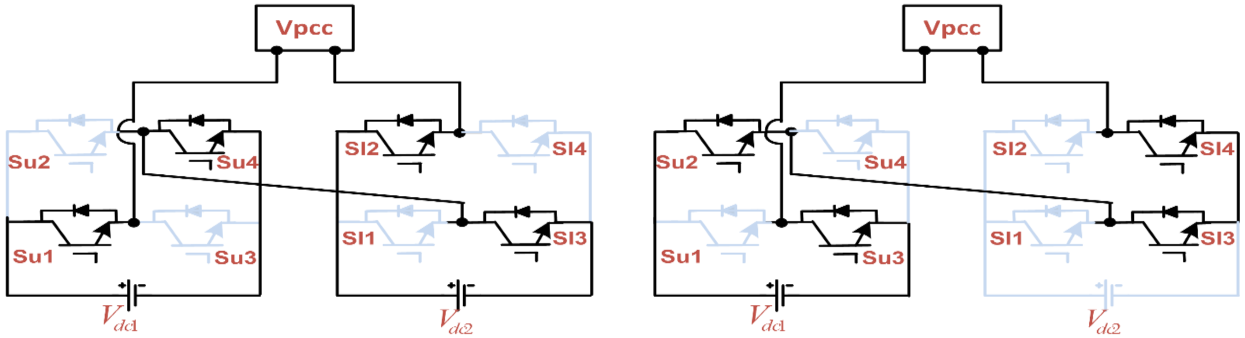

Mode 3: +0 Vdc **Mode 4: - Vdc**

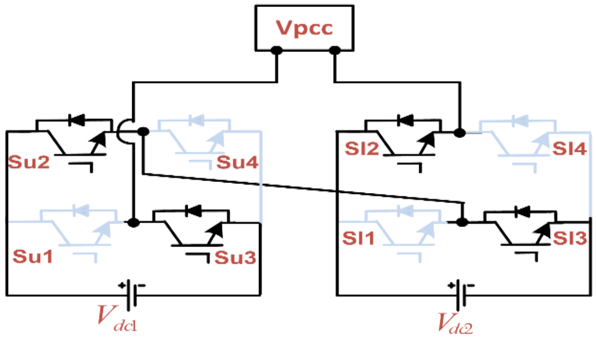

Mode 5: - 2 Vdc

Fig 5.3 Different modes of switching operation in 5L CHB-MLI

5.4 Design and Control of MLI based DSTATCOM using Notch Filter

The complete control algorithm including both the control of DC links and details of Notch filter are shown in Fig 5.4. The controller description comprises the calculation of unit template (u_p), the estimation of the fundamental current (i_f), the estimation of active loss component (i_{loss}) and the reference supply current (i_{ref}). The estimated weight signal is updated in real time to estimate the fundamental value of load current. A PI controller is realized over the total DC-link voltage to regulate it to 200V reference so as to estimate the weight loss component. The summation of both fundamental current (i_f) and loss component (i_{loss}) is considered as the effective current i_T which is multiplied with unit template to generate reference current i_{ref}. The reference current is perfectly sinusoidal (i_{ref}) and the actual supply current i_s is passed through PWM current controller to generate gating pulses for IGBT switching operation to control DSTATCOM. This ensures the grid current is perfectly sinusoidal and the entire reactive power demand of the load is met by the compensator.

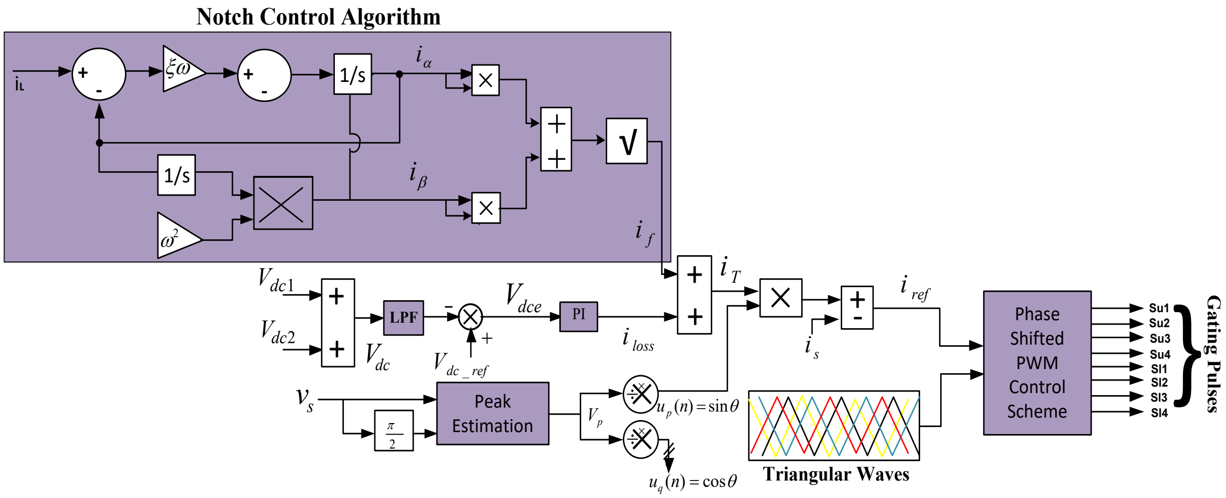

Fig 5.4 Control diagram of Notch Filter

5.4.1 Estimation of Fundamental Current

The load current fundamental active magnitude is extracted using Notch filter controller by using the Eq. 5.1.

$$i_f = \sqrt{(i_\alpha)^2 + (i_\beta)^2} \qquad (5.1)$$

where if is the fundamental current of notch filter.

5.4.2 Estimation of current Loss Component:

The DC link voltage must be raised to a minimum reference value for active shunt filtering. The sum of both DC link voltage V_{dc1}; V_{dc2} (i.e $V_{dc} = V_{dc1} + V_{dc2}$) is passed through a low pass filter to compute

V_{dc} of DSTATCOM. The error V_{dce} is generated by using DC reference voltage V_{dc_ref} and V_{dc} in Eq. (5.2). Now, the error V_{dce} is fed to the Proportional Integral (PI) controller to obtain the current loss component.

$$V_{dce} = V_{dc\_ref} - V_{dc} \tag{5.2}$$

$$i_{loss} = i_f + [k_P\{V_{dce}(n+1) - V_{dce}(n)\} + k_i\{V_{dce}(n+1)\}] \tag{5.3}$$

where, the k_p and k_i are the constants denoting the proportional and integral controller gains.

5.4.3 Calculation of Unit Templates

For the calculation of the unit template, the grid voltage (v_s) along with its phase shifted quadrature component (v_c) are passed through peak estimation block as shown in Fig 5.4 to calculate v_p as shown in the Eq. (5.4-5.6).

$$v_s = v_p \sin \omega t \tag{5.4}$$

$$v_c = v_p (\sin \omega t + \frac{\pi}{2}) \tag{5.5}$$

Now, the peak voltage is estimated as

$$v_p = \sqrt{v_s^2 + v_c^2} \tag{5.6}$$

Now, the unit template is computed as,

$$u_p(n) = \frac{v_s}{v_p} = \sin \omega t \tag{5.7}$$

5.4.4 Estimation of Reference Current and Gating Signal

Now, the fundamental active component extracted by Notch filter is added to fundamental DC loss component. This is used to obtain effective current i_T which is used for the generation of reference current.

$$i_T = i_f + i_{loss} \tag{5.8}$$

$$i_{ref} = i_T * u_p \tag{5.9}$$

The generation of pulses and output voltage of five level CHB converter is shown in Fig 5.5.

5.5 Simulation Results using Notch Filter Control Algorithm

A model of the proposed system is developed and analyzed in MATLAB/Simulink environment. Figs 5.6-5.8 show the simulation results under various conditions. The closed loop control system is developed for 110V, 50Hz. Detailed parameters are mentioned in Appendix B.

The system's dynamic behavior for the Notch control algorithm is shown in Fig. 5.6. This figure displays the waveforms of the grid voltage (v_s), grid current (i_s), nonlinear load current (i_L), inverter voltage (v_{inv}), compensatory current via DSTATCOM (i_c), and total DC link voltage (V_{dc}). It is investigated to observe load perturbations effect on controller performance. The load is raised from 3A to 5A at time t=0.8s and lowered down to the starting level of 3A at time t=1s. When the load changes, the dc link voltage (V_{dc}) exhibits a slight disruption during the load rise or drop; nevertheless, the PI controller's action causes the Vdc voltage to settle back to 200 V. Fig. 5.6 also displays the output response of a 5-L CHB inverter voltage (v_{inv}) of 200V. After corrective action by CHB inverter, it is noted that the source current stays sinusoidal and in phase with the PCC voltage.

Fig 5.7 shows nonlinear load current (i_L), fundamental current (i_f), source current (i_s), and unit template (u_p). During load change the fundamental current is observed to increase at time t=0.8s and then it decreases at t=1s as per the changes in the actual loading conditions. This result shows that the extraction of fundamental current signal using Notch technique is in accordance with change in load current. A highly distorted compensating current ensures the supply current is perfectly sinusoidal. The unit template (u_p) is maintained in the range of ±1.

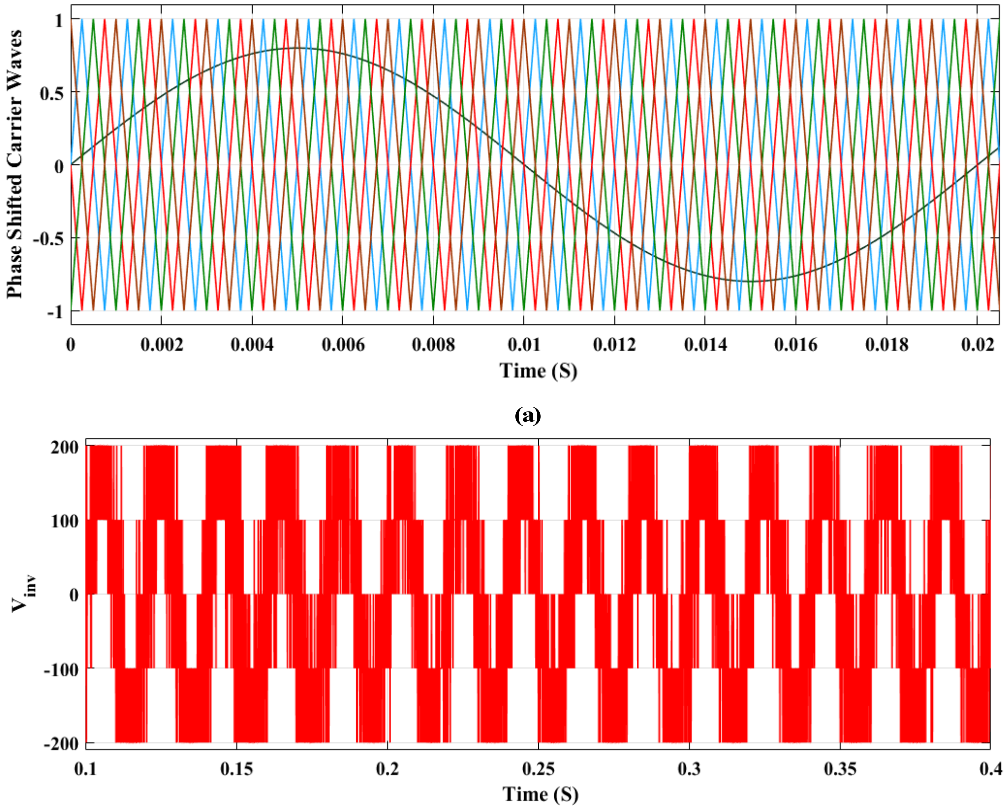

(a)

(b)

Fig 5.5 Waveform showing (a) Phase Shifted -PWM techniques of 5L-CHB converter (b) five level converter voltage output of CHB.

The analysis of the THD profiles in the source voltage (v_s) exhibits harmonic performance with a negligible THD of 0.48%. The source current (i_s) shows a THD of 3.17% which reflecting good harmonic quality. In contrast, the load current displays significant distortion with a THD of 30.69% as shown in Fig 5.8.

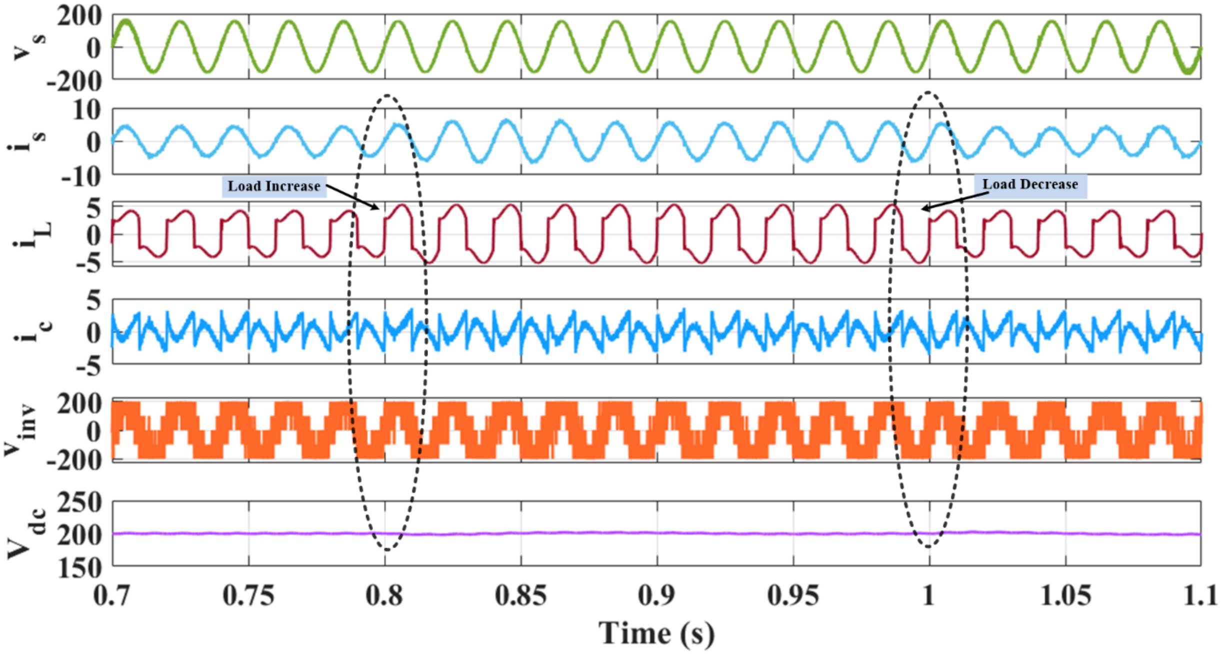

Fig 5.6 Simulation waveforms of source voltage (v_S), source current (i_S), load current (i_L), compensating current (i_C), inverter voltage (v_{inv}), DC link voltage (V_{dc}) during dynamic condition using NF.

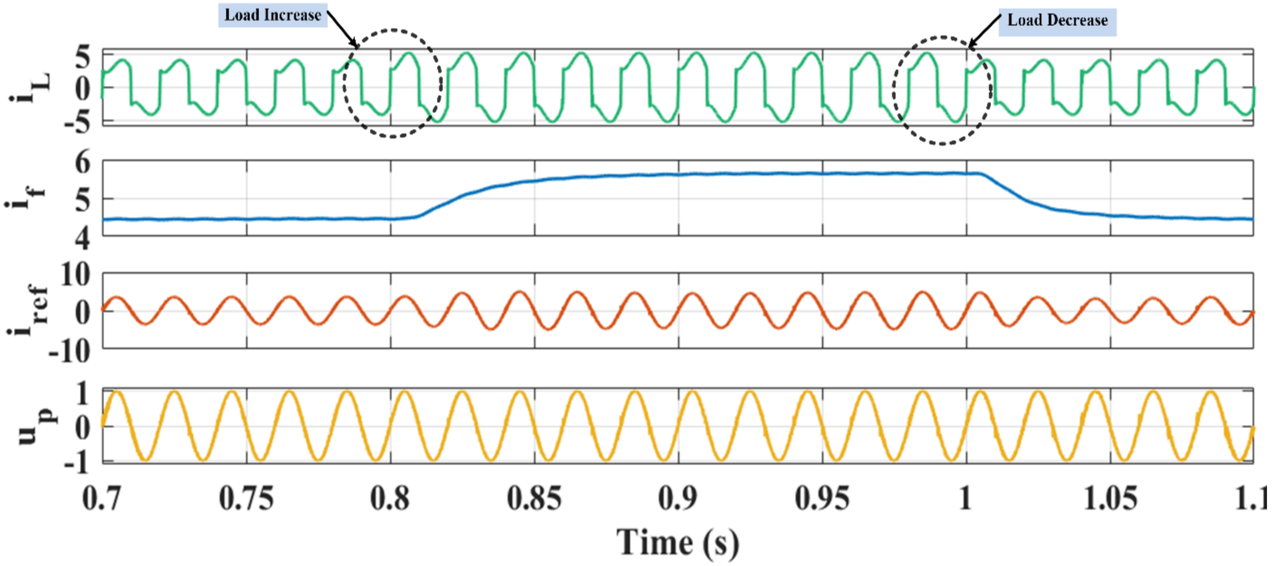

Fig 5.7 Simulation waveforms of load current (i_L), fundamental current (i_f), reference current (i_{ref}), unit template (u_p) during dynamic condition using NF.

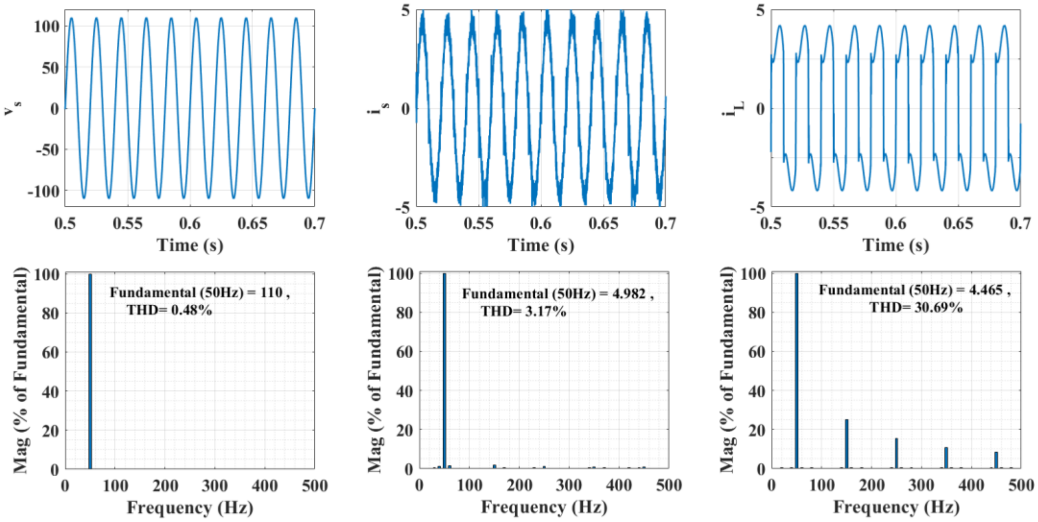

Fig 5.8 Simulation results : Harmonic analysis of a). v_s , THD = 0.48% b). i_s , THD = 3.17% c). i_L , THD = 30.69% during steady state conditions using NF.

5.6 Experimental Results using Notch Filter Control Algorithm

A prototype model is designed in the laboratory as shown in Fig 5.9. The simulation results are verified with experimental setup. The proposed system is working at 110 V and 50 Hz AC supply. The prototype hardware also shows nonlinear load modeled as R-L load at the DC side of rectifier. A DSTATCOM is connected at the PCC for providing compensating currents through interfacing inductors. Various LEM current sensors (LA-25P) for sensing (i_s, i_L) and voltage sensors (LV-25P) for sensing (v_s, V_{dc1}, V_{dc2}) are connected and interfaced with DSP dSAPCE1104 board. Gating pulses from the DSP are fed to DSTATCOM for proper control of the system. A DSO is used to

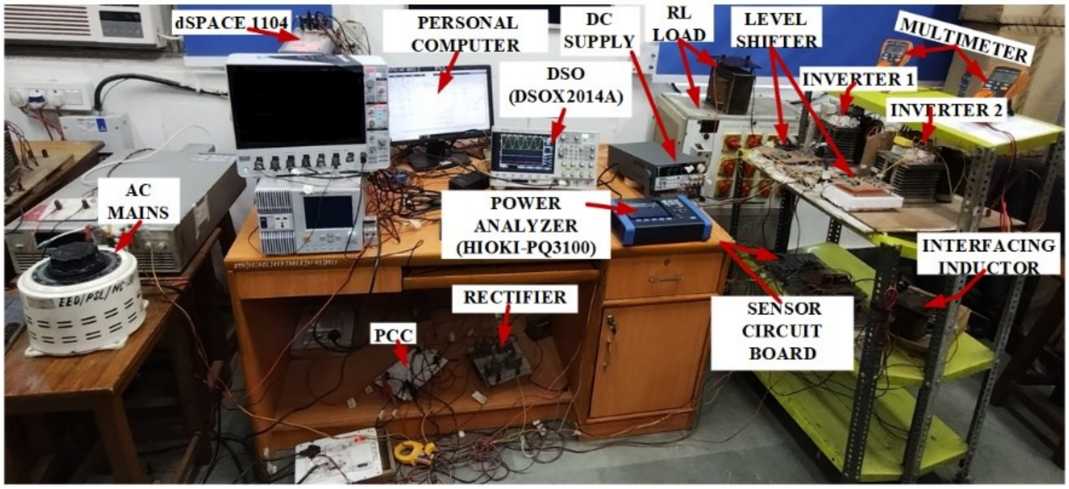

Fig. 5.9 Experimental hardware setup of grid integrated multilevel inverter

capture various hardware dynamic results. The experimental results of power, current and its harmonics are captured through power analyzer (HIOKI PQ3100). The experimental parameters are mentioned in the Appendix B.

(a). Steady State Results

The proposed system's steady-state experimental findings and the waveforms of source voltage (v_s) along with source current (i_s), load current (i_L)and compensating current (i_c) are shown in Fig 5.10 (a-c). Here, the source voltage (v_s) along with source current (i_s) and load current are in same phase as shown in Fig 5.10 (a-b) but load current is distorted. In Fig 5.10 (c), the source voltage with compensating current (i_c) is use to mitigate harmonics present in source current.

Fig 5.10 (d-f) shows the steady-state active and reactive power flow with the present technique. The load's active and reactive power requirements are 324 W and 138 VAR respectively. The switching loss amounts to 0.017 kW. The DSTATCOM meets the load's reactive power demand of 138 VAR, providing power factor (P.F) improvement from 0.920 to 0.983 as seen in Fig 5.8 (d-e). The load has a real and reactive power requirement of 324W and 138 VAR, respectively and the DSTATCOM matches the load's reactive power need by providing 145VAR as seen in Fig 5.10 (f). The grid offers 344W to fit the load's actual power and also meets switching losses.

After compensation, the THD of the source current is reduced to 4.78% and is almost sinusoidal. Moreover, the voltage distortion is 2.29% as shown in Fig 5.11 (a). Before compensation, a high

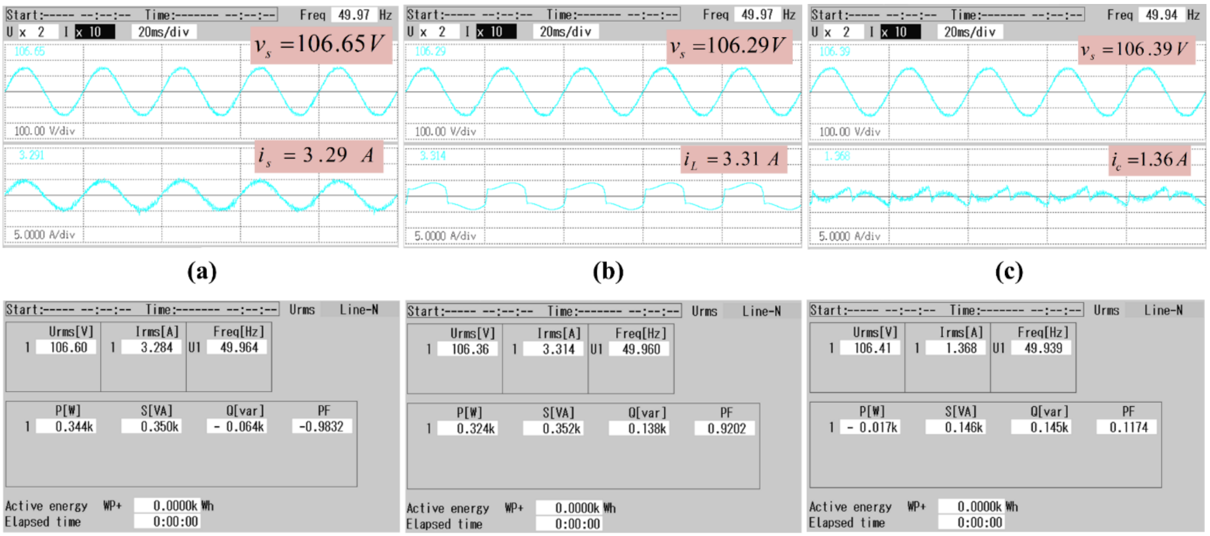

(a) (b) (c)

```
Start:----- --:--:--  Time:------- --:--:--  Urms   Line-N
    Urms[V]      Irms[A]     Freq[Hz]
 1  106.60    1  3.284   U1  49.964

    P[W]       S[VA]      Q[var]      PF
 1  0.344k     0.350k     - 0.064k    -0.9832

Active energy  WP+   0.0000k Wh
Elapsed time         0:00:00
```

```
Start:----- --:--:--  Time:------- --:--:--  Urms   Line-N
    Urms[V]      Irms[A]     Freq[Hz]
 1  106.36    1  3.314   U1  49.960

    P[W]       S[VA]      Q[var]      PF
 1  0.324k     0.352k     0.138k      0.9202

Active energy  WP+   0.0000k Wh
Elapsed time         0:00:00
```

```
Start:----- --:--:--  Time:------- --:--:--  Urms   Line-N
    Urms[V]      Irms[A]     Freq[Hz]
 1  106.41    1  1.368   U1  49.939

    P[W]       S[VA]      Q[var]      PF
 1  - 0.017k   0.146k     0.145k      0.1174

Active energy  WP+   0.0000k Wh
Elapsed time         0:00:00
```

(d) (e) (f)

Fig 5.10 Experimental results of a). v_s,i_s b). v_s,i_L c). v_s,i_C d). Supply power P_S e). Load power P_L f). Compensator power P_C during steady state condition using NF.

content of harmonic distortion of 28.62% can be observed in Fig 5.11(b). The injected DSTATCOM compensating current cancels the harmonics produced by the nonlinear load. The source current is sinusoidal in shape and in phase with the source voltage. The observed waveforms show that the Notch control algorithm works appropriately and the obtained %THD of source current (i_s) is within the IEEE-519 standard limit of 5%.

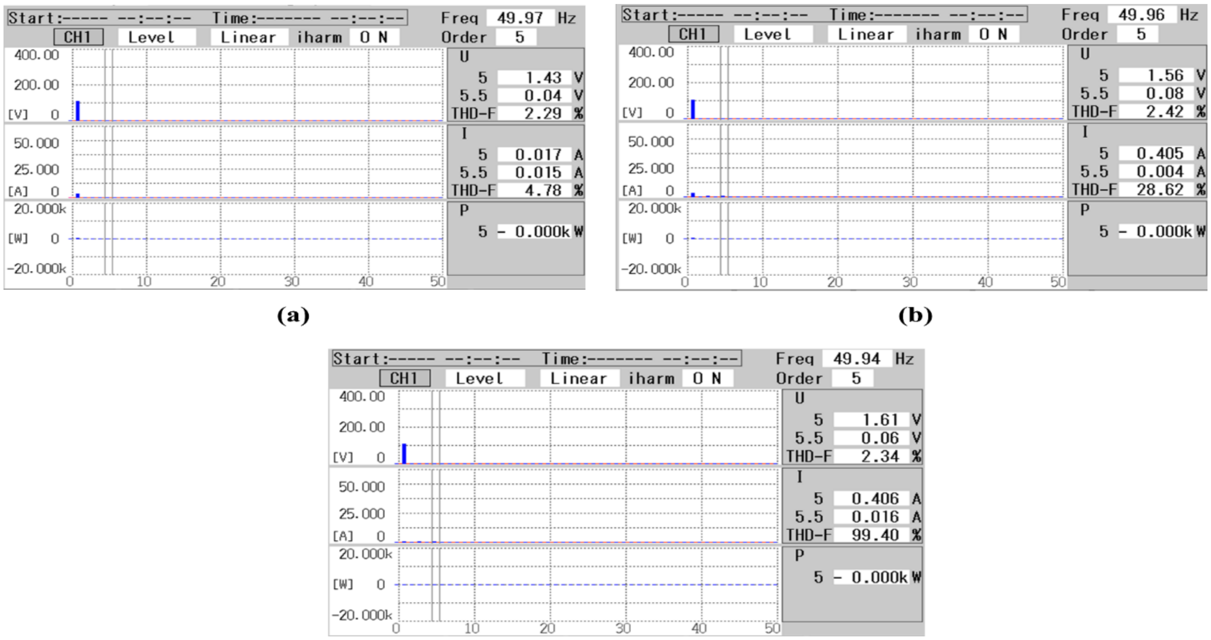

Start:----- --:--:-- Time:------- --:--:--
CH1 Level Linear iharm ON
Freq 49.97 Hz
Order 5
U
5 1.43 V
5.5 0.04 V
THD-F 2.29 %
I
5 0.017 A
5.5 0.015 A
THD-F 4.78 %
P
5 - 0.000k W

(a)

Start:----- --:--:-- Time:------- --:--:--
CH1 Level Linear iharm ON
Freq 49.96 Hz
Order 5
U
5 1.56 V
5.5 0.08 V
THD-F 2.42 %
I
5 0.405 A
5.5 0.004 A
THD-F 28.62 %
P
5 - 0.000k W

(b)

Start:----- --:--:-- Time:------- --:--:--
CH1 Level Linear iharm ON
Freq 49.94 Hz
Order 5
U
5 1.61 V
5.5 0.06 V
THD-F 2.34 %
I
5 0.406 A
5.5 0.016 A
THD-F 99.40 %
P
5 - 0.000k W

(c)

Fig 5.11 Experimental results: Harmonic analysis of a). v_s,i_s with THD = 4.78% b). v_s,i_L with THD = 28.62% c). v_s,i_C with THD = 99.40% during steady state condition using NF.

(b). Dynamic State Results

Figs 5.12 (a-d) present the system's dynamic response under varied load circumstances. The parameters source voltage (v_s), source current (i_s), load current (i_L), DC link voltage of first H-bridge (V_{dc1}), DC link voltage of second H-bridge (V_{dc2}), total DC link voltage (V_{dc}), compensating current (i_c), fundamental current (i_f), reference current (i_{ref}), and unit template (u_p) are displayed during load variations. Fig 5.12(a-b) shows the waveforms of v_s, i_s, i_L, $V_{dc,}$ i_c during load change. The waveform of source voltage, source current and load current are in same phase and the DC link voltage settles to 200V. The compensating current (i_c) is injected at PCC through DSTATCOM to provide sinusoidal grid current.

Fig 5.12(c) shows the waveforms of i_L, V_{dc1}, V_{dc2}, V_{dc} with the change in load. The waveforms show that the voltages at the two DC capacitors settle to100 V within a few cycles. As a result,

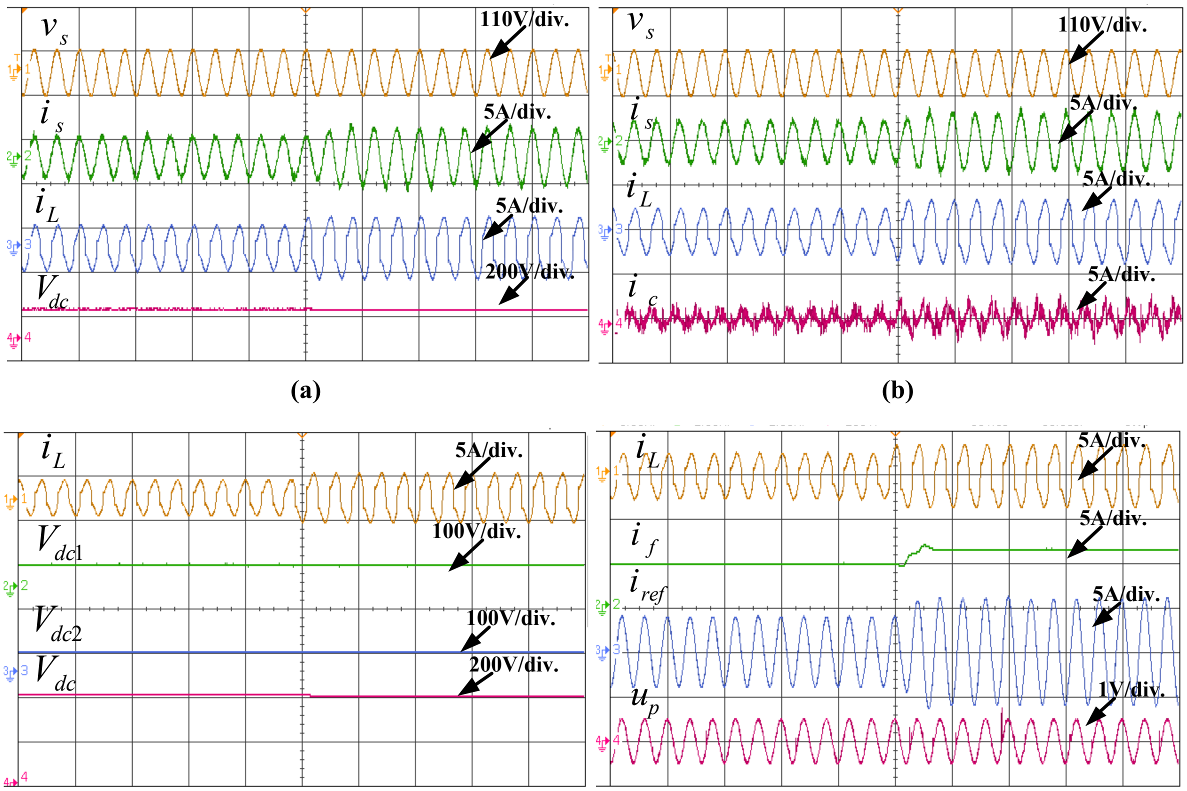

(a) (b)

(c) (d)

Fig 5.12 Experimental waveforms of a). v_s,i_s,i_L,V_{dc} b). v_s,i_s,i_L,i_C c). i_L,i_s,,i_f,i_{ref} and d). i_L, i_f,i_{ref} ,u_p during dynamic condition using NF.

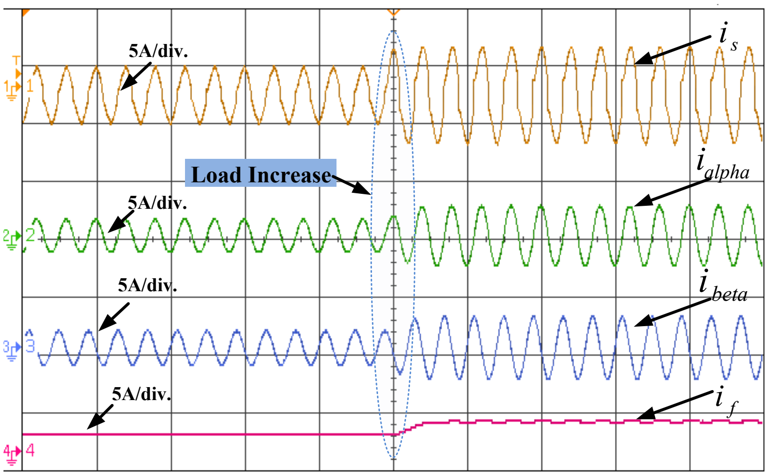

Fig. 5.13 Experimental waveforms of i_L, i_α, i_β,i_f during dynamic load condition using NF.

even under dynamic load conditions, the total DC link voltage stays steady and well-regulated around 200V.

Fig 5.12(d) shows the plots of i_L, i_f, i_{ref}, u_p. It presents the system's gets performance when the load current increases. The waveform shows the fundamental weight is changed due to change in load current as predicted by Notch control algorithm. The reference current also follows the change in load but the sine template remains unity.

The intermediate waveforms of i_α, i_β and i_f of Notch control algorithm with load current i_L are shown in Fig 5.13. The waveforms are observed that the i_α, i_β and i_f track the load current (i_L). Further, the waveforms of 90^0 phase shift between i_α and i_β is also observed.

5.7 Design and Control of MLI based DSTATCOM using ALLMF Control Algorithm

The complete control algorithm including both the control of DC links and details of ALLMF are shown in Fig 5.14. The controller description comprises the calculation of unit template, the estimation of the fundamental weight signal, the estimation of active weight loss component and the reference supply current. The estimated weight signal is updated in real time to estimate the fundamental weight of load current. A PI controller is realized over the total DC-link voltage to regulate it to 200V reference so as to estimate the weight loss component. The summation of both weights viz. fundamental (i_f) and loss component (i_{loss}) is effective weight i_T which is multiplied with unit template to generate reference current (i_{ref}). The reference current is perfectly sinusoidal (i_{ref}) and the actual supply current is is passed through PWM current controller to generate gating pulses for IGBT switching operation to control DSTATCOM. This ensures the grid current is perfectly sinusoidal and the entire reactive power demand of the load is met by the compensator.

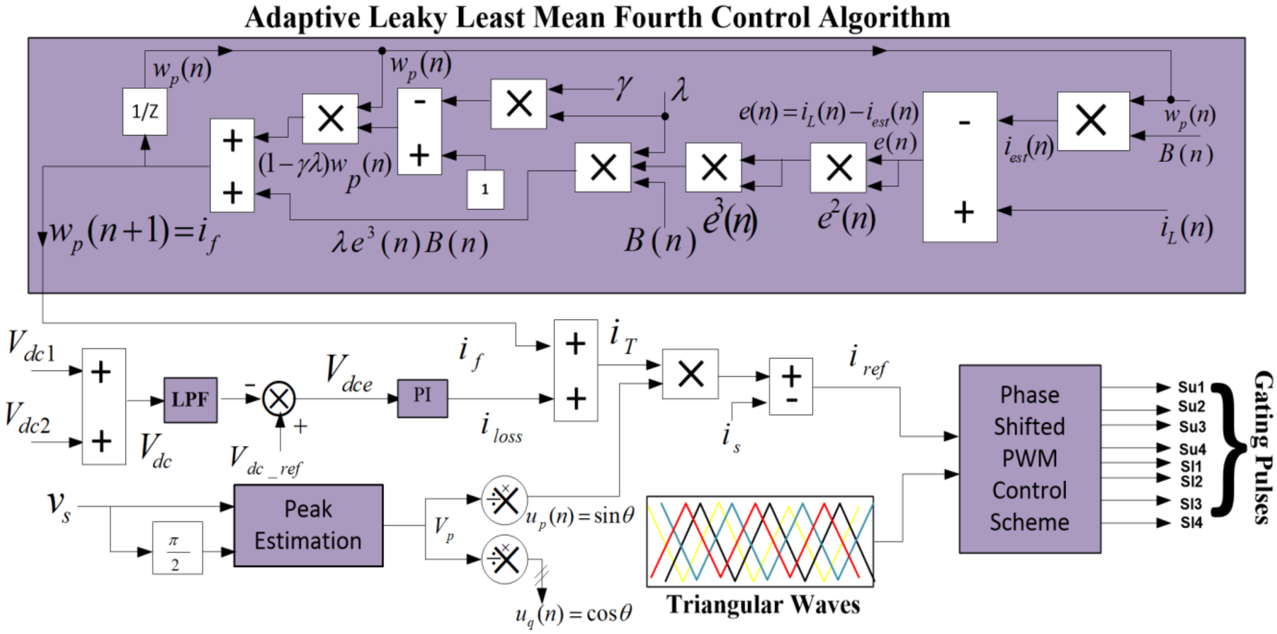

Fig 5.14 Control diagram using ALLMF algorithm

5.7.1 Estimation of Fundamental Current

The load current fundamental active magnitude is extracted using ALLMF controller by using the Eq.5.10.

$$w_p(n+1) = w_p(n) - \lambda[\{\gamma\, w_p(n) - e^3(n)B(n)\}] = i_f \tag{5.10}$$

where $w_p(n+1) = i_f$ corresponds to the fundamental component of load current and λ is the learning rate, e(n) is the error signal.

5.7.2 Estimation of Current Loss Component

The estimation of current loss component is same as per section 5.4.2. The error V_{dce} and current loss component (i_{loss}) are shown in Eq.5.11 and Eq.5.12 respectively.

$$V_{dce} = V_{dc\_ref} - V_{dc} \tag{5.11}$$

$$i_{loss} = i_f + [k_P\{V_{dce}(n+1) - V_{dce}(n)\} + k_i\{V_{dce}(n+1)\}] \tag{5.12}$$

where, the k_p and k_i are the constants denoting the proportional and integral controller gains.

5.7.3 Estimation of Unit Template

Similar to section 5.4.3, the calculation of unit template is shown in Eq. 5.13.

$$u_p(n) = \frac{v_s}{v_p} = \sin \omega t \tag{5.13}$$

5.7.4 Estimation of Reference Current

Similarly, as discussed in section 5.4.4 in NF algorithm based system, the calculation of reference current (i_{ref}) is shown in Eq.5.15

$$i_T = i_f + i_{loss} \tag{5.14}$$

$$i_{ref} = i_T * u_p \tag{5.15}$$

5.8 Simulation Results using ALLMF Algorithm

The MATLAB/Simulink environment is used to develop and analyze a model of the proposed system. Fig 5.15 - 5.17 shows the simulation results under various conditions. The closed loop control system is developed for 110V, 50Hz.

Fig 5.15 shows the dynamic behavior of proposed system for ALLMF control algorithm. In this figure, the waveform of grid voltage (v_s), grid current (i_s), nonlinear load current (i_L), compensating current through DSTATCOM (i_c), Inverter Voltage (v_{inv}) and total DC link voltage (V_{dc}) are shown. Effect of load perturbation on controller performance is studied. At time t=0.8s, the load is increased from 3A to 5A and at time t=1s, the load is decreased back to initial level of 3A. At the instant of load change, V_{dc} shows sudden disturbance during load increase/decrease but V_{dc} voltage again settles to 200 V due to action of PI controller. The output response of 5-L CHB inverter voltage (v_{inv}) of 200V is also shown in Fig 5.15. It is also observed that the source current remains sinusoidal and in phase with the PCC voltage after compensation. This proves the effectiveness of the ALLMF control technique under dynamic load conditions.

Fig 5.16 shows the load current i_L (A), fundamental current i_f, reference current i_{ref} and unit template (u_p). During load change the fundamental weight is observed to increase at time t=0.8s and then it decreases at t=1s as per the changes in the actual loading conditions. This result shows that the extraction of fundamental weight current using ALLMF technique is in accordance with the change in load current and reference current. It also observed that, there is no change in waveforms of unit template during load change and it is maintained to ±1.

The analysis of the THD profiles in the source voltage (v_s) exhibits harmonic performance with a negligible THD of 0.06%. The source current (i_s) shows a THD of 2.72% which reflecting good harmonic quality. In contrast, the load current displays significant distortion with a THD of 30.64% as shown in Fig 5.17.

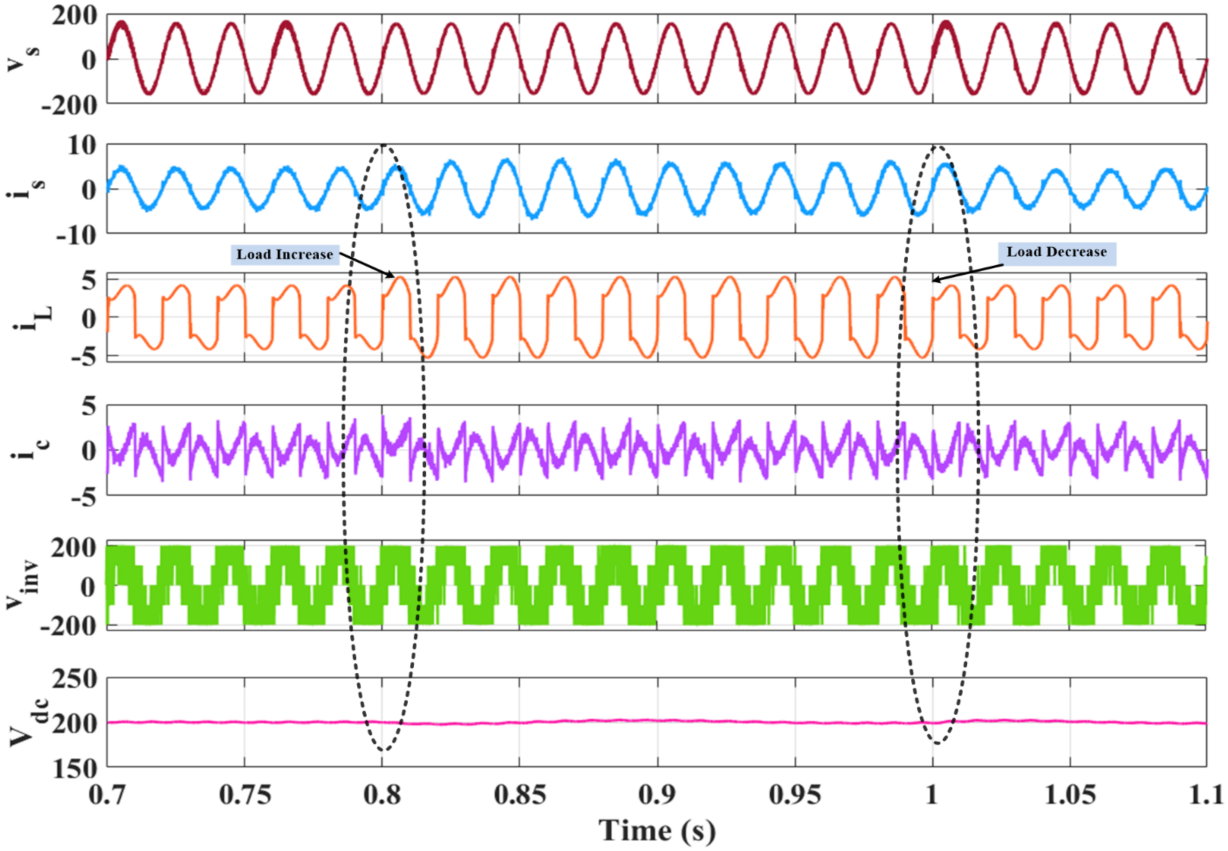

Fig 5.15 Simulation waveforms of source voltage (v_s), source current (i_s), load current (i_L), compensating current (i_C), inverter voltage (v_{inv}), DC link voltage (V_{dc}) during dynamic condition using ALLMF.

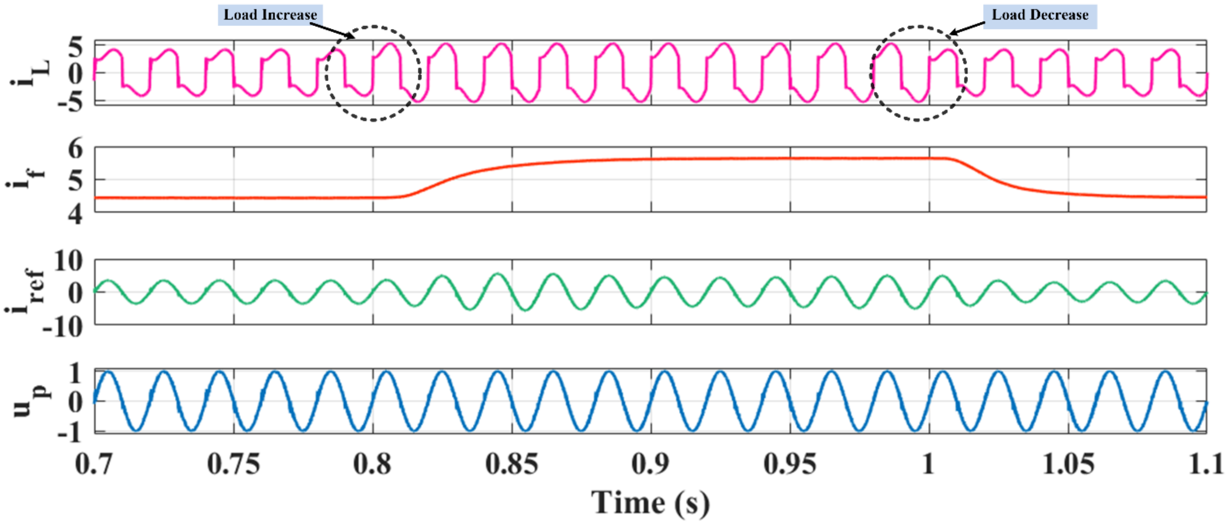

Fig 5.16 Simulation waveforms of load current (i_L), fundamental current (i_f), reference current (i_{ref}), unit template (u_p) during dynamic condition using ALLMF.

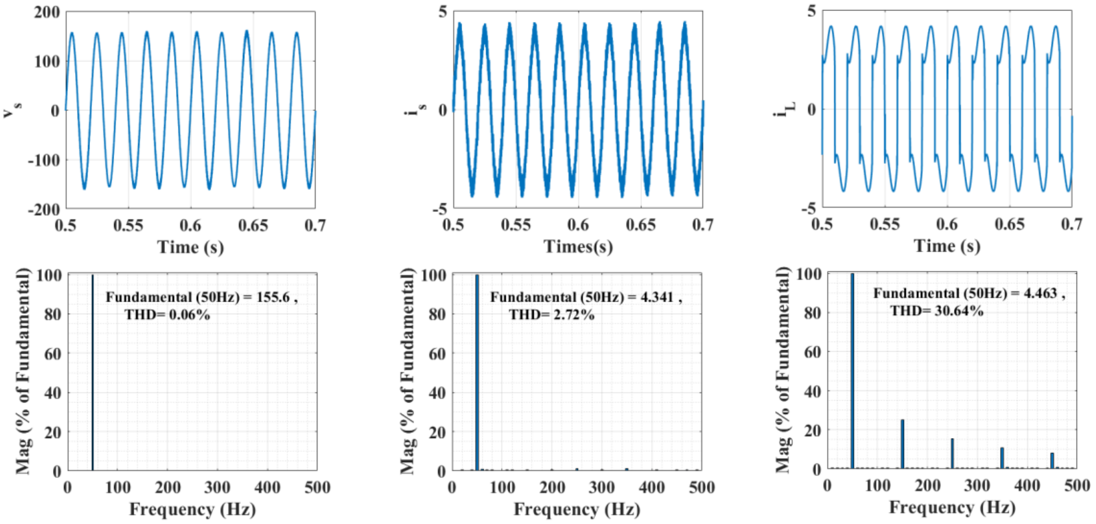

Fig 5.17 Experimental results : Harmonic analysis of a). v_s , THD = 0.06% b). i_s , THD = 2.72% c). i_L , THD = 30.64% during steady state condition using ALLMF.

5.9 Experimental Results using ALLMF Algorithm

The proposed system hardware model is being developed in the laboratory. The simulation results are validated with an experimental setup. The suggested system is powered by an alternating current source of 110 V and 50 Hz. The prototype hardware also consists of a nonlinear load modelled as an R-L load on the rectifier's DC side. A 5-level CHB DSTATCOM is linked to the PCC to provide compensating current via interface inductors. Several LEM current sensors (LA-

25P) for sensing (i_s, i_L) and voltage sensors (LV-25P) for measuring (v_s, V_{dc1}, V_{dc2}) are linked and interfaced with the DSP dSAPCE1104 board. Gating pulses from the DSP are supplied to DSTATCOM for proper system control. A DSO is used to record different hardware dynamic results. The power analyser (HIOKI PQ3100) captures the experimental data of power, current, and their harmonics. Appendix B includes information on the experimental parameters.

(a). Steady State Results

The proposed system's steady-state experimental findings and the waveforms of source voltage vs along with source current (is), load current (iL)and compensating current (ic) are shown in Fig 5.18(a-c). Here, the source voltage (vs) along with source current (is) and load current are in same phase as shown in Fig 5.18 (a-b) but load current is distorted. In Fig 5.18(c), the source voltage with compensating current (ic) is use to mitigate harmonics present in source current. Fig 5.18(d-f) depicts the steady-state active and reactive power flow using the present technique. The load's active and reactive power requirements are 0.327 kW and 0.139 kVAR, respectively. The switching loss equals 0.021 kW. The DSTATCOM fulfils the load's reactive power demand of 0.139 kVAR, resulting in a power factor (P.F) improvement from 0.920 to 0.978, as shown in Fig 5.18 (d-e). The DSTATCOM meets the load's reactive power need by delivering 0.137kVAR, as shown in Fig 5.18(c). The grid provides 0.350kW to match the load's actual power while also accommodating switching losses.

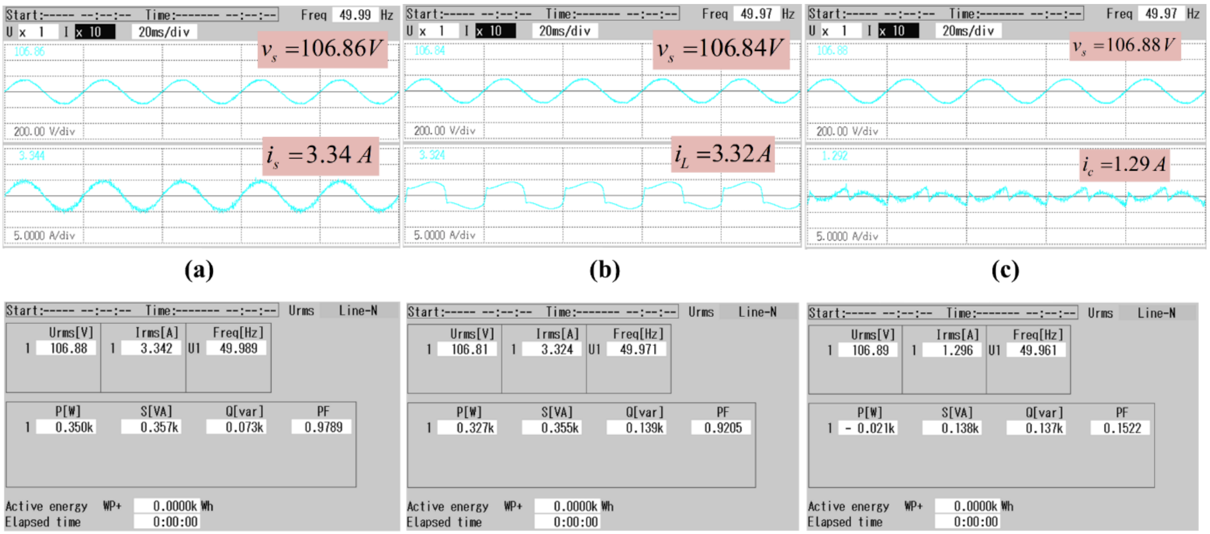

(a) (b) (c)

(d)
Urms[V] 1 106.88 Irms[A] 1 3.342 Freq[Hz] U1 49.989
P[W] 1 0.350k S[VA] 0.357k Q[var] 0.073k PF 0.9789
Active energy WP+ 0.0000k Wh
Elapsed time 0:00:00

(e)
Urms[V] 1 106.81 Irms[A] 1 3.324 Freq[Hz] U1 49.971
P[W] 1 0.327k S[VA] 0.355k Q[var] 0.139k PF 0.9205
Active energy WP+ 0.0000k Wh
Elapsed time 0:00:00

(f)
Urms[V] 1 106.89 Irms[A] 1 1.296 Freq[Hz] U1 49.961
P[W] 1 - 0.021k S[VA] 0.138k Q[var] 0.137k PF 0.1522
Active energy WP+ 0.0000k Wh
Elapsed time 0:00:00

Fig 5.18 Experimental results of a). v_s,i_s b). v_s,i_L c). v_s,i_C d). Supply power P_S e). Load power P_L f). Compensator power P_C during steady state condition using ALLMF.

Fig 5.19 shows the percentage THD of v_s, i_s, i_L and i_c. In Fig 5.19(a), the source current's THD is decreased to 3.86% which is nearly sinusoidal and the voltage distortion is 2.09%. Fig 5.19(b) shows a significant harmonic distortion content of 28.93% in the load current. The DSTATCOM inject compensating current to cancels out the harmonics produced by the nonlinear load. The source current is sinusoidal in shape and synchronised with the source voltage. The observed waveforms demonstrate that the ALLMF method functions properly, and the obtained %THD of source current (i_s) is within the IEEE-519 standard limit of 5%.

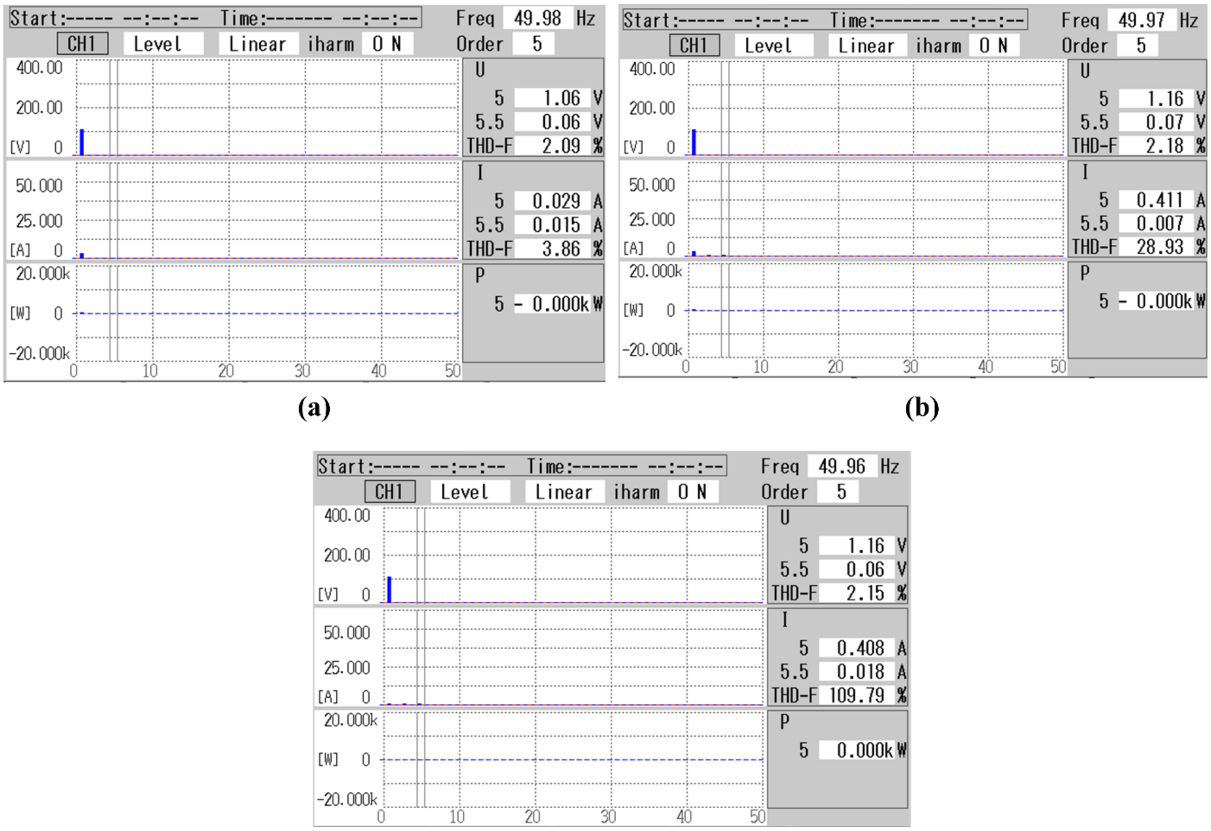

(a)

Start:----- --:--:-- Time:------- --:--:-- Freq 49.98 Hz
CH1 Level Linear iharm ON Order 5
U: 5 1.06 V; 5.5 0.06 V; THD-F 2.09 %
I: 5 0.029 A; 5.5 0.015 A; THD-F 3.86 %
P: 5 - 0.000k W

(b)

Start:----- --:--:-- Time:------- --:--:-- Freq 49.97 Hz
CH1 Level Linear iharm ON Order 5
U: 5 1.16 V; 5.5 0.07 V; THD-F 2.18 %
I: 5 0.411 A; 5.5 0.007 A; THD-F 28.93 %
P: 5 - 0.000k W

(c)

Start:----- --:--:-- Time:------- --:--:-- Freq 49.96 Hz
CH1 Level Linear iharm ON Order 5
U: 5 1.16 V; 5.5 0.06 V; THD-F 2.15 %
I: 5 0.408 A; 5.5 0.018 A; THD-F 109.79 %
P: 5 0.000k W

Fig. 5.19 Experimental results: Harmonic analysis of a). v_s,i_s with THD = 3.86% b). v_s,i_L with THD = 28.93% c). v_s,i_C with THD = 109.79% during steady state condition using ALLMF.

(b). Dynamic State Results

The system's dynamic response under different load conditions with ALLMF algorithm is shown in Figs 5.20(a–d). During load variations, the following parameters are displayed: source voltage (v_s), source current (i_s), load current (i_L), DC link voltage of first H-bridge (V_{dc1}), DC link voltage of second H-bridge (V_{dc2}), total DC link voltage (V_{dc}), compensating current (i_c), fundamental weight current (i_f), reference current (i_{ref}), and unit template (u_p). Fig 5.20(a-b) depicts the waveforms of v_s, i_s, i_L,i_c and V_{dc} as load changes. The waveforms of source current, load current and compensating current are increased due to change in load and also observed that the source voltage is remains unchanged. The DC link voltage stabilizes to 200V. The compensating current (i_c) is injected at PCC through DSTATCOM to provide sinusoidal grid current.

The waveforms of i_L, V_{dc1}, V_{dc2}, and V_{dc} as the load changes are shown in Fig 5.20(c). Due to change in load current, each DC-link voltages V_{dc1}, V_{dc2} settles down to 100V in a few cycles. Consequently, even when dynamic load conditions are present, the total DC link voltage is able to maintain its stability and be well-regulated at around 200V.

Fig 5.20(d) shows the dynamic waveforms of i_L, i_f, i_{ref} and u_p. Due to increase in load current the fundamental weight current and reference current increase but unit template maintains to ±1 limit. The intermediate waveforms of error (e) and fundamental current (i_f) with source current (i_s) and load current (i_L) are shown in Fig 5.21. It is observed that during, a sudden increase in load, the intermediate parameters error (e) and fundamental current (i_f) also change and attain new steady state position.

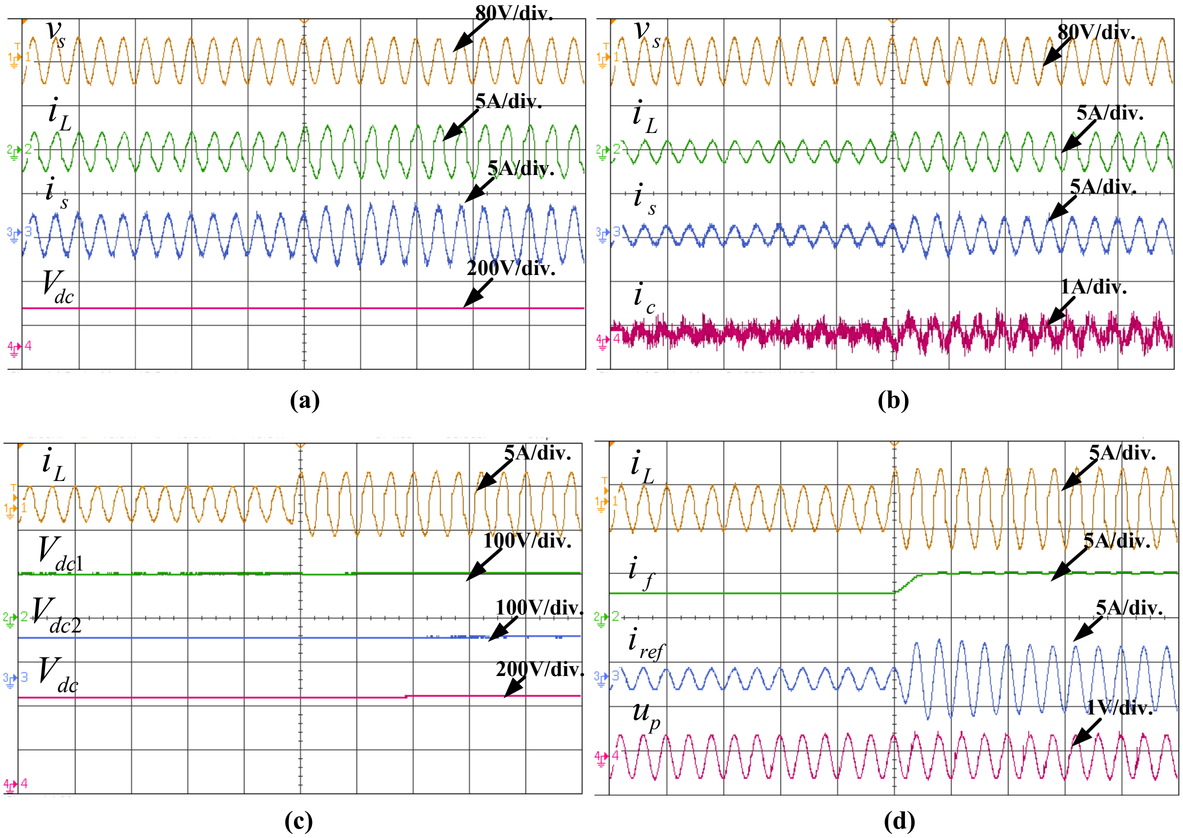

(a) **(b)**

(c) **(d)**

Fig 5.20 Experimental waveforms of a). v_s,i_s,i_L,V_{dc} b). v_s,i_s,i_L,i_C c). i_L,i_s,,i_f,i_{ref} and d). i_L, i_f,i_{ref} ,u_p during dynamic condition using ALLMF.

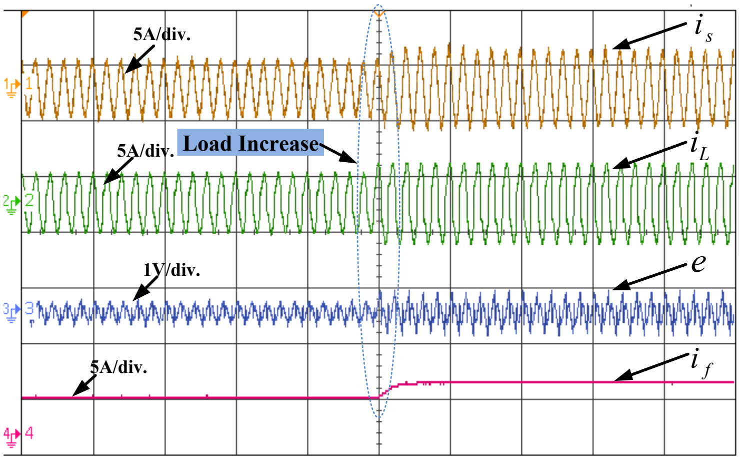

Fig 5.21 Experimental waveforms of i_s ,i_L,e, i_f during dynamic load condition using ALLMF.

5.10 Design and Control Estimation of MLI based DSTATCOM using ARBFNN Control Algorithm

The complete control algorithm including both the control of DC links and ARBFNN algorithm are presented in Fig 5.22. The controller description comprises the calculation of unit template (u_p), the estimation of the fundamental weight signal (i_f), the estimation of active weight loss component (i_{loss}) and the reference supply current (i_{ref}). The estimated weight signal is updated in real time to estimate the fundamental weight of load current. A PI controller is realized over the total DC-link voltage to regulate it to 200V reference so as to estimate the weight loss component. The summation of both weights viz. fundamental (i_f) and loss component (i_{loss}) is effective weight (i_T) which is multiplied with unit template to generate reference current iref. The reference current is perfectly sinusoidal (i_{ref}) and the actual supply current is (i_s) passed through PWM current controller to generate gating pulses for IGBT switching operation to control DSTATCOM. This ensures the grid

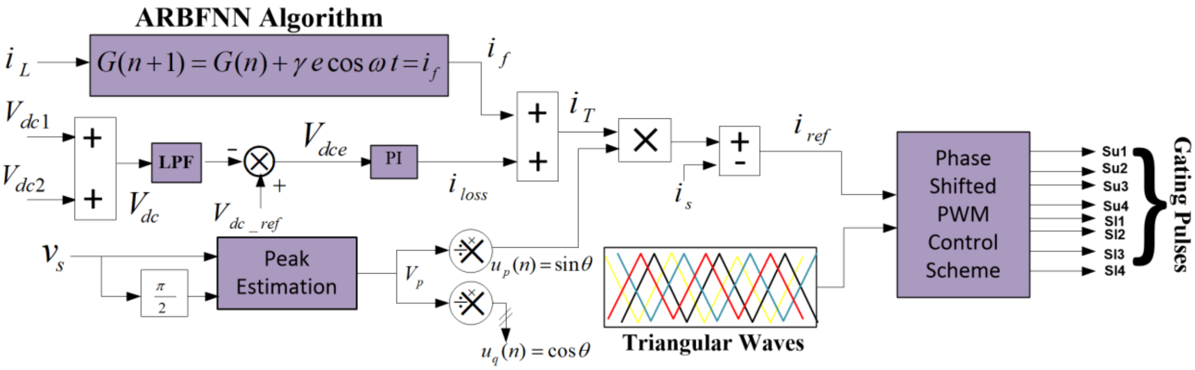

Fig 5.22 Control diagram of ARBFNN algorithm

current is perfectly sinusoidal and the entire reactive power demand of the load is met by the compensator.

5.10.1 Estimation of Fundamental Current

In ARBFNN technique, the dynamics of the weight is control with the help of Adaptive varying gain G as shown in Eq. (5.16).

$$G(n+1) = G(n) - \gamma \frac{\partial w_{pr}}{\partial G} \tag{5.16}$$

The output 'w_{pr}' is calculated for one neuron (n=1) is shown in Eq. 5.17.

$$w_{pr} = \int G(n) e \sin\omega t \; d\omega t \tag{5.17}$$

$$\therefore w_{pr} = -G(n) e \cos\omega t \tag{5.18}$$

The partial derivative of the cost function with respect to the weight vector is

$$\frac{\partial w_{pr}}{\partial G(n)} = -e\cos\omega t \tag{5.19}$$

Using Eq. (5.16), Eq. (5.18) and Eq. (5.19)

$$G(n+1) = G(n) + \gamma e \cos\omega t = i_f \quad .. \tag{5.20}$$

Thus, the gain varies adaptively in A-RBFNN technique until convergence is obtained. The active magnitude of current fundamental is extracted using A-RBFNN controller is given in the Eq. 5.20. The gain varies adaptively in A-RBFNN technique until convergence is obtained.

where G(n+1) = i_f corresponds to the fundamental component of load current and ϒ is the learning rate, 'e' is the error signal.

5.10.2 Estimation of the Active Current Loss Component:

The estimation of active weight loss component in ARBFNN controller based system is shown in Eq. 5.22.

$$V_{dce} = V_{dc\_ref} - V_{dc} \tag{5.21}$$

$$i_{loss} = i_f + [k_P\{V_{dce}(n+1) - V_{dce}(n)\} + k_i\{V_{dce}(n+1)\}] \tag{5.22}$$

5.10.3 Calculation of Unit Templates

The formula of the unit template is shown in the Eq.5.23.

$$u_p(n) = \frac{v_s}{v_m} = \sin\omega t \tag{5.23}$$

5.10.4 Estimation of Reference Current and Gating Signal

The equation of reference current is shown in Eq. 5.25

$$w_T = w_p(n) + w_{loss} \tag{5.24}$$

$$i_p^* = w_T * u_p(n) \tag{5.25}$$

5.11 Simulation Results using ARBFNN Algorithm

In the MATLAB/Simulink software, a model of the suggested system with ARBFNN algorithm is designed and evaluated. The simulation results under different conditions are displayed in Figs 5.23–5.25. The system is designed for 110V, 50Hz applied for testing of closed loop control system.

Fig 5.23 shows the dynamic waveforms of source voltage v_s, source current i_s, load current i_L, compensator current i_c, inverter voltage (v_{inv}) and DC link voltage V_{dc}. The load is increased from 3A to 5A at time t=0.8s and decreased to its initial level of 3A at time t=1s. Due to load change, the load current, source current and compensating current are also changes but source voltage, inverter voltage and DC link voltage remains unchanged. It is observed that the source current

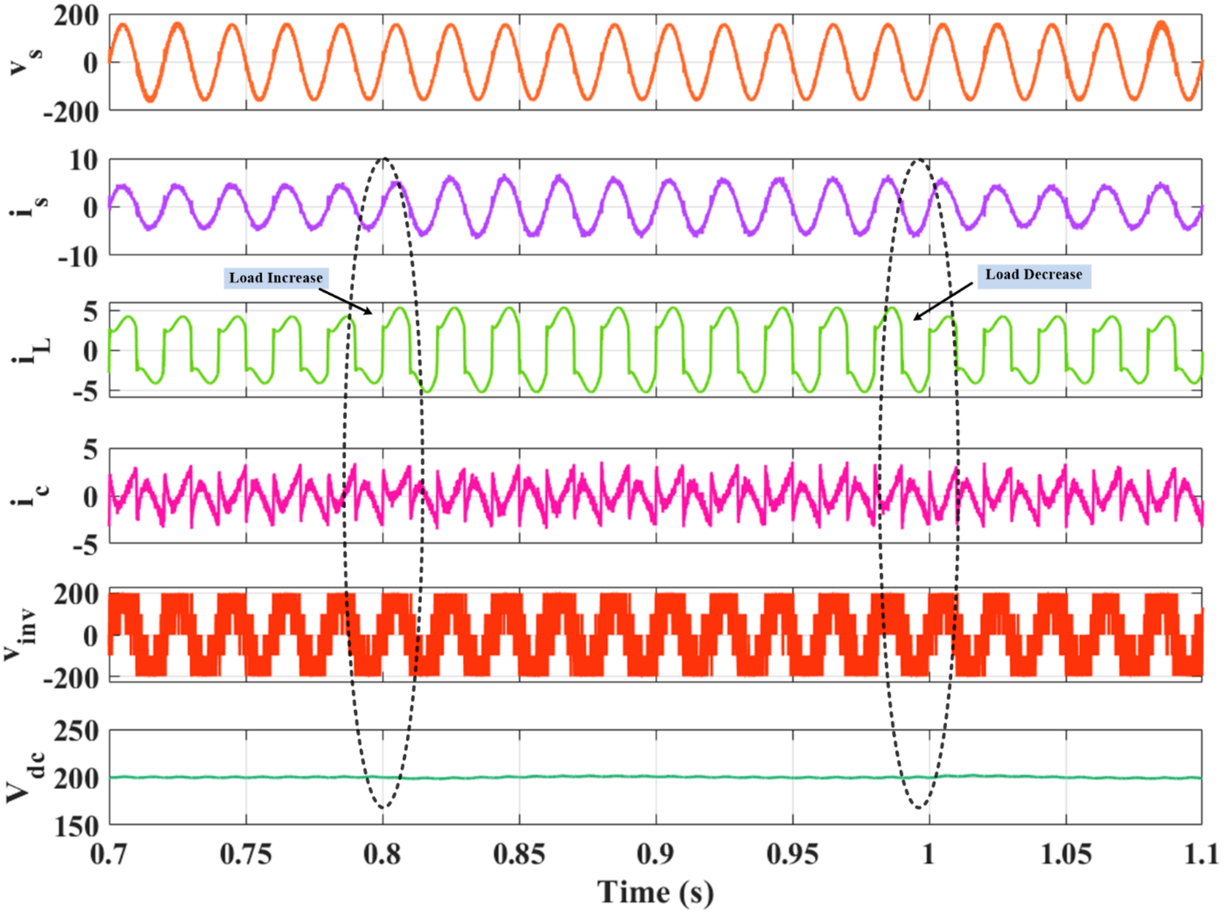

Fig 5.23 Simulation waveforms of source voltage (v_s), source current (i_s), load current (i_L), compensating current (i_C), inverter voltage (v_{inv}) , DC link voltage (V_{dc}) during dynamic condition using ARBFNN.

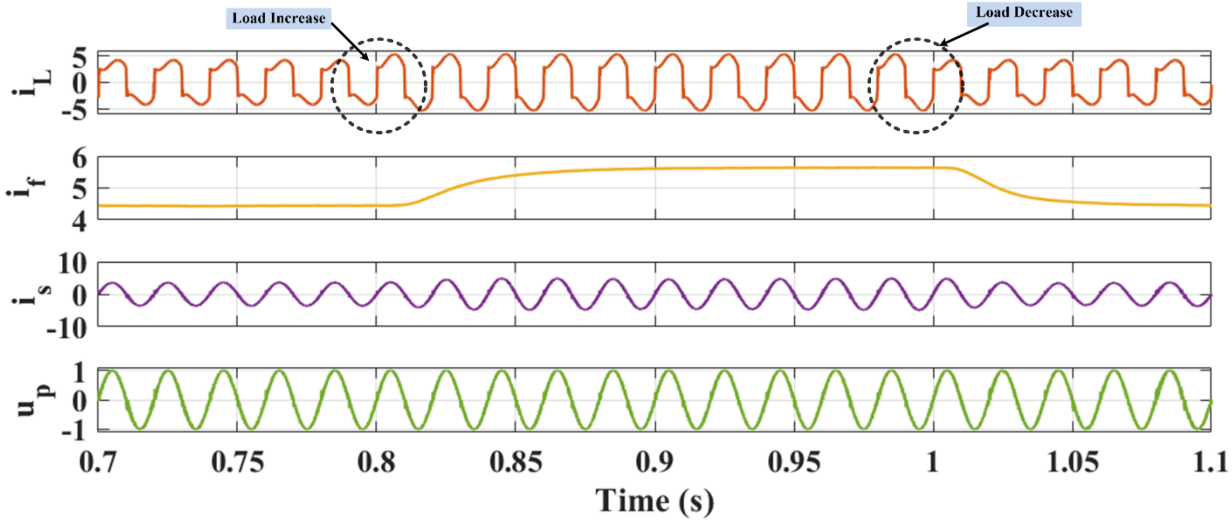

Fig 5.24 Simulation waveforms of load current (i_L), fundamental current (i_f), reference current (i_{ref}), unit template (u_p) during dynamic condition using ARBFNN.

stays sinusoidal and in phase with the source voltage after compensation. Additionally, Fig 5.23 also displays the output response of a 5-L CHB inverter voltage (v_{inv}) of 200V. The DC link voltage is well regulated and maintained to its reference value of 200V under load dynamics.

The waveform of i_L, i_f, i_{ref} and u_p are shown in Fig 5.24. The fundamental current is observed to increase at time t=0.8s and then decrease at t=1s in accordance with the variations in the actual loading conditions during a load change. The fundamental current is extracted by utilizing ARBFNN algorithm. The reference current also changes with change in load current but the unit

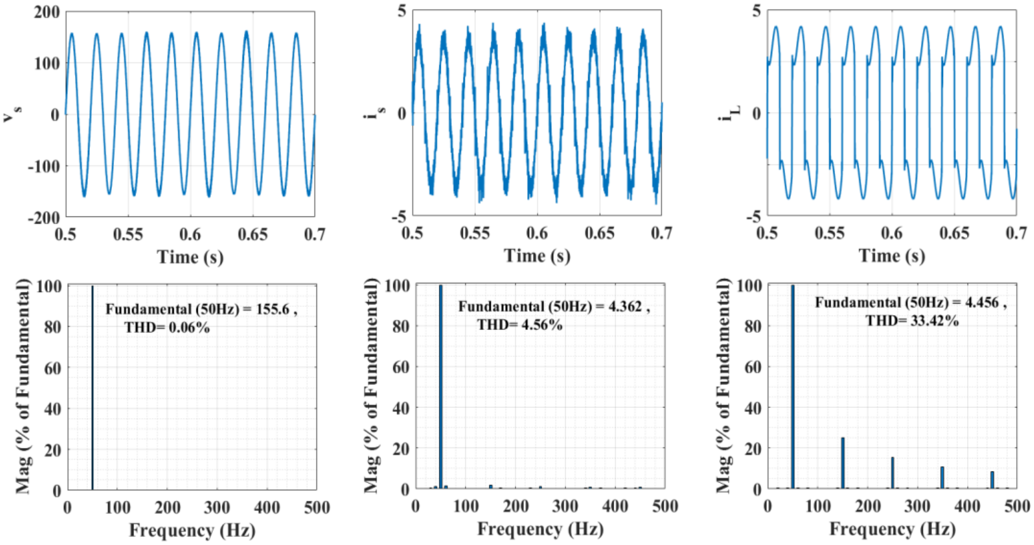

Fig 5.25 Experimental results : Harmonic analysis of a). v_s , THD = 0.06% b). i_s , THD = 4.56% c). i_L , THD = 33.42% during steady state condition using ARBFNN.

template's waveforms remained constant at unity. Also, the fundamental current increases and reaches a new steady state value within less than one cycle, due to the A-RBFNN algorithm's effective control action.

The analysis of the THD profiles in the source voltage (v_s) exhibits harmonic performance with a negligible THD of 0.06%. The source current (i_s) shows a THD of 4.56% which reflecting good harmonic quality. In contrast, the load current displays significant distortion with a THD of 33.42% as shown in Fig 5.25.

5.12 Experimental Results of ARBFNN Algorithm

In the laboratory, single phase system incorporating 5L CHB converter is developed to verify the feasibility of proposed technique. The system rating is 110V rms and 50 Hz frequency. The hardware setup for 5L converter features three voltage sensors (LV-25P) for sensing (v_s, V_{dc1}, V_{dc2}) and two current sensors (LA-25P) for sensing (i_s, i_L). These sensed voltage and current signals are processed by DSP (dSPACE 1104) to generate eight gating pulses for 5L-CHB converter. The 5L CHB converters are controlled to inject compensating current at point of common coupling. Hardware results for steady state and dynamic states are captured using Power Analyzer and DSO respectively.

(a). Steady State Results

The results for the 5L CHB based DSTATCOM configuration are now discussed. Fig 5.26 (a-c) shows the supply voltage (v_s) along with source current i_s, load current i_L and compensating current

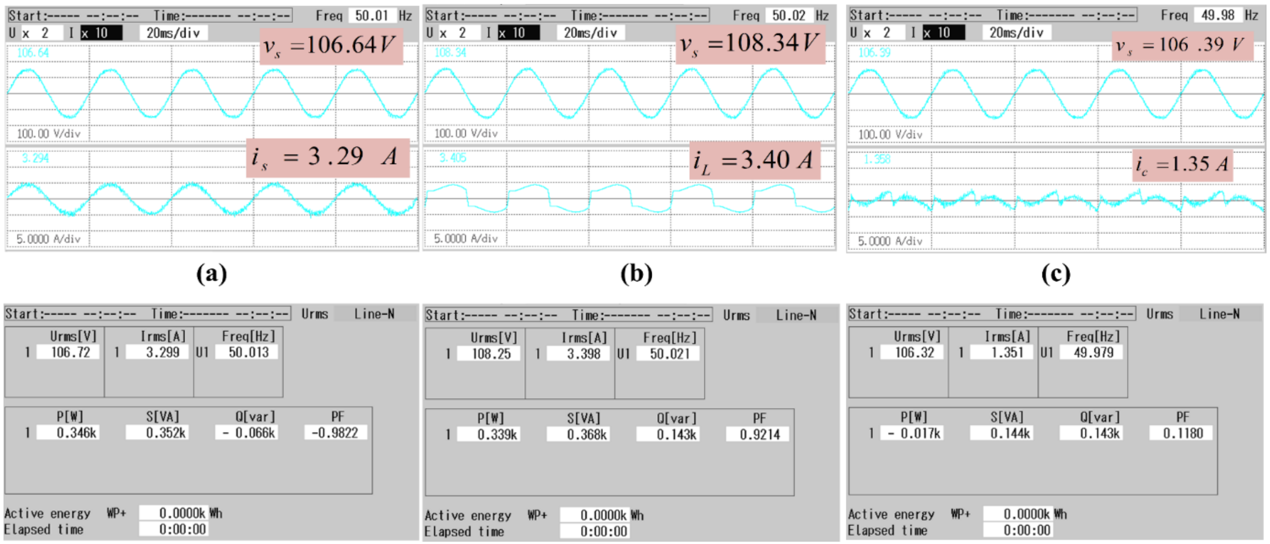

(a) (b) (c)

(d) (e) (f)

Fig 5.26 Experimental results of a). v_s,i_s b). v_s,i_L c). v_s,i_C d). Supply power P_S e). Load power P_L f). Compensator power P_C during steady state condition using ARBFNN.

i_c. After compensation, the supply current (i_s) is observed to be in phase with supply voltage and sinusoidal as shown in Fig 5.26(a) while the load current i_L is distorted as shown in Fig 5.26(b). The steady state active and reactive powers are shown in Fig 5.26(d-f). The active and reactive power demand of load is 339W and 143VAR. The grid supplies 346W active and 66VAR reactive power respectively. The compensator powers are 17W and 143VAR respectively. It is observed that the system active power demand is met by grid whereas most of the reactive power is provided by compensator. Thus, power factor at the supply end is improved from 0.9214 to 0.9822.

The harmonic spectrum of source voltage vs, source current is, and load current iL is shown in Fig 5.27 (a-b). It is observed that after compensation, the THD of iL is reduced from 29.18% to 4.87% in is and THD of vs is 2.76%. The source current THD has been reduced due to DSTATCOM action and brought within prescribed IEEE standard.

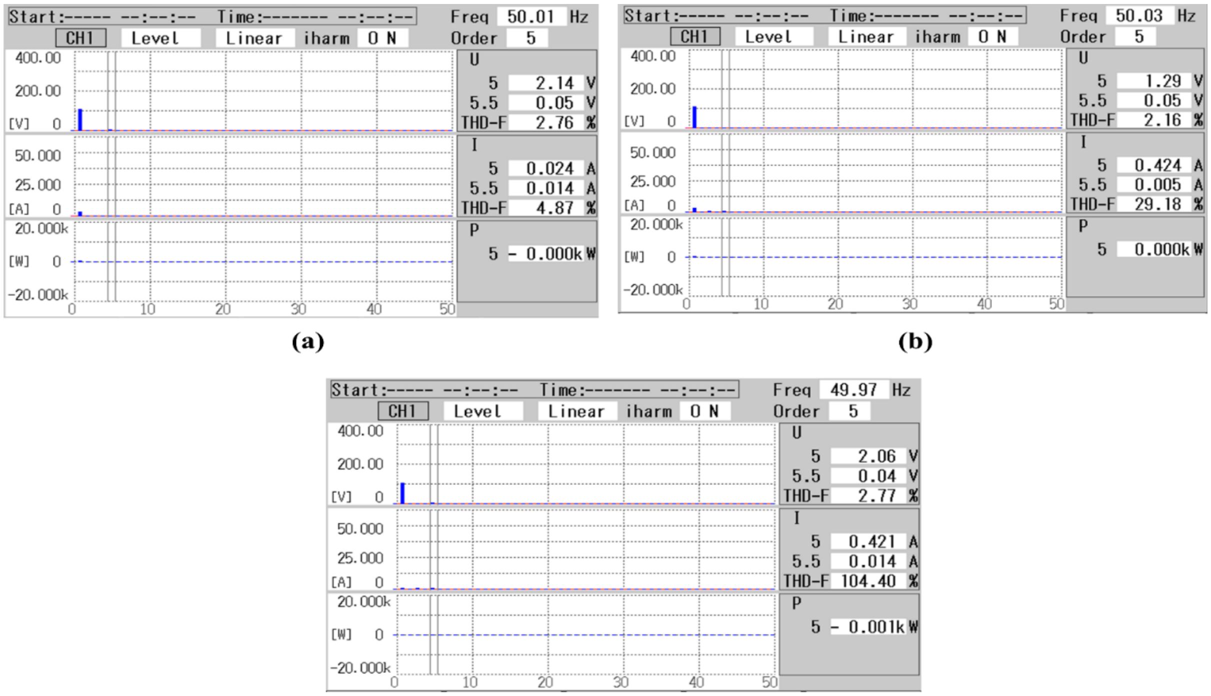

(a) Freq 50.01 Hz, Order 5, iharm 0 N; U: 5 2.14 V, 5.5 0.05 V, THD-F 2.76 %; I: 5 0.024 A, 5.5 0.014 A, THD-F 4.87 %; P: 5 - 0.000k W

(b) Freq 50.03 Hz, Order 5, iharm 0 N; U: 5 1.29 V, 5.5 0.05 V, THD-F 2.16 %; I: 5 0.424 A, 5.5 0.005 A, THD-F 29.18 %; P: 5 0.000k W

(c) Freq 49.97 Hz, Order 5, iharm 0 N; U: 5 2.06 V, 5.5 0.04 V, THD-F 2.77 %; I: 5 0.421 A, 5.5 0.014 A, THD-F 104.40 %; P: 5 - 0.001k W

(a) **(b)**

(c)

Fig 5.27 Experimental results: Harmonic analysis of a). v_s,i_s with THD = 4.87% b). v_s,i_L with THD = 29.18% c). v_s,i_C with THD = 104.40% during steady state condition using ARBFNN.

(b). Dynamic State Results

Fig 5.28(a-b) shows the waveforms of source voltage v_s, source current i_s, load current i_L, DC link voltage V_{dc} and compensating current i_c under load increase condition. The DC link voltage is well regulated to its reference value of 200V under load dynamics as shown in Fig 5.28(a). Fig 5.28(b) shows, the supply voltage and current are in same phase before and after load increase. The compensating current (i_c) is also changed due to load change and it also inject compensating current to improve the waveform of source current.

Fig 5.28(c) shows the waveforms of i_L, V_{dc1}, V_{dc2}, V_{dc}. It is observed that when there is sudden increase in load, the DC link voltage drops but it soon settles down to its steady state value.

The waveform of i_L , i_f ,i_{ref} and u_p are shown in Fig 5.28(d). It is to be observed that, the load and fundamental current both increase as expected. In less than one cycle, the fundamental active current also increases and reaches a new steady state value due to effective control action of A-RBFNN algorithm. The reference current also changes with change in load current and sine template maintains ±1 as expected.

Fig 5.29 shows the intermediate signal waveforms of is, i_L , e, i_f . It is seen that the intermediate parameters (e, i_f) also change whenever there is a sudden increase in load current. It is observed that the error (e) is nearly zero under dynamic load condition.

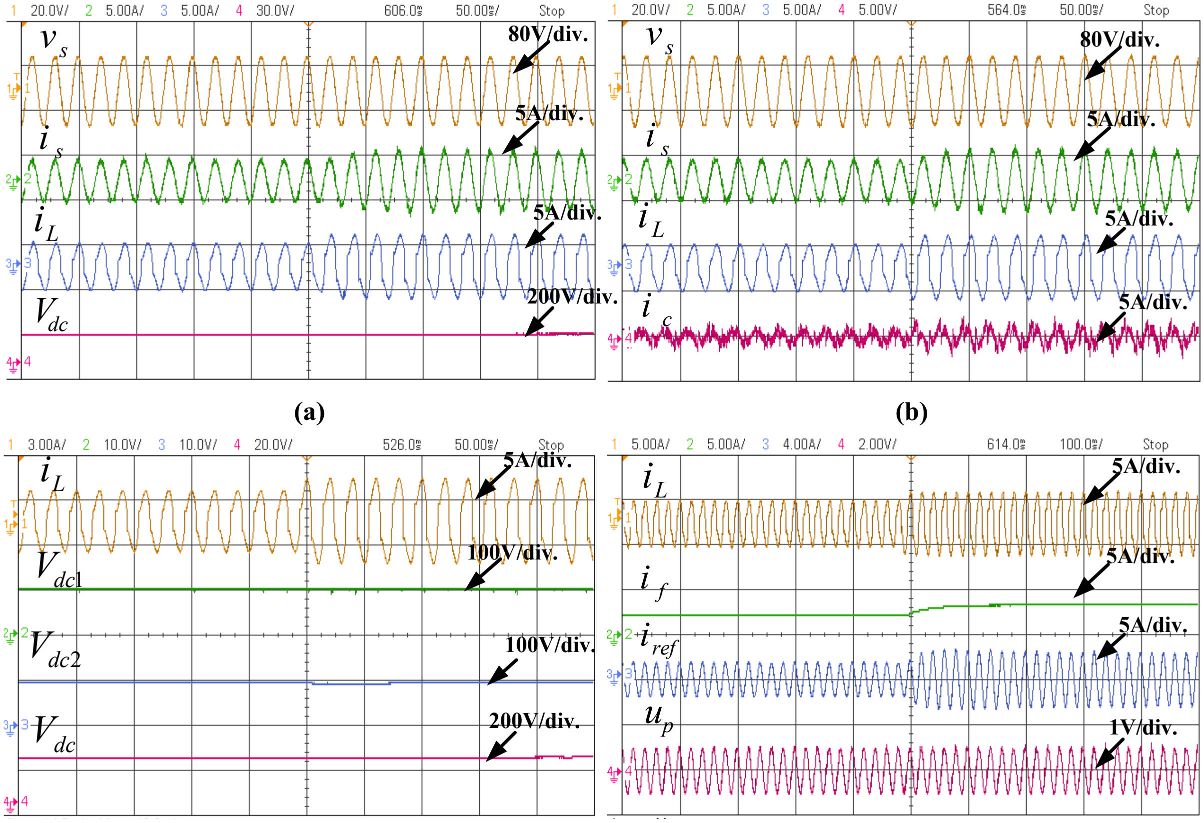

(a) (b)

(c) (d)

Fig 5.28 Experimental waveforms of a). v_s,i_s,i_L,V_{dc} b). v_s,i_s,i_L,i_C c). i_L,i_s,,i_f,i_{ref} and d). i_L, i_f, i_{ref} ,u_p during dynamic condition using ARBFNN.

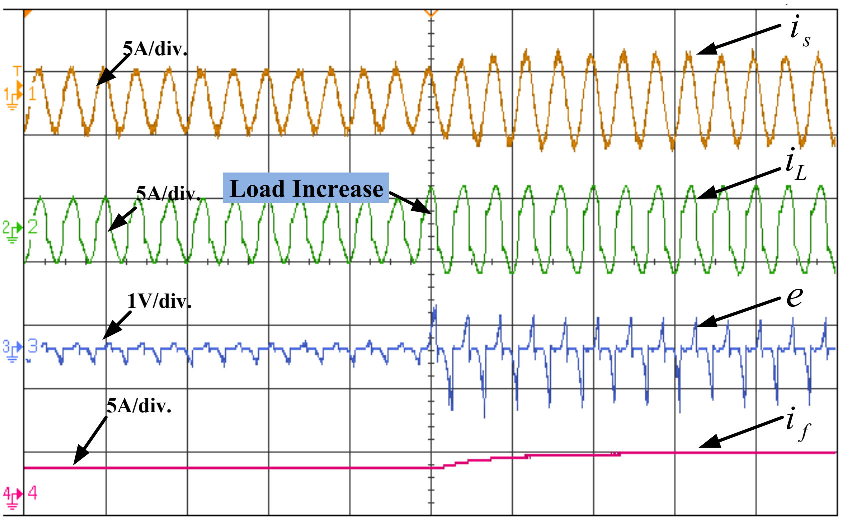

Fig 5.29 Experimental waveforms of i_s ,i_L,e, i_f during dynamic load condition using ARBFNN.

5.13 Comparative Analysis of NF, ALLMF and ARBFNN Control Algorithm

The proposed control algorithms were tested on 5-level CHB converter connected as DSTATCOM at PCC. The comparison of all the three algorithms is discussed based on the extraction of the fundamental current of load current whose response are displayed in Fig 5.30. The comparative analysis of 5L CHB converters with different algorithms (Notch filter, ALLMF and ARBFNN) are also shown in Table 5.2. The topology and performance results for 5-level converters are thoroughly analysed. It is observed that the weight convergence is fastest for ALLMF controller and also the

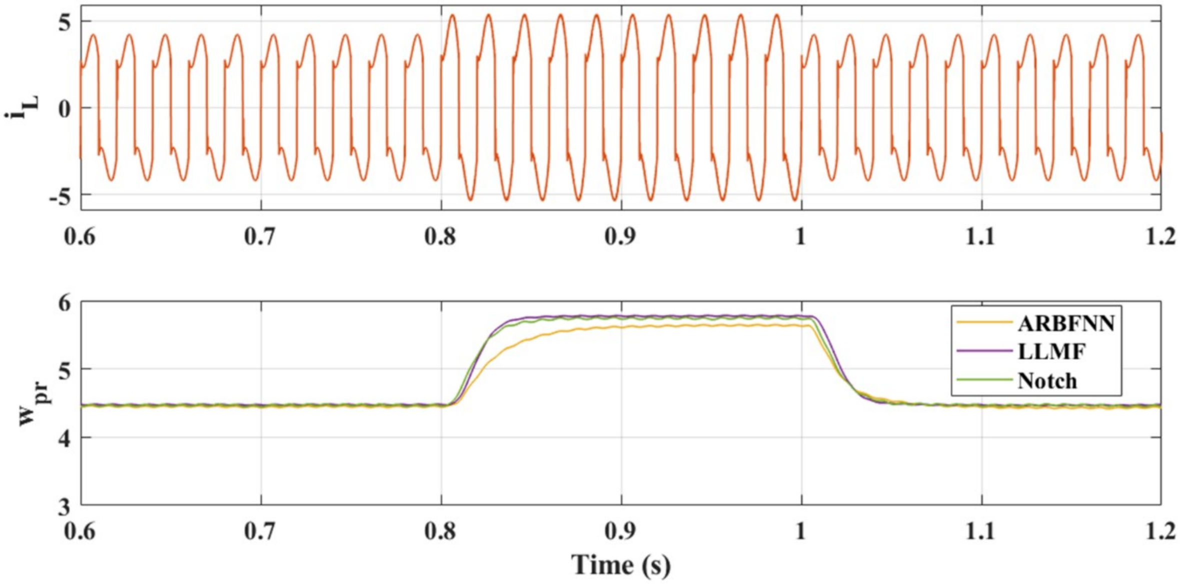

Fig 5.30 Comparative waveforms of load current (i_L) with fundamental current (i_f) at different algorithms

extracted fundamental current does not contain any oscillations. Whereas in other two algorithms, oscillations are observed. The ALLMF controller is adaptive algorithm while the Notch filter is a conventional, non-adaptive filter technique and the ARBFNN is the neural network-based algorithm. The harmonic content of the source current is obtained to be 4.87% and 4.78% for ARBFNN and Notch algorithms respectively, whereas the ALLMF technique achieves 3.86% THD for the load current has THD of 28.93%. The Convergence is also fastest within two cycles with 3V DC link voltage variations under load change. Fast weight convergence guarantees that the proposed approach performs better and maintains closed-loop stability under varied load situations. It is concluded that 5L-CHB converter configuration based DSTATCOM with ALLMF algorithm shows better response in terms of THD of source current with other algorithms as shown in Table 5.3. It is also observed that the lower switching losses and fast transient response in case of ALLMF algorithms.

Table: 5.2 Comparison table of NF, ALLMF and ARBFNN algorithms

S.no	Parameters	NF	ARBFNN	ALLMF
1	Filter type	Non-Adaptive	Adaptive	Adaptive
2	THD of i_s	4.78%	4.87%	3.86%
3	Estimation of fundamental currents	Consist sustained oscillations	Consist small oscillations	Oscillations are absent
4	Oscillations Magnitude	±4%	±5%	Zero
5	Complexity	Medium	Medium	Medium
6	Sampling Time (T_s)	$50\mu s$	$50\mu s$	$50\mu s$
7	Degree of optimization	NA	Second order	Fourth order
8	DC link Voltage variations	4V	4-5V	3V
9	Convergence	Faster than ARBFNN (3~4 cycles)	Slow (4~6 cycles)	Fastest (2 cycles)

Table: 5.3 %THD analysis of NF, ALLMF and ARBFNN algorithms

Algorithms		**%T.H.D (v_s)**	**%T.H.D (i_s)**	**%T.H.D (i_L)**
Notch	Simulation	0.48	3.17	30.69
	Experimental	2.29	4.78	28.62
ALLMF	Simulation	0.06	**2.72**	30.64
	Experimental	2.09	**3.86**	28.93
A-RBFNN	Simulation	0.06	4.56	33.42
	Experimental	2.76	4.87	29.18

5.14 Conclusion

In this chapter, three different algorithms viz. NF, ALLMF and ARBFNN algorithms are applied to a single-phase grid connected 5L-CHB based DSTATCOM for mitigation of power quality issues. All the three control techniques are able to estimate the magnitude of fundamental load current effectively. It is observed that the performance of the simulated as well as hardware system with ALLMF algorithm is better in terms of source current THD (3.86%). The ALLMF also shows faster dynamic response along with improved steady state response in comparison to other two algorithms. A detailed comparison is also discussed in this chapter based upon simulation and hardware results.

Chapter 6

Performance Analysis of Single Phase Grid Interfaced EV Charging System

This chapter presents the analysis of single phase grid connected EV charging system to operate under Grid to Vehicle (G2V) and Vehicle to Grid (V2G) condition. The harmonic analysis of this system is also studied during charging and discharging mode. Three various control algorithms viz Rodrigues Jacobi Polynomial (RJP), Least Mean Square (LMS) and Second Order Generalised Integrator (SOGI) are applied to the proposed system and its mathematical calculation with comparative analysis are discussed in the chapter. The simulation and experimental results are also presented and analysed.

6.1 Introduction

Fig. 6.1 displays a complete circuit diagram of the constructed system that includes the grid, a bidirectional AC-DC converter, and a bidirectional DC-DC converter for an EV charger. At the PCC, a nonlinear load that can be powered by a single-phase AC source is connected. The source resistance and inductance are shown in Fig 6.1 as R_S and L_S, respectively. It is observed that the

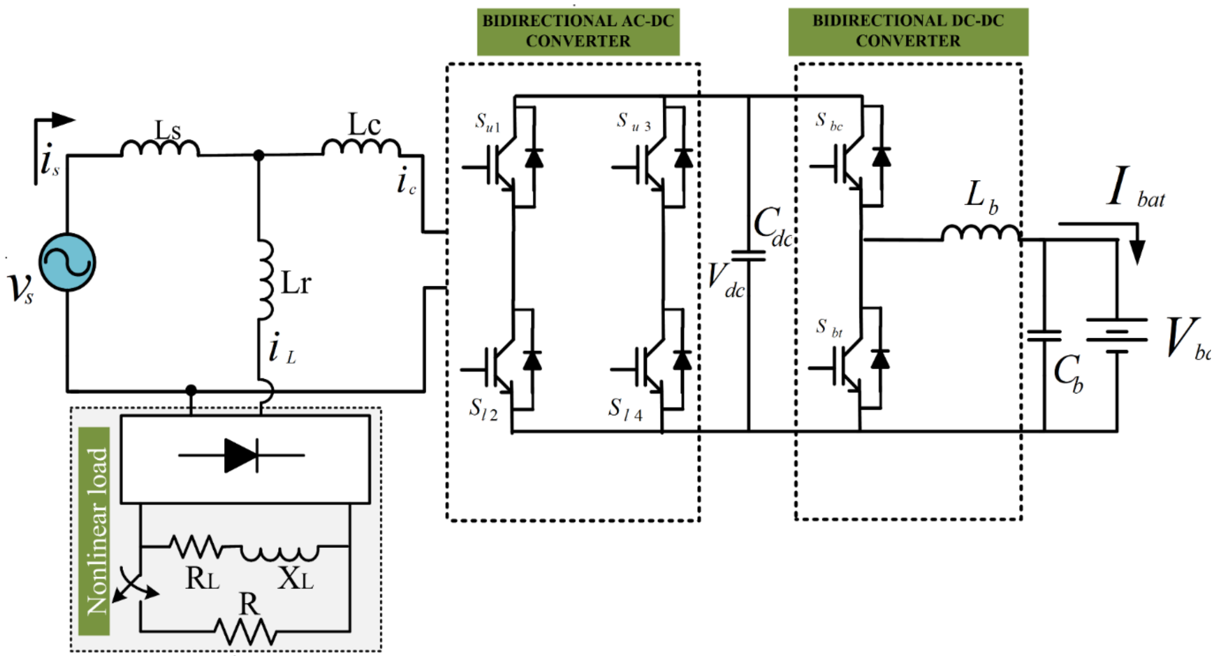

Fig 6.1: System Diagram of single phase grid connected EV charging system

connected load is nonlinear which distort the load as well as source current. A shunt configuration of AC-DC converter is applied as an active filter to reduce supply-side current harmonics. The proposed system's control is based on input variables such as source voltage (v_s), source current (i_s), load current (i_L), DC link voltage (V_{dc}), battery voltage (V_{bat}) and battery current (I_{bat}). These variables are measured using LEM-based current and voltage sensors. These measured voltage and current signals are subsequently analysed by the Real Time System (RTS's) controller through ADC channels. The designed control technique is applied to create the pulses of gate terminal via digital I/O channels. The gate pulses have a magnitude of +5V, which is amplified to +15V by the level shifter circuit. An interface inductor (Lc) is interfaced with the bidirectional AC-DC converter to suppress the output ripples from the inverter.

6.2 Brief theory and Mathematical Analysis of Different Control Algorithms

In this section, the mathematical analysis of different control algorithms like Second Order Generalized Integrator (SOGI), Least Mean Square (LMS) and Rodrigues Jacobi Polynomial (RJP) are described below.

6.2.1 Conventional Second Order Generalised Integrator (SOGI)

The SOGI controller is used to create two orthogonal components in alpha-beta reference frame from the input. The fundamental component of load current as well as unit template is generated using SOGI controller and it is described in following section.

The SOGI controller developed for extraction of load fundamental current is as shown in Fig 6.2. The error between input and alpha component of the output signal is amplified by a factor of ‘K’ and it is compared to the beta component signal. The total performance of SOGI is influenced by the parameter ‘K’. To make the system flexible to frequency changes, SOGI controller employs the angular frequency block created by the second half of the circuit as shown in Fig 6.2. The higher

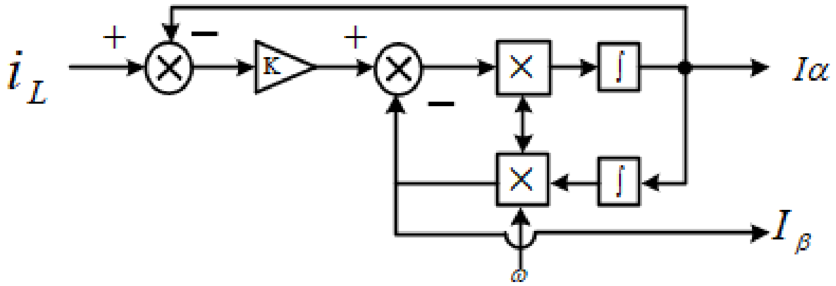

Fig 6.2: Circuit diagram of the SOGI controller

order frequency component occurs in the measured sample can be removed using SOGI block [282].

where, TF is the transfer function of SOGI and 'ω' depicts the resonance frequency, often known as the angular frequency of fundamental. The transfer function of closed loop for α and β current is shown in equation (6.2) and (6.3), respectively.

$$TF = \frac{ws}{w^2 + s^2} \tag{6.1}$$

$$H_\alpha(s) = \frac{i_\alpha(s)}{i(s)} = \frac{Kws}{s^2 + Kws + w^2} \quad ..(6.2)$$

$$H_\beta(s) = \frac{i_\beta(s)}{i(s)} = \frac{Kw^2}{s^2 + Kws + w^2} \tag{6.3}$$

6.2.2 Adaptive Least Mean Square (LMS) Control Algorithm

The LMS control algorithm is commonly used adaptive filter for control applications. It is a type of gradient descent algorithm used for finding the updated weights in a linear regression problem. The LMS algorithm is based on the principle of steepest descent, which involves minimizing the mean squared error (MSE) between the predicted output and the actual output [283]. To reduce the difference between the predicted and actual outputs, the algorithm iteratively modifies the filter coefficients. The algorithm determines the error between the intended and predicted outputs at each iteration, and then uses the gradient of the error with respect to the filter coefficients to update the filter coefficients.

The circuit diagram of LMS control algorithm is shown in Fig 6.3. This circuit estimate the fundamental weight w(n) and changes it in real time of operation. It has been observed that using LMS control technique reduces the error to zero.

As per circuit diagram, the estimated load current is,

$$i_{est}(n) = w(n)B(n) \tag{6.4}$$

Let, $i_L(n)$ be the actual nonlinear load current and $i_{est}(n)$ be an estimated current to evaluate the error signal e(n).

$$e(n) = i_L(n) - w_p(n)u_p(n) \tag{6.5}$$

In case of LMS algorithm, the cost function to be minimized is given by

$$C_{LMS}(n) = \frac{1}{2}[e^2(n)] \tag{6.6}$$

$$=\frac{1}{2}[\{i_L(n)-w(n)u_p(n)\}]^2 \tag{6.7}$$

As a result, the gradient estimation is defined as the partial derivative of the cost function with respect to the weight vector.

$$\frac{\partial C(n)}{\partial w(n)}=[-e(n)u_p(n)] \tag{6.8}$$

The minimum of C(n) can be sought recursively using the gradient method is known as weight update equation of the LMS is

$$w(n+1)=w(n)-\lambda\frac{\partial C(n)}{\partial w(n)} \tag{6.9}$$

$$=w(n)+\lambda e(n)u_p(n) \tag{6.10}$$

The updated weight equation for the LMS algorithm is fundamental current (i_f) given by:

$$w(n+1)=w(n)+\lambda e(n)u_p(n)=i_f \tag{6.11}$$

where, λ is the adaptation constant, e(n) is the error and $u_p(n)$ is unit template

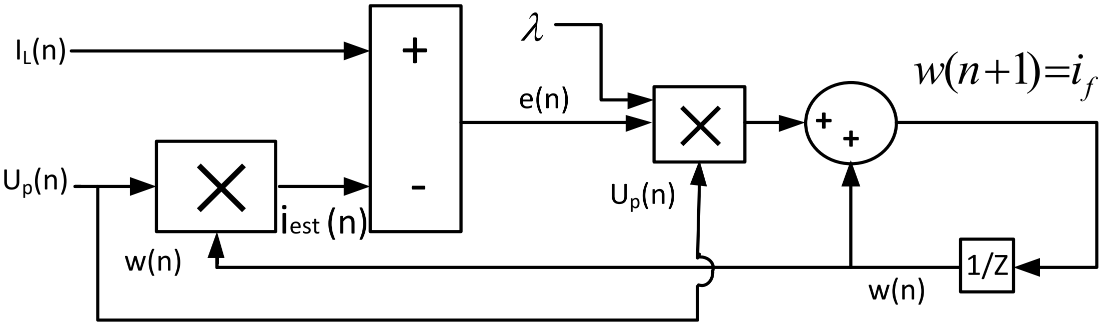

Fig. 6.3 Circuit diagram of LMS control algorithm

6.2.3 Rodrigues Jacobi Polynomial (JP) based Control Algorithm

The classical orthogonal polynomial $P_m^{(\delta,\gamma)}$ is known as Jacobi Polynomial [284]. It is orthogonal in terms of weight $(1-x)^\delta(x+1)^\gamma$ on the interval [1,-1]. Whenever, the choice of the given parameters δ and γ belongs to real (δ,γ ϵ $\Re$) and both are more than -1 (δ>-1 and γ>-1). It is denoted by the relation shown in Eq.6.12.

$$P_m^{(\delta,\gamma)}(x)=\sum_{n=0}^{m}\frac{(1+\delta)_m(1+\gamma)_m(x-1)^n(x+1)^{m-n}}{2^m\, n!(m-n)!(1+\delta)_n(1+\gamma)_{m-n}} \tag{6.12}$$

This can be written as

$$P_m^{(\delta,\gamma)}(x)=\frac{(x-1)^{-\delta}(x+1)^{-\gamma}}{2^m}\sum_{n=0}^{m}\frac{(1+\delta)_m(1+\gamma)_m(x-1)^{n+\delta}(x+1)^{m-n+\gamma}}{n!(m-n)!(1+\delta)_n(1+\gamma)_{m-n}} \tag{6.13}$$

$$D^s(x^{k+\delta}) = (k+\delta)(k+\delta-1)......(k+\delta-s+1)\,x^{k-s+\delta} \tag{6.14}$$
$$= \frac{(1+\delta)_k}{(1+\delta)_{k-s}} x^{k-s+\delta}$$

where, m is the degree of polynomial and $(1+\delta)_m$ is Pochhammer's symbol.

Let us assume, s and k are non-negative integers, the differential term $D^s(x^{k+\delta})$ can be written as

Similarly,

$$D^{m-n}[(x-1)^{m+\delta}] = \frac{(1+\delta)_m (x-1)^{n+\delta}}{(1+\delta)_n} \tag{6.15}$$

Putting this value in Eq.6.13, it becomes

$$P_m^{(\delta,\gamma)}(x) = \frac{(x-1)^{-\delta}(x+1)^{-\gamma}}{2^m\, m!} \sum_{n=0}^{m} \frac{m!}{n!(m-n)!} [D^n[(x+1)^{m+\gamma}][D^{m-n}[(x-1)^{m+\delta}] \tag{6.16}$$

Then, by Leibnitz theorem [ ], we get

$$P_m^{(\delta,\gamma)}(x) = \frac{(x-1)^{-\delta}(x+1)^{-\gamma}}{2^m\, m!} [D^m[(x+1)^{m+\gamma}(x-1)^{m+\delta}] \tag{6.17}$$

Thus, the Rodrigues Jacobi Polynomial can be expressed as

$$P_m^{(\delta,\gamma)}(x) = \frac{(-1)^n (1-x)^{-\delta}(1+x)^{-\gamma}}{2^m\, m!} [D^m[(1+x)^{m+\gamma}(1-x)^{m+\delta}] \tag{6.18}$$

Now, the first few terms of Rodrigues Jacobi Polynomial are calculated for different values of 'm'. Substituting, m=0 for the first term and m=1 for the second term gives Rodrigues Jacobi polynomials as shown in Eq.6.19-6.20.

For m=0, the first Rodrigues Jacobi polynomial reduces to

$$P_0^{(\delta,\gamma)}(x) = 1 \tag{6.19}$$

For m=1, the second Rodrigues Jacobi Polynomial reduces to

$$P_1^{(\delta,\gamma)}(x) = \frac{1}{2}[2(1+\delta) + (\delta+\gamma+2)(x-1)] \tag{6.20}$$

The sum of these two terms is mainly responsible for fundamental $P_m^{(\delta,\gamma)}(x)$ generation using Rodrigues Jacobi Polynomial.

$$P_m^{(\delta,\gamma)}(x) = [1 + \frac{1}{2}\{2(1+\delta) + (\delta+\gamma+2)(x-1)\}] \tag{6.21}$$

Other higher order Rodrigues Jacobi Polynomials can be obtained by substituting different values of 'm' but these have not been considered further for analysis.

6.3 Control Structure of Single Phase Grid Interfaced EV Charging Systems using SOGI filter

The control of bidirectional AC-DC converters and bidirectional DC-DC converters is thoroughly examined in this section, and the control diagram is illustrated in Fig 6.4 (a-b).

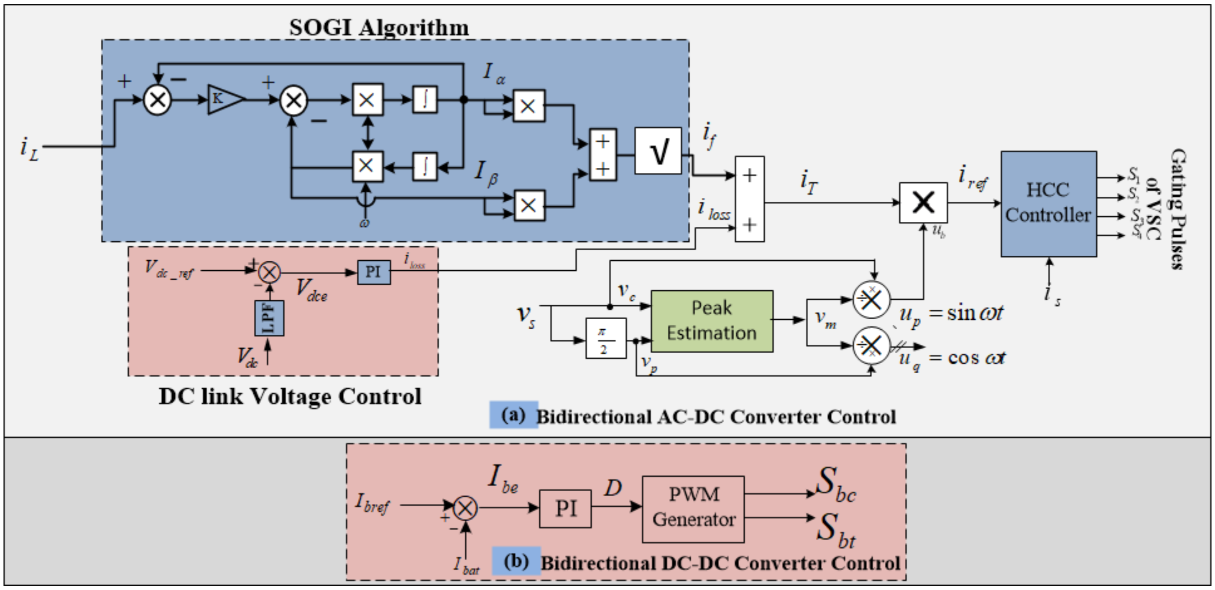

Fig 6.4 Control diagram of SOGI algorithm

6.3.1 Control of Bidirectional AC-DC Converter

Fig 6.4 (a) illustrates the complete control algorithm, which incorporates fundamental component extraction using Second Order Generalised Integrator (SOGI) and DC link voltage control. Important components of the controller description include the computation of the unit template (u_p), estimation of the fundamental current (i_f), determination of the loss current component (i_{loss}), and calculation of the reference supply current (i_{ref}). The main aim of the Second Order Generalised Integrator (SOGI) based controller is to extract the fundamental component (if) of the load current. The PI controller processes the voltage of the DC-link to provide an estimate of the current loss (i_{loss}) component. The Second Order Generalised Integrator (SOGI) controller calculates the fundamental load current component, which is subsequently combined with this output to produce the effective current. Further, the effective current magnitude and unit template are employed to generate reference current, which is then processed through HCC to produce four gating pulses for the bidirectional AC-DC converter. Regardless of the non-linear connected demand, the control algorithm guarantees enhanced power quality on the grid side.

6.3.2 Calculation of Fundamental Component of Load Current

The fundamental component of the load current is estimated by utilising the output of the Second Order Generalised Integrator (SOGI), as illustrated in Fig 6.4 (a). The fundamental current is generated by passing the load current through dominant Second Order Generalised Integrator (SOGI) controller. The fundamental load current is ultimately represented in Eq. 6.22 as

$$i_f = \sqrt{(i_\alpha)^2 + (i_\beta)^2} \tag{6.22}$$

6.3.3 Calculation of Unit Templates

The peak estimate block, shown in Fig 6.4 (a) is used to compute the unit template by processing the grid voltage (v_s) and its phase-shifted quadrature component (v_p). This technique produces the v_m as shown in Eq. (6.24-6.25).

$$v_s = v_m \sin \omega t \tag{6.23}$$

The 90° phase shifted component of v_s can be depicted by v_p and shown in Eq.6.24

$$v_p = v_m (\sin \omega t + \frac{\pi}{2}) \tag{6.24}$$

Now, the peak voltage can be estimated as

$$v_m = \sqrt{v_p^2 + v_s^2} \tag{6.25}$$

The calculation of in-phase unit template (u_p) is shown in Eq.6.26.

$$u_p = \frac{v_s}{v_m} = \sin \omega t \tag{6.26}$$

6.3.4 Estimation of Reference Current and Gating Signals

The contribution of the Second Order Generalised Integrator (SOGI) is responsible to generate fundamental current component (i_f). This component is added to the DC loss current (i_{loss}) to produce an effective current (i_T) as per Eq.6.27. Thereafter, this effective current (i_T) is multiplied with the unit template to generate reference current as shown in Eq.6.28.

$$i_T = i_f + i_{loss} \tag{6.27}$$

$$i_{ref} = i_T * u_p \tag{6.28}$$

Once the reference supply current (i_{ref}) is generated, it is compared with the actual supply current (i_s) using an HCC block to generate four switching pulses for driving the inverter.

6.3.5 Control of Bidirectional DC-DC Converter

The control of bidirectional DC-DC converter is shown in Fig 6.4 (b). The feedback current is the battery current (I_{bat}) fed with reference battery current (I_{bref}) to obtain error (I_{be}) as seen in Eq.6.29. This error is tuned with PI controller to obtain duty cycle (D). Now, the tuned output of PI controller is applied with Pulse Width Modulation (PWM) generator to operate two switches having gate pulse S_{bc} (buck) and S_{bt} (boost).

$$I_{be} = I_{bref} - I_{bat} \tag{6.29}$$

6.4 Simulation Results using SOGI Control Algorithm

The outcomes of the system after testing in the MATLAB/Simulink environment are shown in Figs 6.5-6.6. These simulations provide several waveforms for closed-loop control systems throughout the charging and discharging processes. The parameters of the Simulink model are detailed in the appendix C, and the results are elaborated below.

(a). Simulation Results under Charging Condition

The system's behaviour under charging condition is shown in Fig 6.5, which is obtained from the suggested SOGI controller architecture. The waveforms of the source voltage (v_s), source current (i_s), nonlinear load current (i_L), compensatory current via the active filter (i_c), DC link voltage (V_{dc}), battery voltage (V_{bat}), and battery current (I_{bat}) are shown. Fig 6.5 illustrates an examination of the effects of load disturbance on controller performance during the charging procedure. At time t=0.8s, the current is augmented from 2A to 3A. An increase in source current (i_s) occurs without any change in source voltage (v_s). Due to load variations, the DC-link voltage (V_{dc}) temporarily decreases, but the PI controller promptly reinstates it to the 200V reference level. Furthermore, the source current stays sinusoidal and in phase with the source voltage throughout the charging mode, illustrating the efficacy of the control mechanism based on the SOGI algorithm under dynamic

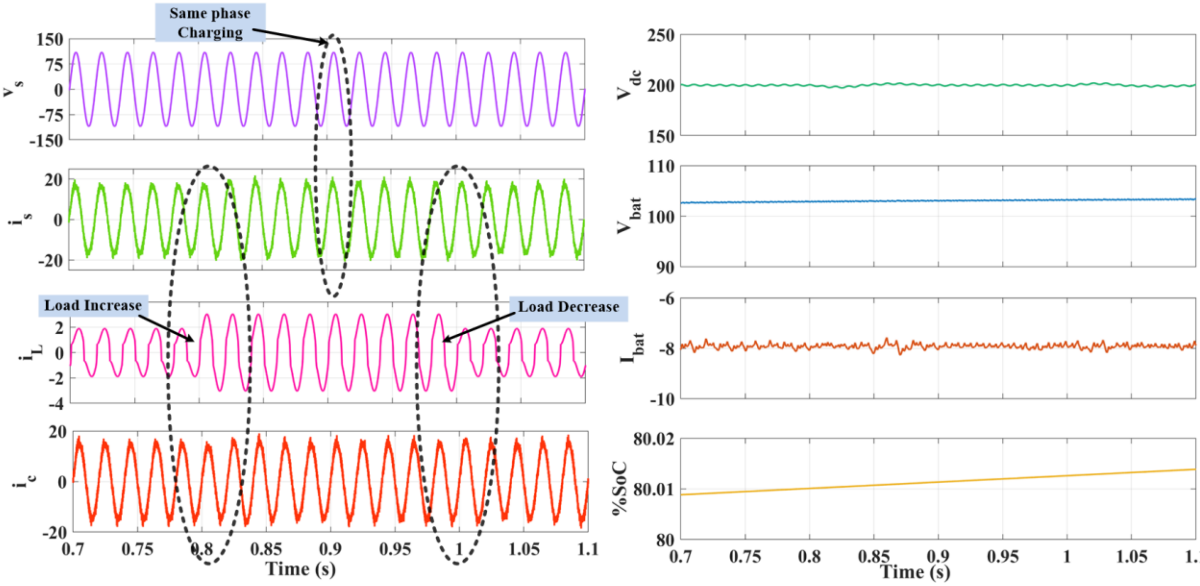

Fig.6.5 Single phase waveform of v_s, i_s, i_L, i_c, V_{dc}, V_{bat}, I_{bat} and %SoC at charging mode using SOGI.

load conditions. Simultaneously, the battery current (I_{bat}) remains at -8A while the voltage consistently increases to 96V. The state of charge (SOC) begins at 80% and continues to increase. The Simulink harmonics content in the source voltage (v_s), source current (i_s), and load current (i_L) during the charging condition is shown in Figs 6.6. The source current's total harmonic distortion (THD) is reduced to 3.17% after the injection of compensating current, as 17.69% for i_L due to non-linear load. Additionally, the supply voltage's THD is 0.48% during charge (b). Simulation Results under Discharging Condition

Fig 6.7 displays the dynamic behaviour of the system while utilising the proposed controller under discharge conditions. The waveforms of several voltages and currents: grid voltage (v_s) with grid current (i_s), nonlinear load current (i_L), compensatory current via DSTATCOM (i_c), DC link voltage (V_{dc}), battery voltage (V_{bat}), and battery current (I_{bat}) are shown in the Fig 6.7. In a procedure analogous to charging, the electric vehicle's battery is used to meet the increased load current demand from 2A to 3A, with the surplus current being returned to the grid. The supply voltage and current are not in phase during discharging, which should be noticed. This is seen clearly in the first plot in Fig 6.7. The DC-link capacitance voltage is maintained at 200V using the tuned PI controller. The electric vehicle's battery voltage drops from 96V which is linked to the grid and is providing power throughout the discharge process. The percentage state of charge (SoC) of 80% is continuously decreasing in nature. The battery current stays at 8A as planned while it is being discharged.

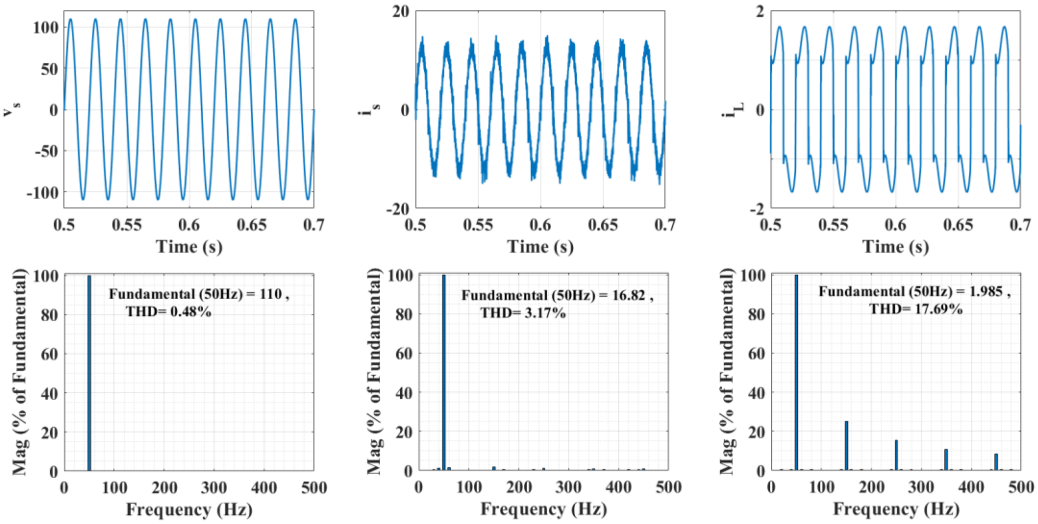

Fig 6.6 Simulink results : Harmonic analysis of a). v_s , THD = 0.48% b). i_s , THD = 3.17% c). i_L , THD = 17.69% during steady state condition at charging mode using SOGI.

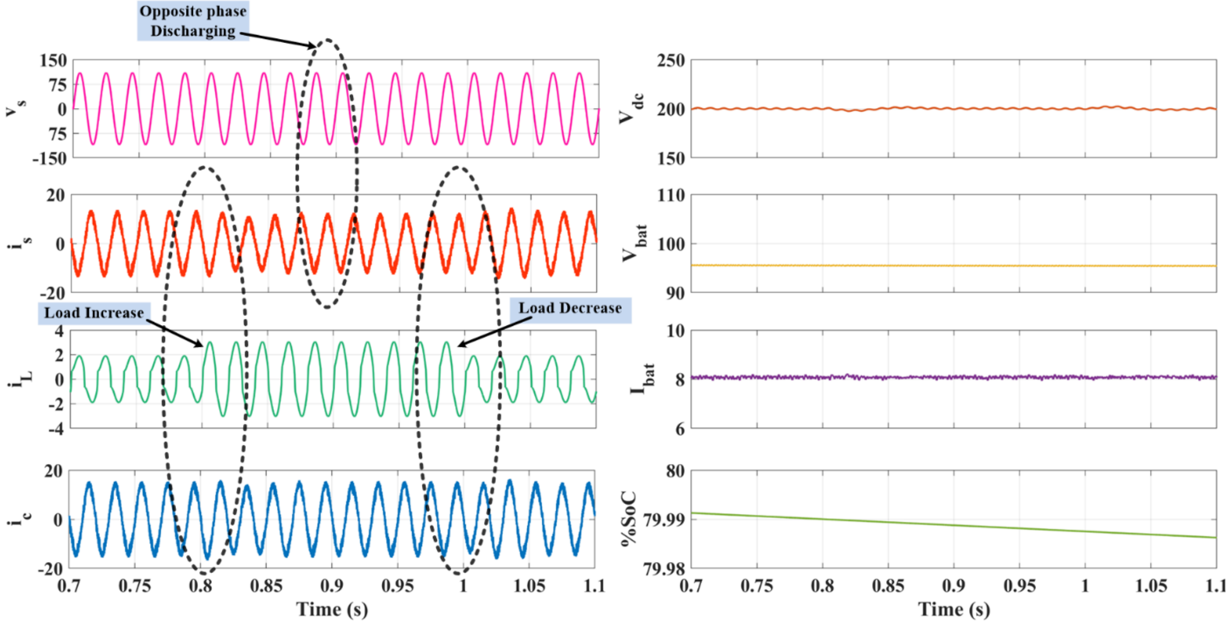

Fig.6.7 Single phase waveform of $v_{s,}$ $i_{s,}$ $i_{L,}$ $i_{c,}$ V_{dc},V_{bat}, I_{bat} and %SoC in discharging mode using SOGI.

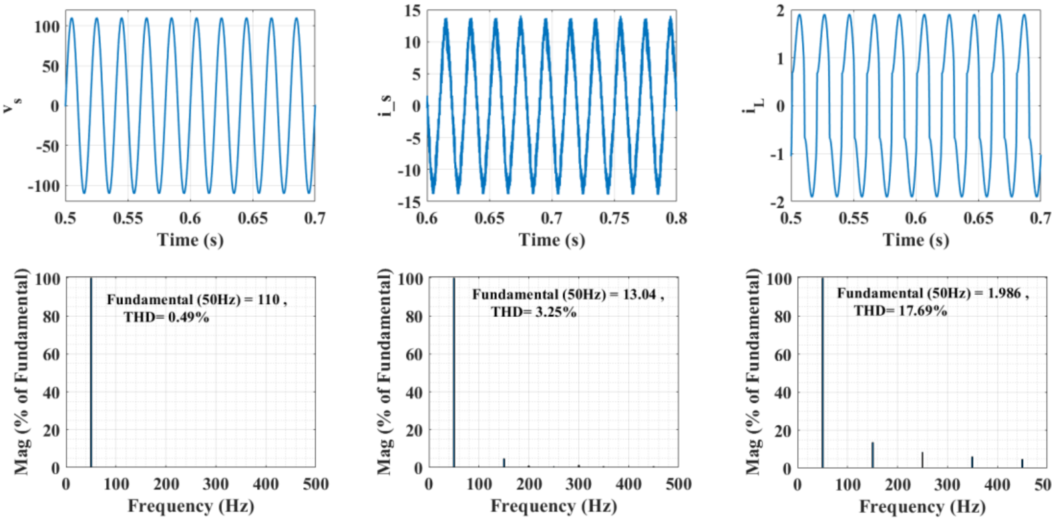

Fig 6.8 Experimental results : Harmonic analysis of a). v_s , THD = 0.49% b). i_s , THD = 3.25% c). i_L , THD = 17.69% during steady state condition at discharging mode using SOGI.

The Simulink harmonics content in the source voltage (v_S), source current (i_S), and load current (i_L) during the discharging condition is shown in Fig 6.8. The source current's total harmonic distortion (THD) is reduced to 3.25% after the injection of compensating current, as 17.69% for i_L due to non-linear load. Additionally, the supply voltage's THD is 0.49% during discharge.

6.5 Experimental Results using SOGI Control Algorithm

A constructed experimental set up is developed in the.laboratory as shown in Fig 6.9. The constructed model is evaluated at 40V (rms) and 50Hz alternating current supply, which powers a nonlinear load and incorporates an integrated EV charger. The nonlinear load is arranged as a series combination of load resistance (R) and inductance (L) on the DC side of the bridge rectifier. The bidirectional AC-DC converter is supplied at the point of common coupling (PCC), enabling compensating currents to be sent via interface inductors. The bidirectional buck-boost converter is supplied by the DC link of the AC-DC converter. Multiple LEM sensors, namely the voltage sensor (LV-25P), are used for measuring v_s, V_{dc1}, and V_{bat}, while current sensors (LA-25P) are used to measure i_s, i_L, and I_{bat}. The Real Time System (RTS) controller is linked for communicating with these sensors. The developed controller ensures proper regulation of the AC side converter, with four gating pulses from the RTS driving the converter. A DSO records various signals obtained from the hardware, while a power analyser (HIOKI PQ3100) evaluates experimental characteristics such as power, current, and harmonics. The comprehensive details of the experimental setup are included in the Appendix C.

a). Experimental Results during Charging Operation with SOGI controller

This section thoroughly analyses the experimental performance during charging operations under steady-state and dynamic conditions, as seen in Figs 6.10-6.12.

Fig. 6.9 Experimental setup up single phase grid interfaced EV charging systems

a). *Steady State Conditions*

Figs 6.10-6.11 show the various waveforms, harmonics, and power is captured during the charging process.

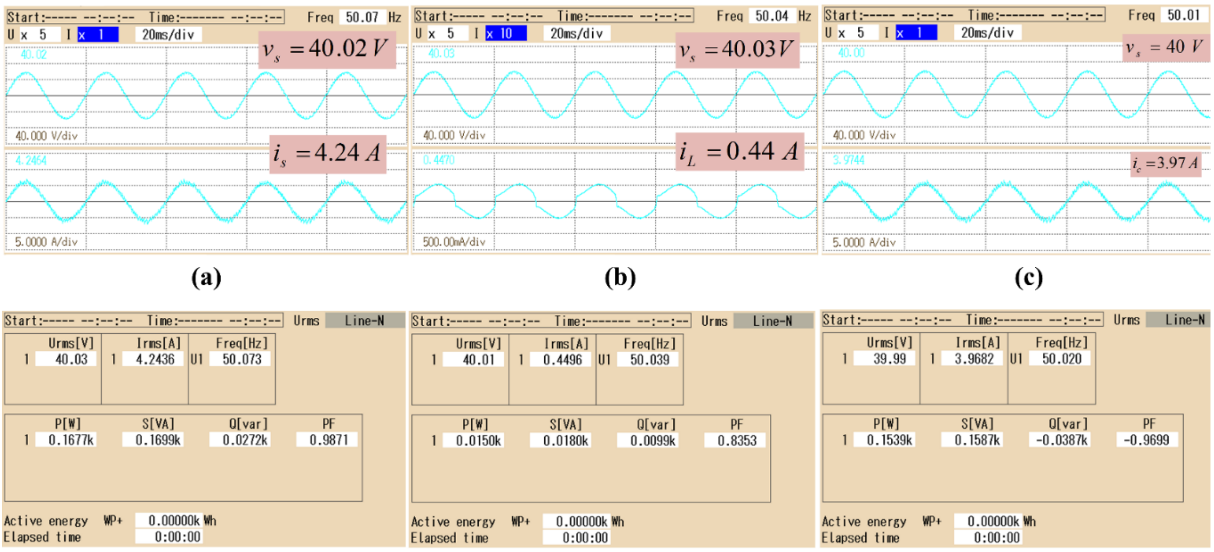

(a) (b) (c)

(d)

Start:----- --:--:-- Time:------- --:--:-- Urms Line-N

Urms[V]	Irms[A]	Freq[Hz]
1 40.03	1 4.2436	U1 50.073

P[W]	S[VA]	Q[var]	PF
1 0.1677k	0.1699k	0.0272k	0.9871

Active energy WP+ 0.00000k Wh
Elapsed time 0:00:00

(e)

Start:----- --:--:-- Time:------- --:--:-- Urms Line-N

Urms[V]	Irms[A]	Freq[Hz]
1 40.01	1 0.4496	U1 50.039

P[W]	S[VA]	Q[var]	PF
1 0.0150k	0.0180k	0.0099k	0.8353

Active energy WP+ 0.00000k Wh
Elapsed time 0:00:00

(f)

Start:----- --:--:-- Time:------- --:--:-- Urms Line-N

Urms[V]	Irms[A]	Freq[Hz]
1 39.99	1 3.9682	U1 50.020

P[W]	S[VA]	Q[var]	PF
1 0.1539k	0.1587k	-0.0387k	-0.9699

Active energy WP+ 0.00000k Wh
Elapsed time 0:00:00

Fig. 6.10 Experimental results of a). v_s,i_s b). v_s,i_L c). v_s,i_C d). Supply power P_S e). Load power P_L f). Compensator power P_C during steady state condition using SOGI.

Fig 6.10 illustrates the results of the system's steady-state experiments, representing the waveforms of the source voltage (v_s), source current (i_s), load current (i_L), and compensating current (i_c). The distortion of the load current due to the connection of a non-linear load is most clearly seen in Fig 6.10 b. Charging operations have sinusoidal characteristics, as seen in Fig 6.10 a, with the supply voltage (v_s) and current (i_s) being in phase. Fig 6.10 c demonstrates that while an electric vehicle is charging, current is drawn into the battery pack via a bidirectional AC converter and a bidirectional DC-DC converter.

During charging operation, Fig 6.10 (d-f) shows the steady-state active and reactive power flow. The reactive power required by the load is 0.0099 kVAR, while the active power need is 0.015 kW. The active filter raises the load's power factor (P.F.) from 0.83 to 0.98 by reducing its reactive power demand by 0.0099 kVAR, as seen in Fig 6.10 (d-e). The load's actual power demand plus switching losses is covered by the 0.167 kW which is supplied by the grid.

The harmonic spectrum of source voltage v_s, source current i_s, and load current i_L is shown in Figs 6.11 (a-c). It is observed that after compensation, the THD of i_L is reduced from 15.55% to 4.90% in is and THD of vs is 2.13%. The compensator current, which is utilised to mitigate harmonics in a non-linear load, exhibits a THD of 6.26%, as shown in Fig 6.11 c.The harmonics generated by the nonlinear load are effectively cancelled by the injection of AC-DC converter compensating current, resulting in a sinusoidal and in-phase source current.

The waveforms that were observed plainly demonstrate that the source current's %THD adheres to the IEEE-1547 and its standard limit of 5%.

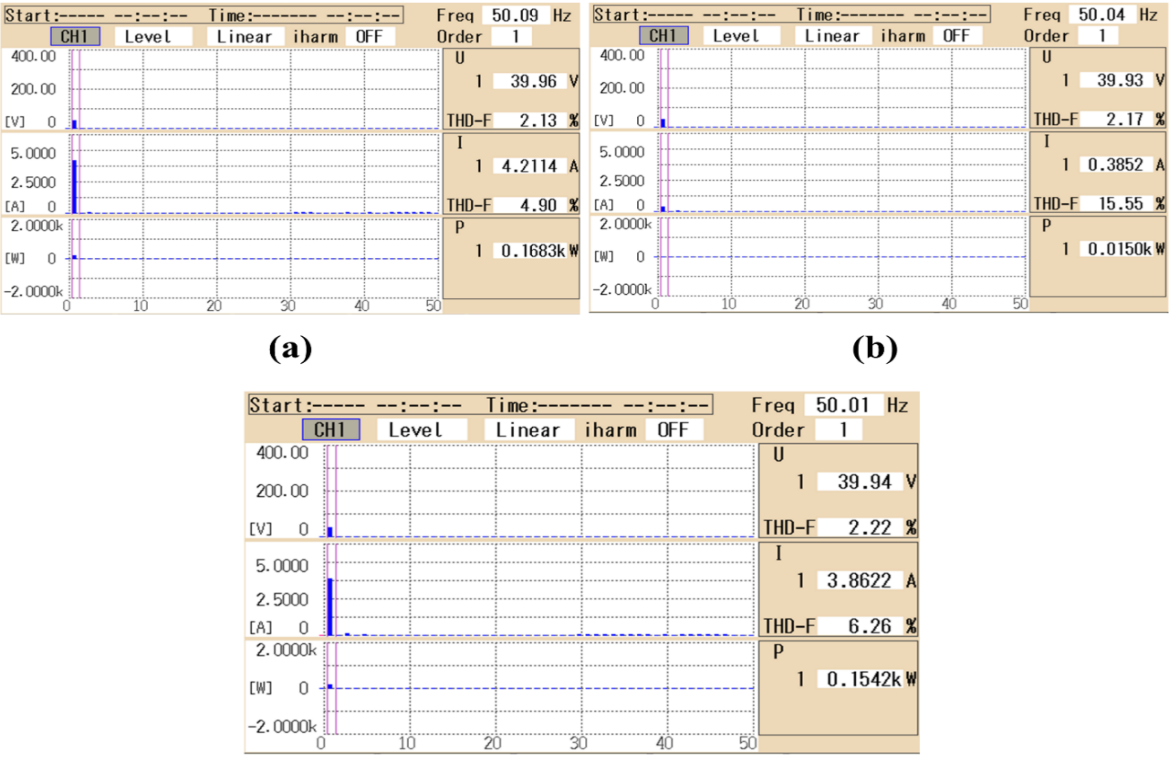

(a) **(b)**

(c)

Fig. 6.11 Experimental results Harmonic analysis of a). v_s,i_s with THD = 4.90% b). v_s,i_L with THD = 15.55% c). v_s,i_C with THD = 6.26% during steady state condition using SOGI.

This further corroborates the fact that the SOGI-based control algorithm has been well-designed and functions correctly.

b). *Dynamic State Conditions*

Fig 6.12 (a–d) shows the dynamic results of the proposed system under different load conditions while it is charging. The waveforms show waveforms that can change, such as source voltage (v_s), source current (i_s), load current (i_L), total DC link voltage (V_{dc}), compensating current (i_c), fundamental weight (I_f), unit template (u_p), reference current (i_{ref}), battery voltage (V_{bat}), and battery current (Ibat), while the load changes during charging.

Fig 6.12 (a–b) shows the patterns of v_s, i_s, i_L, V_{dc}, and i_c as the load changes. The source current changes when the load changes, but the DC link voltage stays at 80V. The voltage on the DC link is well-regulated, and changes in the load have little effect on how well it regulates. The fact that the waves v_s and i_s are seen to be in the same phase indicating charging process.

Fig 6.12 c depicts the waveforms of the variables i_s, i_L, I_{bat}, and V_{bat} respectively. While the charging procedure is being carried out, the battery current (I_{bat}) is maintained at a constant value of -2A. The battery voltage gradually increases from 48V irrespective of the load.

Fig 6.12 d illustrates the waveforms of load current (i_L), fundamental current (i_f), battery current (I_{bat}), and unit template (u_p). The waveforms indicate a change in the fundamental current caused by fluctuations in the load current. The SOGI controller-based control algorithm accurately estimate fundamental load current. The battery current maintains consistently at -2A during the charging condition, as previously stated.

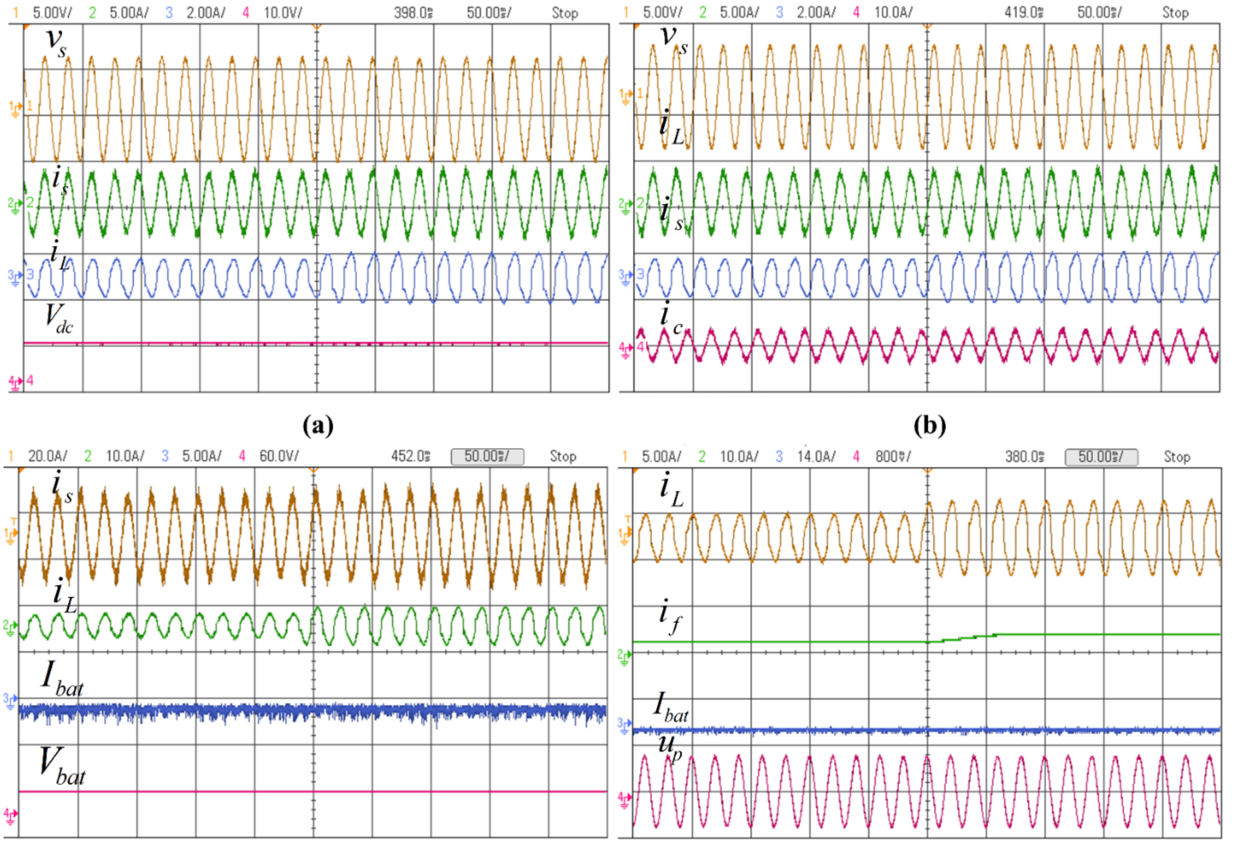

(a) **(b)**

(c) **(d)**

Fig. 6.12 Experimental waveforms of a). v_s,i_s,i_L,V_{dc} b). v_s,i_L, i_s ,i_C c). i_s ,i_L,,I_{bat},V_{bat} and d). i_L, i_f, I_{bat} ,u_p during dynamic condition using SOGI.

b). Experimental Results during Discharging Operation with SOGI controller

Fig 6.13-6.15 illustrates the experimental performance analysis that is described in this part. This section focusses on the steady state and dynamic condition experimental performance analysis that takes place throughout the discharging process.

a). *Steady State Conditions*

In Fig 6.13–6.14, waveforms, power analysis, and THDs are displayed during discharging operation. Fig 6.13 (a-c) depicts the discharging mode operation and source voltage, source current, load current, and compensatory current waveforms. Fig 6.13 a shows source current and voltage in phase opposition. The distorted load current (i_L) and source voltage (v_s) curve in Fig 6.10 b is shown during EV discharging. As shown in Fig 6.13 c, the active filter injects compensating current (i_c) to negate load current nonlinearity and injects a net excess current to the supply side grid when discharging. This can be shown by source voltage inphase opposition to source current. These observations also confirm the simulation results depicted in Fig 6.6.

Figs 6.13 (d-f) illustrate the power balance during the discharging condition. The active and reactive power requirements of the load are +0.0165kW and +0.0054kVAR, respectively. The compensator injects active and reactive power of 0.064kw and 0.0217kVAR to meet the load power demand. Consequently, the grid is supplied with a surplus electricity of -0.0486kw and -0.0161kVAR.

The harmonics content in the source voltage (v_s), source current (i_s), and load current (i_L) during

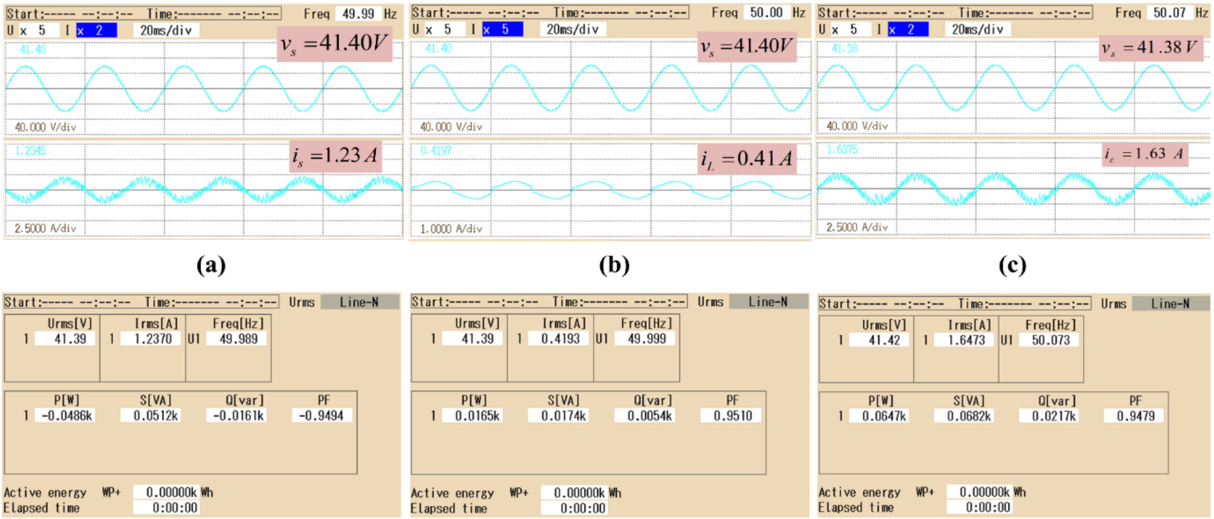

(a) (b) (c)

Start:----- --:--:-- Time:------- --:--:-- Urms Line-N
Urms[V] 1 41.39 Irms[A] 1 1.2370 Freq[Hz] U1 49.989
P[W] 1 -0.0486k S[VA] 0.0512k Q[var] -0.0161k PF -0.9494
Active energy WP+ 0.00000k Wh
Elapsed time 0:00:00

Start:----- --:--:-- Time:------- --:--:-- Urms Line-N
Urms[V] 1 41.39 Irms[A] 1 0.4193 Freq[Hz] U1 49.999
P[W] 1 0.0165k S[VA] 0.0174k Q[var] 0.0054k PF 0.9510
Active energy WP+ 0.00000k Wh
Elapsed time 0:00:00

Start:----- --:--:-- Time:------- --:--:-- Urms Line-N
Urms[V] 1 41.42 Irms[A] 1 1.6473 Freq[Hz] U1 50.073
P[W] 1 0.0647k S[VA] 0.0682k Q[var] 0.0217k PF 0.9479
Active energy WP+ 0.00000k Wh
Elapsed time 0:00:00

(d) (e) (f)

Fig. 6.13 Experimental results of a). v_s,i_s b). v_s,i_L c). v_s,i_C d). Supply power P_S e). Load power P_L f). Compensator power P_C during steady state condition using SOGI.

the discharging condition is shown in Figs 6.14 (a–c). The source current's total harmonic distortion (THD) is reduced to 6.94% after the injection of compensating current, as opposed to 15.24% for i_L. Additionally, the supply voltage's THD is 1.90% during discharge. According to Fig 6.14 c, the

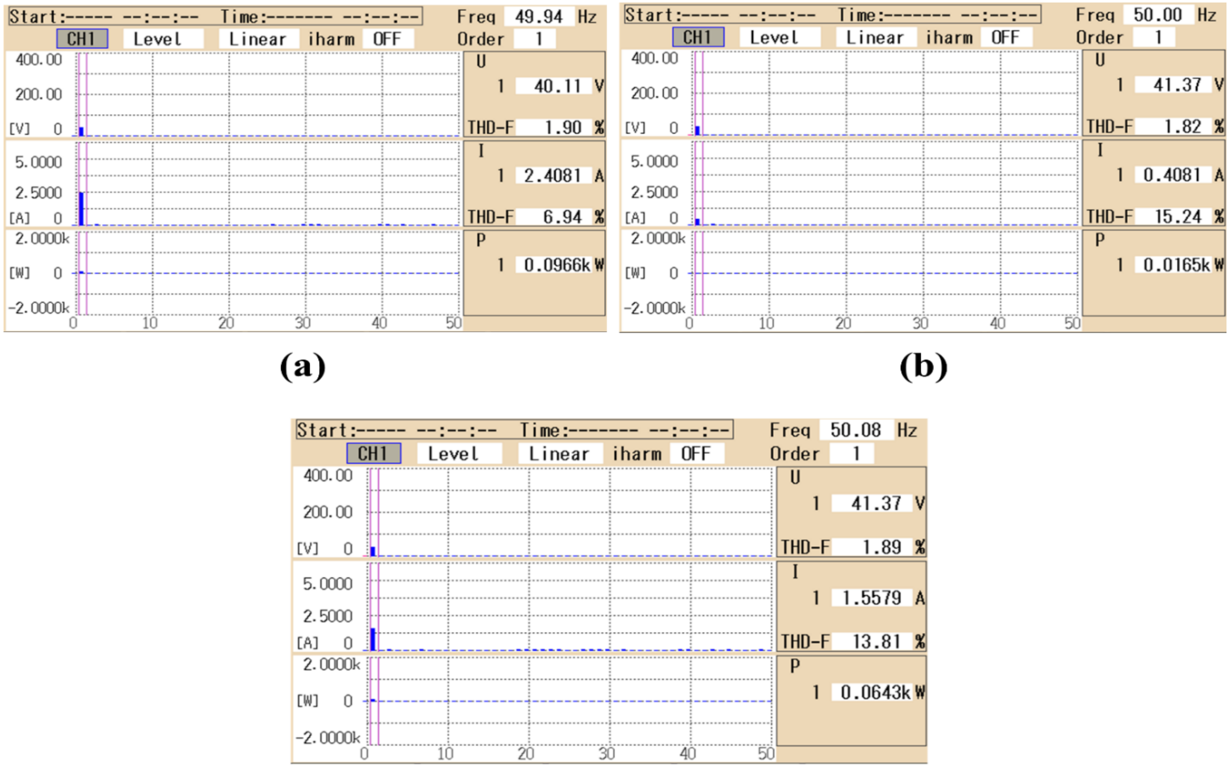
Start:----- --:--:-- Time:------- --:--:--
Freq 49.94 Hz
CH1 Level Linear iharm OFF
Order 1
U 1 40.11 V
THD-F 1.90 %
I 1 2.4081 A
THD-F 6.94 %
P 1 0.0966k W

Start:----- --:--:-- Time:------- --:--:--
Freq 50.00 Hz
CH1 Level Linear iharm OFF
Order 1
U 1 41.37 V
THD-F 1.82 %
I 1 0.4081 A
THD-F 15.24 %
P 1 0.0165k W

Start:----- --:--:-- Time:------- --:--:--
Freq 50.08 Hz
CH1 Level Linear iharm OFF
Order 1
U 1 41.37 V
THD-F 1.89 %
I 1 1.5579 A
THD-F 13.81 %
P 1 0.0643k W

(a) **(b)**

(c)

Fig. 6.14 Experimental results: Harmonic analysis of a). v_s,i_s with THD = 6.94% b). v_s,i_L with THD = 15.24% c). v_s,i_C with THD = 13.81% during steady state condition using SOGI.

compensator current has a THD of 13.81% and is employed to compensate for harmonics in the non-linear load. The harmonics generated by the nonlinear load are effectively eliminated by injecting a compensating current through AC-DC converter, which results in a sinusoidal and out-of-phase source current. The waveforms that have been observed clearly indicate that the source currents follow the opposite waveform of the source voltage, indicating a discharging operation. This demonstrates that the SOGI-based control method has been meticulously constructed, and satisfactory results have been obtained.

b). *Dynamic State Conditions*

Fig 6.15 (a-d) illustrates the various waveforms of source voltage (v_s), source current (i_s), load current (i_L), DC link voltage (V_{dc}), compensating current (i_c), fundamental current (i_f), unit template (u_p), battery current (I_{bat}), and battery voltage (V_{bat}) during the discharging mode condition.

The dynamics of source voltage (v_s), source current (i_s), load current (i_L), DC link voltage (V_{dc}), and compensating current (i_c) during a load transition are illustrated in Figure 6.15 a-b. The system discharging mode is demonstrated by the fact that the source voltage (v_s) remains stable and is in opposition to the source current (i_s). Consequently, the DC-link voltage remains consistent at 80V during dynamic load conditions. During the discharging operation, the compensator is responsible for injecting current to the load and transferring the surplus current to the grid.

Furthermore, the waveforms of i_s, i_L, I_{bat}, and V_{bat} are illustrated in Fig 6.15 c. The current is and iL are in accordance with the change in burden during V2G operation. The battery voltage gradually decreases from 48V, while the battery current remains constant at 2A. Similarly, in Fig 6.15 d, the load current (i_L) and fundamental current (i_f) are increased during a load change; however, the unit template remains sinusoidal with a range of ±1. While the EV battery is being discharged, the battery current remains constant at 2A.

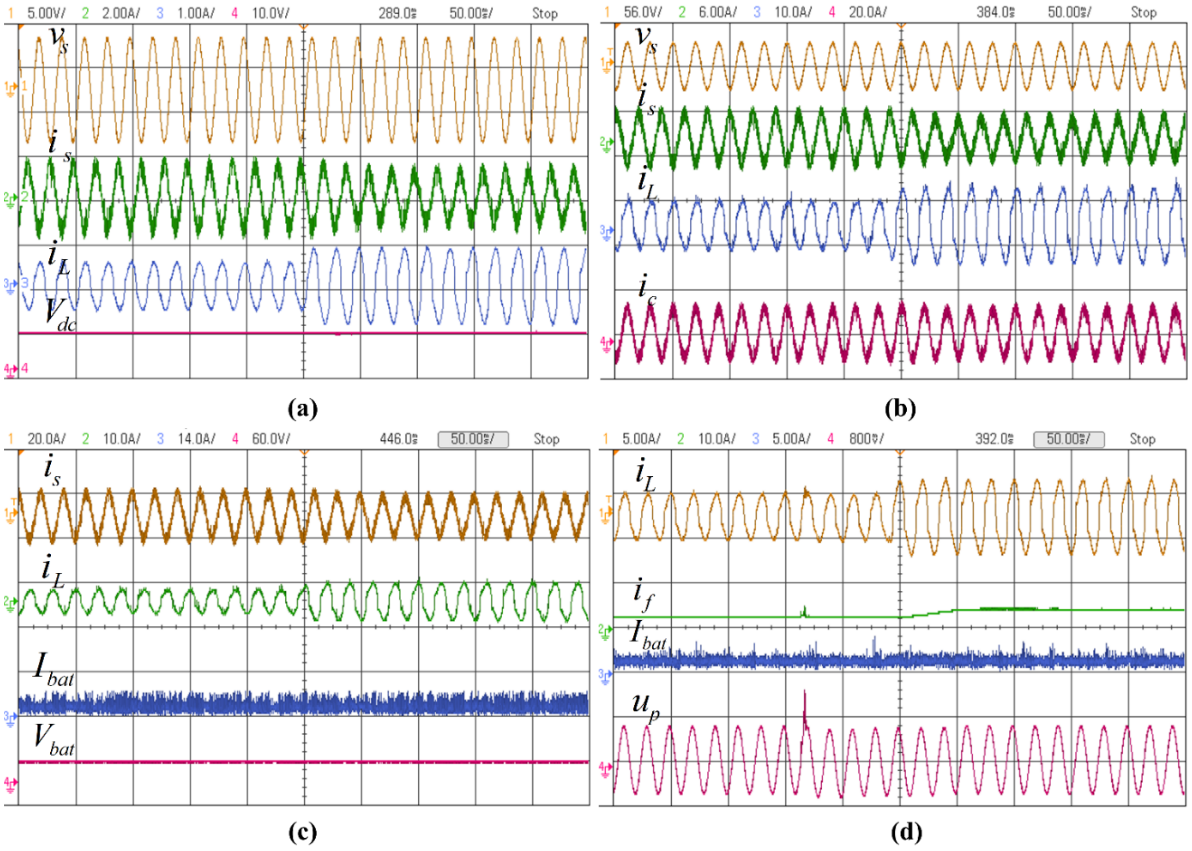

Fig. 6.15 Experimental waveforms of a). v_s,i_s,i_L,V_{dc} b). v_s, i_s ,$i_{L,}$ i_C c). i_s ,i_L,,I_{bat},V_{bat} and d). i_L, i_f, I_{bat} ,u_p during dynamic condition using SOGI.

6.6 Control Structure of Single Phase Grid Interfaced EV Charging Systems using LMS algorithm

The control of bidirectional AC-DC converters and bidirectional DC-DC converters is thoroughly examined in this section, and the control diagram is shown in Fig 6.16 (a-b).

6.6.1 Control of Bidirectional AC-DC Converter

The complete control algorithm, which includes fundamental component extraction using Least Mean Square (LMS) and DC link voltage control, is illustrated in Fig 6.16 (a). In the controller description, the computation of the unit template (u_p), estimation of the fundamental current (i_f), determination of the loss current component (i_{loss}), and calculation of the reference supply current (i_{ref}) are critical components. The fundamental component of load current has been extracted by utilising adaptive Least Mean Square (LMS) controller. The current loss component (i_{loss}) is estimated by the PI controller by processing the voltage of the DC-link. The effective current is obtained by adding this output to the essential load current component calculated by the Least Mean Square (LMS) controller. Lastly, the effective current magnitude and unit template are employed to generate reference current, which is then processed through HCC to produce four gating pulses for the bidirectional AC-DC converter. The control algorithm guarantees enhanced power quality on the grid side, regardless of the non-linear connected demand.

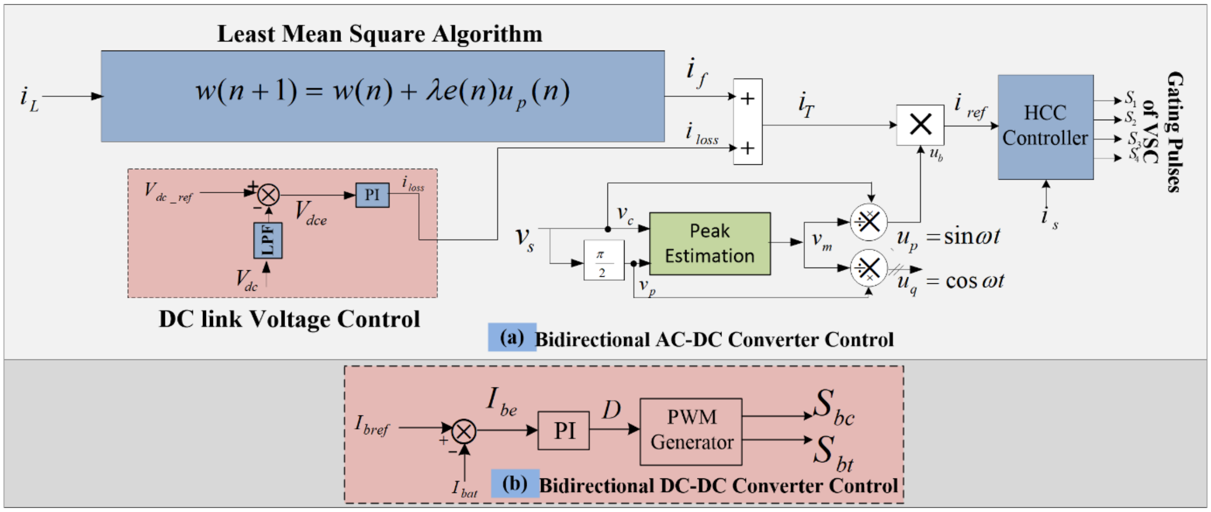

Fig 6.16 Control diagram using LMS algorithm

6.6.2 Calculation of Fundamental Component of Load Current

The fundamental component of the load current is estimated by utilising the output of the Least Mean Square (LMS), as illustrated in Fig 6.16 (a). The fundamental current is generated by passing the load current through adaptive Least Mean Square (LMS) controller. The fundamental load current ($w(n+1) = i_f$) is ultimately represented in Eq. 6.30 as

$$w(n+1) = w(n) + \lambda e(n)u = i_f \tag{6.30}$$

6.7 Simulation Results using LMS algorithm

The system's results after testing in the MATLAB/Simulink environment are displayed in Figs 6.17-6.18. These simulations results are shown for closed-loop control systems during charging and draining. The simulink model's parameters are presented in the appendix C, and the findings are further discussed below.

(a). Charging Condition

The behaviour of the system during charging conditions is illustrated in Fig 6.17, which is based on the proposed Least Mean Square (LMS) controller design. It displays the waveforms of the source voltage (v_s) with source current (i_s), nonlinear load current (i_L), compensating current via active filter (i_c), DC link voltage (V_{dc}), battery voltage (V_{bat}), and battery current (I_{bat}). In Fig 6.17 shows an investigation into the impact of load disturbance on controller performance during charging operation. At time t=0.8s, the load is increased from 2A to 3A. A rise in source current (i_s) is accompanied with no change in source voltage (v_s). As a result of changes in the load, the DC-link voltage (V_{dc}) experiences a brief drop, but the PI controller quickly restores it to the 200V reference value. In addition, the source current remains sinusoidal and in phase with the source voltage during charging mode, demonstrating the effectiveness of the control mechanism based on

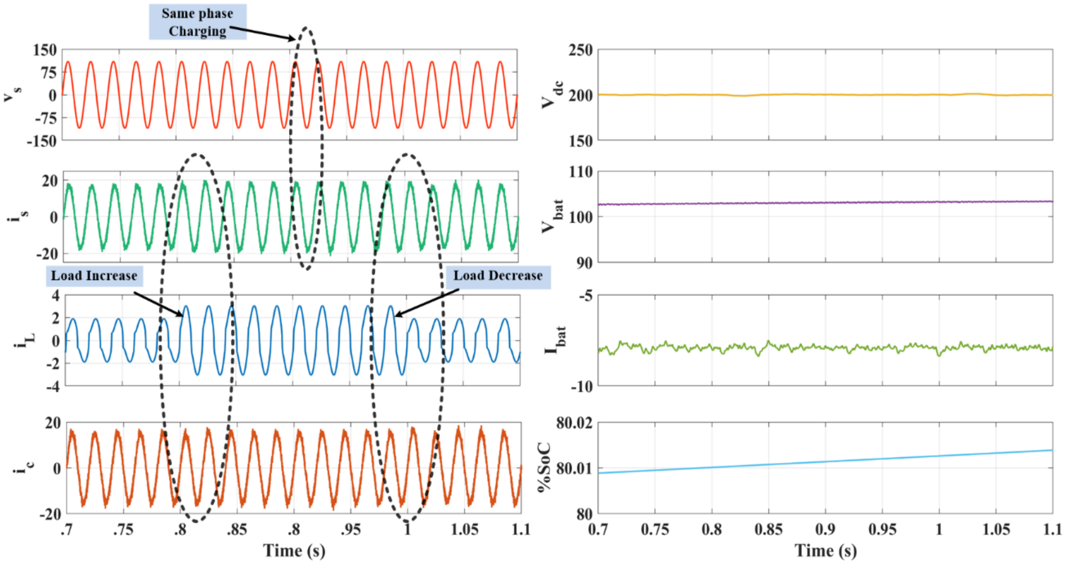

Fig 6.17 Single phase waveform of v_s, i_s, i_L, i_c, V_{dc}, V_{bat}, I_{bat} and %SoC at charging mode using LMS.

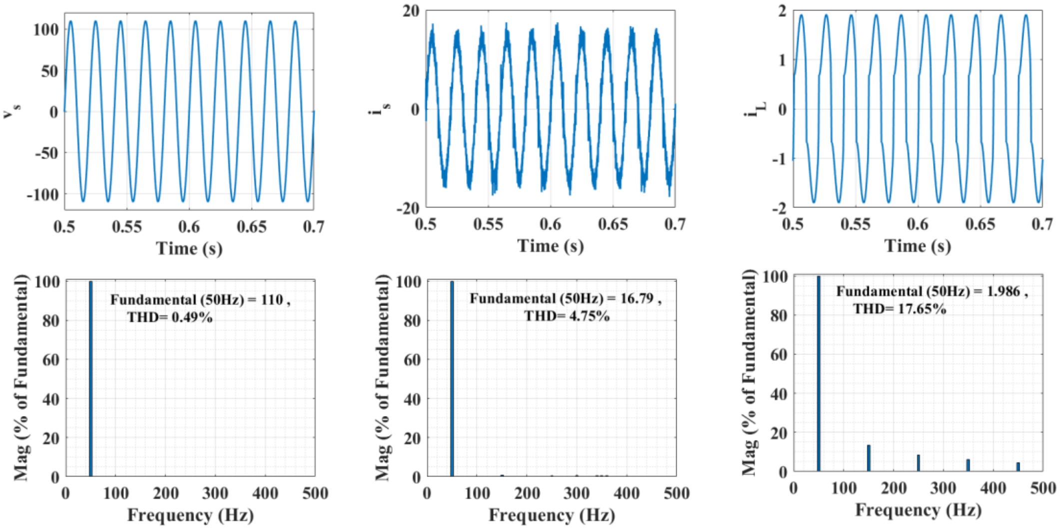

Fig 6.18 Experimental results : Harmonic analysis of a). v_s , THD = 0.49% b). i_s , THD = 4.75% c). i_L , THD = 17.65% during steady state condition at charging mode using LMS.

LMS algorithm under dynamic load circumstances. Meanwhile, the battery current (I_{bat}) stays at -8A and the voltage charges steadily to 96V. The state of charge (SOC) starts at 80% and keeps going up.

The Simulink harmonics content in the source voltage (v_s), source current (i_s), and load current (i_L) during the charging condition is shown in Figs 6.18. The source current's total harmonic distortion (THD) is reduced to 4.75% after the injection of compensating current, as 17.65% for i_L due to non-linear load. Additionally, the supply voltage's THD is 0.49% during charge mode.

(b). Discharging Condition

Fig 6.19 shows the system's dynamic behaviour under discharging circumstances using the suggested controller. Waveforms of the following voltages and currents are displayed: grid voltage (v_s) with grid current (i_s), nonlinear load current (i_L), compensatory current via DSTATCOM (i_c), DC link voltage (V_{dc}), battery voltage (V_{bat}), and battery current (I_{bat}). In a process similar to charging, the load current is increased from 2A to 3A, which is fulfilled by the electric vehicle's battery, and the extra current is sent back into the grid. It should be noted that during discharging, the supply voltage and current are out of phase. The first plot in Fig 6.19 clearly shows this. In order to keep the DC-link capacitance voltage constant at 200V, the tuned PI controller is used. During the discharge process, the electric vehicle battery is connected to the grid side and is delivering electricity. The SOC curve shows a continual decline from 80%, which corresponds to

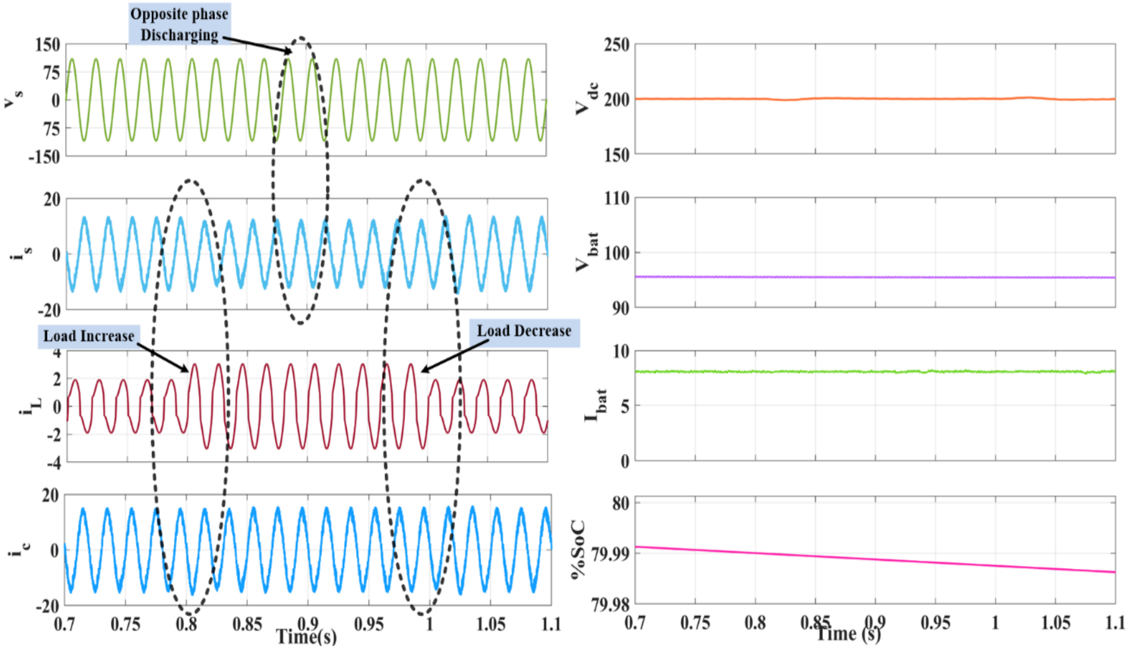

Fig 6.19 Single phase waveform of $v_{s,}$ $i_{s,}$ $i_{L,}$ $i_{c,}$ V_{dc}, V_{bat}, I_{bat} and %SoC at discharging mode using LMS.

a gradual reduction in the battery voltage from 96V when in discharging mode. Under discharging conditions, the battery current remains constant at the intended amount of 8A.

The Simulink harmonics content in the source voltage (v_s), source current (i_s), and load current (i_L) during the discharging condition is shown in Figs 6.20. The source current's total harmonic distortion (THD) is reduced to 4.97% after the injection of compensating current, as 17.69% for i_L due to non-linear load. Additionally, the supply voltage's THD is 0.50% during discharge.

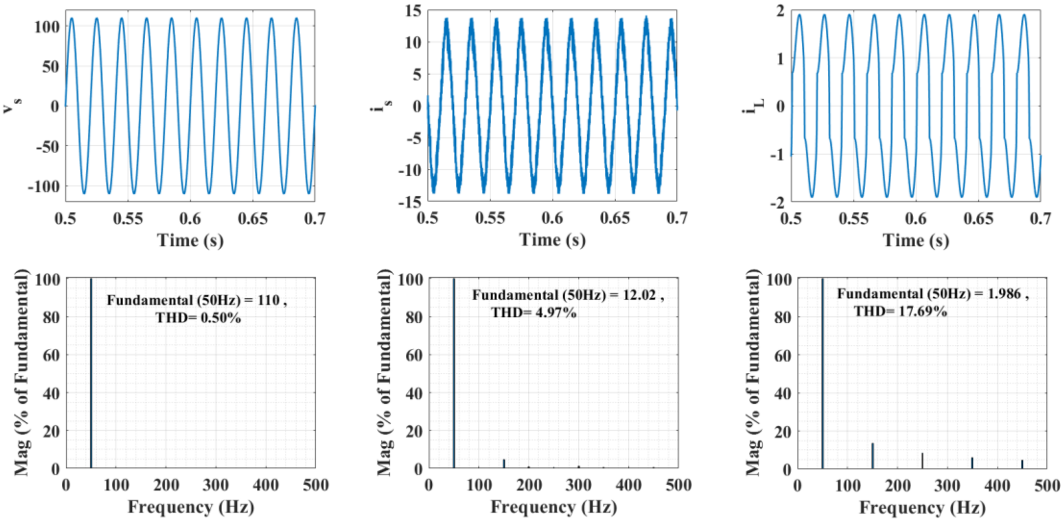

Fig 6.20 Experimental results : Harmonic analysis of a). v_s , THD = 0.50% b). i_s , THD = 4.97% c). i_L , THD = 17.69% during steady state condition at discharging mode using LMS.

6.8 Experimental Results using LMS algorithm

The experimental setup is same as discussed in section 6.5. The only difference is to use LMS algorithm in place of SOGI controller.

a). Experimental Results during Charging Operation with LMS algorithm

The steady state and dynamic condition experimental performance analysis during charging operation are thoroughly examined in this section, as shown in Figs. 6.21-6.23.

a). *Steady State Conditions*

Figs 6.21-6.22 illustrates the various waveforms, harmonics, and power analysis that occur during the charging process.

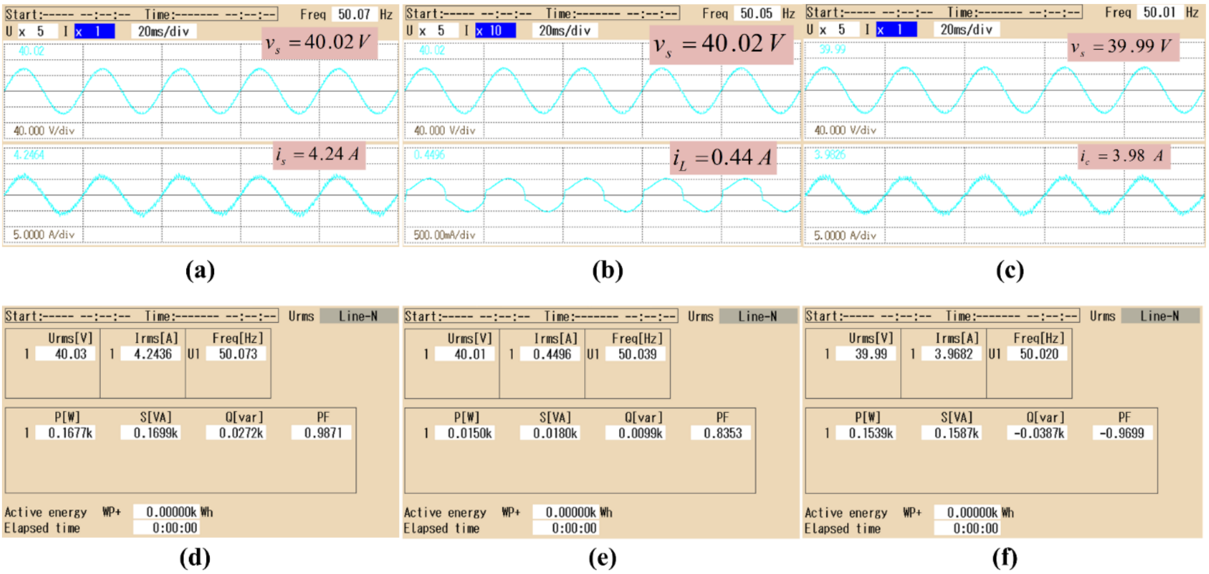

(a) (b) (c)

Urms[V]	Irms[A]	Freq[Hz]
1 40.03	1 4.2436	U1 50.073

P[W]	S[VA]	Q[var]	PF
1 0.1677k	0.1699k	0.0272k	0.9871

Active energy WP+ 0.00000k Wh
Elapsed time 0:00:00

Urms[V]	Irms[A]	Freq[Hz]
1 40.01	1 0.4496	U1 50.039

P[W]	S[VA]	Q[var]	PF
1 0.0150k	0.0180k	0.0099k	0.8353

Active energy WP+ 0.00000k Wh
Elapsed time 0:00:00

Urms[V]	Irms[A]	Freq[Hz]
1 39.99	1 3.9682	U1 50.020

P[W]	S[VA]	Q[var]	PF
1 0.1539k	0.1587k	-0.0387k	-0.9699

Active energy WP+ 0.00000k Wh
Elapsed time 0:00:00

(d) (e) (f)

Fig. 6.21 Experimental results of a). v_s,i_s b). v_s,i_L c). v_s,i_C d). Supply power P_S e). Load power P_L f). Compensator power P_C during steady state condition using LMS.

Fig 6.21 (a-c) shows the steady-state experimental results of the system, which shows the source voltage (v_s), source current (i_s), load current (i_L), and compensating current (i_c) waveforms. The supply voltage (v_s) and current (i_s) are in phase with sinusoidal nature during charging operation as shown in Fig 6.21 (a). Fig 6.21 (b) demonstrate that the load current is distorted when a non-linear load is connected. The fig 6.21 (c) shows that during charging operation EV is drawing current via bidirectional AC converter and bidirectional DC-DC converter to store the charge in the EV battery.

Fig 6.21 (d-f) shows the steady-state active and reactive power flow during the charging operation. The load demands 0.0099 kVAR of reactive power and 0.015 kW of active power. The active filter enhances the load's power factor (P.F.) from 0.83 to 0.98 by addressing its reactive power demand of 0.0099 kVAR, as illustrated in Figs 6.21 (d-e). The grid supplies 0.167kW to satisfy the load's actual power needs and account for switching losses.

Figs 6.22 (a-c) shows the harmonic content of the source voltage (v_s), source current (i_s), and load current (i_L). The source current's total harmonic distortion (THD) reduces to 4.9% after compensation, compared to the THD of iL, which is 15.55%. In addition, the supply voltage's THD is 2.13% during the charging process. In Fig 6.22 (c), the compensator current exhibits a THD of 6.36%, which is employed to mitigate harmonics that are present in a non-linear load. By injecting compensating current into the AC-DC converter, the harmonics generated by the nonlinear load are effectively cancelled, resulting in a sinusoidal and in-phase source current. The waveforms that were observed plainly demonstrate that the source current's %THD adheres to the IEEE-1547 and its standard limit of 5%. This further corroborates the fact that the LMS-based control algorithm has been well-designed and functions correctly.

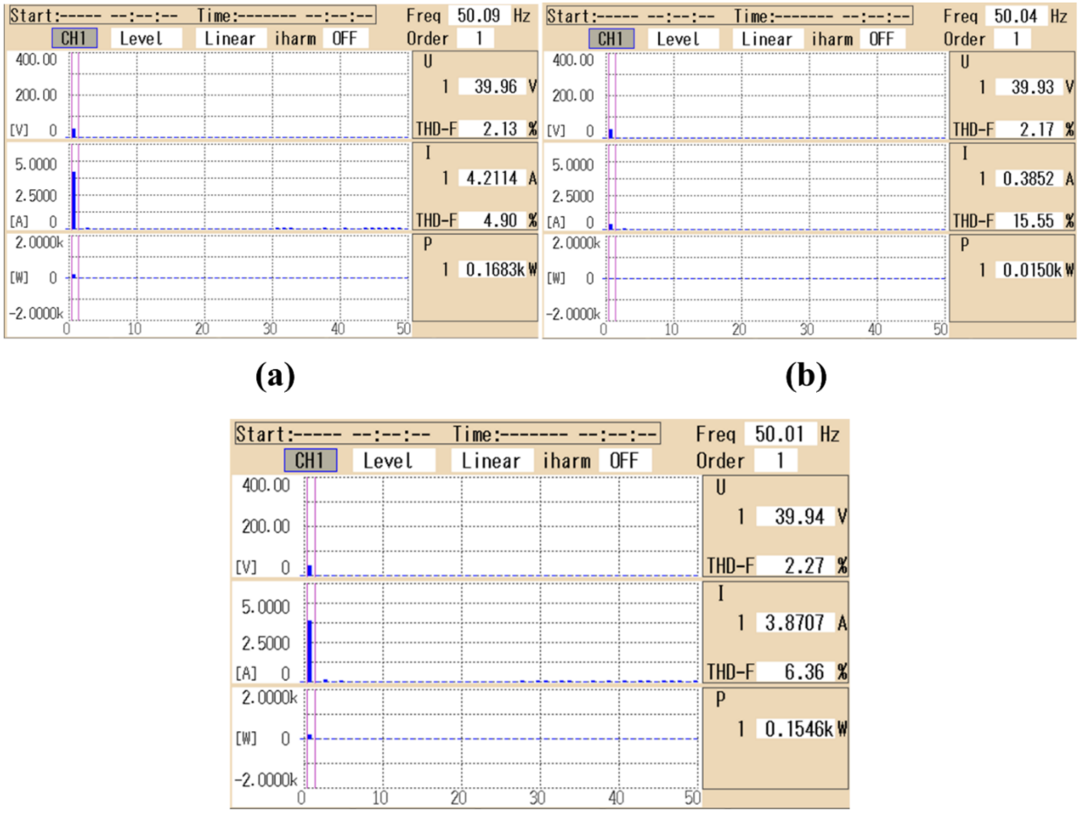
```
Start:----- --:--:--  Time:------- --:--:--   Freq  50.09  Hz
CH1  Level  Linear  iharm  OFF                Order  1
U     1  39.96  V      THD-F  2.13  %
I     1  4.2114 A      THD-F  4.90  %
P     1  0.1683k W
```
(a)

```
Start:----- --:--:--  Time:------- --:--:--   Freq  50.04  Hz
CH1  Level  Linear  iharm  OFF                Order  1
U     1  39.93  V      THD-F  2.17  %
I     1  0.3852 A      THD-F  15.55 %
P     1  0.0150k W
```
(b)

```
Start:----- --:--:--  Time:------- --:--:--   Freq  50.01  Hz
CH1  Level  Linear  iharm  OFF                Order  1
U     1  39.94  V      THD-F  2.27  %
I     1  3.8707 A      THD-F  6.36  %
P     1  0.1546k W
```
(c)

Fig. 6.22 Experimental results: Harmonic analysis of a). v_s,i_s with THD = 4.90% b). v_s,i_L with THD = 15.55% c). v_s,i_C with THD = 6.36% during steady state condition using LMS.

b). *Dynamic State Conditions*

The dynamic results of the designed system are illustrated in Fig 6.23 (a-d) at various load conditions during the charging operation. The waveforms show the following variables: source voltage (v_s), source current (i_s), load current (i_L), total DC link voltage (V_{dc}), compensating current (i_c), fundamental weight (I_f), unit template (u_p), reference current (i_{ref}), battery voltage (V_{bat}), and battery current (I_{bat}) during a charging operation with load variations.

The waveforms of v_s, i_s, i_L, V_{dc}, and i_c during load variations are depicted in Fig 6.23 (a-b). The source current is altered and the DC link voltage is maintained at 80V during a load change. The regulation performance of the DC link is minimally affected by load disturbance, and the voltage is well-regulated. The charging operation is demonstrated by the fact that the waveforms vs and is are in the same phase.

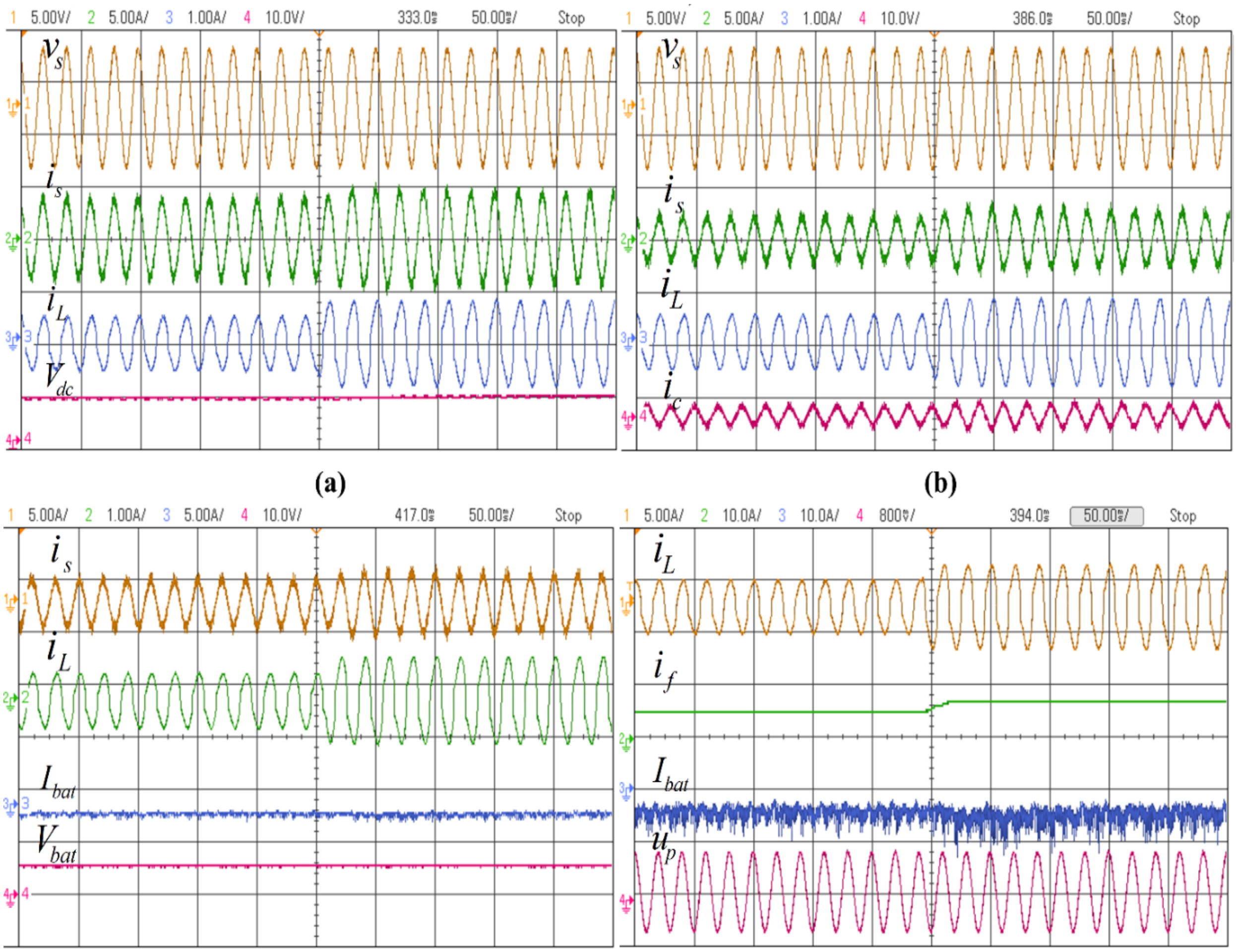

(a) (b)

(c) (d)

Fig. 6.23 Experimental waveforms of a). v_s,i_s,i_L,V_{dc} b). v_s, i_s,i_L,i_C c). i_s, i_L,,I_{bat},V_{bat} and d). i_L, i_f, I_{bat} ,u_p during dynamic condition using LMS.

Fig 6.23 c illustrates the waveforms of i_s, i_L, I_{bat}, and V_{bat}. The battery current (I_{bat}) remains constant at -2A throughout the charging process, as intended. During load disturbances, the battery voltage gradually recharges to 48V.

The waveform of the load current (i_L), fundamental current (i_f), battery current (I_{bat}), and unit template (u_p) is depicted in Fig 6.23 (d). A shift in the fundamental current is evident in the waveform of i_f, which is induced by fluctuations in the load current. The load current of the fundamental component is accurately predicted by the control algorithm that is based on Least Mean Square. As previously stated, the battery current remains constant at -2A during the charging process.

b). Experimental Results during Discharging Operation with LMS algorithm

The experimental performance analysis of the steady state and dynamic conditions during the discharging operation is thoroughly discussed in this section, as illustrated in Fig 6.24-6.26

a). *Steady State Conditions*

Figs 6.24-6.25 illustrates the waveforms, power analysis, and THD that are observed during the discharging operation. Currently, Fig 6.24 (a-c) illustrates the discharging mode operation, as well as the waveforms of the source voltage (v_s), source current (i_s), load current (i_L), and compensating current (i_c). This is evident in Fig 6. 24 (a), where the source voltage and current are in phase opposition which indicate that the system is in a discharging state. Fig 6. 24 (b) shows the source voltage (v_s) with distorted load current (i_L). As illustrated in Fig 6. 24 c, the active filter injects

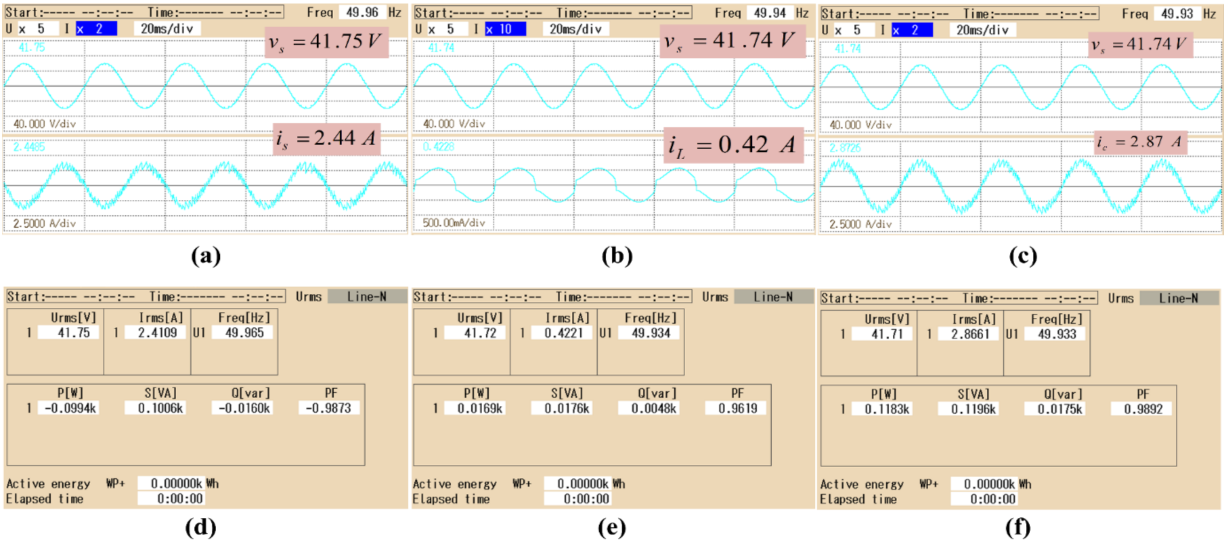

```
Start:----- --:--:-- Time:------- --:--:--  Urms  Line-N
      Urms[V]       Irms[A]       Freq[Hz]
 1    41.75     1   2.4109   U1   49.965
      P[W]          S[VA]         Q[var]        PF
 1    -0.0994k      0.1006k       -0.0160k      -0.9873
Active energy  WP+  0.00000k Wh
Elapsed time        0:00:00
```

```
Start:----- --:--:-- Time:------- --:--:--  Urms  Line-N
      Urms[V]       Irms[A]       Freq[Hz]
 1    41.72     1   0.4221   U1   49.934
      P[W]          S[VA]         Q[var]        PF
 1    0.0169k       0.0176k       0.0048k       0.9619
Active energy  WP+  0.00000k Wh
Elapsed time        0:00:00
```

```
Start:----- --:--:-- Time:------- --:--:--  Urms  Line-N
      Urms[V]       Irms[A]       Freq[Hz]
 1    41.71     1   2.8661   U1   49.933
      P[W]          S[VA]         Q[var]        PF
 1    0.1183k       0.1196k       0.0175k       0.9892
Active energy  WP+  0.00000k Wh
Elapsed time        0:00:00
```

Fig. 6.24 Experimental results of a). v_s,i_s b). v_s,i_L c). v_s,i_C d). Supply power P_S e). Load power P_L f). Compensator power P_C during steady state condition using LMS.

compensating current (i_c) to cancel out non-linearity in the load current, and a net surplus current is injected into the supply side grid during the discharging condition. Thus, the relationship between the source voltage and the out-of-phase source current is substantiated. The simulation results depicted in Figs 6. 24 are also validated by these results.

Figs 6. 24 (d-f) illustrate the power balance during the discharging condition. The active and reactive power requirements of the load are +0.0169kW and +0.0048kVAR, respectively. The compensator injects active and reactive power of 0.0118kw and 0.0175kVAR to satisfy the load power demand. Consequently, the grid is supplied with a surplus electricity of -0.0990kw and -0.016kVAR.

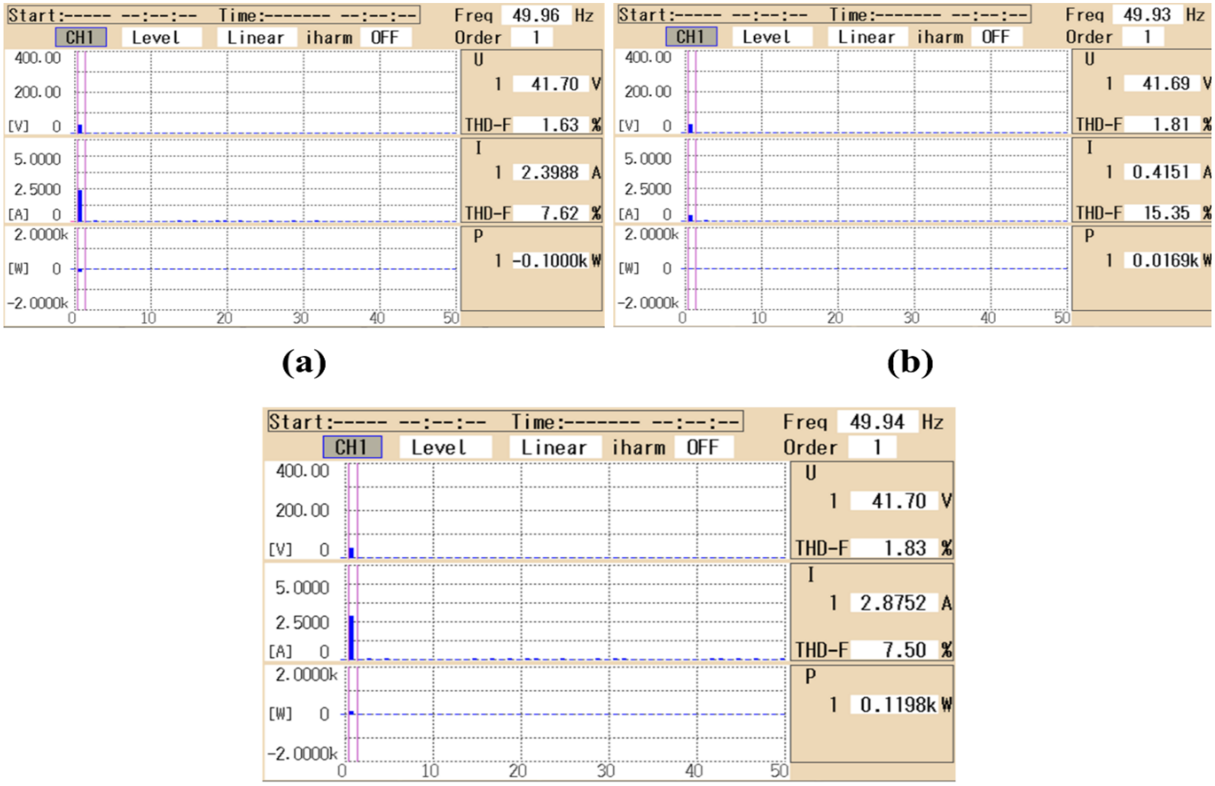

(a) (b)

(c)

Fig. 6.25 Experimental results : Harmonic analysis of a). v_s,i_s with THD = 7.62% b). v_s,i_L with THD = 15.35% c). v_s,i_C with THD = 7.50% during steady state condition using LMS.

The harmonics content in the source voltage (v_s), source current (i_s), and load current (i_L) during the discharging condition is illustrated in Figs 6.25 (a–c). The source current's total harmonic distortion (THD) is reduced to 7.62% after the injection of compensating current, as opposed to 15.35% for i_L. Additionally, the supply voltage's THD is 1.63% during discharge. According to Fig 6.25 c, the compensator current has a THD of 7.50% and is employed to compensate for harmonics in the non-linear load. The harmonics generated by the nonlinear load are effectively eliminated by injecting a compensating current into the AC-DC converter, which produces a sinusoidal and out-of-phase source current. The waveforms that have been observed clearly indicate that the source currents follow the opposite waveform of the source voltage, indicating a discharging operation. This demonstrates that the Least Mean Square-based control method has been meticulously constructed, and satisfactory results have been obtained.

b). *Dynamic State Conditions*

Figs 6.26 (a-d) illustrates the various waveforms of source voltage versus source current, including the load current (i_L), DC link voltage (V_{dc}), compensating current (i_c), fundamental current (i_f), unit template (u_p), battery current (I_{bat}), and battery voltage (V_{bat}) during the discharging mode condition.

The dynamics of source voltage (v_s), source current (i_s), load current (i_L), DC link voltage (V_{dc}), and compensating current (i_c) during a load transition are illustrated in Fig 6.26 a-b. The system discharging mode is demonstrated by the fact that the source voltage (v_s) remains stable and is in

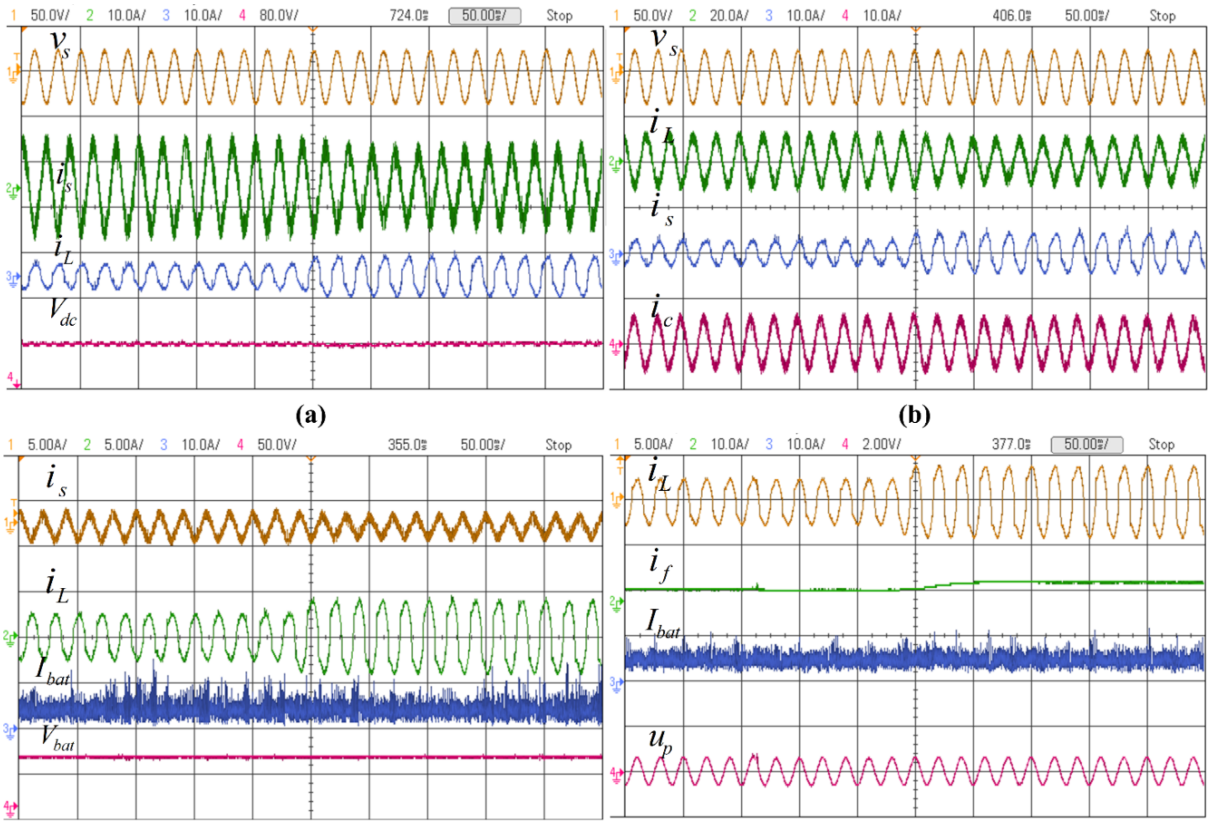

(a) **(b)**

(c) **(d)**

Fig. 6.26 Experimental waveforms of a). v_s,i_s,i_L,V_{dc} b). v_s, i_s ,i_L, i_C c). i_s , i_L,,I_{bat},V_{bat} and d). i_L, i_f, I_{bat} ,u_p during dynamic condition using LMS.

opposition to the source current (i_s). Consequently, the DC-link voltage remains consistent at 80V during dynamic load conditions. During the discharging operation, the compensator is responsible for injecting current to the load and transferring the surplus current to the grid.

Furthermore, the waveforms of i_s, i_L, I_{bat}, and V_{bat} are illustrated in Fig 6.26 c. The current is and iL are in accordance with the change in burden during V2G operation. The battery voltage gradually decreases from 48V, while the battery current remains constant at 2A.

In the same way, the load current (i_L) and fundamental current (i_f) are increased during a load change in Fig 6.26 d. However, the unit template remains sinusoidal with a range of ±1. For the duration of the EV battery's discharge, the battery current remains constant at 2A.

6.9 Control Structure of Single Phase Grid Interfaced EV Charging Systems using RJP algorithm

In this section, the control of bidirectional AC-DC converter and bidirectional DC-DC converter are discussed in detail and its control diagram is shown in Fig 6.27 (a-b).

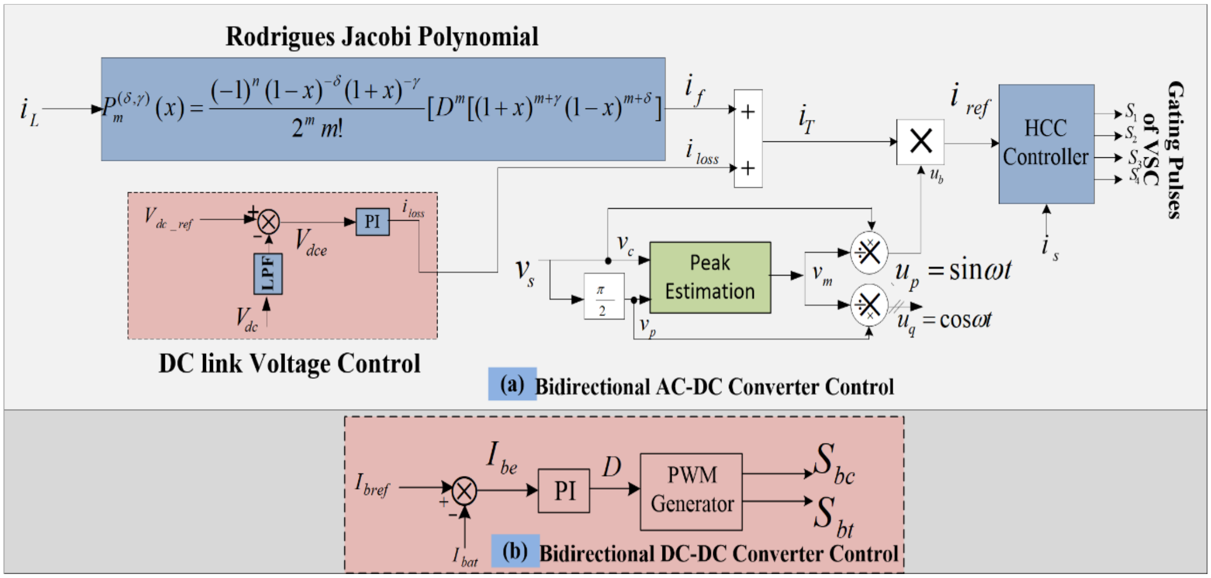

Fig 6.27 Control diagram using RJP

6.9.1 Control of Bidirectional AC-DC Converter

Fig 6.27 (a) depicts the entire control algorithm, which includes both DC link voltage control as well as fundamental component extraction using Rodrigues Jacobi polynomials. The computation of the unit template (u_p), estimation of the fundamental current (i_f), determination of the loss current component (i_{loss}) and calculation of the reference supply current (i_{ref}) are important parts of the controller description. The dominant terms of Rodrigues Jacobi polynomial based controller have been utilized specifically to extract the fundamental component of load current. The voltage of the DC-link is processed by the PI controller to estimate the current loss component. This output is then added to the fundamental load current component calculated by Rodrigues Jacobi polynomial controller to yield the effective current. Finally, reference current is generated using the effective current magnitude and unit template and processed via HCC to generate four gating pulses for the bidirectional AC-DC converter's. The control algorithm ensures improved power quality at the grid side irrespective of the non-linear connected load.

6.9.2 Calculation of Fundamental Component of Load Current

As shown in Fig 6.27 (a), the output of Rodrigues Jacobi polynomial is utilised to estimate the load currents fundamental component. The load current is passed through dominant Rodrigues Jacobi polynomial terms to generate fundamental current i_f. Hence, the term x in Eq.6.31 represents the input load current (i_L) and the output $P_m^{(\delta,\gamma)}(x)$ is equal to i_f. The fundamental load current is finally expressed in Eq.6.31 as

$$P_m^{(\delta,\gamma)}(x) = [1 + \frac{1}{2}\{2(1+\delta) + (\delta+\gamma+2)(x-1)\}] \tag{6.31}$$

$$i_f = [1 + \frac{1}{2}\{2(1+\delta) + (\delta+\gamma+2)(i_L-1)\}] \tag{6.32}$$

6.10 Simulation Results using RJP algorithm

The developed system is tested out in MATLAB/Simulink environment and the results performance are presented in Fig 6.28-6.29. These simulation present different plots under charging and discharging condition for closed-loop control system. The parameters of the simulink model are mentioned in the Appendix C and the results are discussed in detail below.

(a). Charging Condition

Fig 6.28 depicts the behaviour of the system during charging conditions using the proposed Rodrigues Jacobi polynomial based controller. It shows the waveforms of the source voltage (v_s) with source current (i_s), nonlinear load current (i_L), compensating current via active filter (i_c), DC link voltage (V_{dc}), battery voltage (V_{bat}) and battery current (I_{bat}). The effect of load disturbance on controller performance is also investigated during charging operation in Fig 6.28. The load is raised from 2A to 3A at t=0.8s time. The source current (i_s) also increases but source voltage (v_s) remains same. The small transient dip is observed in the DC-link voltage (V_{dc}) due to load variations but the PI controller stabilises it back to the reference value of 200V. Furthermore, during charging mode, the source current stays sinusoidal nature and same phase with the source voltage, showing the efficiency of Rodrigues Jacobi polynomial control mechanism under

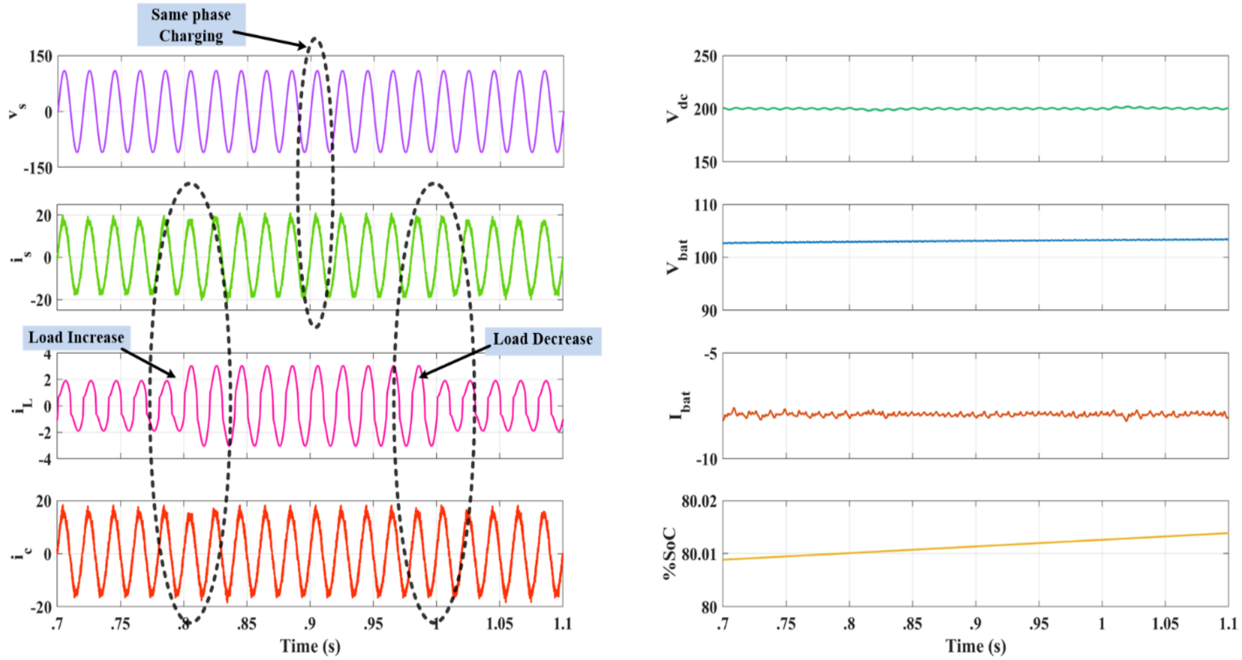

Fig 6.28 Single phase waveform of $v_{s,}$ $i_{s,}$ $i_{L,}$ $i_{c,}$ V_{dc}, V_{bat}, I_{bat} and %SoC at charging mode using RJP.

dynamic load conditions. Also, the battery voltage slowly charges at 96V and the battery current (I_{bat}) remains same to -8A. The state of charge (SOC) continuously increases from 80%.

The harmonics content in the source voltage (v_s), source current (i_s), and load current (i_L) is shown in Fig 6.29. After compensation, the source current's total harmonic distortion (THD) drops to 1.82% from the THD of i_L having 17.69%. Additionally, the THD of the supply voltage is 0.48%

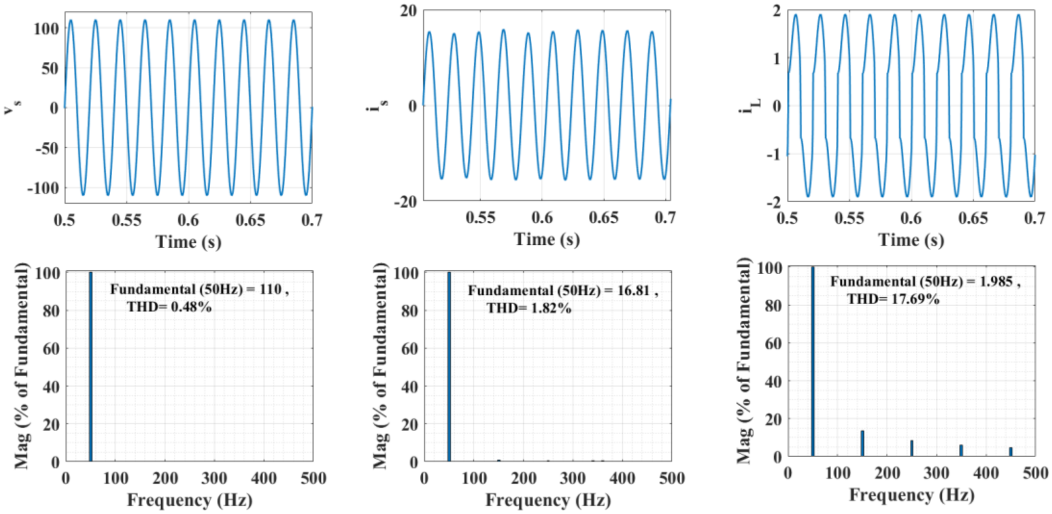

Fig 6.29 Experimental results : Harmonic analysis of a). v_s , THD = 0.48% b). i_s , THD = 1.82% c). i_L , THD = 17.69% during steady state condition at charging mode using RJP.

during charging operation. A sinusoidal and in-phase source current is obtained by successfully cancelling the harmonics generated by the nonlinear load by the injection of AC-DC converter compensating current.

(b). Discharging Condition

Fig 6.30 depicts the dynamic behaviour of the system during discharging conditions using the proposed RJP controller. It shows the waveforms of the grid voltage (v_s) with grid current (i_s), nonlinear load current (i_L), compensating current via DSTATCOM (i_c), DC link voltage (V_{dc}), battery voltage (V_{bat}) and battery current (I_{bat}).

Similar to charging operation, the requirement of load current is changed from 2A to 3A, which is fulfilled by EV (battery) and additional current is injected back into the grid. It is noted that, the supply current and supply voltage are not in phase during discharging operation. This is evident from the first plot of Fig 6.30. The tuned PI controller is utilised to maintain the DC- link capacitance voltage constant at 200V. The setup of EV battery is supplying power to the grid side during the discharging operation. The battery voltage slowly decreases from 96V in the discharging mode and it can be noticed from the SOC plot which is continuously decreasing from 80%. The battery current is constant to desired value of 8A during discharging condition.

The harmonics content in the source voltage (v_s), source current (i_s), and load current (i_L) is shown in Fig 6.31. The source current's total harmonic distortion (THD) drops to 1.33% from the THD

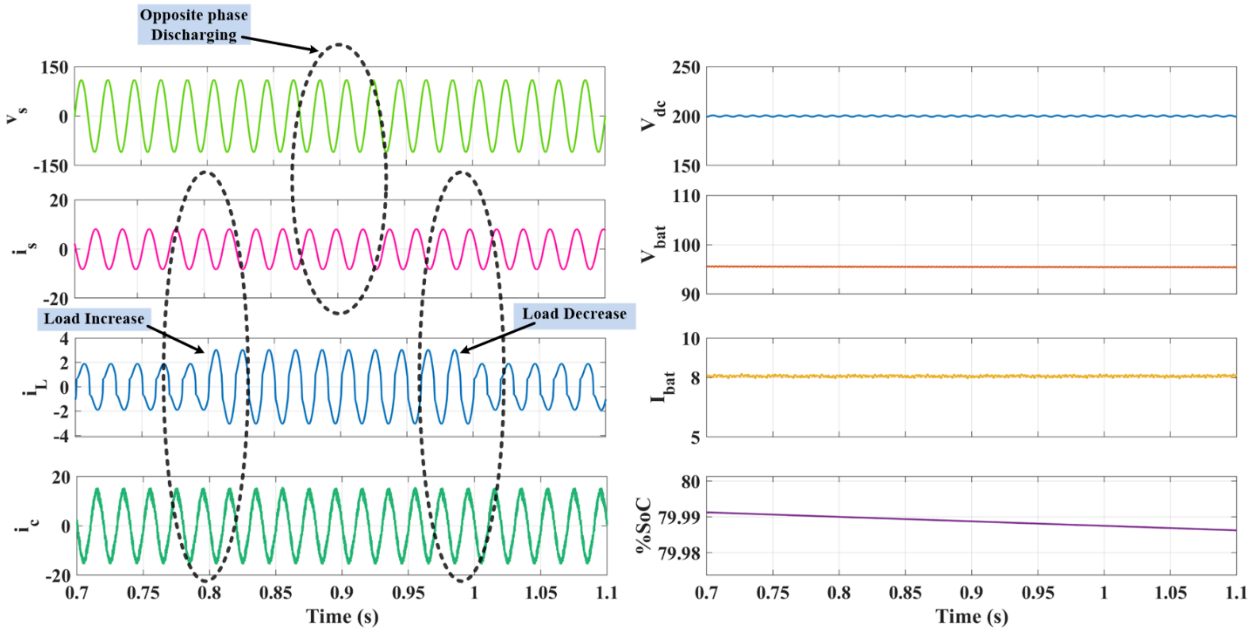

Fig 6.30 Single phase waveform of v_s, i_s, i_L, i_c, V_{dc}, V_{bat}, I_{bat} and %SoC at discharging mode using RJP.

of i_L having 18.68%. Additionally, the THD of the supply voltage is 0.50% during discharging operation.

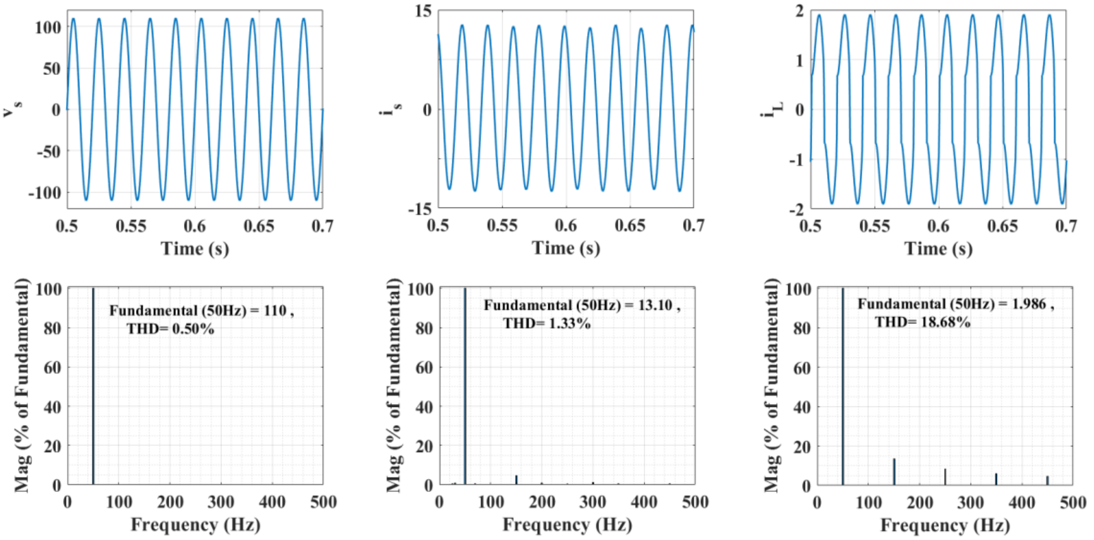

Fig 6.31 Experimental results : Harmonic analysis of a). v_s , THD = 0.50% b). i_s , THD = 1.33% c). i_L , THD = 18.68% during steady state condition in discharging mode using RJP.

6.11 Experimental Results using RJP algorithm

A developed model in the laboratory is verify to confirm and validate the simulation results. The designed model is tested at 40V (rms), 50Hz alternating current supply which feeds nonlinear load and also has an integrated EV charger. The nonlinear load is configured as a series combination of load resistance (R) and inductance (L) on the rectifier's DC-side. The bidirectional AC-DC converter is fed at the point of common coupling (PCC) which allows compensatory currents to be provided via interfacing inductors. The bidirectional buck-boost converter is fed at DC link of AC-DC converter. Various LEM sensors viz. voltage (LV-25P) is utilized for sensing v_s, V_{dc1}, V_{bat} and the i_s, i_L, I_{bat} is sensed by current sensors (LA-25P). The Real Time System (RTS) controller is connected for interfacing with these sensors. Proper control of the AC side converter is ensured by the designed controller and the four gating pulses coming from the RTS drive the converter. A DSO is used to record different signals captured from the hardware, and a power analyser (HIOKI PQ3100) analyses experimental parameters like power, current, and harmonics. The complete specification of the experimental setup is provided in Appendix C.

a). Experimental Results during Charging Operation with RJP algorithm

In this section, the steady state and dynamic condition experimental performance analysis during charging operation are discussed well and it is shown in Figs 6.32-6.34.

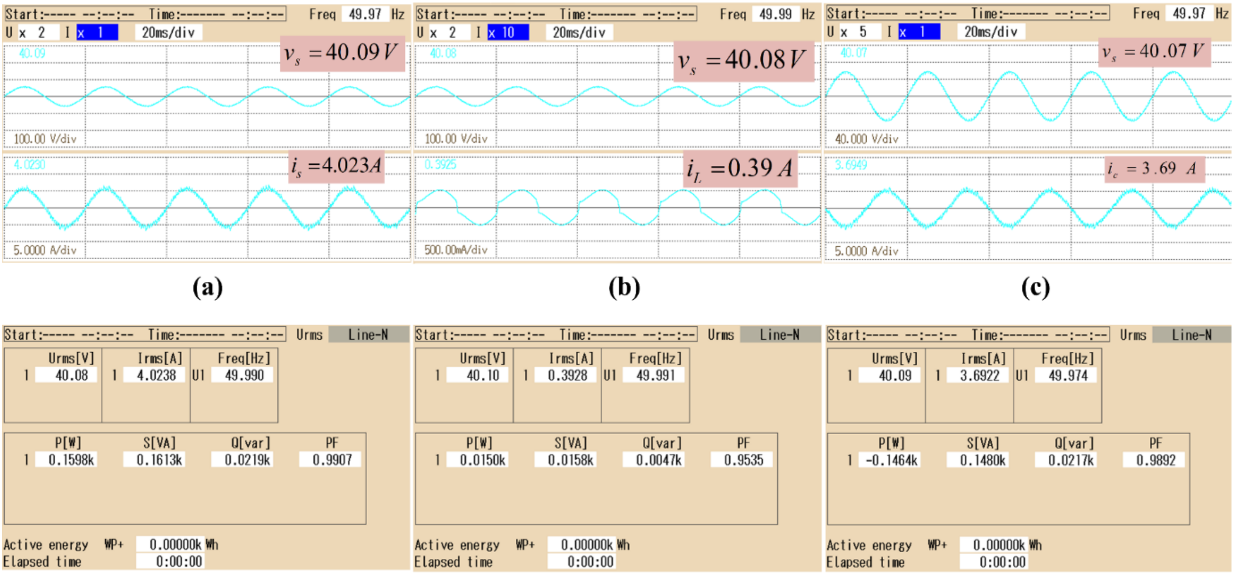

(a) (b) (c)

(d)

Urms[V] 1 40.08 | Irms[A] 1 4.0238 | U1 Freq[Hz] 49.990

P[W] 1 0.1598k | S[VA] 0.1613k | Q[var] 0.0219k | PF 0.9907

Active energy WP+ 0.00000k Wh

Elapsed time 0:00:00

(e)

Urms[V] 1 40.10 | Irms[A] 1 0.3928 | U1 Freq[Hz] 49.991

P[W] 1 0.0150k | S[VA] 0.0158k | Q[var] 0.0047k | PF 0.9535

Active energy WP+ 0.00000k Wh

Elapsed time 0:00:00

(f)

Urms[V] 1 40.09 | Irms[A] 1 3.6922 | U1 Freq[Hz] 49.974

P[W] 1 -0.1464k | S[VA] 0.1480k | Q[var] 0.0217k | PF 0.9892

Active energy WP+ 0.00000k Wh

Elapsed time 0:00:00

Fig. 6.32 Experimental results of a). v_s,i_s b). v_s,i_L c). v_s,i_C d). Supply power P_S e). Load power P_L f). Compensator power P_C during steady state condition using RJP.

a). *Steady State Conditions*

The different waveforms, harmonics and power analysis are shown in Fig 6.32-6.34 during charging operation.

The system's steady-state experimental findings are shown in Figs 6.32, where the source voltage (v_s), source current (i_s), load current (i_L), and compensating current (i_c) waveforms are displayed. Notably, Fig 6. 32 b show that the load current is distorted as non-linear load is connected. The supply voltage (v_s) and current (i_s) are in phase with sinusoidal nature during charging operation as shown in Fig 6. 32 a. Fig 6. 32 c shows that during charging operation EV is drawing current via bidirectional AC converter and bidirectional DC-DC converter to store the charge in the EV battery.

The steady-state active and reactive power flow during charging operation is depicted in Figs 6. 32 (d-f). The load requires 0.015 kW of active power and 0.0047 kVAR of reactive power. As shown in Figs 6. 32 (d-e), the active filter improves the load's power factor (P.F.) from 0.95 to 0.99 by addressing its reactive power demand of 0.0047 kVAR. In order to meet the load's real power requirement and account for switching losses, the grid provides 0.159kW.

The harmonics content in the source voltage (v_s), source current (i_s), and load current (i_L) is shown in Figs 6.33 (a-c). After compensation, the source current's total harmonic distortion (THD) drops to 4.69% from the THD of i_L having 15.33%. Additionally, the THD of the supply voltage is 1.94% during charging operation. Fig 6.33 c shows that the compensator current shows THD of 6.30% which is used to compensate harmonics present in non-linear load. A sinusoidal and in-phase source current is obtained by successfully cancelling the harmonics generated by the nonlinear load by the injection of AC-DC converter compensating current. The observed waveforms clearly show the source current's %THD is follow the IEEE-519 and its standard limit of 5% which further verifies that the Rodrigues Jacobi polynomial based control algorithm has been well designed and operates properly.

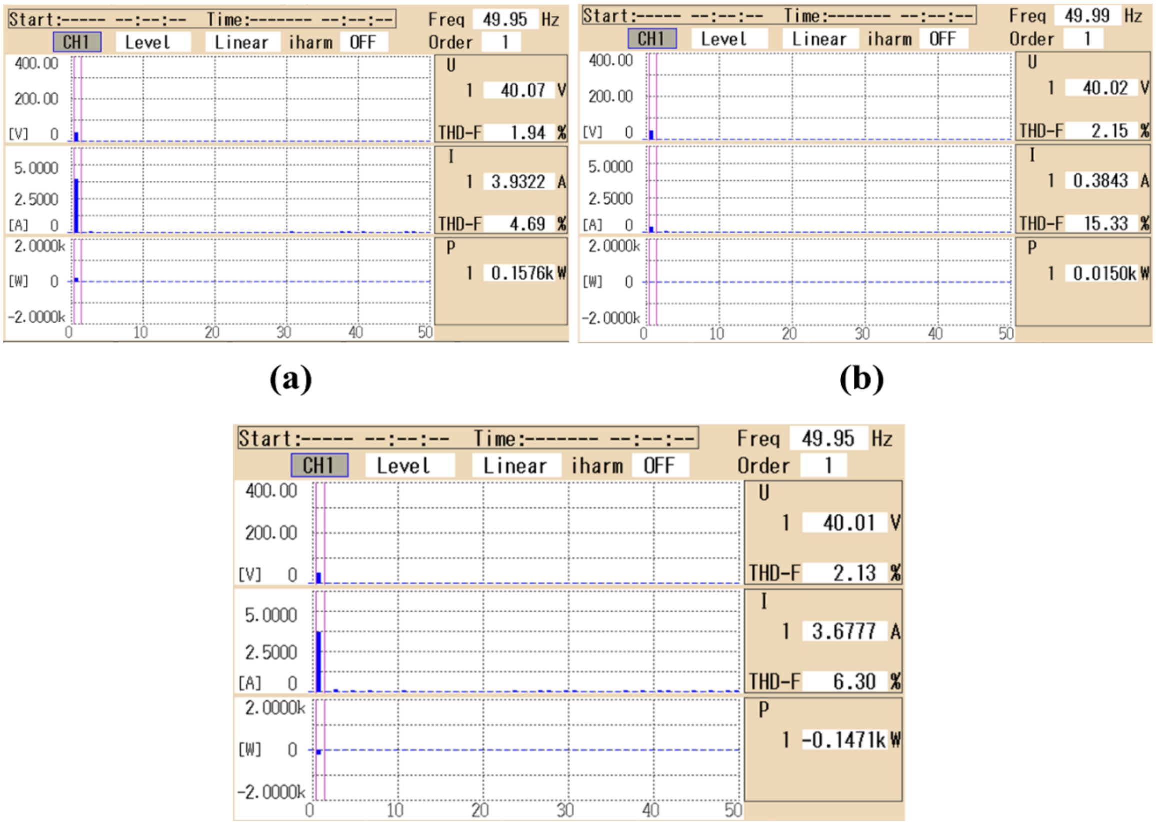

(a)

Freq 49.95 Hz
Order 1
U 1 40.07 V
THD-F 1.94 %
I 1 3.9322 A
THD-F 4.69 %
P 1 0.1576k W

(b)

Freq 49.99 Hz
Order 1
U 1 40.02 V
THD-F 2.15 %
I 1 0.3843 A
THD-F 15.33 %
P 1 0.0150k W

(c)

Freq 49.95 Hz
Order 1
U 1 40.01 V
THD-F 2.13 %
I 1 3.6777 A
THD-F 6.30 %
P 1 -0.1471k W

Fig. 6.33 Experimental results: Harmonic analysis of a). v_s,i_s with THD = 4.69% b). v_s,i_L with THD = 15.33% c).v_s,i_C with THD = 6.30% during steady state condition using RJP.

b). *Dynamic State Conditions*

The dynamic results of the designed system are depicted in Fig 6.34 (a-d) at different load condition during charging operation. The waveforms show variables like source voltage (v_s), source current (i_s), load current (i_L), total DC link voltage (V_{dc}), compensating current (i_c), fundamental weight (i_f), unit template (u_p), reference current (i_{ref}), battery voltage (V_{bat}) and battery current (I_{bat}) respectively, during load variations in charging operation.

The waveforms of v_s, i_s, i_L, V_{dc} and i_c during load variations are shown in Fig 6.34 (a-b). During load change, the source current changes and DC link voltage maintained to 80V. The DC link voltage is well-regulated and load disturbance has little effect on its regulation performance. The waveforms v_s and i_s are observed in same phase is the proof of charging operation.

The waveforms of i_s, i_L, I_{bat} and V_{bat} are shown in Fig 6.34 c. The battery current (I_{bat}) remains constant to -2A during charging operation as desired. The battery voltage slowly charges to 48V during load disturbances.

In Fig 6.34 d, the waveform of load current (i_L), fundamental current (i_f), battery current (I_{bat}) and unit template (u_p) are shown. The waveform of i_f shows a shift in the fundamental current brought during the load current variations. The control algorithm based on Rodrigues Jacobi polynomials

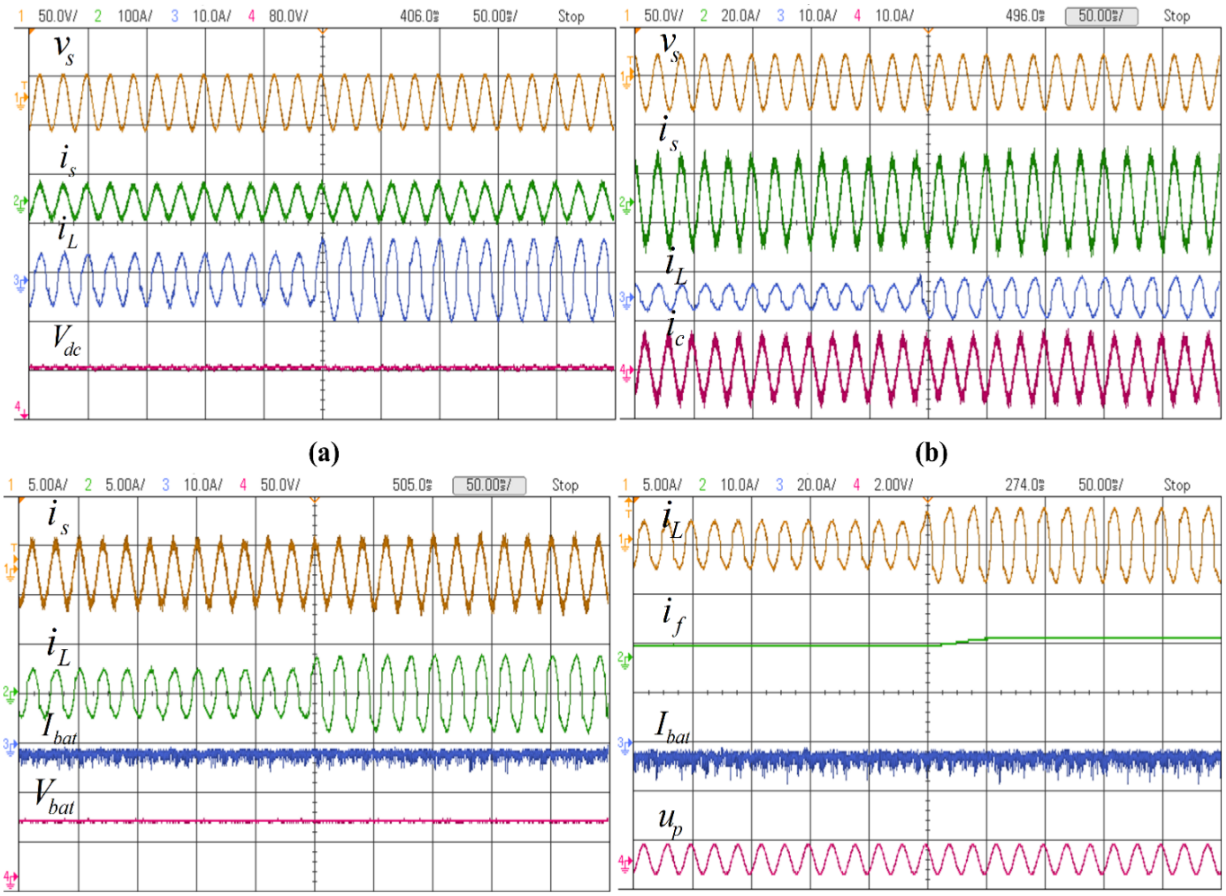

(a) (b)

(c) (d)

Fig. 6.34 Experimental waveforms of a). v_s,i_s,i_L,V_{dc} b). v_s, i_s ,$i_{L,}$ i_C c). i_s , i_L,,I_{bat},V_{bat} and d). i_L, i_f, I_{bat} ,u_p during dynamic condition using RJP. (charging mode) correctly predicts the load current of fundamental component. The battery current remains constant to -2A for charging condition as before.

b). Experimental Results during Discharging Operation with RJP algorithm

The experimental efficiency evaluation under steady state as well as dynamic conditions during discharging operation is fully discussed in this part and is shown in Figs. 6.35–6.37.

a). *Steady State Conditions*

The waveforms, power analysis and THD are shown in Fig 6.35 - 6.36 during discharging operation. Now, Figs 6.35 (a-c) shows the discharging mode operation and the waveforms of source voltage v_s along with source current (i_s), load current (i_L)and compensating current (i_c). It can be noted that the source current and source voltage is in phase opposition as seen in Fig 6.35

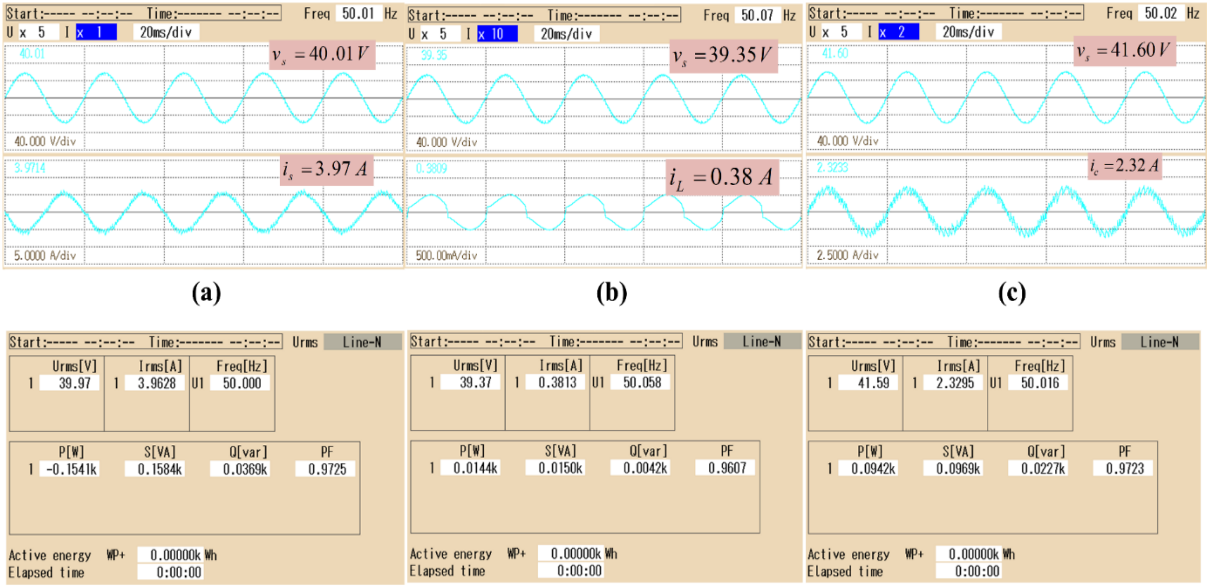

(a) (b) (c)

(d) (e) (f)

Fig. 6.35 Experimental results of a). v_s,i_s b). v_s,i_L c). v_s,i_C d). Supply power P_S e). Load power P_L f). Compensator power P_C during steady state condition using RJP.

a. The distorted load current (i_L) and source voltage (v_s) plot is shown in Fig 6.35 b, that is the system operates in discharging condition. The active filter injects compensating current (i_c) to cancel out non linearity in load current and a net surplus current is injected to the supply side grid during discharging condition as seen in Fig 6.35 c. This justifies the relationship between the source voltage with the out of phase source current. These results also validate the simulation results shown in Fig 6.30.

The power balance during discharging condition is shown in Figs 6.35 (d-f). The requirement of load active and reactive power is +0.014kW and +0.0042kVAR. The demand of load power is delivered by compensator which inject active and reactive power of 0.094kW and 0.022kVAR. Hence a surplus power of -0.154kW and -0.0369kVAR is injected to the grid.

Figs 6.36 (a–c) demonstrate the harmonics content in the source voltage (v_s), source current (i_s), and load current (i_L) during discharging condition. After injecting compensating current, the source current's total harmonic distortion (THD) is reduced to 5.85%, compared to 15.35% for i_L. Furthermore, the THD of the supply voltage is 2.04% when discharging. Fig 6.36 c indicates that the compensator current has a THD of 8.93%, which is utilized to correct for harmonics in the non-linear load. The harmonics created by the nonlinear load are successfully cancelled by injecting AC-DC converter compensating current, resulting in a sinusoidal and out of phase source current. The observed waveforms clearly reveal that the source current's follow the opposite waveform of source voltage i.e discharging operation and it demonstrate that the Rodrigues Jacobi polynomial-based control method has been carefully constructed and satisfactory results found.

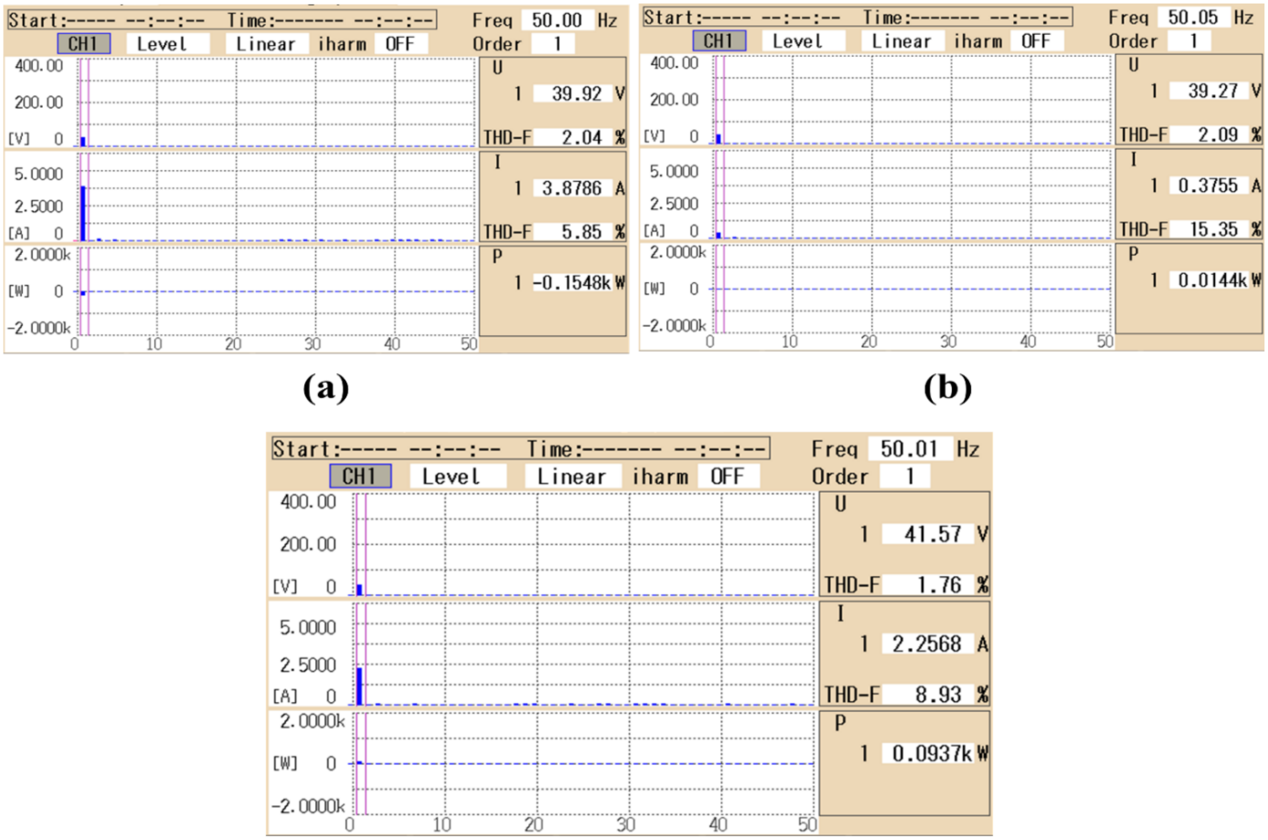

Freq 50.00 Hz
Order 1
U 1 39.92 V
THD-F 2.04 %
I 1 3.8786 A
THD-F 5.85 %
P 1 -0.1548k W

(a)

Freq 50.05 Hz
Order 1
U 1 39.27 V
THD-F 2.09 %
I 1 0.3755 A
THD-F 15.35 %
P 1 0.0144k W

(b)

Freq 50.01 Hz
Order 1
U 1 41.57 V
THD-F 1.76 %
I 1 2.2568 A
THD-F 8.93 %
P 1 0.0937k W

(c)

Fig. 6.36 Experimental results: Harmonic analysis of a). v_s,i_s with THD = 5.85% b). v_s,i_L with THD = 15.35% c). v_s,i_C with THD = 8.93% during steady state condition using RJP.

b). Dynamic State Conditions

The different waveforms of source voltage v_s, source current i_s, load current (i_L), DC link voltage (V_{dc}), compensating current (i_c), fundamental current (i_f), unit template (u_p), battery current (I_{bat}) and battery voltage (V_{bat}) are shown in Fig 6.37 (a-d) during discharging mode condition.

Fig 6.37 a-b shows the dynamics behaviour of source voltage (v_s), source current (i_s), load current (i_L), DC link voltage (V_{dc}) and compensating current (i_c) during load change. The source voltage (v_s) remain stable and opposite phase with source current (i_s) is the proof of system discharging mode. As a result, the entire DC-link voltage stays stable and maintained 80V at dynamic load situations. The compensator is responsible to inject current to the load and feed the surplus current to the grid during discharging operation.

Additionally in Fig 6.37 c, the waveforms of i_s, i_L, I_{bat} and V_{bat} are shown. The current i_s and i_L follow the load change during V2G operation. The battery current remains stable to 2A and battery voltage slowly discharges from 48V.

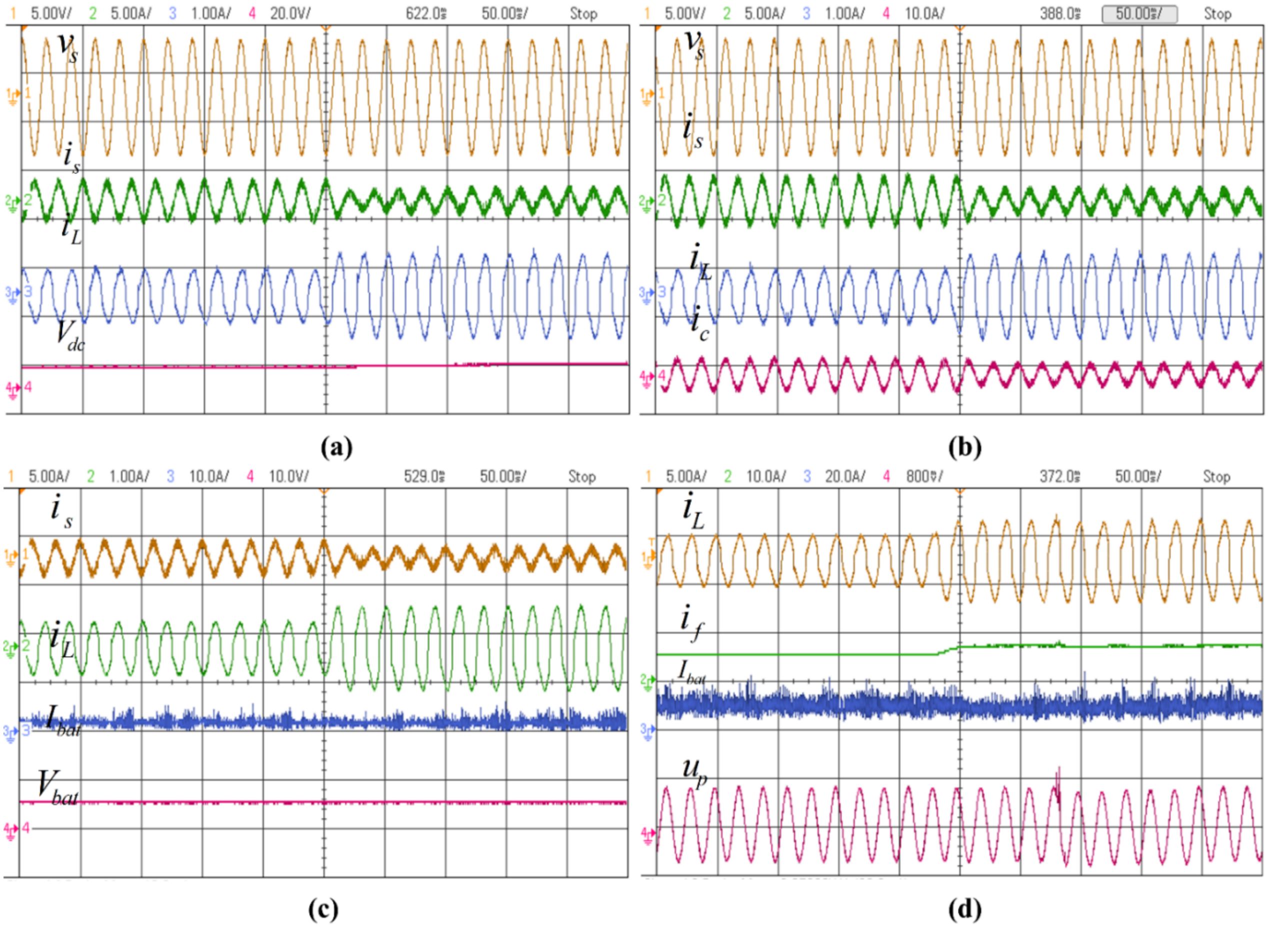

Fig. 6.37 Experimental waveforms of a). v_s,i_s,i_L,V_{dc} b). v_s, i_s ,i_L, i_C c). i_s , i_L,,I_{bat},V_{bat} and d). i_L, i_f, I_{bat},u_p during dynamic condition using RJP.

Similarly, in Fig 6.37 d, during load change, the load current (i_L) and fundamental current (i_f) get interchanged but unit template maintains sinusoidal with range ±1. The battery current remains stable to 2A during the discharge of the EV battery.

6.12 Comparative Analysis of SOGI, RJP and LMS Control Algorithm

In this section, the developed Rodrigues Jacobi Polynomial algorithm is compared with SOGI and LMS control method under identical load conditions. The comparison of extraction of fundamental component of load current with these three algorithms under dynamic load current changes as depected in Fig 6.38. The RJP controller is utilized and shows the fastest response in extracting fundamental current (i_f) with respect to SOGI and LMS based algorithms. In this Figure, it is clearly seen that there is no oscillation present in the extracted fundamental current using RJP. The Table 6.1 shows the analysis of all three control algorithms and it is observed that the proposed RJP controller performs better and the fundamental current is estimated fast with negligible oscillations.

(a) Comparative %T.H.D analysis of single phase grid connected EV system during charging operation

The Total Harmonic Distortion (THD) percentages for the three algorithms RJP, LMS, and SOGI are shown in Table 6.2 across the three current components (v_s, i_s, and i_L) during charging operation. The RJP method has provide lower %THD 1.82% (experimental) and 4.69% (Simulink) than SOGI and LMS algorithms.

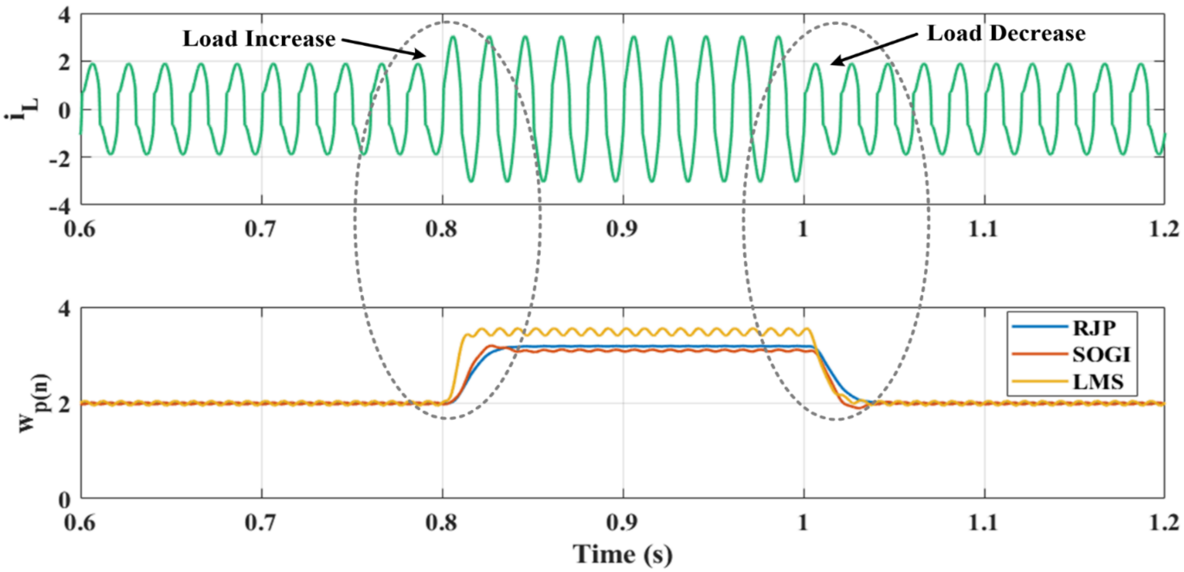

Fig. 6.38 Comparative waveforms of load current (i_L), with fundamental current (i_f) at different algorithms

Table: 6.1 Comparison table of SOGI, LMS and RJP algorithms

S.no	Parameters		SOGI	LMS	RJP
1	Filter type		Non-Adaptive	Adaptive	Adaptive
2	Simulation %THD of i_s	Charging	3.17%	4.75%	1.82%
		Discharging	3.25%	4.97%	1.33%
3	Estimation of fundamental currents		Consist smalloscillations	Consist sustained oscillations	Oscillations are absent
4	Complexity		Medium	Medium	Simple
5	Sampling Time (T_s)		$50\mu s$	$50\mu s$	$50\mu s$
6	DC link Voltage variations		3V	4-5V	2V
7	Convergence		Faster (3~4 cycles)	Slow (4~6 cycles)	Fastest (2 cycles)

Table 6.2: %THD analysis of SOGI, LMS and RJP algorithms during charging mode

Algorithms		**%T.H.D (v_s)**	**%T.H.D (i_s)**	**%T.H.D (i_L)**
SOGI	Simulation	0.48	3.17	17.69
	Experimental	2.13	4.90	15.55
LMS	Simulation	0.49	4.75	17.65
	Experimental	2.13	4.90	15.55
RJP	Simulation	0.48	**1.82**	17.69
	Experimental	1.94	**4.69**	15.33

(b) Comparative %T.H.D analysis of single phase grid connected EV system during discharging operation

Similarly, the %THD of the three algorithms RJP, LMS, and SOGI are shown in Table 6.3 across the three current components (i_s, i_L, and i_c) during discharging operation. The RJP method has

Table 6.3: %THD analysis of SOGI, LMS and RJP algorithms during discharging mode

Algorithms		**%T.H.D (v_s)**	**%T.H.D (i_s)**	**%T.H.D (i_L)**
SOGI	Simulation	0.50	3.25	18.68
	Experimental	1.90	6.94	15.24
LMS	Simulation	0.49	4.97	17.69
	Experimental	1.63	7.62	15.35
RJP	Simulation	0.50	1.33	17.69
	Experimental	2.04	**5.85**	15.35

provide lower %THD 5.85% (experimental) and 1.33% (Simulink) than SOGI and LMS algorithms.

6.13 Conclusion

In this chapter three algorithms SOGI, LMS and RJP are developed for grid connected EV charging operation along with mitigation of PQ issues on the grid side. Various parameters are carefully chosen and a prototype hardware is developed in the laboratory. On the basis of extensive simulation as well as hardware results during dynamics and steady state it is observed that all the three algorithms are able to mitigate grid side PQ issues as well as demonstrated stable G2V and V2G modes. Also, at the end, a comparison of all the three techniques is performed. Based upon the comparison it is observed that RJP algorithm is performing better that other algorithm. The work in this chapter also demonstrates large scale extension is feasible and realisable in V2G and G2V modes of operation in the near future.

Chapter 7

Performance Analysis of Three Phase Grid interfaced Solar PV and EV Charging System

---

This chapter discusses the performance analysis of three phase grid interfaced Solar PV and EV charging systems. Three control techniques Rodrigues Jacobi Polynomial (RJP), Least Mean Square (LMS) and Second Order Generalised Integrator (SOGI) are incorporated to test the system. Results obtained using Matlab software for three phase grid interfaced EV with PV and without PV are presented and compared in this chapter.

7.1 Introduction

In this chapter, the complete system comprises three phase sources, three phase VSC, battery bank with bidirectional Buck Boost converter and Solar PV array as shown in Fig 7.1. The three phase AC voltage supply (v_a,v_b,v_c) feeds power to the system. In Vehicle to Grid (V2G) mode the grid may also absorb power from the system. The source impedances (Z_a, Z_b and Z_c) are also shown in the figure. A non linear load (R_L,X_L with bridge rectifier) is connected at the load end to simulate the non-linear behaviour. A three-phase VSC is connected at Point of Common Coupling (PCC). This three phase VSC is controlled to inject compensating currents (i_{ca},i_{cb},i_{cc}) at PCC through

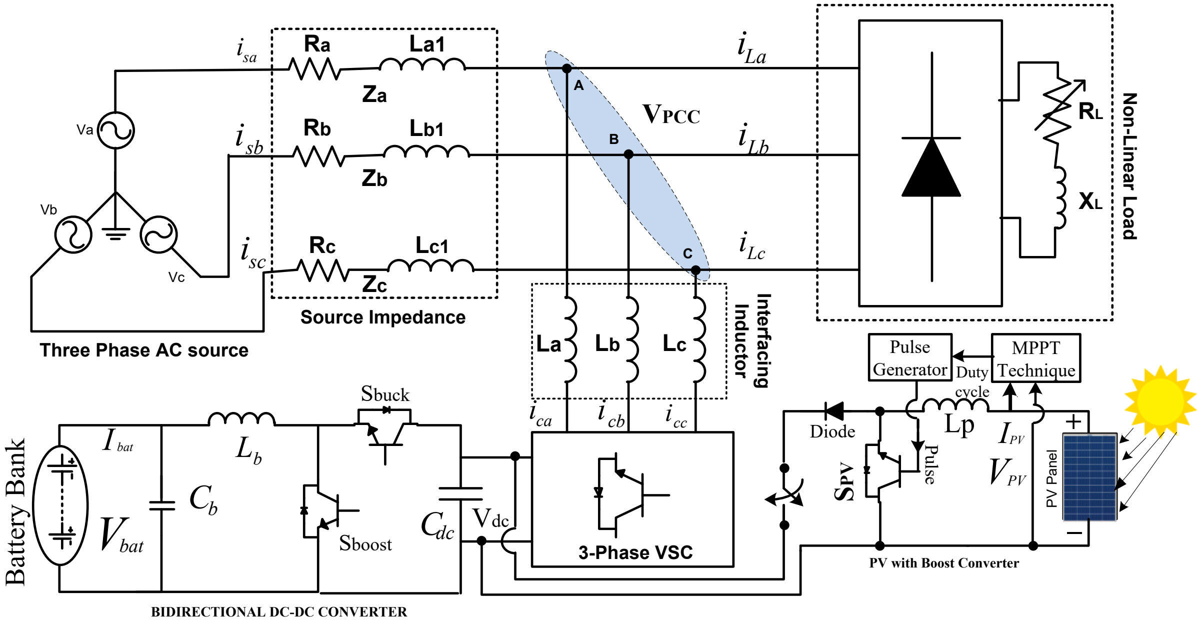

Fig 7.1: System diagram of three phase grid connected solar PV and EV charging system

interfacing inductor (L_a,L_b,L_c) so as to make supply currents (i_{sa},i_{sb},i_{sc}) sinusoidal whereas the load currents are nonlinear (i_{La},i_{Lb},i_{Lc}). The battery bank with bidirectional buck-boost converter is connected at DC link side of the VSC so as to enable charging and discharging control. The control techniques used are Rodrigues Jacobi Polynomial (RJP), Least Mean Square (LMS) and Second Order Generalised Integrator (SOGI) for solar PV array, P & O based MPPT techniques is used. The complete control techniques is discussed in the following subsections. The parameters are shown in Appendix D.

7.2 Calculation of Unit Templates

The unit templates (u_a, u_b, u_c) are necessary for proper synchronization of VSC operation. each phase is calculated by using PCC terminal voltage (V_t) as

$$u_a = \frac{v_{sa}}{V_t}; u_b = \frac{v_{sb}}{V_t}; u_c = \frac{v_{sc}}{V_t}$$

where, the PCC voltage is

$$V_t = \sqrt{\frac{2}{3} v_{sa}^2 + v_{sb}^2 + v_{sc}^2} \tag{7.1}$$

7.3 Estimation of Reference Current and Gating Signals

The product of active weight component obtained using RJP, LMS and SOGI algorithms and unit template of each phase gives three reference currents as

$$i_{sa}^* = i_T * u_a \; ; \; i_{sb}^* = i_T * u_b \, ; i_{sc}^* = i_T * u_c \tag{7.2}$$

The reference currents and source currents are compared using Hysteresis Current Controller (HCC) block so as to generate six gating pulses to control three phase voltage source converters.

7.4 Control strategy of EV Charger

The control method of charging/discharging battery of the EV is as shown in Fig 7.2. The difference of reference battery current (I_{bref}) and actual battery current (I_{bat}) is generated and this error (I_{bate}) is further processed in PI controller. The output of PI block is fed to PWM block which provides pulses of two gating switch. One pulse is S_{buck} pulse used to charge the battery and another is S_{boost} pulse used to perform the discharge operation of the battery.

7.5 Control strategy of Solar PV Array

The solar PV is interconnected at DC link of VSC via boost converter to inject power to the grid. The control strategy incorporating MPPT is depicted in Fig 7.2. The PV voltage V_{pv}, current I_{pv} is passed through the Perturb and Observe MPPT block and then Pulse Width Modulation (PWM) technique is used to generate pulse (S_{pv}). The pulse S_{pv} is connected to the IGBT switch of the boost converter. The output of boost converter is connected at the DC link.

7.6 Control Structure of Three Phase Grid Interfaced EV Charging Systems using SOGI algorithm

In this section, the control strategy of three phase VSC developed using Second Order Generalized Integrator (SOGI) algorithm and calculation of fundamental currents magnitude is discussed in detail.

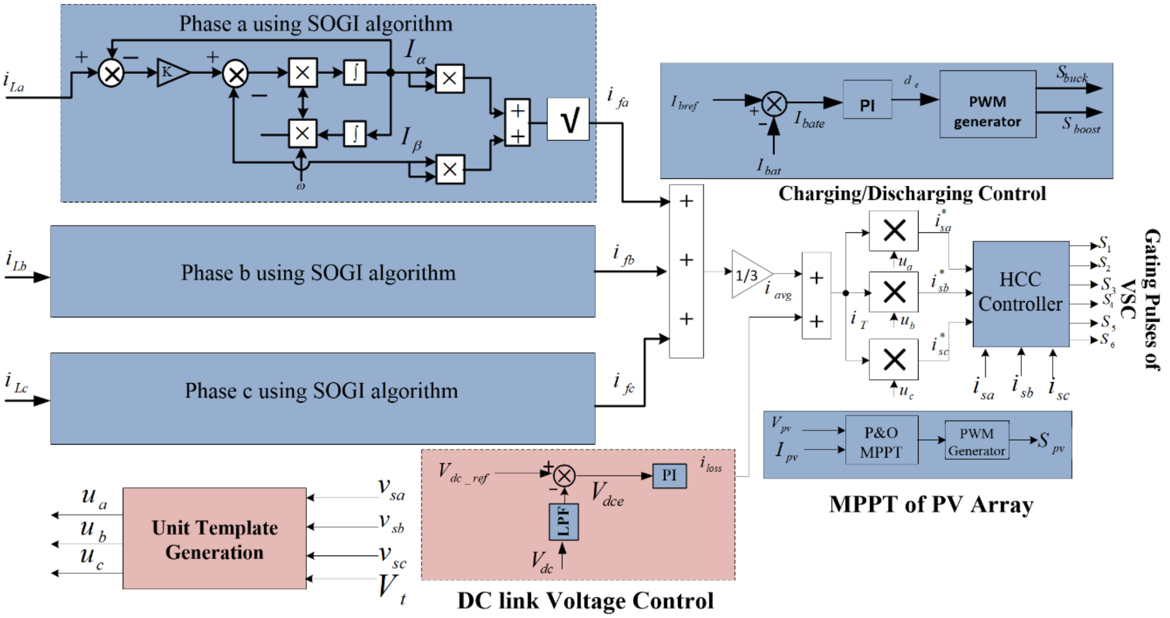

Fig 7.2: Control diagram using SOGI algorithm

7.6.1 Control of Three Phase VSC

The VSC is controlled by the combination of Unit templates (u_a, u_b, u_c), the fundamental current component (i_{fa}, i_{fb}, i_{fc}), active loss component (i_{loss}), reference currents (i_{sa}^*, i_{sb}^*, i_{sc}^*) and hysteresis controller which are shown through Fig 7.2. The fundamental currents (i_{fa}, i_{fb}, i_{fc}) is extracted by injecting each phase load current in SOGI controller. The average current (i_{avg}) is one third of the sum of fundamental currents. A PI controller is realized over the total DC-link voltage to regulate it to 400V reference so as to estimate the current loss component. The summation of both average fundamental current (i_{avg}) and loss component (i_{loss}) is effective total current i_T which is multiplied with unit templates (u_a, u_b, u_c) to generate reference currents (i_{sa}^*, i_{sb}^*, i_{sc}^*). The reference currents (i_{sa}^*, i_{sb}^*, i_{sc}^*) are perfectly sinusoidal and the actual supply currents (i_{sa}, i_{sb}, i_{sc}) is passed through hysteresis current controller (HCC) to generate six gating pulses for IGBT switching operation to control three phase VSC. This ensures the grid currents is perfectly sinusoidal and the entire reactive power demand of the load is met by the compensator. The detailed mathematic analysis is shown below.

7.6.2 Calculation of Fundamental Component of Load Current

The fundamental weight components for each phase i_{fa}, i_{fb} and i_{fc} is extracted by SOGI controller and given by Eq. (7.3 – 7.5)

$$i_{fa} = \sqrt{(i_{\alpha a})^2 + (i_{\beta a})^2} \tag{7.3}$$

$$i_{fb} = \sqrt{(i_{\alpha b})^2 + (i_{\beta b})^2} \tag{7.4}$$

$$i_{fc} = \sqrt{(i_{\alpha c})^2 + (i_{\beta c})^2} \tag{7.5}$$

Now, the average weight is calculated as

$$i_{avg} = \frac{1}{3}(i_{fa} + i_{fb} + i_{fc}) \tag{7.6}$$

7.6.3 Simulation Results using SOGI Algorithm

Fig 7.3-7.6 depicts the results of three phase system including battery system. Results are discussed with / without PV integration under both charging and discharging modes of the battery in detail. The three phase grid supply feeds power to the battery i.e G2V operation to charge the battery. Fig. 7.3 shows the waveforms of the system in which PV is not connected. The waveforms of three phase voltages (v_{sa}, v_{sb}, v_{sc}) of 230V RMS value (L-N), three phase source currents (i_{sa}, i_{sb}, i_{sc}) of 15A peak, load currents (i_{La}, i_{Lb}, i_{Lc}) for three phase load of 5A peak, a DC link (V_{dc}) having reference value of 400V, battery voltage (V_{bat}) is maintained constant at 100V, Ipv = 0A and I_{bat} is constant at -20A where negative sign represents charging behavior of battery. In addition, SoC is seen to be increasing from 80%. Furthermore, a load change at 0.7s is applied to study the dynamic behavior of the system. The system performs satisfactorily under dynamic state. The supply current is observed to be sinusoidal due to good performance of SOGI filter.

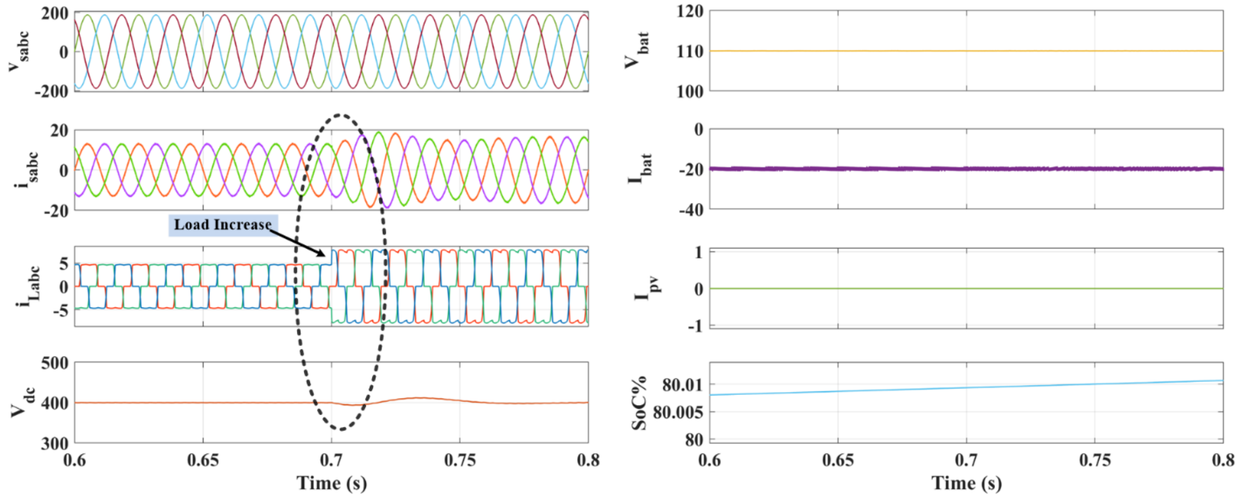

Fig 7.3 Three phase waveform of $V_{s(abc)}$, $I_{s(abc)}$, $I_{L(abc)}$, V_{dc}, V_{bat}, I_{bat}, I_{pv} and %SoC at charging mode (without PV) using SOGI.

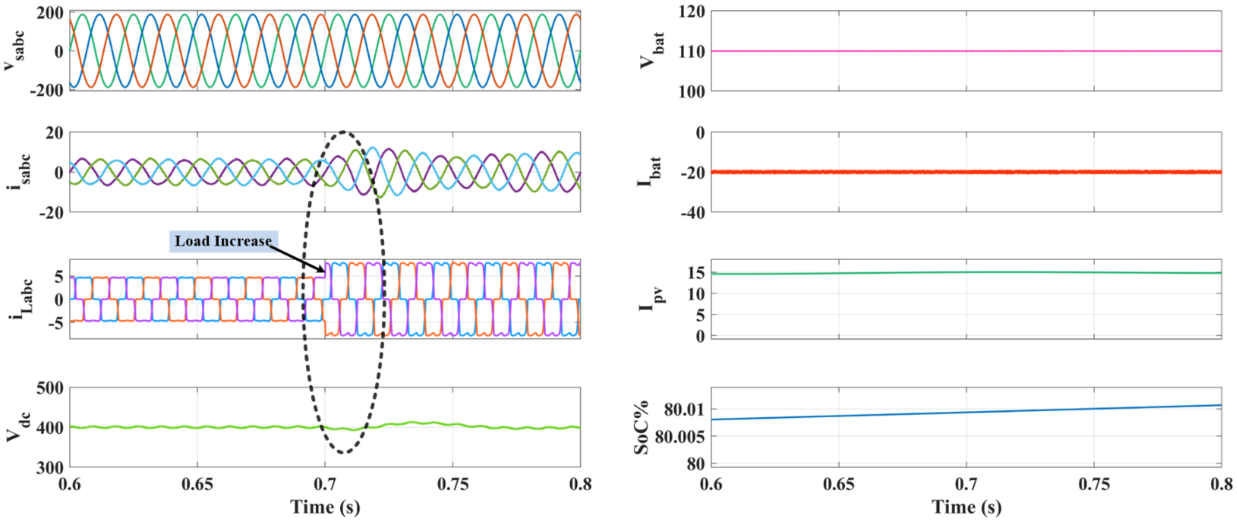

Fig 7.4 Three phase waveform of $v_{s(abc)}$, $i_{s(abc)}$, $i_{L(abc)}$, V_{dc}, V_{bat}, I_{bat}, I_{pv} and %SoC at charging mode (with PV) using SOGI.

Fig.7.4 shows the waveform related to the system integrated with PV under charging mode of operation of battery. The waveforms of three phase voltages (v_{sa}, v_{sb}, v_{sc}) of 230V RMS value (L-N), three phase source currents (i_{sa}, i_{sb}, i_{sc}) of 7A peak, load currents (i_{La}, i_{Lb}, i_{Lc}) for three phase loads of 5A peak, a DC link (V_{dc}) having value close to 400V reference, V_{bat} is maintained constant at 100V and I_{bat} is constant at -20A where negative sign represents charging behavior of battery. In addition, SoC is seen to be increasing in nature for the charging phenomenon. The PV is connected to the system to support load, battery and its current is I_{pv}=15A. Furthermore, a load

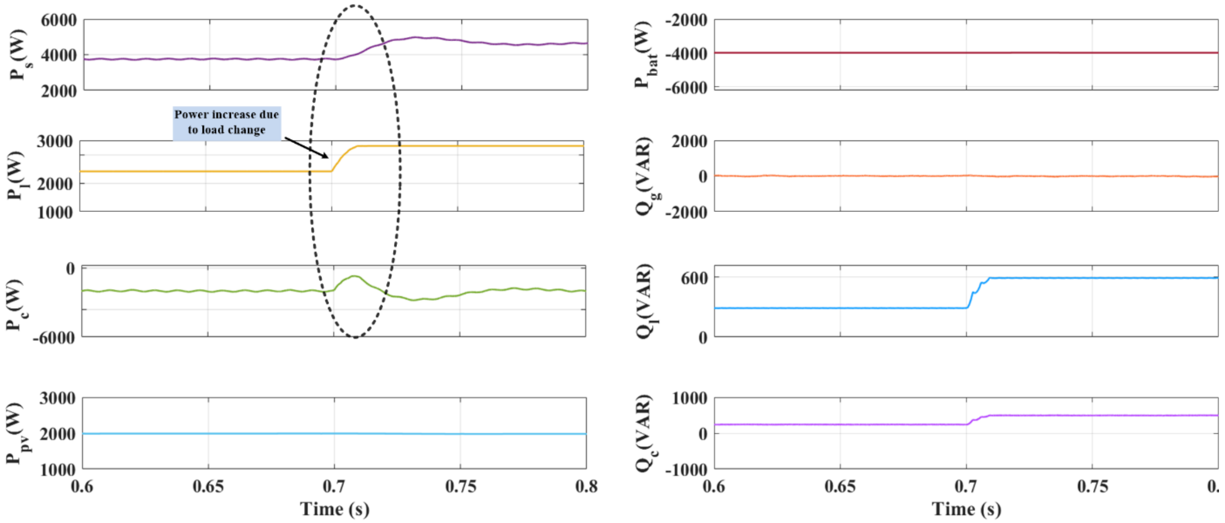

Fig 7.5 Waveform of grid power Pg, load power P_L, compensator power P_c, PV power P_{pv}, battery power P_{bat}, grid reactive power Qg, load reactive power Q_L, compensator reactive power Qc under charging mode using SOGI.

change at 0.7s is carried out to observe the effect under dynamic changes. Satisfactory dynamic performance of the system is observed from the results shown in Fig.7.4.

Power balance for the system in charging mode is shown in Fig 7.5, where, 4 kW power is provided by the grid with PV connected. A constant load power (P_L) of 2.2 kW and 300VAR is seen, compensating power of -1.6 kw is observed and the PV power i.e P_{pv}=2kW. Furthermore, Battery power (P_{bat}) of -4.4 kW is maintained constant in this mode. The reactive power is also observed to be balanced. The Q_g is maintained constant at 0 VAR which shows zero reactive power is supplied from the grid. At 0.7sec load changes, the powers again rebalance to P_{grid}=4.5kW, P_L=2.9kW, Q_L=600VAR and Q_c= 500VAR.

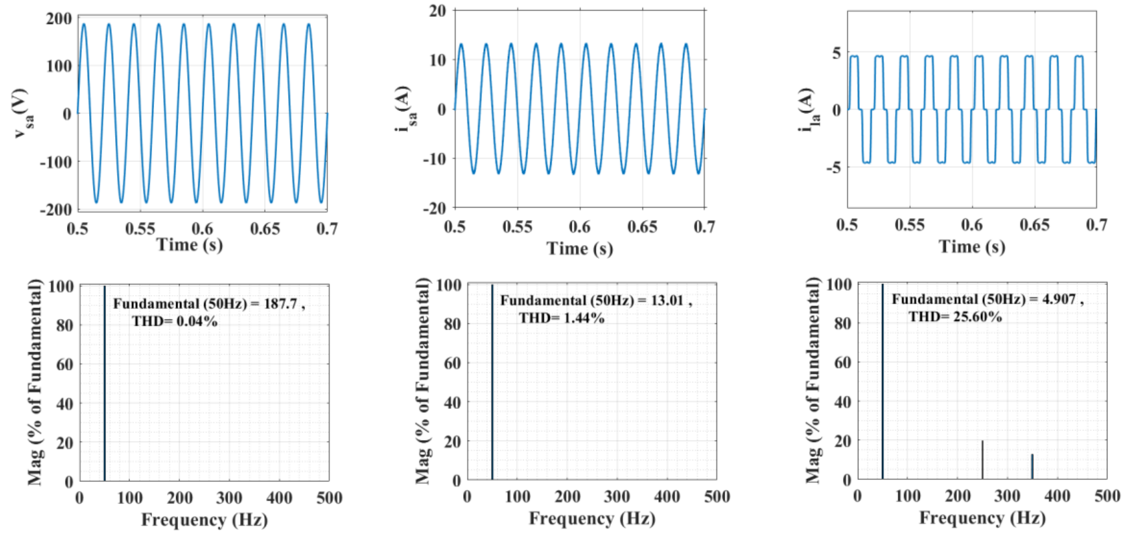

Fig 7.6 Simulation results : Harmonic analysis of a). v_{sa} , THD = 0.04% b). i_{sa} , THD = 1.44% c). i_L , THD = 25.60% during steady state condition at charging mode using SOGI.

The analysis of the THD profiles during the electric vehicle's charging mode reveals that the source voltage (v_{sa}) exhibits excellent harmonic performance with a negligible THD of 0.04%, indicating a clean waveform dominated by the 50 Hz fundamental component (187.7V) as shown in Fig 7.6. The source current (i_{sa}) shows a slightly higher THD of 1.44% with a fundamental magnitude of 13.01A, reflecting good harmonic quality. In contrast, the load current (i_{La}) displays significant distortion with a THD of 25.60% and a fundamental magnitude of 4.907A, likely due to non-linear charging effects. Graphical data in the file include time-domain waveforms and frequency-domain spectra that illustrate these harmonic characteristics across the system.

Fig.7.7 shows the discharging behavior of the system without PV integration. The results obtained are similar to Fig. 7.3 except for polarity of the battery current. The waveforms of three phase voltages (v_{sa}, v_{sb}, v_{sc}) of 230V RMS value (L-N), three phase source currents (i_{sa}, i_{sb}, i_{sc}) of 3A peak, load currents (i_{La}, i_{Lb}, i_{Lc}) for three phase loads of 5A peak, a DC link (V_{dc}) having reference value of 400V, battery voltage (V_{bat}) is maintained constant at 100V, Ipv = 0A and I_{bat} is constant at +20A where positive sign represents discharging behavior of battery. In addition, SoC is seen to be decreasing from 80%. Furthermore, a load change at 0.7s is applied to study the dynamic

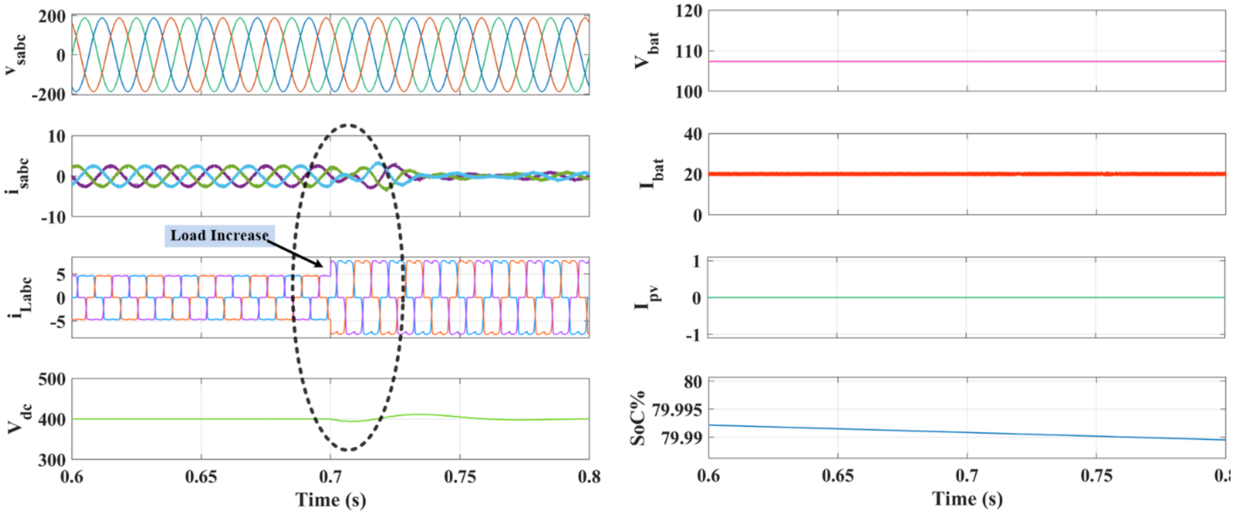

Fig.7.7 Three phase waveform of $v_{s(abc)}$, $i_{s(abc)}$, $i_{L(abc)}$, V_{dc}, V_{bat}, I_{bat}, I_{pv} and %SoC at discharging mode (without PV) using SOGI.

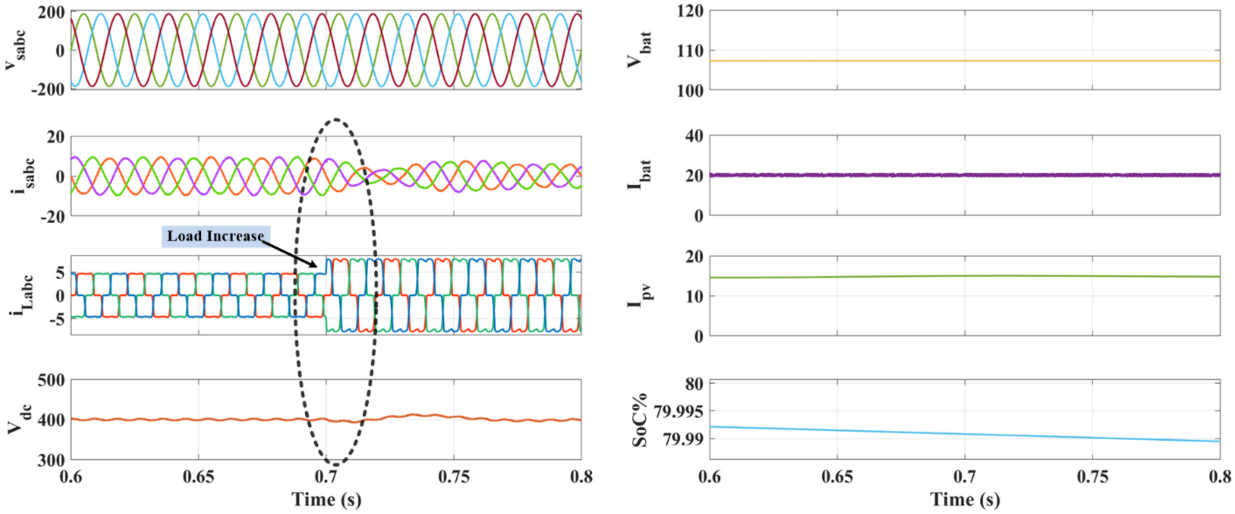

Fig 7.8 Three phase waveform of $v_{s(abc)}$, $i_{s(abc)}$, $i_{L(abc)}$, V_{dc}, V_{bat}, I_{bat}, I_{pv} and %SoC at discharging mode (with PV) using SOGI.

behavior of the system. The system performs satisfactorily under dynamic state. The supply current is observed to be sinusoidal due to good performance of SOGI filter.

Fig. 7.8 shows the discharging behavior with PV connected. Similar characteristics as that of Fig 7.4 are observed except for the polarity of 20A battery current. The PV is connected to the system to support grid, load, battery and its current is I_{pv}=15A. Furthermore, a load change at 0.7s is carried out to observe the effect under dynamic changes. Satisfactory dynamic performance of the system is observed as observed from the results shown in Fig.7.8.

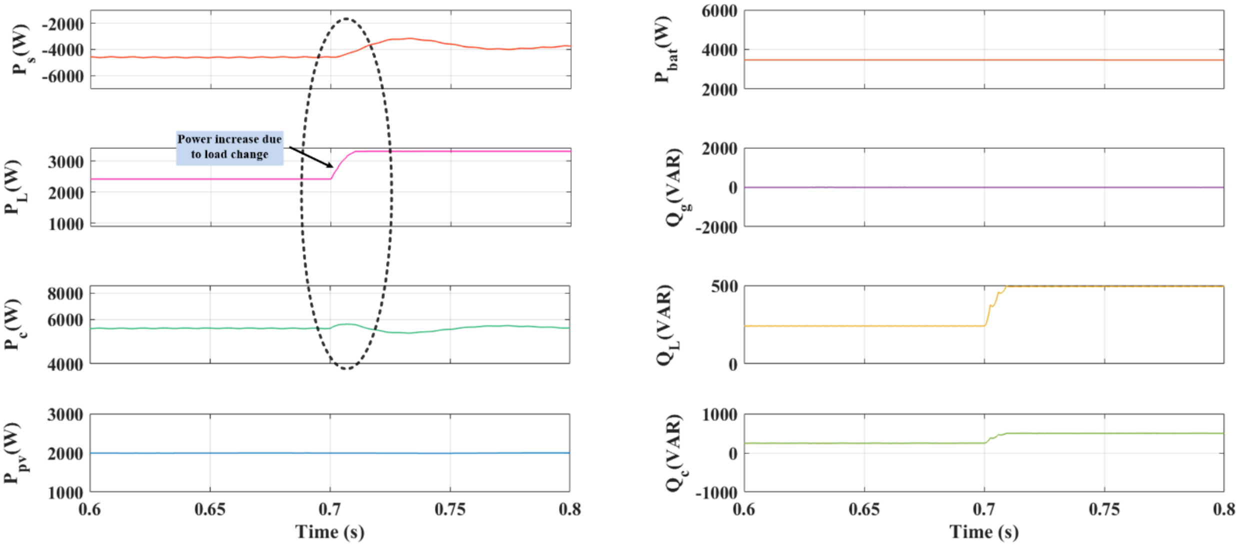

Fig.7.9 Results of grid power P_g, load power P_L, compensator power P_c, PV power P_{pv}, battery power P_{bat}, grid reactive power Q_g, load reactive power Q_L, compensator reactive power Q_c under discharging mode using SOGI.

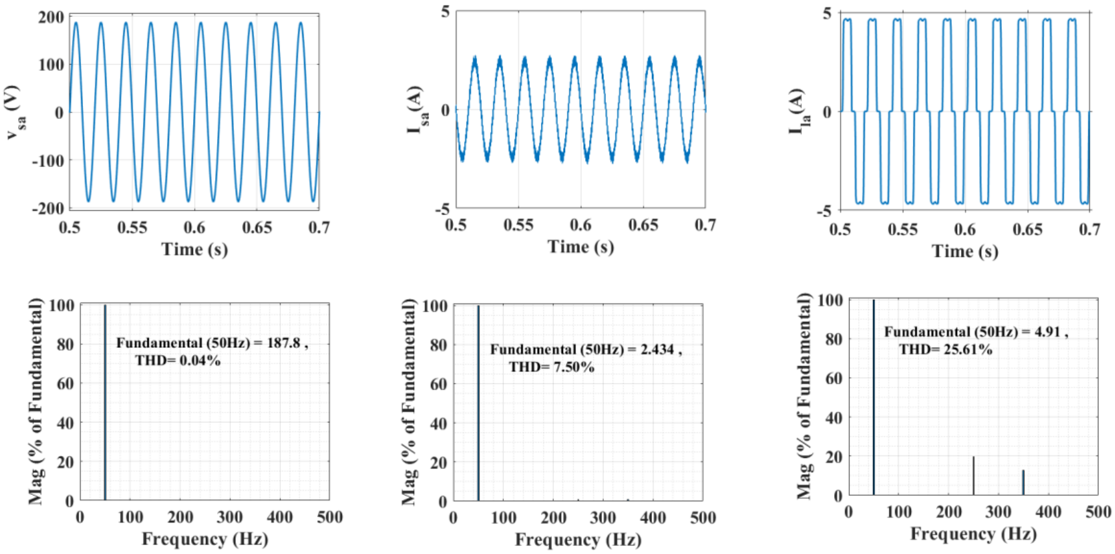

Fig 7.10 Simulation results : Harmonic analysis of a). v_{sa} , THD = 0.04% b). i_{sa} , THD = 7.50% c). i_{La} , THD = 25.61% during steady state condition at discharging mode using SOGI.

Fig. 7.9 shows the results of grid power (P_s, Q_s), load power (P_L, Q_L), compensator power (P_c, Q_c), PV power (P_{pv}) and battery power (P_{bat}) during discharging condition. The load demands 2.2kW and 300VAR. The battery power 3.5kW and PV power 2kW use to form compensator power 5.7kW and 300 VAR. Now, the load is change at t=0.7s, the power becomes Pg= 4kW, Qg = 0VAR, P_L= 3.2kW, Q_L= 500VAR.

During the discharging mode of the electric vehicle battery, the source voltage (v_{sa}) typically maintains a low THD (i.e 0.04%), reflecting a stable supply with minimal harmonic distortion. The THD of source current (i_{sa}) is 7.5% during V2G operation as shown in Fig 7.10. However, the load current (i_{La}), often subject to non-linearities introduced by the discharging circuitry, exhibits a significantly higher THD which is 25.61%. This distortion arises from switching devices used during discharging, which can inject harmonics into the current waveform. These observations highlight the interplay of harmonic performance across system components in discharging mode.

7.7 Control Structure of Three Phase Grid Interfaced EV Charging Systems using LMS algorithm

In this section, the control strategy of three phase VSC developed using Least Mean Square (LMS) algorithm and calculation of fundamental currents is discussed in detail.

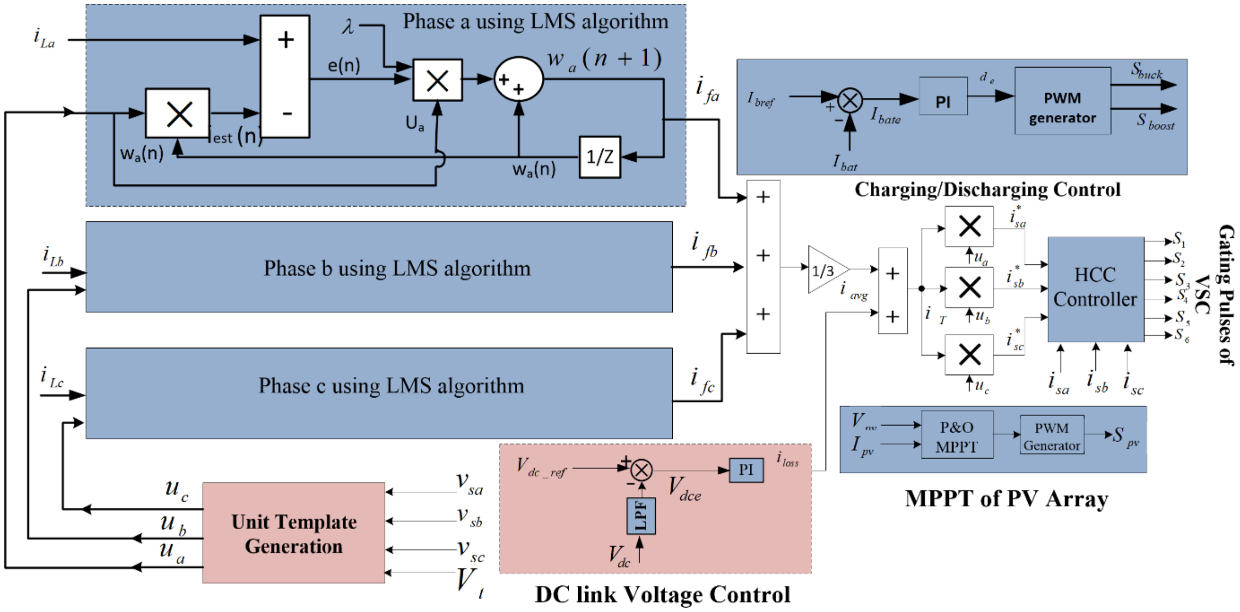

Fig 7.11: Control diagram using LMS algorithm

7.7.1 Control of Three Phase VSC

Fig 7.11 shows the control diagram using LMS algorithm to control three phase VSC. The load currents of each phase are fed with separate LMS algorithm to generate fundamental currents (i_{fa},

i_{fb}, i_{fc}) of each phase. The mean of these fundamental currents is average current (i_{avg}). A PI controller is fed with the total DC-link voltage to regulate it to 400V reference so as to estimate the current loss component (i_{loss}). The summation of both average fundamental current (i_{avg}) and loss component (i_{loss}) is effective total current i_T which is multiplied with unit templates (u_a, u_b, u_c) to generate reference currents (i_{sa}^*, i_{sb}^*, i_{sc}^*). It is observed that the reference currents (i_{sa}^*, i_{sb}^*, i_{sc}^*) are perfectly sinusoidal and the actual supply currents (i_{sa}, i_{sb}, i_{sc}) is fed through hysteresis current controller (HCC) to generate six gating pulses for IGBT switching operation to control three phase VSC. These VSC injecting compensating current to fulfill reactive power demand of the load and ensures the grid currents is perfectly sinusoidal.

7.7.2 Calculation of Fundamental Component of Load Current

The fundamental weight components for each phase i_{fa}, i_{fb} and i_{fc} is extracted by LMS algorithm given by Eq. (7.7 – 7.9). The details of LMS techniques is discussed in Section 6.6.2.

$$w_a(n+1) = w_a(n) + \lambda e(n)u_a = i_{fa} \tag{7.7}$$

$$w_b(n+1) = w_b(n) + \lambda e(n)u_b = i_{fb} \tag{7.8}$$

$$w_c(n+1) = w_c(n) + \lambda e(n)u_c = i_{fc} \tag{7.9}$$

Now, the average weight is calculated as

$$i_{avg} = \frac{1}{3}(i_{fa} + i_{fb} + i_{fc}) \tag{7.10}$$

7.7.3 Simulation Results using LMS algorithm

The real time simulation results of with / without PV integration in three phase EV charging systems are discussed in detail which are shown in Fig 7.12-7.15.

The G2V and V2G operation is applied to charge and discharge of the battery via bidirectional DC-DC converter. Fig 7.12 shows the without PV integrated waveforms of three phase voltages (v_{sa}, v_{sb}, v_{sc}), three phase source currents (i_{sa}, i_{sb}, i_{sc}), load currents (i_{La}, i_{Lb}, i_{Lc}), a DC link (V_{dc}) having reference value of 400V, battery voltage (V_{bat}), without PV integrated current of Ipv = 0A and battery current (I_{bat}) under dynamic load condition. The I_{bat} is constant at -20A i.e negative sign represents charging behavior of battery. In addition, SoC is seen to be increasing from 80%. Furthermore, a load change at 0.7s is applied to study the dynamic behavior of the system. The system performs satisfactorily and it is observed that the supply current is to be sinusoidal.

The waveform of PV integrated three phase EV charging system are shown in Fig 7.13. The waveforms of three phase voltages (v_{sa}, v_{sb}, v_{sc}), three phase source currents (i_{sa}, i_{sb}, i_{sc}), load currents (i_{La}, i_{Lb}, i_{Lc}) for three phase loads of 5A peak, a DC link (V_{dc}), V_{bat} and I_{bat} are shown in Fig 7.13.

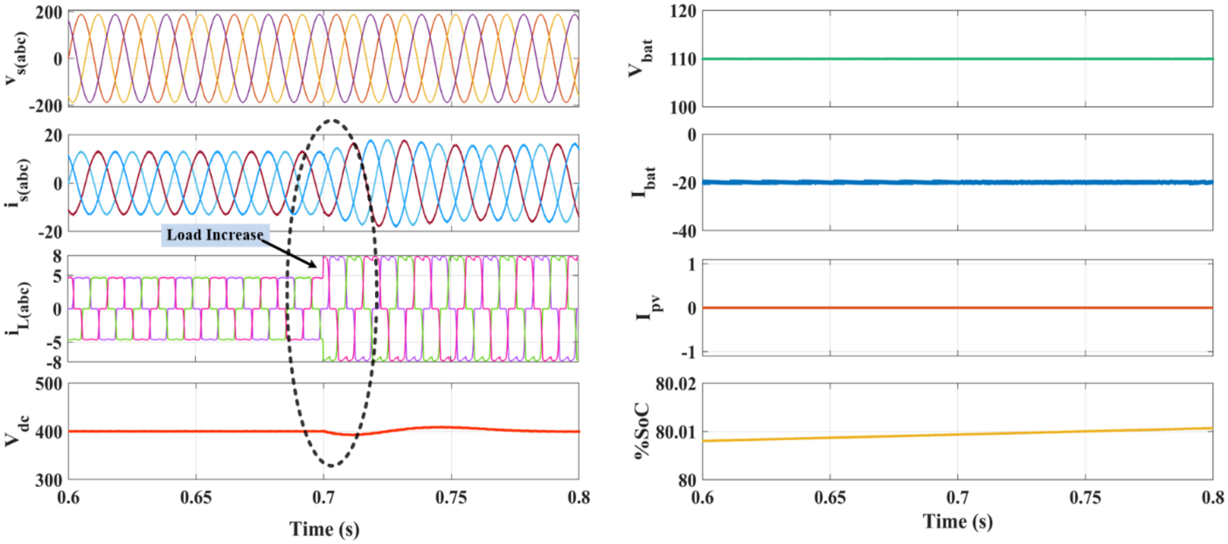

Fig.7.12 Three phase waveform of $v_{s(abc)}$, $i_{s(abc)}$, $i_{L(abc)}$, V_{dc}, V_{bat}, I_{bat}, I_{pv} and %SoC at charging mode (without PV)

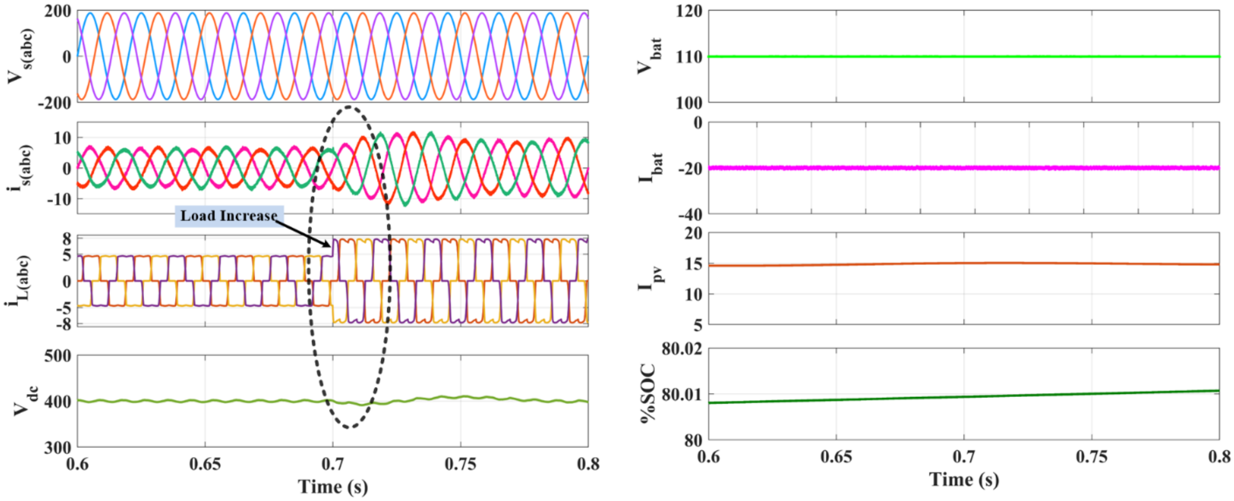

Fig.7.13 Three phase waveform of $V_{s(abc)}$, $I_{s(abc)}$, $I_{L(abc)}$, V_{dc}, V_{bat}, I_{bat}, I_{pv} and %SoC at charging mode (with PV) using LMS.

Also, the SoC is seen to be increasing in nature for the charging phenomenon. The PV is connected to the system to support load and battery via buck converter. Furthermore, the performance of the waveforms is found satisfactory and observed that the waveforms of source current maintained sinusoidal during load change at 0.7s.

The Power of the system in G2V is shown in Fig 7.14, where, 3.8 kW power is provided by the grid with PV connected. A load power demands (P_L) of 1.5 kW and compensating power of -1.6 kw is observed and the PV power i.e P_{pv}=2kw. Furthermore, Battery power (P_{bat}) of -4.4 kw is maintained constant in this mode. The reactive power is also observed to be balanced. The Q_g is maintained constant at 0 VAR which shows zero reactive power is supplied from the grid. At 0.7sec load changes, the powers again rebalances to P_{grid}=4.5kW, P_L=2.9kW, Q_L=600VAR and Q_c= 500VAR.

The Fig. 7.15 shows that the THD of v_{sa}, i_{sa} and i_{La} during charging of the EV battery is 0.0412%, 4.41% and 25.23% respectively.

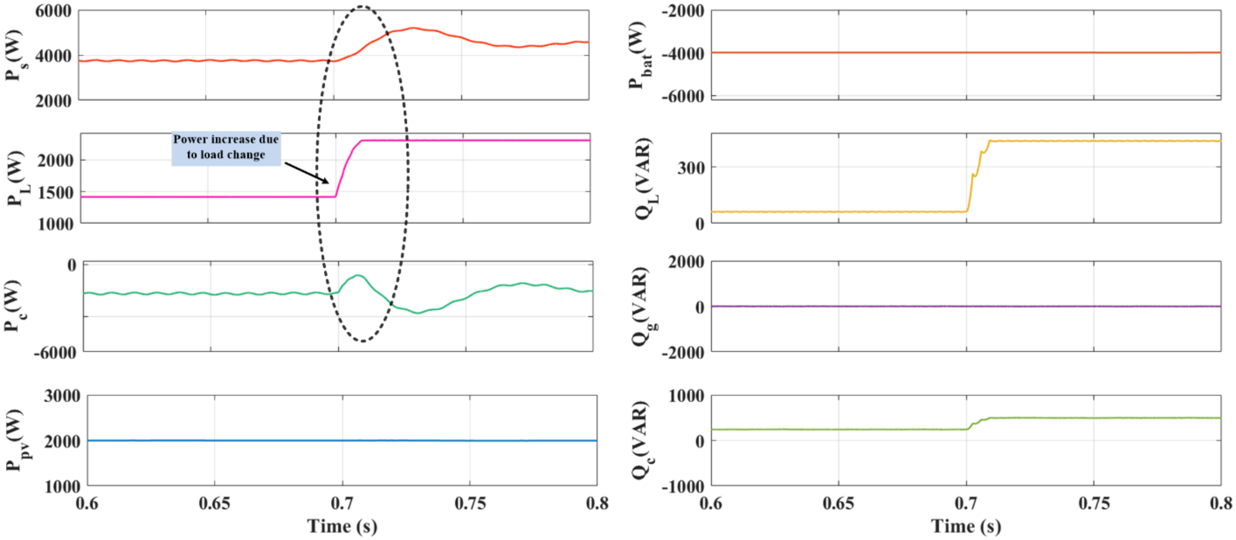

Fig 7.14 Waveform of grid power Pg, load power P_L, compensator power P_c, PV power P_{pv}, battery power P_{bat}, grid reactive power Qg, load reactive power Q_L, compensator reactive power Qc under charging mode using LMS.

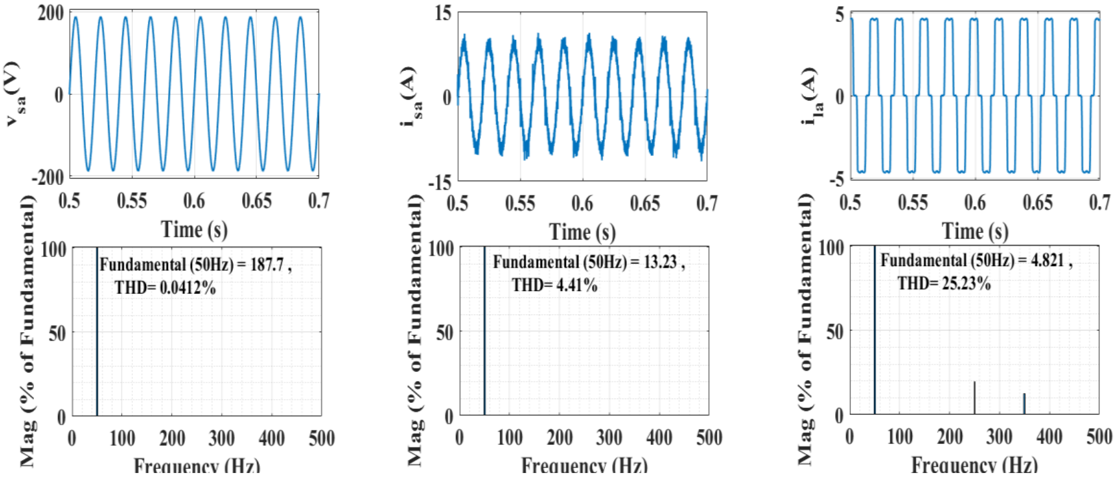

Fig 7.15 Simulation results : Harmonic analysis of a). v_{sa} , THD = 0.0412% b). i_{sa} , THD = 4.41% c). i_L , THD = 25.23% during steady state condition at charging mode using LMS.

The without PV integrated in three phase grid connected EV charging system during discharging condition are shown in Fig 7.16. The waveforms obtained are similar to Fig 7.12 except for polarity of the battery current. During discharging conditions in three phase grid connected EV and without PV shows the waveforms of three phase voltages (v_{sa}, v_{sb}, v_{sc}) of 230V RMS value (L-N), three phase source currents (i_{sa}, i_{sb}, i_{sc}) of 3A peak, load currents (i_{La}, i_{Lb}, i_{Lc}) of 5A peak, a DC link voltage (V_{dc}), battery voltage (V_{bat}), without PV integrated current of Ipv = 0A and I_{bat} is constant

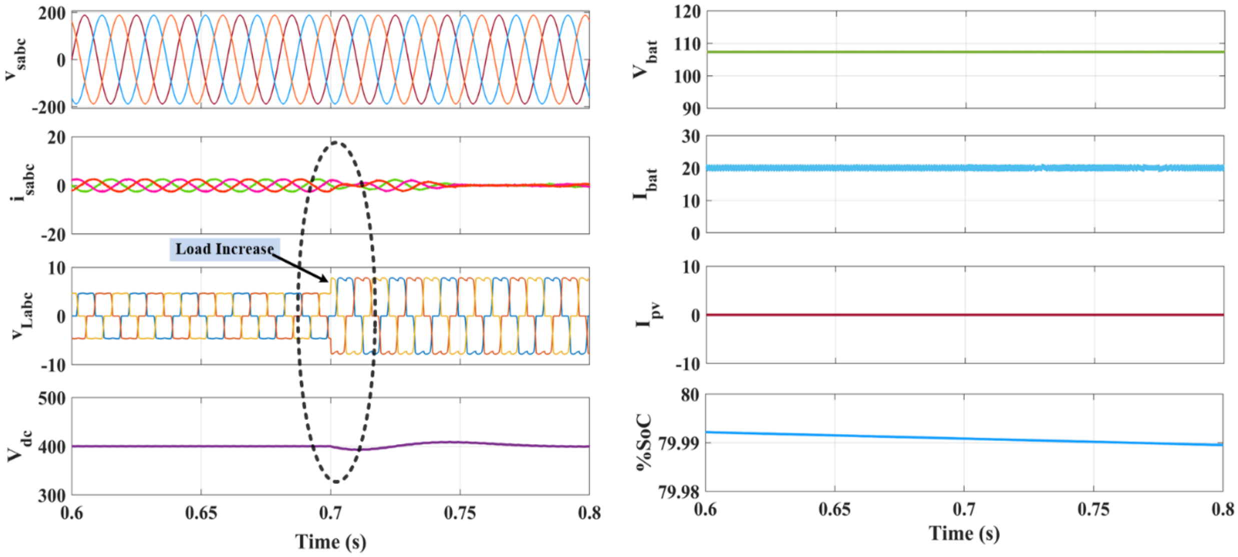

Fig.7.16 Three phase waveform of $v_{s(abc)}$, $i_{s(abc)}$, $i_{L(abc)}$, V_{dc}, V_{bat}, I_{bat}, I_{pv} and %SoC at discharging mode (without PV) using LMS.

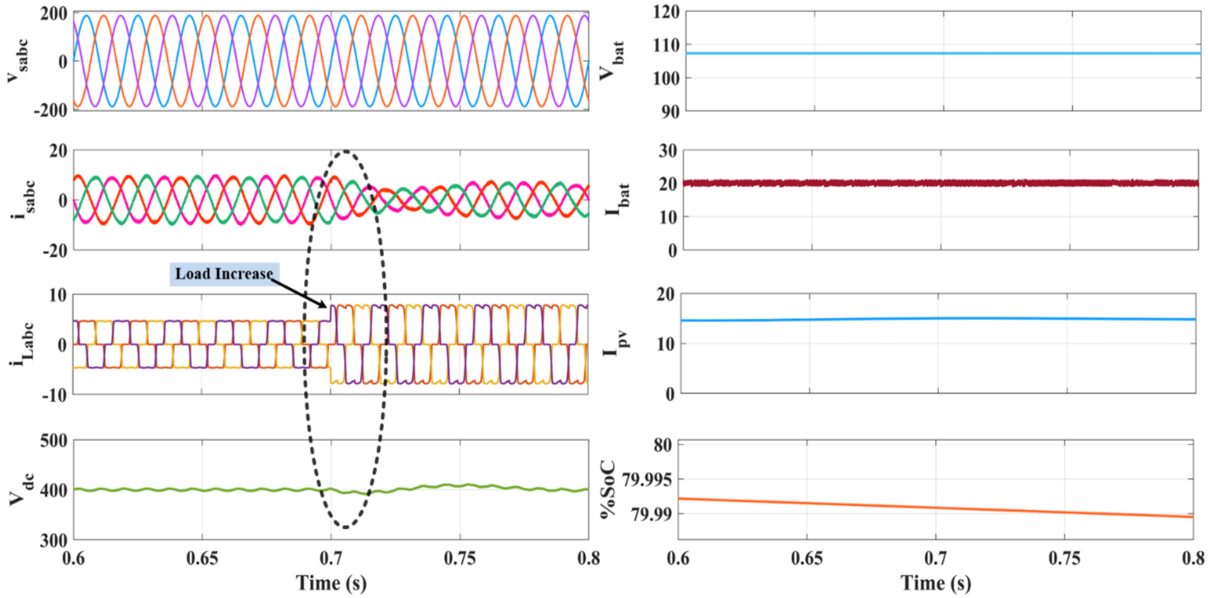

Fig.7.17 Three phase waveform of $v_{s(abc)}$, $i_{s(abc)}$, $i_{L(abc)}$, V_{dc}, V_{bat}, I_{bat}, I_{pv} and %SoC at discharging mode (with PV) using LMS.

at +20A. The continuous decrease in SoC at 80% is another proof of discharging condition. The dynamic response is analysed and observed that the battery supports the load and the grid during V2G mode.

The real time simulation results of PV and EV integrated with three phase grid connected system are shown in Fig 7.17. Similar characteristics as that of Fig 7.13 are observed except for the polarity

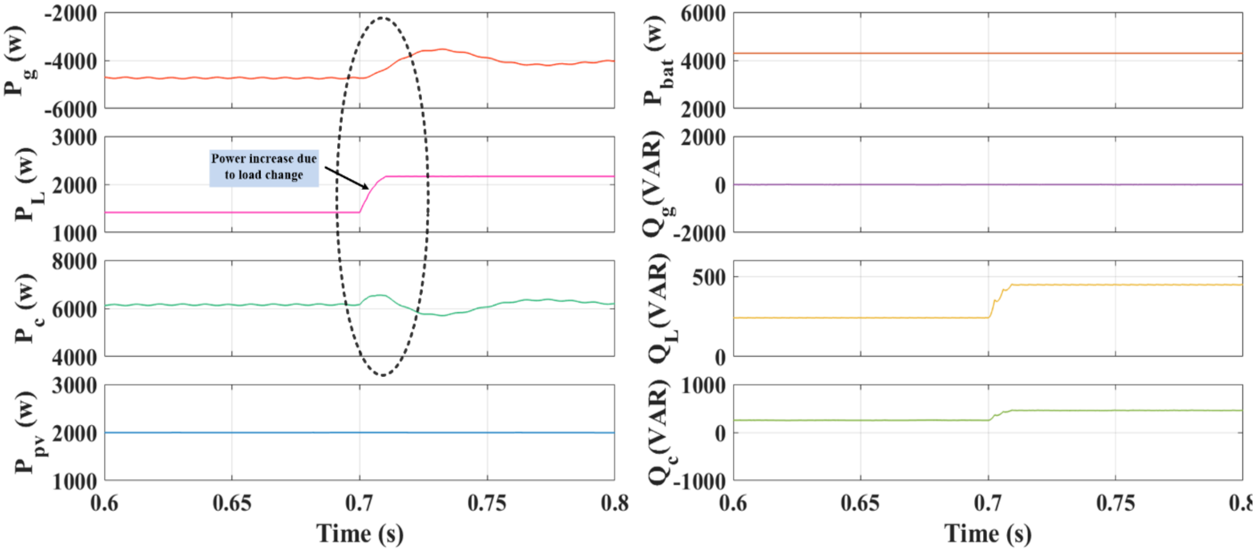

Fig.7.18 Results of grid power P_g, load power P_L, compensator power P_c, PV power P_{pv}, battery power P_{bat}, grid reactive power Q_g, load reactive power Q_L, compensator reactive power Q_c under discharging mode using LMS.

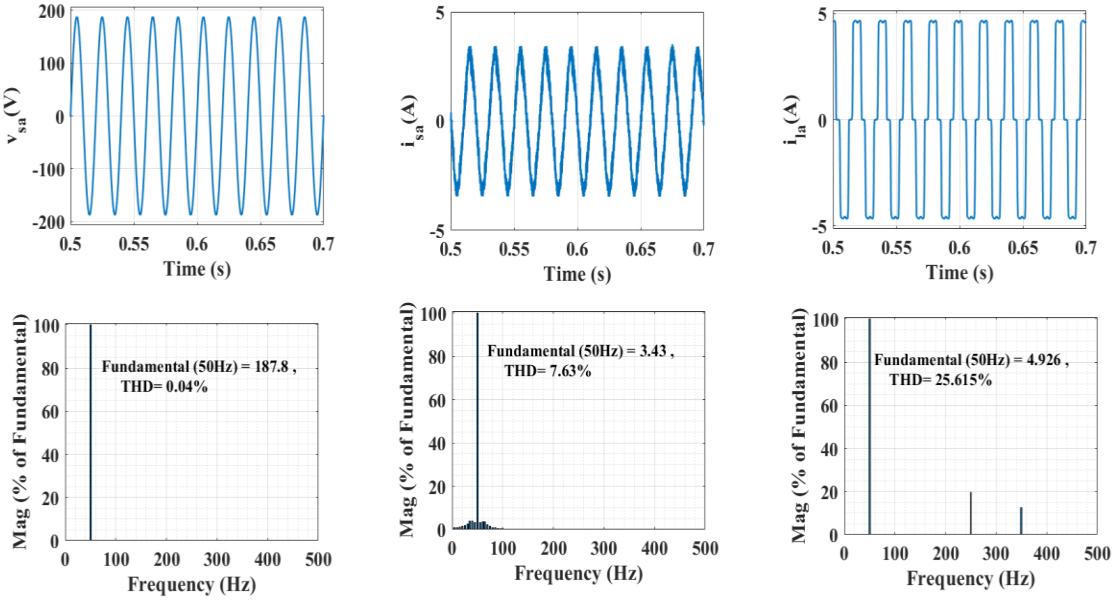

Fig 7.19 Simulation results : Harmonic analysis of a). v_{sa} , THD = 0.04% b). i_{sa} , THD = 7.63% c). i_L , THD = 25.615% during steady state condition using LMS. (discharging mode)

of 20A battery current. The PV and EV is connected to the three phase system to support grid and load during V2G condition. Furthermore, the dynamic response of the system is observed satisfactory.

Fig.7.18 presents the result of grid power P_g=4.5kW, load power P_L=1.5kW, compensator power P_c=6kW, PV power P_{pv}=2kW, battery power P_{bat}=4kW, grid reactive power Q_g=0VAR, load reactive power Q_L=250VAR and compensator reactive power Q_c = 250VAR are observed during discharging mode using LMS algorithm.

The Fig. 7.19 shows that the THD of v_{sa}, i_{sa} and i_{La} during discharging of the EV battery is 0.04%, 7.63% and 25.615% respectively.

7.8 Control Structure of Three Phase Grid Interfaced EV Charging Systems using RJP algorithm

The control diagram of Rodrigues Jacobi Polynomials (RJP) algorithm based three phase grid connected EV with/ without PV based charging operation are shown in Fig. 7.20. The details of the control of three phase VSC and calculation of fundamental currents is discussed.

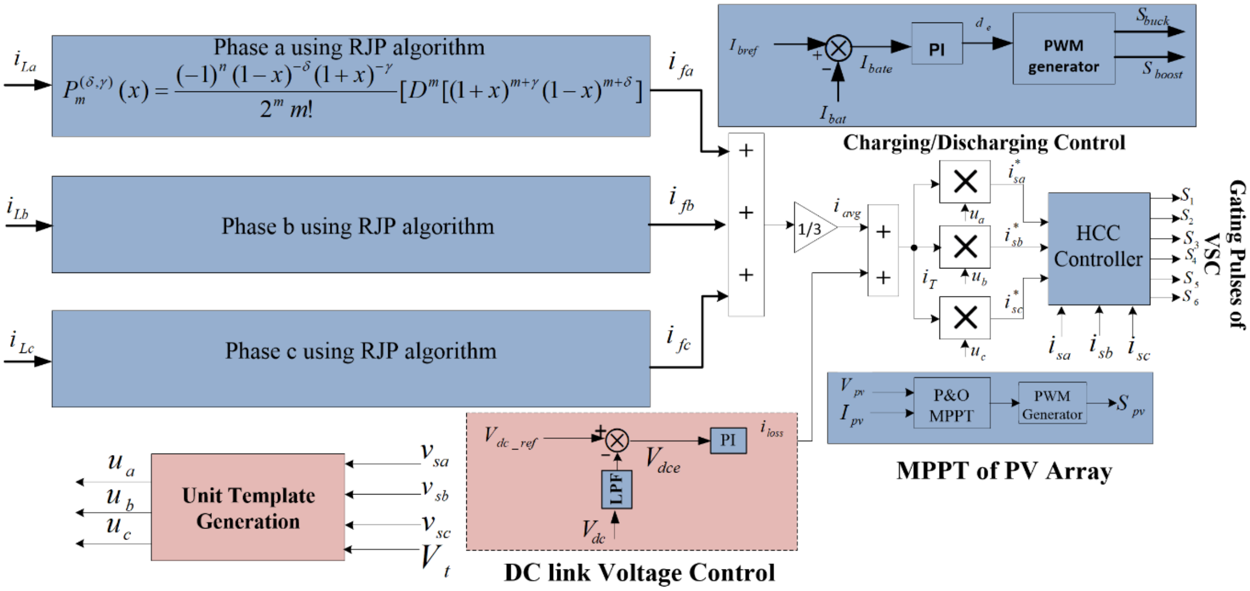

Fig 7.20: Control diagram of RJP algorithm

7.8.1 Control of Three Phase VSC

The proposed RJP algorithm is utilized to control three phase VSC. The six gating pulses (S_1, S_2, S_3, S_4, S_5 and S_6) extracted by combination of Unit templates, the fundamental current component, active loss component, reference currents and hysteresis controller which are shown in Fig 7.20.

The fundamental currents (i_{fa}, i_{fb}, i_{fc}) is extracted by injecting phase load current in RJP controller. The one third of the sum of all fundamental currents is average current (i_{avg}). A DC-link voltage and its reference voltage is compared and fed with PI controller to estimate the current loss component (i_{loss}). The effective total current i_T is the addition of both average fundamental current (i_{avg}) and loss component (i_{loss}). Further, it is multiplied with unit templates (u_a, u_b, u_c) to generate reference currents (i_{sa}^*, i_{sb}^*, i_{sc}^*). The actual supply currents (i_{sa}, i_{sb}, i_{sc}) aa well as reference currents (i_{sa}^*, i_{sb}^*, i_{sc}^*) are now passed in HCC to provide gating pulses of three phase VSC. The VSC with interfacing inductor injects compensating current to improve the grid currents waveform.

7.8.2 Calculation of Fundamental Component of Load Current

The load currents (i_{La}, i_{Lb}, i_{Lc}) is fed with RJP algorithm to extract fundamental weight currents (i_{fa}, i_{fb} and i_{fc}) as given by Eq. (7.11 – 7.13)

$$i_{fa} = [1 + \frac{1}{2}\{2(1+\delta) + (\delta + \gamma + 2)(i_{La} - 1)\}] \tag{7.11}$$

$$i_{fb} = [1 + \frac{1}{2}\{2(1+\delta) + (\delta + \gamma + 2)(i_{Lb} - 1)\}] \tag{7.12}$$

$$i_{fc} = [1 + \frac{1}{2}\{2(1+\delta) + (\delta + \gamma + 2)(i_{Lc} - 1)\}] \tag{7.13}$$

Now, the calculation of average weight current is

$$i_{avg} = \frac{1}{3}(i_{fa} + i_{fb} + i_{fc}) \tag{7.14}$$

7.8.3 Simulation Results of RJP algorithm

The real time simulation results of three phase grid connected EV with / without PV integration at DC link of VSC are discussed as shown in Fig 7.21-7.25. The charging operation is done via DC-DC buck converter and analysed that the smooth waveforms are obtained as shown in Fig 7.21-7.23. The waveforms of three phase voltages (v_{sa}, v_{sb}, v_{sc}), three phase source currents (i_{sa}, i_{sb}, i_{sc}), load currents (i_{La}, i_{Lb}, i_{Lc}), a DC link (V_{dc}) having reference value of 400V, battery voltage (V_{bat}), without PV integrated current of Ipv = 0A and battery current (I_{bat}) under dynamic load condition is shown in Fig 7.21. The I_{bat} is constant at -20A i.e negative sign represents charging behavior of battery. Further, the continuous increasing waveform from 80% is SoC. The dynamic behavior of the system is also analyzed and satisfactory waveforms are found.

The PV are integrated with three phase EV charging systems waveform are shown in Fig 22. The waveforms of three phase voltages (v_{sa}, v_{sb}, v_{sc}), three phase source currents (i_{sa}, i_{sb}, i_{sc}), load currents (i_{La}, i_{Lb}, i_{Lc}) for three phase loads of 5A peak, a DC link voltage (V_{dc}) of 400V, V_{bat}, I_{bat}, PV current (Ipv) are shown in Fig 7.22. The charging operation is observed by increasing nature of SoC. The grid and PV are responsible to charge the battery bank and also support to the nonlinear load. Furthermore, it is found that the quick response in the waveforms during dynamic condition and also maintains sinusoidal waveforms of source current.

The power system in charging mode effectively demonstrates dynamic balance across its components. Initially, a grid power supply P_{grid} of 4 kW is combined with photovoltaic (PV) power Ppv of 2 kW to meet a constant load demand P_L of 1.4 kW. Simultaneously, the compensator

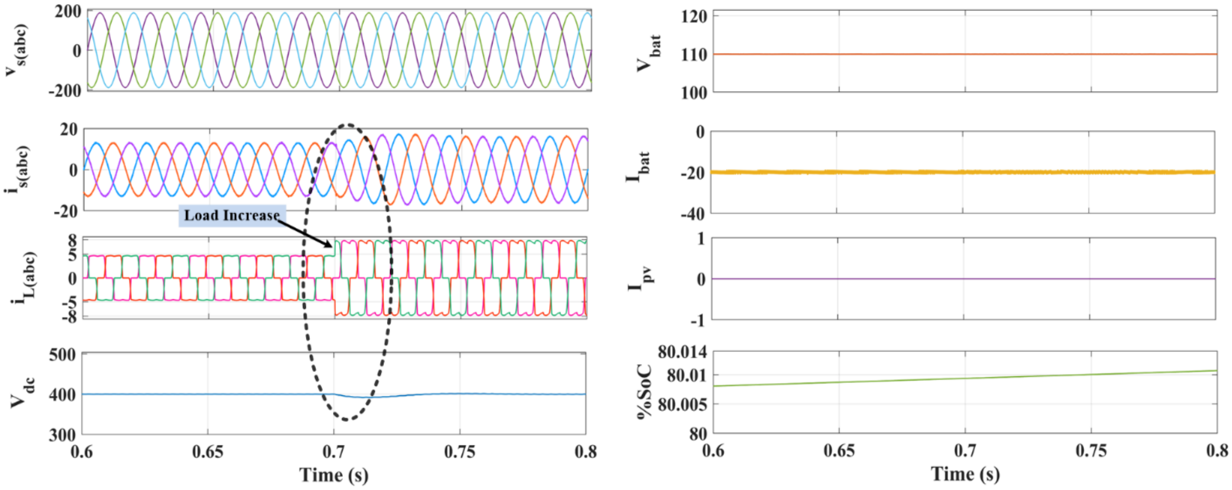

Fig.7.21 Three phase waveform of $V_{s(abc),}$ $I_{s(abc),}$ $I_{L(abc),}$ V_{dc}, V_{bat}, I_{bat}, I_{pv} and %SoC at charging mode (without PV) using RJP.

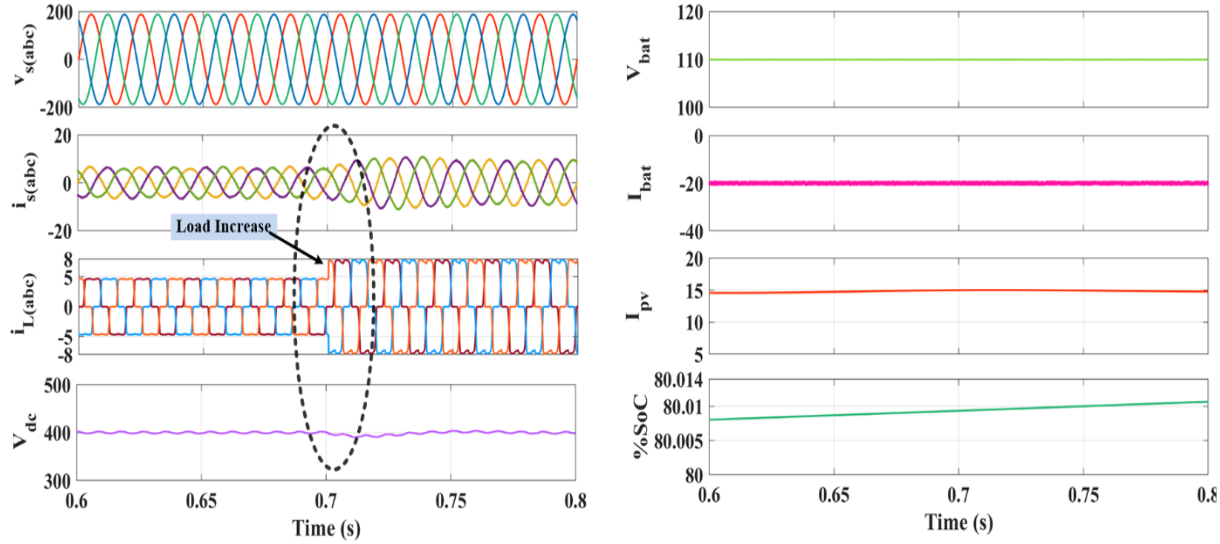

Fig. 7.22 Three phase waveform of $V_{s(abc),}$ $I_{s(abc),}$ $I_{L(abc),}$ V_{dc}, V_{bat}, I_{bat}, I_{pv} and %SoC at charging mode (with PV) using RJP.

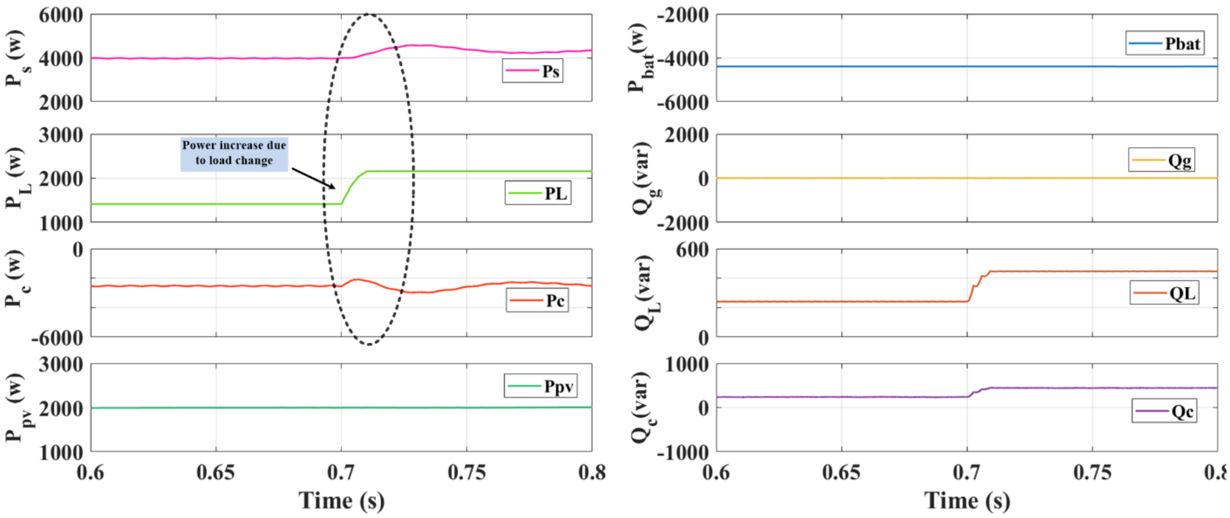

Fig 7.23 Waveform of grid power Pg, load power P_L, compensator power P_c, PV power P_{pv}, battery power P_{bat}, grid reactive power Qg, load reactive power Q_L, compensator reactive power Qc under charging mode using RJP.

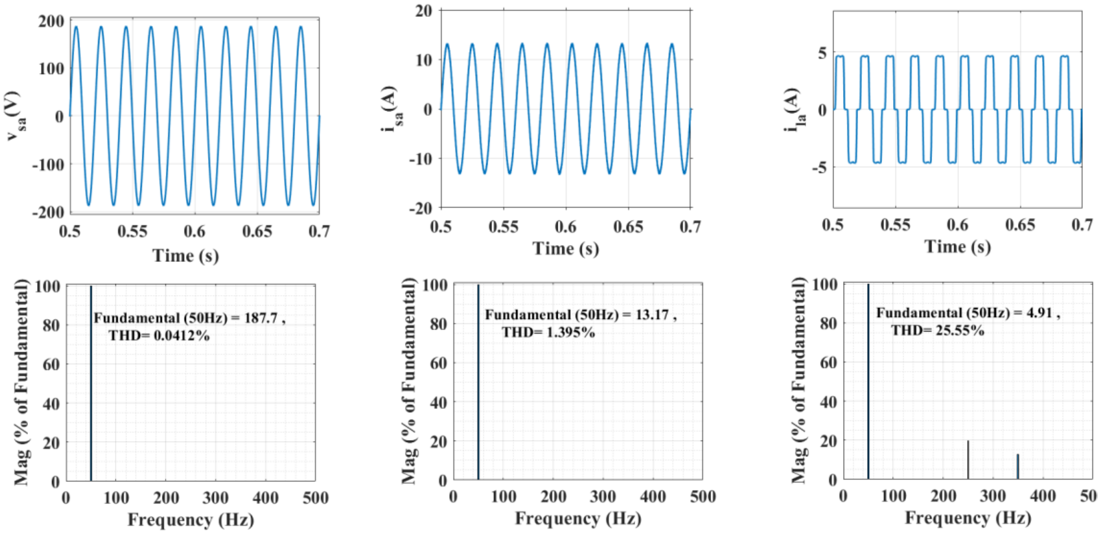

Fig 7.24 Simulation results : Harmonic analysis of a). v_{sa} , THD = 0.0412% b). i_{sa} , THD = 1.395% c). i_L , THD = 25.55% during steady state condition at charging mode using RJP.

provides a power of -2.6 kW to manage system discrepancies, and the battery absorbs energy at a steady rate of -4.4 kW, ensuring efficient charging. Notably, the system maintains zero reactive power Qg supplied by the grid, indicating reactive power neutrality. At 0.7 seconds, a load change occurs, increasing the load power P_L from 1.4 kW to 2.2 kW. The system rebalances by adjusting P_{grid} to 4.5 kW while reactive power Q_L is balanced at 450 VAR for both load and compensator. These transitions highlight the system's capability to dynamically adapt while maintaining stability.In addition, when the load changes at 0.7 seconds, significant shifts occur in the system's power distribution. The power injected into the grid decreases from -4.6 kW to -4 kW, reflecting a reduced reliance on grid support for system balance. The load power P_L increases from 1.4 kW to 2.2 kW, while the compensator power Pc remains constant at 6 kW, ensuring consistent stabilization. The battery power adjusts slightly to 4.3 kW, complementing the system's needs for stability. Photovoltaic power Ppv remains constant at 2 kW throughout the operation, contributing to sustainable energy integration. Reactive power remains consistently balanced across the load, source, and compensator. Fig. 7.23 illustrates the robustness of the system in dynamically managing power flow while maintaining a seamless balance under varying operational conditions.

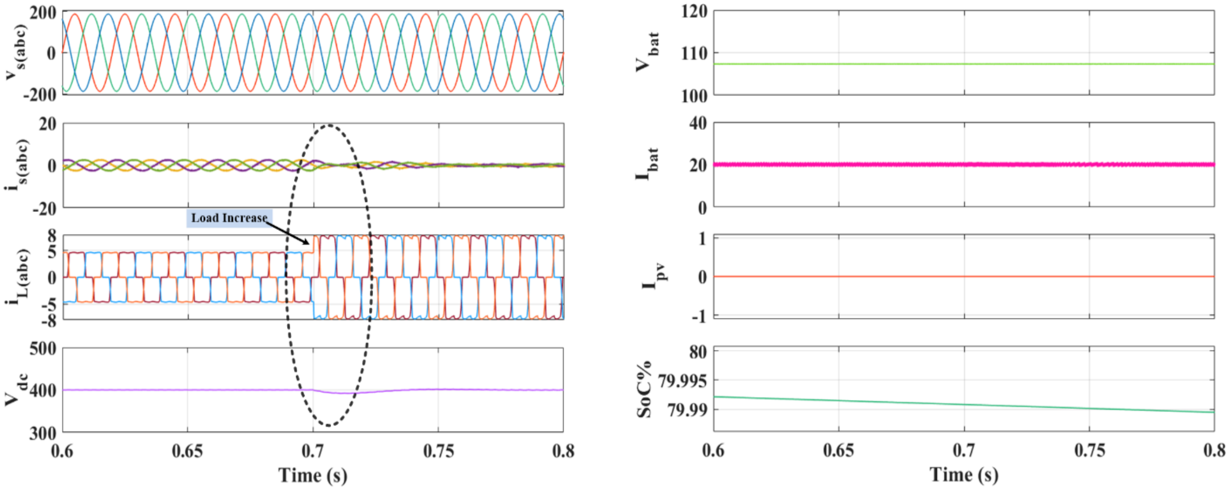

Fig.7.25 Three phase waveform of $v_{s(abc)}$, $i_{s(abc)}$, $i_{L(abc)}$,V_{dc},V_{bat}, I_{bat}, I_{pv} and %SoC at discharging mode (without PV) using RJP.

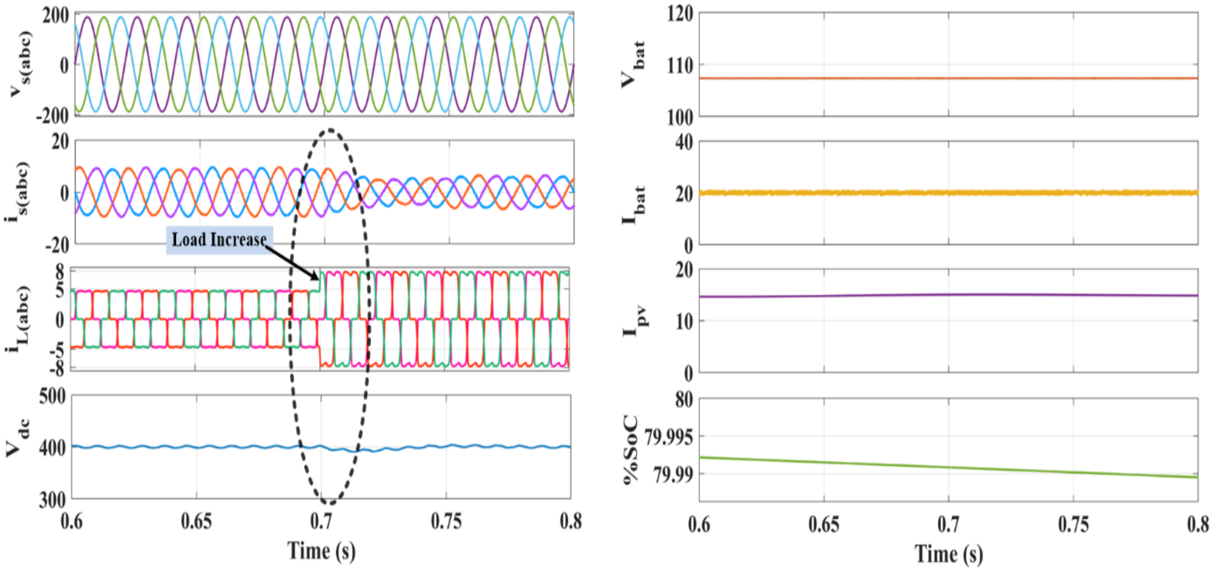

Fig.7.26 Three phase waveform of $V_{s(abc)}$, $I_{s(abc)}$, $I_{L(abc)}$, V_{dc},V_{bat}, I_{bat}, I_{pv} and %SoC at discharging mode (with PV) using RJP.

Charging of the EV battery can be clearly depicted from the waveforms such that in-phase operation of the source voltage and source current. Furthermore, the THDs of the voltage source, source current and load current are 0.0412%, 1.395% and 25.55% respectively as shown in Fig. 7.24. Also, the THD of the source current is within the IEEE standards (i.e <5%).

Similarly, the without PV connected waveforms are observed like Fig. 7.16. The difference is that the battery bank with DC-DC boost converter is responsible to supply power to load and surplus power injected to the grid during discharging operation as shown in Fig. 7.25. The dynamic response is analysed and observed that the battery supports the load and the grid during V2G mode. Here, the similar waveforms like Fig. 7.17 are shown. The discharging nature waveforms of grid connected EV and PV are presented in Fig. 7.26. The positive polarity of 20A battery current represents a system operate in V2G mode. The PV is always injecting power in proposed system which are connected at DC link of VSC.

The system's dynamic behavior underscores the need for robust control strategies to manage the fluctuations in power generation and absorption during discharging operation. A more responsive and intelligent compensator at the Point of Common Coupling (PCC) could significantly enhance system performance. In addition, approx. 6kW power of compensator is distributed to load (≈1.4kW) and grid (≈4.5kW) as shown in Fig. 7.27. By integrating predictive algorithms, the compensator could preemptively manage power imbalances, ensuring a seamless energy transfer between the grid, the load, and storage systems. Additionally, real-time monitoring of load

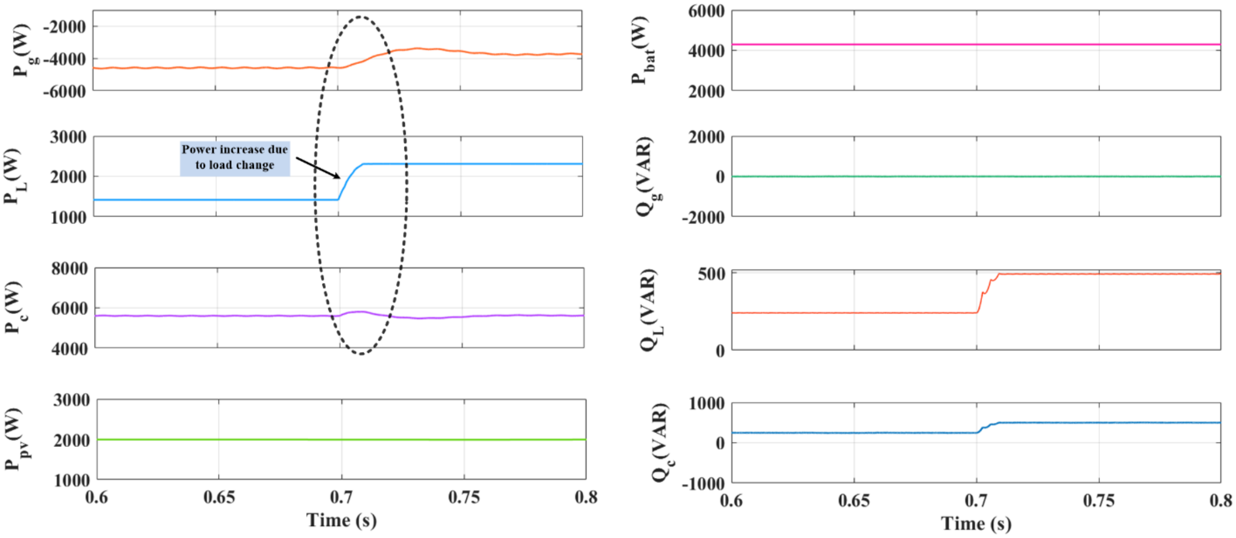

Fig.7.27 Waveform of grid power P_g, load power P_L, compensator power P_c, PV power P_{pv}, battery power P_{bat}, grid reactive power Q_g, load reactive power Q_L, compensator reactive power Q_c under discharging mode using RJP.

demands and grid conditions could allow for adaptive power redistribution, further minimizing transient fluctuations and maintaining grid stability under varying operating conditions.

The discharging mode of operation of the EV battery results in the out-phase with the source current and source voltage. The Fig. 7.28 shows that the THD of v_{sa}, i_{sa} and i_{La} during discharging of the EV battery is 0.04%, 6.98% and 25.66% respectively.

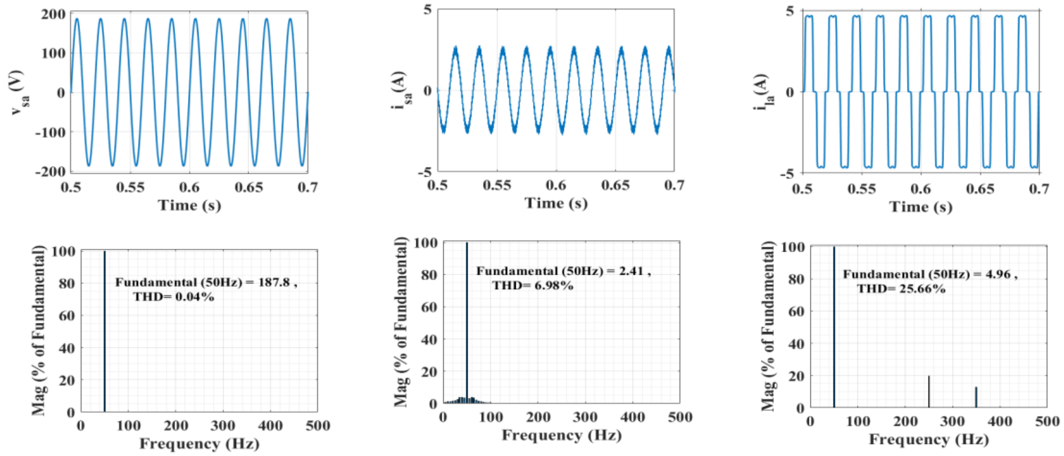

Fig 7.28 Simulation results : Harmonic analysis of a). v_{sa} , THD = 0.04% b). i_{sa} , THD = 6.98% c). i_L , THD = 25.66% during steady state condition at discharging mode using RJP.

7.9 Comparative Analysis of SOGI, RJP and LMS Control Algorithms

The comparative analysis of the proposed controller with SOGI and RJP algorithms is shown in Fig 7.29. When the load current is increased and decreased at 0.8s and 1s respectively it is observed

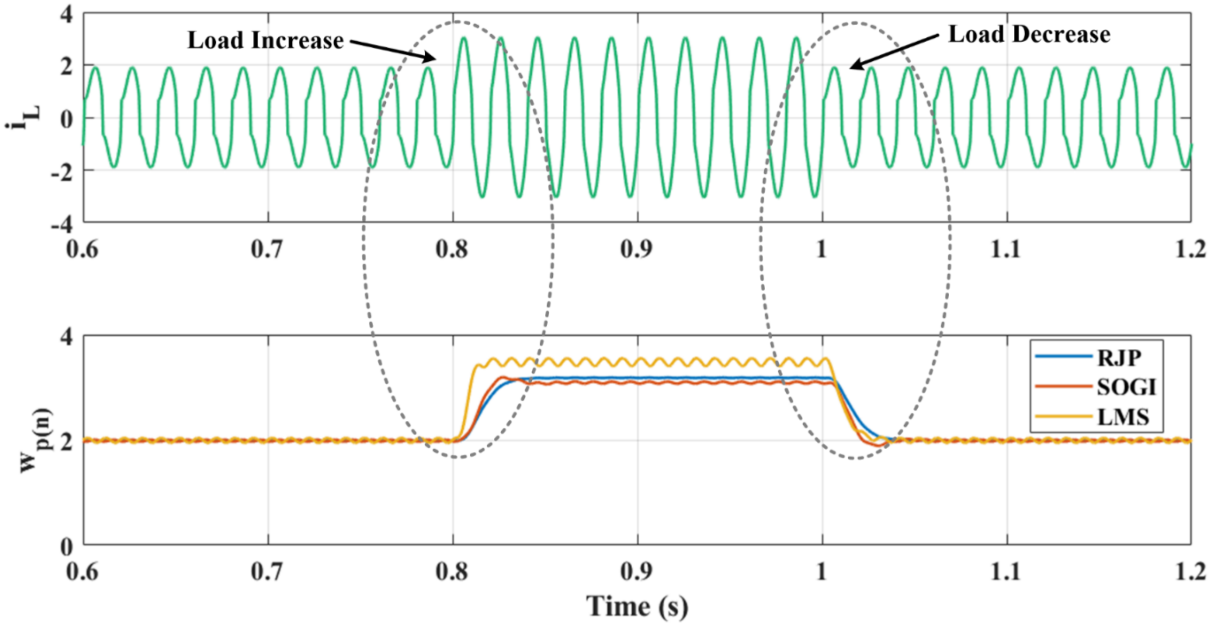

Fig. 7.29 Comparative waveforms of load current (i_L), with fundamental current (i_{fa}) at different algorithms

that the fundamental currents extracted by SOGI and LMS algorithms are oscillating in nature. But Rodrigues Jacobi Polynomial (RJP) algorithm extracts oscillation free i_{fa} and satisfactory results are obtained. The % THD analysis of SOGI, LMS and RJP algorithm are shown in Table 7.1 and Table 7.2 respectively during charging and discharging condition. It is observed that the THD of RJP algorithm is less in comparison to SOGI and LMS algorithm.

Table 7.1: % THD analysis of SOGI, LMS and RJP algorithm during charging condition

Algorithms	**%T.H.D (v_s)**	**%T.H.D (i_s)**	**%T.H.D (i_L)**
SOGI	0.04	1.44	25.60
LMS	0.0412	4.41	25.23
RJP	**0.0412**	**1.395**	**25.55**

Table 7.2: % THD analysis of SOGI, LMS and RJP algorithm during discharging condition

Algorithms	**%T.H.D (v_s)**	**%T.H.D (i_s)**	**%T.H.D (i_L)**
SOGI	0.04	7.50	25.61
LMS	0.04	7.63	25.615
RJP	**0.04**	**6.98**	**25.66**

7.10 Conclusion

This chapter discusses three phase grid connected PV-EV system. A MATLAB model is developed and the system is analyzed using three algorithms namely Rodrigues Jacobi Polynomial (RJP), Least Mean Square (LMS) and Second Order Generalized Integrator (SOGI). The G2V and V2G mode of operation are also demonstrated. From the comparative section it can be inferred that the RJP controller is more robust and effective as compared to LMS and SOGI controller. The results using Simulink supports this conclusion.

Chapter 8

Single Phase Grid Connected Reduced Switch Five Level Inverter (RSFLI) with Solar PV and EV Charging System

---

In this chapter, implementation of single phase grid connected Reduced Switch Multilevel Inverter (RSFLI) with PV and EV charging system is presented. The integration of PV and EV to the grid in single-phase system with simulation waveforms is also summarized in this chapter. The results are validated using OPAL-RT and captured using MSO.

8.1 Introduction

Fig. 8.1 shows the complete system block having a combination of RSFLI inverter, bidirectional DC-DC converter, non-linear load, utility grid and renewable source like PV array. The grid is modeled as a sinusoidal voltage source (v_s) having grid impedance (L_s), which feeds non-linear load having load resistance (R_L) and inductance (X_L) at the full output of wave bridge rectifier DC side. The proposed RSFLI is interfaced to the grid via interfacing inductor (L_i) at PCC.

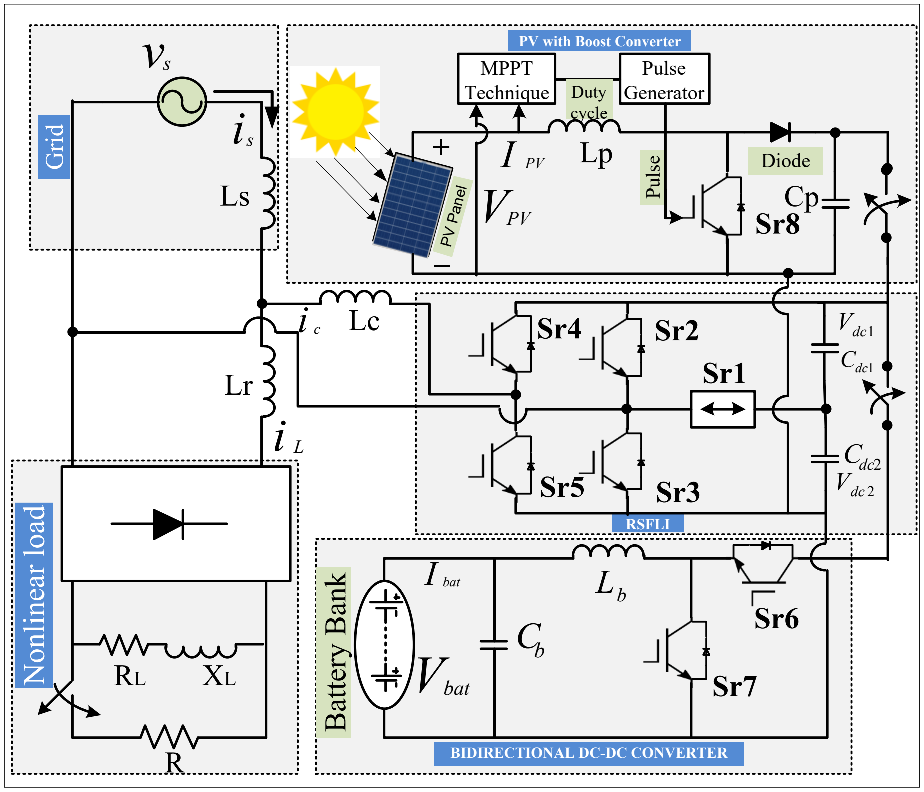

Fig. 8.1 System Configuration of proposed RSFLI

The novel RSFLI inverter is controlled to inject compensating current (i_c) at PCC to improve the power quality of source current (i_s). The proposed converter configuration shows five switches (S_{r1}, S_{r2}, S_{r3}, S_{r4} and S_{r5}) and two DC link capacitors (C_{dc1}, C_{dc2}). The switch S_{r1} is a bidirectional switch and remaining four switches are Insulated Gate Bipolar Transistor (IGBT) switches. The bidirectional DC-DC converter section comprises EV battery voltage (V_{bat}), with filter inductor (L_b), capacitor (C_b) and two IGBT switches (S_{r6}, S_{r7}). This section is responsible for charging and discharging of the EV battery. Additionally, the solar photovoltaic array supplies voltage (V_{pv}) and current (I_{pv}) through boost converter and the switch (S_{r8}) is controlled by Perturb and Observe MPPT technique. The PV array with a boost converter is also connected at DC link of RSFLI to deliver power either to the load, grid or to the battery bank for charging as per the desired need and available conditions. The parameters are shown in Appendix E.

8.2 Modelling of Reduced Switch Five Level Inverter (RSFLI)

In this section, modeling of RSFLI is shown and calculation related to transfer function, modes of operation of RSFLI are discussed in detail.

8.2.1 Configuration and Mathematical Modelling of Proposed RSFLI

The small signal analysis is used to derive a linear model of RSFLI and also the transfer function of the proposed inverter configuration. It is assumed that the system is in steady state condition to develop the linear model of RSFLI. The RSFLI is as shown in Fig 8.2. The transfer function for proposed inverter configuration is defined as the ratio of DC link output (V_{dc}) to the input current (i_c) of RSFLI inverter. The average rate of the power exchange is calculated in between input (AC side) to the output (DC link side) of the RSFLI.

According to Fig 8.2, by equating the average rate of change of energy in RSFLI across interfacing inductor (P_{Lc}), capacitor (P_{Cdc}) and DC link capacitor gives [285]

$$P_{Cdc} = P_{RCFLI} - P_{Lc} - P_{Rc} \tag{8.1}$$

where, P_{Cdc} is the total rate of change of energy absorbed in capacitor, P_{RSFLI} denotes the Reduced Switch Five Level Inverter power input, P_{Lc} is the rate of energy absorbed in interfacing inductor and P_{Rc} is the power loss across resistance.

Total power across DC link capacitance is

$$P_{Cdc} = [P_{Cdc1} + P_{Cdc2}] \tag{8.2}$$

$$P_{Cdc1} = \frac{d}{dt}[\frac{1}{2} C_{dc1} V_{dc1}^2] \tag{8.3}$$

$$P_{Cdc2} = \frac{d}{dt}[\frac{1}{2}C_{dc2}V_{dc2}^2] \tag{8.4}$$

$$\therefore P_{Cdc} = \frac{1}{2}\mathrm{C}_{dc}\mathrm{V}_{dc}\frac{\mathrm{d}}{\mathrm{dt}}\mathrm{V}_{dc} \tag{8.5}$$

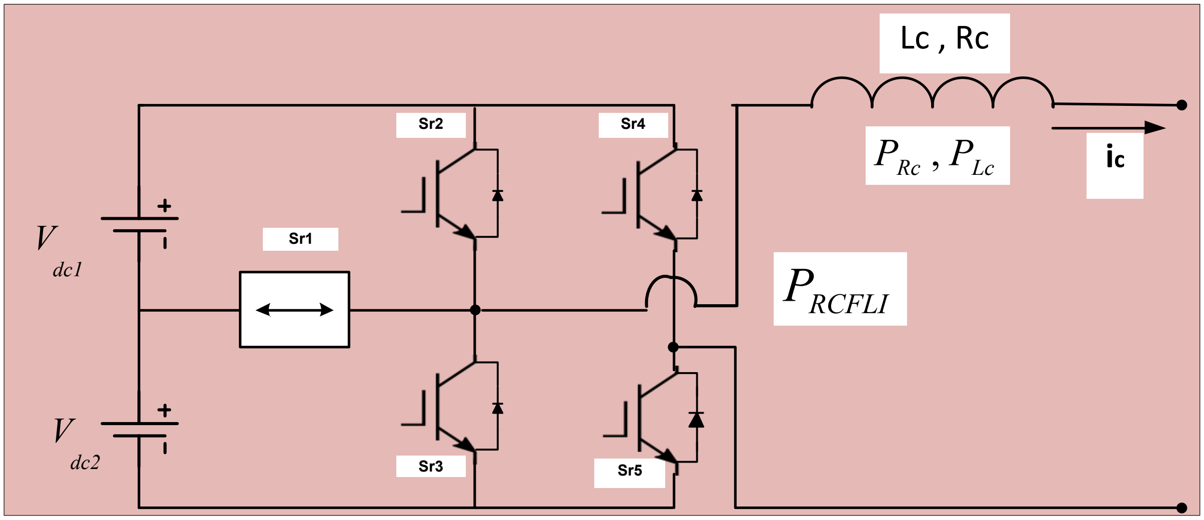

Fig. 8.2: Configuration of the reduced switch five level converter.

where, the DC link capacitance is assumed to be same [$C_{dc1} = C_{dc2} = C_{dc}$] and the DC link voltage across each capacitance is half of the voltage DC link [$V_{dc1} = V_{dc2} = V_{dc}/2$].

The RSFLI power input is,

$$P_{RCFLI} = v_s i_c \tag{8.6}$$

The power loss across resistance is,

$$P_{Rc} = i_c^2 R_c \tag{8.7}$$

The power absorbed across interfacing inductor is

$$P_{Lc} = \frac{d}{dt}[\frac{1}{2}L_c i_c^2] \tag{8.8}$$

Putting these values from Eq. 8.6-8.8 in Eq. 8.1 gives

$$\frac{1}{2}\mathrm{C}_{dc}\mathrm{V}_{dc}\frac{\mathrm{d}}{\mathrm{dt}}\mathrm{V}_{dc} = [\mathrm{v}_s\mathrm{i}_c - \mathrm{i}_c^2\mathrm{R}_c - \mathrm{L}_c\mathrm{i}_c\frac{\mathrm{d}}{\mathrm{dt}}\mathrm{i}_c] \tag{8.9}$$

A small disturbance is applied to the input converter current (Δi_c) to linearize the power equation. Assume the DC link voltage is also disturbed by a small voltage ΔV_{dc}.

Replacing $i_c = i_{co} + \Delta i_c$ and $V_{dc} = V_{dco} + \Delta V_{dc}$ and neglecting higher order terms in Eq. (8.9).

$$\frac{1}{2}\mathrm{C}_{dc}\mathrm{V}_{dco}\frac{\mathrm{d}}{\mathrm{dt}}\Delta\mathrm{V}_{dc} = [\mathrm{v}_s\mathrm{i}_{co} + \mathrm{v}_s\Delta\mathrm{i}_c - \mathrm{i}_{co}^2\mathrm{R}_c - 2i_{co}\Delta i_c R_c - \mathrm{L}_c\mathrm{i}_{co}\frac{\mathrm{d}}{\mathrm{dt}}\Delta\mathrm{i}_c] \tag{8.10}$$

where, i_{co} and V_{dco} denote the operating point under steady state condition.

Under steady state condition, the Eq. 8.10 is written as

$$C_{dc}V_{dco}\frac{d}{dt}\Delta V_{dc} = 2[v_s\Delta i_c - 2i_{co}\Delta i_c R_c - L_c i_{co}\frac{d}{dt}\Delta i_c] \tag{8.11}$$

Taking Laplace Transform of Eq. 8.11 results in

$$C_{dc}V_{dco}s\Delta V_{dc} = 2[v_s\Delta i_c - 2i_{co}\Delta i_c R_c - L_c i_{co}s\Delta i_c] \tag{8.12}$$

The transfer function of RSFLI (G_{TF}) is

$$G_{TF} = \frac{\Delta V_{dc}}{\Delta i_c} = \frac{2[v_s - 2i_{co}R_c - L_c i_{co}s]}{[C_{dc}V_{dco}s]} \tag{8.13}$$

On putting the values of R_c,L_c, C_{dc}, v_s in Eq 8.13 is

$$G_{TF} = \frac{\Delta V_{dc}}{\Delta i_c} = [\frac{454 - 0.05s}{s}] \tag{8.14}$$

8.2.2 Switching operation of RSFLI

In the RSFLI, five number of switches (S_{r1}, Sr_2, S_{r3}, S_{r4} and S_{r5}) are used, which is less in comparison to the eight switches used in the cascaded H-bridge inverter. The RSFLI topology uses a single bidirectional switch Sr_1 and four IGBT switches (S_{r2}, S_{r3}, S_{r4} and S_{r5}). The switching operation of RSFLI is shown in Table 8.1.

Table 8.1: Switching operation of RSFLI

Steps	Conducting Switches 1 = ON ; 0 = OFF					Output Voltage $V_{dc1}= V_{dc2}= V_{dc}$
	Sr_1	Sr_2	Sr_3	Sr_4	Sr_5	
1	0	1	0	0	1	$+2V_{dc}$(step 1)
2	1	0	0	0	1	$+1V_{dc}$(step 2)
3	0	0	1	0	1	$0V_{dc}$(step 3)
4	1	0	0	1	0	$-1V_{dc}$(step 4)
5	0	0	1	1	0	$-2V_{dc}$(step 5)

The five steps of operation of RSFLI are discussed with layout diagram shown in Fig. 8.3.

Step1: To obtain maximum voltage output ($+2V_{dc}$) as per Fig 8.3 (a), the switches S_{r2} and S_{r5} are turned ON and remaining switches S_{r1}, S_{r3}, S_{r4} are turned OFF.

Step2: To obtain voltage output of $+V_{dc}$ as discussed in Fig 8.3(b), the switches S_{r1}, S_{r5} are turned ON and remaining switches S_{r2}, S_{r3}, S_{r4} are turned OFF.

Step3: To obtain voltage output of $0V_{dc}$ as per discuss in Fig 8.3(c), the switches S_{r3}, S_{r5} are turned ON and remaining switches S_{r1}, S_{r2}, S_{r4} turned OFF.

Step4: To obtain voltage output of -V_{dc} as per discuss in Fig 8.3(d), the switches S_{r1}, S_{r4} are turned ON and remaining switches S_{r2}, S_{r3}, S_{r5} are turned OFF.

Step5: To obtain voltage output of -2V_{dc} as per discuss in Fig 8.3(e), the switches S_{r3}, S_{r4} are turned ON and remaining switches S_{r1}, S_{r2}, S_{r5} are turned OFF.

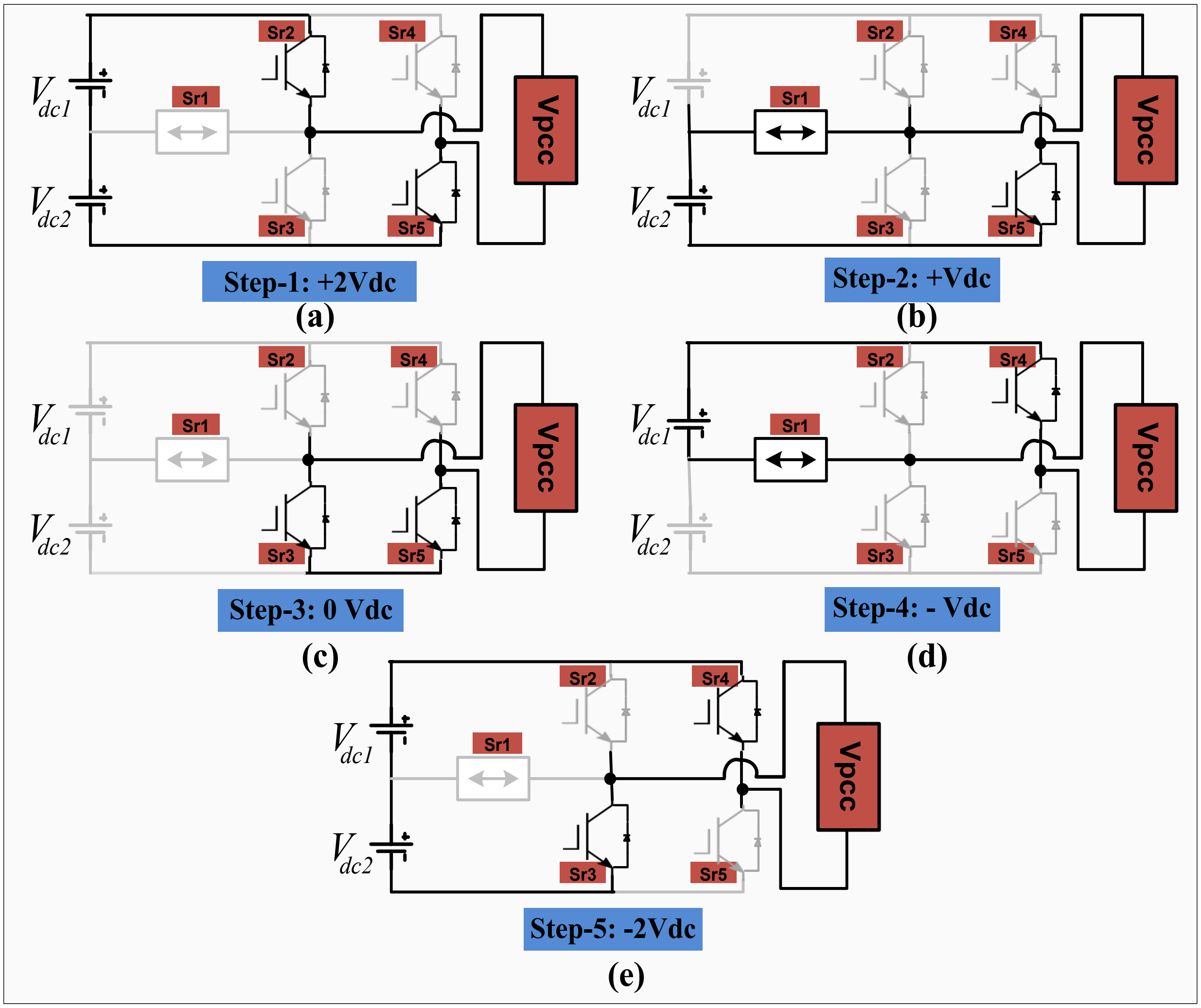

Fig. 8.3: Different modes of operation of RSFLI

8.3 Control Structure of Single Phase Grid Interfaced RSFLI With Solar PV and EV Charging Systems

Fig. 8.4 (a-c) shows the control structure of the complete system. In this section, the control of RSFLI inverter, control of bidirectional DC-DC converter and control of Solar PV array are discussed in detail. Also, the calculation of unit template, fundamental current magnitude, loss current magnitude, generation of reference current and gating signals are discussed in detail.

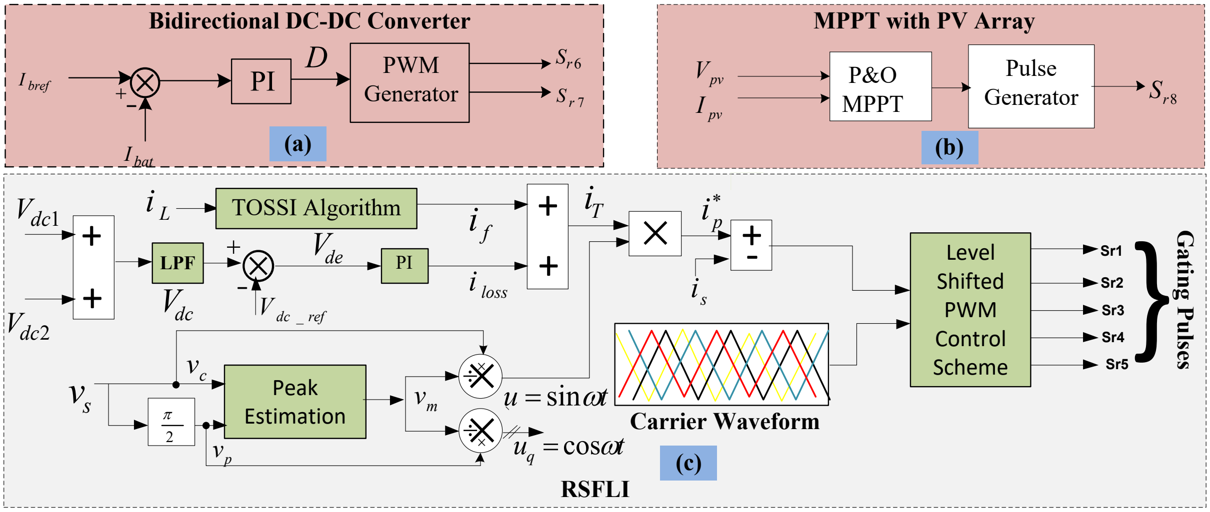

Fig. 8.4 Control of RSFLI with PV and EV systems

8.3.1 Control of RSFLI:

The control strategy of proposed RSFLI converter is shown in Fig. 8.4(c). The fundamental current is estimated with the help of TOSSI algorithm and loss current magnitude is calculated by comparing the sum of two DC link voltages (V_{dc1},V_{dc2}) with reference voltage of 400 V. The sum of these components (i_f and i_{loss}) is multiplied with unit template to obtain reference current (i_{ref}). Now, the difference of reference current (i_{ref}) and source current (i_s) is compared with triangular carrier waveform by a level shifted pulse width modulation control scheme so as to generate five gating pulses to control RSFLI. Below is the description of estimation of fundamental current, loss current, unit template, reference current and generation of gating signals in detail.

8.3.1.1 Estimation of Fundamental Current using TOSSI Algorithm

The circuit diagram of TOSSI algorithm to extract fundamental current (i_f) as shown in Fig. 8.5. The load current (i_L) is passed through the Third Order Generalised Integrator (TOSSI) block to extract two orthogonal components. One component is in-phase current (i_α) and another one is quadrature current (i_β) [286].

Two tuning parameters are required for this filter which are selected to be g_1=1.2, g_2=2.5 with damping factor ξ=0.707. The relation between the input load current (i_L), in-phase current (i_α) and quadrature current (i_β) in terms of transfer function are shown in Eq 8.15-8.16.

$$T_\alpha(s) = \frac{i_\alpha}{i_L} = \frac{g_1\omega^2 s}{s^3 + g_2\omega s^2 + (1+g_1)\omega^2 s + g_2\omega^3} \tag{8.15}$$

$$T_\beta(s) = \frac{i_\beta}{i_L} = \frac{g_1\omega^3}{s^3 + g_2\omega s^2 + (1+g_1)\omega^2 s + g_2\omega^3} \tag{8.16}$$

The amplitude of fundamental current (i$_f$) is calculated as Eq. 8.17.

$$i_f = \sqrt{i_\alpha^2 + i_\beta^2} \tag{8.17}$$

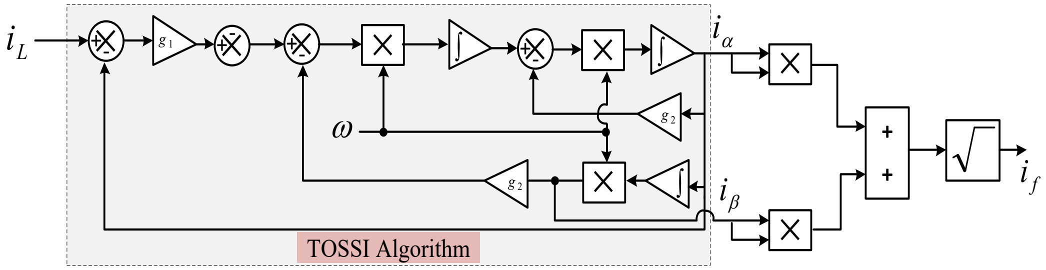

Fig. 8.5: Extraction of Fundamental Current Component using TOSSI Algorithm

8.3.1.2 Generation of Loss Current

The sum of both DC link voltage $V_{dc1}; V_{dc2}$ ($i.e\ V_{dc} = V_{dc1} + V_{dc2}$) is passed through a low pass filter to compute V_{dc}as shown in Fig. 8.4 (c).

The comparison of both DC-link voltage V_{dc} and DC-link reference voltage V_{dc_ref} generates error V_{dce} as per Eq. (8.18). The errorV_{dce} is now fed into the Proportional Integral (PI) controller, which calculates the loss component i_{loss} using Eq. (8.19).

$$V_{dce} = V_{dc\_ref} - V_{dc} \tag{8.18}$$

$$i_{loss} = i_L(n) + [k_P\{V_{dce}(n+1) - V_{dce}(n)\} + k_i\{V_{dce}(n+1)\}] \tag{8.19}$$

8.3.1.3 Calculation of Unit Templates

The source voltage (v$_s$) and its quadrature phase shifted component as shown in Fig 8.6 are passed through peak estimation block to calculation peak voltage v_m as per Eq. 8.20-8.22.

$$v_s = v_m sin\omega t \tag{8.20}$$

$$v_{\mathrm{p}} = v_m(sin\omega t + \frac{\pi}{2}) \tag{8.21}$$

Now, the peak voltage is,

$$\therefore V_m = \sqrt{v_{\mathrm{p}}^2 + v_s^2} = V_t \tag{8.22}$$

These two components are fed with peak voltage to generate unit template u(n) as shown in Eq. 8.23. Now, the unit template is computed as,

$$u(n) = \frac{v_s}{V_m} = sin\omega t \tag{8.23}$$

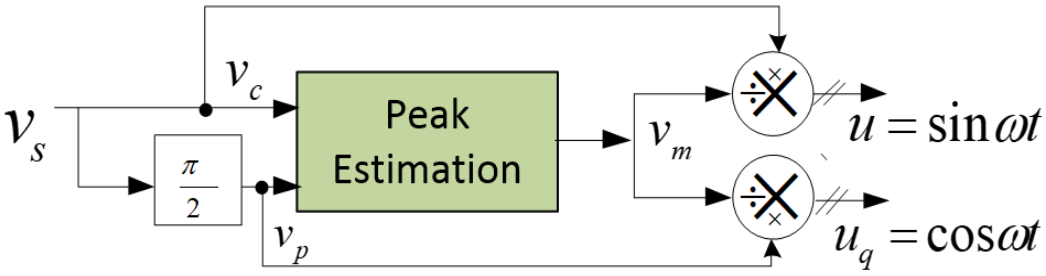

Fig. 8.6 Generation of unit template.

8.3.1.4 Estimation of Reference Current and Pulse Generation

The TOSSI algorithm's extracted fundamental current component is now added with fundamental DC current loss component. In order to observe effective current component (i_T) which is needed to generate reference current.

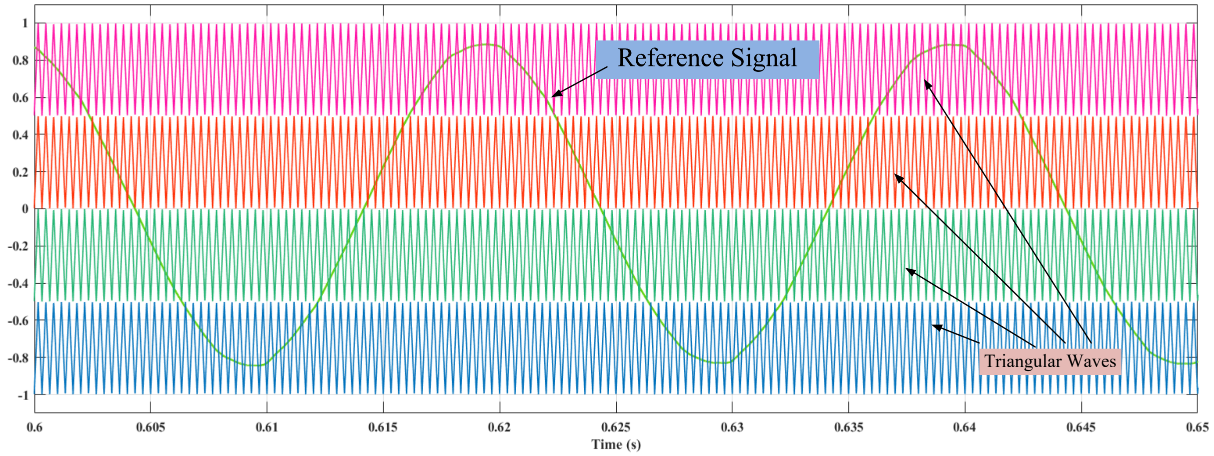

(a). LS-PWM control techniques

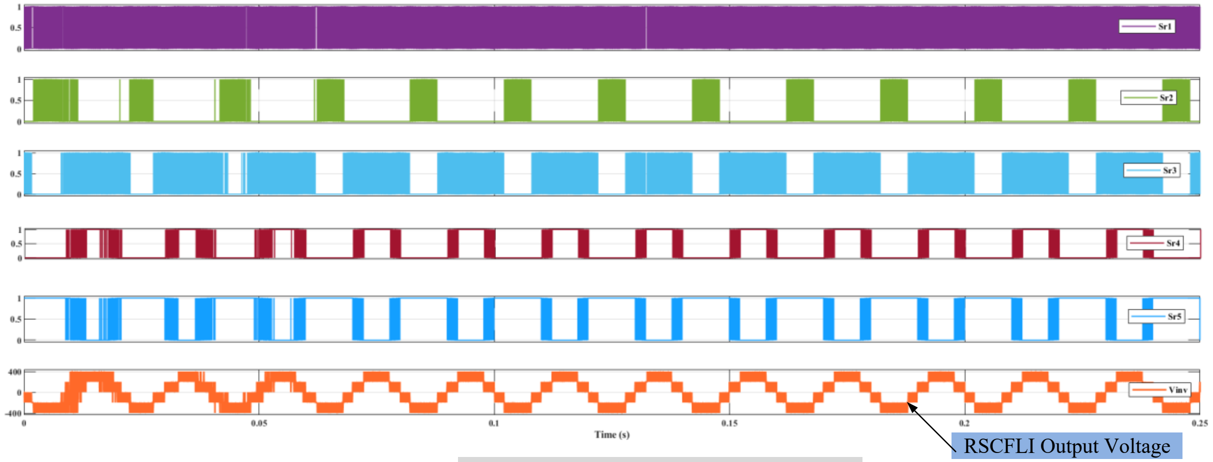

(b). Pulses of RSCFLI and Inverter Voltage Output

Fig. 8.7: waveform of (a). LS-PWM control technique and (b). Pulses of RSFLI with output five level inverter voltage

$$i_T = i_f + i_{loss} \tag{8.24}$$

$$i_{ref} = i_T * u(n) \tag{8.25}$$

The reference current i_{ref} is obtained by multiplying the effective current component i_T by the unit template u(n). In order to regulate the RSFLI, five switching pulses are generated by comparing the reference current (i_{ref}) with a triangle signal fed by level shift PWM techniques. The waveform of the level-shifted PWM control techniques and gating pulses of RSFLI with five level output inverter voltage are shown in Fig. 8.7(a–b).

8.3.2 Control of Bidirectional DC-DC Converter

The EV's battery charging and discharging control mechanism is depicted in Fig. 8.4 (a) The PI controller processes the error (I_{bate}) that results from the calculation of the difference between the reference battery current (I_{bref}) and the actual battery current (I_{bat}) as shown in Eq.26.Two gating pulses are produced by the PWM generator block, which receives the input from the PI controller. The battery is charged by one pulse, known as the S_{r6} pulse, and discharged by another pulse, known as the S_{r7} pulse. Bidirectional Buck Boost Converter is used to connect the PV array and batteries to the DC link. The two modes of operation for the bidirectional converter are boost mode and buck mode, which are for charging and discharging, respectively.

$$I_{bate} = I_{bref} - I_{bat} \tag{8.26}$$

8.3.3 Control of Solar PV Array

Fig. 8.4(b) displays the MPPT control diagram with solar PV array. The 700 W PV array is connected to the VSC's DC link via a boost converter. To get the most power out of the PV array, the Perturb and Observe (P&O) MPPT algorithm regulates the duty cycle of the DC-DC boost converter.

8.4 Simulation Results of Single Phase Grid Interfaced RSFLI with Solar PV and EV Charging Systems

The simulation results of dynamic state waveforms and %THD are discuss in detail.

a). Charging Operation/G2V mode

Fig 8.8 depicts the behaviour of the system during charging conditions using the Third Order Sinusoidal Integrator (TOSSI) controller based controller. It shows the waveforms of the source voltage (v_s) with source current (i_s), nonlinear load current (i_L), compensating current via active filter (i_c), DC link voltage (V_{dc}), fundamental current (i_f), reference current (i_{ref}), PV current (I_{pv}), battery current (I_{bat}) and battery voltage (V_{bat}) during G2V mode. The effect of load disturbance on controller

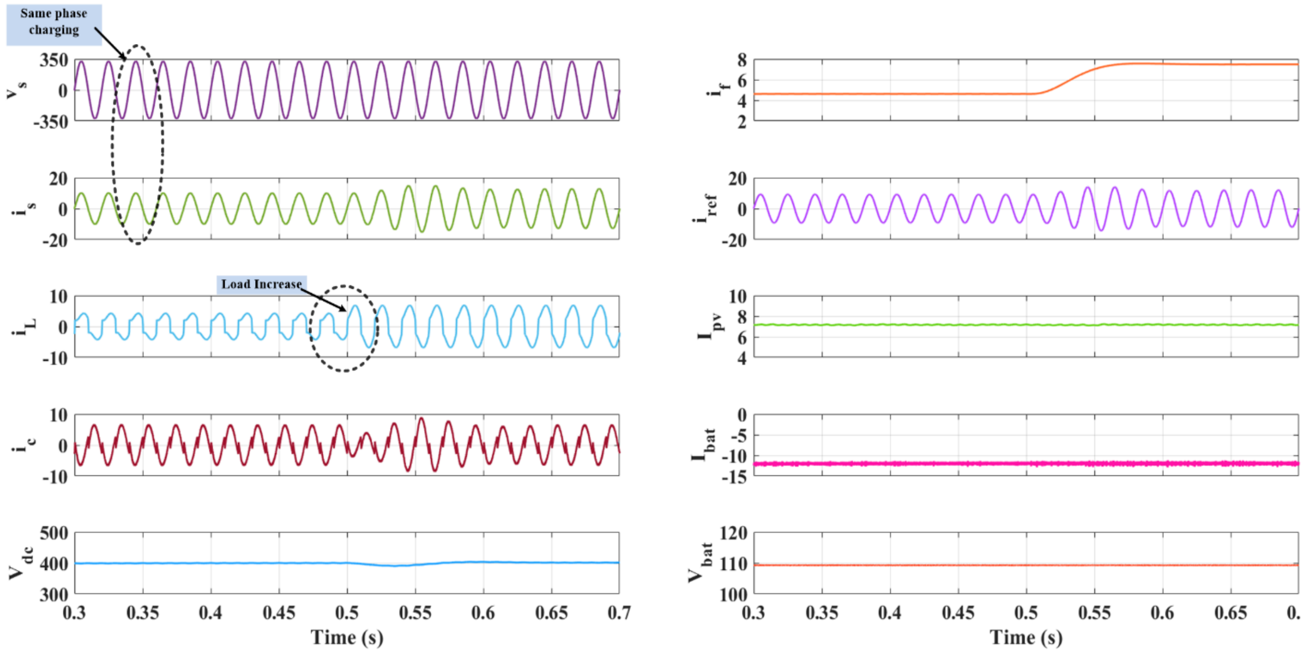

Fig.8.8 Simulation results of $v_s, i_s, i_L, i_c, V_{dc}, i_f, i_{ref}, I_{pv}, I_{bat}$ and V_{bat} at charging mode.

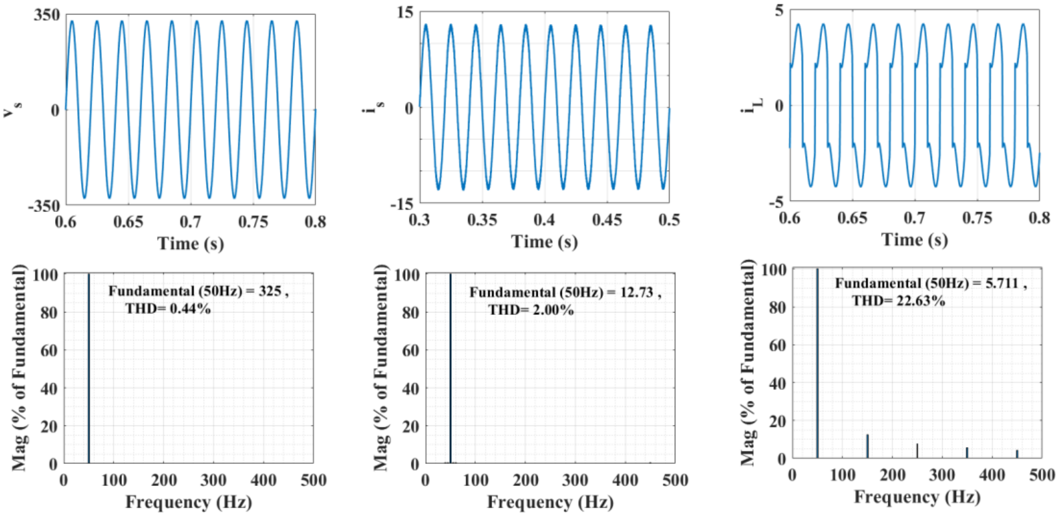

Fig 8.9 Simulation results : Harmonic analysis of a). v_s , THD = 0.044% b). i_s , THD = 2.00% c). i_L , THD = 22.63% during steady state condition at charging mode.

performance is also investigated during charging operation. The load is raised from 5A to 8A at t=0.5s time. The source current (i_s), fundamental current (i_f) and reference current (i_{ref}) also increases but source voltage (v_s) remains same. The small transient dip is observed in the DC-link voltage (V_{dc}) due to load variations but the PI controller stabilises it back to the reference value of 400V.

Furthermore, during charging mode, the source current stays sinusoidal nature and same phase with the source voltage, showing the efficiency of TOSSI control mechanism under dynamic load conditions. Also, the battery voltage slowly charges at 96V and the battery current (I_{bat}) remains same to -12A. The PV also support to load, battery, grid and the current of PV (I_{pv}) is 7A.

The analysis of the THD profiles is shown in Fig. 8.9 across the source voltage (v_s) exhibits harmonic performance with a negligible THD of 0.44%. The source current (i_s) shows a THD of 2.00% which reflecting good harmonic quality. In contrast, the load current displays significant distortion with a THD of 22.63%.

b). Discharging Operation/ V2G mode

Fig 8.10 depicts the dynamic behaviour of the system during discharging conditions using the proposed controller. It shows the waveforms of the source voltage (v_s) with source current (i_s), nonlinear load current (i_L), compensating current via active filter (i_c), DC link voltage (V_{dc}), fundamental current (i_f), reference current (i_{ref}), PV current (I_{pv}), battery current (I_{bat}) and battery voltage (V_{bat}) during discharging mode.

Similar to charging operation, the requirement of load current is changed from 5A to 8A, which is fulfilled by EV (battery) and additional current is injected back into the grid. It is noted that, the supply current and supply voltage are not in phase during discharging operation. The tunned PI

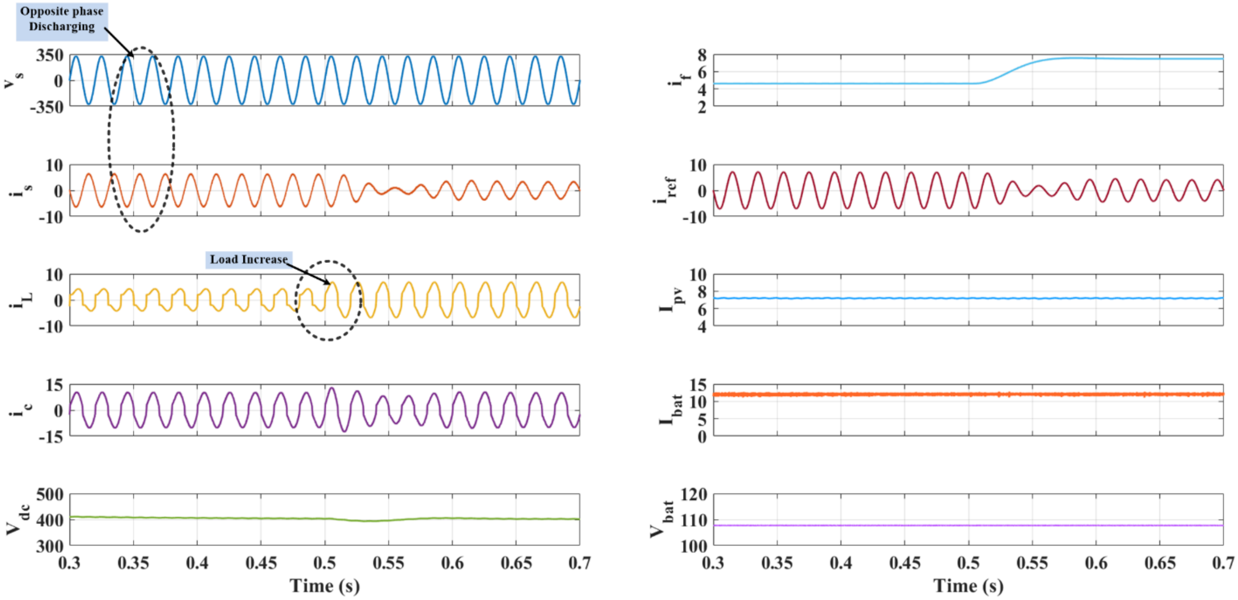

Fig.8.10 Simulation results of $v_s, i_s, i_L, i_c, V_{dc}, i_f, i_{ref}, I_{pv}, I_{bat}$ and V_{bat} at discharging mode.

controller is utilised to maintain the DC- link capacitance voltage constant at 400V. The setup of EV battery is supplying power to the grid side during the discharging operation. The battery voltage slowly decreases from 96V in the discharging mode. The battery current is constant to desired value of 12A during discharging condition.

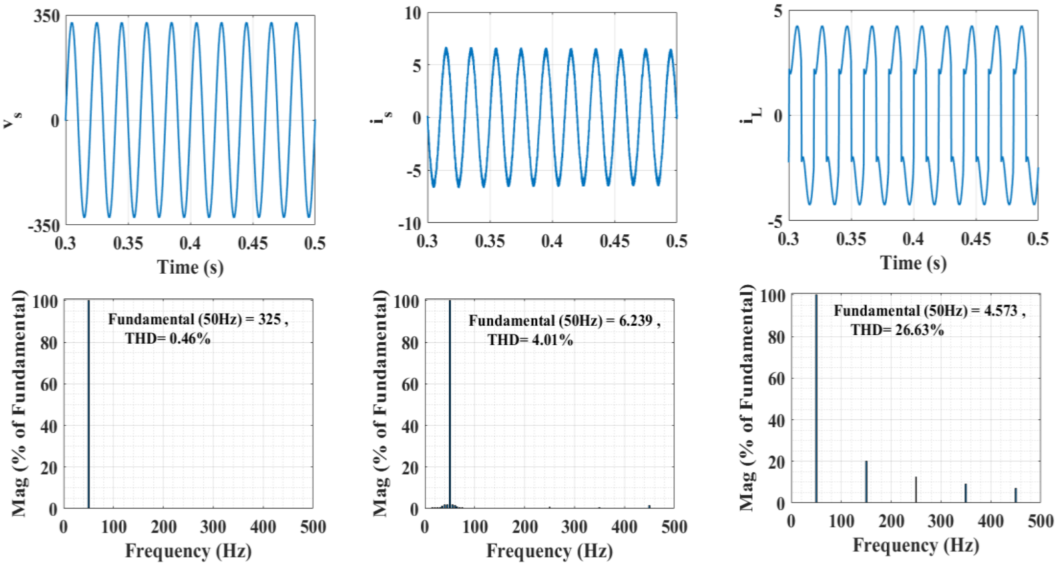

Fig 8.11 Simulation results : Harmonic analysis of a). v_s , THD = 0.46% b). i_s , THD = 4.01% c). i_L , THD = 26.63% during steady state condition at discharging mode.

Fig 8.11 demonstrate the Simulink harmonics content in the source voltage (v_S), source current (i_S), and load current (i_L) during discharging condition. After injecting compensating current, the source current's total harmonic distortion (THD) is reduced to 4.01%, compared to 26.63% for i_L. Furthermore, the THD of the supply voltage is 0.46% when discharging. The harmonics created by the nonlinear load are successfully cancelled by injecting AC-DC converter compensating current, resulting in a sinusoidal and out of phase source current. The observed waveforms clearly reveal that the source current's follow the opposite waveform of source voltage i.e discharging operation.

8.5 Opal-RT Results of Single Phase Grid Interfaced RSFLI with Solar PV and EV Charging Systems

In the laboratory, an OPAL-RT set-up is developed as shown in Fig 8.12. This setup contains OPAL-RT, Control desk and DSO. The matlab/simulink model is dump in control desk and interface with ADC channel of OPAL-RT. The DAC channel of OPAL-RT is connected DSO to capture waveforms of G2V and V2G mode. operation is discussed in details below. In this section, the charging and discharging operation are discussed in details.

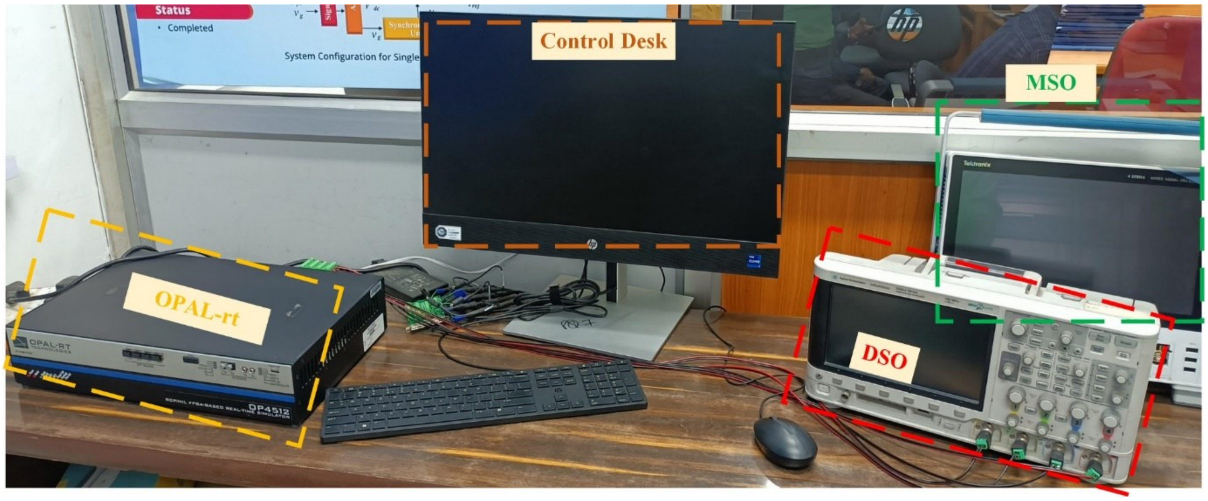

Fig. 8.12 Opal-RT Setup

a). Charging Operation/G2V mode

In G2V mode of operation the battery gets charged via buck mode of bidirectional DC-DC converter. Figs (8.13-8.14) show the results for G2V mode for various dynamic conditions.

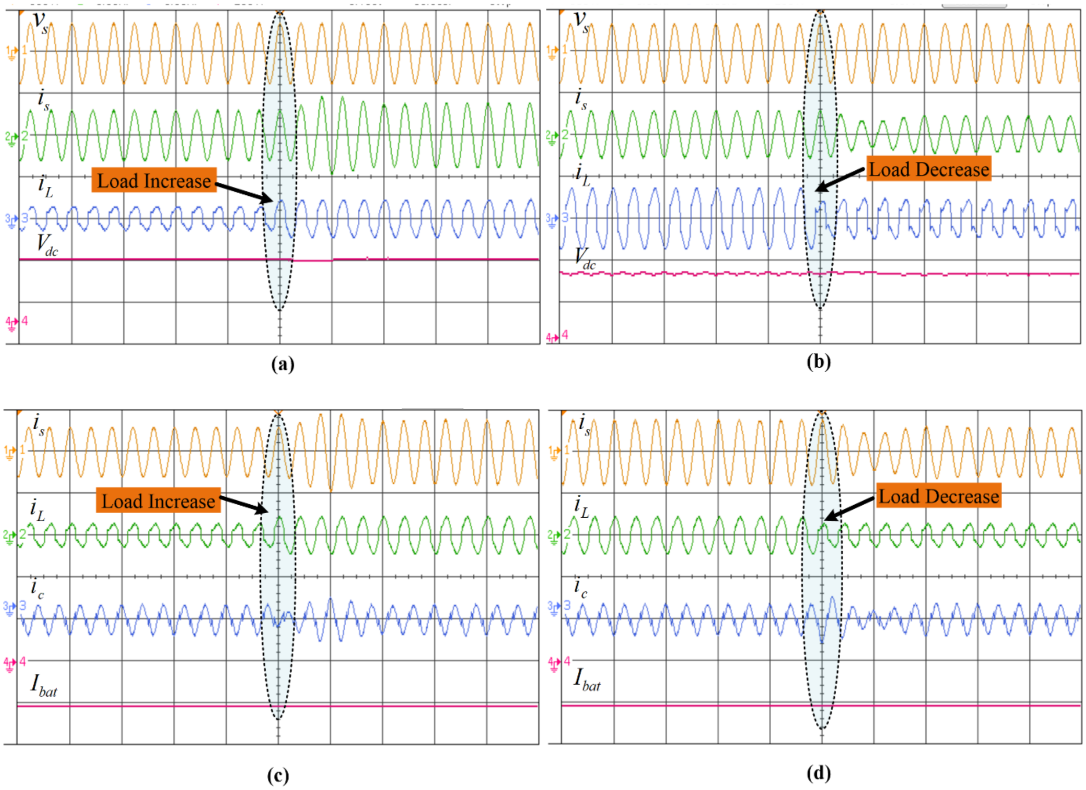

Fig. 8.13 Opal-RT Results during charging operation

Fig. 8.13 shows the waveform of source voltage (v_s), source current (i_s), load current (i_L), compensating current (i_c), DC link voltage (V_{dc}) and battery current (I_{bat}) for G2V mode. In this mode of operation, the load current magnitude is changed due to change in load which also follow the change in source current at same instant. The source voltage (v_s) and DC link voltage (V_{dc}) remain unchanged and well regulated during all disturbances. The DC link voltage remains stable at 400V due to PI controller action. Here, the v_s and i_s are in phase. During charging operation, it is observed that the battery charging current has not changed when distribution is introduced in the system. The battery is charged with $I_{bat} = -12A$.

Fig. 8.14 shows the waveform of i_s, i_L, i_f, i_{ref}, V_{bat} and I_{bat} for G2V mode. When the load is changed, the source current, fundamental current and reference current are also changed accordingly. At the same time, the battery voltage and battery current remain unchanged. The supply current is observed to be sinusoidal and in phase with the load current.

b). Discharging Operation/ V2G mode

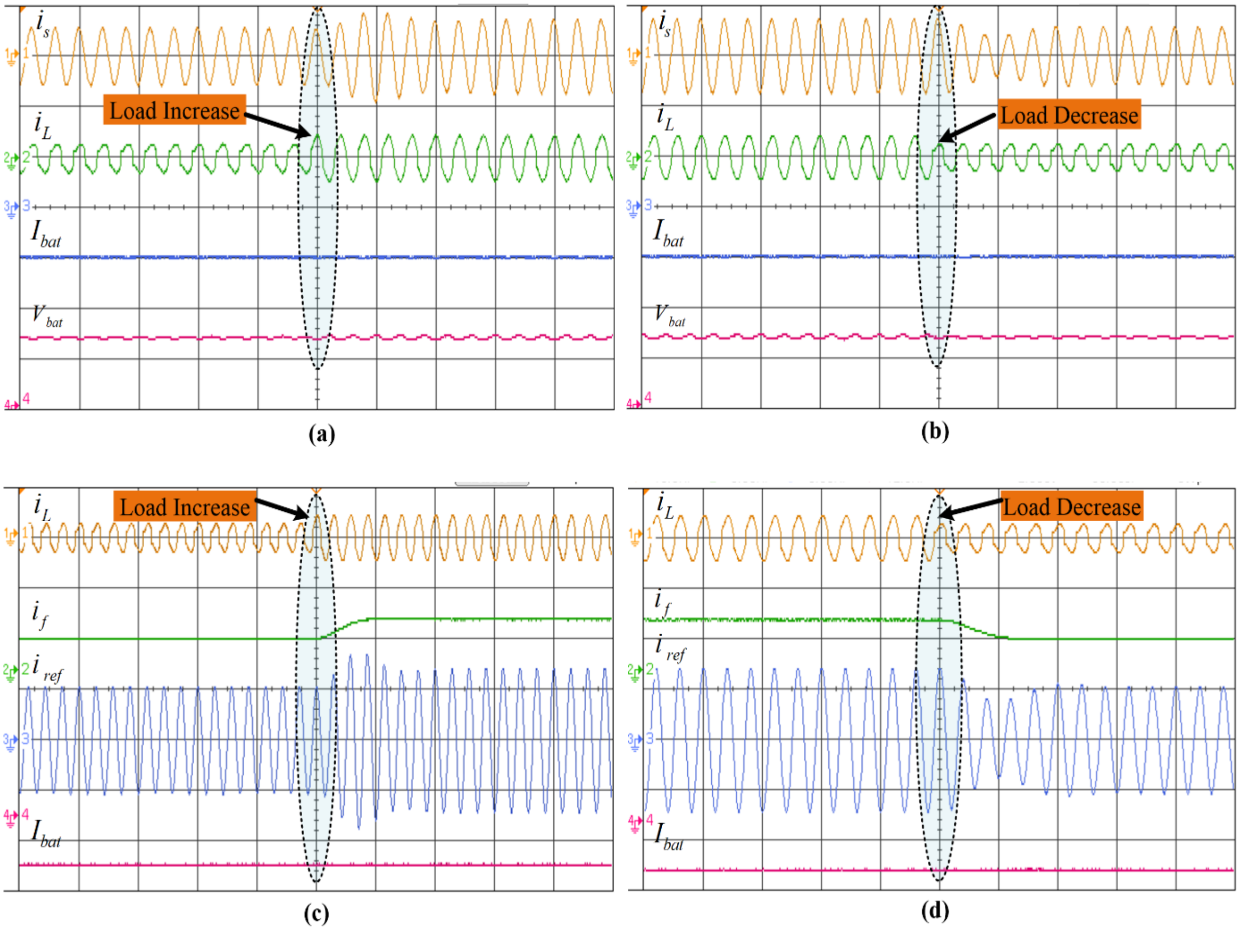

(a) (b)

(c) (d)

Fig. 8.14 Opal-RT Results during charging operation

In V2G mode of operation the battery gets discharged via boost mode of bidirectional DC-DC converter to feed the load/grid. Here, the v_s and i_s are in out of phase, hence V2G operation is taking place to discharge the battery with $I_{bat} = 12A$. Figures (8.15-8.16) show the results for V2G mode for various dynamic conditions. Fig. 8.15 shows the waveform of source voltage (v_s), source current (i_s), load current (i_L), compensating current (i_c), DC link voltage (V_{dc}), and battery current (I_{bat}). From Fig. 8.15, it is observed that the source current magnitude is decreased/increased. It is due to higher/lower demand from the load respectively during load change. Since the battery output is constant and if the extra power which was feeding to the load is now diverted to the grid side. The source voltage, DC link voltage and battery current remains same. This has a repercussion on the source current as shown in Fig 8.15 in the form of a decrease in the magnitude of source current. All other waveforms are observed to be unchanged. When the load is changed, the supply current also changes. Since in this condition source current and source voltage has opposite polarity. The supply current remains sinusoidal and in phase opposition to the grid voltage

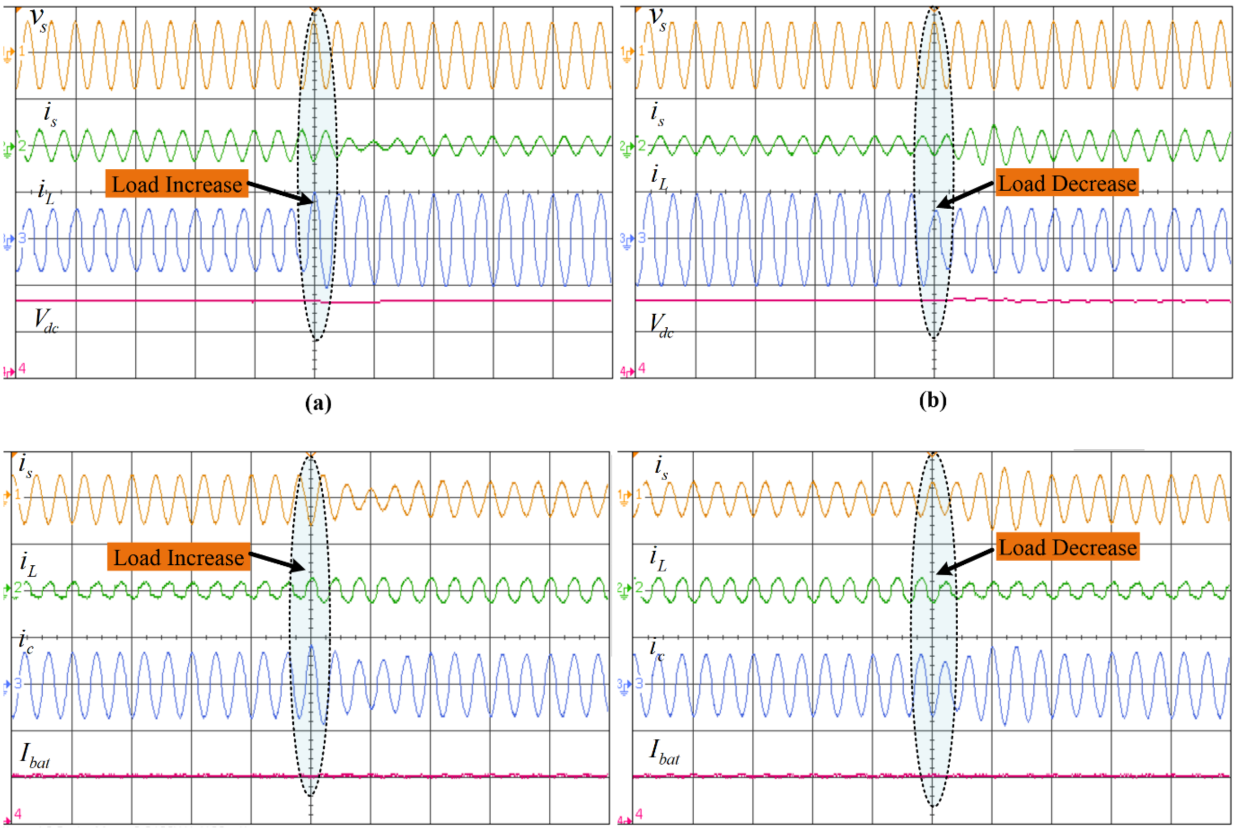

(a) (b)

(c) (d)

Fig. 8.15 Opal-RT Results during Discharging operation

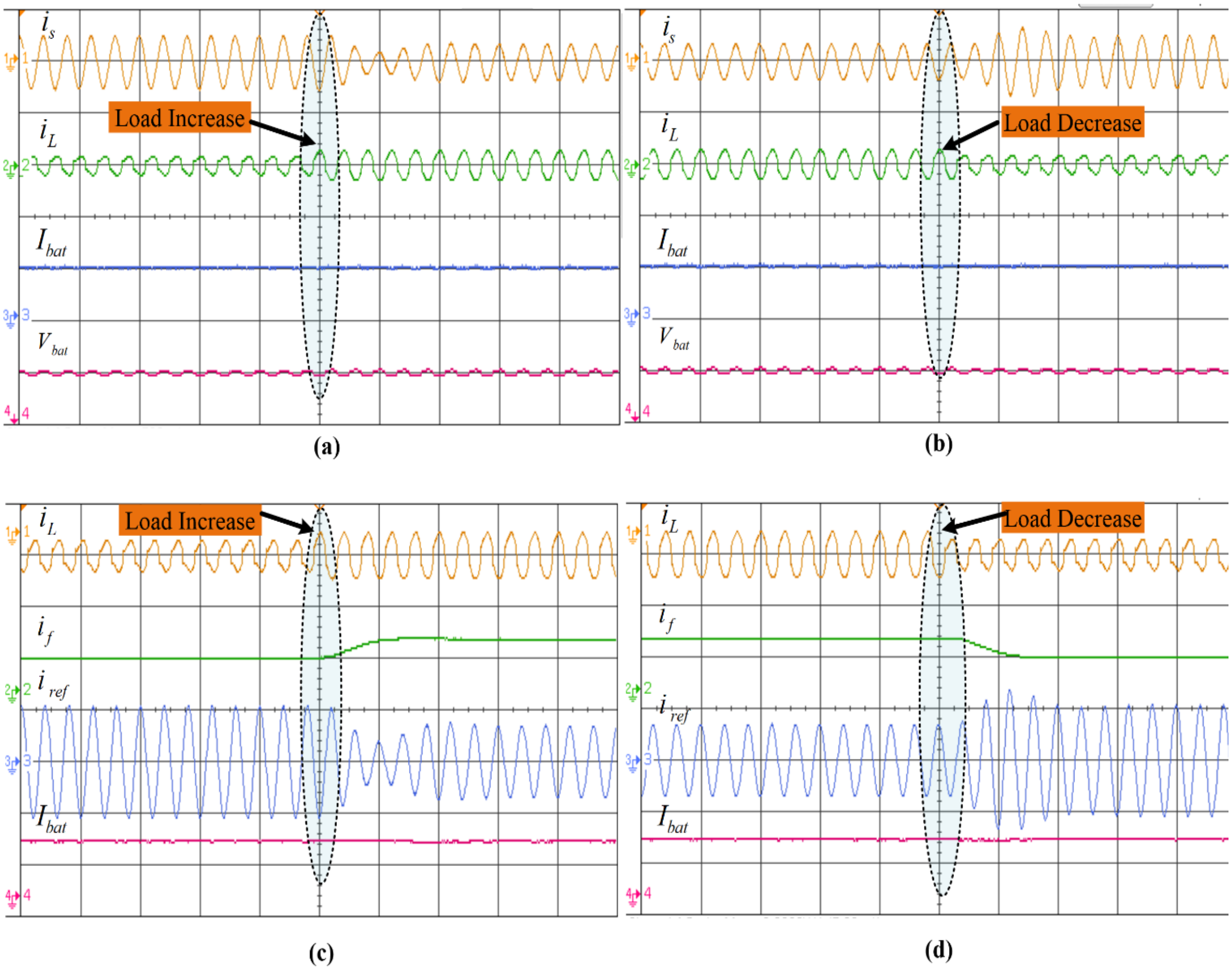

Fig. 8.16 Opal-RT Results during Discharging operation (V2G mode)

during all time indicating that PV and EV supply more power to the grid side as compared to the demand of the load current.

Fig. 8.16 shows the waveform of i_s, i_L, i_f, i_{ref}, V_{bat} and I_{bat} for a change in load. All the AC side currents (i_s, i_{ref}, i_L) get changed when the load is changed. So, an increase in load is reflected by a corresponding reduction in the value of source current since both i_s and i_L are in phase opposition. The battery voltage and battery current remain same.

8.6 Comparative analysis of Single Phase Grid Interfaced RSFLI with Solar PV and EV Charging Systems

In this section, the proposed RSFLI is compared with DC-MLI, FC- MLI and CHB multilevel inverter. The Table 8.2 shows the comparison between different configurations of MLI. The RSFLI, five number (one is bidirectional switch and remaining four is IGBT switches) of switches are required but in all other MLIs eight switches are used. There are only two capacitors required in RSFLI which is less in comparison to DC-MLI (required four capacitors) and FC-MLI (required ten capacitors). It is also observed that, RSFLI have simple structure and design, easy to operate, less complex as compared to other five level multilevel inverter. The overall cost of RSFLI is also less. So, this design of RSFLI can easily be implemented for various power system operations. It is also observed that the %THD of source current is minimum as shown in Table 8.3.

Table.8.2 Comparison table of RSFLI with another MLI

Parameters	**DC-MLI [287]**	**FC-MLI [288]**	**CHB-MLI [289]**	**RSFLI (Proposed)**
No. of levels	5	5	5	5
No. of switches	8	8	8	5 (1-bidirectional switch)
No. of DC voltage source	1	1	2	2
No. of DC link capacitors	4	10	2	2
No. of diodes	12	-	-	-
Modulation strategies	Level Shifted	Level Shifted	Level Shifted	Level Shifted
Complexity	higher	higher	moderate	less
Structure	Complex	Complex	Simple	Very simple

Table.8.3 %THD of RSFLI using TOSSI algorithm during charging and discharging condition

TOSSI Algorithms	**%T.H.D (v_s)**	**%T.H.D (i_s)**	**%T.H.D (i_L)**
Charging	**0.44**	2.00	**22.63**
Discharging	**0.46**	4.01	**26.63**

8.7 Conclusions

A novel Reduced Switch Five Level Inverter topology is presented in this chapter. The RSFLI is used to improve the current waveform on the source side where as the load is taken as nonlinear.

The PV array along with EV is connected at the DC-link of RSFLI. Both G2V and V2G mode of operation were tested on MATLAB simulation as well as on a system based on OPAL-RT which was developed in the laboratory. The RSFLI, DC-DC boost converter, Bidirectional DC-DC converter was controlled independently to study various grid/load condition. A thorough OPAL-RT results analysis is performed in this chapter. A comparative study of the proposed RSFLI with other MLIs is also presented. The proposed model of RSFLI has got several advantages over other MLIs in terms of a simple structure, improved performance available at a lower cost. Overall, it can be concluded that RSFLI provides a very good alternative to other costly and complex MLIs.

Chapter 9

Conclusion and Future Scope

In this chapter conclusion from each chapter is summarized and also works of the future scope is discussed.

Chapter 1: This chapter discusses the importance of power quality (PQ) improvement, PQ standards and, introduction to single, three phase and multilevel inverters.

Chapter 2: This chapter presents a through literature survey on the grid connected DSTATCOM and different configurations such as (single phase VSC, three phase VSC, and Multilevel inverter), single phase grid connected EV charging system, three phase grid connected solar PV and EV charging systems. This chapter also discusses literature survey regarding different control algorithms under various grid (single phase and three phase conditions). A brief review on single phase grid connected multilevel inverter based EV charger is also discussed in this.

Chapter 3: This chapter includes the design aspects of different converter configurations. The design of DC link voltage, DC link capacitance, interfacing inductor, design of voltage and current sensors, design of gating circuit, Design of DC-DC bidirectional converter etc. are presented in this chapter.

Chapter 4: In this chapter discusses the analysis of the single phase and three-phase grid-connected DSTATCOM system. The designed system is modeled in MATLAB/Simulink. The steady state and dynamic waveforms for different control algorithms are presented analysed.

The prototype experimental setup of both single phase and three phase is discussed in this chapter. The experimental setup is developed using Power Analyser, DSO, dSPACE 1104, microlab box 1202, multimeter etc. The performance of the different control algorithms is compared and conclusion are made.

Chapter 5: This chapter includes the analysis of multilevel inverter based DSTATCOM system. The configuration and switching operation of five level multilevel inverter are discussed. The mathematical modeling of different control algorithms with control diagram and their comparison of fundamental current is also presented in the thesis.

Chapter 6: This chapter presents the analysis of single phase grid connected EV charging system to perform G2V and V2G operations. The harmonic content analysis of this system is also shown during charging and discharging mode. The various control algorithms and their mathematical calculations with comparative analysis are discussed in the chapter. The simulation and experimental results are also presented and analysed.

Chapter 7: This chapter discusses the performance analysis of three phase grid interfaced Solar PV - EV charging system. The Simulation results of three phase grid interfaced EV with PV and without PV are presented and compared.

Chapter 8: In this chapter implementation of single phase grid connected reduced switch multilevel inverter with PV and EV charging system is presented. The integration of PV and EV to the grid in single-phase system using reduced switch MC1 is performed using multiple control technique.

Scope of Future Work

The present study discusses thorough analysis on different converter configurations which are presented in detailed in the thesis. Still the work can be extended to the following future scope of work

1. In all simulation works and system configuration a stiff grid was considered. In place of stiff grid weak/distorted grid can be examined to better understand the impact of distributed generation in near future. A weak/distorted grid has high THD content in the supply voltage. To tackle this there is need to developed advanced PLL which can extract proper phase and frequency from the supply voltage signal which is needed to mitigate PQ issues in the grid side and also to integrate PV and EV to the conventional grid.
2. Modern control algorithms incorporating new and robust Reduced Switch Configuration of the MLI DSTATCOM could be explored more into depth. A reduced switch configuration of the DSTTACOM provides similar results as compared to convention DSTATCOM but at a lower cost, so if we use multiple such reduced switch DSTATCOM in our power system then definitely the overall cost will lower down.
3. The multilevel inverter configuration incorporating G2V and V2G could be explored for AI based control techniques. The EV is emerging as a futuristic solution for current fossile fuel issue, and to utilize EV in near future to act not only as load but also as source could enable us to create virtual system inertia. Due to this our power system will be more stable and it has less disturbances due to increased renewable energy sources penetration.

4. Impact of large penetration of V2G could be explored. Since it is expected that the large scale PV or wind integration could have adverse effects on the system performance as well as grid stability. So, it becomes quite necessary to study the impact of large scale integration of V2G mode also.

5. Impact of fast charging station on the PQ of the grid could be explored. Since the future mobility may be more depended on the EV and the automobile market is already seeing a huge demand of fast charging stations. So, if fast charging stations are increased in near future then since it will act as DC load so there could be huge PQ disturbances. So, this could be a main future scope of study.

References:

[1] Mariscotti, Andrea. "Power quality phenomena, standards, and proposed metrics for dc grids." Energies 14.20 (2021): 6453.

[2] Ouyang, Min. "Review on modeling and simulation of interdependent critical infrastructure systems." Reliability engineering & System safety 121 (2014): 43-60.

[3] Khaleel, Mohamed, et al. "Assessing the financial impact and mitigation methods for voltage sag in power grid." Int. J. Electr. Eng. and Sustain. (2023): 10-26.

[4] Han, Yang, et al. "Cause, classification of voltage sag, and voltage sag emulators and applications: A comprehensive overview." IEEE Access 8 (2019): 1922-1934.

[5] Moghassemi, Ali, and Sanjeevikumar Padmanaban. "Dynamic voltage restorer (DVR): a comprehensive review of topologies, power converters, control methods, and modified configurations." Energies 13.16 (2020): 4152.

[6] Foroushani, Elnaz Sarrami, et al. "Nature-Inspired Healing: Biomimetic Nanomaterials for Advanced Wound Management." Materials Today Sustainability (2024): 100975.

[7] Hossain, Eklas, et al. "Analysis and mitigation of power quality issues in distributed generation systems using custom power devices." Ieee Access 6 (2018): 16816-16833.

[8] Lebrouhi, B. E., et al. "Key challenges for a large-scale development of battery electric vehicles: A comprehensive review." Journal of Energy Storage 44 (2021): 103273.

[9] Sathiyan, S. Paul, et al. "Comprehensive assessment of electric vehicle development, deployment, and policy initiatives to reduce GHG emissions: opportunities and challenges." IEEE Access 10 (2022): 53614-53639.

[10] Liguo, Xin, et al. "Evaluating the role of innovation in hybrid electric vehicle-related technologies to promote environmental sustainability in knowledge-based economies." Technology in Society 74 (2023): 102283.

[11] Hasan, Mohammad Kamrul, et al. "Review of electric vehicle energy storage and management system: Standards, issues, and challenges." Journal of energy storage 41 (2021): 102940.

[12] Yildiz, Baran, Jose I. Bilbao, and Alistair B. Sproul. "A review and analysis of regression and machine learning models on commercial building electricity load forecasting." Renewable and Sustainable Energy Reviews 73 (2017): 1104-1122.

[13] Mastoi, Muhammad Shahid, et al. "An in-depth analysis of electric vehicle charging station infrastructure, policy implications, and future trends." Energy Reports 8 (2022): 11504-11529.

[14] Lebrouhi, B. E., et al. "Key challenges for a large-scale development of battery electric vehicles: A comprehensive review." Journal of Energy Storage 44 (2021): 103273.

[15] Mohanty, Asit, et al. "Enhancing power quality in contemporary utility systems: A comprehensive analysis of active power filters and control strategies." Energy Reports 11 (2024): 5575-5592.

[16] Ilyushin, Pavel, et al. "State-of-the-Art Literature Review of Power Flow Control Methods for Low-Voltage AC and AC-DC Microgrids." Energies 16.7 (2023): 3153.

[17] Khadkikar, Vinod. "Enhancing electric power quality using UPQC: A comprehensive overview." IEEE transactions on Power Electronics 27.5 (2011): 2284-2297.

[18] Sangar, Brijendra, Madhusudan Singh, and Mini Sreejeth. "An improved ANFIS model predictive current control approach for minimizing torque and current ripples in PMSM-driven electric vehicle." Electrical Engineering (2024): 1-11.

[19] Singh, Girish Kumar. "Power system harmonics research: a survey." European Transactions on Electrical Power 19.2 (2009): 151-172.

[20] Hernández-Mayoral, Emmanuel, et al. "A comprehensive review on power-quality issues, optimization techniques, and control strategies of microgrid based on renewable energy sources." Sustainability 15.12 (2023): 9847.

[21] Kumar, Pradeep, Niranjan Kumar, and A. K. Akella. "A simulation based case study for control of DSTATCOM." ISA transactions 53.3 (2014): 767-775.

[22] Sharma, Angshuman, and Santanu Sharma. "Review of power electronics in vehicle-to-grid systems." Journal of Energy Storage 21 (2019): 337-361.

[23] Kumar, Yellapragada Venkata Pavan, et al. "Fuzzy hysteresis current controller for power quality enhancement in renewable energy integrated clusters." Sustainability 14.8 (2022): 4851.

[24] Aravind, R., et al. "Multi-port non-isolated DC-DC converters and their control techniques for the applications of renewable energy." IEEE Access (2024).

[25] Dubey, Alok Kumar, Jyoti Prakash Mishra, and Amritesh Kumar. "Modified CCF based shunt active power filter operation with dead-band elimination for effective harmonic and unbalance compensation in 3-phase 3-wire system." IEEE Transactions on Power Delivery 37.3 (2021): 2131-2142.

[26] Tavakoli, Ahmad, et al. "Impacts of grid integration of solar PV and electric vehicle on grid stability, power quality and energy economics: A review." IET Energy Systems Integration 2.3 (2020): 243-260.

[27] Sreenivasarao, D., Pramod Agarwal, and Biswarup Das. "Neutral current compensation in three-phase, four-wire systems: A review." Electric Power Systems Research 86 (2012): 170-180.

[28] Molzahn, Daniel K., et al. "A survey of distributed optimization and control algorithms for electric power systems." IEEE Transactions on Smart Grid 8.6 (2017): 2941-2962.

[29] Ali, Ziad M., et al. "Complexities of Power Quality and Harmonic-Induced Overheating in Modern Power Grids Studies: Challenges and Solutions." IEEE Access (2024).

[30] Kim, Young-Jin, Jianhui Wang, and Xiaonan Lu. "A framework for load service restoration using dynamic change in boundaries of advanced microgrids with synchronous-machine DGs." IEEE Transactions on Smart Grid 9.4 (2016): 3676-3690.

[31] Cai, Siyuan, et al. "Security risk intelligent assessment of power distribution internet of things via entropy-weight method and cloud model." Sensors 22.13 (2022): 4663.

[32] Mbuli, Nhlanhla. "Dynamic Voltage Restorer as a Solution to Voltage Problems in Power Systems: Focus on Sags, Swells and Steady Fluctuations." Energies 16.19 (2023): 6946.

[33] Ali, Ziad M., et al. "Complexities of Power Quality and Harmonic-Induced Overheating in Modern Power Grids Studies: Challenges and Solutions." IEEE Access (2024).

[34] Saxena, Vivek, et al. "Navigating the complexities of distributed generation: Integration, challenges, and solutions." Energy Reports 12 (2024): 3302-3322.

[35] Blaabjerg, Frede, et al. "Distributed power-generation systems and protection." Proceedings of the IEEE 105.7 (2017): 1311-1331.

[36] Mariscotti, Andrea. "Power quality phenomena, standards, and proposed metrics for dc grids." Energies 14.20 (2021): 6453.

[37] Mariscotti, Andrea, and Alessandro Mingotti. "The Effects of Supraharmonic Distortion in MV and LV AC Grids." Sensors 24.8 (2024): 2465.

[38] Lopes, JA Pecas, et al. "Integrating distributed generation into electric power systems: A review of drivers, challenges and opportunities." Electric power systems research 77.9 (2007): 1189-1203.

[39] Alkahtani, Ammar Ahmed, et al. "Power quality in microgrids including supraharmonics: Issues, standards, and mitigations." IEEE access 8 (2020): 127104-127122.

[40] Khan, Shazma, Balvinder Singh, and Prachi Makhija. "A review on power quality problems and its improvement techniques." 2017 Innovations in Power and Advanced Computing Technologies (i-PACT) (2017): 1-7.

[41] Kumar, Amit. "Power Quality Issues and Harmonics Performance Analysis for Non-Linear Load in Power Distribution System." 2022 19th International Conference on Electrical Engineering, Computing Science and Automatic Control (CCE). IEEE, 2022.

[42] Habib, Salman, Muhammad Kamran, and Umar Rashid. "Impact analysis of vehicle-to-grid technology and charging strategies of electric vehicles on distribution networks–a review." Journal of Power Sources 277 (2015): 205-214.

[43] Rodriguez, Jose A., Fernando Salcedo, and Stephen B. Bayne. "Investigating the Effects of Non-Linear Loads on Generator Sets." 2021 IEEE Pulsed Power Conference (PPC). IEEE, 2021.

[44] Ali, Ziad M., et al. "Complexities of Power Quality and Harmonic-Induced Overheating in Modern Power Grids Studies: Challenges and Solutions." IEEE Access (2024).

[45] Hossain, Eklas, et al. "Analysis and mitigation of power quality issues in distributed generation systems using custom power devices." Ieee Access 6 (2018): 16816-16833.

[46] Amin, S. Massoud. "Smart grid: Overview, issues and opportunities. advances and challenges in sensing, modeling, simulation, optimization and control." European Journal of Control 17.5-6 (2011): 547-567.

[47] Prasad, Miska, and Ashok Kumar Akella. "Mitigation of power quality problems using custom power devices: A review." Indonesian Journal of Electrical Engineering and Informatics (IJEEI) 5.3 (2017): 207-235.

[48] Heenkenda, Anisha, et al. "Unified power quality conditioners based different structural arrangements: A comprehensive review." IEEE Access 11 (2023): 43435-43457.

[49] Heng, Han, Mohamad Hazwan Mohd Ghazali, and Wan Rahiman. "Exploring the application of ant colony optimization in path planning for Unmanned Surface Vehicles." Ocean Engineering 311 (2024): 118738.

[50] Abdulghani, B. A., and M. A. Abdulghani. "A comprehensive review of Ant Colony Optimization in swarm intelligence for complex problem solving." Acadlore Trans. Mach. Learn 3.4 (2024): 214-224.

[51] Mallala, Balasubbareddy, P. Venkata Prasad, and Kowstubha Palle. "Analysis of power quality issues and mitigation techniques using HACO algorithm." International Conference on Intelligent Sustainable Systems. Singapore: Springer Nature Singapore, 2023.

[52] Ahmed, Shakir D., et al. "Grid integration challenges of wind energy: A review." Ieee Access 8 (2020): 10857-10878.

[53] Vishnu, Kandakatla, et al. "Advancing Power Quality in Smart Grids Through Tailored UPQC Modifications." 2024 IEEE International Conference on Information Technology, Electronics and Intelligent Communication Systems (ICITEICS). IEEE, 2024.

[54] Subhani, S., V. Cuk, and J. F. G. Coben. "A literature survey on power quality disturbances in the frequency range of 2–150 kHz." Proceedings of the International Conference on Renewable Energies and Power Quality (ICREPQ'14), Málaga, Spain. 2017.

[55] Alkahtani, Ammar Ahmed, et al. "Power quality in microgrids including supraharmonics: Issues, standards, and mitigations." IEEE access 8 (2020): 127104-127122.

[56] Xu, Shuang, Yaosuo Xue, and Liuchen Chang. "Review of power system support functions for inverter-based distributed energy resources-standards, control algorithms, and trends." IEEE open journal of Power electronics 2 (2021): 88-105.

[57] Mwasilu, Francis, et al. "Electric vehicles and smart grid interaction: A review on vehicle to grid and renewable energy sources integration." Renewable and sustainable energy reviews 34 (2014): 501-516.

[58] Sen, Souvik, and Sourav Ganguly. "Opportunities, barriers and issues with renewable energy development–A discussion." Renewable and sustainable energy reviews 69 (2017): 1170-1181.

[59] Khalid, Muhammad. "Smart grids and renewable energy systems: Perspectives and grid integration challenges." Energy Strategy Reviews 51 (2024): 101299.

[60] Altaf, Humeera, and Abdul Hamid Bhat. "Performance investigation of a transistor clamped H-bridge inverter-based dynamic voltage restorer for mitigating various power quality problems." International Journal of Power Electronics 17.1 (2023): 29-52.

[61] Prasad, K. N. V., et al. "Realization of cascaded H-bridge 5-Level multilevel inverter as Dynamic Voltage Restorer." 2013 International Conference on Computer Communication and Informatics. IEEE, 2013.

[62] Devi, T. Anuradha, et al. "Hybrid optimal-FOPID based UPQC for reducing harmonics and compensate load power in renewable energy sources grid connected system." Plos one 19.5 (2024): e0300145.

[63] Yadav, Shravan Kumar, and Krishna Bihari Yadav. "Performance analysis of hybrid metaheuristic assisted collateral FO controller for HRES system integrated UPQC." Computers and Electrical Engineering 120 (2024): 109664.

[64] Surasmi, N. L., G. Shiny, and B. R. Vinod. "Grid Integrated Hybrid Renewable Energy System for Power Quality Improvement Using Open End Winding Transformer." 2024 International Conference on E-mobility, Power Control and Smart Systems (ICEMPS). IEEE, 2024.

[65] Hannan, M. A., Lipu, M. H., Ker, P. J., Begum, R. A., Agelidis, V. G., & Blaabjerg, F. (2019). Power electronics contribution to renewable energy conversion addressing emission reduction: Applications, issues, and recommendations. Applied energy, 251, 113404.

[66] Mbhombhi, S. J. "Evaluation of key factors influencing a South African based electrical utility to utilise smart grid technologies for power quality management." PhD diss., North-West University (South Africa), 2019.

[67] Kyriakopoulos, Grigorios L., and Garyfallos Arabatzis. "Electrical energy storage systems in electricity generation: Energy policies, innovative technologies, and regulatory regimes." Renewable and Sustainable Energy Reviews 56 (2016): 1044-1067.

[68] Liang, Xiaodong. "Emerging power quality challenges due to integration of renewable energy sources." IEEE Transactions on Industry Applications 53.2 (2016): 855-866.

[69] Ong, Shih Jong Benjamin, and Yeong Jia Cheng. "An overview of international harmonics standards and guidelines (IEEE, IEC, EN, ER and STC) for low voltage system." 2007 International Power Engineering Conference (IPEC 2007). IEEE, 2007.

[70] Gui, Yonghao, Sufan Jiang, Linquan Bai, Yaosuo Xue, Hong Wang, Jacob Reidt, Samuel Ojetola, and David A. Schoenwald. "Review of challenges and research opportunities for control of transmission grids." IEEE Access (2024).

[71] Khan, Musa, Wenchuan Wu, and Li Li. "Grid-forming control for inverter-based resources in power systems: A review on its operation, system stability, and prospective." IET Renewable Power Generation 18, no. 6 (2024): 887-907.

[72] Alkahtani, Ammar Ahmed, et al. "Power quality in microgrids including supraharmonics: Issues, standards, and mitigations." IEEE access 8 (2020): 127104-127122.

[73] Sepasi, Saeed, Celia Talichet, and Abrar Shahriar Pramanik. "Power quality in microgrids: A critical review of fundamentals, standards, and case studies." IEEE Access 11 (2023): 108493-108531.

[74] Wu, Yuan-Kang, Jhih-Hao Lin, and Huei-Jeng Lin. "Standards and guidelines for grid-connected photovoltaic generation systems: A review and comparison." IEEE Transactions on Industry Applications 53.4 (2017): 3205-3216.

[75] Ahmed, Ibrahim. "Comparative evaluation of different power quality issues of variable speed wind turbines." PhD diss., Brunel University London, 2017.

[76] Sepasi, Saeed, Celia Talichet, and Abrar Shahriar Pramanik. "Power quality in microgrids: A critical review of fundamentals, standards, and case studies." IEEE Access 11 (2023): 108493-108531.

[77] Kumar, Dinesh, Firuz Zare, and Arindam Ghosh. "DC microgrid technology: system architectures, AC grid interfaces, grounding schemes, power quality, communication networks, applications, and standardizations aspects." Ieee Access 5 (2017): 12230-12256.

[78] Abubakar, Ukashatu. "Digital Protection of Power Converters Employed in Doubly-fed Induction Generator and Induction Motor Using Wavelet Transform." PhD diss., University of Malaya (Malaysia), 2021.

[79] Muhammed, Adil Hussein. "High frequency transformer design and modelling using finite element technique." PhD diss., Newcastle University, 2000.

[80] Gursoy, Mehmetcan, and Behrooz Mirafzal. "Direct vs. indirect control schemes for grid-forming inverters–Unveiling a performance comparison in a microgrid." IEEE Access (2023).

[81] BT, Venu Gopal. "Comparison between direct and indirect field oriented control of induction motor." Int. J. Eng. Trends Technol 43, no. 6 (2017): 364-369.

[82] Tian-yuan, Tan, et al. "Comparison of direct and indirect current control strategy for DSTATCOM." 2006 International Conference on Power System Technology. IEEE, 2006.

[83] Kalair, A., et al. "Review of harmonic analysis, modeling and mitigation techniques." Renewable and Sustainable Energy Reviews 78 (2017): 1152-1187.

[84] Fallows, Daniel, et al. "Harmonic reduction methods for electrical generation: a review." IET Generation, Transmission & Distribution 12.13 (2018): 3107-3113.

[85] Salam, Zainal, Perng Cheng Tan, and Awang Jusoh. "Harmonics mitigation using active power filter: A technological review." Elektrika Journal of Electrical Engineering 8.2 (2006): 17-26.

[86] Akagi, Hirofumi. "The state-of-the-art of active filters for power conditioning." 2005 European Conference on Power Electronics and Applications. IEEE, 2005.

[87] Salmerón, Patricio, and Jesús R. Vázquez. "Active Power-line conditioners." Power quality: mitigation technologies in a distributed environment. London: Springer London, 2007. 231-291.

[88] K., Soujanya., J., Upendar. (2024). Investigation and Reduction of Harmonic in Grid Connected PV Fed DSTATCOM System. International journal of electrical & electronics research, doi: 10.37391/ijeer.120125

[89] Faris, R. Aboo, Mohanrajan S. Rajendran, and V. Prashobh Suresh. "Performance Analysis of Modulation Techniques for Three-Phase High-Frequency VSC." In 2023 IEEE 20th India Council International Conference (INDICON), pp. 1068-1075. IEEE, 2023.

[90] Monica, Swetha, Alok Kumar Singh, and D. Vijaya Kumar. "Design and implementation of GCMBO control strategy for grid integrated SPV-DSTATCOM." e-Prime-Advances in Electrical Engineering, Electronics and Energy 6 (2023): 100356.

[91] Sahu, Gokulananda, et al. "An Adaline model predictive control strategy based DSTATCOM for power quality enhancement." International Journal of Applied Power Engineering (IJAPE) 13.3.

[92] Bansal, Praveen, and Alka Singh. "Control of DSTATCOM with Parallel Tangent Method Based Adaptive Control Algorithm under Distorted Grid Conditions." Electric Power Components and Systems (2024): 1-13.

[93] D'silva, Silvanus, Mohammad Shadmand, Sertac Bayhan, and Haitham Abu-Rub. "Towards grid of microgrids: Seamless transition between grid-connected and islanded modes of operation." IEEE Open Journal of the Industrial Electronics Society 1 (2020): 66-81.

[94] Khadse, Dushyant, and Ankur Beohar. "Enhancement of power quality problems using DSTATCOM: An optimized control approach." Solar Energy 268 (2024): 112260.

[95] Chenchireddy, Kalagotla, et al. "A review on D-STATCOM control techniques for power quality improvement in distribution." 2021 5th International conference on electronics, communication and aerospace technology (ICECA). IEEE, 2021.

[96] Masand, Deepika, Shailendra Jain, and Gayatri Agnihotri. "Control algorithms for distribution static compensator." 2006 IEEE International Symposium on Industrial Electronics. Vol. 3. IEEE, 2006.

[97] Ram, Atma, Parsh Ram Sharma, and Rajesh Kumar Ahuja. "Enhancement of power quality using U-SOGI based control algorithm for DSTATCOM." Ain Shams Engineering Journal 15.1 (2024): 102296.

[98] Devanshu, Ambrish, Kundan Kumar, and Ramesh Kumar. "Implementation of SRF theory to DSTATCOM for power quality improvement." 2022 IEEE Delhi Section Conference (DELCON). IEEE, 2022.

[99] Behera, Manoja Kumar, and Lalit Chandra Saikia. "A novel spontaneous control for autonomous microgrid vsc system using bpf droop and improved hysteresis band control scheme." Electric Power Systems Research 220 (2023): 109262.

[100] Arya, Sabha Raj, Rakesh Maurya, and Jayadeep Srikakolapu. "DSTATCOM using model predictive control associated with LMS control." International Journal of Electronics 111.2 (2024): 238-258.

[101] Singh, Bhim, Krishan Kant, and S. Arya. "Notch filter based fundamental frequency component extraction to control DSTATCOM for mitigating current related power quality problems." IET Power Electron (2015).

[102] Jayaraman, Ramesh, et al. "Analysis of sliding mode controller based DSTATCOM for power quality improvement in distribution power system." Materials Today: Proceedings 80 (2023): 3675-3681.

[103] Bala, Nishi, and Sanjeev Kumar Mallik. "Control algorithm for an island microgrid under DSTATCOM using a Third Order Sinusoidal Integrator (TOSSI) to improve power quality for a local nonlinear load." Engineering Research Express 6.2 (2024): 025354.

[104] Trinh, Quoc-Nam, and Hong-Hee Lee. "An enhanced grid current compensator for grid-connected distributed generation under nonlinear loads and grid voltage distortions." IEEE Transactions on Industrial Electronics 61, no. 12 (2014): 6528-6537.

[105] Chindris, M., A. Cziker, and Anca Miron. "UPQC—The best solution to improve power quality in low voltage weak distribution networks." In 2017 international conference on modern power systems (MPS), pp. 1-8. IEEE, 2017.

[106] Adaptive control algorithms for DSTATCOM (Distribution Static Compensator) are essential for the improvement of power quality by managing reactive power and reducing harmonics.

[107] Lolamo, Mathewos, Rajan Kumar, and Veena Sharma. "Enhancing power quality of PV-DSTATCOM integrated grid with modified adaptive LMS control." Electrical Engineering (2024): 1-14.

[108] Sadiq, Alishba, Muhammad Usman, Shujaat Khan, Imran Naseem, Muhammad Moinuddin, and Ubaid M. Al-Saggaf. "q-lmf: Quantum calculus-based least mean fourth algorithm." In Fourth International Congress on Information and Communication Technology: ICICT 2019, London, Volume 1, pp. 303-311. Springer Singapore, 2020.

[109] Bansal, Praveen, and Alka Singh. "Control of DSTATCOM with Parallel Tangent Method Based Adaptive Control Algorithm under Distorted Grid Conditions." Electric Power Components and Systems (2024): 1-13.

[110] Grisales-Noreña, Luis Fernando, Oscar Danilo Montoya, Walter Julian Gil-González, Alberto-Jesus Perea-Moreno, and Miguel-Angel Perea-Moreno. "A comparative study on power flow methods for direct-current networks considering processing time and numerical convergence errors." Electronics 9, no. 12 (2020): 2062.

[111] Colak, Ilhami, and Ersan Kabalci. "Developing a novel sinusoidal pulse width modulation (SPWM) technique to eliminate side band harmonics." International Journal of Electrical Power & Energy Systems 44, no. 1 (2013): 861-871.

[112] Hussin, H., A. Saparon, M. Muhamad, and M. D. Risin. "Sinusoidal pulse width modulation (SPWM) design and implementation by focusing on reducing harmonic content." In 2010 Fourth Asia International Conference on Mathematical/Analytical Modelling and Computer Simulation, pp. 620-623. IEEE, 2010.

[113] Zakaria, Magdi, A. S. Mabrouka, and Shahenda Sarhan. "Artificial neural network: a brief overview." neural networks 1 (2014): 2.

[114] Kovacic, Zdenko, and Stjepan Bogdan. Fuzzy controller design: theory and applications. CRC press, 2018.

[115] Gite, Akhil V., Raksha M. Bodade, and Bhagyashri M. Raut. "ANFIS controller and its application." International Journal of Engineering Research and Technology 2.2 (2013).

[116] Huang, Guang-Bin, Qin-Yu Zhu, and Chee-Kheong Siew. "Real-time learning capability of neural networks." IEEE Transactions on Neural Networks 17.4 (2024): 863-878.

[117] Zhang, Jingyi, et al. "Dynamics Power Quality Cost Assessment Based on a Gradient Descent Method." Energies 17.9 (2024): 2104.

[118] Samanta, Indu Sekhar, et al. "A comprehensive review of deep-learning applications to power quality analysis." Energies 16.11 (2023): 4406.

[119] Srikanth, Islavatu, and Pradeep Kumar. "Neural Network Based DSTATCOM Control for Power Quality Enhancement." Robotics, Control and Computer Vision: Select Proceedings of ICRCCV 2022. Singapore: Springer Nature Singapore, 2023. 313-322.

[120] Singh, Alka, and Amarendra Pandey. "Performance of adaptive radial basis functional neural network for inverter control." Electrical Engineering 105.2 (2023): 921-933.

[121] Rai, Kanchan Bala, Narendra Kumar, and Alka Singh. "Design and analysis of Hermite function-based artificial neural network controller for performance enhancement of photovoltaic-integrated grid system." International Journal of Circuit Theory and Applications 51.3 (2023): 1440-1459.

[122] Das, Soumya Ranjan, et al. "Improvement of power quality in a three-phase system using an adaline-based multilevel inverter." Frontiers in Energy Research 8 (2020): 23.

[123] Badoni, Manoj, Alka Singh, and Bhim Singh. "Adaptive neurofuzzy inference system least-mean-square-based control algorithm for DSTATCOM." IEEE Transactions on industrial informatics 12.2 (2016): 483-492.

[124] Mittal, Sudhanshu, Alka Singh, and Prakash Chittora. "Design and development of leaky least mean fourth control algorithm for single-phase grid-connected multilevel inverter." International Journal of Circuit Theory and Applications 52.1 (2024): 328-345.

[125] Rai, Kanchan Bala, Narendra Kumar, and Alka Singh. "Design and Control of DVR Based on Adaptive Bateman Polynomial for Power Quality Improvement." International Journal of Circuit Theory and Applications (2024).

[126] Barbie, Eli, Raul Rabinovici, and Alon Kuperman. "Analytical formulation and optimization of Weighted Total Harmonic Distortion in three-phase staircase modulated multilevel inverters." Energy 215 (2021): 119137.

[127] Rai, Kanchan Bala, Narendra Kumar, and Alka Singh. "Performance Analysis of UPQC using Mittag Leffler Polynomial based Neural Network Control." 2022 IEEE 2nd International Symposium on Sustainable Energy, Signal Processing and Cyber Security (iSSSC). IEEE, 2022.

[128] Hassani, Hossein, et al. "Generalized Bernoulli–Laguerre Polynomials: Applications in Coupled Nonlinear System of Variable-Order Fractional PDEs." Journal of Optimization Theory and Applications 200.1 (2024): 371-393.

[129] Lolamo, Mathewos, Rajan Kumar, and Veena Sharma. "Enhancing power quality of PV-DSTATCOM integrated grid with modified adaptive LMS control." Electrical Engineering (2024): 1-14.

[130] Chawda, Gajendra Singh, et al. "Performance Evaluation of Second Order Generalized Integrator-Quadrature Algorithm for DSTATCOM in Non-ideal Grid." IECON 2020 The 46th Annual Conference of the IEEE Industrial Electronics Society. IEEE, 2020.

[131] Singh, Bhim, Krishan Kant, and S. Arya. "Notch filter based fundamental frequency component extraction to control DSTATCOM for mitigating current related power quality problems." IET Power Electron (2015).

[132] Xu, Shihe, and Stephen A. Boyd. "Cationic surfactant adsorption by swelling and nonswelling layer silicates." Langmuir 11, no. 7 (1995): 2508-2514.

[133] Arya, Sabha Raj, et al. "Power quality improvement in isolated distributed power generating system using DSTATCOM." IEEE Transactions on Industry Applications 51.6 (2015): 4766-4774.

[134] Zhang, Zeyu, Pingping Gong, and Ziguang Lu. "A Lyapunov Theory-Based SEIG–STATCOM Voltage Regulation Control Strategy." Energies 17.19 (2024): 4992.

[135] Mittal, Sudhanshu, Alka Singh, and Prakash Chittora. "Solar PV array based grid-connected bi-directional EV charger controlled using NARLMMN algorithm." 2023 9th IEEE India International Conference on Power Electronics (IICPE). IEEE, 2023.

[136] Kumar, Nishant, Bhim Singh, and Bijaya Ketan Panigrahi. "ANOVA kernel Kalman filter for multi-objective grid integrated solar photovoltaic-distribution static compensator." IEEE Transactions on Circuits and Systems I: Regular Papers 66.11 (2019): 4256-4264..

[137] Kumar, Avdhesh, Rachana Garg, and Priya Mahajan. "Performance improvement of grid-integrated PV system using novel robust least mean logarithmic square control algorithm." Electrical Engineering 104.5 (2022): 3207-3224.

[138] Özer, Ali Sait, et al. "Enhanced control method for voltage regulation of DSTATCOM based SEIG." Energy Reports 8 (2022): 839-847.

[139] Singh, Yashi, et al. "Power quality improvement in single phase grid tied solar PV-APF based system using improved LTI-EPLL based control algorithm." 2017 7th International Conference on Power Systems (ICPS). IEEE, 2017.

[140] Levi, Emil. "Advances in converter control and innovative exploitation of additional degrees of freedom for multiphase machines." IEEE Transactions on Industrial Electronics 63, no. 1 (2015): 433-448.

[141] Golestan, Saeed, Josep M. Guerrero, and Juan C. Vasquez. "Three-phase PLLs: A review of recent advances." IEEE Transactions on Power Electronics 32, no. 3 (2016): 1894-1907.

[142] Zhou, Jiayu, Fen Tang, Zhen Xin, Songwei Huang, Poh Chiang Loh, and Jiuchun Jiang. "Differences between continuous single-phase and online three-phase power-decoupled converters." IEEE Transactions on Power Electronics 34, no. 4 (2018): 3487-3503.

[143] Nair, Divya, et al. "Mitigation of power quality issues using DSTATCOM." 2012 International Conference on Emerging Trends in Electrical Engineering and Energy Management (ICETEEEM). IEEE, 2012.

[144] Dash, Arobinda, Durgesh Prasad Bagarty, Prakash Kumar Hota, Utkal Ranjan Muduli, Khalifa Al Hosani, and Ranjan Kumar Behera. "Performance evaluation of three-phase grid-tied SPV-DSTATCOM with DC-offset compensation under dynamic load condition." IEEE Access 9 (2021): 161395-161406.

[145] Yang, Yuanxi, and Weiguang Gao. "An optimal adaptive Kalman filter." Journal of Geodesy 80 (2006): 177-183.

[146] Sinopoli, Bruno, Luca Schenato, Massimo Franceschetti, Kameshwar Poolla, Michael I. Jordan, and Shankar S. Sastry. "Kalman filtering with intermittent observations." IEEE transactions on Automatic Control 49, no. 9 (2004): 1453-1464.

[147] Fujii, Keisuke. "Extended kalman filter." Refernce Manual 14 (2013): 41.

[148] Shah, Priyank, Ikhlaq Hussain, and Bhim Singh. "Fuzzy logic based FOGI-FLL algorithm for optimal operation of single-stage three-phase grid interfaced multifunctional SECS." IEEE Transactions on Industrial Informatics 14, no. 8 (2017): 3334-3346.

[149] Badoni, Manoj, Alka Singh, and Bhim Singh. "Power quality enhancement using euclidean direction search based control technique." IEEE Transactions on Industrial Electronics 67, no. 3 (2019): 2231-2240.

[150] Chittora, Prakash, Alka Singh, and Madhusudan Singh. "Chebyshev functional expansion based artificial neural network controller for shunt compensation." IEEE transactions on industrial informatics 14, no. 9 (2018): 3792-3800.

[151] Chen, Lin, Ivor W. Tsang, and Dong Xu. "Laplacian embedded regression for scalable manifold regularization." IEEE transactions on neural networks and learning systems 23, no. 6 (2012): 902-915.

[152] Mukundan, Nirmal, Yashi Singh, Syed Bilal Qaiser Naqvi, Bhim Singh, and Jayaprakash Pychadathil. "Multi-objective solar power conversion system with MGI control for grid integration at adverse operating conditions." IEEE Transactions on Sustainable Energy 11, no. 4 (2020): 2901-2910.

[153] Singh, Bhim, Chinmay Jain, and Sagar Goel. "ILST control algorithm of single-stage dual purpose grid connected solar PV system." IEEE Transactions on Power Electronics 29, no. 10 (2013): 5347-5357.

[154] Eckhardt, Klaus. "How to construct recursive digital filters for baseflow separation." Hydrological Processes: An International Journal 19, no. 2 (2005): 507-515.

[155] Chaudhary, Priyanka, and M. Rizwan. "QNBP NN-based I cos ϕ algorithm for PV systems integrated with LV/MV grid." Soft Computing 25, no. 4 (2021): 2599-2614.

[156] Jain, Vandana, Ikhlaq Hussain, and Bhim Singh. "A HTF-based higher-order adaptive control of single-stage grid-interfaced PV system." IEEE Transactions on Industry Applications 55, no. 2 (2018): 1873-1881.

[157] Garcia, Carlos E., David M. Prett, and Manfred Morari. "Model predictive control: Theory and practice—A survey." Automatica 25, no. 3 (1989): 335-348.

[158] Grimm, Gene, Michael J. Messina, Sezai Emre Tuna, and Andrew R. Teel. "Model predictive control: for want of a local control Lyapunov function, all is not lost." IEEE Transactions on Automatic Control 50, no. 5 (2005): 546-558.

[159] Nagulu, Shaik, T. A. Rameshkumar, and Jonnala Rohith Balaji. "Hybrid Naïve Back Propagation Based iCOSϕ Algorithm for Enriching the Grid Performance with Photovoltaics/Battery/Ultracapacitor/Fuel Cell." Electric Power Components and Systems (2023): 1-16.

[160] Arya, Sabha Raj, Bhim Singh, Ambrish Chandra, and Kamal Al-Haddad. "Learning-based anti-Hebbian algorithm for control of distribution static compensator." IEEE Transactions on Industrial Electronics 61, no. 11 (2014): 6004-6012.

[161] Badoni, Manoj, Alka Singh, and Bhim Singh. "Variable forgetting factor recursive least square control algorithm for DSTATCOM." IEEE Transactions on Power Delivery 30, no. 5 (2015): 2353-2361.

[162] Kesharvani, Sachin Kumar, Alka Singh, and Manoj Badoni. "Conductance based fryze algorithm for improving power quality for non-linear loads." In 2014 International Conference on Signal Propagation and Computer Technology (ICSPCT 2014), pp. 703-708. IEEE, 2014.

[163] Singh, Amresh Kumar, Ikhlaq Hussain, and Bhim Singh. "Double-stage three-phase grid-integrated solar PV system with fast zero attracting normalized least mean fourth based adaptive control." IEEE Transactions on Industrial Electronics 65, no. 5 (2017): 3921-3931.

[164] Samuel, Omaji, Nadeem Javaid, Sheeraz Aslam, and Muhammad Hassan Rahim. "JAYA optimization based energy management controller for smart grid: JAYA optimization based energy management controller." In 2018 International Conference on Computing, Mathematics and Engineering Technologies (iCoMET), pp. 1-8. IEEE, 2018.

[165] Kumar, Nishant, Bhim Singh, Bijaya Ketan Panigrahi, and Lie Xu. "Leaky-least-logarithmic-absolute-difference-based control algorithm and learning-based InC MPPT technique for grid-integrated PV system." IEEE Transactions on Industrial Electronics 66, no. 11 (2019): 9003-9012.

[166] Chittora, P., Badoni, M., Singh, A., Singh, M., & Bagla, V. (2024, April). Multi-Functional Capabilities of Self Tuned Filter in Three Phase Four Wire Polluted Grid Distribution System. In 2024 IEEE Third International Conference on Power Electronics, Intelligent Control and Energy Systems (ICPEICES) (pp. 672-677). IEEE.

[167] Badoni, M., Singh, A., Singh, A. K., Saxena, H., & Kumar, R. (2021). Grid tied solar PV system with power quality enhancement using adaptive generalized maximum Versoria criterion. CSEE Journal of Power and Energy Systems, 9(2), 722-732.

[168] Peerzadah, Ehsanul Haque, Rehana Perveen, and Abdul Hamid Bhat. "Power quality improvement of utility-distribution system using reduced-switch DSTATCOM in grid-tied solar-PV system based on modified SRF strategy." International Journal of Emerging Electric Power Systems 0 (2023).

[169] Singh, Bhim, Maulik Kandpal, and Ikhlaq Hussain. "Control of grid tied smart PV-DSTATCOM system using an adaptive technique." IEEE transactions on smart grid 9, no. 5 (2016): 3986-3993.

[170] Govil, Vinamra Kumar, Kuldeep Sahay, and S. M. Tripathi. "Enhancing power quality through DSTATCOM: a comprehensive review and real-time simulation insights." Electrical Engineering (2024): 1-30.

[171] Bagheri, Mehdi, Venera Nurmanova, Oveis Abedinia, and Mohammad Salay Naderi. "Enhancing power quality in microgrids with a new online control strategy for DSTATCOM using reinforcement learning algorithm." IEEE access 6 (2018): 38986-38996.

[172] Chenchireddy, Kalagotla, V. Kumar, Khammampati R. Sreejyothi, and P. Tejaswi. "A review on D-STATCOM control techniques for power quality improvement in distribution." In 2021 5th International conference on electronics, communication and aerospace technology (ICECA), pp. 201-208. IEEE, 2021.

[173] Qutaina, Wafa IS. Modeling and Control of SAPF in MV Applications. Diss. Birzeit University, 2019.

[174] Behera, Rashmi Rekha, Ashish Ranjan Dash, Satyasis Mishra, Anup Kumar Panda, and Demissie Jobir Gelmecha. "Implementation of a hybrid neural network control technique to a cascaded MLI based SAPF." Scientific Reports 14, no. 1 (2024): 8614.

[175] Ray, Soumyadeep, Nitin Gupta, and R. A. Gupta. "Power quality improvement using multilevel inverter-based active filter for medium-voltage high-power distribution system: a comprehensive review." International Journal of Power Electronics 14, no. 1 (2021): 1-36.

[176] Chokkalingham, Bharatiraja, Sanjeevikumar Padmanaban, and Frede Blaabjerg. "Investigation and comparative analysis of advanced PWM techniques for three-phase three-level NPC-MLI drives." Electric Power Components and Systems 46, no. 3 (2018): 258-269.

[177] Ahmed, Rokan Ali, Enas Dawood Hassan, and Adham Hadi Saleh. "A new flying capacitor multilevel converter topology with reduction of power electronic components." International Journal of Power Electronics and Drive Systems (IJPEDS) 14, no. 2 (2023): 1011-1023.

[178] Sarwar, Mohammad Irfan, Adil Sarwar, Shoeb Azam Farooqui, Mohd Tariq, Mohammad Fahad, Abdul R. Beig, and Basem Alamri. "A hybrid nearest level combined with PWM control strategy: analysis and implementation on cascaded H-bridge multilevel inverter and its fault tolerant topology." IEEE Access 9 (2021): 44266-44282.

[179] Nabae, Akira, Isao Takahashi, and Hirofumi Akagi. "A new neutral-point-clamped PWM inverter." IEEE Transactions on industry applications 5 (1981): 518-523.

[180] Meynard, T. A., and H. Foch. "Multi-level choppers for high voltage applications." EPE journal 2, no. 1 (1992): 45-50.

[181] Maheshkumar, N., V. Maheskumar, and M. Divya. "The new topology in flying capacitor multilevel inverter." In 2013 International Conference on Computer Communication and Informatics, pp. 1-6. IEEE, 2013.

[182] Baker, Richard H., and Lawrence H. Bannister. "Electric power converter." U.S. Patent 3,867,643, issued February 18, 1975.

[183] Kala, Peeyush, and Sudha Arora. "A comprehensive study of classical and hybrid multilevel inverter topologies for renewable energy applications." Renewable and Sustainable Energy Reviews 76 (2017): 905-931.

[184] Sivapriya, A., and N. Kalaiarasi. "A Review on Cascaded H-Bridge and Modular Multilevel Converter: Topologies, Modulation Technique and Comparative Analysis." Advanced Power Electronics Converters for Future Renewable Energy Systems (2023): 195-222.

[185] Ray, Soumyadeep, Nitin Gupta, and Ram Avtar Gupta. "A comprehensive review on cascaded H-bridge inverter-based large-scale grid-connected photovoltaic." IETE Technical review 34, no. 5 (2017): 463-477.

[186] Elsanabary, Ahmed Ibrahim, Georgios Konstantinou, Saad Mekhilef, Christopher David Townsend, Mehdi Seyedmahmoudian, and Alex Stojcevski. "Medium voltage large-scale grid-connected photovoltaic systems using cascaded H-bridge and modular multilevel converters: A review." IEEE Access 8 (2020): 223686-223699.

[187] Barth, Christopher B., Pourya Assem, Thomas Foulkes, Won Ho Chung, Tomas Modeer, Yutian Lei, and Robert CN Pilawa-Podgurski. "Design and control of a GaN-based, 13-level, flying capacitor multilevel inverter." IEEE Journal of Emerging and Selected Topics in Power Electronics 8, no. 3 (2019): 2179-2191.

[188] Rahimi, Tohid, Mehdi Fallah, Ehsan Pashajavid, Josep Pou, Ali Arefi, and Ka Hong Loo. "Single-phase 15-level inverters for uninterruptible power supply applications: fault-tolerant strategies." IEEE transactions on consumer electronics 69, no. 4 (2023): 1055-1067.

[189] Anu, P., R. Divya, and Manjula G. Nair. "STATCOM based controller for a three phase system feeding single phase loads." In 2015 International Conference on Technological Advancements in Power and Energy (TAP Energy), pp. 333-338. IEEE, 2015.

[190] Bhargav, Allu, and Alka Singh. "Performance analysis of SLMS based control for PV-STATCOM using a CHB-MLI." International Journal of Electronics 108, no. 10 (2021): 1710-1732.

[191] Sudiharto, Indhana, and Ony Asrarul Qudsi. "Application of D-STATCOM to reduce unbalanced load using synchronous reference frame theory." In 2020 10th Electrical Power, Electronics, Communications, Controls and Informatics Seminar (EECCIS), pp. 65-70. IEEE, 2020.

[192] Kumar, Pradeep, Asheesh K. Singh, and Naresh K. Kummari. "pq theory based modified control algorithm for load compensating using DSTATCOM." In 2014 16th International Conference on Harmonics and Quality of Power (ICHQP), pp. 591-595. IEEE, 2014.

[193] Yuvaraj, T., D. Lakshmi, S. Sivarajeswari, R. Essaki Raj, and D. Buvana. "Application of Salp Swarm Algorithm for optimal placement of DSTATCOM in the radial distribution networks." In AIP Conference Proceedings, vol. 3044, no. 1. AIP Publishing, 2024.

[194] Srikakolapu, Jayadeep, Sabha Raj Arya, and Rakesh Maurya. "Distribution static compensator using an adaptive observer based control algorithm with salp swarm

optimization algorithm." CPSS Transactions on Power Electronics and Applications 6, no. 1 (2021): 52-62.

[195] Dash, Arobinda, Utkal Ranjan Muduli, Khaled Al Jaafari, Khalifa Al Hosani, Atif Iqbal, and Ranjan Kumar Behera. "Harmonic mitigation and dc offset rejection for grid-tied dstatcom with cesogi-wpf control." In 2022 3rd International Conference on Smart Grid and Renewable Energy (SGRE), pp. 1-6. IEEE, 2022.

[196] Myneni, Hareesh, and Ganjikunta Siva Kumar. "Simple algorithm for current and voltage control of LCL DSTATCOM for power quality improvement." IET Generation, Transmission & Distribution 13, no. 3 (2019): 423-434.

[197] Sah, Pranjali, and B. K. Singh. "Power quality improvement using distribution static synchronous compensator." Computers and Electrical Engineering 106 (2023): 108599.

[198] Rai, Kanchan Bala, Narendra Kumar, and Alka Singh. "Three-phase Grid Connected Shunt Active Power Filter based on Adaptive q-LMF Control Technique." IEEE Transactions on Power Electronics (2024).

[199] Dash, Arobinda, Utkal Ranjan Muduli, Surya Prakash, Khalifa Al Hosani, Sandhya Rani Gongada, and Ranjan Kumar Behera. "Modified proportionate affine projection algorithm based adaptive dstatcom control with increased convergence speed." IEEE Access 10 (2022): 43081-43092.

[200] NarasimhaRaju, V. S. N., M. Premalatha, S. Pragaspathy, NSD Prakash Korlepara, and M. Mathan Kumar. "Implementation of Instantaneous Symmetrical Component Theory based Hysteresis Controller for DSTATCOM." In 2021 International Conference on Advancements in Electrical, Electronics, Communication, Computing and Automation (ICAECA), pp. 1-8. IEEE, 2021.

[201] Karthik, Markala, Venkata Ramana Naik N, and Anup Kumar Panda. "A variable step size robust normalized least mean absolute third-based control scheme for a grid-tied multifunctional photovoltaic system." International Journal of Circuit Theory and Applications 51, no. 10 (2023): 4817-4838.

[202] Bansal, Praveen, and Alka Singh. "Nonlinear adaptive normalized least mean absolute third algorithm for the control of five-level distribution static compensator." International Journal of Circuit Theory and Applications 49, no. 9 (2021): 2840-2864.

[203] Badoni, Manoj, Alka Singh, and Bhim Singh. "Implementation of immune feedback control algorithm for distribution static compensator." IEEE Transactions on Industry Applications 55, no. 1 (2018): 918-927.

[204] Badoni, Manoj, Alka Singh, and Bhim Singh. "DSP based implementation of an immune feedback algorithm for control of shunt compensator." In 2016 IEEE 6th International Conference on Power Systems (ICPS), pp. 1-6. IEEE, 2016.

[205] Dash, Arobinda, Durgesh Prasad Bagarty, Prakash Kumar Hota, Utkal Ranjan Muduli, Khalifa Al Hosani, and Ranjan Kumar Behera. "Performance evaluation of three-phase grid-tied SPV-DSTATCOM with DC-offset compensation under dynamic load condition." IEEE Access 9 (2021): 161395-161406.

[206] Bommana, Babji, JSV Siva Kumar, Ramakrishna SS Nuvvula, Polamarasetty P. Kumar, Baseem Khan, Suresh Muthusamy, and Ravikiran Inapakurthi. "A comprehensive examination of the protocols, technologies, and safety requirements for electric vehicle charging infrastructure." Journal of Advanced Transportation 2023, no. 1 (2023): 7500151.

[207] Mateen, Suwaiba, Mohmmad Amir, Ahteshamul Haque, and Farhad Ilahi Bakhsh. "Ultra-fast charging of electric vehicles: A review of power electronics converter, grid stability and optimal battery consideration in multi-energy systems." Sustainable Energy, Grids and Networks (2023): 101112.

[208] Akhtar, Mohammad Faisal, Siti Rohani S. Raihan, Nasrudin Abd Rahim, Mohammad Nishat Akhtar, and Elmi Abu Bakar. "Recent developments in DC-DC converter topologies for light electric vehicle charging: a critical review." Applied Sciences 13, no. 3 (2023): 1676.

[209] Hassan, Syeda Anam, Inayatul Haq, Ejaz Ahmad Khattak, Abdelmohsen A. Nassani, Khalid Zaman, and Mohamed Haffar. "Transitioning from gridlock to sustainability: advancing transport strategies for eco-friendly solutions in high-income countries." Environmental Science and Pollution Research (2024): 1-24.

[210] Dik, Abdullah, Siddig Omer, and Rabah Boukhanouf. "Electric vehicles: V2G for rapid, safe, and green EV penetration." Energies 15, no. 3 (2022): 803.

[211] Meckling, Jonas, and Jonas Nahm. "The politics of technology bans: Industrial policy competition and green goals for the auto industry." Energy policy 126 (2019): 470-479.

[212] Zhang, Xingping, Jian Xie, Rao Rao, and Yanni Liang. "Policy incentives for the adoption of electric vehicles across countries." Sustainability 6, no. 11 (2014): 8056-8078.

[213] Rietmann, Nele, Beatrice Hügler, and Theo Lieven. "Forecasting the trajectory of electric vehicle sales and the consequences for worldwide CO2 emissions." Journal of cleaner production 261 (2020): 121038.

[214] Ali, Ziad M., Martin Ćalasan, Francisco Jurado, and Shady HE Abdel Aleem. "Complexities of Power Quality and Harmonic-Induced Overheating in Modern Power Grids Studies: Challenges and Solutions." IEEE Access (2024).

[215] Kumar, Dinesh, Firuz Zare, and Arindam Ghosh. "DC microgrid technology: system architectures, AC grid interfaces, grounding schemes, power quality, communication networks, applications, and standardizations aspects." Ieee Access 5 (2017): 12230-12256.

[216] Habib, Salman, Muhammad Mansoor Khan, Farukh Abbas, Lei Sang, Muhammad Umair Shahid, and Houjun Tang. "A comprehensive study of implemented international standards, technical challenges, impacts and prospects for electric vehicles." IEEe Access 6 (2018): 13866-13890.

[217] Acharige, Sithara SG, Md Enamul Haque, Mohammad Taufiqul Arif, Nasser Hosseinzadeh, Kazi N. Hasan, and Aman Maung Than Oo. "Review of electric vehicle charging technologies, standards, architectures, and converter configurations." IEEE Access 11 (2023): 41218-41255.

[218] Shahed, Md Tanvir, and ABM Harun-ur Rashid. "Battery charging technologies and standards for electric vehicles: A state-of-the-art review, challenges, and future research prospects." Energy Reports 11 (2024): 5978-5998.

[219] Dini, Pierpaolo, Sergio Saponara, and Antonio Colicelli. "Overview on battery charging systems for electric vehicles." Electronics 12, no. 20 (2023): 4295.

[220] Nasr Esfahani, Fatemeh, Ahmed Darwish, Xiandong Ma, and Peter Twigg. "Non-Integrated and Integrated On-Board Battery Chargers (iOBCs) for Electric Vehicles (EVs): A Critical Review." Energies 17, no. 10 (2024): 2285.

[221] Panchanathan, Suresh, Pradeep Vishnuram, Narayanamoorthi Rajamanickam, Mohit Bajaj, Vojtech Blazek, Lukas Prokop, and Stanislav Misak. "A comprehensive review of the bidirectional converter topologies for the vehicle-to-grid system." Energies 16, no. 5 (2023): 2503.

[222] Arya, Sabha Raj, Mittal M. Patel, Sayed Javed Alam, Jayadeep Srikakolapu, and Ashutosh K. Giri. "Phase lock loop–based algorithms for DSTATCOM to mitigate load created power quality problems." International transactions on electrical energy systems 30, no. 1 (2020): e12161.

[223] Bansal, Pranshu, Prashant Bharati, Sambhav Jeswani, and Ankita Arora. "Power Quality Improvement using Hopfield Neural Network in Grid Distribution System." In 2023 International Conference on Power, Instrumentation, Energy and Control (PIECON), pp. 1-6. IEEE, 2023.

[224] Arora, Ankita, and Alka Singh. "Fractional delay Newton structure for Lagrangian interpolation in PV integrated grid connected system." International Journal of Circuit Theory and Applications 52, no. 3 (2024): 1095-1115.

[225] Liu, Zhan, Bin Li, Yang Yang, Peiyuan Li, and Guifeng Wang. "Active power filter based on DS-SDFT harmonic detection method with MPC." Electrical Engineering (2024): 1-12.

[226] Rai, Kanchan Bala, Narendra Kumar, and Alka Singh. "Design and analysis of the shunt active power filter with the ε-NSRLMMN adaptive algorithm for power quality improvement in the distribution system." IETE Journal of Research 70, no. 2 (2024): 2105-2119.

[227] Pandey, Amarendra, and Alka Singh. "Laguerre polynomial function-based inverter control with low-voltage ride-through capabilities." International Journal of Circuit Theory and Applications 51, no. 2 (2023): 764-786.

[228] Sakipour, Ramin, and Hamdi Abdi. "Voltage stability improvement of wind farms by self-correcting static volt-ampere reactive compensator and energy storage." International Journal of Electrical Power & Energy Systems 140 (2022): 108082.

[229] Srivastava, Kalash, Rakesh Maurya, and Shailendra Kumar. "A STC-DAB converter for PV–EV battery-based hybrid system with a unified power management scheme in a grid-integrated and islanded condition." Electrical Engineering (2024): 1-16.

[230] Naseem, Hamid, and Jul-Ki Seok. "Reactive Power Controller for Single Phase Dual Active Bridge DC-DC Converters." IEEE Access (2023).

[231] Chilakalapudi, Ganesh, and Amritesh Kumar. "Optimal reactive power control for dual-active-bridge converter using improved dual-phase-shift modulation strategy for electric vehicle application." International Journal of Circuit Theory and Applications 51, no. 3 (2023): 1204-1223.

[232] Feng, Yangyang, Jiatao Yang, Rui Li, Mingxia Xu, Yiming Wang, and Po Xu. "Modulation strategy of a DAB-type isolated DC-AC converter with reactive power support capabilities." In IET Conference Proceedings CP880, vol. 2024, no. 6, pp. 878-882. Stevenage, UK: The Institution of Engineering and Technology, 2024.

[233] Wang, Lu, Zian Qin, Tim Slangen, Pavol Bauer, and Thijs Van Wijk. "Grid impact of electric vehicle fast charging stations: Trends, standards, issues and mitigation measures-an overview." IEEE Open Journal of Power Electronics 2 (2021): 56-74.

[234] Oswald, Niall, Philip Anthony, Neville McNeill, and Bernard H. Stark. "An experimental investigation of the tradeoff between switching losses and EMI generation with hard-switched all-Si, Si-SiC, and all-SiC device combinations." IEEE Transactions on Power Electronics 29, no. 5 (2013): 2393-2407.

[235] Hartmann, Michael, Hans Ertl, and Johann W. Kolar. "EMI filter design for a 1 MHz, 10 kW three-phase/level PWM rectifier." IEEE Transactions on Power Electronics 26, no. 4 (2010): 1192-1204.

[236] Mariscotti, Andrea. "Harmonic and supraharmonic emissions of plug-in electric vehicle chargers." Smart Cities 5, no. 2 (2022): 496-521.

[237] Kumar, Anup, Mohan V. Aware, B. S. Umre, and Manoj A. Waghmare. "Single-Phase Grid-Connected Fault Tolerant Bi-directional Power Flow Converter for Electric Vehicle Charging System." In 2023 International Conference on Future Energy Solutions (FES), pp. 1-5. IEEE, 2023.

[238] Barah, Sushree Smrutimayee, and Sasmita Behera. "An optimize configuration of H-bridge multilevel inverter." In 2021 1st International Conference on Power Electronics and Energy (ICPEE), pp. 1-4. IEEE, 2021.

[239] Kumar, Abhishek, Mohan V. Aware, and Anup Kumar. "Single-Phase Grid-Connected High DC-Gain Flyback Converter for EV Battery Charging." In 2022 IEEE 19th India Council International Conference (INDICON), pp. 1-6. IEEE, 2022.

[240] Li, Shenghu. "Power flow modeling to doubly-fed induction generators (DFIGs) under power regulation." IEEE transactions on power systems 28, no. 3 (2013): 3292-3301.

[241] Carvalho, Pedro MS, Pedro F. Correia, and Luís AFM Ferreira. "Distributed reactive power generation control for voltage rise mitigation in distribution networks." IEEE transactions on Power Systems 23, no. 2 (2008): 766-772.

[242] Senthil Kumar, S., C. Srinivasan, and P. Sridhar. "Enhancing grid stability and efficiency in buildings through forecasting and intelligent energy management of distributed energy resources." Electrical Engineering (2024): 1-18.

[243] Patel, Manish D., and Rajendra R. Aparnathi. "Simulation Design of Three Phase Grid Integrated EV Charging Station with Renewables." Journal of Electrical Systems 20, no. 7s (2024): 1625-1637.

[244] Jain, Vandana, Seema Kewat, and Bhim Singh. "Three phase grid connected PV based EV charging station with capability of compensation of reactive power." IEEE Transactions on Industry Applications 59, no. 1 (2022): 367-376.

[245] Ullah, Wahab. "Novel Bidirectional Charging/Discharging Schemes in PV Supported EV-Battery Charging Station in a Hybrid AC/DC Microgrid." (2023).

[246] Imam, Amir A., and Yusuf A. Al-Turki. "Techno-economic feasibility assessment of grid-connected PV systems for residential buildings in Saudi Arabia—A case study." Sustainability 12, no. 1 (2019): 262.

[247] Suvvala, Jayaprakash, C. Dhananjayulu, Hossam Kotb, and Ali Elrashidi. "Integration of renewable energy sources using multiport converters for ultra-fast charging stations for electric vehicles: An overview." Heliyon (2024).

[248] Szinai, Julia K., Colin JR Sheppard, Nikit Abhyankar, and Anand R. Gopal. "Reduced grid operating costs and renewable energy curtailment with electric vehicle charge management." Energy Policy 136 (2020): 111051.

[249] Dimitriadou, Konstantina, Nick Rigogiannis, Symeon Fountoukidis, Faidra Kotarela, Anastasios Kyritsis, and Nick Papanikolaou. "Current trends in electric vehicle charging infrastructure; opportunities and challenges in wireless charging integration." Energies 16, no. 4 (2023): 2057.

[250] Tyagi, Shalvi, and Bhim Singh. "Solar Photovoltaic–Small Hydro-Based Charging: Infrastructure for a Three-Phase, Four-Wire Distribution Network." IEEE Industry Applications Magazine (2024).

[251] Ullah, Zahid, Iqrar Hussain, Assia Mahrouch, Kaleem Ullah, Rafiq Asghar, Muhammad Talha Ejaz, Muhammad Minam Aziz, and Syed Fahad Murtaza Naqvi. "A survey on enhancing grid flexibility through bidirectional interactive electric vehicle operations." Energy Reports 11 (2024): 5149-5162.

[252] Bhaskar, Mahajan Sagar, Nikita Gupta, Sanjeevikumar Padmanaban, Jens Bo Holm-Nielsen, and Umashankar Subramaniam, eds. Power electronics for green energy conversion. John Wiley & Sons, 2022.

[253] Wang, Rui, Chunyue Song, Wenjun Huang, and Jun Zhao. "Improvement of battery pack efficiency and battery equalization based on the extremum seeking control." International Journal of Electrical Power & Energy Systems 137 (2022): 107829.

[254] Zhou, Kai, Huayu Yang, Yuxin Zhang, Yuhe Che, Yiwen Huang, and Xiaohan Li. "A review of the latest research on the topological structure and control strategies of on-board charging systems for electric vehicles." Journal of Energy Storage 97 (2024): 112820.

[255] Lenka, Rajesh Kumar, Anup Kumar Panda, Ashish Ranjan Dash, Laxmidhar Senapati, and Nishit Tiwary. "A unified control of grid-interactive off-board EV battery charger with

improved power quality." IEEE Transactions on Transportation Electrification 9, no. 1 (2022): 920-933.

[256] Majid Gulzar, Muhammad, Huma Tehreem, and Muhammad Khalid. "Modified Finite Time Sliding Mode Controller for Automatic Voltage Regulation under Fast-Changing Atmospheric Conditions in Grid-Connected Solar Energy Systems." International Journal of Intelligent Systems 2023, no. 1 (2023): 8863346.

[257] Heydari-doostabad, Hamed, and Terence O'Donnell. "A wide-range high-voltage-gain bidirectional DC–DC converter for V2G and G2V hybrid EV charger." IEEE Transactions on Industrial Electronics 69, no. 5 (2021): 4718-4729.

[258] Mittal, Sudhanshu, Alka Singh, and Prakash Chittora. "Design and development of Reduced Switch Five Level Inverter for interfacing renewable energy sources and EV charger." Electrical Engineering (2024): 1-15.

[259] Sami, I., Z. Ullah, K. Salman, I. Hussain, S. M. Ali, B. Khan, C. A. Mehmood, and U. Farid. "A bidirectional interactive electric vehicles operation modes: Vehicle-to-grid (V2G) and grid-to-vehicle (G2V) variations within smart grid." In 2019 international conference on engineering and emerging technologies (ICEET), pp. 1-6. IEEE, 2019.

[260] Verma, Anjeet, Bhim Singh, Ambrish Chandra, and Kamal Al-Haddad. "An implementation of solar PV array based multifunctional EV charger." IEEE Transactions on Industry Applications 56, no. 4 (2020): 4166-4178.

[261] Vega-Fuentes, Eduardo, and Mouloud Denai. "Enhanced electric vehicle integration in the UK low-voltage networks with distributed phase shifting control." IEEE Access 7 (2019): 46796-46807.

[262] Muttaqi, Kashem M., Obaidur Rahman, Danny Sutanto, MS Hossain Lipu, Maher GM Abdolrasol, and M. A. Hannan. "High-frequency ripple injection signals for the effective utilization of residential EV storage in future power grids with rooftop PV system." IEEE Transactions on Industry Applications 58, no. 5 (2022): 6655-6665.

[263] Jain, Vandana, and Bhim Singh. "A grid connected PV array and battery energy storage interfaced EV charging station." IEEE Transactions on Transportation Electrification 9, no. 3 (2023): 3723-3730.

[264] Boström, Tobias, Bilal Babar, Jonas Berg Hansen, and Clara Good. "The pure PV-EV energy system–A conceptual study of a nationwide energy system based solely on photovoltaics and electric vehicles." Smart Energy 1 (2021): 100001.

[265] Bhatti, Abdul Rauf, Zainal Salam, Mohd Junaidi Bin Abdul Aziz, and Kong Pui Yee. "A critical review of electric vehicle charging using solar photovoltaic." International Journal of Energy Research 40, no. 4 (2016): 439-461.

[266] Mahajan, Vasundhara, Pramod Agarwal, and Hari Om Gupta. "Implementation of high-voltage multilevel harmonic filter based on rotated carrier modulation and artificial intelligence-based controllers." Arabian Journal for Science and Engineering 39 (2014): 7127-7143.

[267] Garg, Grisham, Dhruv Talan, Gaurav Yadav, and Mukhtiar Singh. "Implementing ML and DL Based Controllers for Improving Efficiency in EV Charging Application." In 2024 IEEE Third International Conference on Power Electronics, Intelligent Control and Energy Systems (ICPEICES), pp. 235-240. IEEE, 2024.

[268] Dai, Haifeng, Bo Jiang, Xiaosong Hu, Xianke Lin, Xuezhe Wei, and Michael Pecht. "Advanced battery management strategies for a sustainable energy future: Multilayer design concepts and research trends." Renewable and Sustainable Energy Reviews 138 (2021): 110480.

[269] Yadav, Gaurav, and Mukhtiar Singh. "Real-time investigation of grid-interactive EV charger with two-stage bidirectional converter under wide voltage range scenarios." Electrical Engineering (2024): 1-13.

[270] Wan, Muchun, Heyang Yu, Yingning Huo, Kan Yu, Quanyuan Jiang, and Guangchao Geng. "Feasibility and Challenges for Vehicle-to-Grid in Electricity Market: A Review." Energies 17, no. 3 (2024): 679.

[271] Zhang, Chengquan, Hiroshi Kitamura, and Mika Goto. "Feasibility of vehicle-to-grid (V2G) implementation in Japan: A regional analysis of the electricity supply and demand adjustment market." Energy 311 (2024): 133317.

[272] P. Chittora, “Analysis and Control of Shunt Compensator in Distribution System”, PhD dissertation, Delhi Technological University, 2018.

[273] B. Singh, S. Dwivedi, I. Hussain, and A. K. Verma, “Grid integration of solar pv power generating system using qpll based control algorithm,” in 2014 6th IEEE Power India International Conference (PIICON), pp. 1–6, 2014.

[274] Bansal, Praveen, and Alka Singh. "Closed Loop Control Using RSAPS Algorithm for 5-Level CHB Multilevel Inverter." Journal of Control, Automation and Electrical Systems (2022): 1-14.

[275] Tsunoda, Asuka, Youhei Hinago, and Hirotaka Koizumi. "Level-and phase-shifted PWM for seven-level switched-capacitor inverter using series/parallel conversion." IEEE Transactions on Industrial Electronics 61.8 (2013): 4011-4021.

[276] Arora A. Singh A.: ‘Design and analysis of functional link artificial neural network controller for shunt compensation’, IET Gener. Transm. Distrib., 2019, 13, (11), pp. 2280–2289.

[277] Xu X, Zheng C, Hu C, Lu Y, Wang Q. Design of Bi-directional DC-DC converter. In2016 IEEE 11th conference on industrial electronics and applications (ICIEA) 2016 Jun 5 (pp. 2283-2287). IEEE.

[278] Badoni, Manoj, et al. "Fractional-order notch filter for grid-connected solar PV system with power quality improvement." IEEE Transactions on Industrial Electronics 69.1 (2021): 429-439.

[279] Mirzaeinejad, Hossein. "Robust predictive control of wheel slip in antilock braking systems based on radial basis function neural network." Applied soft computing 70 (2018): 318-329.

[280] Khattak, Obaid Ur Rehman, and Azzedine Zerguine. "Leaky least mean fourth adaptive algorithm." IET Signal Processing 7.2 (2013): 134-145.

[281] Singh B, Singh BN, Chandra A, Al-Haddad K, Pandey A, Kothari DP. A review of single-phase improved power quality AC-DC converters. IEEE Transactions on industrial electronics. 2003 Oct 7;50(5):962-81.

[282] Mittal S, Singh A, Chittora P. EV Control in G2V and V2G modes using SOGI Controller. In2022 IEEE 3rd Global Conference for Advancement in Technology (GCAT) 2022 Oct 7 (pp. 1-6). IEEE.

[283] Arya SR, Maurya R, Srikakolapu J. DSTATCOM using model predictive control associated with LMS control. International Journal of Electronics. 2024 Feb 1;111(2):238-58.

[284] Bonneux, Niels. "Exceptional Jacobi polynomials." Journal of Approximation Theory 239 (2019): 72-112.

[285] Pandey A, Singh A. Design and analysis of Levenberg–Marquardt-based adaptive SOGI. IET Generation, Transmission & Distribution. 2020 Dec;14(26):6569-79.

[286] Bala N, Mallik SK. Control algorithm for an island microgrid under DSTATCOM using a Third Order Sinusoidal Integrator (TOSSI) to improve power quality for a local nonlinear load. Engineering Research Express. 2024 Jun 13;6(2):025354.

[287] Abd Halim, W., et al. "Review of multilevel inverter topologies and its applications." Journal of Telecommunication, Electronic and Computer Engineering (JTEC) 8.7 (2016): 51-56.

[288] Aishwarya, Venkittaraman, et al. "Review of reduced-switch multilevel inverters for electric vehicle applications." International Journal of Circuit Theory and Applications 49.9 (2021): 3053-3110.

[289] Mahato, Bidyut et al. "Generalized symmetrical/asymmetrical single-phase MLI topology." 2018 International Conference on Recent Trends in Electrical, Control and Communication (RTECC). IEEE, 2018.

List of Publications

The following are some publications in journals and conferences related to this research work.

❖ Publications in National/International Journals

[1] **S. Mittal**, A. Singh, P. Chittora, “Design and development of leaky least mean fourth control algorithm for single-phase grid-connected multilevel inverter”, International Journal of Circuit Theory and Applications, vol. 52, no. 1, pp. 328-345, year 2024. doi:10.1002/cta.3746.

[2] **S. Mittal**, A. Singh, P. Chittora, “Design and Development of Reduced Switch Five Level Inverter for Interfacing Renewable Energy Sources and EV charger”, Electrical Engineering, year 2024.

[3] **S. Mittal**, A. Singh, P. Chittora, “Power quality enhancement in single phase two level/five level converters using adaptive-RBFNN algorithm”, Electrical Engineering. 2024 May 21:1-4.

[4] **S. Mittal**, A. Singh, P. Chittora, “Rodrigues Jacobi Polynomial Based Control Technique for On Board EV Charger in Single Phase Power Distribution System,” Electrical Power System Research. (under review)

[5] **S. Mittal**, A. Singh, P. Chittora, G. Kaushik, “Implementation of Bell Polynomial Based Controller for a Novel Five Level Converter used in Single Phase EV-PV based Microgrid,” International Journal of Circuit Theory and Applications. (communicated)

❖ Publications in National/International Conferences

[1] **S. Mittal**, A. Singh and P. Chittora, "EV Control in G2V and V2G modes using SOGI Controller," 2022 IEEE 3rd Global Conference for Advancement in Technology (GCAT), Bangalore, India, 2022, pp. 1-6, doi: 10.1109/GCAT55367.2022.9972182

[2] **S. Mittal**, A. Singh and P. Chittora, " Solar PV Array Based Grid-Connected Bi-Directional EV Charger Controlled Using NARLMMN Algorithm," 2023 9th IEEE India International Conference on Power Electronics (IICPE), Murthal, India, 2024.

Appendix A

Performance Analysis of Single Phase and Three Phase Grid Connected DSTATCOM

Single phase system DSTATCOM

Simulation parameters

Supply voltage (v_s)= 110 V, load resistance and inductance (nonlinear) R=30Ω and L=100mH, DC link voltage capacitance (C_{dc}) = 1500 µF, K_p=0.1, K_i =5, $V_{dc\text{-}ref}$ = 200 V, interfacing inductor (L_c)= 3.5mH, switching frequency (f_{sw})= 20 kHz, sampling time= 50 µs.

Experimental parameters

Supply voltage (v_s)= 110 V, resistive and inductive R=120Ω and L=80mH (nonlinear load), DC link capacitance voltage (C_{dc}) = 1500 µF, K_p=0.15, K_i =5, $V_{dc\text{-}ref}$ = 200 V, interfacing inductor (L_c)= 3.5mH, switching frequency (f_{sw})= 10 kHz, sampling time= 50 µs.

Three phase system DSTATCOM

Simulation parameters

Supply voltage (v_s)= 110 V, load resistance and inductance (nonlinear) R=30Ω and L=100mH, DC link voltage capacitance (C_{dc}) = 3300 µF, K_p=0.5, K_i =2, $V_{dc\text{-}ref}$ = 200 V, interfacing inductor (L_c)= 4.8mH, switching frequency (f_{sw})= 20 kHz, sampling time= 50 µs.

Experimental parameters

Supply voltage (v_s)= 110 V, resistive and inductive R=120Ω and L=80mH (nonlinear load), DC link capacitance voltage (C_{dc}) = 4700 µF, K_p=0.08, K_i =0.1, $V_{dc\text{-}ref}$ = 200 V, interfacing inductor (L_c)= 5mH, switching frequency (f_{sw})= 10 kHz, sampling time= 50 µs.

Appendix B

Performance Analysis of Grid integrated Multilevel Inverter to Improve Power Quality

Simulation parameters

Supply voltage (v_s)= 110 V, load resistance and inductance (nonlinear) R=30Ω and L=100mH, DC link voltage capacitance (C_{dc}) = 2400 µF, K_p=0.1, K_i =5, $V_{dc\text{-}ref}$ = 200 V, interfacing inductor (L_c)= 5mH, switching frequency (f_{sw})= 20 kHz, sampling time= 50 µs.

Experimental parameters

Supply voltage (v_s)= 110 V, resistive and inductive R=120Ω and L=80mH (nonlinear load), DC link capacitance voltage (C_{dc}) = 2500 µF, K_p=0.05, K_i =2, $V_{dc\text{-}ref}$ = 200 V, interfacing inductor (L_c)= 5mH, switching frequency (f_{sw})= 5 kHz, sampling time= 50 µs.

Appendix C

Performance Analysis of Single Phase Grid Interfaced EV Charging System

Simulation parameters

Supply voltage (v_s)= 110 V, load resistance and inductance (nonlinear) R=30Ω and L=100mH, DC link voltage capacitance (C_{dc}) = 1500 µF, $V_{dc\text{-}ref}$= 200 V, V_{bat}=96V, interfacing inductor (L_c)= 5mH, sampling time= 50 µs, D=0.6, K_p=0.5, K_i =10, switching frequency (f_{sw})= 20 kHz (for AC-DC Converter), K_p=0.5, K_i =5, switching frequency (f_{sw})= 5 kHz (for DC- DC Converter)

Experimental parameters

Supply voltage (v_s)= 40 V, resistive and inductive R=120Ω and L=80mH (nonlinear load), DC link capacitance voltage (C_{dc}) = 1500 µF, $V_{dc\text{-}ref}$= 80 V, V_{bat}=48V, interfacing inductor (L_c)= 5mH, sampling time= 50 µs, D=0.6, K_p=0.08, K_i =0.15, switching frequency (f_{sw})= 10 kHz (for AC- DC Converter), K_p=0.1, K_i =5, switching frequency (f_{sw})= 5 kHz (for DC- DC Converter)

Appendix D

Performance Analysis of Three Phase Grid interfaced Solar PV and EV Charging System

Simulation parameters

Supply voltage (v_{sa})= 230 V, load resistance and inductance (nonlinear) R=50Ω and L=100mH, DC link voltage capacitance (C_{dc}) = 1640 µF, $V_{dc\text{-}ref}$= 400 V, interfacing inductor (L_{ca})= 3.4mH, switching frequency (f_{sw})= 10 kHz, sampling time= 50 µs, P_{pv}=2kW, K_p=0.1, K_i =10, switching frequency (f_{sw})= 20 kHz (for AC- DC Converter), K_p=0.1, K_i =5, switching frequency (f_{sw})= 20 kHz (for DC- DC Converter), V_{bat} = 100V , I_{bat} = ±20A

Appendix E

Single Phase Grid Connected Reduced Switch Five Level Inverter (RSFLI) with Solar PV and EV Charging System

Simulation parameters

Supply voltage (v_s)= 230 V, resistive and inductive R=125Ω and L=80mH (nonlinear load), DC link capacitance voltage (C_{dc}) = 2400 µF, K_p=0.05, K_i =0.5, $V_{dc\text{-}ref}$= 400 V, interfacing inductor (L_c)= 5mH, switching frequency (f_{sw})= 10 kHz, sampling time= 50 µs, K_p=0.29, K_i =1.5, switching frequency (f_{sw})= 20 kHz (for AC- DC Converter), K_p=0.4, K_i =5, switching frequency (f_{sw})= 10 kHz (for DC- DC Converter),V_{bat} = 100V , I_{bat} = ±12A